2010-04-08

Wind Energy Conversion Systems based on DFIG Technology used as Active Filters: Steady-State and Transient Analysis

Grazia Todeschini
Worcester Polytechnic Institute

WIND ENERGY CONVERSION SYSTEMS BASED ON DFIG TECHNOLOGY USED AS ACTIVE FILTERS: STEADY STATE AND TRANSIENT ANALYSIS

Candidate

Grazia Todeschini

A Dissertation

Submitted to the Faculty

of the

WORCESTER POLYTECHNIC INSTITUTE

in partial fulfillment of the requirements for the

Degree of Doctor of Philosophy

in

Electrical and Computer Engineering

February 2010

APPROVED:

Dr. Alexander E. Emanuel, WPI, Research Advisor

Dr. Alexandar Stankovic, Northeastern University

Dr. Marc T. Thompson, WPI and Thompson Consulting Inc.

Abstract

This thesis deals with the performance of a Wind Energy Conversion System operating as a power generator and Active Filter simultaneously. As a power generator, the Wind Energy Conversion System converts wind energy into electric energy; as an Active Filter, it sinks the harmonic currents injected by Non-Linear Loads connected at the same feeder.

Three control systems are developed to ensure the described operation; a specific study regarding the compensation of the triplen harmonics is carried out; Doubly-Fed Induction Generator derating is defined; and an engineering economic analysis is performed to determine the profitability of the proposed operation.

The Wind Energy Conversion System performance as generator and Active Filter has been studied for steady-state analysis, fast transients and low transients.

It is concluded that the proposed control systems allow operating the Wind Energy Conversion System as power generator and harmonic compensator both during steady state and transient operation; the described operation causes power loss increase and voltage distortion that determine the choice of the component and require system derating.

Table of Contents

Acronyms

AF	Active Filter
AWEA	American Wind Energy Association
CB	Circuit Breaker
CM	Combined Modulation
CUF	Current Unbalance Factor
DFIG	Doubly Fed Induction Generator
EMI	Electromagnetic Interference
FERC	Federal Energy Regulatory Commission
FRT	Fault Ride Through
HVdc	High-Voltage direct current
IG	Induction Generator
IEC	International Electrotechnical Commission
LSC	Line Side Converter
LVRT	Low Voltage Ride Through
NERC	North American Electric Reliability Corporation

NLL	Non-Linear Load
PCC	Point of Common Coupling
PF	Power Factor
PI	Proportional Integral controller
PLL	Phase Locked Loop
PMSG	Permanent Magnet Synchronous Generator
PWM	Pulse Width Modulation
RSC	Rotor Side Converter
SVC	Static Voltage Compensator
THD	Total Harmonic Distortion
TF	Transfer Function
WECC	Western Electricity Coordinating Council
WECS	Wind Energy Conversion System
VCO	Voltage Controlled Oscillator
VUF	Voltage Unbalance Factor

List of Symbols

Table 1 - Representation of electric quantities in different domains

$y(t)$ or y	time varying quantity
$\overline{Y}$	phasor
Y	constant
$Y_{rms} = \sqrt{\frac{1}{T}\int_0^T y^2(t)dt}$	rms value
$Y(s) = \int_{-\infty}^{+\infty} y(t)e^{-st}dt$	Laplace transform
$\hat{Y}$	peak value
$\dot{y} = \frac{dy(t)}{dt}$	time derivative
$\overline{y} = y_d + iy_q$	space vector in the dq reference frame

Table 2 - Superscripts

M^{-1}	inverse matrix
$\overline{y}^*$	complex conjugate
M^T	transposed matrix

Table 3 - Subscripts

$+$	positive sequence
$-$	negative sequence
0	zero sequence
a,b,c	three-phase quantities
α,β	fixed reference frame coordinates
d,q	rotating reference frame coordinates
dc	direct current
g	grid
h	single harmonic
H	sum of harmonic
l	leakage
LL	line-to-line
m	mutual
$meas$	measured
n	rated or neutral
r	rotor
ref	reference
rms	root mean square
s	stator
w	wind
t	turbine

Table 4 - Symbols (Part I)

Symbol	**Unit**	**Definition**
$a = e^{j2\pi/3}$		Fortescue operator
A		Fortescue matrix
A_s	(m^2)	slot area
A_{Cu}	(m^2)	copper area
A_t	(m^2)	turbine swept area
C_p		power coefficient
c_s	(J/(Kg °C))	specific thermal capacitance
C_{th}	(J/ °C)	thermal capacitance
$\mathscr{D}$		derating factor
$\mathbb{F}$		friction factor
E_{sw}	(J/pulse)	switching energy loss
f_1	(Hz)	fundamental frequency
f_{con}	(Hz)	control signal frequency (PWM)
f_i	(Hz)	PLL input signal frequency
f_o	(Hz)	PLL output signal frequency
f'_o	(Hz)	VCO free running frequency
$f_r = \mathbb{S}\ f_1$	(Hz)	rotor voltage frequency
f_{tri}	(Hz)	modulating signal frequency (PWM)
G	(s)	inertia constant
h		harmonic order
H(s)		transfer function
k		skin effect coefficient
J	(A/m^2)	current density

Table 5 - Symbols (Part II)

Symbol	Unit	Definition
l	(m)	airgap width
ℓ	(km)	line length
L_{lr}	(H)	rotor leakage inductance
L_{ls}	(H)	stator leakage inductance
$L_r = L_{lr} + M$	(H)	rotor self inductance
$L_s = L_{ls} + M$	(H)	stator self inductance
M	(H)	mutual inductance
m		number of layers
m_a		amplitude modulation index (PWM)
m_f		frequency modulation index (PWM)
$\mathbb{N}$		set of integer numbers
N_{gb}		gearbox ratio
N_s		number of windings in each stator slot
$N_{sr} = N_s/N_r$		stator to rotor turns ratio
N_r		number of windings in each rotor slot
n_b		number of blades
$\mathbb{P}$		number of pole pairs
P_{airgap}	(W)	airgap power
P_H	(W)	total harmonic power
P_m	(W)	mechanical power
P_s	(W)	stator active power
P_r	(W)	rotor active power
P_n	(W)	rated active power

Table 6 - Symbols (Part III)

Symbol	**Unit**	**Definition**
$P_{n,\mathrm{RSC}}$	(W)	rotor side converter rated active power
$P_{n,\mathrm{LSC}}$	(W)	line side converter rated active power
$P_t = P_s + P_r$	(W)	DFIG total power
$p = v_d\ i_d + v_q\ i_q$	(W)	instantaneous active power
P_w	(W)	kinetic power in moving air
$\mathbb{R}$		set of real numbers
R_{on}	(Ω)	switch 'on-resistance'
$\mathbb{Q}$		set of rational numbers
$q = v_d\ i_q - v_q\ i_d$	(VA)	instantaneous imaginary power
R	(m)	blade radius
R_{th}	(°C/W)	thermal resistance
$\overline{s} = p + jq$	(VA)	instantaneous apparent power
$\mathbb{S} = \dfrac{\omega_1 - \omega_m}{\omega_1} = \dfrac{\dot{\vartheta}_s - \dot{\vartheta}_r}{\dot{\vartheta}_s}$	(p.u.)	slip (fundamental)
$\mathbb{S}_h = \dfrac{h\ \omega_1 - \omega_m}{h\ \omega_1}$	(p.u.)	slip (harmonic frequency)
s		Laplace operator
T	(°C)	temperature
T_a	(°C)	ambient temperature
T_e	(Nm)	electromagnetic torque
v_u	(m/s)	upstream wind speed
X	(Ω)	reactance
W_μ	(J)	energy stored in the magnetic field
Z	(Ω)	impedance

Table 7 - Greek letters (Part I)

Symbol	**Unit**	**Definition**
α		non-linear load current modulator or scale parameter (Figure 7.2)
β	(rad)	blade pitch angle or scale parameter (Figure 7.2)
ε	(deg)	phase shift between three-phase voltages
Γ		tip speed ratio
γ	(kg/m^3)	density
γ_a	(kg/m^3)	air density
γ_r	(rad)	remainder of the division $\vartheta_m/2\pi$
ΔI, ΔV		difference between the reference (current, voltage) value and the measured (current, voltage) value
ΔP_s	(W)	stator winding loss
ΔP_r	(W)	rotor winding loss
Δt	(s)	voltage dip duration
ΔT	(°C)	temperature increase
δ	(rad)	phase shift of $\overline{V}_r$ with respect to $\overline{V}_s$ in the equivalent DFIG circuit
δ_h	(rad)	phase shift of h=order harmonic current

Table 8 - Greek letters (Part II)

Symbol	**Unit**	**Definition**
ϑ_a	(rad)	angle between stator phase a_s and d-axis in the generic reference frame (Figure B.6)
ϑ_1	(rad)	angle between stator phase a_s and d-axis in the stator reference frame (Figure 4.5)
ϑ_r	(rad)	angle between rotor phase a_r and d-axis (Figure B.6)
$\vartheta_m = \vartheta_a - \vartheta_r$	(rad)	angle between rotor phase a_r and stator phase a_s (Figure B.6)
λ	(Wb)	magnetic flux
ρ	(Ωm)	electric conductivity
χ	(m)	penetration depth
cosφ		power factor in sinusoidal operation
ψ	(Wb)	flux linkage
ω_a	(rad/s)	dq axes rotating speed in the general reference frame
$\omega_1 = \dot{\vartheta}_1 = \frac{2\,\pi f_1}{\mathbb{P}}$	(rad/s)	dq axes rotating speed axes in the stator reference frame
$\omega_m = \dot{\vartheta}_m$	(rad/s)	rotor mechanical speed in electrical radians
$\omega_{\text{mech}} = \frac{\omega_m}{\mathbb{P}}$	(rad/s)	actual rotor mechanical speed
$\omega_r = \mathbb{S}\,\omega_1 = \dot{\vartheta}_r$	(rad/s)	rotor current angular frequency
ω_t	(rad/s)	turbine angular speed

Acknowledgments

I don't think I can express my gratitude to all the people who help me to be here as a doctor today, but at least I want to remember their names.

Prof. Emanuel has been the best advisor I could wish, but I have to recognize that his example, encouragement and support during my doctorate have been even more valuable than the technical knowledge he transmitted to me.

Deepest gratitude is due to the members of the thesis committee, Prof. Stankovic e Prof. Thompson, for their suggestions and comments that resulted in significant improvements of my work. I am particularly grateful to Prof. Thompson for the detailed grammar and stylistic review of my dissertation: his observations have been priceless.

Special thanks go also to the faculty, staff and students from the ECE Department, for having provided a supportive and friendly environment where I could work with serenity and efficiency. In particular, I want to thank Prof. Looft, Prof. Makarov, Bob, Cathy, Colleen and Stacie.

In writing this page, I keep thinking to my family: thank you to mum, dad, Andrea and Matilda for your endless love that surpasses any physical distance.

Also, many thanks to my friends for their patience and help, and for having shared with me moments of joy as well as difficulty. I want in particular to mention: Aastha, Angela, Anikò, Brenda, Davide, Isabella, Joszef and Paulo. I want also to thank here Rodi Emanuel, for her care and attention in all these years.

Finally, I want to thank God for all the gifts He offers to me every day to me and for His continuous presence and protection.

Introduction

Overview of wind power plant evolution

Distributed generation represents an answer to the growing demand of electric energy and to increasing environmental concerns. Among alternative sources, wind energy is one of the most promising technologies.

In the developed countries, wind capacity has been growing at a rate of 20% to 30% a year over the last decade [1, 2]. At the moment of this writing, the countries with higher installed wind capacity are United States, Germany, China and Spain [3, 4]. In terms of relative installed capacity, the market is dominated by Denmark, with 20 % installed capacity [5].

Regarding the United States, the national total power capacity at the end of 2009 was about 32000 MW, and approximately 6000 MW are under construction. The total installed wind capacity in US provides about 1% of the total energy consumption in the United States. Texas is the leader in wind market [6, 7], with 9000 MW installed. A study published in 2008 by the Department of Energy delineates a scenario of 20% wind power penetration by 2030 [8].

The rapid growth of the wind industry is due to different factors, including:

1. supporting government policies [9],
2. advance in wind power technology that cause reduction of costs and improvement in performance [2],
3. environmental concerns [3],
4. the deregulation process [10].

Until the early 1970s, wind energy filled a small niche market, providing mechanical energy for grinding grain and pumping water [11]. The main hurtle against wind turbine development was the incompatibility of a variable speed generator with an electric grid operating at a fixed frequency. The availability of fossil fuels in high quantity and low cost was another limiting factor for the investment in alternative sources of energy [3].

Power conditioning was a milestone in the development of wind energy technology [12], because it allowed the decoupling between the turbine and the grid frequencies. At the end of the '80s power converters were fitted to 50 kW-class wind power plants.

In the last part of the 20th century radical improvements in wind technology resulted in an explosion of wind turbine installations. For example, blades once made of sail or sheet metal, are now made of fiberglass composite; dc generators and synchronous generators have been replaced by induction generators; digital control has been introduced; turbine size has increased, passing from the average rated power of 50 kW in the early 1980s to the average rated power of 1.5 MW in 2006; and blades size has grown from 8 m in 1980s to more than 70 m in many modern systems [13].

Given the advances in power electronics and controls, applications such as reactive power compensation, static transfer switches, energy storage, variable-speed generation, voltage control and dynamic reactive power support are commonly found in modern wind power plants [14, 15]. As a result of the above listed improvements, the cost per VA of wind technology have been dropping, while reliability, efficiency and performances have been increasing [16].

Modern power plant reach a total installed power of 200 MW and more. In the United States, wind plants recently completed, currently under construction or recently announced include: the Gulf Wind Project in Texas (300 MW phase I with total of 1,200 MW by the completion of phase IV), Cedar Creek wind plant in Colorado (300 MW) and the Prince Wind Plant in Ontario (200 MW).

When wind power plant were small and their impact on the grid operation was minimal, the rules governing wind generation were relaxed to encourage development [16]. In the last year, the increase of wind power plant installations showed that this lack of regulations is a threat to the stability and power quality of the grid [14, 17, 18, 19]. As a consequence, the requirements for interconnecting wind power plants to the grid are becoming stricter and more similar to the ones developed for traditional generation [20, 21] and wind plants are transitioning from a simple energy source to a power plant that delivers significant grid support [16].

Modern control technologies allow operating wind power plants below their maximum power rating for most of the time while trading some energy capture for grid ancillary services[1] [22, 23].

[1] The ancillary services represent a number of services required by the power system operators, such as voltage control, in order to secure safe and reliable grid operation.

Research objectives

The scope of this research is to investigate the use of a Wind Energy Conversion System (WECS) as a power generator and harmonic compensator simultaneously. Power generation is the primary application, while harmonic compensation is an ancillary service provided to improve the quality of the electric energy delivered to the loads.

The proposed use of the WECS has many practical implementations, since the number of Non-Linear Loads (NLLs) connected to the grid is continuously increasing, thus resulting in high amounts of harmonic currents flowing in the grid. Since only a small amount of distortion is allowed on the grid [24, 25, 26], devices such as Passive and Active Filters (AFs) are installed to sink the sink the harmonic currents injected by the NLL.

To study the use of a WECS as a power generator and harmonic compensator, one must address the following topics:

- The design of the control system for the WECS operation, taking into account the different dynamics involved (electric generator, power converters and wind turbine);
- The effects of the proposed application on the WECS operation, in terms of power loss increase and voltage distortion;
- The performances and limitations of the proposed control system for different wind speeds and NLL current spectra;
- The analysis of transient operation to verify the system response to voltage variations and wind speed variations.

Related research

Several studies in the literature deal with methods to improve the performances of WECS; however, only a few of them addresses how to use the WECSs as a harmonic compensator and power generator.

An introductory study to this application is conducted in [23]: the control of a power converter connected to a distributed generator is presented. This study shows how to use the power converter to sink harmonic currents injected by a NLL.

The WECS studied in the present work is based on DFIG technology, since this is the most common configuration for modern WECSs [27]. Active Filter operation of WECS based on DFIG has been investigated by three research groups, guided by M. T. Abolhassani

[28, 29, 30], B. Toufik [31] and E. Tremblay [32]. Additional details regarding the studies conducted in the literature are provided in chapter 3.

The studies conducted in the literature prove that the proposed application is feasible, by showing the improvement of the grid current and voltage oscillograms when the above described operation is implemented. The present research investigates further aspects of the use of a WECS as an AF, described in the following section.

Thesis original contributions

This dissertation presents the following original contributions in the areas of control system design, WECS integration and power quality:

1. Three alternative control systems to perform the described operation are designed and their performances are compared. The studied system is representative of a real installation and takes into consideration several design parameters that affects the system performances, such as the equivalent impedance of the line that connects the stator to the Point of Common Coupling (PCC) and of the transmission line.

2. Compensation of the zero-sequence currents is addressed. Zero-sequence currents are very common in power system due to load unbalance and to the operation of residential and industrial loads such as consumer electronics and motor drives. The compensation of the zero-sequence currents requires a different approach with respect to the positive- and negative-sequence current, that has not been investigated by the previous studies on the subject.

3. The increasing power loss and consequent temperature rise in the WECS components is studied: it is verified that current increase may result in unacceptable temperature rise and therefore DFIG derating is needed to limit the power loss. DFIG derating is effective for all three control systems.

4. Voltage distortion due to the harmonic current flow within the WECS is investigated. The harmonic voltage drop on the line impedance may lead to stator peak voltages above the rated value. The length of the line connecting the stator to the PCC is an important parameter when the stator is injecting harmonic currents, since a longer transmission line leads to more severe voltage distortion, thus resulting in higher peak voltage at the stator terminals.

5. Several results are obtained from the analysis of the control system response to voltage dips: Low-Voltage Ride Through (LVRT) capability is verified; the capability of the

system to perform harmonic compensation in spite of the voltage variations is verified; and derating allows protecting the WECS devices in the instants following the voltage dip, because it reduces the amplitude of the currents flowing through the generator and the power converters.

6. The control system response to wind variation is addressed and it is shown that sudden and severe wind variations may affect the voltage amplitude at the PCC. Therefore, reactive power compensation is necessary to limit the voltage oscillations

7. Since derating causes a reduced income from the sale of the electric energy, a preliminary economic analysis is conducted to verify the feasibility of the proposed methodology.

Thesis results

A number of contributions have been made in the study of the use of a WECS as an AF. The effectiveness of the proposed control system to cancel any harmonic currents (positive-, negative-, zero-sequence, interharmonics, subharmonics) is proved.

Analytical expressions are provided to quantify the effects of the proposed application: voltage distortion at the DFIG terminals requires a conservative design of the windings insulation, and temperature rise implies derating of the machine. Stator and rotor derating formulations as a function of the current spectrum injected by the NLL are carried out.

Transient analysis allows verifying that harmonic compensation is implemented in spite of voltage variation and wind speed variations. It is verified that if the transmission line is long, the voltage at the PCC may experience severe oscillations, and reactive power control is designed to reduce the voltage fluctuations.

The economic analysis allows identifying the conditions under which the proposed approach is convenient.

Thesis organization

The thesis is organized in three parts:

Part I is an introduction to wind generation technology:

Chapter 1 describes the state-of-art wind technology and the challenges posed by the interconnection of wind resources to the grid;

Chapter 2 describes the DFIG principles, equivalent circuit and power and torque definitions.

Part II provides the steady-state analysis of the WECS operating as power generator and harmonic compensator:

Chapter 3 presents the principles of harmonic compensation, studies the effects of the proposed application on the WECS, and describes DFIG derating in detail;

Chapter 4 describes the control system that results in compensation by means of RSC modulation;

Chapter 5 deals with the control to implement compensation by means of LSC modulation;

Chapter 6 introduces compensation by means of combined modulation.

Part III deals with the transient analysis of the system under study, operated by means of combined modulation:

Chapter 7 studies the system response to voltage variation and discuss the Low Voltage Ride Through (LVRT) ability;

Chapter 8 presents a model of the mechanical system and verifies the system response to wind variation and the implementation of voltage regulation.

Several appendices complete the work. Appendix A provides the systems parameters; appendix B presents the generalized *dq* transformation applied to electrical machines, appendix C introduces the principles of wind turbines aerodynamics and of variable speed operation. The other appendices describe some of the tools used to develop the work, including: the principles of control systems and Phase Locked Loop (PLL) design (appendix D), the theory of instantaneous powers (appendix E), the Fortescue transformation for poly-phase systems (appendix F), elements for an economic valuation of the proposed control system (appendix G), and the principles of Pulse Width Modulation for the power converters control (appendix H).

Part I

Wind Power Technology

Introduction to Part I

The scope of Part I is to frame the research on Active Filter operation of WECSs within the most recent developments of Wind Energy Technology.

The common configurations for wind generation and a synthesis of the challenges posed by the connection of wind power plants to the power system are presented in chapter 1. Given the fact that the majority of the WECS installations are based on Doubly-Fed Induction Generators (DFIGs), chapter 2 is dedicated to the steady-state analysis of this electrical machine.

The principles of wind turbine aerodynamics are presented in appendix C: a basic knowledge of these topics helps identifying the effects of wind turbines operation on the grid.

Chapter 1

WECS Configuration and Interconnection to the Grid

1.1 Introduction

This chapter presents the most common configurations used for modern WECSs, and the principal challenges presented by their connection to the grid.

1.2 Configuration of modern WECSs

In the earlier applications of wind generation, dc machines were used to convert wind energy into electric energy to decouple the mechanical system from the electric grid that is operating at constant frequency [11].

Power electronics advances enabled in the replacement of the dc-machine with the synchronous and induction generators [33]. At the moment, many technological alternatives are available to achieve electromechanical conversion in wind power plants [9, 11, 13, 34, 35, 36]. The different configurations are obtained by combining an induction or synchronous machine to a full-scale or partial scale power converters[2], as illustrated in Figure 1.1 [33]. In this diagram, the different stages that implement the conversion of mechanical energy into electric energy are visualized in different rows; for each stage, the technological alternatives are presented. Different vertical paths can be identified to perform the energy conversion.

Among the solution presented in Figure 1.1, four machine/power converters combinations encompass the majority of the present installations and they are known as [10, 33, 37]:

Type A: Fixed speed,

Type B: Dynamic slip control,

Type C: Doubly-Fed Induction Generator (DFIG) with back-to-back converters,

[2]Full-scale power converters are rated for the generator power, while partial-scale power converters are rated for a portion of the generator power. The power flow can be one-directional or bi-directional.

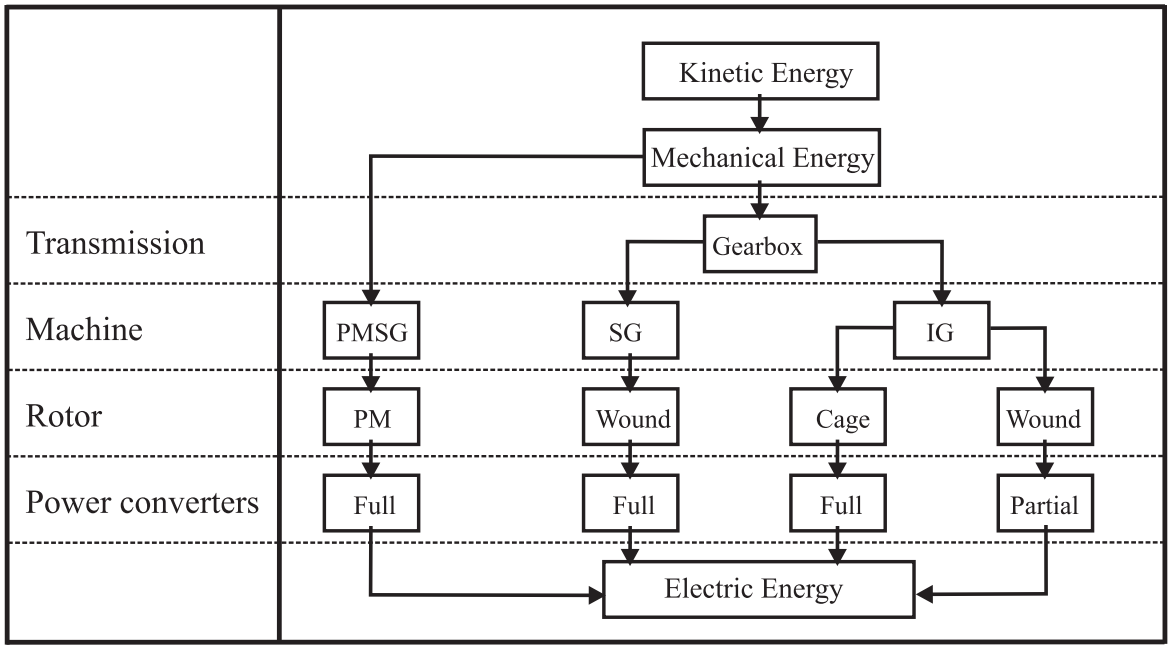

Figure 1.1 - Road-map for wind energy conversion [33].

Type D: Direct Drive.

1.2.1 Type A - Fixed speed

Fixed speed wind generators represent the oldest and simplest configuration. As illustrated in Figure 1.2, the induction generator rotor is short circuited, and the stator is connected to the grid. The induction generator shaft is connected to the wind turbine through a gear-box. A reactive compensator is installed at the stator terminals to provide reactive power to the generator.

This solution is simple because it does not require the installation of power converters, however the fixed speed operation does not allow optimal power capture (appendix C), and the reactive compensator is necessary to provide the magnetizing current. The two major drawbacks of Type A configuration are as follows:

- the time necessary to pay back the investment is higher than the one for configurations based on variable speed operation due to the fact that the annual energy extracted from the wind is lower;
- the system is unable to damp the turbulences of wind speed, that are directly transmitted to the grid.

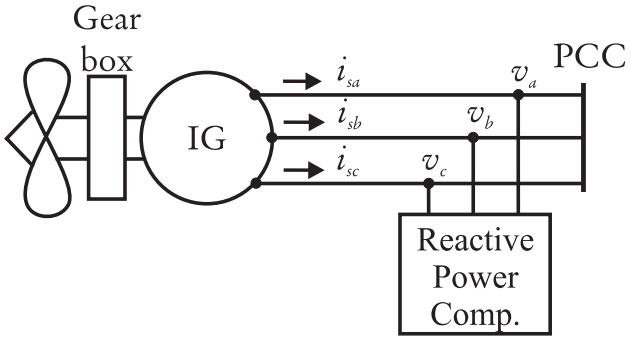

Figure 1.2 - Type A configuration: Fixed speed.

1.2.2 Type B - Dynamic slip control

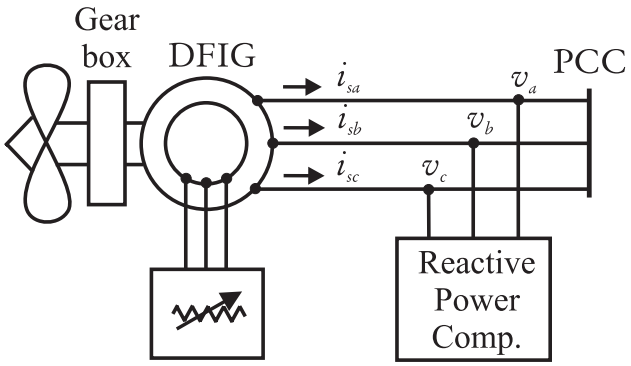

Figure 1.3 - Type B configuration: Dynamic slip control.

The design known as Dynamic Slip control has been introduced by the Danish manufacturer Vestas in 1999 (Vestas OptiSlip technology [38]). The main difference between this design and Type A is the variable resistance added in series to the rotor windings, as shown in Figure 1.3. The variable resistance is controlled through power electronics, and allows variable speed operation with a maximum slip equal to 0.03-0.05.

Type B design results in higher costs due to increased complexity of the design, but variable speed operation allows a higher power capture and in a smoother control of the power delivered to the grid.

This configuration is renowned because it represented a milestone toward the implementation of variable speed operation, but at the moment it has been superseded by DFIG technology (Type C configuration).

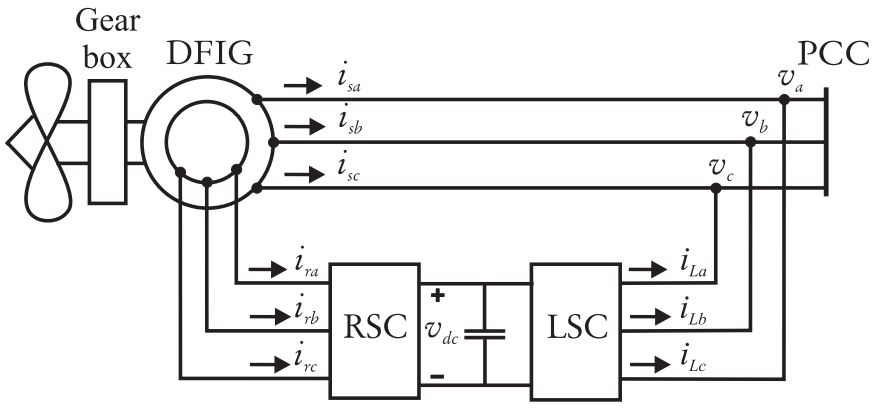

Figure 1.4 - Type C configuration: DFIG with back-to-back converters.

1.2.3 Type C - DFIG with back-to-back Converters

The Doubly-Fed Induction Generator (DFIG) conceptual schematic is shown in Figure 1.4. The stator is directly connected to the suppling bus; the rotor is supplied by two back-to-back connected power converters: the Rotor Side Converter (RSC) and the Line Side Converters (LSC) interfaced by means of a dc-link. This configuration allows impressing a rotor voltage with adjustable amplitude and frequency.

In spite of its complexity, this configuration is the most popular for wind generation due to several advantages, that can be summarized as follows:

1. Only 25%-30% of the total power flows through the power converters which can be designed for a low-rated power (partial-scale converter), resulting in lower cost, size, and weight, and smaller losses compared to the system with full-scale power converters connected to the stator [36, 39, 40, 41, 42].

2. Both active and reactive power exchange with the grid can be adjusted; since this operation is performed by controlling the power converters, regulation of active and reactive power is very fast (in the range of few milliseconds [43, 44]) and precise.

3. Variable speed operation leads to a higher energy yield given the same wind regime, and reduces the dynamic loads on the tower and the gearbox.

4. DFIGs have the ability to output more than the rated power without becoming overheated and are able to transfer maximum power over a wide speed range [35].

5. A reactive compensator is not needed

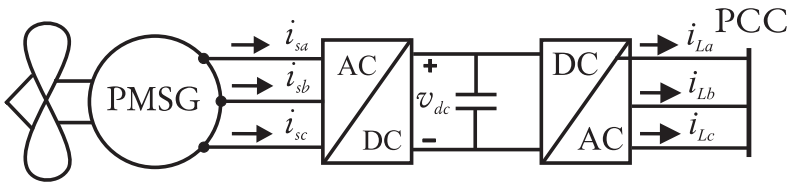

Figure 1.5 - Type D configuration: Direct drive.

DFIG technology presents drawbacks as well: due to the stator's direct connection to the grid, DFIGs are very sensitive to grid disturbances, especially to voltage dips [40, 43]. A decrease in the supply voltage may cause high rotor voltages and currents that constitute a threat for the sensitive solid state devices installed in the RSC and LCS[3].

1.2.4 Type D - Direct drive

The direct drive design is relatively recent and makes use of a Permanent Magnet Synchronous Generator (PMSG) with a high number of poles. A gear box is not needed because the PMSG is able to generate electricity at relatively low speed. To decouple the turbine varying rotating speed from the constant grid frequency, the stator windings are connected to the grid through full-rated converters.

Type D configuration results in the use of full-scale converter and in higher cost with respect to Type C. The high cost of the permanent magnets contributed limits the application of this configuration to WECS with low rated power. However, the absence of the gearbox increases significantly the reliability of the installation while reducing maintenance costs. For this reason many research efforts are going in the direction of increasing the applications of gearless solutions [45, 46, 47, 48, 49].

1.2.5 Market share of wind generation technologies

According to [27, 33], the wind technology market in 2002 was shared as shown in Table 1.1. At the moment of this writing (2010), the Type C configuration is still the most popular technology; however Type D is increasing its impact in the market [50].

1.2.6 Off-shore wind farms

The configurations for off-shore wind farm are chosen among the ones described above for in-land plants: for example, off-shore wind farms in Denmark are based on Type A and Type

[3]A detailed analysis of the transient response of a specific WECS based on DFIG technology is provided in chapter 7.

Turbine Technology	World-Market Share
Type A	28 %
Type B	5 %
Type C	47 %
Type D	20 %

Table 1.1 - Wind Turbine Technology Market in 2002

C configurations [33]. Although turbines of up to 5 MW have been installed, the majority of the off-shore projects range from 2.0 MW to 3.6 MW. In the United States, several offshore project proposals have been presented but most of these projects have not been implemented yet due to environmental concerns [6, 8, 9, 51]. In the future, it is expected that off-shore wind power installations will increase significantly worldwide [8, 33], due to the enormous energy potential of wind energy on the sea.

The increase of off-shore wind farm installation may lead to the development of different configurations: for example, the long distance between the off-shore wind power plant locations and the loads combined with the transfer of large amounts of power make off-shore wind power a suitable candidate for the implementation of High Voltage dc (HVdc) transmission lines [33, 52, 53, 54].

In-land wind farms the installations have been tested for many years and their performance are well known. Off-shore wind power plants are mainly in a research or prototype stage and currently there is not a dominant technology for the plants or for transmission of the wind power to land.

1.3 WECS effects on the grid operation

The connection of wind turbines to the grid present several challenges, some of them are summarized as follows [9, 12, 55, 56]:

1. Wind generation, as any power sources depending on natural elements, is characterized by variability and availability of wind. Therefore wind energy is not as dispatchable as the energy obtained by traditional plants.

2. Wind power plant technology is not as familiar or well characterized as conventional generating equipment. Moreover, each configuration (Types A-D) has different dynamical characteristics and impacts differently the grid operation.

3. Grid requirements for wind generators are gradually moving toward those applied to

other types of generation, such as gas and steam turbines. For example, some grid code require that wind power plants assist the grid in maintaining or regulating the system voltage. The requirements for wind generator interconnections are becoming more demanding due to the increasing size of the WECSs and of their impact on the grid operation [9].

4. Many wind plants are built in remote areas far from load centers, where the transmission network is less developed and requires reinforcement to accommodate the additional power flow caused by wind generation [9]. This phenomenon is critical in deregulated markets where transmission and generation are functionally separated [7, 8]. Transmission owners are not motivated to build new high-voltage transmission lines to remote areas where there may be a high potential wind energy resource but little existing generation or load. Wind plant developers cannot build new wind power plants in remote wind-rich areas, if the transmission line is not capable of transferring the plant output to major load centers. Given the fact that the transmission line construction requires longer times than the completion of the generating units, it results that wind power plants are often located in regions that are closer to existing transmission lines but that are not the richest in wind energy [7]. Policies in a few states (including Texas, Minnesota, Colorado and California) support the creation of transmission first in advance of generation [7].

At the time of this writing, the regulations for wind plant generator are still evolving worldwide. This is principally due to the following reasons:

- The increasing number of wind power installations continuously poses new challenges to the stability and reliability of the grid
- Wind power technology is changing, together with the static and dynamic performances of wind power plant.
- The differences in terms of requirements for conventional and distributes resources has not been yet established.

In the following sections, some of the most important challenges posed by the connection of WECSs to the grid are briefly analyzed.

1.3.1 Voltage fluctuations and flicker

Reduction of voltage quality due to the connection of wind generators are caused by variations of the wind speed [9, 14, 18, 57]. Wind fluctuations are caused by several phenomena;

the most important are described in appendix C.

In general, wind speed fluctuations result in a variation of the power absorbed by the turbine. In the case of a weak transmission line, the connection of large wind plants causing severer power fluctuations may be limited in a given part of the electrical network [58].

In other cases, wind power can improve the voltage quality and benefit the service in remote rural systems. For example, in areas where wind may have a high correlation with the seasonal loads (e.g. seasonal tourism in windy areas), the local integration of distributed resources into the grid may avoid to build new transmission lines [58].

Flicker[4] produced by grid connected wind turbines is mainly caused by fluctuations in the output power due to wind speed variations, the wind gradient and the tower shadow effect (appendix C). Many factors affect flicker emission of grid-connected wind turbines during continuous operation, such as wind characteristics (e.g. mean wind speed, turbulence intensity) and grid conditions (e.g. short circuit capacity, grid impedance angle, load type) [60, 61, 62].

The WECS configuration significantly affects the level of flicker emissions. Variable-speed wind turbines show reduced flicker levels in comparison with fixed speed wind turbines [60, 61, 62]. This phenomenon has the following explanation: during variable speed operation fast power variations are not transmitted to the grid but are smoothed by the flywheel action of the rotor. Although variable speed wind turbine produces lower flicker levels, the study of flicker emissions is necessary for each installation since the wind power penetration level is increasing and the global effect may be detrimental.

1.3.2 Reactive power regulation

The first standards for interconnection of wind generators to the grid (such as [63]) specified that wind generators should not actively regulate distribution system voltages since the the wind generator control could conflict with the regulation schemes applied by the utility.

Even if a distribute resource does not participate actively to voltage regulation, it can still cause a voltage increase or decrease along the feeder, depending on the generator type, control method, its delivered power and feeder parameters and loading [18] [5]. Wind generators based on squirrel cage induction machines create a reactive power burden for the power system and they often degrade system voltage performance [9].

Recent changes in the grid standards require wind plants to actively participate in the voltage regulation [9, 64]. Such regulation is implemented by controlling the reactive power

[4]Flicker is 'an impression of unsteadiness of visual sensation induced by a light stimulus, whose luminance or spectral distribution fluctuates with time' [59] which can cause consumer annoyance and complaint.

[5]The effect of a WECS operation on the transmission voltage will be presented in details in chapter 7

exchanged between the wind generator and the grid, different methodologies are available to perform this task.

Capacitors can be used to correct power factor to near unity, but they may induce self-excitation, resonance and harmonics in response to change in system voltage or frequency [14, 44]. Since the capacitor bank regulation is slow, this solution does not provide fine, continuous control, and does not allow to follow the small changes in voltage commonly seen in a weak grid or caused by gusty wind conditions.

To add speed and flexibility, some wind plants use static VAR compensators (SVC). By choosing the correct size of an inductor and capacitor, the SVC can be operated to either generate or absorb reactive power. For example, with a 100-MVAR capacitor and a 200-MVAR inductor, a range of $\pm$100 MVAR can be achieved and adjusted continuously. If negative reactive power is not required, a combination of a 100-MVAR capacitor and a 100-MVAR inductor provides a range of 0 MVAR to +100 MVAR [14]. In [14] simulations are carried out for the wind power plant of Tehachapi (CA) where SVC are installed. Simulation results show that without reactive power compensation the voltage drop due to variations in the wind is unacceptable (the bus voltage reaches 0.905 p.u.), while with proper compensation the voltage drops only to 0.95 p.u.. At the same time, the reactive power flow from the grid drops significantly when the reactive power is compensated locally.

A more sophisticated solution is applied in the the Aragonne Mesa wind plant in New Mexico. A distributed static compensator (DSTATCOM) controls the power factor to unity and a feedback signal of the actual reactive power at the point of interconnection is used to make any correction to the reactive power output of the DSTATCOM [9]. Wind plants that provide closed-loop control of utility system voltages, like the one installed in Aragonne Mesa wind plant, provide two major benefits: the impact of active power fluctuations on the grid voltage is minimized and precise voltage control strengthens the grid [9].

Many modern wind generators provide reactive power compensation directly from the power electronics that control the real power operation of the machine. Such performances may be obtained by using wind power plants based on the Type C configuration [9].

For many wind farms, especially large and remote ones located in systems with relatively low short-circuit ratio, traditional approaches to managing reactive power are not adequate, because they may result in unsatisfactory voltage performances and in flicker [9]. For each installation, the interconnection study helps determining the best method to implement reactive power control.

At the moment many operators prefer unity power factor operation since the active power delivered to the grid results in an economical reward. Reactive power would be produced only if there are sufficient financial incentives [42, 43]. Reactive power production

from the WECS may be beneficial for the grid operation: recent advancements in wind turbine generator technology may allow continuous control of reactive power output even when the wind turbine is motionless. Currently, wind turbines stop both reactive and active power production in response to wind speed value either below a minimum threshold (cut-in speed) or above a maximum value (cut-out speed) as explained in appendix C. While loss of real power production is easily adjusted by the utility, the loss of controlled reactive power production can be locally disruptive. Some variable-speed wind turbines generators that rely on a power-electronic based converter can be configured to deliver reactive power regardless of whether the turbine is turning: this feature will provide effective grid reinforcements by implementing continuous voltage regulation, while this benefit is not possible with conventional thermal or hydro generation.

1.3.3 Power Factor at the WECS terminal

According to the regulations for connection of wind power plants to the grid issued in many European countries, the Power Factor (PF) at the WECS terminals must be maintained above 0.95 under any operating condition. Since the active power delivered by the DFIG is a function of the slip and of the wind speed, it results that the limitations on the maximum reactive power are changing in time. In [64, 65] a throughout analysis is developed to identify the PQ curves of a single wind turbine and of a wind plant.

1.3.4 Harmonics and resonance

If the reactive power compensation system in the WECS makes use of shunt capacitor banks, even a small amount of distortion on current delivered by the the transmission network may be detrimental [9, 66]. The transmission network sees the the capacitor banks as connected in series with the substation transformer [9, 14]: this LC combination may result in a small impedance at low order harmonic frequency, allowing distorted currents to flow from the network. Overloading of capacitor banks and high harmonic voltage distortion on the medium-voltage bus are two of the problems that might be caused by this configuration.

Capacitor banks may also lead to resonance phenomena [66]: for the reasons listed above, together with their slow and coarse control, capacitor banks are not generally used to implement reactive power compensation in WECS. In the majority of wind installations, that are based on Type C and D configurations, the power converters are used to implement this task.

It is recognized that wind turbines are not a significant source of harmonic distortion although they are connected to the grid by means of power converters [66], since inverter

manufacturers adopted the switching inverter technology that results in current distortion well below the one allowed by the IEEE Standard P1457 [63].

1.3.5 Dynamic response to voltage dips and faults

The first standards for the interconnection of WECS to the grid stated that the wind power plant was expected to disconnect from the system during faults [18, 39]. A drawback of this regulation is that separation of wind turbines from the grid during the fault leads to loss of a portion of power generation instead of providing grid support.

For this reason, the most recent standards [55, 67, 68] the generator must support the grid in the event of faults and it is not allowed to disconnect during a network disturbance such as voltage dip [43]. The Low Voltage Ride Through (LVRT) requirement was firstly issued by E.ON Netz [68] in Germany and is now becoming a universal feature for wind power generation.

As an example, the LVRT requirement for UK is shown in Figure 1.6. The normalized voltage at the point of common coupling is plotted as a function of time: the shaded area indicates the region where the WECS is allowed to disconnect from the grid. For example, if the PCC voltage amplitude is equal to 0.15 for 2.5 s. then the WECS can be disconnected. The curve applies for three-phase faults: it is worth to notice that according to the UK requirement, the turbine is supposed to stay connected for a zero-voltage symmetrical fault with duration up to 140 ms. A comparison of LVRT requirements in different countries is carried out in [58]. The analysis of the US regulations is carried out in section 1.5.

1.3.6 Dispatchability

Power grids are operated in such a way that generation resources meet supply demands: traditional generators are programmed to follow dispatch order, and failure to deliver power per dispatch orders results in financial penalties [7, 9].

Wind generation does not fit this control scheme, because the power output of wind plant is function of the wind speed. This characteristic is common to all distributed resources that rely on natural environment: generation can be estimated in advance by using forecasting tools [69], but power output cannot follow dispatch orders. For this reason, distributed resources are generally defined as 'intermittent'. Spatial planning and the connection of different distributed power sources to the grid allows to smooth the power production curve (For this reason, some authors prefer to replace the adjective 'intermittent' with 'variable' [19, 58]).

Given the above considerations, it results that the increasing amount of distributed

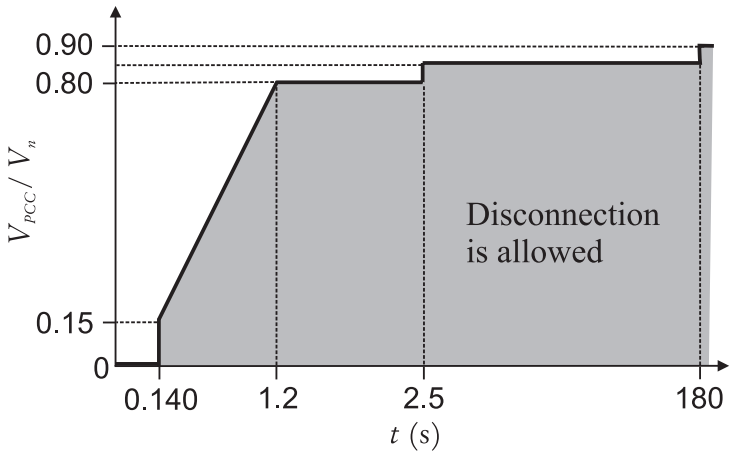

Figure 1.6 - LVRT requirement according to UK National Grid [67]. The normalized voltage at the PCC is plotted in function of time, and the region where the WECS is allowed to disconnect is indicated by the gray area. For voltage variations above the black trajectory, the WECS must stay connected to the grid.

resources installed on the grid results in a simultaneous increase of the reserves to keep the system in balance. The estimation of the amount of reserve is an optimization problem: from one side, lack of reserve results in system unbalance and in penalties, on the other side, excess of reserves results in a too high cost [8]. The experience of European countries with a significant installation of renewable energies (Denmark, Spain and Germany) allows estimating an increase of the reserves equal to 1%. This minimal increase is due principally to the interconnection of the electric systems within the European countries and may be not sufficient in other countries where the short circuit ratio is low.

At the moment, energy storage is not competitive enough to constitute a solution to mitigate intermittency of renewable energy productivity [3, 21], therefore other solutions need to be adopted to ensure maintenance of the power balance. Statistical analysis can be used to balance loads, by observing that energy production and consumption are positive and negative contribution to the power balance, respectively. The smart grid technology may be used to promote the integration of wind energy into the grid, by allowing a more efficient and fast monitoring of energy production and load consumption.

1.4 Assessment of power quality - IEC standard

The survey carried out in the previous sections allows the identification of many sources of power quality concerns related to WECS connection to the grid.

The power quality standard of grid connected wind turbines IEC61400-21 [70] issued by the International Electrotechnical Commission (IEC) defines the parameters that characterize the quality of energy delivered by wind turbines and provides recommendations to carry out measurements of power characteristics. The factors and characteristics with highest influence on the power quality of wind turbines identified by the standards can be summarized as follows [58, 66]:

- Wind turbine technology (type of electrical generator, gearbox or gearless transmission, direct/controlled connection to the grid).
- Grid conditions at the PCC (short circuit power and X/R ratio, interconnection voltage level and regulation, type of interconnecting transformers, earth system, coordination of the protections)
- Wind farm design and control (number and nominal power of the wind turbines, wind farm internal power collecting system characteristics (X/R), possible capacity effects from the wind farm internal cabling system, added power/voltage control and regulation).
- Wind flow local characteristics (turbulence intensity, turbine operation under wake flow, spectrum of the wind 3D components, spatial variability of the wind [71])
- Wind turbine constructive parameters (nominal and reference power, reactive power versus active power)
- Wind power fluctuations (Steady-state: flicker emission, long and short term emission. Transient performance: wind turbine cut-in and cut-out, voltage dips)
- Imbalances and harmonics (current harmonics and inter-harmonics)

1.5 FERC Order 661 and 661A

The requirements for interconnection of WECS in the US are determined by the Federal Energy Regulatory Commission (FERC).

In May 2005, FERC emitted the 'Final Rule' on Interconnection for Wind Energy, Order No. 661 [72]. This order 'requires public utilities that own, control, or operate facilities for transmitting electric energy in interstate commerce to append to their standard ... procedures and technical requirements for the interconnection of large wind generation'. This order has been modified in December 2005 under request of several entities (including

AWEA, ISO New England, National Grid and NERC) thus resulting in FERC Order 661-A [73].

Any wind power plants intended to be connected to the grid must demonstrate the following requirements according to Order 661-A:

1. LVRT capability for voltage dip down to zero residual voltage measured at the high side of the wind generating plant step-up transformer.

2. Power factor regulation within the range of 0.95 leading to 0.95 lagging if the interconnection study conducted by the Transmission Operator shows that this requirement is necessary to ensure safety or reliability; the PF is measured at the PCC.

3. Supervisory control and data acquisition (SCADA) capability to transmit data and receive instructions from the Transmission Provider, to protect the system reliability.

1.6 Future trends and conclusions

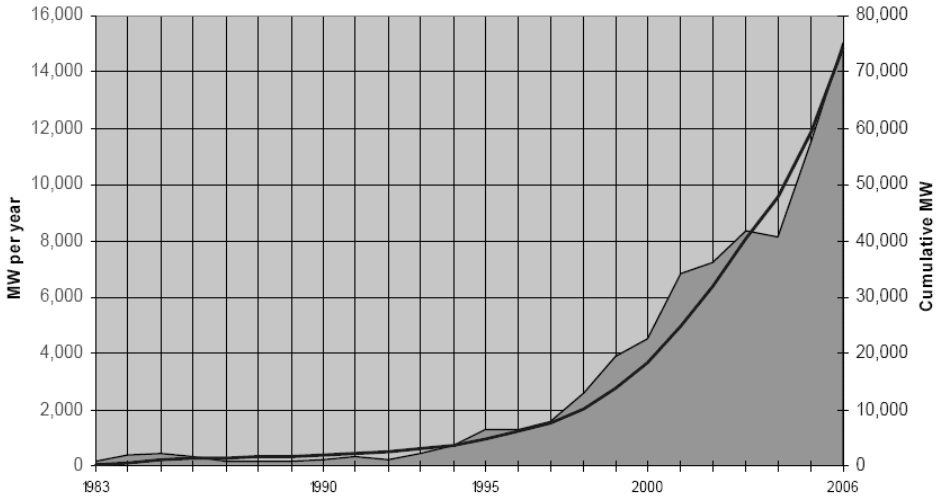

Figure 1.7 - Installed wind power worldwide: the annual and cumulative distributions are shown as a function of time [74].

In spite of the technical challenges posed by the interconnection of wind turbines to the grid and of the more stringent requirements that wind power plants are required to satisfy, the number of WECSs installed worldwide is continuously and rapidly increasing. Figure 1.7 helps quantifying this concept, by showing the annual and cumulative distribution of wind power worldwide as a function of time. The MW of wind power installed per year have

been increasing continuously since the '90s, thus resulting in an almost exponential growth of the cumulative wind power. The trend presented in Figure 1.7 is expected to continue since in many countries, including United States, wind energy still provides a small portion of the installed generation.

A technical report prepared by the US Department of Energy studies the scenario where wind energy will represent 20% of the energy production in 2030 [8]: this projection means that the impact of WECSs on the grid operation will become more significant in the future, and will require further improvements of the WECSs performances and of their control system.

Chapter 2

DFIG Steady-State Analysis

2.1 Introduction

In this chapter, a detailed analysis of the DFIG steady-state performances is carried out and the following items are presented:

- Induction machine configuration and operating principles,
- DFIG equivalent circuit,
- Power and torque expressions.

2.2 Configuration and equivalent circuit

2.2.1 Singly-fed induction machine: principles of operation and notation

The three-phase induction machine idealized configuration is shown in Figure 2.1.a [75, 76, 77, 78]. The stator terminals are labeled as a_s, b_s and c_s. The rotor terminals are labeled as a_r, b_r and c_r. The stator and the rotor are separated by a uniform air gap of width l.

In the singly-fed induction machine, the rotor terminals are short-circuited and the stator terminals are connected to the three-phase power supply. When the singly-fed induction machine is used as a motor, the rotor windings are replaced by conductive bars that form a squirrel-cage structure

The current flowing in each stator winding produces a magnetic field in the air gap; if the leakage field is ignored, the air gap magnetic field distribution created by current flow in one winding is a square wave [78]. Figure 2.1.b shows the magnetic field distribution produced by stator phase a_s current for the machine depicted in Figure 2.1.a., assuming that a dc current with amplitude I_s flows in each conductor.

At the end of the XIX century [79], G. Ferraris [80] and N. Tesla [81] proved that if the stator windings are supplied by a symmetrical and sinusoidal poly-phase supply, the stator currents induce a sinusoidal flux wave (rotating magnetic field) in the air gap. In practice, the sinusoidal flux distribution is obtained by distributing properly the windings

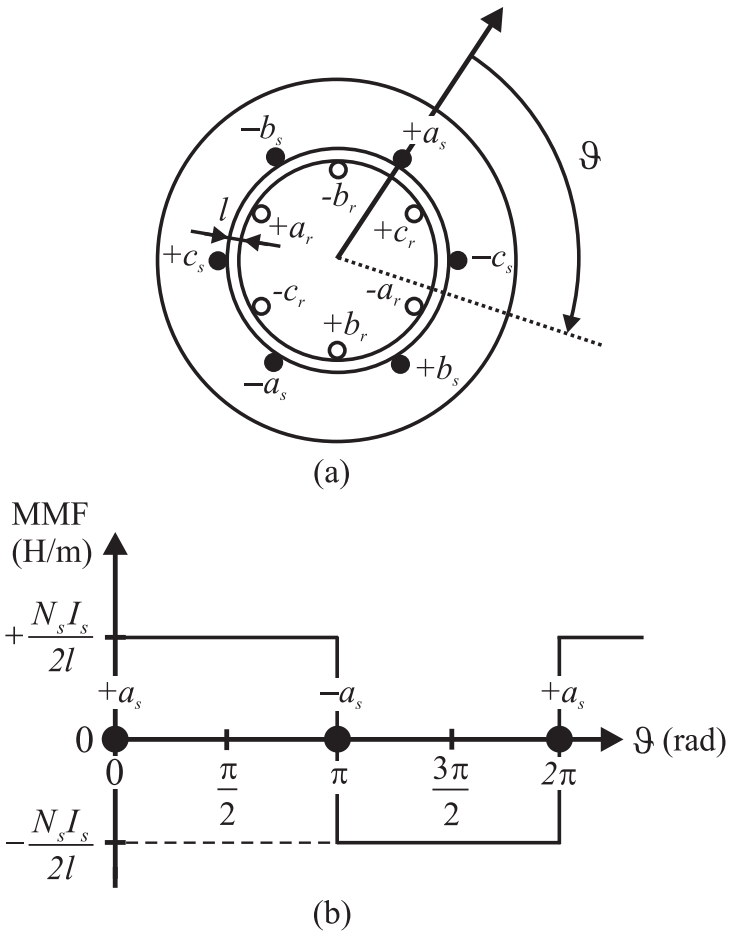

Figure 2.1 - Idealized singly-fed induction machine: (a) stator and rotor winding distribution and reference frame for the air gap magnetic field representation. (b) Magnetic field distribution produced by a dc current I_s flowing in each conductor of stator phase a_s, while the current flowing in phases b_s and c_s is zero; N_s is the number of conductors in each stator slot.

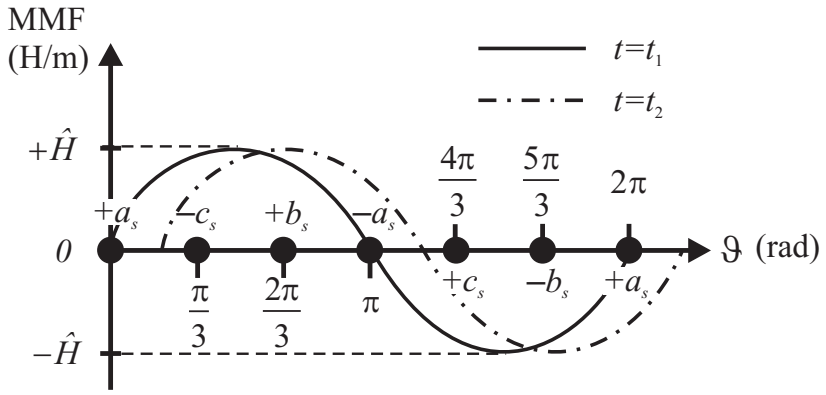

Figure 2.2 - Conceptual representation of the rotating magnetic field generated by the stator windings of the machine shown in Figure 2.1 when supplied with a symmetrical three-phase voltage. At different time instants, the wave flux position changes. The flux wave speed is ω_1.

of each phase on the stator perimeter and the induction machine analysis is performed at fundamental frequency. The conceptual representation of the rotating field at fundamental frequency is shown in Figure 2.2: at different time instants t_1 and t_2 the zeros and the peaks of the flux wave are at different positions.

The stator flux wave moves with synchronous speed ω_1 (rad/s); the synchronous speed is related to the supply frequency f_1 by means of the number of pole pairs $\mathbb{P}$ [75, 76, 77, 78, 82]:

$$\omega_1 = \frac{2\pi f_1}{\mathbb{P}} \tag{2.1}$$

The rotating stator field induces three-phase voltages in the rotor windings that in turns produce rotor currents; rotor currents generate a rotor flux wave in the air gap. Electromechanical conversion is possible only if the stator and rotor flux waves rotate with the same speed ω_1 [75, 76]. According to electromagnetic theory [79], the interaction between the air gap flux and the rotor current flow creates a force ('Lorentz Force') on the rotor windings and consequently the rotor turns with mechanical speed ω_{mech}.

In the classical theory of the induction machine, the rotor speed is expressed in electrical radians rather than in mechanical radians; this way, the same units are used for the electrical and the mechanical quantities. In this work, the symbol ω_m is used when the rotor speed is expressed in electrical rad/s, the symbol ω_{mech} is used when the rotor speed is expressed in mechanical rad/s.

The relation between electrical radians and mechanical radians is explained by referring to Figure 2.3 where the configuration of a four poles induction machine and the correspond-

ing rotating field distribution are shown. For the four pole machine, the period of the flux wave is half of the perimeter of the rotor, and to one electrical radiant corresponds half mechanical radiant. In Figure 2.3.b the rotating field distributions for both the two poles machine (Figure 2.1) and the four poles machine (Figure 2.3.a) are depicted to visualize the different flux distribution for machines with different number of pole pairs. For a generic number of pole pairs $\mathbb{P}$, the relation between electrical radians and mechanical radians is the following [75, 76]:

$$\omega_{mech} = \frac{\omega_m}{\mathbb{P}} \quad \left(\frac{\text{rad}}{\text{s}}\right) \tag{2.2}$$

where ω_{mech} is the actual mechanical speed and ω_m is the mechanical speed. In a two poles machine ($\mathbb{P} = 1$), $\omega_{mech} = \omega_m$.

In typical operation of the induction machine, the rotor speed is different from the flux wave speed ($\omega_m \neq \omega_1$); the slip $\mathbb{S}$ [77, 82] is a dimensionless parameter that quantifies this difference and is defined as follows:

$$\mathbb{S} = \frac{\omega_1 - \omega_m}{\omega_1} \tag{2.3}$$

The synchronous speed ω_1 is constant and proportional to the supply frequency (2.1); the value of $\mathbb{S}$ is determined by the rotor speed ω_m and four distinct operating modes are defined:

- If $\mathbb{S} > 1$, the rotor turns in the opposite direction with respect to the rotating field produced by the stator ($\omega_m < 0$) and the machine operates as a brake.
- If $\mathbb{S} = 1$, the rotor is at stand still ($\omega_m = 0$) and the machine operates as a three-phase transformer.
- If $0 < \mathbb{S} < 1$, the rotor turns slower than the rotating field produced by the stator ($0 < \omega_m < \omega_1$) and the machine operates as a motor.
- If $\mathbb{S} < 0$, the rotor turns faster than the rotating field produced by the stator ($\omega_m > \omega_1$) and the machine operates as a generator.

The rotor currents frequency f_r is related to the stator currents frequency f_1 by means of the slip $\mathbb{S}$. Figure 2.4 displays the relations between stator and rotor flux waves speed and the rotor speed. The rotor and stator flux waves move with the same speed ω_1, imposed by the power supply, and the rotor speed is ω_m. The rotor field velocity with respect to the rotor is represented by the symbol ω_r and is defined as follows:

$$\omega_r = \omega_1 - \omega_m = \mathbb{S}\omega_1 \tag{2.4}$$

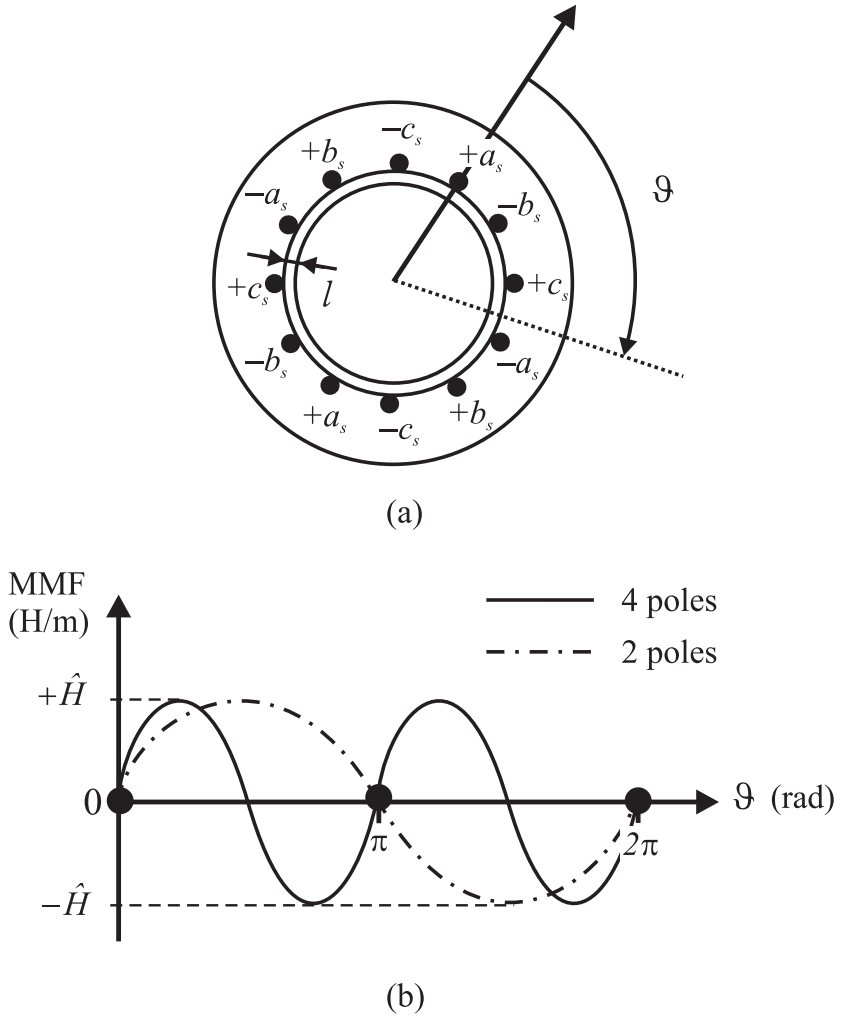

Figure 2.3 - Idealized four poles singly-fed induction machine: (a) schematic representation of the stator and rotor windings distribution; (b) comparison between the air gap rotating field produced by a two poles machine (dashed-dotted line) and by a four poles machine (continuous line) at the same time instant $t = t^*$.

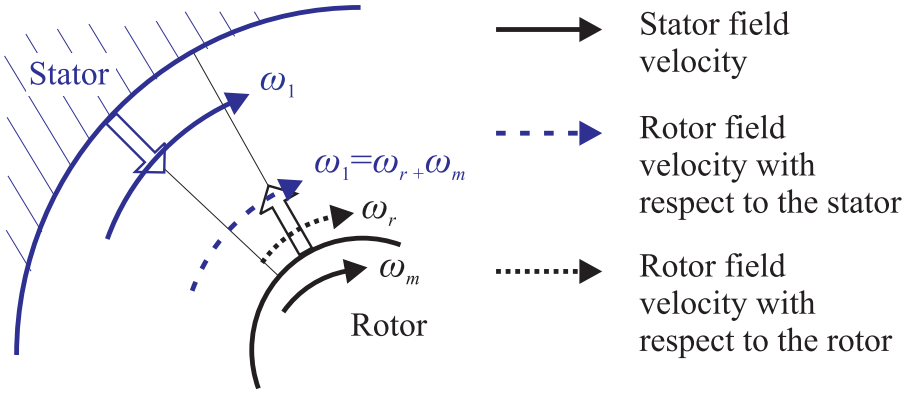

Figure 2.4 - Relation between the stator flux wave speed (ω_1), the rotor speed (ω_m) and the rotor flux wave speed with respect to the rotor (ω_r).

where the slip definition (2.3) has been applied. Dividing all terms by 2π, the rotor current frequency is obtained [77]:

$$f_r = \mathbb{S} f_1 \tag{2.5}$$

2.2.2 DFIG Steady-state analysis and equivalent circuit

The DFIG stator and rotor windings three-phase equivalent circuit is presented in Figure 2.5. The stator side is supplied by the distribution grid with a sinusoidal voltage of amplitude V_s and frequency f_1, the rotor side is connected to a sinusoidal three-phase voltage supply of amplitude V_r and fundamental frequency f_r. The stator and rotor voltages expressions are as follows:

$$\begin{aligned} v_{sa} &= V_s \cos(\omega_1 t) \\ v_{sb} &= V_s \cos(\omega_1 t - 2\pi/3) \\ v_{sc} &= V_s \cos(\omega_1 t - 4\pi/3) \end{aligned} \tag{2.6}$$

and

$$\begin{aligned} v_{ra} &= V_r \cos(\omega_r t) \\ v_{rb} &= V_r \cos(\omega_r t - 2\pi/3) \\ v_{rc} &= V_r \cos(\omega_r t - 4\pi/3) \end{aligned} \tag{2.7}$$

where $\omega_1 = 2\pi f_1/\mathbb{P}$ and $\omega_r = \mathbb{S}\omega_1$ according to (2.1) and (2.4).

The windings are assumed symmetrical and having the following equivalent parameters:

R_s: stator resistance,

R_r: rotor resistance,

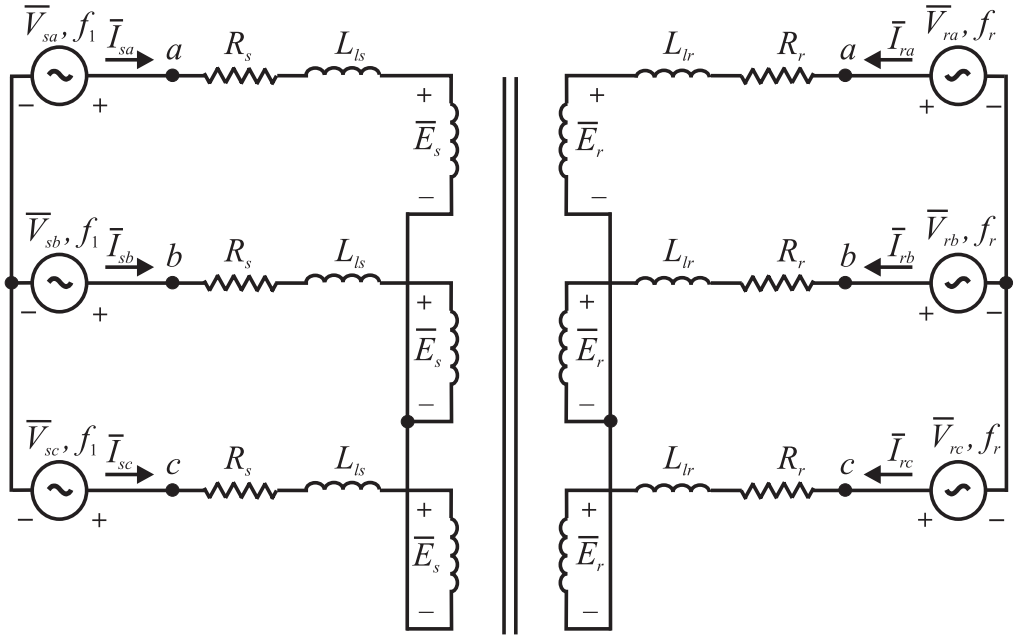

Figure 2.5 - Schematic representation of the DFIG stator and rotor windings in steady state operation. The stator voltage operates at fundamental frequency f_1, the rotor voltage frequency is f_r. The mutual couplings between the windings are not shown to simplify the diagram.

L_{ls}: stator leakage inductance,

L_{lr}: rotor leakage inductance.

To derive the equivalent circuit at fundamental frequency, it is assumed that the windings properties are not function of frequency and temperature [83]: in chapter 3, where the winding loss is calculated at different harmonic frequencies, a more realistic model of the windings is presented.

Using KVL for each phase stator and rotor voltage loops (Figure 2.5) we find:

$$\overline{V}_s = \overline{E}_s + (R_s + j\omega_1 L_{ls})\overline{I}_s \tag{2.8}$$

$$\overline{V}_r^R = \overline{E}_r^R + (R_r^R + j\omega_r L_{lr}^R)\overline{I}_r^R \tag{2.9}$$

where:

$\overline{E}_s$ is the emf self induced by the stator windings at frequency f_1,

$\overline{E}_r$ is the emf self induced by the rotor windings at frequency f_r,

the superscript ^{R} means that the quantity is referred to the rotor windings.

In [84] it is shown that the emf $\overline{E}_r^R$ is the product between the slip $\mathbb{S}$, $\overline{E}_s$ and the ratio between the number of stator and rotor windings (stator to rotor turns ratio) $K_{sr} = N_s/N_r$:

$$\overline{E}_r^R = \mathbb{S}\overline{E}_s K_{sr} \tag{2.10}$$

From the relation above, it is learned that stator and rotor windings behave as primary and secondary windings of a transformer and the stator and rotor frequencies are function of $\mathbb{S}$, according to (2.5).

By substituting (2.4) and (2.10) in (2.9) and dividing both sides by K_{sr}, the following is obtained:

$$\frac{\overline{V}_r^R}{K_{sr}} = \frac{\mathbb{S}\ \overline{E}_s K_{sr}}{K_{sr}} + \Big(\frac{R_r^R}{K_{sr}} + j\mathbb{S}\omega_1 \frac{L_{rl}^R}{K_{sr}}\Big)\overline{I}_r^R \tag{2.11}$$

that is equivalent to:

$$\frac{\overline{V}_r^R}{K_{sr}} = \frac{\mathbb{S}\ \overline{E}_s K_{sr}}{K_{sr}} + \Big(\frac{R_r^R}{K_{sr}^2} + j\mathbb{S}\omega_1 \frac{L_{rl}^R}{K_{sr}^2}\Big)\overline{I}_r^R K_{sr} \tag{2.12}$$

Further rearrangements of (2.12) lead to the rotor voltage formulation:

$$\overline{V}_r = \mathbb{S}\ \overline{E}_s + \Big(R_r + j\mathbb{S}\omega_1 L_{rl}\Big)\overline{I}_r \tag{2.13}$$

where: $R_r = \dfrac{R_r^R}{K_{sr}^2}$; $L_{rl} = \dfrac{L_{rl}^R}{K_{sr}^2}$; $\overline{I}_r = \overline{I}_r^R K_{sr}$; $\overline{V}_r = \dfrac{\overline{V}_r^R}{K_{sr}}$.

By dividing all the terms of (2.13) by $\mathbb{S}$, the following basic equation results:

$$\overline{E}_s + \Big(\frac{R_r}{\mathbb{S}} + j\omega_1 L_{rl}\Big)\overline{I}_r = \frac{\overline{V}_r}{\mathbb{S}} \tag{2.14}$$

The equivalent circuit described by (2.8) and (2.14) is shown in Figure 2.6, where

$$\overline{I}_m = \overline{I}_s + \overline{I}_r \tag{2.15}$$

and M is the magnetizing inductance, assuming:

$$\overline{E}_s = j\omega_1 M \overline{I}_m \tag{2.16}$$

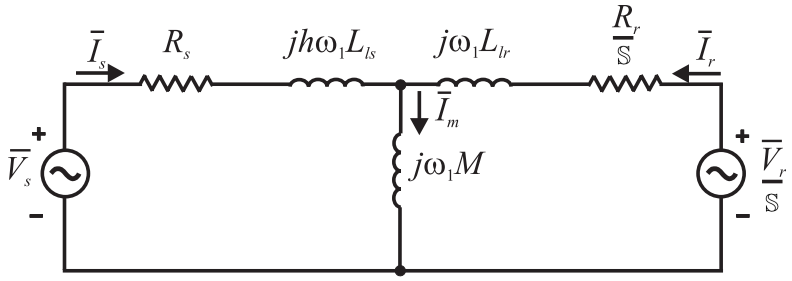

Figure 2.6 - DFIG single-phase equivalent circuit at fundamental frequency f_1 for steady-state analysis.

2.3 DFIG power and torque expressions

2.3.1 Relations between stator, rotor and mechanical active powers

According to the notation of Figure 2.6, the stator and rotor active powers P_s and P_r are expressed as follows:

$$P_s = 3 \text{ Re}\left\{\overline{V}_s \overline{I}_s^*\right\} \tag{2.17}$$

$$P_r = 3 \text{ Re}\left\{\frac{\overline{V}_r}{\mathbb{S}} \overline{I}_r^*\right\} \tag{2.18}$$

The airgap power P_{airgap} is the power stored the air-gap magnetic field:

$$P_{airgap} = P_s - \Delta P_s = T_e \omega_1 \tag{2.19}$$

where

$$\Delta P_s = 3 R_s I_s^2 \tag{2.20}$$

is the stator winding Joule power loss for a constant stator winding resistance R_s and T_e is the air-gap torque.

The total power P_t at the machine terminals is the difference between the input powers (from the stator and from the rotor) and the Joule power loss:

$$P_e = P_s + P_r - \Delta P_s - \Delta P_r \tag{2.21}$$

where

$$\Delta P_r = 3 R_r I_r^2 \tag{2.22}$$

is the rotor winding Joule power loss.

The total power can be written as function of the air-gap torque as follows [76]:

$$P_e = T_e\omega_m = T_e\omega_1\frac{\omega_m}{\omega_1} = P_{airgap}(1-\mathbb{S}) \tag{2.23}$$

where the definition of the slip (2.3) has been applied.

If the Joule loss is ignored ($R_r = R_s = 0$), the following simplifications apply [84, 85, 86, 87]:

1. The stator power is equal to the air-gap power:

$$P_s = P_{airgap} = T_e\omega_1 \tag{2.24}$$

2. The sum of the stator power and the rotor power is equal to the total power:

$$P_s + P_r = P_t \tag{2.25}$$

From (2.25) the rotor power as a function of the stator power and of the slip (under the assumption $\Delta P_s = \Delta P_r = 0$) is obtained:

$$P_r = P_t - P_s = T_e\omega_m - T_e\omega_1 = T_e\omega_1(\frac{\omega_m}{\omega_1} - 1) = -\mathbb{S}P_s \tag{2.26}$$

This last relation shows that the power supplied to the rotor is equal to the product of the stator power and the slip; for this reason, the rotor rated power is named 'slip power' [12, 56, 88]. The RSC and LSC are connected in series to the rotor (Figure 1.4) and they are rated for the slip power [84, 85, 87]:

$$P_{n,\mathrm{RSC}} = P_{n,\mathrm{LSC}} = |P_r| = |\mathbb{S}_{max}|P_s \tag{2.27}$$

From (2.27) it results that if the machine is operating with $|\mathbb{S}| > 1$, the RSC and LSC rated power is greater than the DFIG rated power [87]; for this reason, in the common applications the maximum slip is below unity [84, 85, 89]. For example, if the DFIG operates in the range $0.5 \leq \mathbb{S} \leq -0.5$, the maximum slip is 0.5 and the converters rated power (2.27) is half of the DFIG rated power.

As a final remark, (2.26) teaches that the direction of the rotor power P_r depends on both the sign of the slip and the sign of the stator power. This property of the DFIG leads to the four operating modes of the DFIG, presented in section 2.4.

2.3.2 DFIG as hybrid of synchronous and asynchronous machine

The analysis developed in the previous section results in two main conclusions:

1. The DFIG allows to extract or inject power from the rotor, depending on the sign of the slip and the stator power (2.26);

2. The RSC and LSC rated power (2.27) is equal to the slip power (2.26).

This section provides a further analysis of the DFIG operation, resulting in an interpretation of the operation of the DFIG as an hybrid between the traditional synchronous machine and the induction machine [84, 85, 90].

By ignoring the magnetizing inductance, the equivalent circuit shown in Figure 2.6 is simplified as shown in Figure 2.7, where $\overline{I}_s = -\overline{I}_r = \overline{I}$.

The line-to-neutral stator voltage phasor is:

$$\overline{V}_s = V_s e^{j0} \tag{2.28}$$

The RSC voltage phasor referred to the stator is:

$$\frac{\overline{V}_r}{\mathbb{S}} = \frac{V_r}{\mathbb{S}} e^{j\delta} = \frac{V_r}{\mathbb{S}} \left[\cos\delta + j\sin\delta\right] \tag{2.29}$$

where δ (rad) is the phase shift between the rotor voltage and the stator voltage. The angle δ has a similar role played by the 'torque angle' in the conventional synchronous machine [91, 92] and can be adjusted by regulating the voltage impressed by the power converter connected at the rotor terminals.

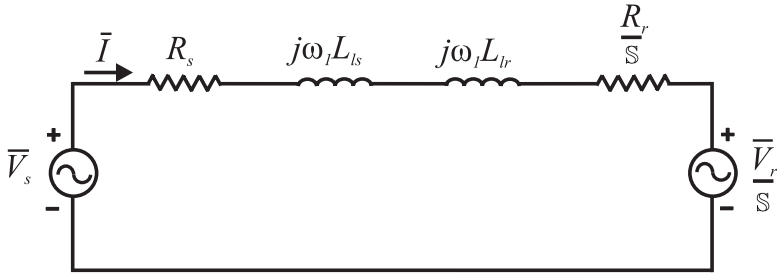

Figure 2.7 - Simplified DFIG equivalent circuit for steady-state analysis. The circuit is obtained from the one presented in Figure 2.6 by ignoring the magnetizing inductance.

The current phasor $\overline{I}$ is obtained by applying KVL to the circuit presented in Figure 2.7:

$$\overline{I} = \frac{\overline{V}_s - \dfrac{V_r[\cos\delta + j\sin\delta]}{\mathbb{S}}}{R + jX} \tag{2.30}$$

where

$$R = R_s + R_r/\mathbb{S}$$

$$X = X_r + X_s$$

By substituting (2.30) in (2.18), one finds the following expression of the stator power [85] (as derived in appendix 2.A):

$$P_s = 3\mathrm{Re}\{\overline{V}_s\overline{I}^*\} = -\frac{V_s}{Z^2}\Big[X\frac{V_r}{\mathbb{S}}\sin\delta - R\Big(V_s - \frac{V_r}{\mathbb{S}}\cos\delta\Big)\Big] \tag{2.31}$$

where $Z^2 = R^2 + X^2$.

According to (2.31), the stator power is a function of the slip $\mathbb{S}$, the magnitude of rotor voltage V_r and the phase shift δ, resulting in a wider range of operation and increased flexibility for the DFIG with respect to the singly-fed machine. The following observations apply to the result expressed by (2.31) [84, 85, 90]:

- The term dependent on $\sin\delta$ resembles the power expression of power in the synchronous machine [76, 91],
- If $V_r = 0$ the stator power expression for the singly-fed induction machine (section 2.1) is obtained:

$$P_s = 3\ \mathrm{Re}\{\overline{V}_s\overline{I}^*\} = 3\frac{\overline{V}_s}{Z^2}\ R \tag{2.32}$$

Figures 2.8 and 2.9 display the stator power waveforms for the machine described in appendix A.

In Figure 2.8 the stator power P_s is expressed in function of $\mathbb{S}$, with δ as a parameter. For small values of the slip, the stator power can be more than ten times higher than the nominal power of the machine. The angle δ is adjusted to avoid this situation. For high value of the slip, the stator power is small for any values assumed by δ. Figure 2.8 results in the conclusion that the values of $\mathbb{S}$ and δ cannot be chosen arbitrarily in order to avoid absorption of large stator power.

In Figure 2.9 the stator power P_s is expressed in function of δ, with $\mathbb{S}$ as a parameter: the power curves resemble the ones typical of the synchronous machine. Figure 2.8 confirms that for some combinations of $\mathbb{S}$ and δ the stator power is higher than the rated power.

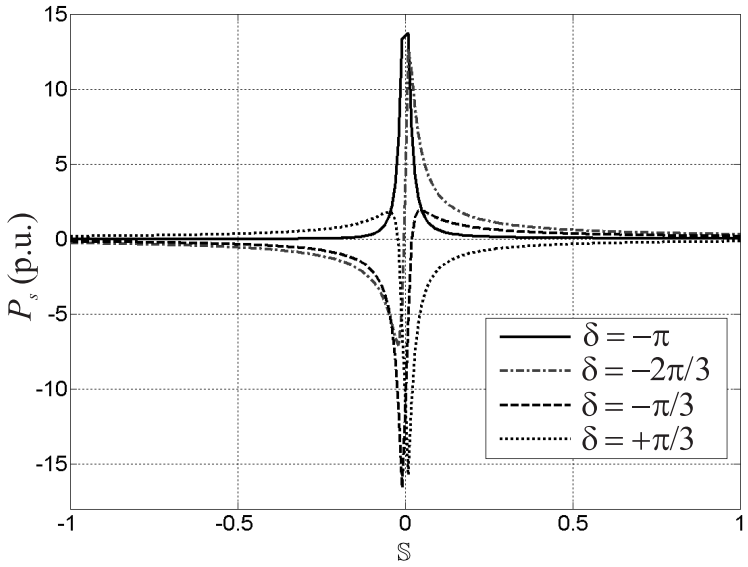

Figure 2.8 - Normalized stator power as a function of $\mathbb{S}$, δ is a parameter.

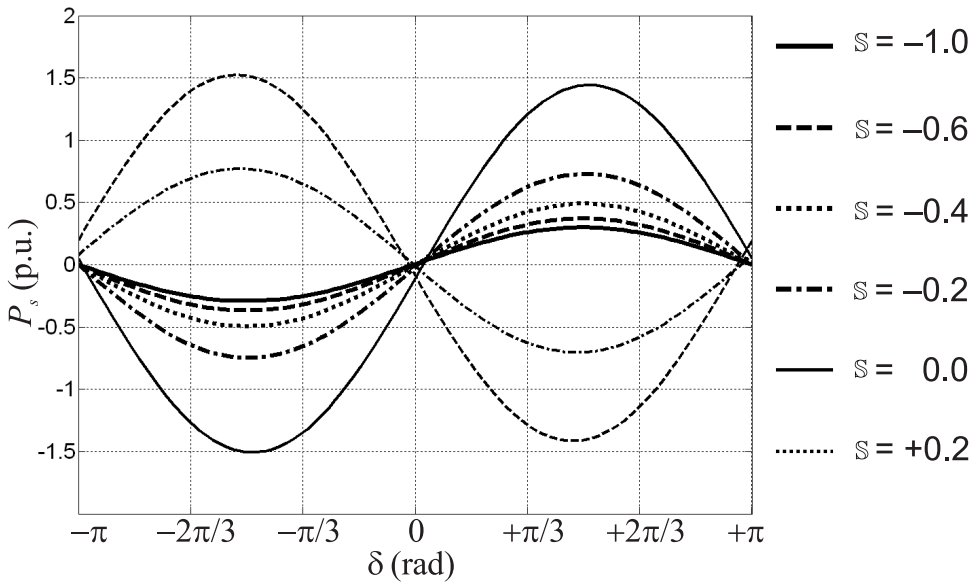

Figure 2.9 - Normalized stator power as a function of δ, $\mathbb{S}$ is a parameter.

Figure 2.8 and 2.9 show that the operating range of DFIG is wide, due to the high number of combinations of values assumed by $\mathbb{S}$ and δ. In the practice, the operating range of the machine is limited by applying several constrains: in particular the limits on mechanical stresses and temperature rise result in a limitation of the stator power flow [86]. For wind power applications, the stator power is related to the wind speed according to the power curve associated to the wind turbine (appendix C) [10, 93, 94].

By rearranging (2.26), the total electric power is expressed as function of stator power:

$$P_t = P_s + P_r = P_s - \mathbb{S}P_s = P_s(1 - \mathbb{S}) \tag{2.33}$$

Figure 2.10 to 2.13 show the stator, rotor and total electric power for different combinations of $\mathbb{S}$ and δ, according to (2.26), (2.31) and (2.33).

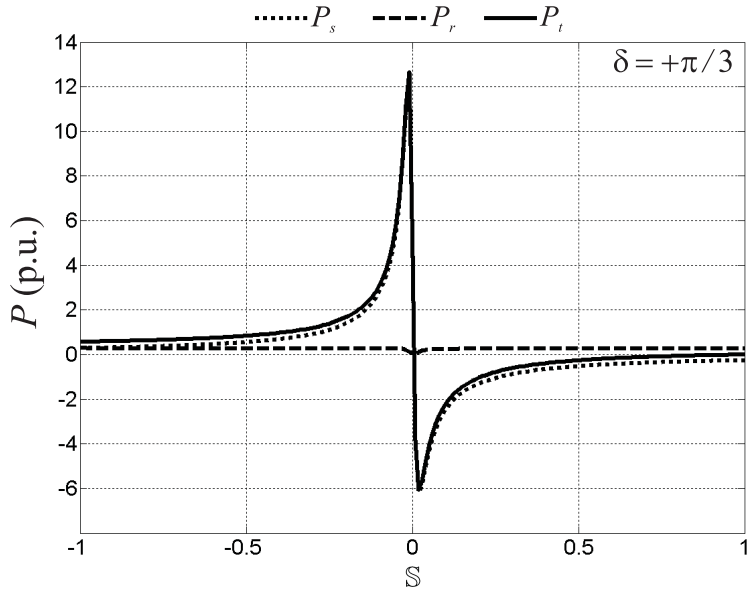

Figure 2.10 - Normalized stator, rotor and total powers as a function of $\mathbb{S}$, $\delta = +\pi/3$.

In Figure 2.10 and 2.11, the normalized stator, rotor and total power are plotted as function of $\mathbb{S}$ for two different values of δ. The rotor power P_r is always a small ratio of the power P_s, according to (2.27). The signs of P_r, P_s and $\mathbb{S}$ are related according to (2.26). For example, in Figure 2.10, for $\mathbb{S} > 0$, $P_s < 0$ results in $P_r > 0$.

In Figure 2.12 and 2.13, P_s, P_r and P_e are plotted as function of δ for two different values of $\mathbb{S}$. The signs and amplitude of P_r, P_s and $\mathbb{S}$ are related according to (2.26). For example, in Figure 2.12 where $\mathbb{S} = +0.4$, when $P_s = +0.8$, $P_r \approx -0.32 = +0.8 \cdot -0.4$.

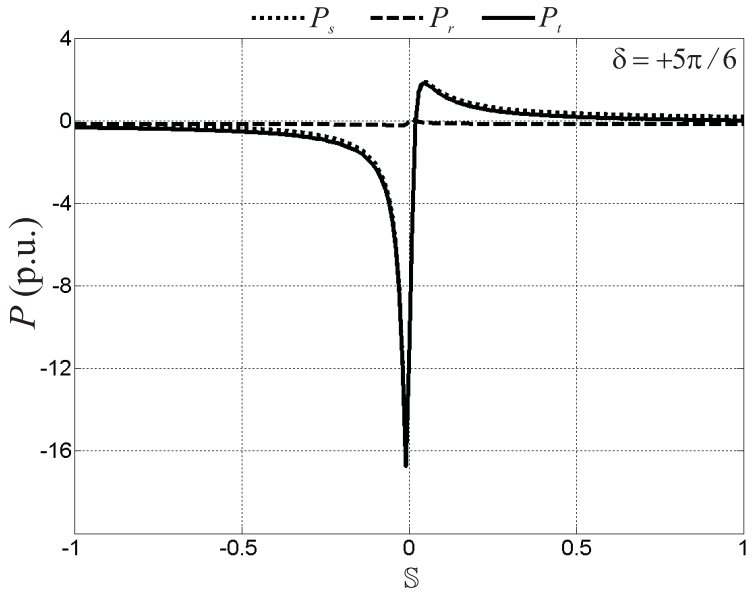

Figure 2.11 - Normalized stator, rotor and total powers as a function of $\mathbb{S}$, $\delta = +5\pi/6$.

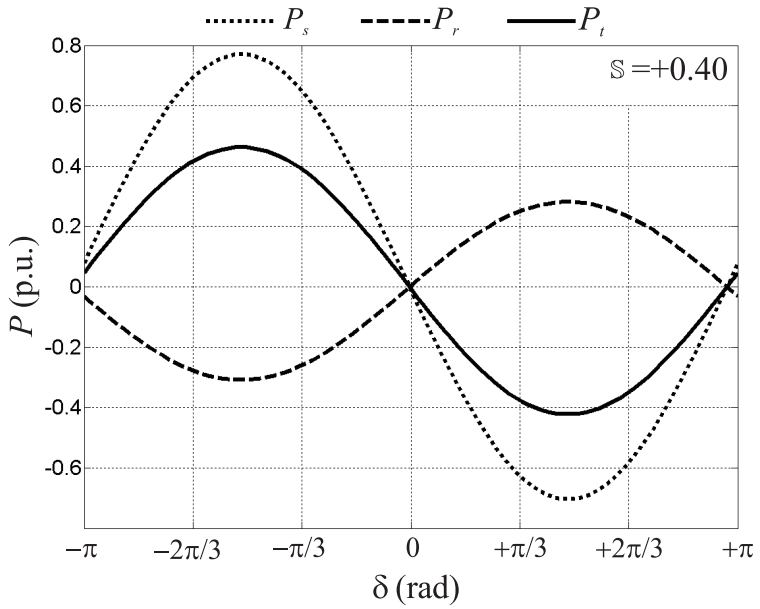

Figure 2.12 - Normalized stator, rotor and total powers as a function of δ, $\mathbb{S} = +0.40$.

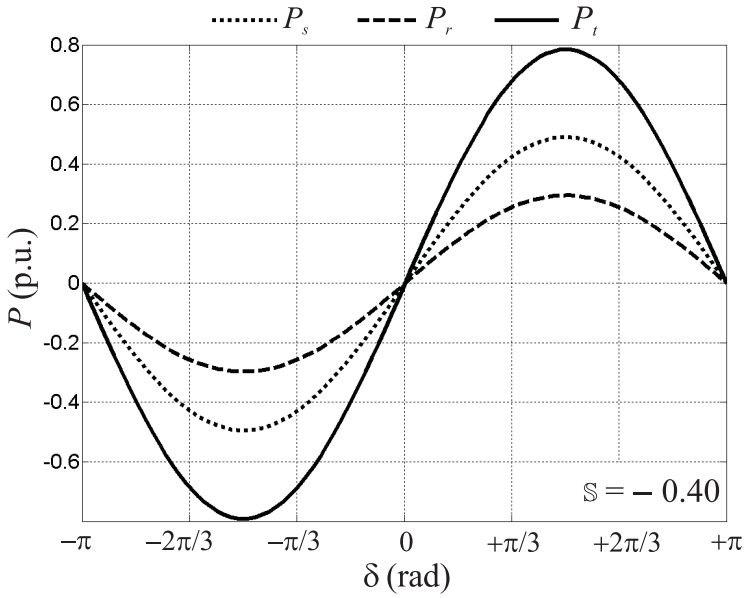

Figure 2.13 - Normalized stator, rotor and total powers as a function of δ, $\mathbb{S} = -0.40$.

The DFIG torque expression derived from (2.19) is:

$$T_e = \frac{P_{airgap}}{\omega_1} = \frac{P_s - \Delta P_s}{\omega_1} \tag{2.34}$$

By substituting (2.20) and (2.31) in (2.34), the torque is obtained as the sum of four components [85] (appendix 2.A):

$$T_e = T_s + T_r + T_{sr,cos}\cos\delta + T_{sr,\sin}\sin\delta \tag{2.35}$$

where:

$$T_s = V_s^2 \frac{R_r}{\mathbb{S}} \frac{1}{\omega_1 Z^2} \tag{2.36}$$

is the torque of the conventional induction machine;

$$T_r = -\Big(\frac{V_r}{\mathbb{S}}\Big)^2 R_s \frac{1}{\omega_1 Z^2} \tag{2.37}$$

is the torque due to rotor excitation;

$$T_{sr,cos} = -\frac{V_r}{\mathbb{S}}\, V_s \Big(\frac{R_r}{\mathbb{S}} - R_s\Big) \frac{1}{\omega_1 Z^2} \tag{2.38}$$

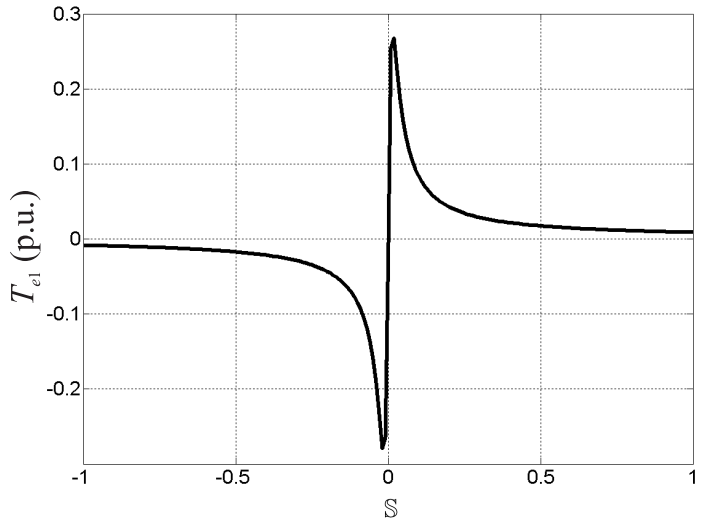

Figure 2.14 - First normalized torque component (2.35) as a function of $\mathbb{S}$ (This component is independent from δ).

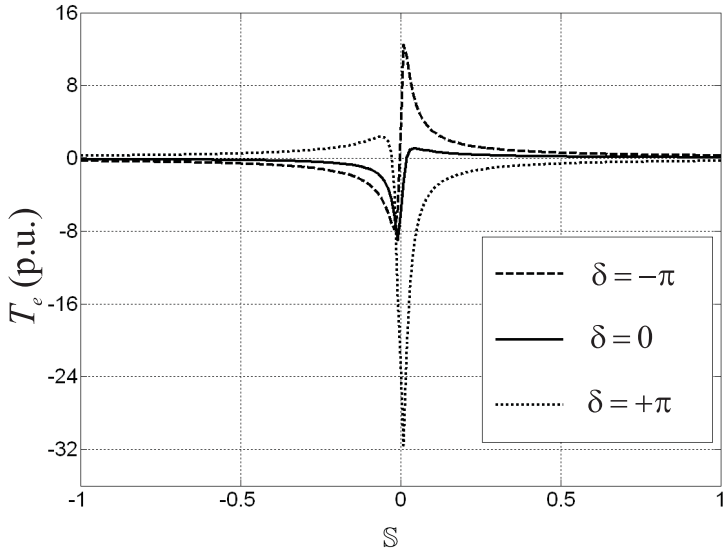

Figure 2.15 - Total normalized torque (2.35) as a function of $\mathbb{S}$, δ is a parameter

.

is the first component of the torque due to the interaction between the rotor and the stator;

$$T_{sr,sin} = -\frac{V_r}{\mathbb{S}} V_s X \frac{1}{\omega_1 Z^2} \tag{2.39}$$

is the second component of the torque due to the interaction between the rotor and the stator.

The first torque component as function of $\mathbb{S}$ is illustrated in Figure 2.14 and corresponds to the typical torque illustration for singly-fed machines: this component is independent of δ. The total torque is a function of both $\mathbb{S}$ (as the singly-fed machine) and δ, as exemplified by Figure 2.15.

2.4 DFIG operating modes

Four operating modes can be defined for the DFIG depending on the values of $\mathbb{S}$ and of δ and they are presented in Figure 2.16 [84, 85].

A reading-by-columns of Figure 2.16 shows the difference between operation as a motor or as a generator.

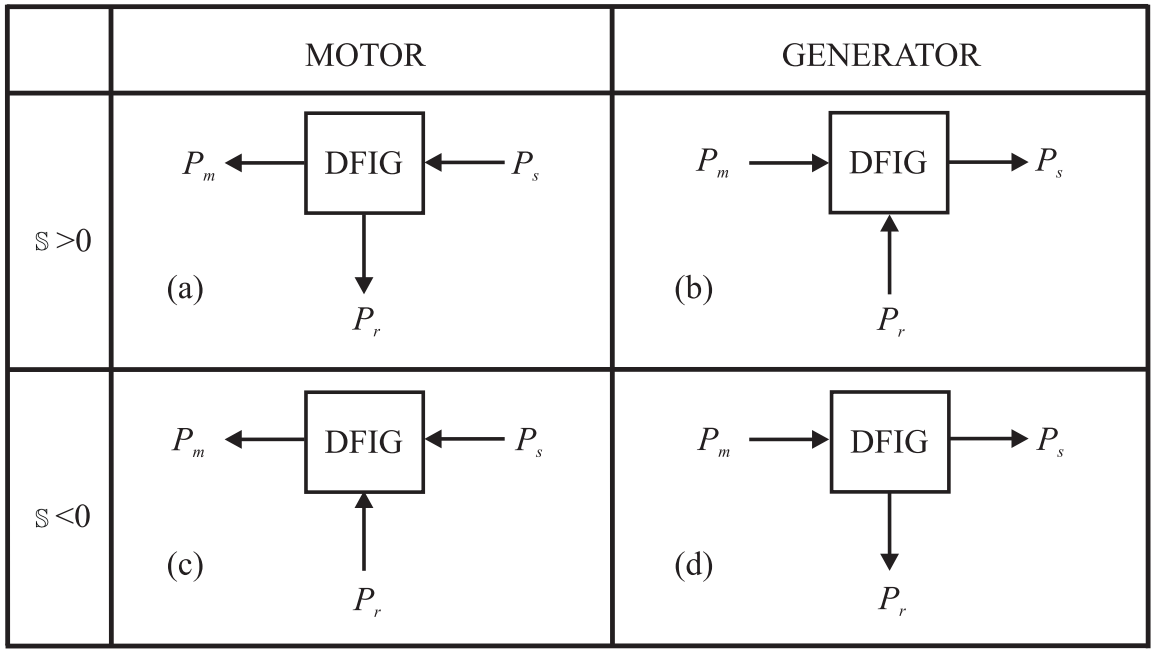

Figure 2.16 - The four operating modes for the DFIG: the operating modes depends on the value of the $\mathbb{S}$ and of δ, and result in variable directions for the stator, rotor and mechanical power flows.

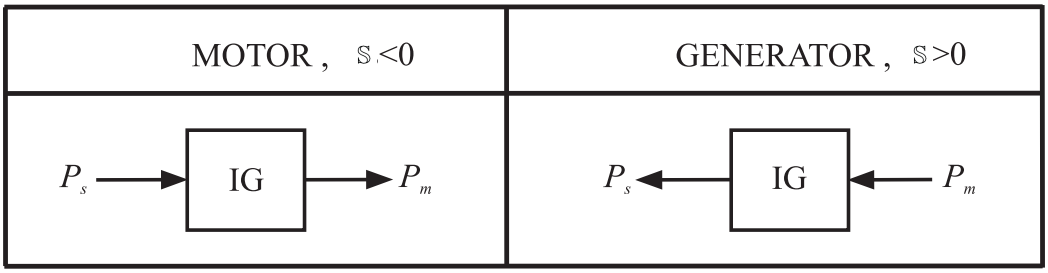

Figure 2.17 - The two operating for the singly-fed induction machine: motor and generator.

The second column of Figure 2.16 illustrates the two operating modes of the DFIG as a motor: for both $\mathbb{S} > 0$ and $\mathbb{S} < 0$, the power P_s is supplied by the grid to the stator and the mechanical power P_m is delivered to the shaft. The rotor power is positive if $\mathbb{S} < 0$ and negative if $\mathbb{S} > 0$, according to (2.26)[6].

The third column of Figure 2.16 describes the two operating modes of the DFIG as a generator: for both $\mathbb{S} > 0$ and $\mathbb{S} < 0$, the power P_s is delivered to the grid by the stator and the mechanical power P_m is supplied by the shaft. The rotor power is positive if $\mathbb{S} > 0$ and negative if $\mathbb{S} < 0$, according to (2.26).

A reading-by-rows of Figure 2.16 shows the effect of the slip sign on the DFIG operation.

The second line of Figure 2.16 illustrates that for $\mathbb{S} > 0$, motor operation is obtained if $P_s > 0$, and $P_r < 0$ results from (2.26); generation is obtained if $P_s < 0$ and $P_r > 0$. The sign of P_s is determined by the regulation of δ, according to (2.31). In the real-world applications, the power flow is adjusted by varying the real and imaginary components of the rotor voltage rather than with the control of the angle δ [82, 95][7].

The third line of Figure 2.16 indicates that for $\mathbb{S} < 0$, motor operation is obtained if $P_s > 0$ and $P_r > 0$; generation is obtained if $P_s < 0$ and $P_r < 0$.

The singly-fed induction machine allows only two operating modes: since $v_r = 0$, it results $P_r = 0$ for any value of $\mathbb{S}$. As explained in section 2.2.1, the singly-fed machine operating mode is determined by the value of $\mathbb{S}$ only, because δ does not appear as a variable. Motor operation corresponds to $P_s > 0$ and $P_m < 0$, generation corresponds to $P_s < 0$ and $P_m > 0$ [8]).

From the comparison of Figure 2.16 with Figure 2.17, one concludes that the higher

[6]In Figure 2.16, the stator power P_s is assumed positive if it is delivered from the turbine to the grid; the rotor power P_r is assumed positive if it is delivered from the RSC to the rotor.

[7]In chapter 4 it is shown that the rotor voltage components affect separately the active and the imaginary rotor power.

[8]Brake operation described in section 2.2.1 is not included in Figure 2.17

flexibility of the DFIG with respect to the singly-fed machine results from the introduction of an additional variable, the angle δ, that is controlled by rotor voltage modulation.

2.5 DFIG power curve for wind generation

The DFIG power curve for wind generation is obtained by coupling the turbine characteristics (Figure C.4.b) with the two generator modes presented in Figure 2.16. The resulting power curve for variable speed operation is shown in Figure 2.18 [84, 85, 96], where the normalized stator, rotor and total active power are shown as function of the normalized rotor speed. The trajectories are drawn under the assumption of ideal system.

The normalized stator active power trajectory (P_s/P_n) coincides with the turbine power curve shown in Figure C.4.b, since the stator active power is equal to the mechanical power extracted from the wind. The normalized rotor active power P_r/P_n is derived from the the stator power by applying (2.26). The sum of rotor power and stator power results in the normalized DFIG total power P_t/P_n.

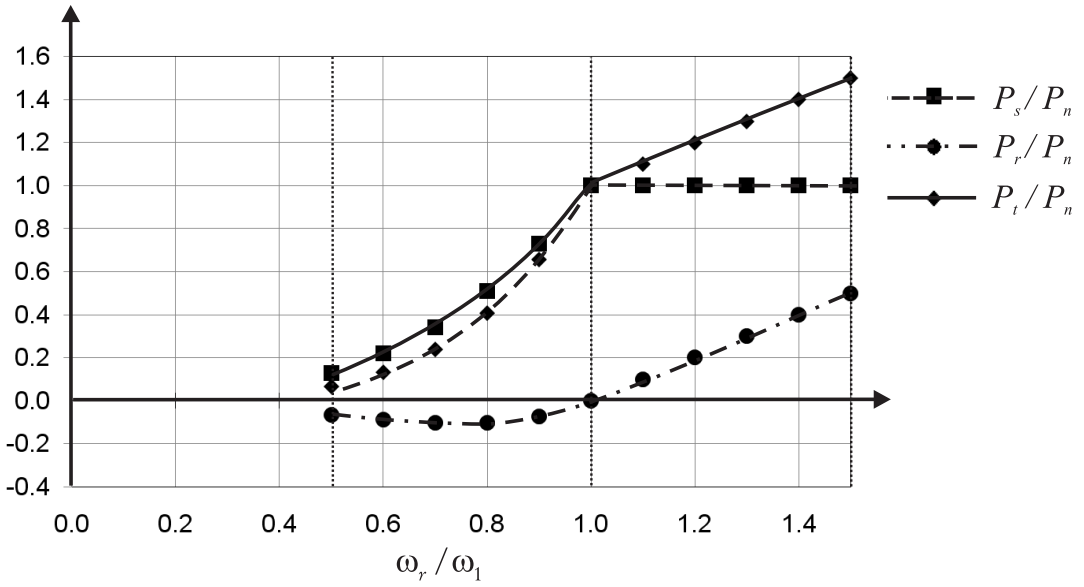

Figure 2.18 - DFIG power curve for variable speed wind generation: the normalized stator active power, rotor power and total power are shown as function of the normalized rotor speed. Base values are the DFIG rated power P_n and the synchronous speed ω_1.

For rotor speeds lower than the synchronous speed ($0.5 < \mathbb{S} < 1$), the stator power is positive and the rotor power is negative. This operating condition results in a total power

delivered to the grid lower than the mechanical power extracted from the wind by the turbine, because the rotor is absorbing power (Figure 2.16, operating mode (b)). The rotor power is a small fraction of the rated power at subsynchronous speeds, and the reduction of the overall power delivered is minimal [64].

For rotor speeds above the synchronous speed($1 < \mathbb{S} < 1.5$), both the stator and rotor active powers are positive and the total power delivered to the grid is higher than the DFIG rated power (Figure 2.16, operating mode (d)). The rotor contribution to the total power is significant because in the region $1 < \mathbb{S} < 1.5$ the stator is injecting full rated power. In particular, for $\mathbb{S} = 1.5$, $P_t = 1.5P_s$.

2.6 Conclusions

The DFIG operation in steady-state has been analyzed. The DFIG presents a more complex configuration than the traditional singly-fed machine, but the possibility to control power flow on the rotor side results in two significant advantages:

1. the DFIG can operate as a motor or as a generator for each value of slip;
2. the rotor power may significantly contribute to increase the power output at super-synchronous speeds.

Appendix 2.A - Derivation of expressions (2.31) and (2.35)

Stator power (2.31)

$$\begin{aligned} P_s &= \mathrm{Re}\{\overline{V}_s\overline{I}^*\} = V_s\ \mathrm{Re}\{\overline{I}^*\} = V_s\ \mathrm{Re}\{\overline{I}\} \\ &= V_s\ \mathrm{Re}\Big\{\frac{V_s - \dfrac{V_r\ [\cos\delta + j\sin\delta]}{\mathbb{S}}}{R + jX}\Big\} \\ &= \frac{V_s}{R^2+X^2}\mathrm{Re}\{(V_s - \frac{V_r}{\mathbb{S}}\ \cos\delta) - j\frac{V_r}{\mathbb{S}}\ \sin\delta)(R - jX)\} \\ &= \frac{V_s}{R^2+X^2}[RV_s - R\frac{V_r}{\mathbb{S}}\ \cos\delta) - X\frac{V_r}{\mathbb{S}}\ \sin\delta] \\ &= \frac{1}{Z^2}[RV_s^2 - RV_s\frac{V_r}{\mathbb{S}}\ \cos\delta - X\frac{V_s\ V_r}{\mathbb{S}}\ \sin\delta] \end{aligned}$$

Torque (2.35)

Starting from (2.34) and substituting (2.20):

$$T_e = \frac{P_{airgap}}{\omega_1} = \frac{P_s - \Delta P_s}{\omega_1} = \frac{P_s - R_s I^2}{\omega_1}$$

where

$$\begin{aligned}
I^2 &= \Big(\frac{V_s - \frac{V_r}{\mathbb{S}}\cos\delta - j\frac{V_r}{\mathbb{S}}\sin\delta}{R + jX}\Big)^2 \\
&= \frac{1}{R^2+X^2}\Big(RV_s - R\frac{V_r}{\mathbb{S}}\cos\delta - X\frac{V_r}{\mathbb{S}}\sin\delta + jXV_s - jX\frac{V_r}{\mathbb{S}}\cos\delta + jR\frac{V_r}{\mathbb{S}}\sin\delta\Big)^2 \\
&= \frac{1}{(R^2+X^2)^2}\Big[R^2V_s^2 + R^2\Big(\frac{V_r}{\mathbb{S}}\Big)^2\cos^2\delta \\
&\quad -X^2\Big(\frac{V_r}{\mathbb{S}}\Big)^2\sin^2\delta + X^2V_s^2 + X^2\Big(\frac{V_r}{\mathbb{S}}\Big)^2\cos^2\delta \\
&\quad +R^2\Big(\frac{V_r}{\mathbb{S}}\Big)^2\sin^2\delta - 2R^2\frac{V_rV_s}{\mathbb{S}}\cos\delta + 2RX\Big(\frac{V_r}{\mathbb{S}}\Big)^2\cos\delta\sin\delta - 2RX\frac{V_rV_s}{\mathbb{S}}\sin\delta - 2X^2\frac{V_rV_s}{\mathbb{S}}\cos\delta \\
&\quad -2RX\Big(\frac{V_r}{\mathbb{S}}\Big)^2\cos\delta\sin\delta + 2RX\frac{V_rV_s}{\mathbb{S}}\sin\delta\Big] \\
&= \frac{1}{(R^2+X^2)^2}[(R^2+X^2)V_s^2 + (R^2+X^2)\Big(\frac{V_r}{\mathbb{S}}\Big)^2 - 2(R^2+X^2)\frac{V_rV_s}{\mathbb{S}}\cos\delta] \\
&= \frac{1}{R^2+X^2}[V_s^2 + \Big(\frac{V_r}{\mathbb{S}}\Big)^2 - 2\frac{V_rV_s}{\mathbb{S}}\cos\delta]
\end{aligned}$$

Using the results for P_s and I^2 in the torque expression (2.35) becomes:

$$\begin{aligned}
T_e &= \frac{P_s - R_sI^2}{\omega_1} \\
&= \frac{1}{\omega_1}\frac{1}{R^2+X^2}[RV_s^2 - R\frac{V_sV_r}{\mathbb{S}}\cos\delta - X\frac{V_sV_r}{\mathbb{S}}\sin\delta - R_s(V_s^2 + \Big(\frac{V_r}{\mathbb{S}}\Big)^2 - 2\frac{V_rV_s}{\mathbb{S}}\cos\delta)] \\
&= \frac{1}{\omega_1 Z^2}[RV_s^2 - R\frac{V_sV_r}{\mathbb{S}}\cos\delta - X\frac{V_sV_r}{\mathbb{S}}\sin\delta - R_sV_s^2 - R_s\Big(\frac{V_r}{\mathbb{S}}\Big)^2 + 2R_s\frac{V_rV_s}{\mathbb{S}}\cos\delta] \\
&= \frac{1}{\omega_1 Z^2}[\frac{R_r}{\mathbb{S}}V_s^2 - R_s\Big(\frac{V_r}{\mathbb{S}}\Big)^2 - X\frac{V_sV_r}{\mathbb{S}}\sin\delta + \Big(R_s - \frac{R_r}{\mathbb{S}}\Big)\frac{V_sV_r}{\mathbb{S}}\cos\delta]
\end{aligned}$$

The last equation leads to the four torques (2.36)-(2.39).

Part II

Harmonic Compensation: Steady-state Analysis

Introduction to Part II

The following chapters deal with the control system design and with the steady-state operation of a WECS used as power generator and Active Filter simultaneously.

Chapter 3 describes the concept of harmonic compensation by using the WECS components and presents the effect on the proposed application in terms of power loss and voltage distortion; chapters 4-6 describe the control system that allows 'compensation by means of RSC modulation', 'compensation by means of LSC modulation' and 'compensation by means of combined modulation', respectively.

For each compensation method, simulation results in steady-state operation are presented, including current and voltage oscillograms and spectra, power loss as a function of the rotor speed, derating curves and Total Harmonic Distortion (THD) values.

Chapter 3

Principles of Harmonic Compensation by Means of a WECS and DFIG Derating

3.1 Introduction

Recent developments in power electronics paved the road for additional applications of WECS in addition to power generation. Such applications are named 'ancillary services' [15, 22, 97, 98]. Harmonic compensation is an ancillary service and in the following sections the principles regulating the use of a specific WECS as harmonic compensator are presented.

The system under study is shown in Figure 3.1:

- The DFIG is connected to the grid by means of a RSC and a LSC (Type C configuration, chapter 1).
- A Non-Linear Load (NLL) injecting harmonic currents is connected to the same PCC[9] through a line with resistance R_h and inductance L_h.
- A step-up transformer allows the connection of the WECS to the distribution or transmission line.
- The power grid is represented by its Thevenin equivalent circuit; the parameters of the Thevenin circuit are the voltage source V_g supplying electric power at fundamental frequency f_1, the line series resistance R_g and inductance L_g[10].
- The line that connects the stator terminals to the PCC is described by the parameters R_c and L_c.

[9] IEEE Standard 519 [25, 26] defines the PCC as a point where multiple customers may be fed from the same distribution point by the utility.

[10] In the present work, the grid equivalent parameters R_g and L_g include the transformer winding resistance and equivalent inductance and therefore the transformer presented in Figure 3.1 is ideal.

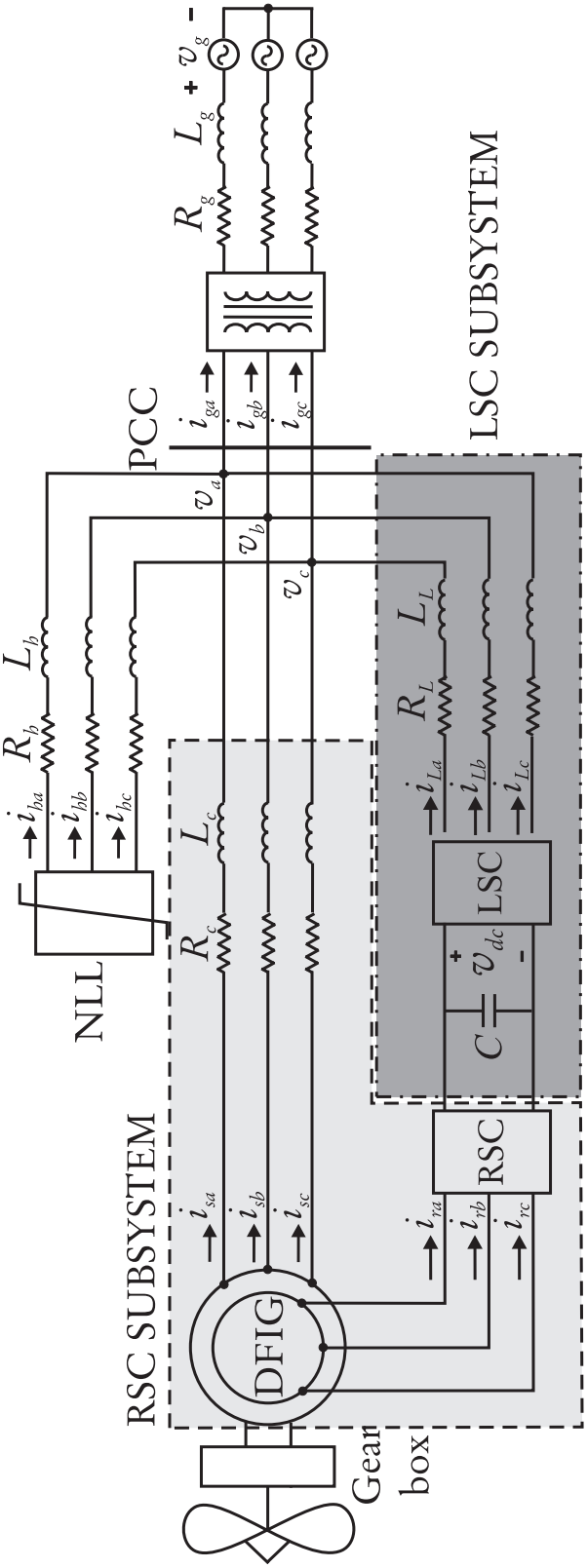

Figure 3.1 - The studied system: a DFIG and a non linear load (NLL) connected to the same point of common coupling (PCC) to the power system.

- The line that connects the LSC terminals to the PCC is described by the parameters R_L and L_L.

According to the configuration shown in Figure 3.1, the grid currents $i_{g,abc}$ contain harmonic components injected by the NLL. The presence of harmonic components in the grid current is common in modern power systems, because in the last decades the amount of harmonic pollution has been increasing due to the proliferation of non linear or time varying loads[11] [34, 99].

The presence of harmonic currents is detrimental for the grid operation, because they cause overheating of supply transformers and of line cables, fatigue or premature failure of drive line fuses, nuisance, tripping of drive circuit breakers and voltage distortion [100]. Due to these effects, international standards [25, 26] place limits on the harmonic currents content in the grid current.

Different solutions for sinking harmonic currents have been proposed [101, 102, 103, 104]. In the last few decades Active Filters (AFs) have become more popular due to the progress in power switching devices technology and more reliable control algorithms [99, 105]. The three-phase inverter [34] is the most common topology of AF [99, 106, 107, 108].

Two compensation methodologies to obtain the cancellation of the harmonic currents $i_{h,abc}$ on the grid side by using a WECS are described in the following sections:

- **Compensation by means of RSC modulation**. The DFIG is used as an AF: the stator windings inject currents $i_{s,abc}$ equal in magnitude and 180^o out of phase with respect to the currents $i_{h,abc}$ injected by NLL, according to the notation shown in Figure 3.1. The stator currents are regulated by controlling the RSC voltage [28, 29, 30, 31, 109, 110]. In [32] it is stated 'it is not clear what are the long term consequences of using the DFIG for harmonic and reactive power compensation'. One of the scope of the present work is to address this concern and to provide an analysis of the effects of harmonic voltages and currents on the DFIG.

- **Compensation by means of LSC modulation**. The LSC is used as 'classical' AF and the currents injected by the the LSC terminals $i_{L,abc}$ are equal to the currents $i_{h,abc}$ injected by NLL, according to the notation shown in Figure 3.1. In the conventional applications of the three-phase inverter as AF [99, 106, 107, 108, 111], a dc voltage source is connected to the dc side. In the proposed application, the LSC is connected back to back to the RSC by means of a dc-link.

[11] In the present work, NLLs include any kind of loads injecting harmonic currents, independently of the mechanism that generates them.

The use of a WECS as an harmonic compensator causes power loss increase in the DFIG and in the power converters. DFIG derating is necessary to reduce the power loss by limiting the fundamental power flow in the WECS components. The second part of this chapter deals with DFIG derating and its application in WECS.

3.2 Compensation by means of RSC modulation

3.2.1 Rotor voltage expression

The objective of this section is to determine the rotor voltage v_r impressed by the RSC that results in harmonic stator currents $i_{sh,abc}$ equal in magnitude and 180^o out of phase with respect to the NLL currents $i_{h,abc}$ (Figure 3.1). In order to accomplish this result, successive simplifications are applied to the circuit of Figure 3.1.

The system shown in Figure 3.1 is first simplified as illustrated in Figure 3.2: the power converters that feed the DFIG rotor are replaced by an independent and controlled voltage source.

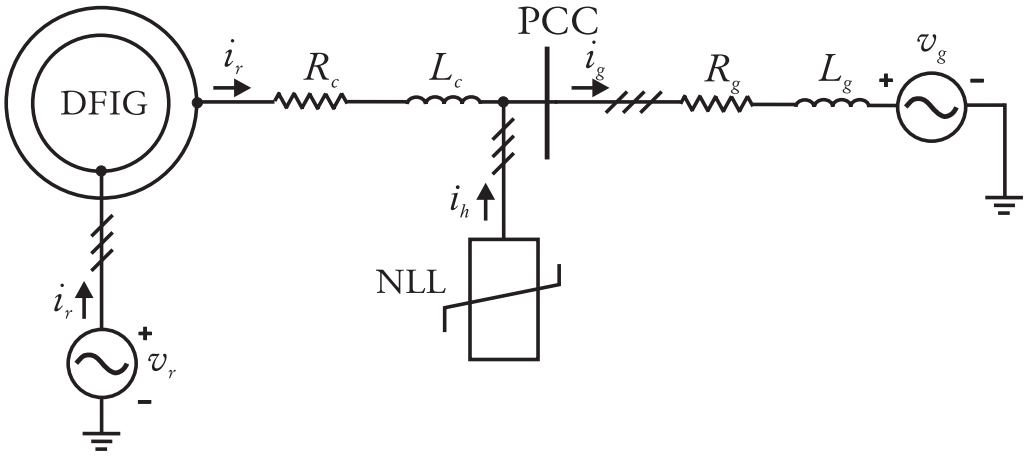

Figure 3.2 - Simplified system for the study of compensation by means of RSC modulation.

The steady state equivalent circuit of the system shown in Figure 3.2 for the h^{th}-order harmonic is depicted in Figure 3.3:

- The DFIG is represented by the steady state equivalent circuit described in chapter 2; the machine reactances are computed for the h^{th}-order harmonic.
- The NLL is represented by the phasor current source $\overline{I}_h$.

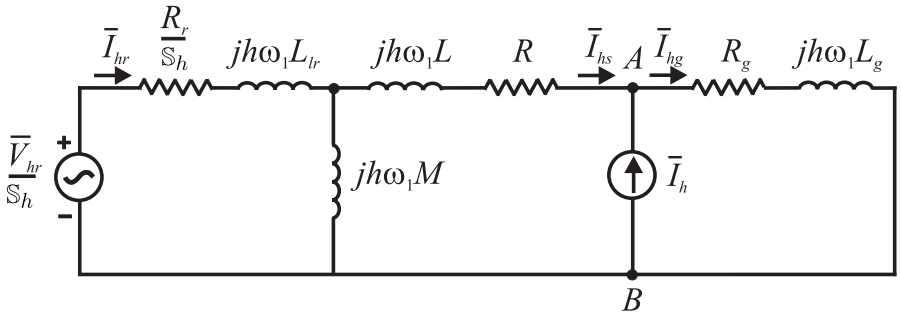

Figure 3.3 - Steady state equivalent circuit of the system shown in Figure 3.2 for the h^{th}-order harmonic.

- The supply voltage $\overline{V}_g$ at fundamental frequency f_1 is not shown since at harmonic h the voltage source $\overline{V}_g$ is a short circuit.
- The equivalent resistance R and inductance L are defined as follows: $R = R_s + R_c$ and $L = L_s + L_c$ (R_s and L_s are the stator resistance and inductance respectively, chapter 2).

If the following condition is fulfilled:

$$\overline{I}_{sh} = -\overline{I}_h \tag{3.1}$$

the grid current is sinusoidal at fundamental frequency and the harmonic current $\overline{I}_{gh}$ in the circuit shown in Figure 3.3 is nil.

The use of the Thevenin equivalent representation of the DFIG results in a further simplification of the circuit shown in Figure 3.3. The components on the left hand side are replaced by an equivalent impedance Z_T and by an equivalent power source V_T as shown in Figure 3.4.

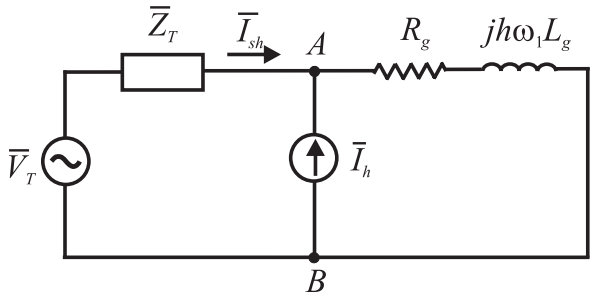

Figure 3.4 - Steady state equivalent circuit of the system shown in Figure 3.2 for the h order harmonic: the DFIG is replaced by its Thevenin equivalent circuit.

The Thevenin equivalent impedance $\overline{Z}_T$ and voltage source $\overline{V}_T$ are obtained according to the following expressions:

$$\overline{Z}_T = (R + j\omega_1\ hL) + \frac{j\omega_1 hM(\frac{R_r}{\mathbb{S}_h} + j\omega_1 hL_{lr})}{\frac{R_r}{\mathbb{S}_h} + j\omega_1 h(M + L_{lr})} \tag{3.2}$$

$$\overline{V}_T = \frac{j\omega_1 hM}{\frac{R_r}{\mathbb{S}_h} + j\omega_1 h(M + L_{lr})} \frac{\overline{V}_{rh}}{\mathbb{S}_h} \tag{3.3}$$

As already observed in chapter 2, $M >> L_{lr}$ in the practical machines and (3.2) and (3.3) can be approximated as follows:

$$\overline{Z}_T \approx (R + \frac{R_r}{\mathbb{S}_h}) + j\omega_1 h(L + L_{lr}) = R_T + jhX_T \tag{3.4}$$

where

$$R_T = R + \frac{R_r}{\mathbb{S}_h} \text{ and } X_T = \omega_1(L + L_{lr})$$

and

$$\overline{V}_T \approx \frac{\overline{V}_{rh}}{\mathbb{S}_h} \tag{3.5}$$

Figures 3.3 and 3.4 are used to determine the relation between the harmonic rotor voltage $\overline{V}_{rh}$ and the harmonic current $\overline{I}_h$. Applying Kirchhoff voltage law to the external loop and assuming that no harmonic current is flowing in R_g and $j\omega hL_g$, the following expression is obtained:

$$\overline{V}_T = \overline{Z}_T \overline{I}_h \tag{3.6}$$

Substitution of (3.5) in (3.6) yields to the approximated relation:

$$\frac{\overline{V}_{rh}}{\mathbb{S}_h} \approx \overline{Z}_T \overline{I}_h \tag{3.7}$$

If both sides of (3.7) are multiplied by $\mathbb{S}_h$ the following is obtained:

$$\overline{V}_{rh} \approx \overline{Z}_T\ \overline{I}_h \mathbb{S}_h \tag{3.8}$$

Substitution of (3.4) in (3.8) gives the expression of the harmonic voltage $\overline{V}_{rh}$ at the

RSC terminals:

$$\overline{V}_{rh} \approx [(R + \frac{R_r}{\mathbb{S}_h}) + j\omega_1 h(L + L_{lr})]\ \overline{I}_h \mathbb{S}_h = \overline{Z}_T \overline{I}_h \mathbb{S}_h \tag{3.9}$$

The voltage (3.9) is obtained by the switching operation of the RSC solid state devices. Different strategies can be used to control the switches operation: in the present work, PWM is assumed and the principles of this method are summarized in appendix H.

In order to verify the feasibility of the proposed approach, the value of $\overline{V}_{rh}$ is normalized with respect to the rated stator voltage. Under the assumption $M >> L_s, L_r$, the rated stator voltage is as follows [76]:

$$\overline{V}_{sn} \approx [(R_s + \frac{R_r}{\mathbb{S}_n}) + j\omega_1 (L_{ls} + L_{lr})]\overline{I}_{sn} \tag{3.10}$$

where $\overline{I}_{sn}$ is the stator rated current.

The magnitudes of the harmonic rotor voltage and of the rated stator voltage are obtained from (3.9) and (3.10):

$$V_{rh} \approx \sqrt{[R_s + \frac{R_r}{\mathbb{S}_h}]^2 + \omega_1^2\ h^2 (L_{ls} + L_{lr})^2} I_h \mathbb{S}_h = \sqrt{R_T^2 + h^2 X_T^2} I_h \mathbb{S}_h \tag{3.11}$$

$$V_{sn} \approx \sqrt{[R_s + \frac{R_r}{\mathbb{S}_n}]^2 + \omega_1^2 (L_{ls} + L_{lr})^2} I_{sn} \tag{3.12}$$

The ratio between (3.11) and (3.12) is as follows:

$$\frac{V_{rh}}{V_{sn}} \approx \sqrt{\frac{R_T^2 + h^2 X_T^2}{[R_s + \frac{R_r}{\mathbb{S}_n}]^2 + \omega_1^2 (L_{ls} + L_{lr})^2}} \frac{I_h}{I_{sn}} \mathbb{S}_h \tag{3.13}$$

This result quantifies the magnitude of the harmonic rotor voltage with respect to the rated stator voltage. An example allows understanding the practical implementations of the above analysis.

Example 3.I - Magnitude of rotor harmonic voltage V_{rh} for single harmonic current injected by the NLL

The magnitude of the rotor harmonic voltage is calculated according to (3.13); in Figure 3.5 the harmonic rotor voltage magnitude is shown as function of the fifth harmonic current I_{s5} for the extreme slip values $\mathbb{S} = \pm 0.5$. Similar results are presented in Figure 3.6 where

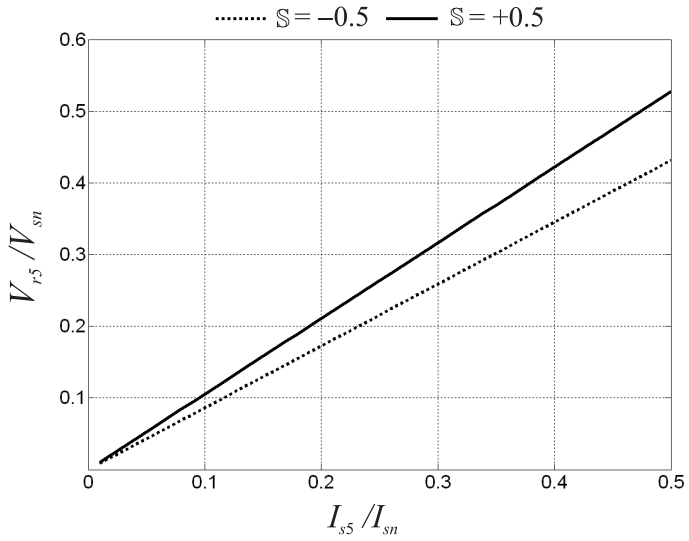

Figure 3.5 - Example 3.I: Rotor voltage V_{r5} as function of harmonic current I_{s5}, according to (3.13), for two values of $\mathbb{S}$.

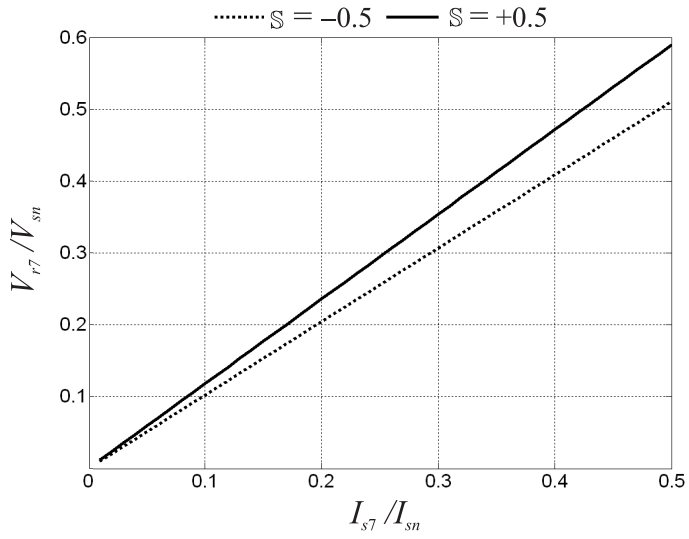

Figure 3.6 - Example 3.I: Rotor voltage V_{r7} as function of harmonic current I_{s7}, according to (3.13), for two values of $\mathbb{S}$.

a seventh harmonic current injection is assumed.

As expected from (3.8), for higher harmonic current injection, the magnitude of the corresponding rotor voltage component increases. The trajectories presented in Figure 3.6 are higher than the ones presented in Figure 3.5 since the equivalent line and windings reactances increases with the harmonic order.

The results shown in Figure 3.5 and obtained by means of the study of the equivalent circuits are confirmed by simulations of the wind power plant shown in Figure 3.1 with the parameters listed in appendix A.

A fifth harmonic current I_5/I_{sn}=0.2 is injected by the NLL and ω_r/ω_1=1.5. The rotor voltage spectrum is shown in Figure 3.7. Two main voltage components are identified:

1. The fundamental rotor voltage component corresponding to the fundamental stator voltage. The frequency of the rotor voltage harmonic component is $f_{r1} = \mathbb{S} \cdot f_1 = 0.5 \cdot 60 = 30$ Hz. The amplitude of the normalized fundamental rotor voltage component is 0.5 p.u.. This result agrees with the analysis described in chapter 2 where it has been proved that $V_{r1} = \mathbb{S}_{max}\ V_{s1} = 0.5 \cdot 1 = 0.5$.

2. The fifth harmonic rotor voltage component. The frequency of the rotor voltage harmonic component is a function of the fifth-order slip. Being for the case study ω_r/ω_1=1.5, it results $\mathbb{S}_5 = 0.7$. Therefore, the stator fifth harmonic component corresponds to the rotor frequency: $f_{r2} = \mathbb{S} \cdot f_5 = 0.7 \cdot 300 = 210$ Hz. The amplitude is approximately 0.2 (p.u.): this result is very close to the value shown in Figure 3.5. Perfect correspondence is not expected since some approximations have been used to carry out (3.13).

3.2.2 Voltage distortion at the DFIG stator and rotor terminals

When the DFIG displayed in Figure 3.1 is used as AF, two different contribution to voltage distortion are identified. Low frequency distortion is produced by the harmonic current components injected by the NLL, and high frequency distortion is generated by the power converter operation. The stator peak voltage $\hat{V}_s$ caused by low frequency harmonic components is calculated by referring to the equivalent circuit at harmonic h depicted in Figure 3.8. The harmonic voltage at the PCC is zero assuming that the grid current is sinusoidal at fundamental frequency. According to compensation by RSC modulation, harmonic currents flow in the line that connects the stator to the PCC causing harmonic voltage drop $\Delta\overline{V}_h$.

The amplitude of the harmonic stator voltage $\overline{V}_{sh}$ at the stator terminals is found by applying Kirchhoff voltage law and by ignoring the line resistance that is several orders of

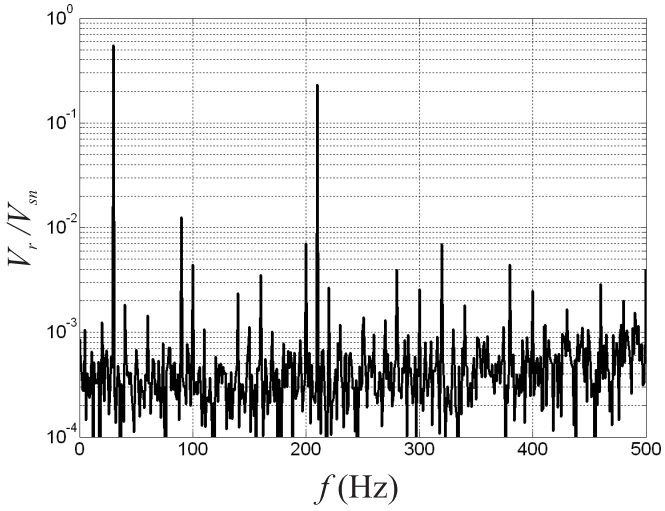

Figure 3.7 - Example 3.I: Normalized line-to-line rotor voltage spectrum, for I_5/I_{sn}=0.2 and $\omega_r/\omega_1 = 1.5$.

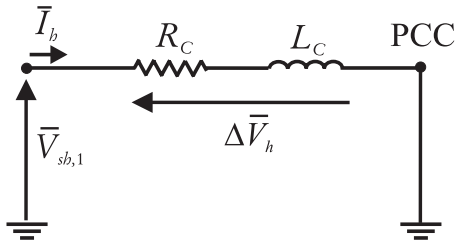

Figure 3.8 - Equivalent circuit for the calculation of the stator harmonic voltage due to low harmonic components.

magnitude smaller than the reactance:

$$V_{sh} = \Delta V_h = X_{ch} I_h = h X_c I_h \tag{3.14}$$

The amplitude of the harmonic stator voltage due to different harmonic current is calculated in Table 3.1 by applying (3.14) and assuming $X_c/Z_n = 0.05$

Table 3.1 - Stator harmonic voltage for different harmonic currents, according to (3.14) and assuming a line impedance X_c/Z_n= 0.05.

Harmonic index h	Harmonic current amplitude	Peak harmonic stator voltage
h=5	$I_5/I_s = 1/5$	$\hat{V}_5/V_s = 0.05$
h=7	$I_7/I_s = 1/7$	$\hat{V}_7/V_s = 0.05$
h=0.05	$I_{0.05}/I_s = 1/10$	$\hat{V}_{0.05}/V_s \approx 2.5 \cdot 10^{-3}$
h=7.5	$I_{7.5}/I_s = 1/10$	$\hat{V}_{7.5}/V_s \approx 0.0375$

Table 3.1 shows that the contribution of the subsynchronous interharmonics ($h < 1$) to the harmonic stator voltage amplitude is small, because the value of the line reactance is proportional to the harmonic order. The higher order interharmonics, on the contrary, may cause a significant voltage distortion at the stator terminals.

In the most conservative case, the harmonic voltage peaks are aligned and the harmonic stator peak voltage $\hat{V}_{sh,1}$ is obtained as follows:

$$\hat{V}_{sh,1} = \sum_h \hat{V}_h \tag{3.15}$$

Substituting in (3.15) the values listed in Table 3.1, the following is obtained:

$$\frac{\hat{V}_{sh,1}}{V_{sn}} = \frac{\hat{V}_1 + \sum_{h \neq 1} V_h}{V_{ns}} \approx 1.14 \text{ p.u.} \tag{3.16}$$

The last result show that the stator peak voltage may be significantly higher than the rated voltage. As a result, if compensation by means of RSC modulation is implemented, it results that the stator winding insulation should be chosen in function of the amplitude and order of the harmonic currents injected by the NLL.

The second contribution to stator voltage distortion is caused by high frequency harmonic components due to the RSC switches operation: the mutual coupling between stator windings and rotor windings causes transmission of the rotor current harmonics to the stator

windings.

The amplitude of the high frequency switching component are quantified by using the equivalent circuit shown in Figure 3.3 at the switching frequency f_{tri}=6480 Hz. A rough estimate of the stator high frequency voltage distortion is obtained by observing that at switching frequency:

- $\mathbb{S}_h \approx 1$,
- the stator, rotor and line resistances are negligible with respect to the impedances,
- the magnetizing impedance acts as an open circuit because is much higher than the stator, rotor and line impedances.

By applying the above simplifications, the following expression for the peak stator harmonic voltage as function of the peak rotor harmonic voltage is carried out:

$$\hat{V}_{sh,2} = \frac{L_{lc}}{L_{ls} + L_{lr}} \hat{V}_{rh} \approx 0.12 \hat{V}_{rh} \tag{3.17}$$

The quantification of the rotor peak voltage is simpler than the stator peak voltage. According to the theory of PWM, the peak rotor voltage is a function of the dc-link voltage v_{dc} as follows:

$$V_{LLr} = \frac{m_a}{2\sqrt{2}} v_{dc}, \tag{3.18}$$

where $0< m_a <1$ is the amplitude modulation index (appendix H).

For the configuration presented in Figure 3.1, the dc-link voltage amplitude is practically constant[12][89]. Therefore, the peak rotor voltage can be immediately quantified, since it is not a function of the harmonic currents injected by the NLL.

3.3 Compensation by means of LSC modulation

The second compensation concept consists in the use of the LSC as an AF: for each harmonic h, the current injected by the LSC is equal and 180^o out of phase with respect to the current injected by the NLL; referring to the notation of Figure 3.1 the following formulation is obtained:

$$i_{Lh} = -i_h \tag{3.19}$$

[12]The control systems for the dc-link voltage control is described in section 4.5.1

The objective of this section is to determine the value of the voltage v_{Lh} impressed at the LSC terminals to obtain the harmonic current i_{Lh}. This result is obtained by applying simplifications to the system studied in Figure 3.1 similar to the ones presented in section 3.2.1.

At first, the system shown in Figure 3.1 is simplified in the one-line diagram presented in Figure 3.9:

- the LSC converter is replaced by a controlled voltage source v_L injecting the current i_L.
- the DFIG is not shown because it does not participate in the compensation of the harmonic currents i_h;

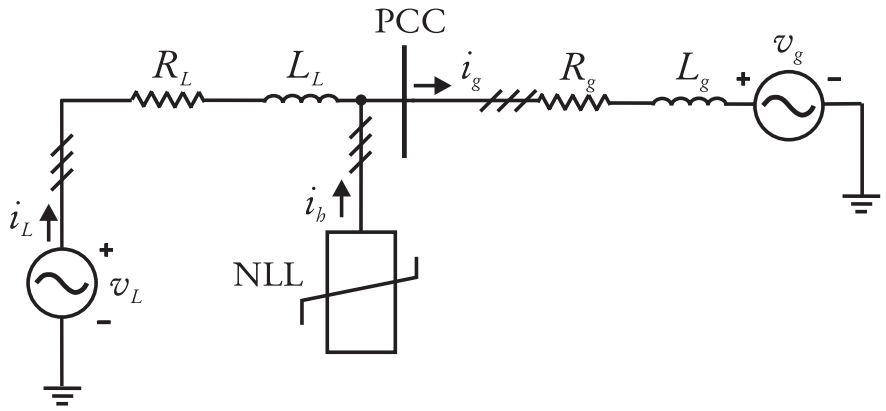

Figure 3.9 - The elementary system for compensation by means of LSC modulation.

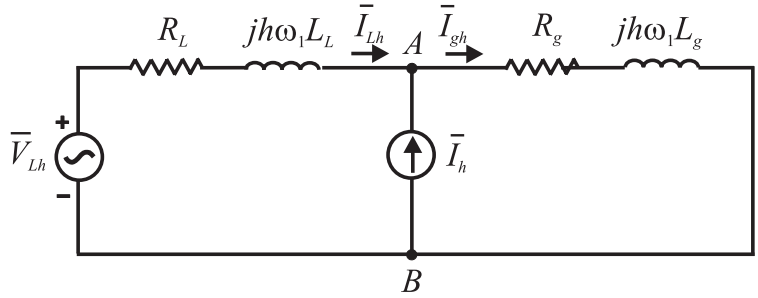

Figure 3.10 - Steady state equivalent circuit of the system shown in Figure 3.9 for the h order harmonic.

The steady state equivalent circuit at harmonic h for the system shown in Figure 3.9 is drawn in Figure 3.10:

- The NLL is represented by the current source $\overline{I}_h$.
- The supply voltage at fundamental frequency f_1 is not shown since at harmonic h the voltage source $\overline{V}_g$ is a short circuit.

If the following condition is fulfilled:

$$\overline{I}_{Lh} = -\overline{I}_h \tag{3.20}$$

the grid current is sinusoidal at fundamental frequency and the harmonic current $\overline{I}_{gh}$ in the circuit shown in Figure 3.10 is nil. The converter harmonic voltage V_{Lh} is obtained by applying Kirchhoff voltage law (Figure 3.10): :

$$\overline{V}_{Lh} = Z_L \overline{I}_h \tag{3.21}$$

where $\overline{Z}_L = R_L + jh\ \omega_1 L_L$. The last expression teaches that the LSC harmonic voltage is equal to the harmonic voltage drop measured between the PCC and the LSC terminals: Example 3.II allows visualizing this result. The fundamental LSC voltage $\overline{V}_{L1}$ is a function of the active power flowing in the LSC to/from the DFIG rotor.

The LSC solid state devices are controlled by means of PWM modulation and the amplitude of the LSC peak voltage is function of the dc-link voltage amplitude v_{dc}, as expressed in (3.17).

When compensation by means of LSC modulation is applied, the stator and rotor voltage distortion is due only to the switches operation, and the amplitudes of the high harmonic voltage components are expressed by (3.17)-(3.18).

Example 3.II: Line-to-line LSC voltage oscillogram and spectrum when compensation by means of LSC modulation is applied

A fifth harmonic current is injected by the NLL, with amplitude $I_5/I_{sn} = 0.2$ and ω_r/ω_1=0.5. The LSC voltage oscillogram and spectrum are shown in Figures 3.11 and 3.12 respectively. The LSC voltage oscillogram is the typical output of a three-phase inverter controlled by means of PWM; the spectrum is dominated by a fundamental and a fifth harmonic. (figures should be LSC not VR)

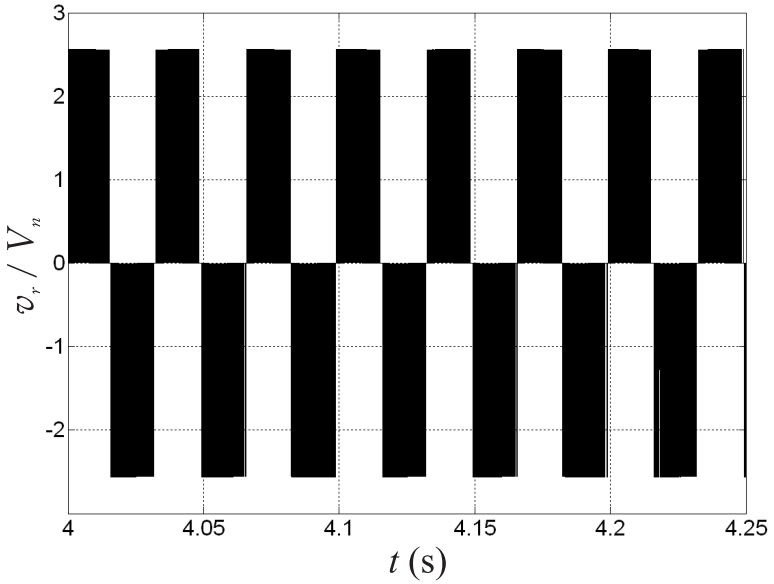

Figure 3.11 - Example 3.II: Line-to-line normalized LSC voltage oscillogram for I_5/I_{sn}=0.2 and ω_r/ω_1=1.5.

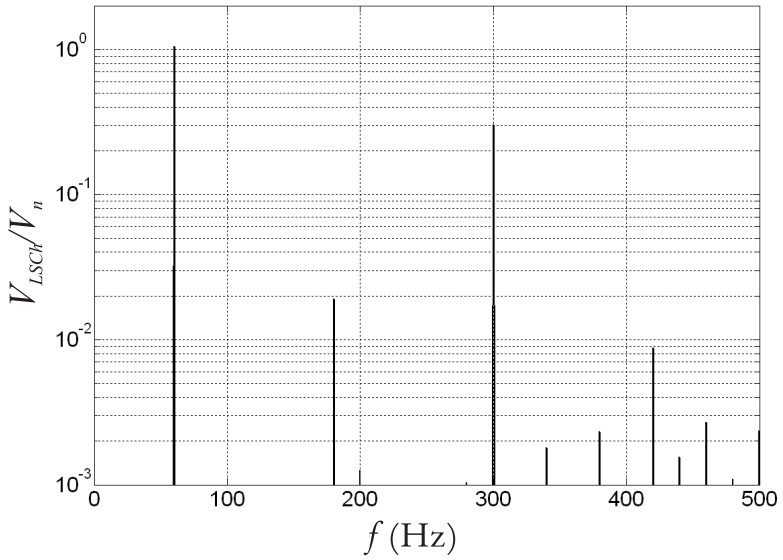

Figure 3.12 - Example 3.II: Line-to-line LSC voltage spectrum for I_5/I_{sn}=0.2 and ω_r/ω_1=1.5.

3.4 DFIG derating

When compensation by means of RSC modulation is applied, the harmonic currents flow in the stator and rotor windings causes additional power loss and temperature increase with respect to rated operation[13]. Due to the skin effect [90, 112], the stator and rotor resistance increases with the harmonic order, thus resulting in higher power loss and temperature rise. Operating the machine at temperature above the rated results in rapid insulation degradation and the reduction of the insulation life-time [76].

DFIG derating[14] is necessary to limit the power loss in presence of harmonic currents and to maintain a safe operating temperature. The DFIG derating consists in a reduction of the fundamental current rms and as a consequence of the active power delivered by the generator.

The temperature rise in squirrel-cage induction machines due to voltage harmonics and the consequent derating have been studied in [83, 115, 116]. In the following sections, DFIG derating is investigated; the original contributions of the analysis are as follows:

1. Due to the winding geometry and insulation, the heat transfer conditions are different in the DFIG and in the squirrel cage case. The skin effect dominates the distribution of current flow in the bars and end ring of the squirrel cage machine. In the DFIG rotor, the skin effect is less harsh [84] and is calculated according to the procedure described in appendix 3.A [112].

2. The effects of both current and voltage harmonics are accounted for, while in the literature only the voltage distortion has been studied.

3. Specific considerations are carried out for the DFIG used as a wind generator.

In the following sections the derating factor for stator and rotor windings will be defined as a function of the harmonic currents flowing in the DFIG stator and rotor windings.

[13] Parasitic (pulsating) torques [75] may result from the flow of harmonic currents in the machine windings: the effect of the torque is jitter in the machine speed and, if the parasitic torque frequency is close to the mechanical frequency of the shaft, vibrations take place. This problem is not investigated in the thesis, but may represent a future work.

[14] According to the IEEE dictionary, derating is defined as 'the intentional reduction of stress/strength ratio (e.g., real or apparent power) in the application of an item (e.g.. transformer), usually for the purpose of reducing the occurrence of stress-related failure (e.g., reduction of lifetime of transformer due to increase temperature beyond rated temperature)' [113, 114].

Definition of derating factor $\mathscr{D}$

The rated winding power loss[15] ΔP_n for a three-phase machine is determined according to the expression:

$$\Delta P_n = 3k_1 R I_n^2 \tag{3.22}$$

where

k_1 is the skin effect coefficient at fundamental frequency and is a function of the geometry of the conductors [112],

I_n is the rms value of the rated current (at fundamental frequency),

R is the per phase dc resistance.

In presence of harmonic currents I_h, the total harmonic winding power loss ΔP_H is:

$$\Delta P_H = 3R \sum_{h \in R}^{n} k_h I_h^2 \tag{3.23}$$

where h is the harmonic order. Theoretically, h can be any positive number corresponding to the ratio between the harmonic frequency f_h and the fundamental frequency f_1. The following cases can be distinguished [100, 102, 117]:

- If h is an integer number, the harmonics are multiple of the fundamental frequency. In common three-phase systems $h = 6\ n \pm 1$, where $n = 1, 2, 3...$ [25, 26, 92].
- Non-integer values of h corresponds to interharmonics ($h > 1$) and to subsynchronous interharmonics ($h < 1$).

The windings are designed to operate at fundamental frequency that correspond to the rated winding loss (3.22). In presence of harmonics, the harmonic winding loss is expressed by (3.23); the nominal temperature rise is maintained if the harmonic winding loss (3.23) is equal to the rated winding loss (3.22):

$$\Delta P_n = \Delta P_H \tag{3.24}$$

[15] In the present work, the name 'winding loss' refers to the calculation of the windings Joule loss including the skin effect losses.

Substitution of (3.22) and (3.23) in (3.24) gives:

$$Rk_1 I_n^2 = R \sum_{h=1}^{n} k_h I_h^2 \tag{3.25}$$

that can be rearranged by separating the fundamental current component:

$$k_1 I_n^2 = k_1 I_1^2 + \sum_{h=2}^{n} k_h I_h^2 \tag{3.26}$$

From (3.26) one obtains:

$$I_1 = \sqrt{I_n^2 - \sum_{h\neq 1} \frac{k_h}{k_1} I_h^2} \tag{3.27}$$

The above result shows that in presence of harmonic currents in the windings, the rated temperature increase is maintained if the magnitude of the fundamental current I_1 is reduced with respect to the rated current I_n.

The derating factor $\mathscr{D}$ is defined as follows:

$$\mathscr{D} = \frac{P_1}{P_n} = \frac{3V_1 I_1 \cos\varphi_1}{3V_n I_n \cos\varphi_n} \tag{3.28}$$

where:

P_1 is the fundamental active power,

P_n is the rated power,

V_1 is the fundamental voltage in presence of harmonic distortion,

I_1 is the fundamental current in presence of harmonic distortion,

$\cos\varphi_1$ is the fundamental power factor in presence of harmonic distortion,

V_n is the rated voltage,

I_n is the rated current,

$\cos\varphi_n$ is the rated power factor.

In the following sections it will be shown that the stator and rotor derating expressions for a DFIG are simpler than the general formulation (3.28).

Stator windings Derating Factor $\mathscr{D}_s$

The derating factor $\mathscr{D}_s$ for the stator windings is obtained from (3.28) by adding the subscript $_s$:

$$\mathscr{D}_s = \frac{P_{s1}}{P_{sn}} = \frac{3V_{s1}I_{s1}\cos\varphi_{s1}}{3V_{sn}I_{sn}\cos\varphi_{sn}} \tag{3.29}$$

where:

P_{s1} is the stator fundamental active power,

P_{sn} is the stator rated power (note that the DFIG stator and rotor windings are designed with different rated power),

V_{s1} is the stator fundamental voltage in presence of harmonic distortion,

I_{1s} is the stator fundamental current in presence of harmonic distortion,

$\cos\ \varphi_{s1}$ is the stator power factor in presence of harmonic distortion,

V_{sn} is the stator rated voltage,

I_{sn} is the stator rated current,

$\cos\ \varphi_{sn}$ is the stator rated power factor.

In the following paragraphs, some considerations are carried out to simplify the derating coefficient for stator windings (3.29).

The phasor voltage $\overline{V}_{1s}$ is determined by using the equivalent circuit at fundamental frequency shown in Figure 3.13. This circuit resembles the one illustrated in Figure 3.8, with the difference that the phasor voltage at the PCC included. The phasor voltage at the PCC is imposed by the grid and is equal to the rated voltage. The maximum voltage drop on the impedance $\overline{Z}_c$ takes place when the rated current $\overline{I}_{sn}$ is delivered/absorbed by the stator windings. The magnitude of the maximum voltage drop is:

$$|\frac{\Delta\overline{V}_1}{\overline{V}_{sn}}| = |\overline{Z}_c\ \frac{\overline{I}_n}{\overline{V}_{sn}}| \tag{3.30}$$

In general, the impedance of the line that connects the stator to the PCC is small, and $\Delta\overline{V}_1$ is negligible. Therefore, the stator voltage is approximately equal to the voltage at the PCC:

$$V_{s1} \approx V_{sn} \tag{3.31}$$

The current I_{1s} is obtained from (3.27) by adding the subscript $_s$:

$$I_{s1} = \sqrt{I_{sn}^2 - \sum_{h\neq 1} \frac{k_{sh}}{k_{s1}} I_{sh}^2} = \sqrt{I_{sn}^2 - \sum_{h\neq 1} \frac{k_{sh}}{k_{s1}} I_h^2} \tag{3.32}$$

where according to the proposed methodology, the stator harmonic current I_{sh} is equal to the NLL harmonic current I_h and k_{sh} is the h-order skin effect coefficient for stator harmonic current I_{sh} (appendix 3.A).

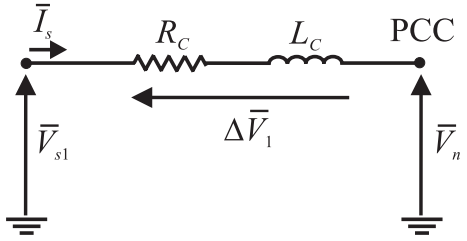

Figure 3.13 - Equivalent circuit for the calculation of the fundamental component of stator voltage.

Since the derating does not alter the phase shift between fundamental current and voltage (it alters only the magnitude of fundamental current), the power factor cos φ_{s1} is equal to the rated power factor:

$$\cos\varphi_{s1} = \cos\varphi_{sn} \tag{3.33}$$

Substituting (3.31), (3.32) and (3.33) in (3.29), the derating factor for stator windings $\mathscr{D}_s$ is simplified as follows:

$$\mathscr{D}_s = \frac{P_{s1}}{P_{sn}} = \frac{3\ V_{sn}\ I_{s1}\cos\varphi_{sn}}{3\ V_{sn}\ I_{sn}\cos\varphi_{sn}} = \frac{I_{s1}}{I_{sn}} = \sqrt{1 - \sum_{h\neq 1} \frac{k_{sh}}{k_{s1}} \left(\frac{I_h}{I_{sn}}\right)^2} \tag{3.34}$$

To reinforce the concept of derating, a simple case is studied, ignoring the skin effect. The stator current spectrum contains the fundamental component and the fifth harmonic; in Figure 3.14 the stator windings loss $\Delta P_s/P_n$ is plotted as function of the magnitude of the fifth harmonic current I_{s5}/I_{ns}. The fundamental harmonic stator winding loss $\Delta P_{s1}/P_n$ and the fifth harmonic stator winding loss $\Delta P_{s5}/P_n$ are shown on the same plot.

For increasing values of I_{s5}, the winding loss due to the fifth harmonic current increases, but derating is implemented to maintain a constant stator winding loss $\Delta P_s = \Delta P_{s1} + \Delta P_{s5}$. This condition is obtained by lowering the amplitude of the fundamental stator current and

consequently by reducing the fundamental harmonic stator winding loss.

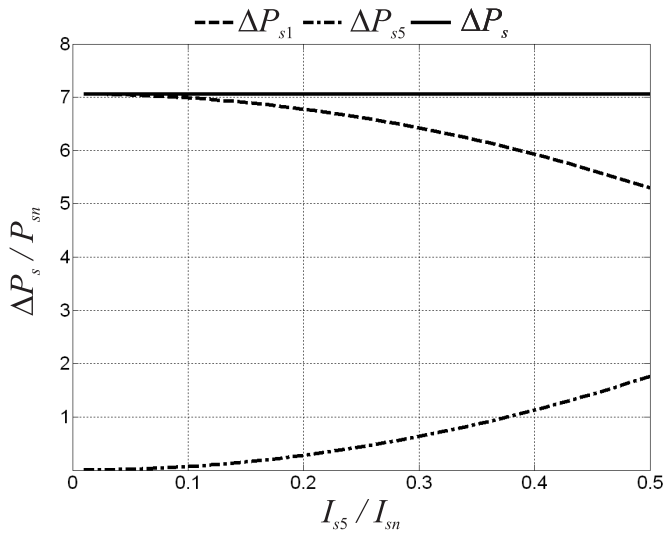

Figure 3.14 - Normalized stator winding power loss as function of the normalized fifth order harmonic current I_{s5}/I_{sn} (skin effect is not taken into account). Three trajectories are presented: ΔP_{s1} is the stator winding power loss due to the fundamental current component when derating is applied, ΔP_{s5} is the stator winding power loss due to the fifth harmonic current and ΔP_s is the total stator winding power loss.

Rotor windings Derating Factor $\mathscr{D}_r$

The derating factor $\mathscr{D}_r$ for the rotor windings is expressed as follows:

$$\mathscr{D}_r = \frac{P_{r1}}{P_{rn}} = \frac{3V_{r1}I_{r1}\cos\varphi_{r1}}{3V_{rn}I_{rn}\cos\varphi_{rn}} \tag{3.35}$$

where:

P_{r1} is the rotor fundamental active power,

P_{rn} is the rotor rated power,

V_{r1} is the rotor fundamental voltage in presence of harmonic distortion,

I_{r1} is the rotor fundamental current in presence of harmonic distortion,

$\cos\varphi_{r1}$ is the rotor power factor in presence of harmonic distortion,

V_{rn} is the rotor rated voltage,

I_{rn} is the rotor rated current,

cos φ_{rn} is the rated rotor power factor.

The objective of this section is to find a relation between the rotor and the stator derating factors; in order to obtain this result, the rotor derating factor (3.34) is expressed in function of the stator derating coefficient (3.34).

From chapter 2, it is known that in wind power applications, the rotor rated power is smaller than the stator power:

$$\begin{gathered} P_{rn} = |\mathbb{S}_{max}| P_{sn} \\ 3\ V_{rn}\ I_{rn} \cos\varphi_{rn} = 3\ |\mathbb{S}_{max}|\ V_{sn}\ I_{sn} \cos\varphi_{sn} \end{gathered} \tag{3.36}$$

where $|\mathbb{S}_{max}| \leq 0.5$. In the DFIG the stator and rotor nominal power factor are very close due to the similar geometry (this assertion has been confirmed by simulating a real-world DFIG):

$$\cos\varphi_{rn} \approx \cos\varphi_{sn} \tag{3.37}$$

By applying (3.37), the second expression of (3.36) is simplified as follows:

$$V_{rn}\ I_{rn} = |\mathbb{S}_{max}|\ V_{sn}\ I_{sn} \tag{3.38}$$

The left hand side of (3.38) is multiplied and divided by the stator to rotor turns ratio N_{sr} and the following is obtained:

$$\left(\frac{V_{rn}}{N_{sr}}\right)\ (N_{sr} I_{rn}) = |\mathbb{S}_{max}|\ V_{sn}\ I_{sn}$$

or

$$V_{nr} I_{rn} = (|\mathbb{S}_{max}|\ N_{sr}\ V_{sn})\ \left(\frac{I_{sn}}{N_{sr}}\right) \tag{3.39}$$

Two fundamental relations result from (3.39):

$$V_{rn} = |\mathbb{S}_{max}|\ N_{sr}\ V_{sn} \tag{3.40}$$

and

$$I_{rn} = \frac{I_{sn}}{N_{sr}} \tag{3.41}$$

The relation (3.40) can be generalized by observing that for any value of the slip, the fundamental component of rotor voltage V_{r1} is related to the fundamental component of stator voltage V_{s1} as follows:

$$V_{r1} = |\mathbb{S}|\ N_{sr}\ V_{s1} \tag{3.42}$$

The relation (3.41) can be generalized too: for any harmonic h, the harmonic rotor current I_{rh} is related to the stator harmonic current I_{sh} by means of the stator to rotor turn ratio N_{sr}

$$I_{rh} = \frac{I_{sh}}{N_{sr}} \tag{3.43}$$

where h can be any integer number or fraction, including the case $h = 1$ that corresponds to fundamental frequency.

The current I_{r1} is computed from (3.27):

$$I_{r1} = \sqrt{I_{rn}^2 - \sum_{h\neq 1} \frac{k_{hr}}{k_{r1}} I_{rh}^2} = \sqrt{I_{rn}^2 - \sum_{h\neq 1} \frac{k_{hr}}{k_{r1}} I_h^2} \tag{3.44}$$

where k_{rh} is the skin effect coefficient for stator harmonic current I_{hr} (appendix 4.A).

By dividing both sides of (3.44) by I_{rn}, the following expression is obtained:

$$\frac{I_{r1}}{I_{rn}} = \sqrt{1 - \sum_{h\neq 1} \frac{k_{hr}}{k_{1r}} \frac{I_{rh}^2}{I_{rn}^2}} \tag{3.45}$$

Substitution of (3.43) in (3.45) allows writing the fundamental component of rotor current as function of harmonic stator currents I_{sh} and fundamental stator current I_{s1}:

$$\frac{I_{r1}}{I_{rn}} = \sqrt{1 - \sum_{h\neq 1} \frac{k_{hr}}{k_{r1}} \frac{\left(\frac{I_{sh}}{N_{sr}}\right)^2}{\left(\frac{I_{s1}}{N_{sr}}\right)^2}} = \sqrt{1 - \sum_{h\neq 1} \frac{k_{hr}}{k_{r1}} \frac{I_{sh}^2}{I_{s1}^2}} \tag{3.46}$$

In wind generators $1 \leq N_{sr} \leq 4$ [84] and the stator and rotor geometries have very similar skin effect coefficients:

$$k_{rh} \approx k_{sh} \quad \text{for any } h \tag{3.47}$$

Substitution of (3.47) in (3.46) results in the following approximation:

$$\frac{I_{r1}}{I_{rn}} = \sqrt{1 - \sum_{h\neq 1} \frac{k_{rh}}{k_{r1}} \frac{I_{sh}^2}{I_{s1}^2}} \approx \sqrt{1 - \sum_{h\neq 1} \frac{k_{sh}}{k_{s1}} \frac{I_{sh}^2}{I_{s1}^2}} = \frac{I_{s1}}{I_{sn}} \tag{3.48}$$

The last expression indicates that the stator and rotor deratings have similar values for the same harmonic current injection. This conclusion applies where the stator and rotor geometries are similar and (3.47) can be applied.

The fundamental rotor power factor cos φ_{r1} is equal to the rotor rated power factor because the derating does not cause a significant change in the phase shift between the fundamental current and voltage phasors:

$$\cos\varphi_{r1} = \cos\varphi_{rn} \tag{3.49}$$

Substitution of (3.39), (3.40) and (3.49) in (3.35) result in a more simplified expression for the rotor derating coefficient:

$$\begin{aligned} \mathscr{D}_r &= \frac{P_{r1}}{P_{rn}} = \frac{3V_{r1}I_{r1}\cos\varphi_{r1}}{3V_{rn}I_{rn}\cos\varphi_{rn}} \\ &= \frac{3|\mathbb{S}|\ N_{sr}\ V_{s1}\ \dfrac{I_{s1}}{N_{sr}}\cos\varphi_{rn}}{3|\mathbb{S}_{max}|\ N_{sr}V_{sn}\dfrac{I_{sn}}{N_{sr}}\cos\varphi_{rn}} \\ &= \frac{\mathbb{S}\ V_{s1}\ I_{s1}}{|\mathbb{S}_{max}|\ V_{sn}I_{sn}} \end{aligned} \tag{3.50}$$

Substituting (3.31) in (3.50) results in the following expression:

$$\mathscr{D}_r = \frac{\mathbb{S}\ V_{sn}\ I_{s1}}{|\mathbb{S}_{max}|\ V_{sn}I_{sn}} = \frac{\mathbb{S}}{|\mathbb{S}_{max}|}\frac{I_{s1}}{I_{sn}} = \frac{\mathbb{S}}{|\mathbb{S}_{max}|}\mathscr{D}_s \tag{3.51}$$

Since $\dfrac{\mathbb{S}}{|\mathbb{S}_{max}|} \leq 1$, (3.51) leads to the inequality:

$$\mathscr{D}_r \leq \mathscr{D}_s \tag{3.52}$$

The following important conclusions are carried out from the analysis derived in this section:

- Relation (3.48) proves that the normalized fundamental stator and rotor currents I_{s1}

and I_{r1} have similar value.

- The fundamental stator and rotor voltages V_{s1} and V_{r1} are related by $\mathbb{S}$ as expressed by (3.42). This implies that the stator and rotor derating coefficients $\mathscr{D}_s$ and $\mathscr{D}_r$ are related by the value of the slip $\mathbb{S}$ as shown in (3.51).
- Derating of the stator windings results in a conservative derating for the rotor windings according to (3.52): in other words, if the stator is derated according to (3.34), the rotor winding loss ΔP_r are below the rated values ΔP_{rn}.

Example 3.III - Derating curves for single stator harmonic current

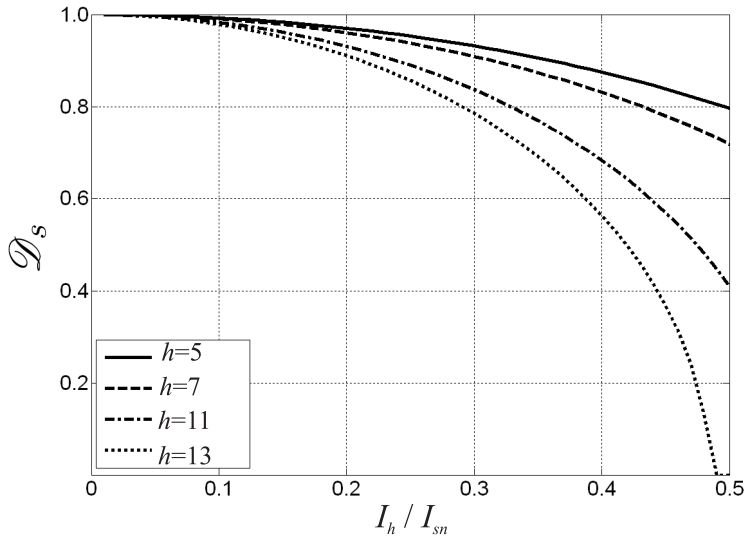

Figure 3.15 - Example 3.III: Stator derating coefficient $\mathscr{D}_s$ as a function of the harmonic current amplitude; the harmonic order h is a parameter. Skin effect is calculated according to [112] and referring to the geometry illustrated in Figure 3.21, with $m = 20$.

The stator supplies a single harmonic current $\overline{I}_{sh}$ and the fundamental current $\overline{I}_{s1}$. The stator derating is calculated by including the skin effect coefficient. The skin effect coefficients are determined for the geometry presented in Figure 3.20 with $m = 20$ and they are plotted in Figure 3.21.

The stator derating coefficient illustrated in Figure 3.15 is expressed in function of the normalized harmonic current amplitude, the harmonic order h is a parameter. For increasing harmonic order the skin effect coefficient and the corresponding Joule loss increase [112]. As

a result, for increasing values of h, stator derating is more severe and the stator fundamental current is lower.

Example 3.IV - Derating curves for multiple stator harmonic currents

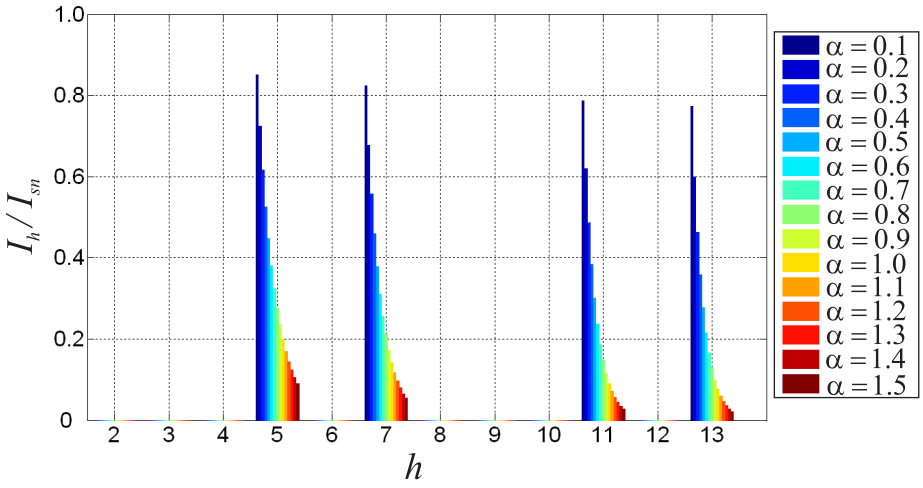

Figure 3.16 - Example 3.IV: Normalized spectrum of the stator current, according to (3.2), where $0.1 < \alpha < 1.5$ and $h = 5, 7, 11, 13$; base value is the stator rated current I_{sn}.

The stator windings supplies multiple harmonic currents. The amplitude of each harmonic of the stator current spectrum (is defined as function of the parameter α:

$$I_h/I_n = \frac{1}{h^\alpha} \tag{3.53}$$

where $0.1 < \alpha < 1.5$ and $h = 5, 7, 11, 13$. Figure 3.16 presents the current spectrum injected by the NLL as a function of the harmonic order, α is a parameter.

The normalized total harmonic current is defined as follows:

$$I_H = \frac{\sqrt{\sum_h I_h^2}}{I_n} \tag{3.54}$$

The derating coefficient $\mathscr{D}_s$ resulting from the current (3.54) is presented in Figures 3.17 and 3.17. In both figures, $\mathscr{D}_s$ is plotted as a function of α; in Figures 3.17, the skin effect coefficient is ignored while Figure 3.18 takes the skin effect coefficient into account. When the skin effect is included, stator derating is more severe: for example, if α=0.6 and I_H=0.9, it results $\mathscr{D}_s$=0.82 when k_s is ignored, and $\mathscr{D}_s$=0.54 when k_s is included.

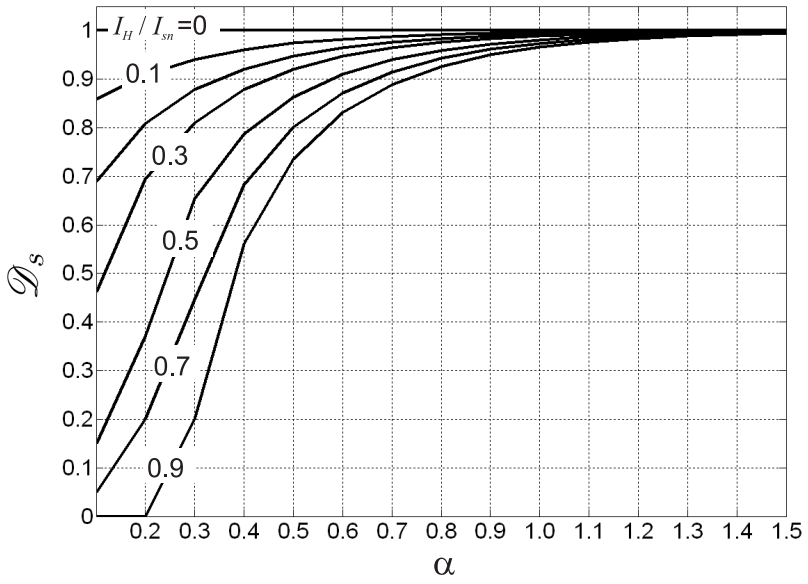

Figure 3.17 - Example 3.IV: Stator derating coefficient $\mathscr{D}_s$ as a function of α; the total harmonic current I_H is a parameter. Skin effect is not included.

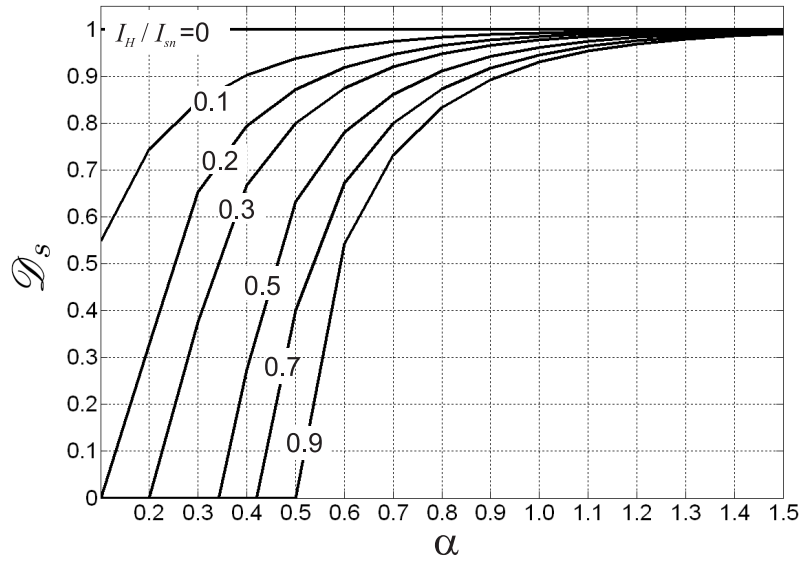

Figure 3.18 - Example 3.IV: Stator derating coefficient $\mathscr{D}_s$ as a function of α, the total harmonic current I_H is a parameter. Skin effect is calculated according to [112] and referring to the geometry illustrated in Figure 3.21, with $m = 20$.

Figures 3.18 and 3.17 indicate that increasing values of α in (3.53) result in a lower derating coefficient: this result is expected since the magnitude of the harmonic current components and of the Joule loss increases with α. In the practice, derating is limited to 0.7, since the power injection is the primary function of the DFIG.

3.5 Considerations about DFIG derating in wind power applications

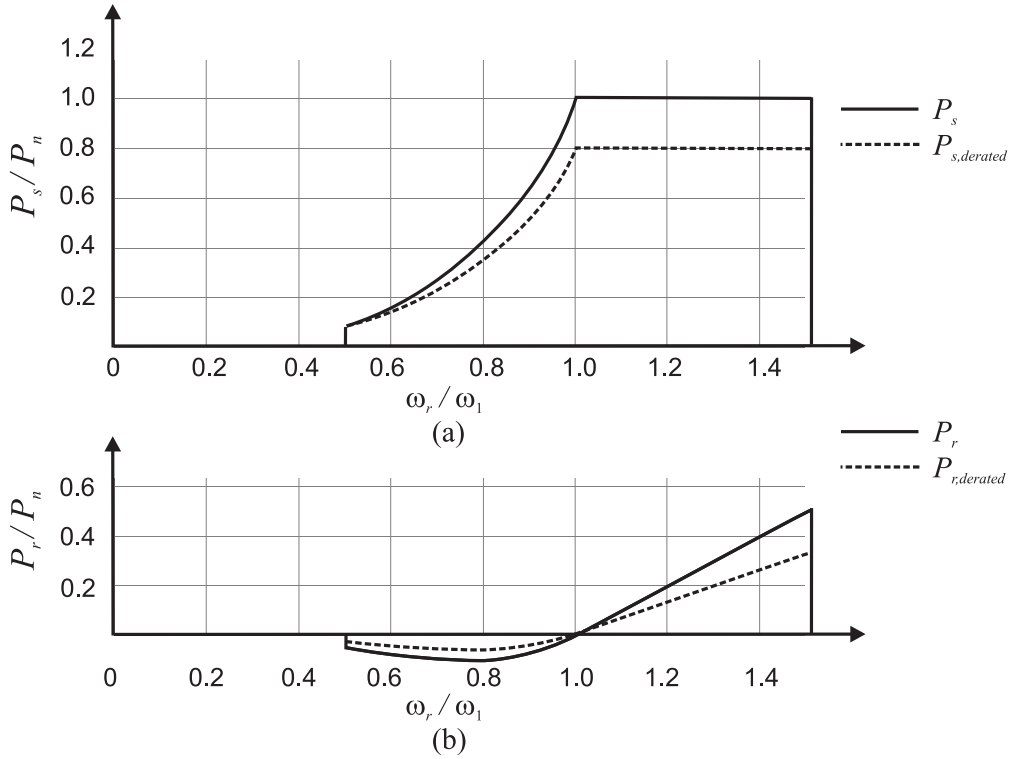

Figure 3.19 - Power curves used for variable speed wind generation: (a) Stator and (b) Rotor. Continuous lines correspond to normal operation, dashed lines correspond to derating.

The stator and rotor power curves used for variable speed wind generation are presented in Figures 3.19.a and .b, respectively. The stator power curve is derived by the tracking characteristic of the turbine, presented in Figure A.1. The rotor power curve is obtained from the stator power curve by applying the relation $P_r = \mathbb{S}P_s$ derived in chapter 2.

The continuous lines correspond to sinusoidal operation; the dotted line correspond to derating. When derating is applied, the value of the fundamental current is lowered with

respect to rated operation and the power extracted from the wind is reduced.

The curves shown in Figure 3.19.a and 3.19.b lead to the following conclusions: when derating is applied, the power capture from the wind is lower with respect to the optimal operation.

In the practice, derating can be obtained by pitching the blade angle: the principles of pitch angle control are presented in section C.4.1.

3.6 RSC and LSC rated power and power loss

The RSC and LSC are connected in series with the rotor and they are rated for the slip power (3.36). The rotor and power converters rating is an important design parameter and depends on many factors. Large power converters mean more weight and more power loss and increased initial cost, but result in higher efficiency. In Figure 3.9 of [118] the DFIG energy efficiency is plotted for different rotor-speed ranges; from this figure one learns that the energy gain increases with the rotor-speed range. In section 1.2.3 it has been explained that the wider is the rotor speed range, the higher is the RSC and LSC rated power.

The RSC and LSC power losses ΔP include the switching power loss, the conduction power loss and the snubber power loss. In [118, 119] a closed form expression for the power converters losses is presented; in the present study the power loss is calculated as the difference between the input power and the output power. This choice is motivated by observing that the expression provided in [118, 119] do not take into consideration all the terms that contribute to the power converter loss and, in spite of the simplifications and approximations, is rather complex.

The choice made in this study is reinforced by observing that in typical motor drives, including the one studied in the present research, the power loss in each power converter is about 5% of the generator rated power. In [113] it is stated that for power electric devices with low efficiency, it is common and acceptable to determine the power loss as difference between input power and output power.

If the value of the power converter loss is above the rated values, the fundamental power can be reduced by implementing DFIG derating. By derating the stator, the power flow in the rotor and in the power converters is automatically reduced thus lowering the power loss.

3.7 Conclusions

Two methodologies to compensate harmonic currents by using a WECS have been presented: 'compensation by means of RSC modulation' and 'compensation by means of LSC modulation'. Both technique result in increasing power loss in the WECS components and in DFIG derating.

Appendix 3.A - Skin effect coefficients calculation

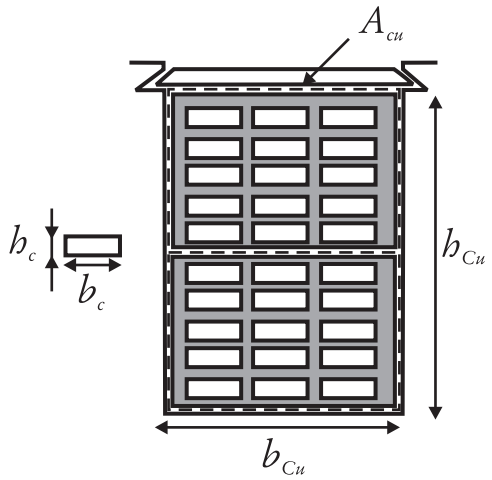

Figure 3.20 - Schematic representation of a wound machine slot.

The procedure for the skin effect coefficients calculation according to [112] is summarized as follows:

1. The rated current I_n of the machine is as follows:

$$I_n = \frac{P_n}{\sqrt{3}V cos\varphi_n}$$

2. The slot area (Figure 3.20) is determined from the value the average density current; in general 4 A/mm^2 $\leq J \leq$ 5 A/mm^2. Then:

$$A_s = \frac{I_n}{J} \text{ (mm}^2\text{)}$$

3. The (stator or rotor) slot dimensions b_{Cu} and h_{Cu} are chosen to satisfy the following

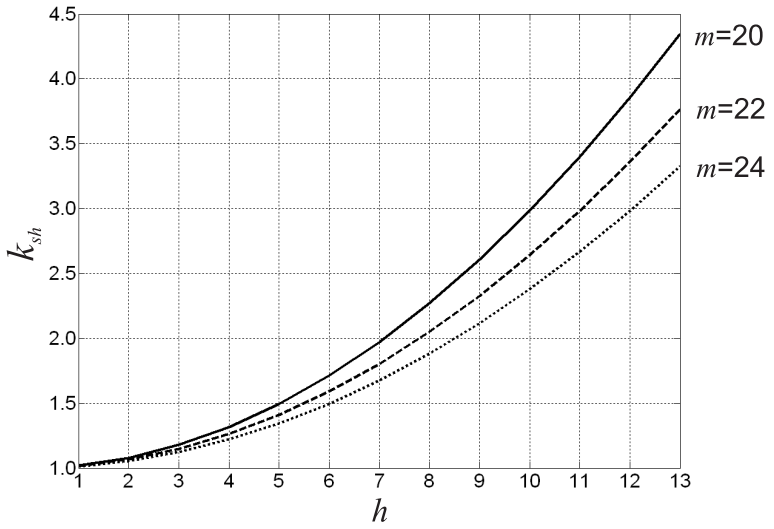

Figure 3.21 - Stator skin effect coefficients as a function of the harmonic order h. The number layers m is a parameter.

relation:

$$b_{Cu} \cdot h_{Cu} = A_{Cu} \geq A_s \text{ mm}^2$$

The above inequality means that the copper area is smaller than the slot area because of the space occupied by the insulation. Figure 3.20 shows that there are three types of insulation: between the conductors and the borders of the slot, between the conductors themselves and between the upper and the lower half.

4. The number of layers m is chosen so that the height of each conductor is less than 2 mm (in the majority of the applications).

$$h_c < \frac{h_{Cu}}{m} \text{ (mm)}$$

5. The penetration depth χ is a function on the harmonic current frequency hf_1 and is calculated as follows:

$$\chi = \sqrt{\frac{\pi \ \mu_0 \ f}{\rho}} = 2\pi\sqrt{\frac{f}{\rho \ 10^7}}(\text{mm})$$

6. The skin effect coefficient k is obtained by using the expression:

$$k = 1 + \frac{m^2 - 0.2}{18} \ \cdot (\chi h_c)^4$$

The skin effect coefficients for the stator windings of the DFIG described in appendix A are illustrated in Figure 3.21, as a function of the harmonic frequency h; the number of layers m is a parameter. With increasing numbers of layers the skin effect coefficient decreases. For the studied problem, the number of layers m must be greater than 20 in order to obtain an acceptable skin effect.

Chapter 4

Compensation by Means of RSC Modulation: Steady-State Analysis

4.1 Introduction

Compensation by means of RSC modulation consists in controlling the RSC voltage to induce stator harmonic currents $i_{s,abc}$ equal in magnitude and 180^o out of phase with respect to the currents $i_{h,abc}$ injected by the NLL (Figure 3.1).

This chapter describes the RSC and LSC control systems that result in the described operation of the WECS [110]. The following topics are presented:

- overview of the control system design,
- Park transformation of the electric and magnetic quantities,
- definition of the RSC and LSC control in the dq domain,
- simulation results.

4.2 Overview of the control system design

This section describes in general terms the control system concepts[16]. The relevant components of the systems under study (Figure 3.1) are:

1. DFIG
2. RSC
3. LSC
4. NLL

Two subsystems are identified:

[16] A short introduction to the basic terminology and fundamental concepts of control system design [75, 120] is presented in appendix D.

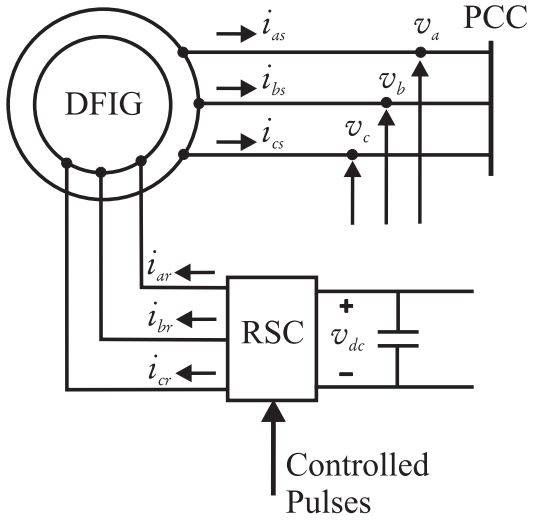

Figure 4.1 - The RSC subsystem including the DFIG and the RSC.

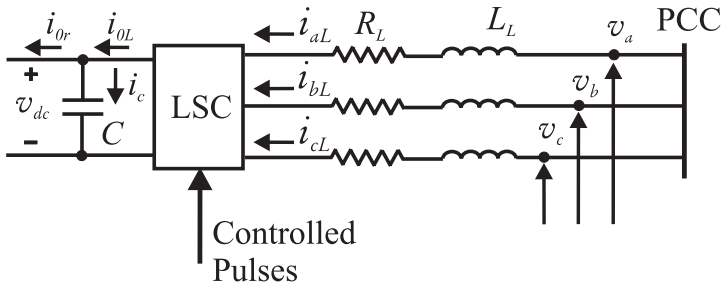

Figure 4.2 - The LSC subsystem including the dc-link and the LSC.

1. The *RSC subsystem* (Figure 4.1) includes the DFIG and the RSC; the inputs are the stator active power[17] P_s and the power factor (PF) measured at the machine terminals, the outputs are the stator currents i_{sa}, i_{sb}, i_{sc}.

2. The *LSC subsystem* (Figure 4.2) includes the dc-link and the LSC: the inputs are the dc-link voltage v_{dc} and the PF at the LSC terminals. The outputs are the grid side converter currents i_{La}, i_{Lb}, i_{Lc}.

The input, output and transfer functions of the two subsystems are independent, thus resulting in a simplified analysis of the system under study.

The control system operation is based on the values assumed by the following quantities[18]:

- Non-Linear Load currents i_{ha},i_{hb},i_{hc};
- stator currents i_{sa},i_{sb},i_{sc};
- rotor currents i_{ra},i_{rb},i_{rc};
- LSC currents i_{La},i_{Lb},i_{Lc};
- grid currents i_{ga},i_{gb},i_{gc};
- voltages at the PCC v_a,v_b,v_c.

After applying the Park transformation[19] the control is defined in the equivalent reference frame for each subsystem.

For the RSC subsystem (Figure 4.1):

- The reference currents $i_{dr,ref}$ and $i_{qr,ref}$ are defined. The reference currents $i_{dr,ref}$ and $i_{qr,ref}$ magnitudes depend on the value of the active and reactive power at the stator terminals; the control operates so that the rotor currents i_{dr} and i_{qb} follow the reference currents.
- The rotor voltages $v_{dr,ref}$ and $v_{qr,ref}$ that generate the reference currents are determined.

[17] The stator power is a function of the wind speed according to the tracking characteristic Figure A.1.

[18] To simplify the notation in the block diagrams, the three phase quantities are often referred as: $i_{ha,b,c}$, $i_{sa,b,c}$ ...

[19] The motivations and the details of the Park transformation are presented in appendix B.

- The switching times of the RSC are controlled to obtain the rotor reference voltages $v_{dr,ref}$ and $v_{qr,ref}$.

For the LSC subsystem (Figure 4.2):

- The reference currents $i_{dL,ref}$ and $i_{qL,ref}$ are defined. The reference currents $i_{dL,ref}$ and $i_{qL,ref}$ magnitude depend on the dc-link voltage V_{dc} and on the PF at the LSC terminals; the control acts so that the output currents i_{dL} and i_{qL} follow the reference currents.
- The converter voltages $v_{dL,ref}$ and $v_{qL,ref}$ that generate the reference currents are determined.
- The switching times of the LSC are controlled to obtain the LSC reference voltages $v_{dL,ref}$ and $v_{qL,ref}$.

The reference currents definition is the core of the control system. The description of the control for each subsystem follows the transformation of the three-phase quantities into the equivalent reference frame.

4.3 Electric quantities transformation into the equivalent $dq0$ frame

The transformation of the three-phase quantities into the $dq0$ domain results in a simplified analysis of electric systems including induction machines and motor drives. Two of the most important simplifications are:

1. the mutual coupling between stator and rotor windings is constant in the equivalent domain (section B.3.2), while in the actual machine it varies on time depending on the rotor windings displacement;
2. the electric quantities have the same frequency in the equivalent domain, while in the DFIG the rotor and stator currents have different frequency (section 2.1).

In the general formulation of the Park transformation (B.10), the speed ω_a of the dq axes can take any arbitrary value. In the present work, the stator voltage reference frame has been chosen: this means that the d axis is aligned with the phase a stator voltage [121] and is rotating with speed $\omega_a = \omega_1$ (Figure 4.7)[20].

[20]Since in the practice the stator resistance is small, the stator voltage orientation (grid-flux orientation) gives the same results obtained by applying the stator-flux orientation [88, 122, 123]. The only difference between the two reference frames is a phase shift of 90 deg.

The reasons for this choice are:

- the measurement of the stator voltage phase and frequency, that determine the position of the *dq* axes is easily obtained by means of a Phase-Locked Loop (PLL) [124],
- the use of the same reference frame for both the converters reduce the number of transformations and simplifies the block diagram with respect to the methods proposed in [28, 29, 89].

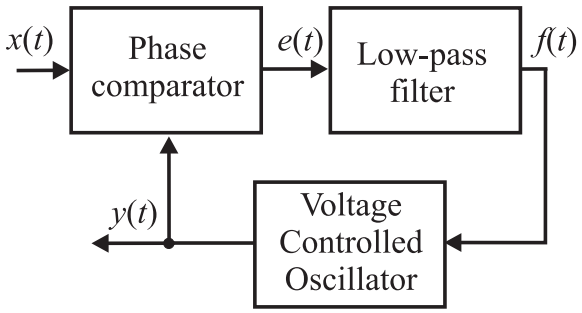

Figure 4.3 - PLL conceptual schematic: $x(t)$ is the input signal, $y(t)$ is the output signal and the feed-back signal. When the PLL is locked, $x(t)$ and $y(t)$ are at the same frequency.

A PLL is used to determine the position and speed of the *dq* axes [125, 126]. The PLL conceptual schematic is illustrated in Figure 4.3: the input signal is $x(t)$ with frequency f_i. The signal $y(t)$ is simultaneously the feedback signal and the output signal with frequency f_o. When the PLL is operating in locked condition, the frequency f_o matches f_i.

The analysis of the PLL operation begins with the assumption of 'not locked' condition: the voltage controlled oscillator (VCO) operates at frequency f'_o (free running frequency), and $f'_o \neq f_i$

The expressions for $x(t)$ and $y(t)$ are:

$$x(t) = V_i \sin(\omega_i t) \tag{4.1}$$

$$y(t) = V_o \sin(\omega'_o t) \tag{4.2}$$

where $\omega_i = 2\pi f_i$ and $\omega'_o = 2\pi f'_o$.

The signals $x(t)$ and $y(t)$ are the phase comparator inputs. The phase comparator is an analog multiplier and it is assumed that its gain is unity. The output of the phase comparator is the signal $e(t)$ obtained as the product of $x(t)$ and $y(t)$:

$$e(t) = x(t)\ y(t) = V_i\ V_o\ \sin(\omega_i t)\ \sin(\omega'_o t) = \frac{V_i\ V_o}{2}\ [\cos(\omega_i t - \omega'_o t) - \cos(\omega_i t + \omega'_o t)] \tag{4.3}$$

The low-pass filter cancels the high frequency component from the error signal (4.3) and yields to the input of the VCO:

$$f(t) = \frac{V_i\ V_o}{2}\ \cos(\omega_i t - \omega'_o t) = \frac{V_i\ V_o}{2}\ \cos(\Delta\omega t) \tag{4.4}$$

where $\Delta\omega = \omega_i - \omega'_o$.

The free running frequency of the VCO is ω'_o; the term $\Delta\omega$ is the input for the VCO and is a correction for the output frequency. Therefore, the output frequency is obtained as follows:

$$\omega_o = \omega'_o \pm \Delta\omega \tag{4.5}$$

and the expression of the output signal is as follows:

$$y(t) = V_o \sin(\omega_o t) = V_o \sin[(\omega'_o \pm \Delta\omega)t] \tag{4.6}$$

The procedure described in (4.2)-(4.6) repeats until when the frequency ω_o equals ω_i and the PLL operates in locked condition. Under this condition, the feedback signal $y(t)$ has the same frequency as the input signal $x(t)$ and is out of phase by the angle[21] ϑ_e:

$$y(t) = V_o \sin(\omega_i t + \vartheta_e) \tag{4.7}$$

If the inputs of phase comparator are (4.1) and (4.7), the output error results as follows:

$$e(t) = x(t)\ y(t) = V_i\ V_o\ \sin(\omega_i t)\ \sin(\omega_i t + \vartheta_e) = \frac{V_i\ V_o}{2}\ [\cos\vartheta_e - \cos(2\omega_i t + \vartheta_e)] \tag{4.8}$$

and the low-pass filter output (4.4) is:

$$f(t) = \frac{V_i\ V_o}{2}\ \cos\vartheta_e \tag{4.9}$$

Any variation of the input frequency f_i within the 'lock range' of the PLL results in a variation of the value of $\cos\vartheta_e$; the VCO input changes according to (4.8) and yields to an output voltage $y(t)$ that follows the variation of f_i.

The use of the PLL has the following motivation: under locked condition the signal $y(t)$ is a 'clean' replica of the input signal $x(t)$ that can be noisy; the filter guarantees the cancellation of the high frequency components, the feedback loop forces to zero the

[21] When the PLL is not locked and the frequencies of the signals $x(t)$ and $y(t)$, the phase angle is not expressed in (4.19) and (4.2) because it has not physical meaning.

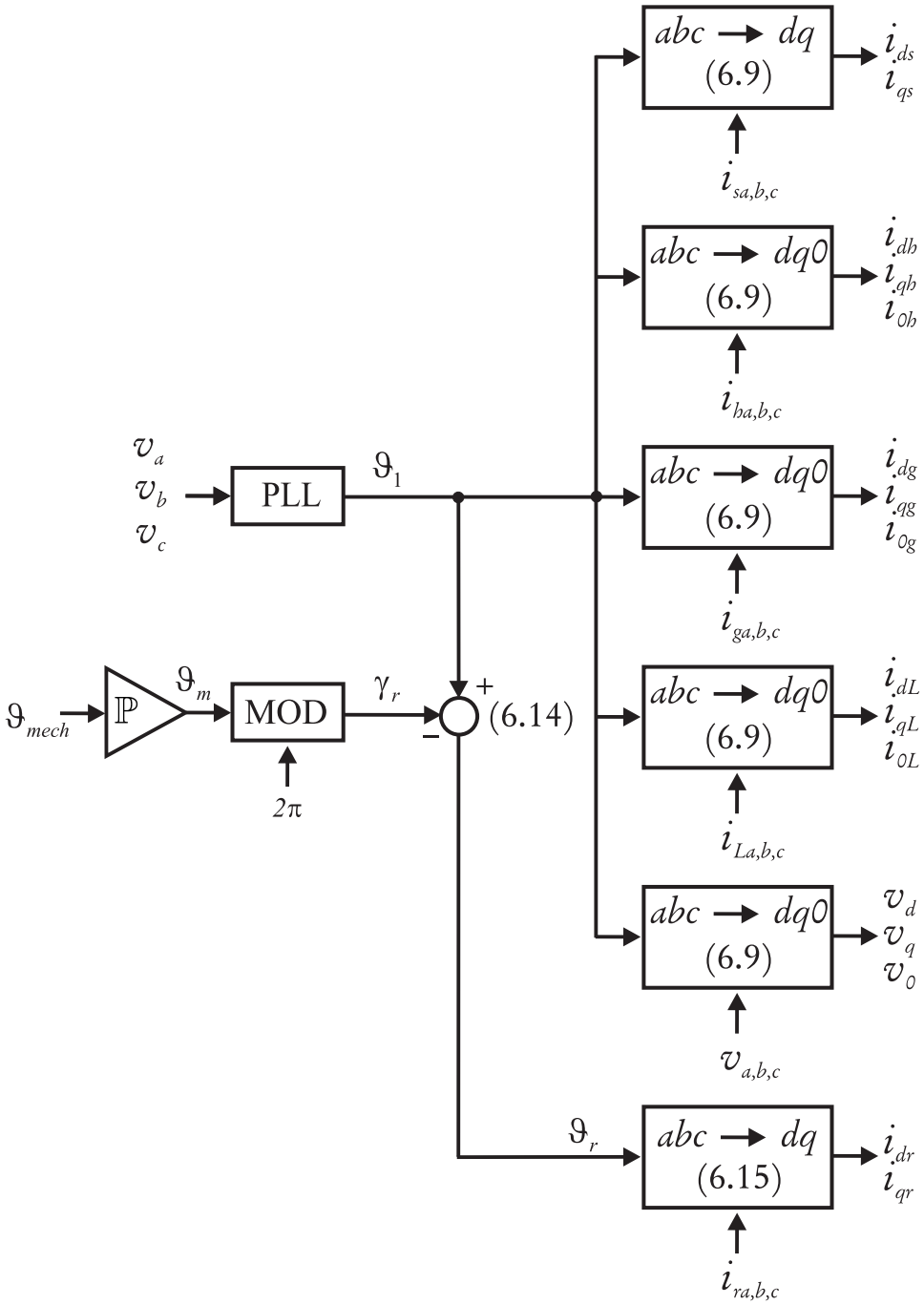

Figure 4.4 - Transformation of the three-phase quantities into the $dq0$ reference frame aligned with stator voltage: the PLL allows deriving the angle ϑ_1 use for the transformation of the stator and grid quantities; the measurement of the rotor displacement ϑ_{mech} is used to derive the transformation angle ϑ_m used for the transformation of the rotor quantities.

difference between input and output frequencies and $\omega_i = \omega_o$

In the present application, the PLL is used to determine the angle ϑ_1 used in the Park transformation. The PLL block diagram and the transformation of the three-phase quantities in the $dq0$ domain are displayed in Figure 4.4.

The voltages $v_{a,b,c}$ are the PLL input; the PLL output is the angle ϑ_1. In the proposed control system, the input of the PLL is a three-phase quantity rather than the single input $x(t)$ considered in Figure 4.3: although the same principles apply, the PLL implementation in the present work is slightly different from the one presented in Figure 4.3 [127].

The angle ϑ_1 defines the position of the phase a stator voltage, that coincides with the position of the d axis in the stator voltage frame [121]. The angle ϑ_1 is supplied to the blocks that perform the Park transformation for the stator and grid quantities ($i_{h,abc}$; $i_{s,abc}$; $i_{L,abc}$; $i_{g,abc}$ and v_{abc}), as indicated in Figure 4.4. The expression of the Park transformation for a generic three phase quantity is obtained by substituting $\vartheta_a = \vartheta_1$ in (B.9):

$$\begin{bmatrix} y_d(t) \\ y_q(t) \\ y_0(t) \end{bmatrix} = \sqrt{\frac{2}{3}} \begin{bmatrix} \cos(\vartheta_1) & \cos(\vartheta_1 - 2\pi/3) & \cos(\vartheta_1 - 4\pi/3) \\ \sin(\vartheta_1) & \sin(\vartheta_1 - 2\pi/3) & \sin(\vartheta_1 - 4\pi/3) \\ \sqrt{1/2} & \sqrt{1/2} & \sqrt{1/2} \end{bmatrix} \begin{bmatrix} y_a(t) \\ y_b(t) \\ y_c(t) \end{bmatrix} \tag{4.10}$$

The zero-sequence component obtained from (B.9) is always nil for the RSC subsystem quantities, since the DFIG windings are never connected to the ground (chapter 2).

The angle ϑ_r used for the transformation of the rotor currents is different from ϑ_1. The relation between the stator and rotor transformation angles is explained in detail in appendix B and some considerations are now recalled.

Figure 4.5 displays the stator winding a_s, rotor winding a_r and d axis and helps to understand the relation between the transformation angles ϑ_1 and ϑ_r.

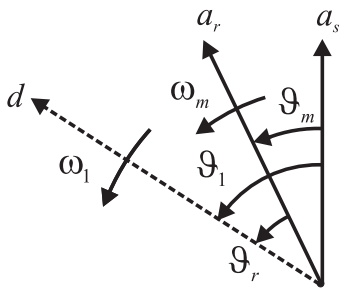

Figure 4.5 - Angles between stator winding a_s, rotor winding a_r and d axis in stator voltage reference frame. This representation is obtained by substituting $\vartheta_a = \vartheta_1$ in Figure B.6.

The stator winding a_s is fixed in space, the rotor winding a_r rotates with electrical speed ω_m (2.2), the d axis rotates with speed ω_1. The angles ϑ_1 and ϑ_m define the position of the d axis and of the rotor winding a_r with respect to the stator winding a_s and are obtained by applying the expressions:

$$\vartheta_1 = \omega_1 t \tag{4.11}$$

$$\vartheta_m = \omega_r t \tag{4.12}$$

The angle ϑ_r expresses the displacement between rotor winding a_r and d axis according to the following expression (Figure 4.5):

$$\vartheta_r = \vartheta_1 - \vartheta_m \tag{4.13}$$

Figure 4.4 shows that in the actual control system a further step is applied and the angle γ_m is replaces ϑ_m in (4.13):

- The mechanical angle ϑ_{mech} is measured (a position sensor [88, 89] can be used for this purpose). The angle ϑ_{mech} defines the position of the rotor winding a_r with respect to the stator winding a_s.
- The electrical angle ϑ_m is determined according to (2.2)
- Since the rotor position increases linearly with time, ϑ_m must be continuously update to a value between 0 and 2 π; this result is obtained by calculating the remainder γ_r of the division $\vartheta_m/2\pi$.

As a result, according to the notation in Figure 4.4, the angle ϑ_r is determined as follows:

$$\vartheta_r = \vartheta_1 - \gamma_r \tag{4.14}$$

The Park transformation for the rotor currents is then obtained by substituting $\vartheta_a = \vartheta_r$ in (B.9):

$$\begin{bmatrix} y_d(t) \\ y_q(t) \\ y_0(t) \end{bmatrix} = \sqrt{\frac{2}{3}} \begin{bmatrix} \cos(\vartheta_r) & \cos(\vartheta_r - 2\pi/3) & \cos(\vartheta_r - 4\pi/3) \\ \sin(\vartheta_r) & \sin(\vartheta_r - 2\pi/3) & \sin(\vartheta_r - 4\pi/3) \\ \sqrt{1/2} & \sqrt{1/2} & \sqrt{1/2} \end{bmatrix} \begin{bmatrix} y_a(t) \\ y_b(t) \\ y_c(t) \end{bmatrix} \tag{4.15}$$

As a result of the Park transformations (4.10) and (4.15), the measured three-phase quantities are referred to the same $dq0$ frame and are shown on the right hand side of Figure 4.4.

4.4 RSC subsystem control

4.4.1 Reference currents definition

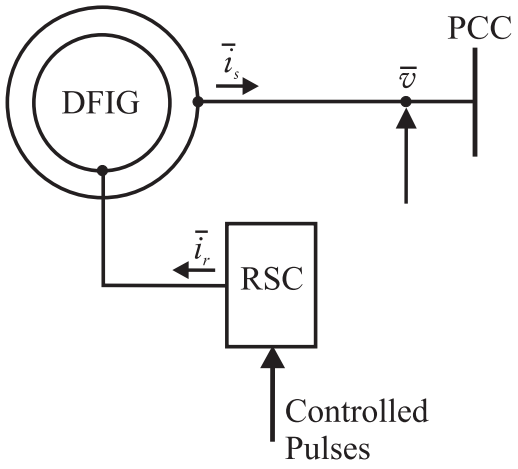

Figure 4.6 - The RSC subsystem in terms of space vectors.

The rotor subsystem in the *dq* domain is shown in Figure 4.6. The control system acts so that the output currents follow the rotor reference currents $i_{dr,ref}$ and $i_{qr,ref}$ that provide the space vector $\bar{i} = i_{dr,ref} + ii_{qr,ref}$.

The rotor reference currents $i_{dr,ref}$ and $i_{qr,ref}$ are the sum of two parts: i_{dr1}, i_{qr1} are the components at fundamental frequency ($h = 1$); the sets i_{drh}, i_{qrh} include the harmonic components ($h \neq 1$):

$$i_{dr,ref} = i_{dr1} + i_{drh} \tag{4.16}$$
$$i_{qr,ref} = i_{qr1} + i_{qrh} \tag{4.17}$$

The following sections deal with the definition of the reference currents: the fundamental and harmonic components are calculated separately and then added in the control system:

Fundamental rotor currents i_{dr1} and i_{qr1}

The fundamental components i_{dr1} and i_{qr1} are obtained from the values of the instantaneous active and imaginary stator powers p_s and q_s [106, 128]. The relation between the rotor currents i_{dr1} and i_{qr1} and the stator powers p_s and q_s is derived from the DFIG model in the equivalent domain.

Figure 4.7 displays the stator voltage and flux components in the stator voltage reference

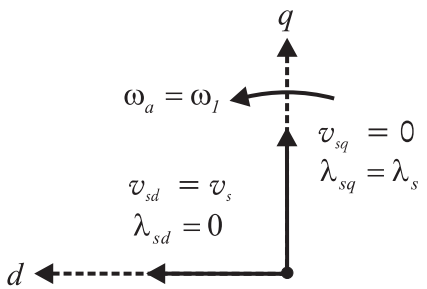

Figure 4.7 - Representation of the stator voltage and flux components in the stator voltage reference frame.

frame:

$$\begin{array}{lcll} \text{the speed of the } dq \text{ axes is the fundamental angular frequency} & : & \omega_a = \omega_1 & \\ \text{the } d \text{ component of stator voltage is the stator voltage} & : & v_{ds} = v_s & \\ \text{the } q \text{ component of stator voltage is nil} & : & v_{qs} = 0 & (4.18) \\ \text{the } d \text{ component of stator flux is nil} & : & \lambda_{ds} = 0 & \\ \text{the } q \text{ component of stator flux is the stator flux} & : & \lambda_{qs} = \lambda_s & \end{array}$$

Substituting the relations (4.18) in (B.27) and (B.29), the machine equations in the stator reference frame are obtained[22] [129]:

$$\begin{cases} v_{ds1} = R_s\ i_{ds1} + \dfrac{d}{dt}\ \lambda_{ds1} - \omega_1\ \lambda_{qs1} = v_s \\ v_{qs1} = R_s\ i_{qs1} + \dfrac{d}{dt}\ \lambda_{qs1} + \omega_1\ \lambda_{ds1} = 0 \\ v_{dr1} = R_r\ i_{dr1} + \dfrac{d}{dt}\ \lambda_{dr1} - (\omega_1 - \omega_r)\ \lambda_{qr1} \\ v_{qr1} = R_r\ i_{qr1} + \dfrac{d}{dt}\ \lambda_{qr1} + (\omega_1 - \omega_r)\ \lambda_{dr1} \end{cases} \tag{4.19}$$

and:

$$\begin{cases} \lambda_{ds1} = L_s\ i_{ds1} + M\ i_{dr1} = 0 \\ \lambda_{qs1} = L_s\ i_{qs1} + M\ i_{qr1} = \lambda_s \\ \lambda_{dr1} = L_r\ i_{dr1} + M\ i_{ds1} \\ \lambda_{qr1} = L_r\ i_{qr1} + M\ i_{qs1} \end{cases} \tag{4.20}$$

where

[22] Some authors use a superscript to indicate the chosen reference frame, such as $^{s,r,e\cdots}$. This choice is recommended if different reference frames are used, as in [28, 29, 89]. In this work all the electric and magnetic quantities are referred to the stator reference frame and the use of the superscript is avoided.

R_s and R_r are the stator and rotor winding resistance respectively;

L_s and L_r are the stator and rotor winding inductance respectively.

In (4.19) and (4.20) the subscript $_1$ is used to emphasize that the system is referring to the fundamental component.

The stator and rotor active and imaginary powers are as follows [106, 128]:

$$\begin{aligned} p_s &= v_{ds1}\ i_{ds1} + v_{qs1}\ i_{qs1} \\ p_r &= v_{dr1}\ i_{dr1} + v_{qr1}\ i_{qr1} \\ q_s &= v_{ds1}\ i_{qs1} - v_{qs1}\ i_{ds1} \\ q_r &= v_{dr1}\ i_{qr1} - v_{qr1}\ i_{dr1} \end{aligned} \tag{4.21}$$

where

p_s and p_r are the stator and rotor instantaneous active powers,

q_s and q_r are the stator and rotor instantaneous imaginary powers.

Substitution of (4.18) in (4.21) yields to the following simplified expressions:

$$\begin{aligned} p_s &= v_{ds1}\ i_{ds1} \\ p_r &= v_{dr1}\ i_{dr1} + v_{qr1}\ i_{qr1} \\ q_s &= v_{ds1}\ i_{qs1} \\ q_r &= v_{dr1}\ i_{qr1} - v_{qr1}\ i_{dr1} \end{aligned} \tag{4.22}$$

The stator powers can be expressed as functions of the fundamental components of rotor currents i_{dr1} and i_{qr1}.

Substitution of the first equation of (4.20) in the first equation of (4.22) results in the following expression for the stator active power:

$$p_s = v_{ds1}\ i_{ds1} = v_s\ \Big(-\frac{M}{L_s} i_{dr1} \Big) = -\frac{M}{L_s} v_s\ i_{dr1} \tag{4.23}$$

Substituting the second equation of (4.20) in the third equation of (4.22) results in the following expression for the stator imaginary power:

$$\begin{aligned} q_s &= v_{ds1}\ i_{qs1} = v_s\ \Big(\frac{\lambda_s}{L_s} - \frac{M}{L_s} i_{qr1} \Big) \\ &= \frac{v_s}{L_s} (\lambda_s - M\ i_{qr1}) \end{aligned} \tag{4.24}$$

From (4.23) and (4.24) it is learned that:

- the stator instantaneous active power p_s (4.23) defines the d-axis component of the rotor fundamental current i_{dr}:

$$i_{dr1} = -\frac{L_s}{M} v_s \; p_s \tag{4.25}$$

When variable speed wind generation is implemented, the tracking characteristic of the turbines uniquely determines the value of the active power p_s as a function of the wind speed (appendix C).

- the stator instantaneous imaginary power q_s (4.24) defines the q-axis component of the rotor fundamental current:

$$i_{qr1} = -\frac{1}{M}(\lambda_s - L_s \frac{q_s}{v_s}) \tag{4.26}$$

where λ_s is computed according to the second equations of (4.20).

The imaginary power q_s depends on the PF at the machine terminals: in section E.2 the relation between the PF and the value of the instantaneous imaginary power is provided (E.11) - (E.21). It results that unity PF corresponds to $q_s = 0$ and to $i_{qr1} = 0$. If PF$\neq$1, then the i_{qr1} components of the current is not zero and $q_s \neq 0$.

In the applications for wind generation presented in [29, 75, 89] the DFIG is controlled to obtain unity PF: this choice is very common since the active power production is the WECS owners objective (chapter 1).

Harmonic rotor currents i_{drh} and i_{qrh}

Compensation by means of RSC modulation implies that the stator injects three-phase harmonic currents equal in magnitude and 180^o out of phase with respect to the NLL harmonic current:

$$i_{dsh} = -i_{dh}$$

$$i_{qsh} = -i_{qh}$$

The harmonic component of the rotor currents i_{drh} and i_{qrh} that correspond to i_{dsh} and i_{qsh} are determined by using (4.20) written for the harmonic component h.

For the d-axis:

$$i_{drh} = \frac{L_s}{M} i_{dsh} = \frac{L_s}{M} i_{dh} \tag{4.27}$$

For the q-axis:

$$i_{qrh} = -\frac{1}{M}(\lambda_s - L_s i_{qsh}) = -\frac{1}{M}(\lambda_s - L_s i_{qh}) \tag{4.28}$$

4.4.2 The RSC transfer function

In the RSC control system, a PI[23] controller is used to force to zero the difference between the actual RSC voltages v_{dr},v_{qr} and the reference voltages $v_{dr,ref}$,$v_{qr,ref}$. The parameters of the PI controller can be determined if the transfer function [56, 130] between rotor voltage and rotor current is known.

The d-axis transfer function is determined as follows: substitution of the third and fourth equation of (4.20) in the third equation of (4.19) gives:

$$v_{dr} = R_r\ i_{dr} + \frac{d}{dt}\ [L_r\ i_{dr} + M\ i_{ds}] - (\omega_1 - \omega_m)\ [L_r\ i_{qr} + M\ i_{qs}] \tag{4.29}$$

The Laplace transform applied to (4.29) yields:

$$V_{dr}(s) = R_r\ I_{dr}(s) + s\ [L_r\ I_{dr}(\mathrm{s}) + M\ I_{ds}(\mathrm{s})] - (\omega_1 - \omega_m)\ [L_r\ I_{qr}(\mathrm{s}) + M\ I_{qs}(\mathrm{s})] \tag{4.30}$$

that is conveniently rearranged:

$$V_{dr}(s) - s\ M\ I_{ds}(s) + (\omega_1 - \omega_m)\ [L_r\ I_{qr}(\mathrm{s}) + M\ I_{qs}(s)] = R_r\ I_{dr}(\mathrm{s}) + s\ L_r\ I_{dr}(\mathrm{s}) \tag{4.31}$$

An auxiliary voltage V'_{dr} is defined:

$$V_{dr}(\mathrm{s})' = V_{dr}(\mathrm{s})) - s\ M\ I_{ds}(\mathrm{s}) + (\omega_1 - \omega_m)\ [L_r\ I_{qr}(\mathrm{s}) + M\ I_{qs}(\mathrm{s})] \tag{4.32}$$

and substituting $V'_{dr}(s)$ in (4.31) results:

$$V'_{dr}(\mathrm{s}) = R_r\ I_{dr}(\mathrm{s}) + s\ L_r\ I_{dr}(\mathrm{s}) \tag{4.33}$$

yielding to the transfer function:

$$\frac{I_{dr}(\mathrm{s})}{V'_{dr}(\mathrm{s})} = \frac{1}{R_r + s\ L_r} \tag{4.34}$$

A similar procedure is applied to the q-axis variables; substitution of the third and

[23]Due to their simplicity and efficiency, Proportional Integral (PI) controllers are widely used in control systems [78, 130]; a brief introduction to the design of PI controllers is provided in appendix D.

fourth equations of (4.20) in the fourth equation of (4.19) gives

$$v_{qr} = R_r\ i_{qr} + \frac{d}{dt}\ [L_r\ i_{qr} + M\ i_{qs}] + (\omega_1 - \omega_r)\ [L_r\ i_{dr} + M\ i_{ds}] \tag{4.35}$$

When the Laplace transform is applied to (4.35) one obtains:

$$V_{qr}(\mathrm{s}) = R_r\ I_{qr}(\mathrm{s}) + s\ [L_r\ I_{qr}(s) + M\ I_{qs}(s)] + (\omega_1 - \omega_r)\ [L_r\ I_{dr}(\mathrm{s}) + M\ I_{ds}(\mathrm{s})] \tag{4.36}$$

and grouping q-axis component on the left and the d-axis components on the right results:

$$V_{qr}(\mathrm{s}) - s\ M\ I_{qs}(\mathrm{s}) + (\omega_1 - \omega_r)\ [L_r\ I_{dr}(\mathrm{s}) + M\ I_{ds}(\mathrm{s})] = R_r\ I_{qr}(\mathrm{s}) + s\ L_r\ I_{qr}(\mathrm{s}) \tag{4.37}$$

The auxiliary voltage V'_{qr} is defined as follows:

$$V'_{qr}(\mathrm{s}) = V_{qr}(\mathrm{s}) - s\ M\ I_{ds}(\mathrm{s}) + (\omega_1 - \omega_r)\ [L_r\ I_{qr}(\mathrm{s}) + M\ I_{qs}(\mathrm{s})] \tag{4.38}$$

and substituting in (4.37) gives:

$$V'_{qr}(\mathrm{s}) = R_r\ I_{qr}(\mathrm{s}) + s\ L_r\ I_{qr}(\mathrm{s}) \tag{4.39}$$

yielding to the transfer function:

$$\frac{I_{qr}(\mathrm{s})}{V'_{qr}(\mathrm{s})} = \frac{1}{R_r + s\ L_r} \tag{4.40}$$

By comparing (4.34) and (4.40) one learns that the same transfer function expression is obtained for the d and q axes. This result can be justified from the geometrical and electrical symmetry of the DFIG (the same parameters for all the three phases).

Figure 4.8 is a feedback system of the type shown in appendix 4.A and is used to show the relation between the system transfer function and the PLL parameters. Figure 4.8, Figure D.1 where:

- The input variable is the reference current $I_{dr,ref}(\mathrm{s})$.
- The output variable is the rotor current $I_{dr}(\mathrm{s})$,
- The current $I_{dr}(\mathrm{s})$ is fed back and the error is obtained as $\Delta I_{dr}(\mathrm{s}) = I_{dr,ref}(\mathrm{s}) - I_{dr}(\mathrm{s})$. The error $\Delta I_{dr}(\mathrm{s})$ is the input for the PI,

- The voltage V'_{dr}(s) is the output of the PLL and the input for the system transfer function.

For the q variables a similar system apply: an identical PI is used because the same transfer function describes the subsystem in the d and q variables.

The block diagram Figure 4.8 shows that the PI controller is not simply a gain, because input and output variables have different units. In the case of Figure 4.8, the input variable is a current (A), the output is a voltage (V), and as a result the gain must be a resistance ($\Omega = V/A$).

The PI parameters are obtained using the phase margin test described in appendix B.

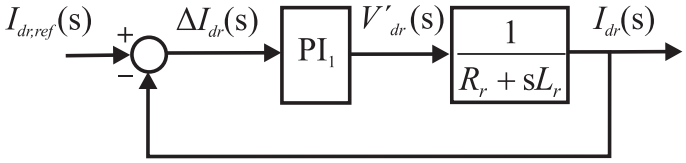

Figure 4.8 - Closed-loop including the PI controller and the d-axis transfer function for the RSC subsystem.

4.4.3 Block diagram for RSC control

The block diagram describing the control of the rotor subsystem is depicted in Figure 4.9. Since in the practical applications the control is implemented in the time domain rather than in the Laplace domain, all the quantities are represented in the continuous time domain.

The diagram of the control process for the d-axis variables is shown in the upper branch. The diagram of the control process for the q-axis variables is presented in the lower level.

The diagram for the d-axis variables is described at first. On the top right corner of Figure 4.9, the reference rotor currents are computed: the fundamental component $i_{dr1,ref}$ is obtained by applying (4.25), the harmonic component $i_{drh,ref}$ is obtained by applying (4.27). The fundamental and harmonic reference currents are then added according to (4.16) and $i_{r,ref}$ is obtained.

The difference between the reference current $i_{dr,ref}$ and the measured current $i_{dr,meas}$ is the error term Δi_{dr}. The error term is the input of the PI controller. The output of the PI controller is the auxiliary voltage v'_{dr}, as explained in the previous paragraph (Figure 4.8).

The actual reference voltage is obtained from the auxiliary voltage according to (4.32):

$$v_{dr,ref} = v'_{dr} + \frac{d}{dt} M\ i_{ds} - (\omega_1 - \omega_m)\ [L_r\ i_{qr} + M\ i_{qs}] \tag{4.41}$$

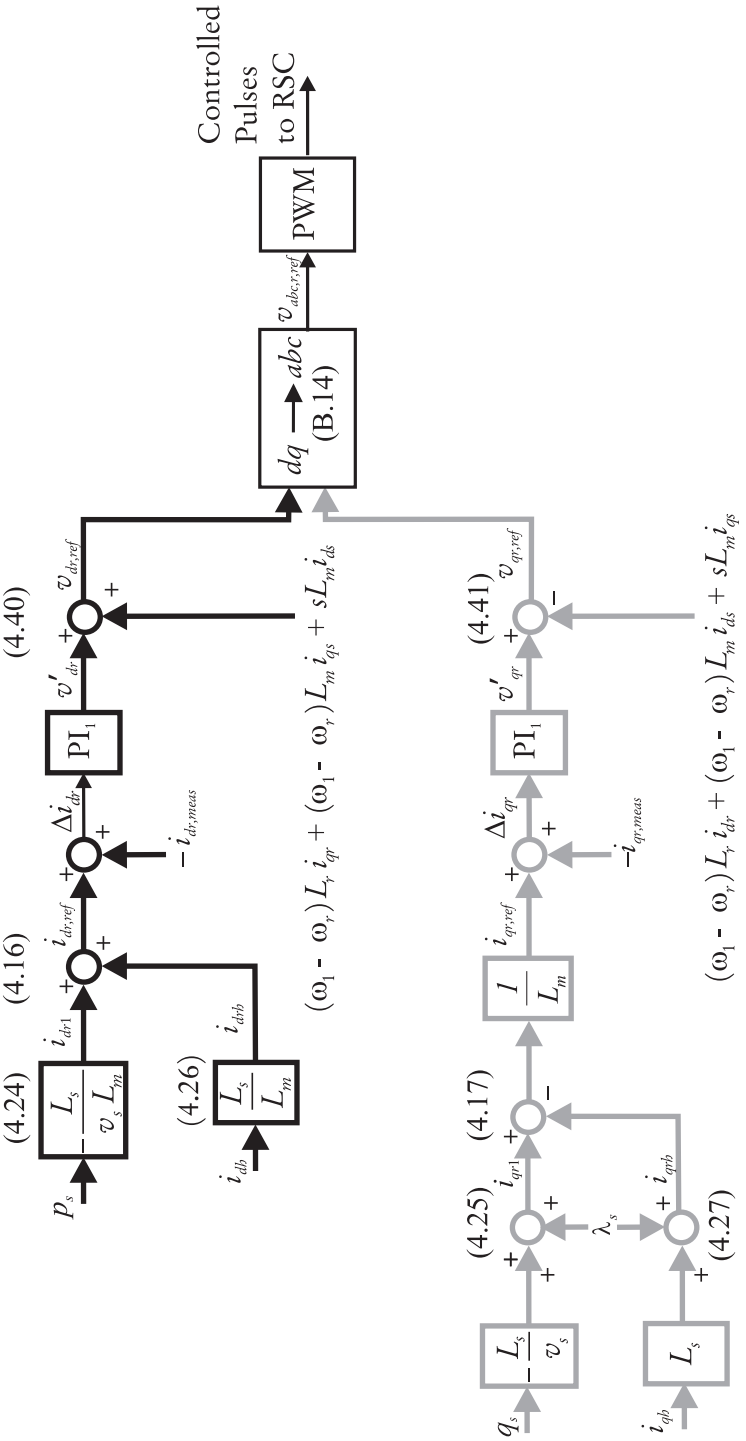

Figure 4.9 - Block diagram for the control of the RSC subsystem, compensation by means of RSC modulation).

The diagram of the control process for the q-axis variables is shown in the lower branch: similar steps are applied to derive the reference voltage $v_{qr,ref}$ from the reference currents $i_{qr1,ref}$ and $i_{qrh,ref}$. The same parameters characterizes the PI controller because the same transfer function describes both the d and the q axes.

The actual reference voltage $v_{qr,ref}$ is obtained from the auxiliary voltage (4.39) as follows:

$$v_{qr,ref} = v'_{qr} + \frac{d}{dt} M \; i_{ds}(\mathrm{s}) + (\omega_1 - \omega_m) \; [L_r \; i_{qr} + M \; i_{qs}] \tag{4.42}$$

The actual reference voltages v_{qr} and v_{dr} are then transformed in the phase domain by applying the inverse Park transform (B.14); the voltages v_{ar},v_{br} and v_{cr} are the reference voltage the rotor terminals and represent the inputs for the PWM pulses generator. The pulses are generated by using PWM, with $m_f = 108$ (appendix H).

In the block diagram 4.9 the transfer functions (4.34) and (4.40) are not shown because they don't come into play in the control system. In the design of the PI controller, the feedback terms is computed using the transfer function, that is the mathematical model of the system, as shown in Figure 4.8. In the real implementations of the control system, the feedback term is measured by sensors to monitor the actual behavior and the phenomena that were not included in the model. As a result, in Figure 4.9 the quantities $i_{d,meas}$ and $i_{q,meas}$ measured by the sensors are shown and the transfer function is not necessary.

4.5 LSC subsystem control

The LSC subsystem in the dq reference frame is shown in Figure 4.10

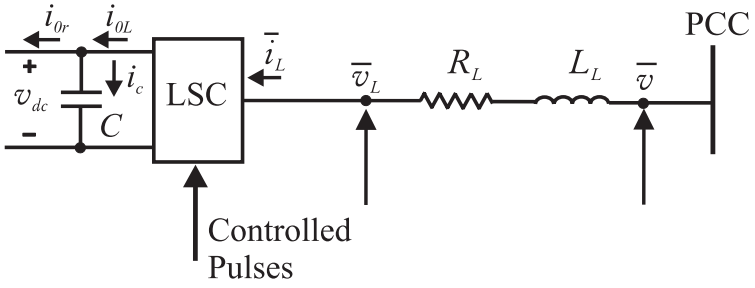

Figure 4.10 - The LSC subsystem in terms of space vectors.

The LSC is controlled to keep constant the dc-link voltage and to regulate the PF at the LSC terminals [89]. When compensation by means of RSC modulation is implemented, the LSC is not intended to compensate harmonic currents and the reference currents i_{dL} and i_{qL} are sinusoidal and at fundamental frequency f_1.

4.5.1 LSC reference currents

The reference currents $i_{dL,ref}$ and $i_{qL,ref}$ are obtained from the active and reactive powers p_L and q_L measured at the LSC terminals [106]:

$$\begin{aligned} p_L &= v_d\ i_{dL} + v_q\ i_{qL} \\ q_L &= v_d\ i_{qL} - v_q\ i_{dL} \end{aligned} \tag{4.43}$$

In the voltage reference frame, the conditions (B.42) apply. Substituting $v_d = v_s$ and $v_q = 0$ in (4.43):

$$\begin{aligned} p_L &= v_s\ i_{dL} \\ q_L &= v_s\ i_{qL} \end{aligned} \tag{4.44}$$

The value of the reference current i_{qL} is obtained from the second equation of (4.44):

$$i_{qL,ref} = \frac{q_L}{v_s} \tag{4.45}$$

The above expression shows that, similarly to the case of the RSC, the value of $i_{qL,ref}$ depends on the choice of q_L. In section E.2 it is proved that if $q_L = 0$ (and consequently $i_{Lq} = 0$), a unity PF results at the LSC terminals. This is the usual mode of operation of the LSC in wind power plants [89].

The value of the reference current $i_{Ld,ref}$ is controlled to maintain a constant dc-link voltage. A PI controller is used to coerce the difference between the reference voltage $V_{dc,ref}$ (a constant value) and the actual voltage v_{dc} to be nil [75]. The transfer function of the dc-link is used to determine the values of the PI controller parameters.

The dc-link (Figure 4.2) is characterized by the following relations [34]:

- the power on the dc side of the LSC is instantaneously equal to the active power on the AC side, if the power loss in the converter is ignored:

$$v_{dc}\ i_{0L} = 3 v_d\ i_{dL}, \tag{4.46}$$

- the following relation applies between the dc-link voltage amplitude and the RMS value of the voltage on the AC side, assuming that PWM modulation is applied:

$$V_{L,rms} = \frac{m_a}{2\sqrt{2}} v_{dc}, \tag{4.47}$$

  where m_a is the amplitude modulation.

- the constitutive relation of the dc-link capacitor is

$$C\ \frac{d}{dt}v_{dc} = i_c = i_{0L} - i_{0r}, \tag{4.48}$$

By applying the Laplace transform to (4.46) - (4.48) the following is obtained:

$$V_{dc}(\mathrm{s})\ I_{0L}(\mathrm{s}) = 3V_L(s)\ I_{dL}(\mathrm{s}) \tag{4.49}$$

$$V_L(\mathrm{s}) = \frac{m_a}{2\sqrt{2}}V_{dc}(\mathrm{s}) \tag{4.50}$$

$$\mathrm{s}C\ V_{dc}(\mathrm{s}) = I_{0L}(\mathrm{s}) - I_{0r}(\mathrm{s}) \tag{4.51}$$

The control acts so that the current $I_{0L}(\mathrm{s})$ compensates the variations of $V_{dc}(s)$ and the current $I_{0r}(\mathrm{s})$ delivered to the rotor side converter is considered as a disturbance [89]. The relation between the current $I_{dL}(\mathrm{s})$ and the dc-link voltage $V_{dc}(\mathrm{s})$ is obtained from the equations (4.49) - (4.51):

$$V_{dc}(\mathrm{s}) = 3\ V_L\frac{I_{dL}(s)}{I_{0L}(\mathrm{s})} = 3\ \left(\frac{m_a}{2\sqrt{2}}V_{dc}(\mathrm{s})\right)\frac{I_{dL}(\mathrm{s})}{I_{0L}(\mathrm{s})} = \frac{3}{2\sqrt{2}}\ m_a\frac{I_{0s}(\mathrm{s})}{\mathrm{s}C}\ \frac{I_{dL}(\mathrm{s})}{I_{0L}(\mathrm{s})} = \frac{3}{2\sqrt{2}}\ m_a\frac{I_{dL}(\mathrm{s})}{\mathrm{s}C} \tag{4.52}$$

The resulting dc-link transfer function is:

$$\frac{V_{dc}(\mathrm{s})}{I_{dL}(\mathrm{s})} = \frac{3}{2\sqrt{2}}\ \frac{m_a}{\mathrm{s}C} \tag{4.53}$$

The control loop for the dc-link is designed according to the block diagram shown in Figure 4.11. In this case, the input of the PI controller is the error voltage ΔV_{dc}, the output is the current I_{dL}. The PI parameters are defined according to the phase margin test described in appendix D.

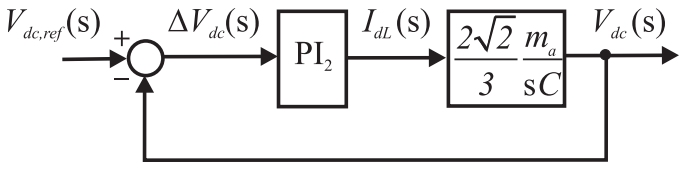

Figure 4.11 - Closed-loop including the PI controller and the dc-link transfer function.

4.5.2 The LSC transfer function

A third PI controller is used to force to zero the difference between the reference voltage $v_{L,ref}$ and the actual voltage v_L. The transfer function between the currents i_{dL} and i_{qL} and the voltages v_{dL} and v_{qL} respectively is used to determine the parameters of the PI controller.

Kirchhoff's voltage law applied to Figure 4.10 gives:

$$\overline{v} = R_L \bar{i}_L + L_L \frac{d}{dt} \bar{i}_L + \overline{v}_L \tag{4.54}$$

where

$\overline{v} = v_d + jv_q$ is the space vector that corresponds to the voltage at the PCC;

$\overline{v}_L = v_{Ld} + jv_{Lq}$ is the space vector that corresponds to the voltage at the LSC terminals.

From (4.54) the following relations are derived for the d and q axis:

$$\begin{cases} v_d = R_L\ i_{dL} + L_L\ \dfrac{d}{dt}\ i_{dL} - \omega_1\ L_L\ i_{qL} + v_{dL} \\ v_q = R_L\ i_{qL} + L_L\ \dfrac{d}{dt}\ i_{qL} + \omega_1\ L_L\ i_{dL} + v_{qL} \end{cases} \tag{4.55}$$

By substituting $v_d = v_s$ and $v_q = 0$ in (4.55) and applying the Laplace transform, the following is obtained:

$$\begin{cases} V_s(\mathrm{s}) &= R_L\ I_{dL}(\mathrm{s}) + \mathrm{s}\ L_L\ I_{dL}(\mathrm{s}) - \omega_1\ L_L\ I_{qL}(\mathrm{s}) + V_{dL}(\mathrm{s}) \\ 0 &= R_L\ I_{qL}(\mathrm{s}) + \mathrm{s}\ L_L\ I_{qL}(s) + \omega_1\ L_L\ I_{dL}(\mathrm{s}) + V_{qL}(\mathrm{s}) \end{cases} \tag{4.56}$$

By rearranging the above relations:

$$\begin{cases} V_s + \omega_1\ L_L\ I_{qL}(\mathrm{s}) - V_{dL}(\mathrm{s}) &= R_L\ I_{dL}(\mathrm{s}) + \mathrm{s}\ L_L\ I_{dL}(\mathrm{s}) \\ -\omega_1\ L_L\ I_{dL}(\mathrm{s}) + V_{qL}(\mathrm{s}) &= R_L\ I_{qL}(\mathrm{s}) + s\ L_L\ I_{qL}(\mathrm{s}) \end{cases} \tag{4.57}$$

and the auxiliary voltages are defined as follows:

$$\begin{cases} V'_{dL}(\mathrm{s}) &= V_s(\mathrm{s}) + \omega_1\ L_L\ I_{qL}(\mathrm{s}) - V_{dL}(\mathrm{s}) \\ V'_{qL}(\mathrm{s}) &= -\omega_1\ L_L\ I_{dL}(\mathrm{s}) + V_{qL}(\mathrm{s}) \end{cases} \tag{4.58}$$

From (4.57) and (4.58) the following expressions are derived:

$$\begin{cases} V'_{dL}(\mathrm{s}) &= R_L\ I_{dL}(\mathrm{s}) + \mathrm{s}\ L_L\ I_{dL}(\mathrm{s}) \\ V'_{qL}(\mathrm{s}) &= R_L\ I_{qL}(\mathrm{s}) + \mathrm{s}\ L_L\ I_{qL}(\mathrm{s}) \end{cases} \tag{4.59}$$

The above system shows that the same transfer function is obtained for the d and q equivalent circuits:

$$\frac{I_{dL}(\mathrm{s})}{V'_{dL}(\mathrm{s})} = \frac{I_{qL}(\mathrm{s})}{V'_{qL}(\mathrm{s})} = \frac{1}{R_L + \mathrm{s}L_L} \tag{4.60}$$

The same transfer function is obtained because the same resistance and inductance characterize the d and q axes equivalent circuits.

The transfer function (4.60) is used in the design of the PI controller for the LSC as shown in Figure 4.12. The input for the PI controller is the current error ΔI_{dL}, the output is the auxiliary voltage V'_{dL}. The PI parameters are defined according to the phase margin test described in appendix D.

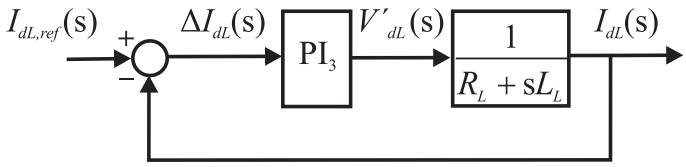

Figure 4.12 - Closed-loop including the PI controller and the LSC transfer function.

4.5.3 Block diagram for the LSC control

In Figure 4.13 the block diagram for the control of the LSC is presented. The structure is similar to the one described for the RSC control (Figure 4.9). Two main differences can be identified between the control systems shown in Figures 4.9 and 4.13:

1. The RSC subsystem reference currents contain harmonic components, the LSC subsystem reference currents are at fundamental frequency only.

2. The block diagram for the LSC has an additional PI controller that limits the variation of the dc-link voltage v_{dc}.

The upper level of the diagram shown in Figure 4.13 refers to the d-axis variables, the lower level refers to the q-axis variables.

The upper level is described at first. In the top left corner of Figure 4.9, the difference between the reference voltage and the measured voltage is computed. According to Figure

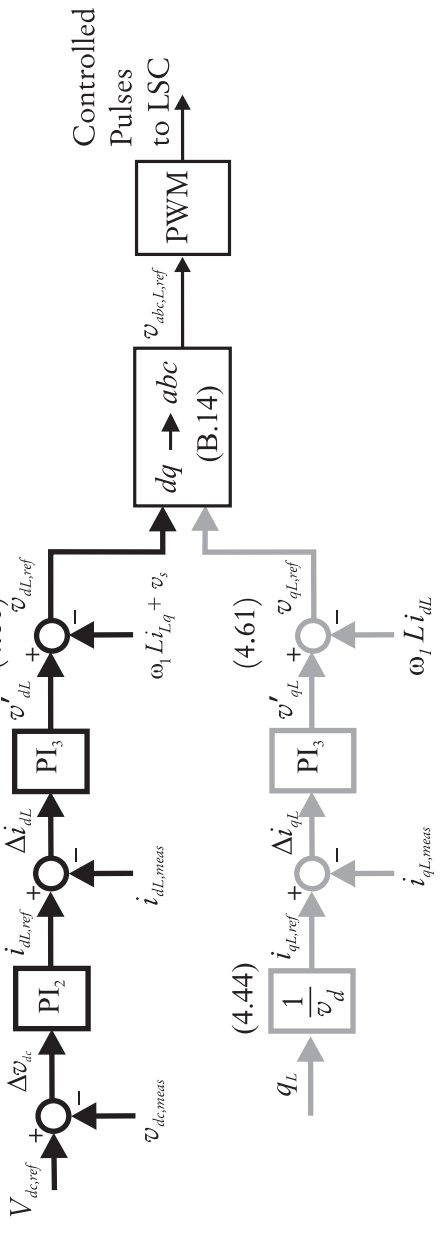

Figure 4.13 - Block diagram for the LSC subsystem control, compensation by means of RSC modulation.

4.11, the difference ΔV_{dc} is the input for the PI controller of the dc-link. The output of the PI controller is the reference current $i_{dL,ref}$.

The difference between the reference current and the measured current Δi_{dL} is the input for the PI controller of the LSC. The output of the PI controller is the auxiliary reference voltage v'_{dL} .

The actual reference voltages $v_{dL,ref}$ is obtained from the auxiliary voltage v'_{dL} according to the first of (4.58):

$$v_{dL,ref}(\mathrm{s}) = v'_{dL}(\mathrm{s}) - \frac{d}{dt}\omega_1 \; L_L \; i_{qL}(\mathrm{s}) + v_s(\mathrm{s}) \tag{4.61}$$

A similar procedure is applied to the q axis variables except for the definition of the reference current i_{qL}. The reference current i_{qL} that is derived from the value of q_c according to (4.45) and does not require a feedback loop.

The actual reference voltages $v_{qL,ref}$ is obtained from the auxiliary voltage v'_{qL} according to the second of (4.58):

$$v_{qL,ref}(\mathrm{s}) = v'_{qL}(\mathrm{s}) + \frac{d}{dt}\omega_1 \; L_L \; i_{dL}(\mathrm{s}) \tag{4.62}$$

4.6 Control system simulation

4.6.1 Software and simulation parameters

The system shown in Figure 3.1 is simulated according to the control strategy explained in sections 4.3 - 4.5. The NLL is replaced by equivalent current sources injecting harmonics. Appendix A contains the machine and lines data, the power converters characteristics, the PI controller parameters and the tracking characteristic of the turbine. The software used is Simulink SimPowerSystems®[82, 127, 131].

A fixed-step discrete time simulation is chosen. This choice is motivated as follows:

1. When power converters are simulated, it is always recommended to discretize a system to speed up the simulation process [131, 132]. The step time used for the simulation is $T_s = 10\mu$s. With this choice, a simulation of a few seconds runs in less then five minutes and the generated waveforms are not truncated. With a continuous time solver, the same simulation takes ten times more without adding any significant improvement to the resulting waveforms. With larger step times, the graphs are not accurate enough; with smaller time steps, the simulation time grows significantly. Other authors [29] chose to simulate the power converters by means of averaged models in

order to speed up the simulation process. In the averaged model, the power converters are represented by equivalent voltage sources generating the AC voltage averaged over one cycle of the switching frequency [130]. The averaged model results in a fast simulation, but it does not allow harmonics simulations, and this is the reason why it cannot be used for this work.

2. Using a fixed-step solver, the Fast Fourier Transform (FFT) of the measured electric quantities can be performed directly from the sampled data [133], and no interpolation is needed.

4.6.2 Study organization

In each example presented in the following sections, the NLL injects harmonic currents with different frequencies and magnitudes. The scope of the simulations is to show that the compensation by means of RSC modulation results in sinusoidal currents at fundamental frequency on the grid for practical situations that apply in moder power systems.

For each example, the following results are provided:

- Current spectra of NLL current i_h, stator current i_s, LSC current i_L and grid current i_g. The current spectra are used to verify the improvement of the grid current harmonic content.
- Stator and rotor winding loss, calculated according to (3.23) and power converter loss, determined as explained in section 3.6. The winding loss calculation allows determining if derating of the DFIG is necessary.
- Stator and rotor voltage oscillogram and spectra. The voltage oscillograms shows the value of the peak voltage.

4.6.3 Example 4.I

Example 4.I - Current oscillograms

The NLL injects a negative sequence fifth harmonic current ($h = 5$); the harmonic current amplitude is $I_5 = I_n/5$, where I_n is the DFIG rated current:

$$\begin{cases} i_{ha} = 0.2 I_n \cos(5\omega_1 t) \\ i_{hb} = 0.2 I_n \cos(5\omega_1 t + 2\pi/3) \\ i_{hc} = 0.2 I_n \cos(5\omega_1 t + 4\pi/3) \end{cases} \tag{4.63}$$

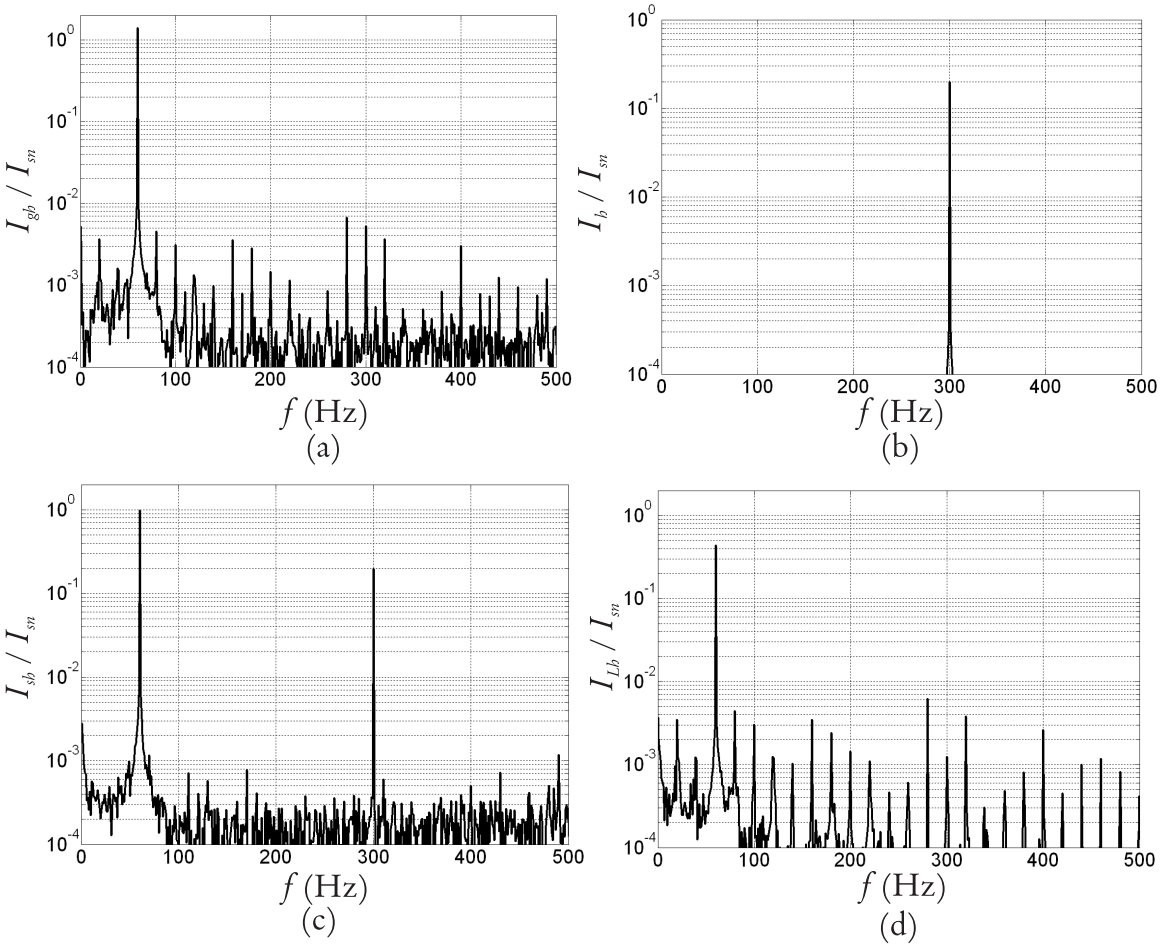

Figure 4.14 - Example 4.I : Normalized current amplitude spectra; (a) grid current, (b) NLL current, (c) stator current and (d) LSC current.

The normalized current amplitude spectra are displayed in Figure 4.14. The stator current spectrum illustrated in Figure 4.14.b and is dominated by two components. The fifth harmonics corresponds to the one injected by the NLL and the first harmonic component results from the mechanical power extracted by the turbine. The value of the mechanical power and therefore of the fundamental current is obtained from the tracking characteristic, Figure A.1.a. In this example, the steady state wind velocity v_u=16 m/s is assumed, corresponding to $\omega_r/\omega_1 = 1.5$ and $P_s = 1$.

The LSC current spectrum is presented in Figure 4.14.d: since the LSC does not participate to the compensation of harmonic currents (section 4.5), the fundamental current component is dominant. The LSC current charges the dc-link capacitor and results in a constant dc voltage; minor harmonic components are caused by the switches operation, since the switches are modeled as real devices with the characteristics listed in appendix A. Moreover, truncation errors contribute to generate a noisy spectrum.

The normalized grid current amplitude spectrum is displayed in Figure 4.14.a: the 60 Hz component is dominant as a result of the AF operation implemented by the WECS.

The current spectra presented in Figure 4.14 show other spectral lines in addition to the fundamental and the fifth components. Those spectral lines are at least two orders of magnitude lower than the fundamental and they are caused by principally two phenomena:

1. Truncation errors caused by the fixed-step solver used.
2. The RSC and LSC IGBTs are modeled according to the manufacturer parameters ([134]): the parasitic parameters included in the model causes discrepancies between the switching times defined by the control and the actual switch operation, thus resembling a real-life application.

Several other simulations have been carried out assuming other steady-state wind speeds, resulting in current spectra very similar to the ones shown in Figure 4.14, with varying amplitude for stator and grid fundamental current component.

Observation - Phase angle

Figures 4.15.a and 4.15.b show the phase angle spectrum of the NLL current and of the stator current respectively. These diagrams show that the difference between the fifth harmonic component of the NLL current and of the stator current is 180^o, thus resulting in harmonic cancellation.

It has been verified that any variations in the phase angle of the harmonic current injected by the NLL is tracked by the control system, thus resulting in an equal change of the harmonic stator current phase angle.

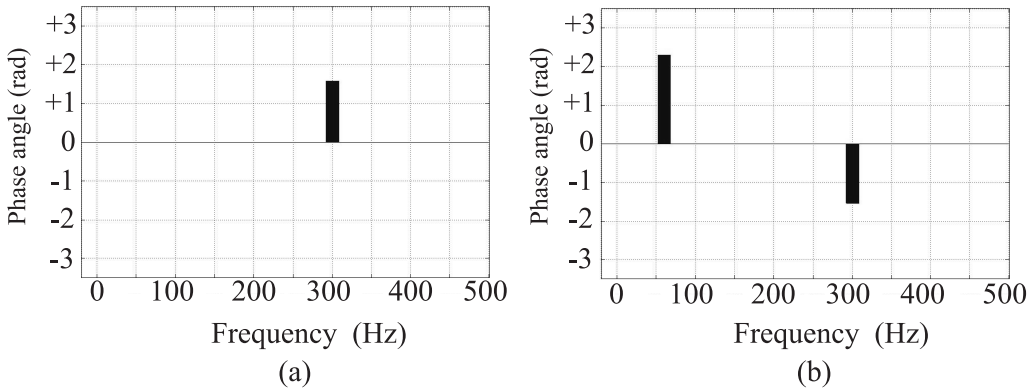

Figure 4.15 - Example 4.I: Current phase angle spectrum; (a) NLL current and (b) stator current.

Example 4.I - Power loss

The normalized stator and rotor winding losses for variable speed operation are plotted in Figure 4.16; base value are the rated stator and rotor winding loss, respectively [24]. On the horizontal axis the normalized rotor speed ω_r/ω_1 is displayed. The winding loss calculation has been calculated according to (3.23), under the assumption that the operation of the DFIG cooling system does not depend on the rotor speed [135].

The patterns of stator and rotor loss almost overlap: this is due to the similar geometry of stator and rotor windings [84] and to the mutual coupling between stator windings and rotor windings.

For subsynchronous speeds ($\omega_r/\omega_1 < 1$), both stator and rotor winding power loss are below the rated value. For supersynchronous speeds ($\omega_r/\omega_1 > 1$), the winding loss is about 10% over the rated losses. This overloading can be tolerated by the machine for a short time. Since high wind speeds, corresponding to $\omega_r/\omega_1 > 1$, are not very frequent, this overloading can be temporarly tolerated by the DFIG without causing winding insulation damage deterioration. As a result, derating is not necessary and the machine can operate according to the tracking characteristic at any wind speed, providing harmonic compensation simultaneously.

The normalized power converters losses are plotted in Figure 4.17; base value is the rated power loss. Two different patterns are presented: the RSC and LSC loss for sinusoidal operation and for harmonic compensation. Since no harmonic currents are injected by the power converters, the two patterns overlap.

[24] The rated power loss values are listed in appendix A.

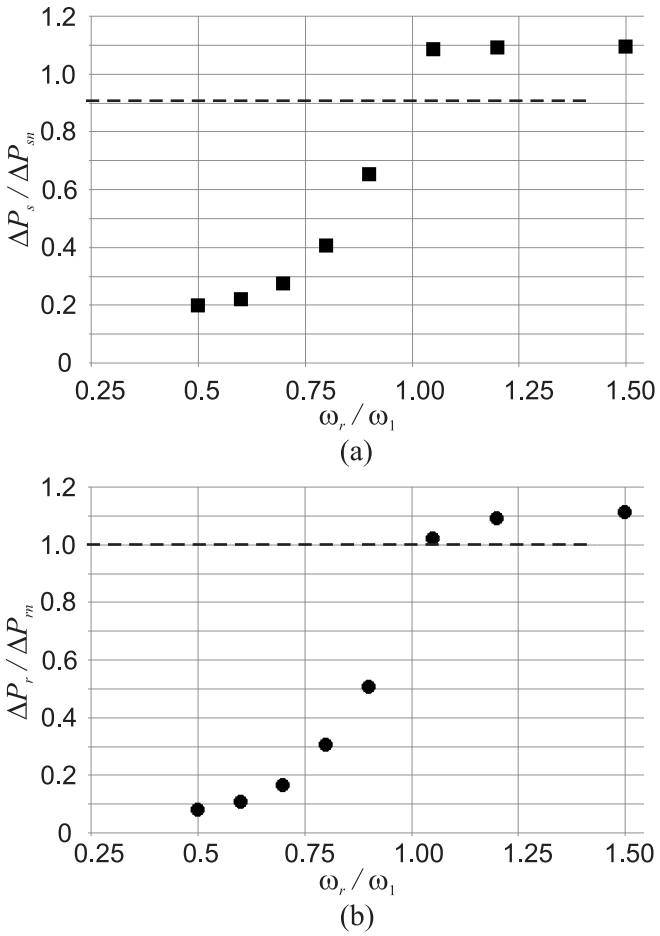

Figure 4.16 - Example 4.I: Normalized windings power loss; (a) Stator and (b) rotor. For subsynchronous speeds ($\omega_r/\omega_1 < 1$), both stator and rotor winding losses are below the rated value. For supersynchronous speeds ($\omega_r/\omega_1 > 1$), both stator and rotor power loss are about 10% above the rated value.

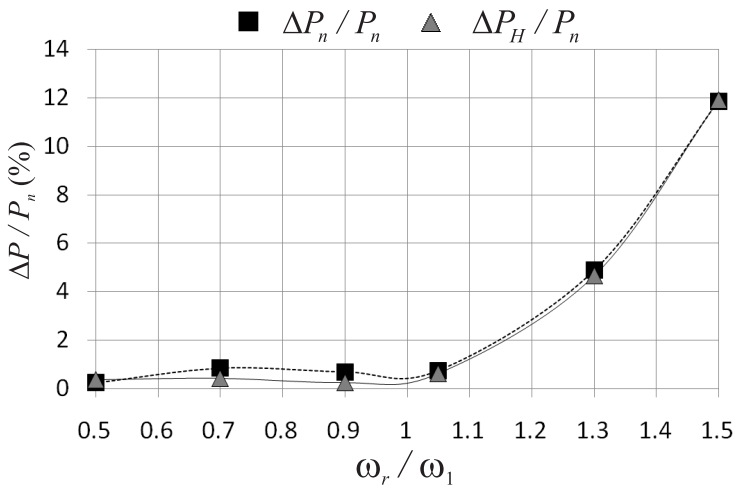

Figure 4.17 - Example 4.I: Normalized power converters loss; the black rectangles correspond to sinusoidal operation, the gray triangles to power generation and harmonic compensation.

Example 4.I - Voltage oscillograms and spectra

The normalized line-to-line rotor oscillogram and spectrum are shown in Figures 4.18 and 4.19, respectively.

The line-to-line rotor voltage is the typical output of a power converter controlled by PWM modulation. The peak rotor voltage depends on the value of the dc-link voltage v_{dc} according to (3.17).

The harmonic components are identified in Figure 4.19:

1. Fundamental component frequency is $f_{r,1} = 30$ Hz, since the slip for the case study is $\mathbb{S}$=0.5 and $f_{r,1} = sf_{s,1} = 0.5 \cdot 60 = 30$ Hz.

2. A low frequency component corresponds to the NLL currents: $f_{r,5} = sf_{s,5} = 0.5 \cdot 300 = 150$ Hz.

3. High frequency components in the region $6000 < f < 7000$ Hz that includes the PWM carrier frequency ($f_{tri} = 6480$ Hz, appendix A). According to the theoretical analysis presented in appendix H, PWM operation generates harmonic frequencies that are multiple of the carrier frequency (Figure H.4): therefore, it is expected to find other harmonic components equally spaced at multiple of the frequency $f_{tri} = 6480$ Hz.

The normalized line-to-neutral stator voltage oscillogram and spectrum are presented in Figures 4.20 and 4.21, respectively.

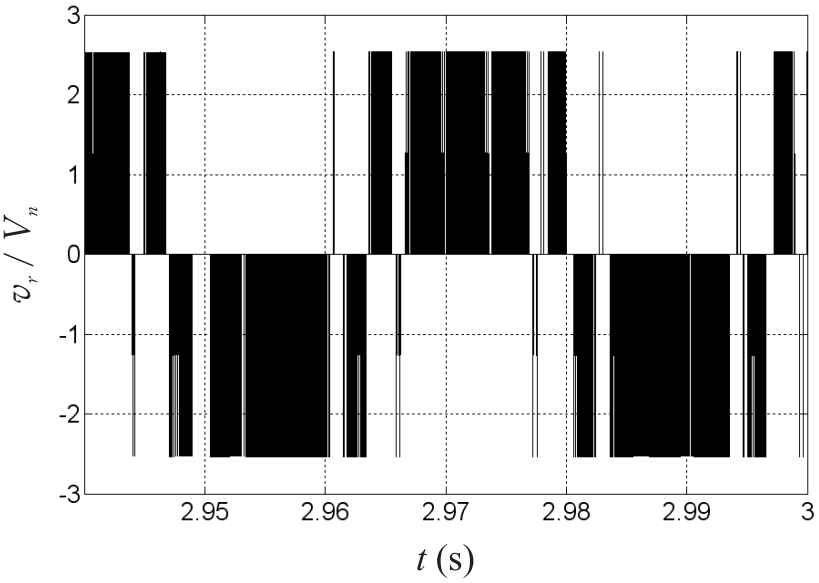

Figure 4.18 - Example 4.I: Normalized line-to-line rotor voltage oscillogram.

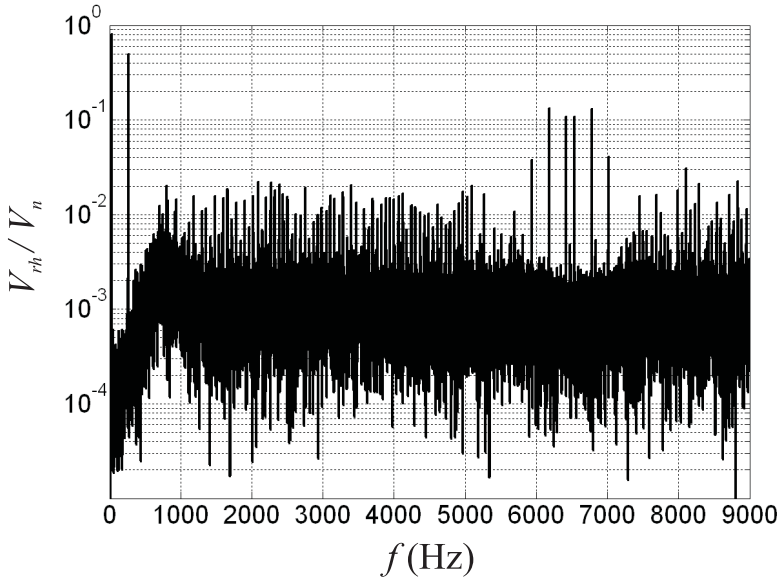

Figure 4.19 - Example 4.I: Normalized line-to-line rotor voltage spectrum.

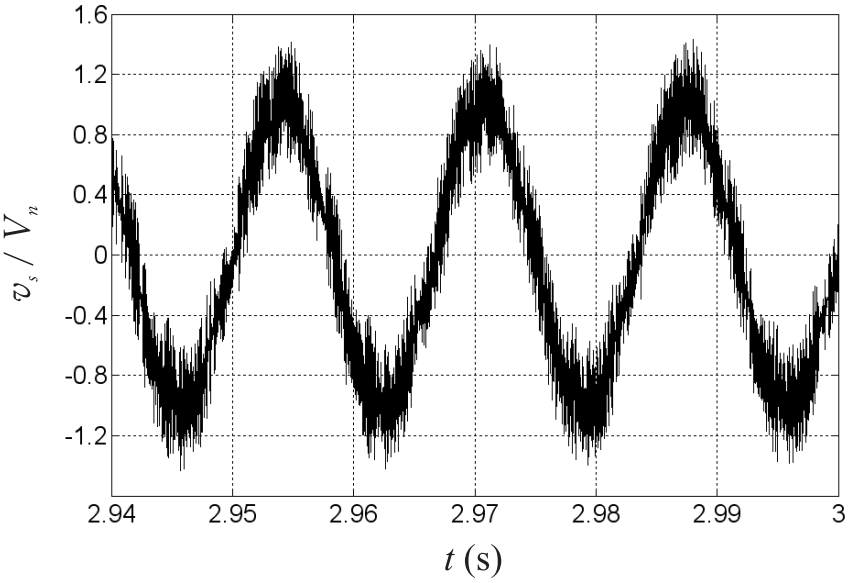

Figure 4.20 - Example 4.I: Normalized line-to-neutral stator voltage oscillogram.

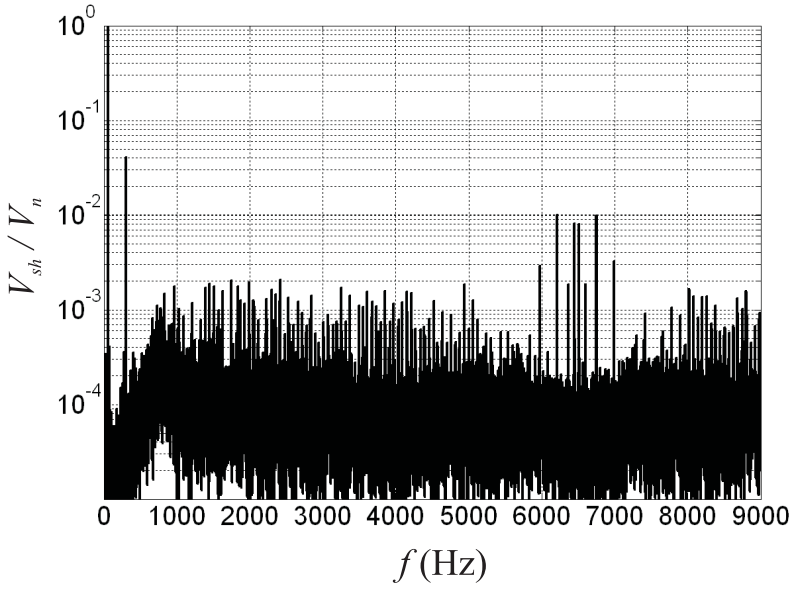

Figure 4.21 - Example 4.I: Normalized line-to-neutral stator voltage spectrum.

The stator voltage peak $\hat{V}_s$ is approximately 1.4 p.u. and is function on the harmonic content of the stator current, as explained in section 3.2.2. The harmonic components to the voltage spectrum are identified in Figure 4.21, similarly to the rotor voltage:

1. Fundamental harmonic at $f_{s,1}$=60 Hz. This component is responsible for the transfer of fundamental active power.

2. A low frequency harmonic at $f_{s,5}$=300 Hz. This component is caused by the flow of the fifth harmonic current in the DFIG stator windings and consequent voltage drop on the line impedance Z_c.

3. High frequency harmonics in the region $6000 < f < 7000$ Hz. The stator voltage high frequency components correspond to the ones illustrated in Figure 4.21 for the rotor voltage spectrum. The amplitudes of the stator voltage harmonic components are smaller than the rotor voltage harmonic components, according to the theoretical extimates provided in chapter 3. For example, for $f = 6200$, $V_{rh}/V_n \approx 0.13$ (Figure 4.19) and according to (3.17), $V_{sh}/V_n = 0.12 * 0.13 \approx 0.0156$ is expected. Figure 4.21 shows that $V_{sh}/V_n \approx 0.01$: this results is consistent with the theoretical results, observing that (3.17) is obtained with the help of approximations and simplifications.

4.6.4 Example 4.II

Example 4.II - Current spectra

The NLL injects a negative sequence fifth harmonic and a positive sequence seventh harmonic current: the amplitude of the harmonic components are listed in Table 4.1.

Table 4.1 - Example 4.II: Harmonic currents injected by the NLL.

h	I_h/I_n	Sequence
5	0.20	+
7	0.14	−

The normalized current amplitude spectra are shown in Figure 4.22: the stator current spectrum (Figure 4.22.c) contains the harmonic currents corresponding to the ones injected by the NLL (Figure 4.22.b). As a consequence, the grid current spectrum (Figure 4.22.a) is dominated by the fundamental current component and this proves the validity of the proposed approach. Similarly to the previous example, the LSC current spectrum dominant

component is at fundamental frequency, since the stator windings only are responsible for harmonic compensation.

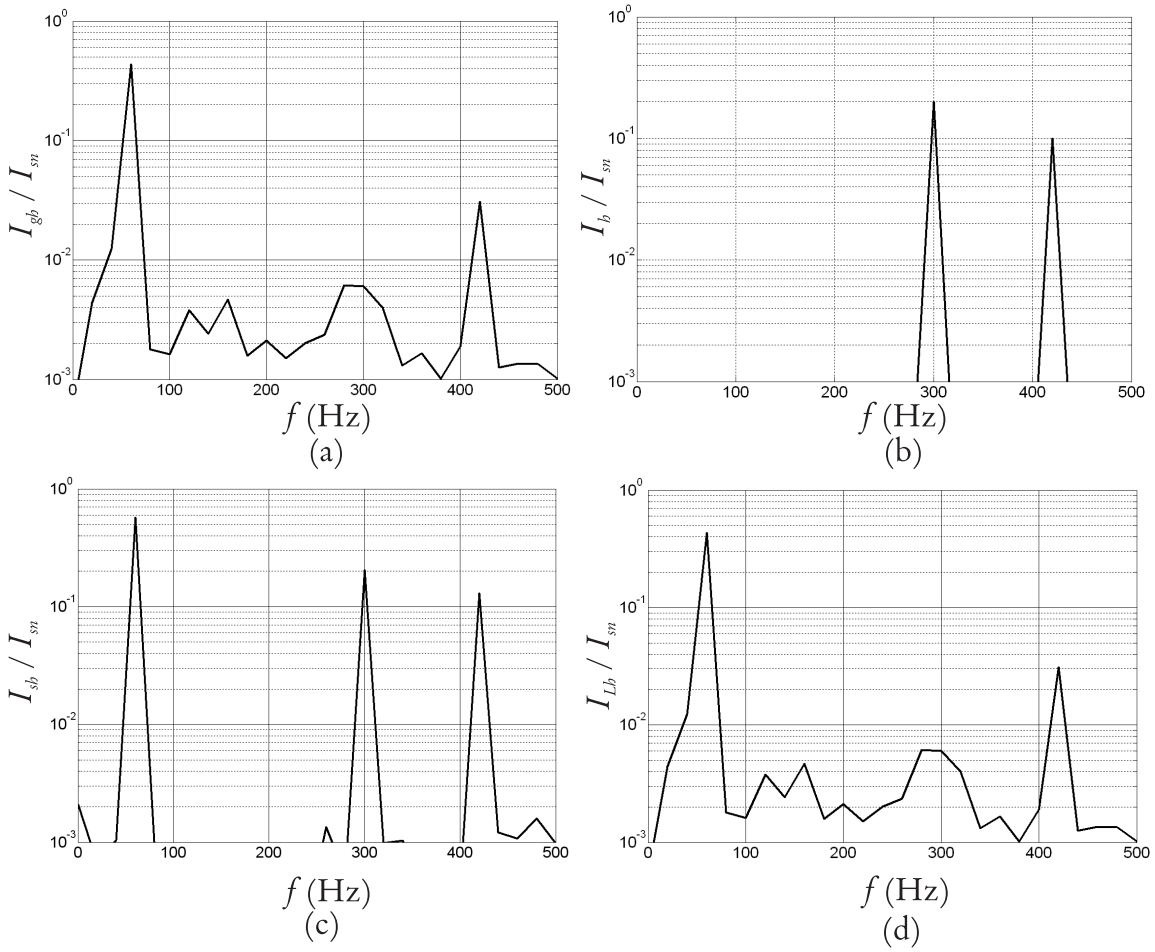

Figure 4.22 - Example 4.II: normalized current amplitude spectra; (a) grid current, (b) NLL current, (c) stator current and (d) LSC current.

Example 4.II - Power loss

The normalized stator and rotor winding losses are plotted in Figure 4.23 as function of the normalized rotor speed ω_r/ω_1 and they are very similar to the ones calculated for Example 4.I. The winding loss in Example 4.II are slightly higher than the winding loss calculated in Example 4.I, since an additional seventh order current is injected by the DFIG in the second example. The difference can be quantified as follows: the amplitude of the seventh harmonic current is $I_7 = 1/7 = 0.43$, the winding loss caused by this current component

(ignoring the skin effect) is:

$$P_7 = (I_7)^2 = \frac{1}{7^2} \approx 0.02 \text{ (p.u.)}$$

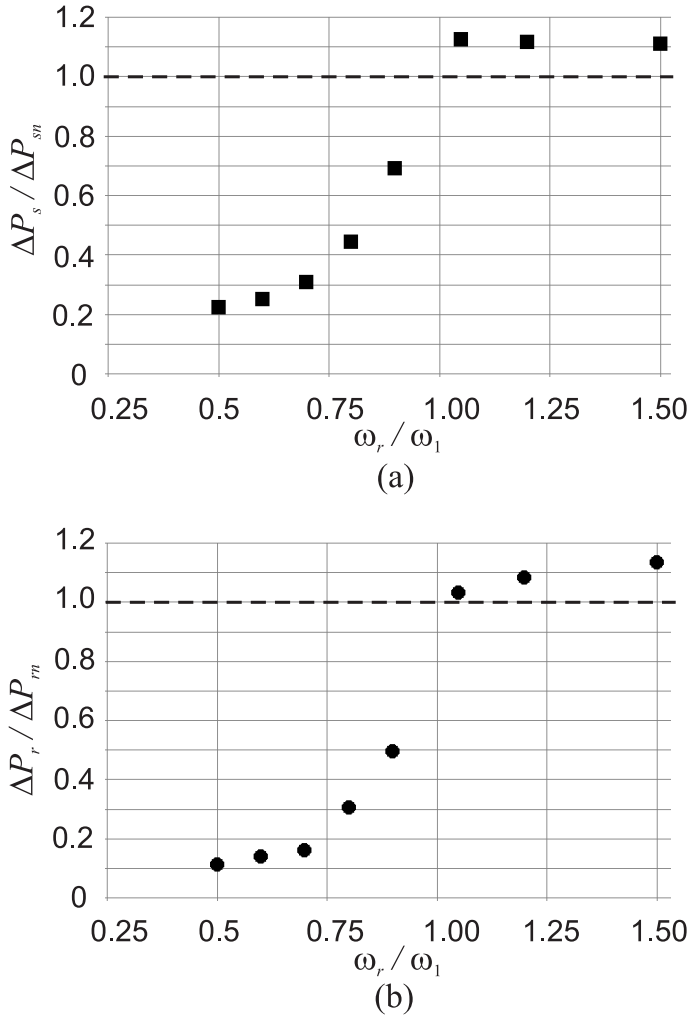

Figure 4.23 - Example 4.II: Normalized winding power loss for Example 4.II; (a) Stator and (b) rotor. For $\omega_r/\omega_1 \leq 1$, the winding loss is below the rated value for both rotor and stator. For $\omega_r/\omega_1 \geq 1$, the winding loss is about 10% over the rated loss for both stator and rotor.

The conclusions carried out from the graphs depicted in Figure 4.23 are very similar to the ones obtained in Example 4.I. The increased power loss due to harmonic compensation does not result in winding insulation damage if high wind speeds corresponding to supersynchronous operation are an intermittent condition.

Example 4.II - Voltage oscillograms and spectra

The normalized line-to-line rotor voltage oscillogram and spectrum are presented in Figures 4.24 and 4.25, respectively.

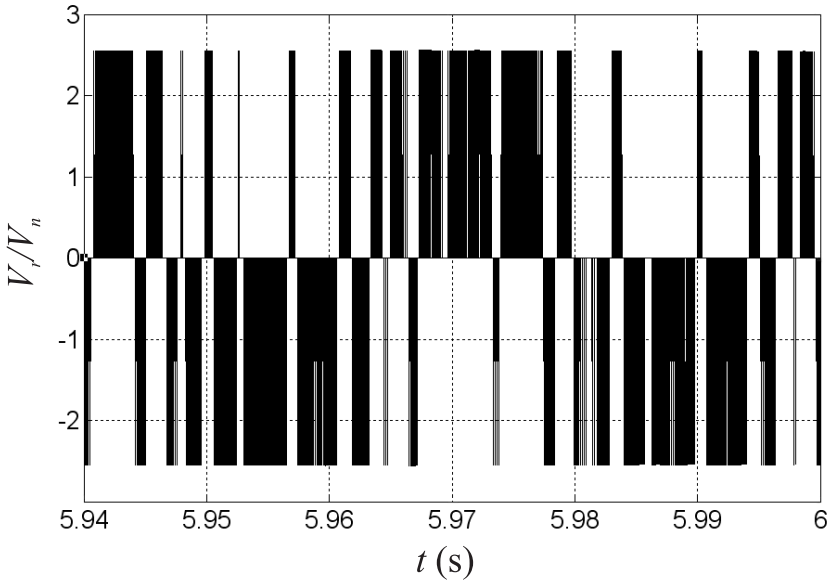

Figure 4.24 - Example 4.II: Normalized line-to-line rotor voltage oscillogram.

The normalized phase-to-neutral stator voltage oscillogram and spectrum are presented in Figures 4.26 and 4.27, respectively.

The voltage oscillograms and spectra show a pattern very similar to the one obtained for the previous example, and the harmonic content is very similar to the one described in aection 4.6.3.

4.6.5 Example 4.III

Example 4.III - Current spectra

The NLL injects a negative sequence fifth harmonic and a positive sequence seventh harmonic current with the amplitudes listed in Table 4.2.

The amplitude spectra for Example 4.III are shown in Figure 4.28. Similarly to Examples 4.I and 4.II, the grid current spectrum (Figure 4.28.a) is dominated by the fundamental component, thus proving the effectiveness of the proposed approach.

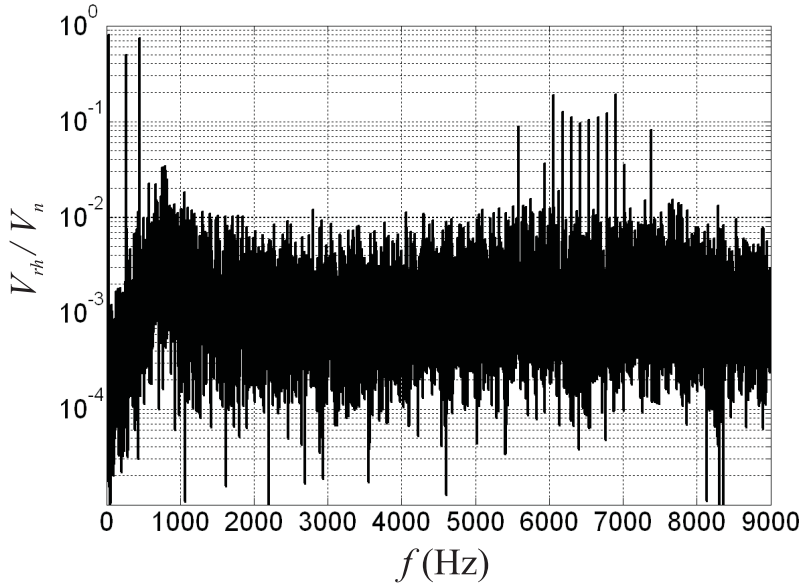

Figure 4.25 - Example 4.II: Normalized line-to-line rotor voltage spectrum.

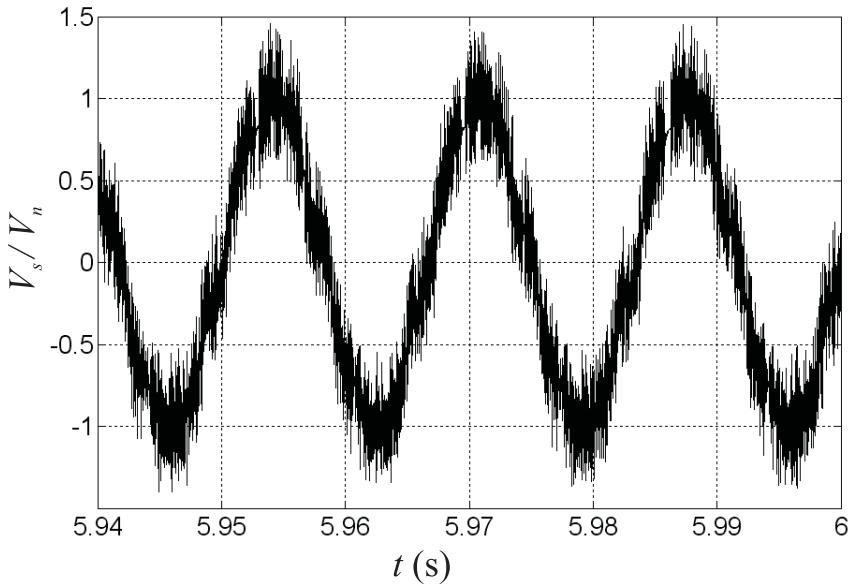

Figure 4.26 - Example 4.II: Normalized phase-to-neutral stator voltage oscillogram.

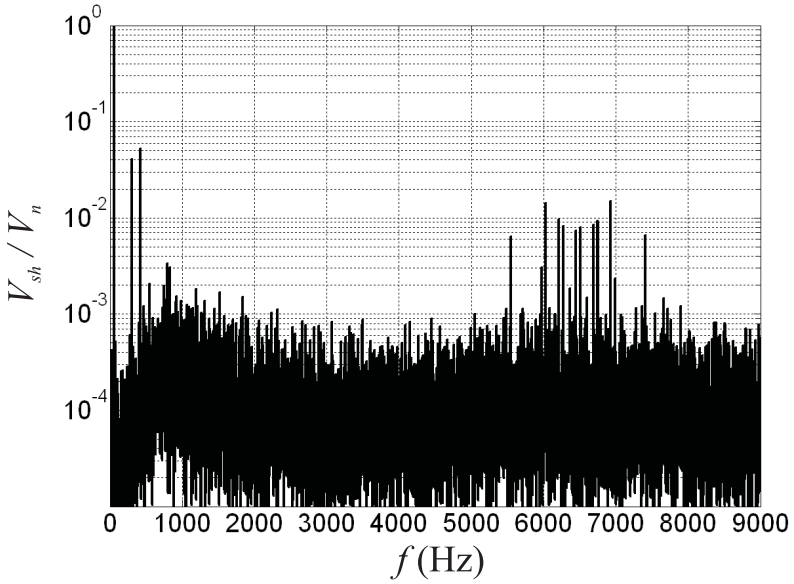

Figure 4.27 - Example 4.II: Normalized phase-to-neutral stator voltage spectrum.

Table 4.2 - Example 4.III: Harmonic currents injected by the NLL.

h	I_h/I_n	Sequence
5	0.2759	+
7	0.2108	−

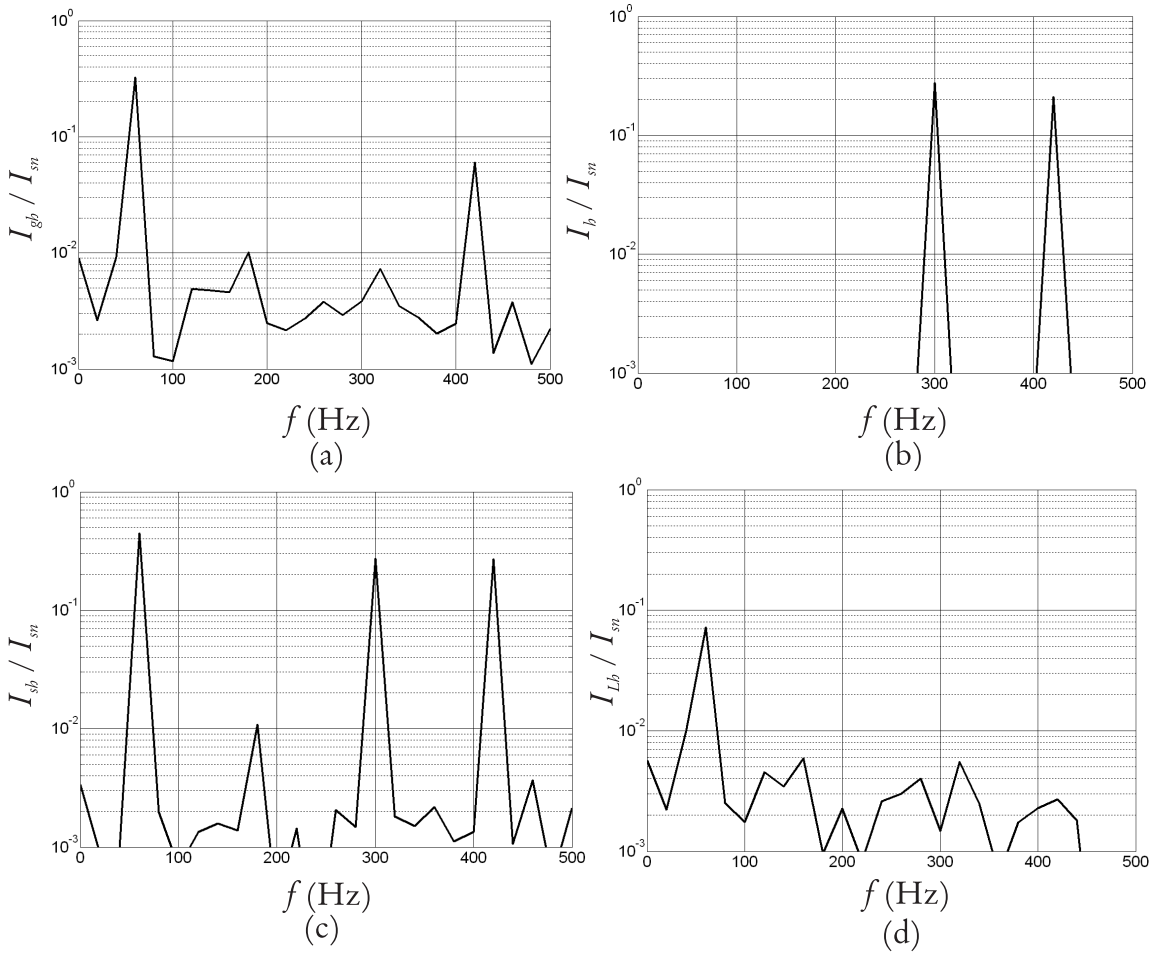

Figure 4.28 - Example 4.III: normalized current amplitude spectra; (a) grid current, (b) NLL current, (c) stator current and (d) LSC current.

Example 4.III - Power loss

The normalized stator and rotor winding loss are displayed in Figure 4.23 as function of the normalized rotor speed ω_r/ω_1. For $\omega_r/\omega_1 \leq 1$, the winding loss in the machine are below the rated rated value. For $\omega_r/\omega_1 \geq 1$, the winding loss are 30 % above the rated value (black markers). Therefore, derating is necessary for $\omega_r > 1$ to reduce the winding loss below the rated value (white markers).

DFIG derating results in the power curve shown in Figure 4.30. Stator active power P_s is shown on the vertical axis as function of the normalized rotor speed ω_r/ω_1. The derating curve for the stator windings is shown since derating of the stator results in an automatic derating of the rotor, according to the analysis carried out in section 3.4.

For subsynchronous speeds ($0.5 \leq \omega_r \leq 1$), the power curve follows the tracking characteristic presented in Figure A.1: the area below the curve corresponds to the fundamental stator power P_{s1}, the area between the tracking characteristic and the rated power corresponds to the harmonic stator power P_{sH}. In Region II a wide area is available for harmonic compensation.

For supersynchronous speeds ($1 \leq \omega_r \leq 1.5$), the fundamental stator power P_{s1} (3.28) is equal to 0.8 p.u. : this corresponds to a lower active power extracted from the wind with respect to the traditional power curve (Figure A.1.a). The area between 0.8 p.u. and 1 p.u. is dedicated to the harmonic stator power P_{sH}.

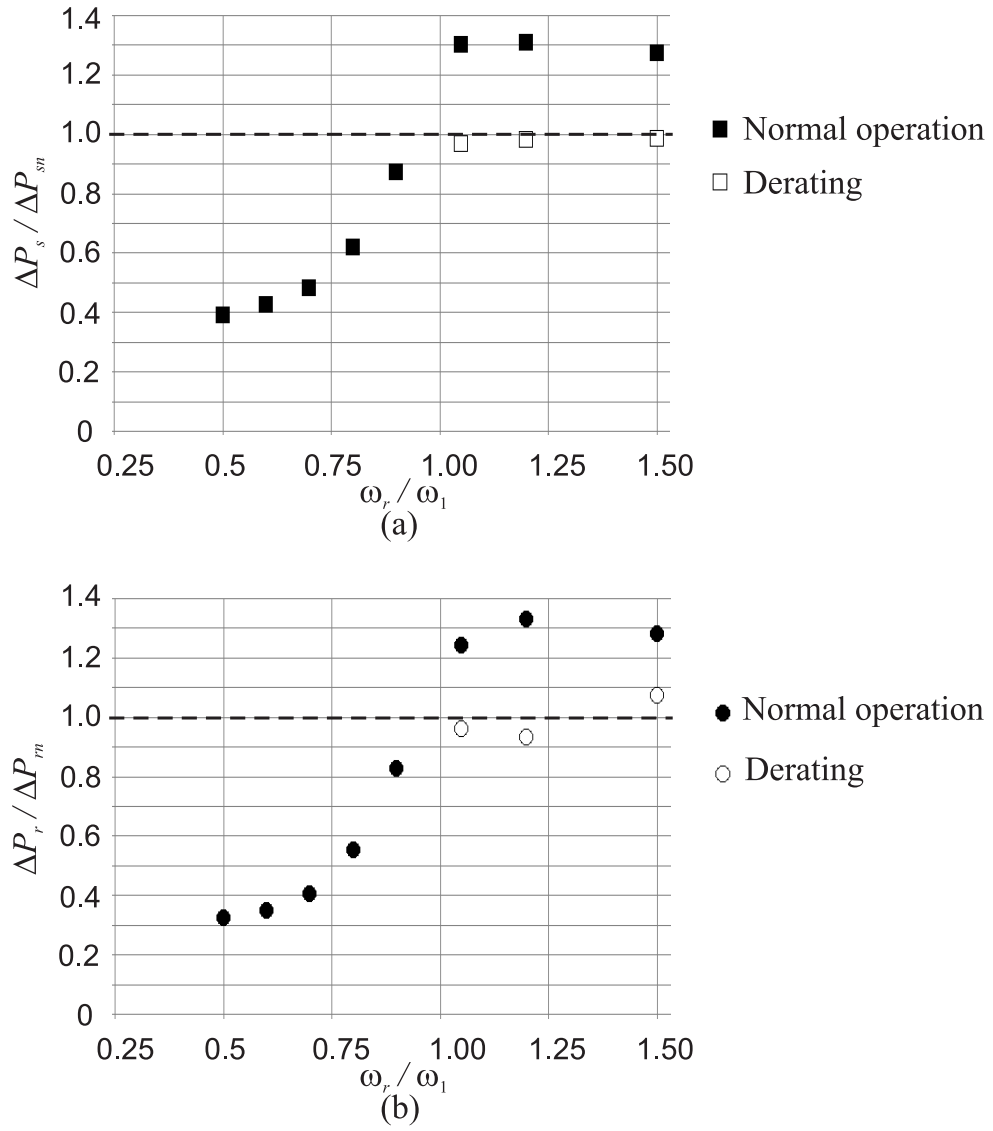

Figure 4.29 - Example 4.III: Normalized winding loss; (a) Stator and (b) rotor. The black markers indicate the winding power loss when AF operation and power generation are implemented simultaneously, the white markers indicate the stator and rotor losses when derating is applied. For ω_r/ω_1, the stator and rotor losses derating is necessary.

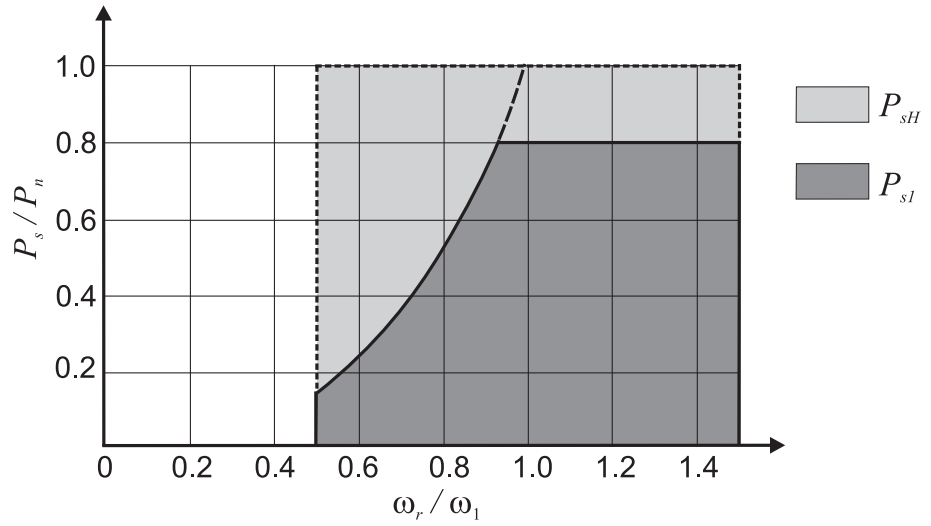

Figure 4.30 - Example 4.III: Modified power curve as function of the normalized rotor speed ω_r/ω_1; derating of the DFIG is implemented at supersynchronous speed $1 \leq \omega_r/\omega_1 \leq 1.5$.

4.6.6 Example 4.IV

Example 4.IV - Current spectra

The last example exemplifies the effectiveness of the proposed control method when several harmonics are injected by the NLL. The harmonic current injected by the NLL are listed in Table 4.3.

Table 4.3 - Example 4.IV - Harmonic currents injected by the NLL.

h	I_h/I_n	Sequence
0.05	0.10	+
5	0.20	+
7	0.14	−
7.5	0.10	+

The current amplitude spectra are presented in Figure 4.31: similarly to the previous examples, the effectiveness of the proposed method is verified and the grid current spectrum is dominated by the fundamental component.

Example 4.IV - Power loss

The normalized winding power loss is shown in Figure 4.32. For supersynchronous speed both the stator and the rotor winding loss are about 20 % above the rated values. As a consequence, the derating is implemented according to Figure 4.33.

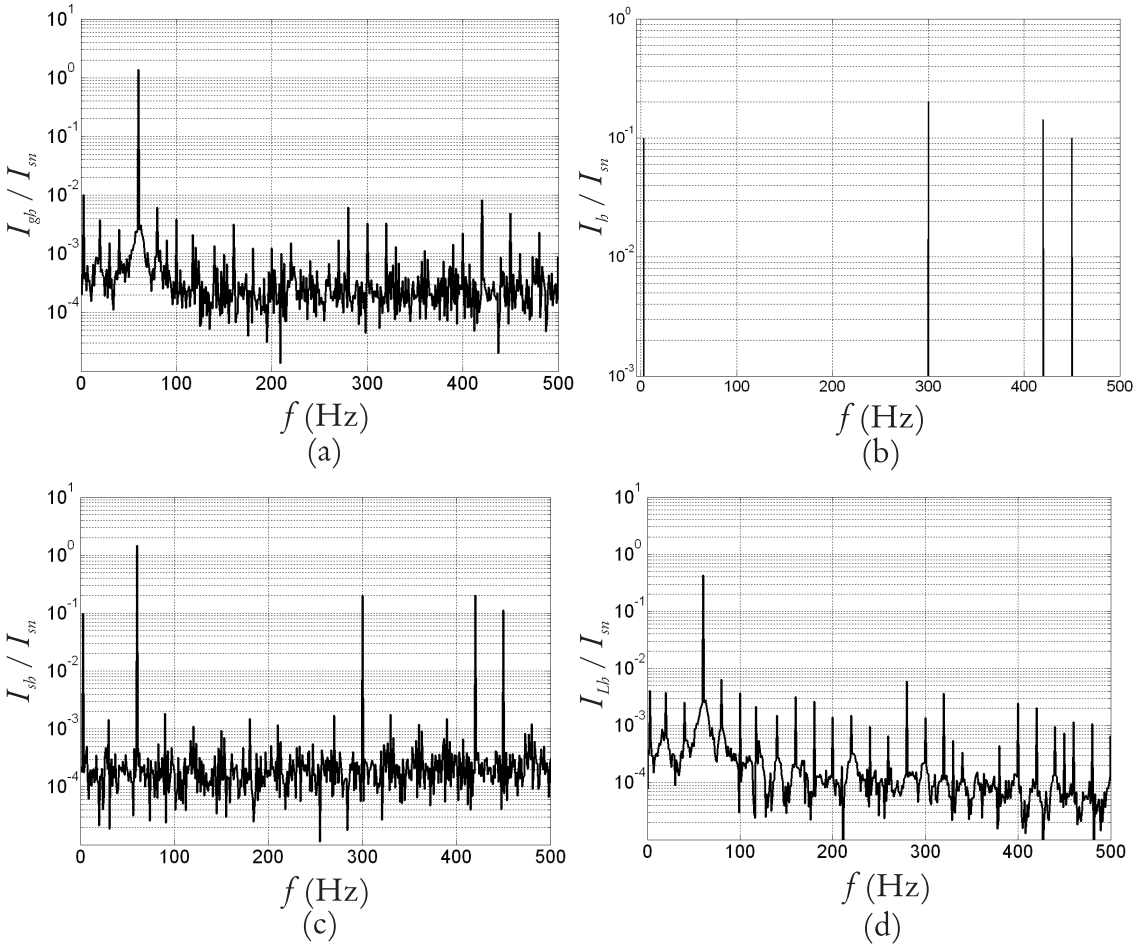

Figure 4.31 - Example 4.IV: Normalized current amplitude spectra for Example 4.VII: (a) grid current, (b) NLL current, (c) stator current and (d) LSC current.

The total power loss in the RSC and LSC is plotted in Figure 4.34 as a function of the normalized rotor speed ω_r/ω_1. If derating of the DFIG is implemented according to the curve depicted in Figure 4.33, the power loss at $\omega_r/omega_1 \geq 1$ are below the rated value, because the value of the fundamental power delivered from the rotor through the power converters is reduced. The above results proves that harmonic compensation does not have side effects on the operation of the power converters, because derating of the machine limits

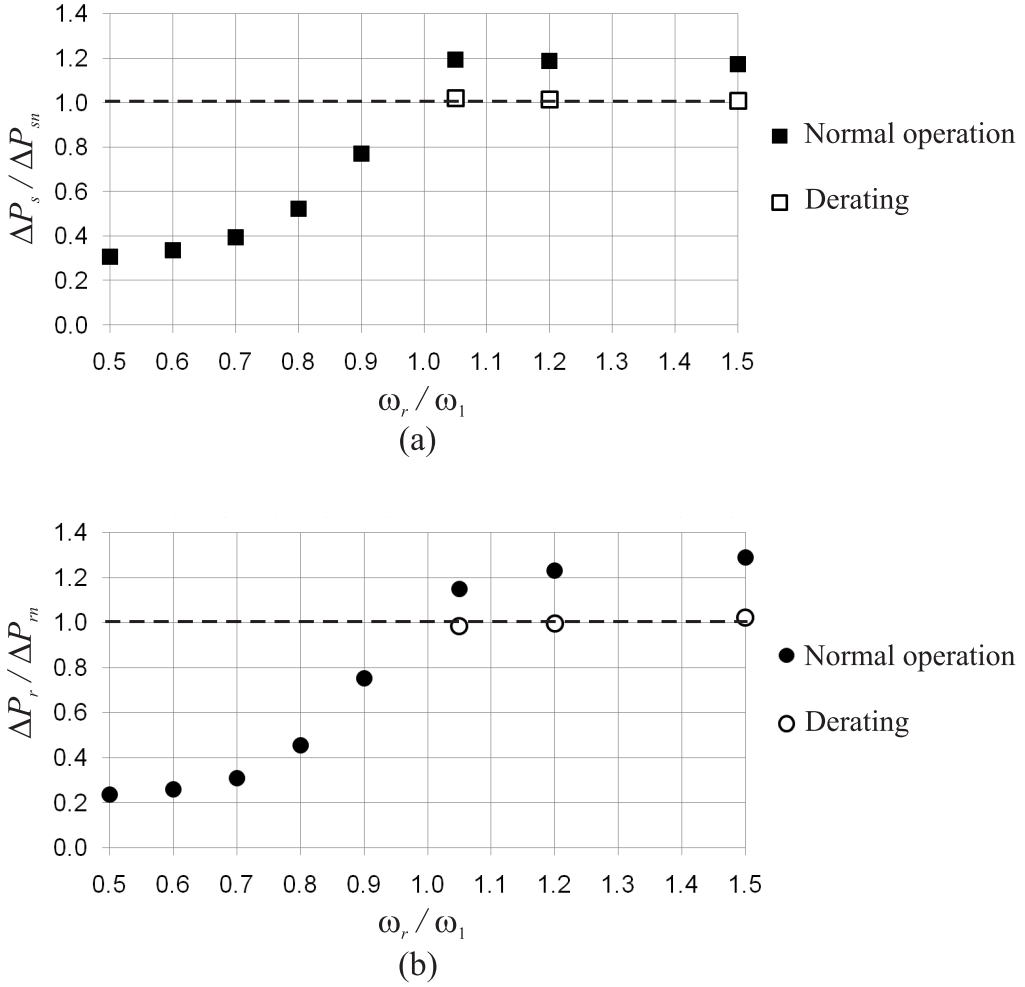

Figure 4.32 - Example 4.IV: Normalized winding loss: (a) Stator and (b) rotor.

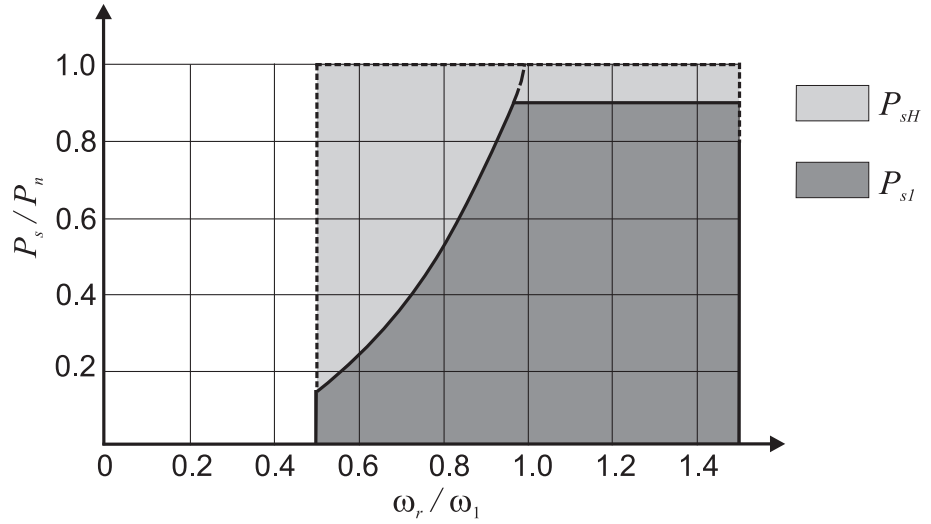

Figure 4.33 - Example 4.IV: Modified power curve as function of the normalized rotor speed ω_r/ω_1; derating of the DFIG is implemented at supersynchronous speed $1 \leq \omega_r/\omega_1 \geq 1.5$. .

their power loss.

Example 4.IV - Voltages oscillograms and spectra

The normalized line-to-line rotor voltage oscillogram and spectrum are illustrated in Figures 4.35 and 4.36, respectively.

The normalized stator voltage oscillogram and spectrum are presented in Figures 4.37 and 4.38, respectively.

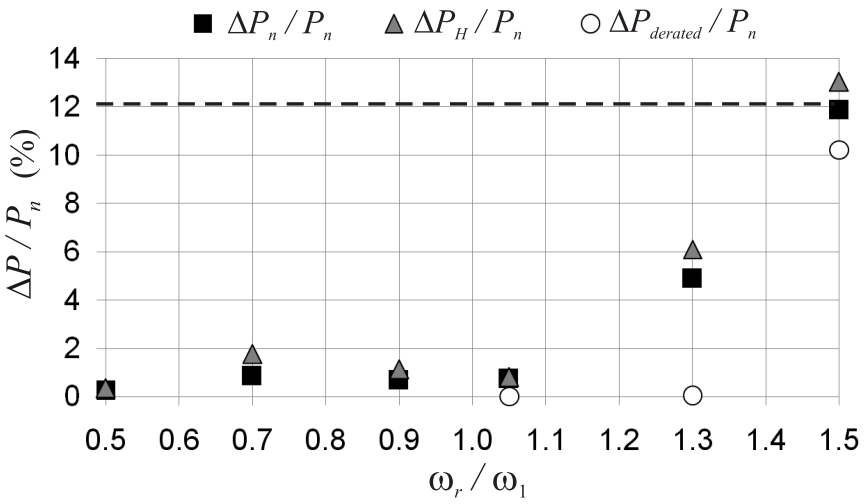

Figure 4.34 - Example 4.IV: Total power loss in the RSC and LSC as function of the normalized rotor speed ω_r/ω_1. Three curves are presented: the rated power loss, the power loss in presence of harmonic compensation and the power loss when derating is implemented according to the curve shown in Figure 4.33 are shown.

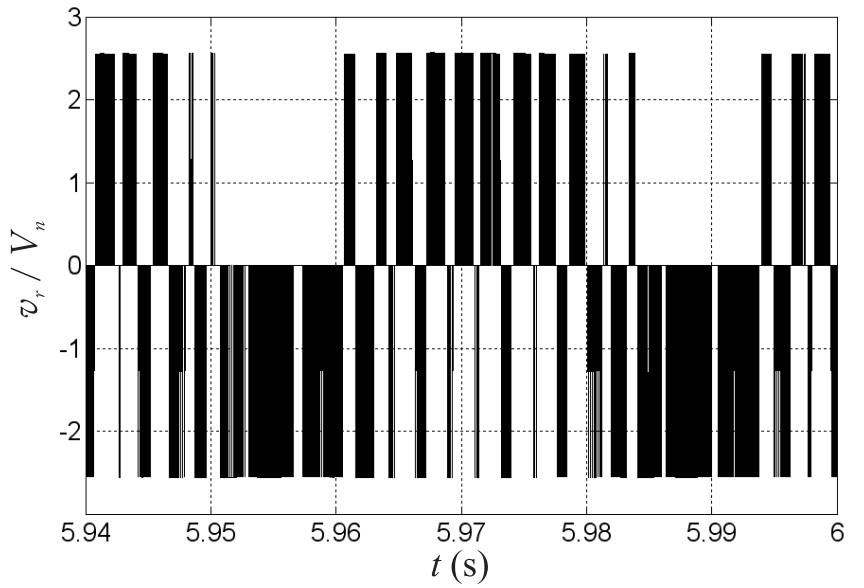

Figure 4.35 - Example 4.IV: Normalized line-to-line rotor voltage oscillogram.

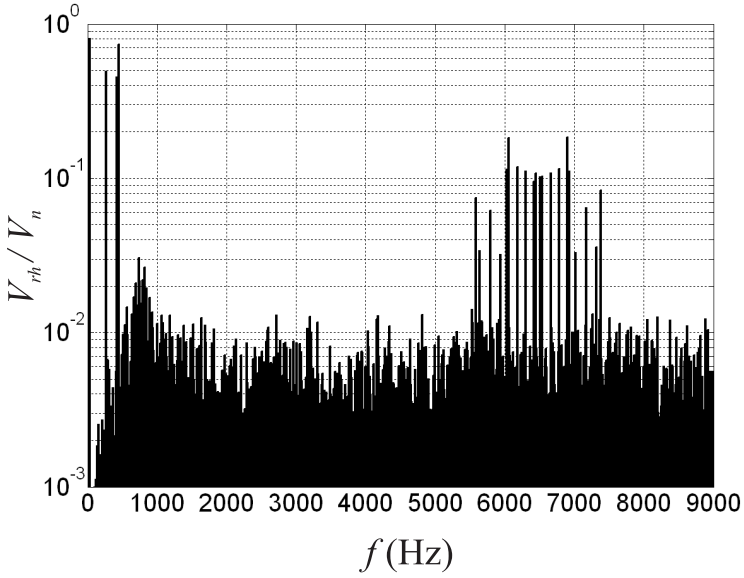

Figure 4.36 - Example 4.IV: Normalized line-to-line rotor voltage spectrum.

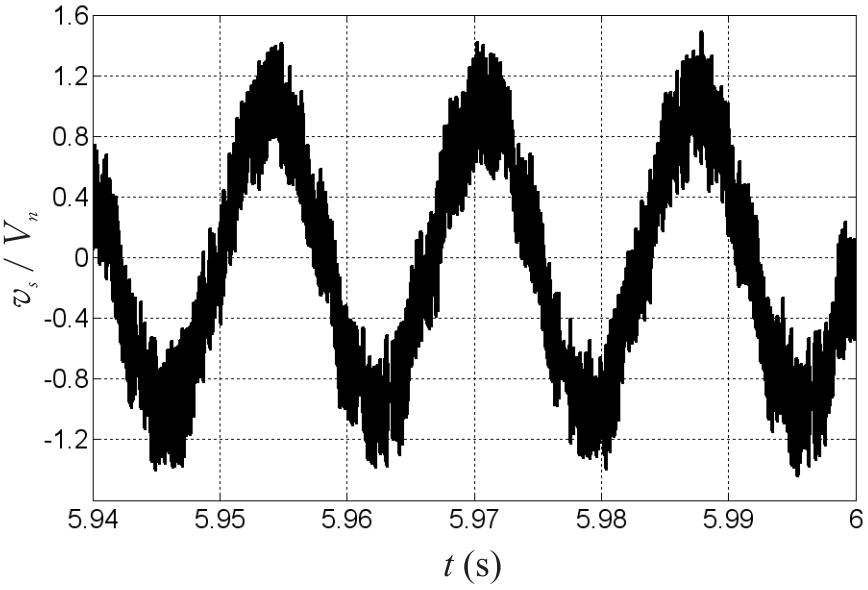

Figure 4.37 - Example 4.IV: Normalized line-to-neutral stator voltage oscillogram.

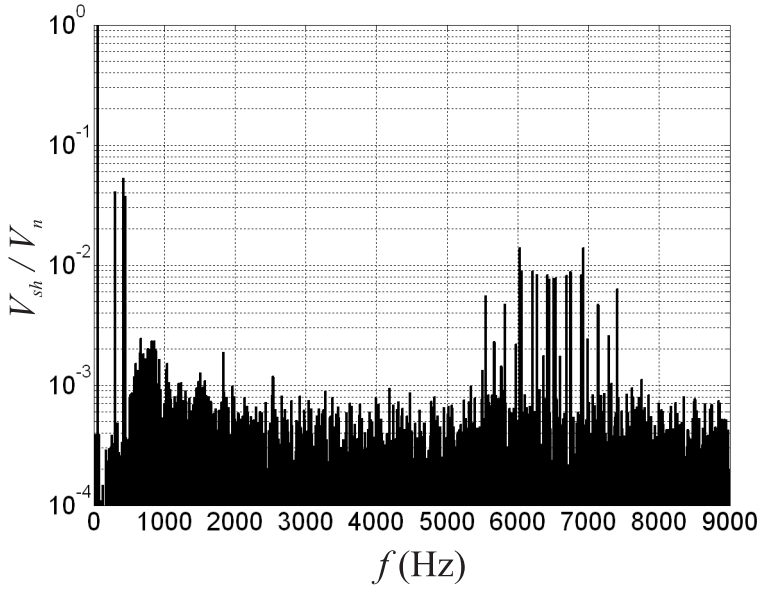

Figure 4.38 - Example 4.IV: Normalized line-to-neutral stator voltage spectrum.

4.7 Conclusions

Compensation by means of RSC modulation has been described and simulation results demonstrate that it can be applied successfully to obtain sinusoidal current on the grid when a NLL is connected in proximity of the WECS.

When the injection of harmonic current from the stator results in overheating of the windings, derating is necessary. If the amplitudes of the harmonic components are too high, the proposed methodology has limitations because the compensation of the harmonic currents results in saturation of the power converters.

In the following chapter, two other methods for harmonic compensation will be described, named 'compensation by means of LSC modulation' and 'compensation by means of combined modulation'. They will be compared with 'compensation by means of RSC modulation'.

Chapter 5

Compensation by Means of LSC Modulation: Steady-State Analysis

5.1 Introduction

This chapter deals with the mathematical formulation of the RSC and LSC control systems to obtain 'compensation by means of LSC modulation' [111]. The analysis is based on a procedure similar to the one described in chapter 4 for 'compensation by means of RSC modulation'. In particular:

- The control system is defined in the stator voltage reference frame as explained in section 4.3.
- The transfer functions (4.40), (4.53) and (4.60) for the DFIG, the dc-link and the LSC derived in chapter 4 are used because the same system configuration is studied. As a consequence, the same PI controllers described in sections 4.4 and 4.5 are used with the parameters listed in appendix A.

The main difference between 'compensation by means of RSC modulation' and 'compensation by means of LSC modulation' is in the definition of the RSC and LSC reference currents, according to the following principles:

1. Compensation by means of RSC modulation: the rotor reference currents contain both fundamental and harmonic components, the LSC reference currents contain only the fundamental component;
2. Compensation by means of LSC modulation: the rotor reference currents contain only the fundamental component; the LSC reference currents contain both first and harmonic components.

In the second part of this chapter it is proved that the connection of the dc-link to the neutral allows the compensation of the triplen harmonics by applying compensation by means of LSC modulation.

5.2 Power converters control

The RSC subsystem (Figure 4.1) and LSC subsystem (Figure 4.2) are analyzed independently; the equivalent subsystems in terms of space vectors are shown in Figures 4.6 and 4.10, respectively.

5.2.1 RSC subsystem control

The DFIG is used as a generator and the rotor winding currents contains the fundamental frequency only. Since no harmonic currents flow in the DFIG windings, the RSC control is simpler than the one described in section 4.4.

The block diagram for the generation of the RSC power switches pulses is obtained by setting the harmonic rotor reference currents i_{drh} (4.27) and i_{qrh} (4.28) to zero, and the result is shown in Figure 5.1.

5.2.2 LSC subsystem control

The LSC reference currents $i_{dL,ref}$ and $i_{qL,ref}$ are the sum of two parts: i_{dL1}, i_{qL1} are the components at fundamental frequency ($h = 1$); the sets i_{dLh}, i_{qLh} include the harmonic components ($h \neq 1$):

$$i_{dL,ref} = i_{dL1} + i_{dLh} \tag{5.1}$$

$$i_{qL,ref} = i_{qL1} + i_{qLh} \tag{5.2}$$

The LSC subsystem is linear and superposition principle is applied. The fundamental reference currents and the harmonic reference currents are defined separately and the two components are summed to obtain the overall reference currents.

Fundamental LSC currents $i_{dL1,ref}$ and $i_{qL1,ref}$

The fundamental reference currents $i_{dL1,ref}$ and $i_{qL1,ref}$ are obtained as described in section 4.5.1; only the final expressions are reported below:

$$i_{dL1,ref}(\mathrm{s}) = \frac{2\sqrt{2}}{3} \frac{d}{dt} \frac{v_{dc}}{m_a} \tag{5.3}$$

$$i_{qL1,ref} = \frac{q_L}{v_s} \tag{5.4}$$

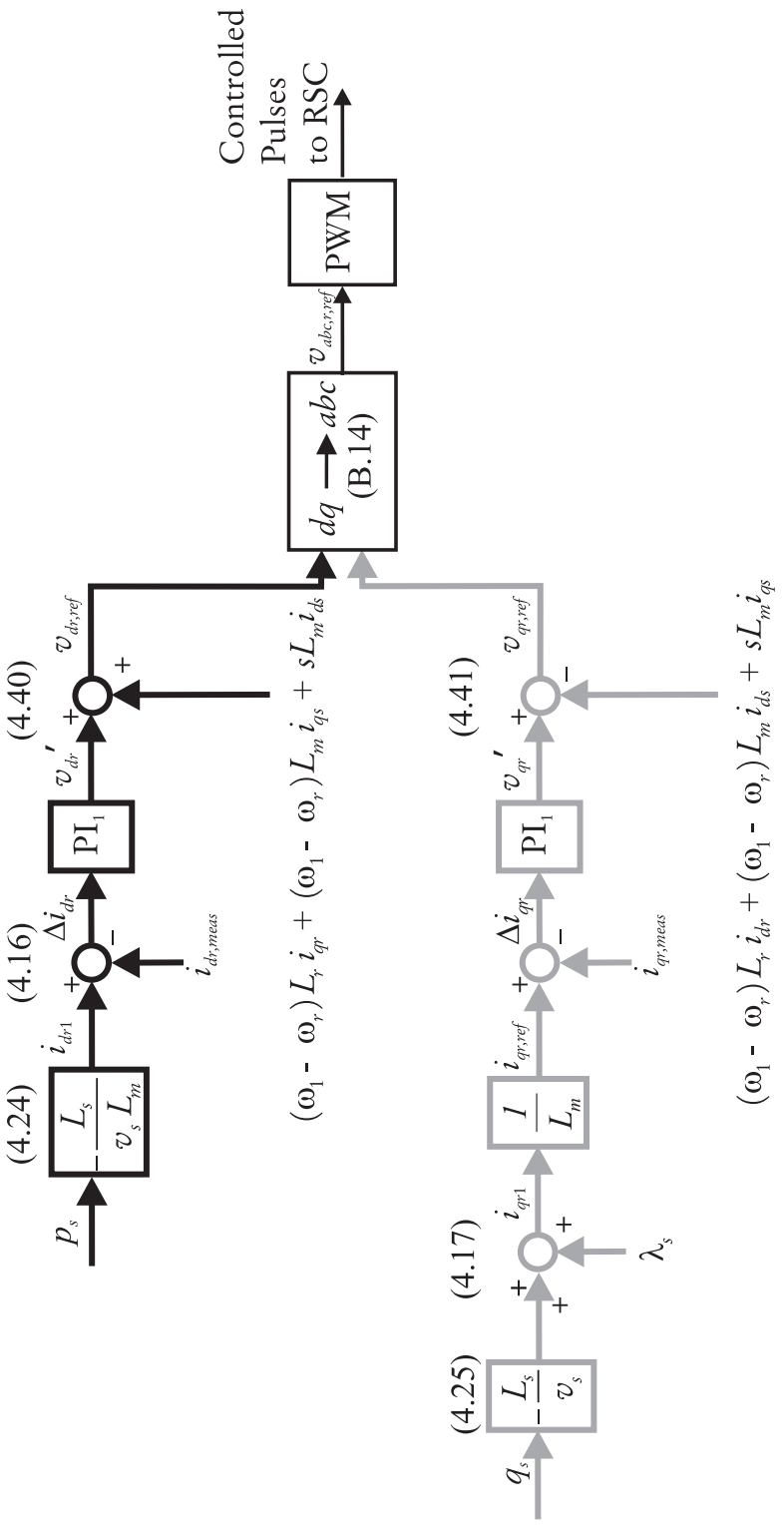

Figure 5.1 - Block diagram for the RSC subsystem control, compensation by means of LSC modulation.

Harmonic LSC currents $i_{dLh,ref}$ and $i_{qLh,ref}$

The harmonic currents $i_{dLh,ref}$ and $i_{qLh,ref}$ are equal in magnitude and 180^o out of phase with respect to the currents injected by the NLL:

$$i_{dLh,ref} = -i_{dh} \tag{5.5}$$

$$i_{qLh,ref} = -i_{qh} \tag{5.6}$$

Block diagram for the LSC subsystem control

The block diagram illustrated in Figure 4.13 is modified as shown in Figure 5.2: the LSC $d-q$ reference currents are the sum of the fundamental and harmonic component, according to (5.1) and (5.2).

5.3 Simulation results

In the following sections, simulations results are shown to prove the effectiveness of compensation by means of LSC modulation. The studied system is the one illustrated in Figure 3.1 and the system parameters are listed in appendix A. The software and simulation parameters are the same used in section 4.6.1.

For each example, the current and voltage oscillogram and spectra and the RSC and LSC power loss are presented. The stator fundamental current curve is displayed when DFIG derating is applied.

5.3.1 Example 5.I

Example 5.I - Current spectra

The NLL injects a negative-sequence fifth harmonic current with amplitude $I_5 = I_n/5$, (4.39).

The current spectra are shown in Figure 5.3. The grid current spectrum is shown in Figure 5.3.a and is relatively clean in spite of the harmonic current injected by the NLL (Figure 5.3.b).

The stator current spectrum (Figure 5.3.c) contains a dominant first harmonic current responsible for the active power flow from the turbine to the grid.

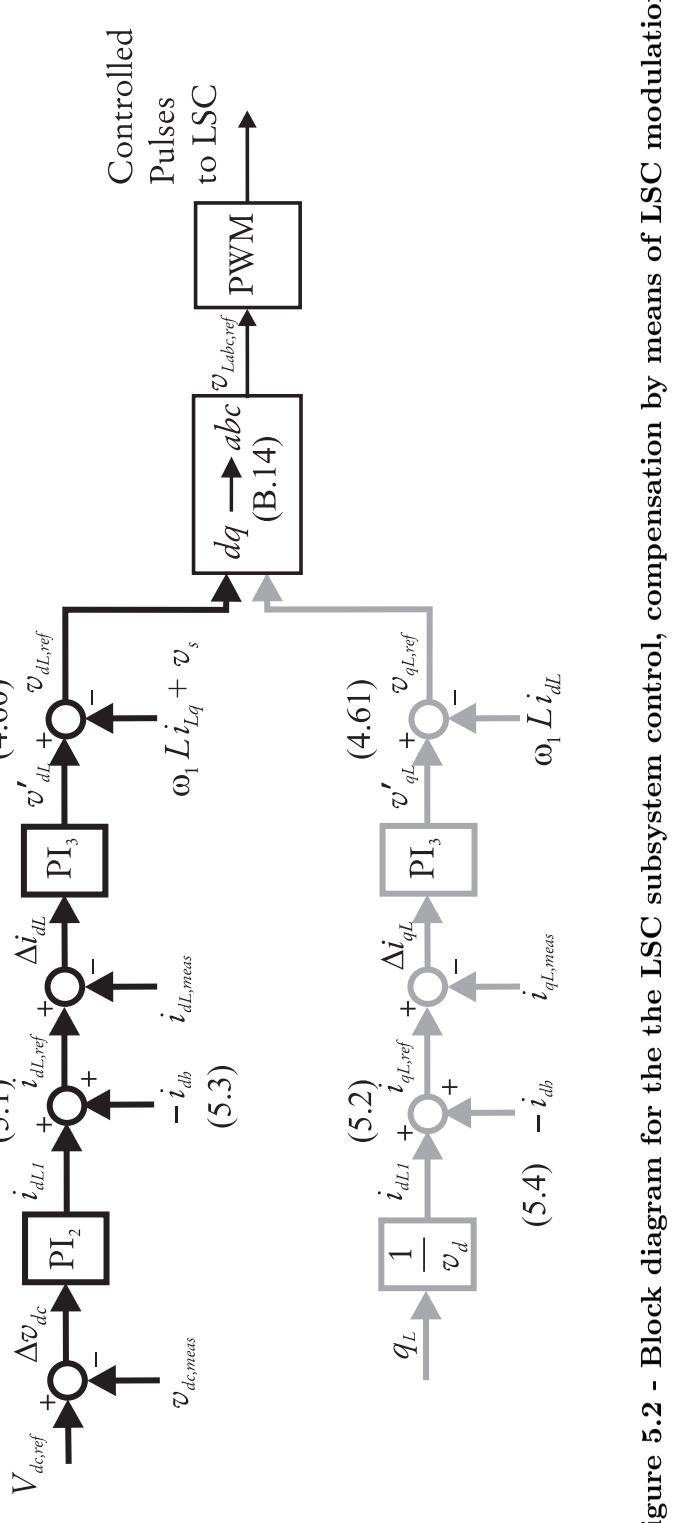

Figure 5.2 - Block diagram for the the LSC subsystem control, compensation by means of LSC modulation.

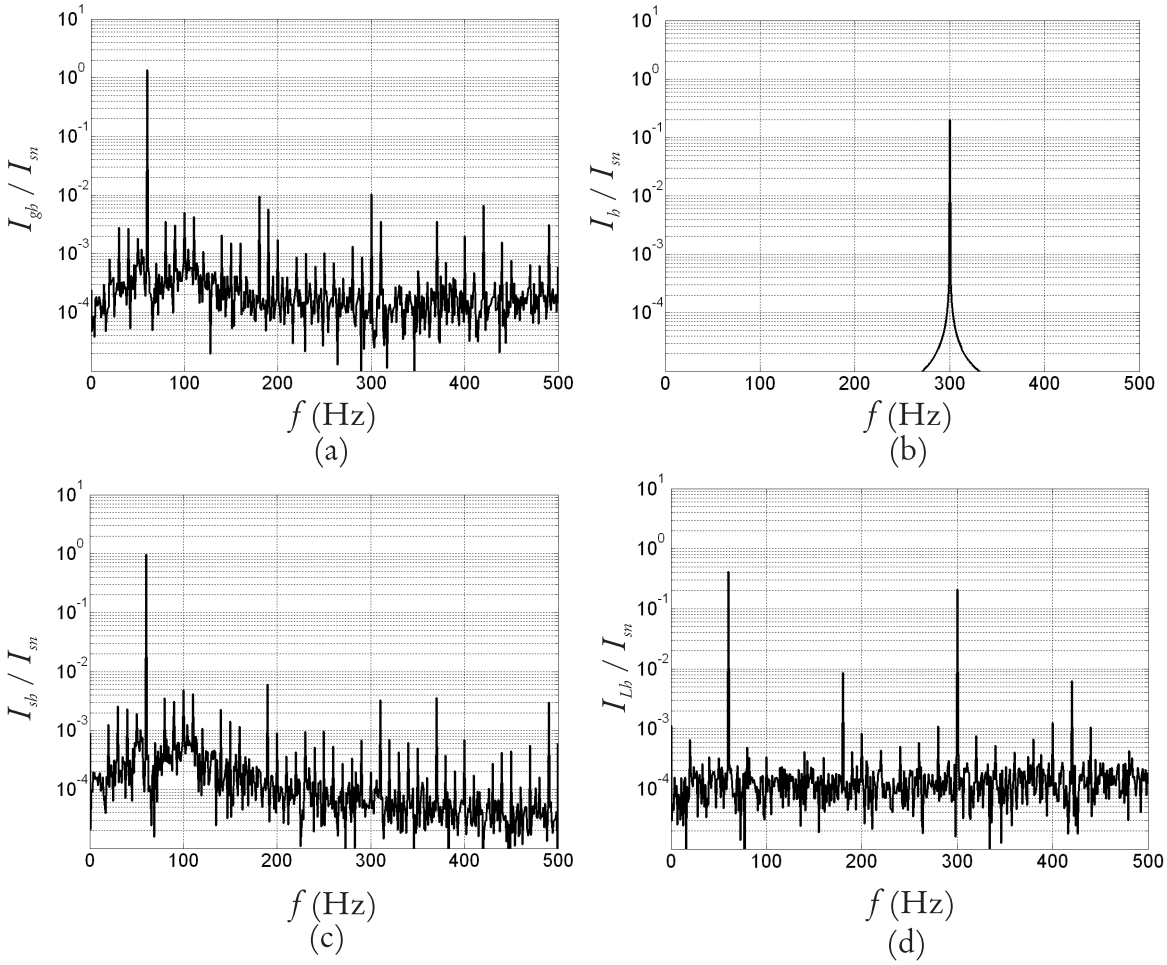

Figure 5.3 - Example 5.I: Normalized current amplitude spectra; (a) grid current, (b) NLL current, (c) stator current and (d) LSC current.

The LSC current spectrum (Figure 5.3.d) contains the first harmonic component responsible to maintain a constant dc-link voltage and a fifth harmonic that cancels the harmonic current injected by the NLL.

Example 5.I - Power loss

The normalized RSC and LSC power loss are shown in Figure 5.4. Two trajectories are presented: one corresponds to power loss for sinusoidal operation; the second shows the power loss when compensation by means of LSC modulation is applied. The power loss is higher in the second case than in the first, due to harmonic power flow in the power converters. However, since only one harmonic current is injected by the LSC, the power loss is always lower than the rated value, except for $\omega_r/\omega_1 = 1.5$. Given these results, derating is not applied in the present case.

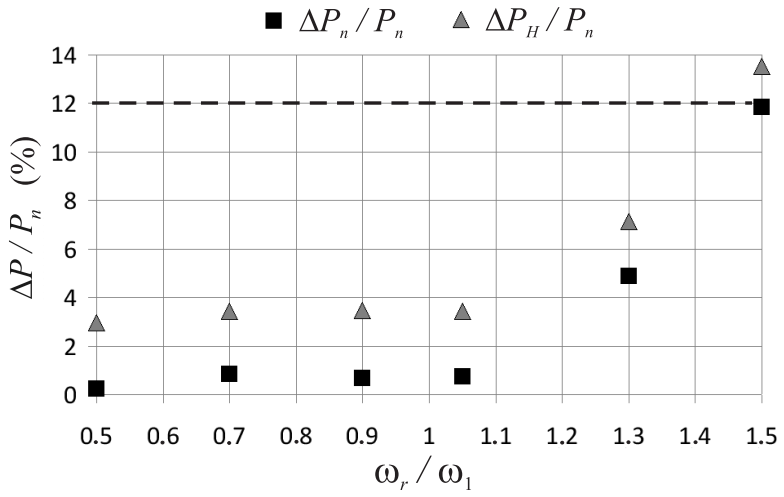

Figure 5.4 - Example 5.I: Normalized power loss in the RSC and LSC as function of the normalized rotor speed; base values are the rated stator power ΔP_n and the synchronous speed ω_1. The rated power loss ratio $\Delta P_n/P_n$ and the power loss ratio when harmonic compensation is implemented $\Delta P_H/P_n$ are shown.

5.3.2 Example 5.II

Example 5.II - Current spectra

The harmonic current injected by the NLL are listed in Table 5.1 and they are as in Example 4.IV to allow comparison of the two compensation methodologies.

The current spectra are shown in Figure 5.5 and they are very similar to the ones

Table 5.1 - Example 5.II - Harmonic currents injected by the NLL.

h	I_h/I_n	Sequence
0.05	0.10	+
5	0.20	+
7	0.14	−
7.5	0.10	+

obtained for Example 5.I. The stator current spectrum (Figure 5.5.c) contains a dominant first harmonic current responsible for the active power flow from the turbine to the grid. The LSC current spectrum (Figure 5.3.d) contains the first harmonic component responsible to maintain a constant dc-link voltage and the harmonic components that cancel the ones injected by the NLL. The LSC current spectrum is very noisy since the LSC is operating in saturation (Figure H.3 in appendix H).

The grid current spectrum shown in Figure 5.3.a is relatively clean in spite of the noise observed for the LSC current spectrum.

Example 5.II - RSC and LSC power loss

The total power loss in the RSC and LSC is plotted in Figure 5.6 as a function of normalized rotor speed ω_r/ω_1. Three trajectories are presented:

1. $\Delta P_n/P_n$: power loss for sinusoidal operation,
2. $\Delta P_H/P_n$: power loss for harmonic compensation
3. $\Delta P_{derating}/P_n$: power loss when DFIG derating is applied.

When harmonic compensation is applied, for any rotor speeds, the power loss in the RSC and in the LSC is significantly higher than the power loss for sinusoidal operation. In particular, for supersynchronous speeds, the power loss is unacceptable for the power converters operation. For this reason, DFIG derating is applied: the reduction of the fundamental power flow in the rotor results in a reduction of the power loss in the RSC and in the LSC.

DFIG derating is implemented according to the curve depicted in Figure 5.7: for speed above the synchronous, the target fundamental current is linearly reduced with respect to the rated current.

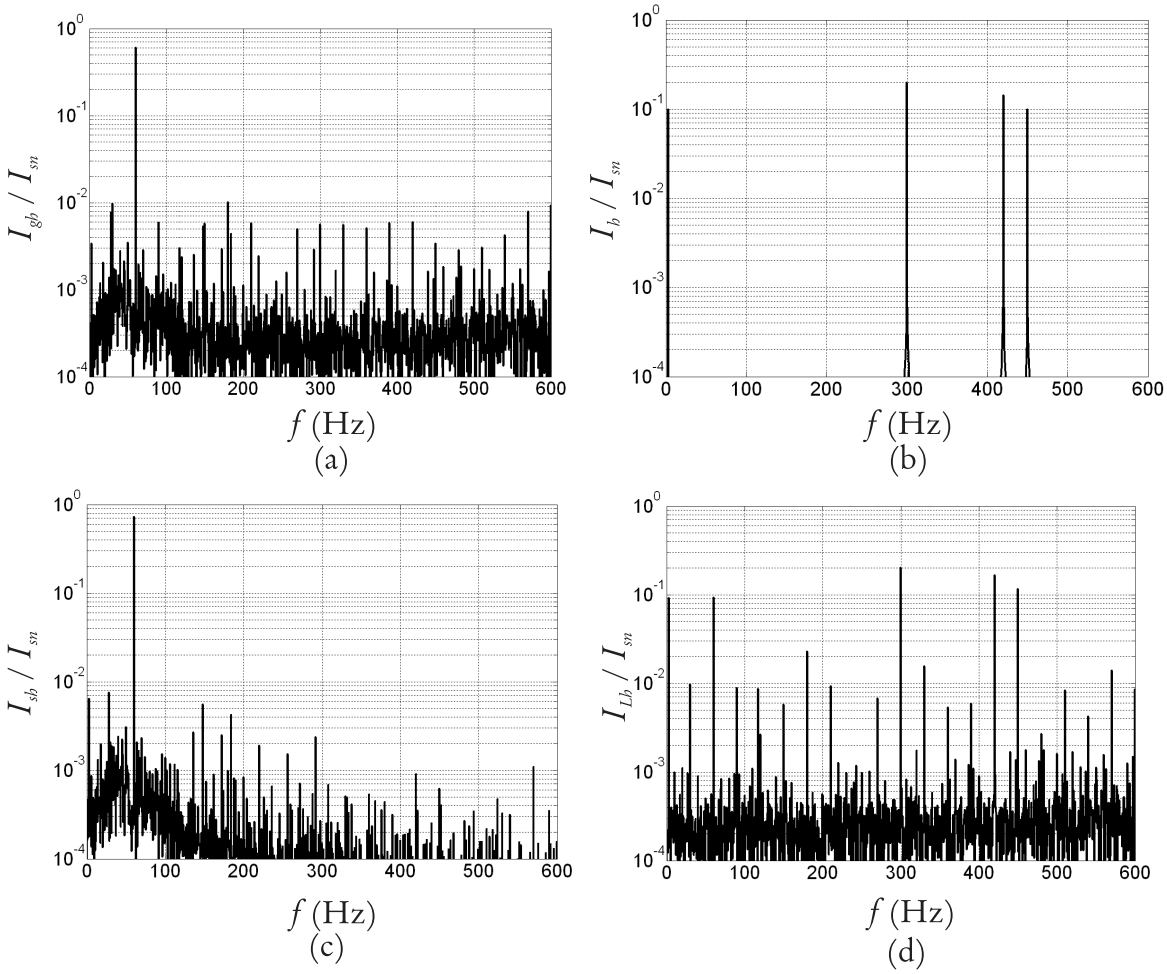

Figure 5.5 - Example 5.II: Normalized current amplitude spectra; (a) grid current, (b) NLL current, (c) stator current and (d) LSC current.

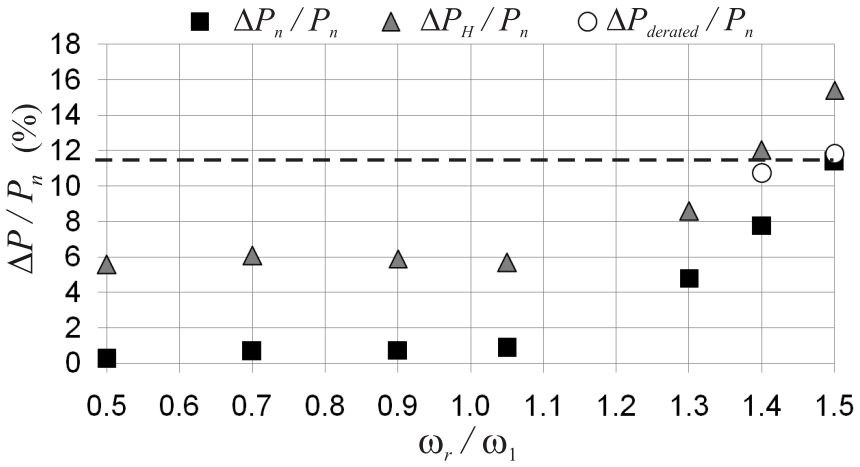

Figure 5.6 - Example 5.II: Normalized RSC and LSC power loss as function of the normalized rotor speed; base values are the rated stator power and the synchronous speed. Three trajectories are illustrated: power loss for sinusoidal operation $\Delta P_n/P_n$, power loss for harmonic compensation $\Delta P_H/P_n$ and power loss when DFIG derating is applied $\Delta P_{derating}/P_n$. Derating is implemented according to the power curve presented in Figure 5.7.

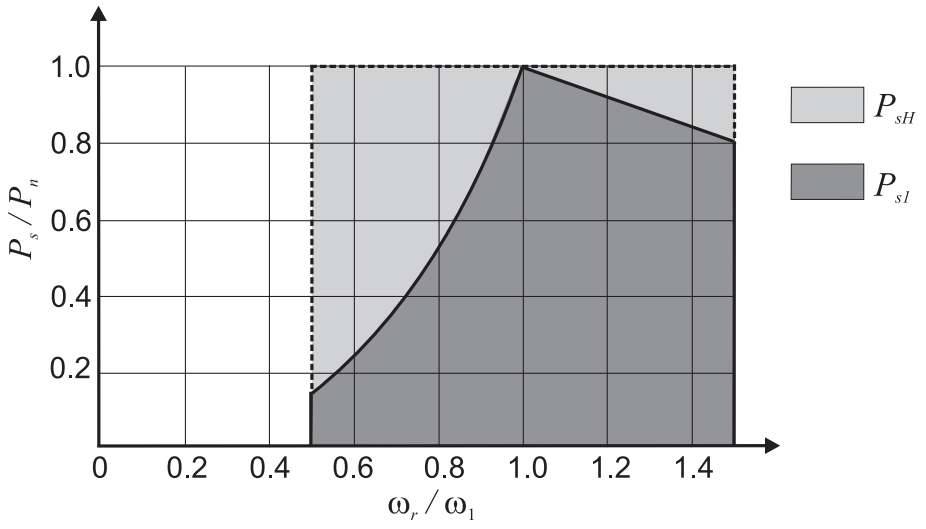

Figure 5.7 - Example 5.II: Modified power curve as function of the normalized rotor speed ω_r/ω_1; DFIG derating is implemented at supersynchronous speed.

Example 5.II - Voltages oscillograms and spectra

The normalized line-to-line rotor voltage oscillogram and spectrum are presented in Figures 5.8 and 5.9, respectively. The results are very similar to the ones presented in chapter 4. However, no low frequency harmonics are identified in the spectrum because the LSC is responsible for harmonic compensation.

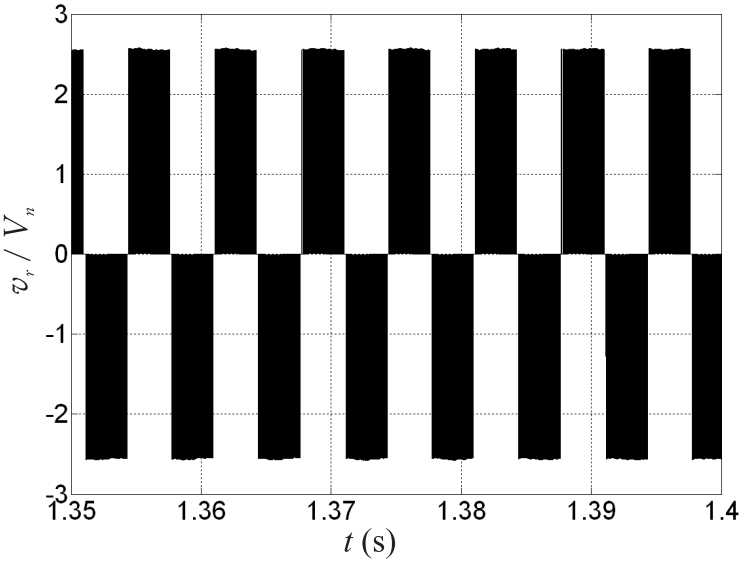

Figure 5.8 - Example 5.II: Normalized line-to-line rotor voltage oscillogram.

The normalized line-to-line rotor voltage oscillogram and spectrum are presented in Figures 5.10 and 5.9, respectively. The results are very similar to the ones obtained for the rotor, since both the LSC and the RSC are controlled by means of PWM and the same carrier frequency is used. However, the LSC voltage spectrum shows the following harmonics:

1. Fundamental component frequency is $f_1 = 60$ Hz.
2. Low frequency components corresponding to the NLL currents frequencies.
3. High frequency components in the region $6000 < f < 7000$ Hz that includes the PWM carrier frequency ($f_{tri} = 6480$ Hz, appendix A).

The normalized line-to-neutral PCC voltage oscillogram and spectrum are illustrated in (Figure 5.12) and Figure 5.12, respectively. The voltage waveform is sinusoidal with a slight distortion. The corresponding spectrum is dominated by the fundamental component;

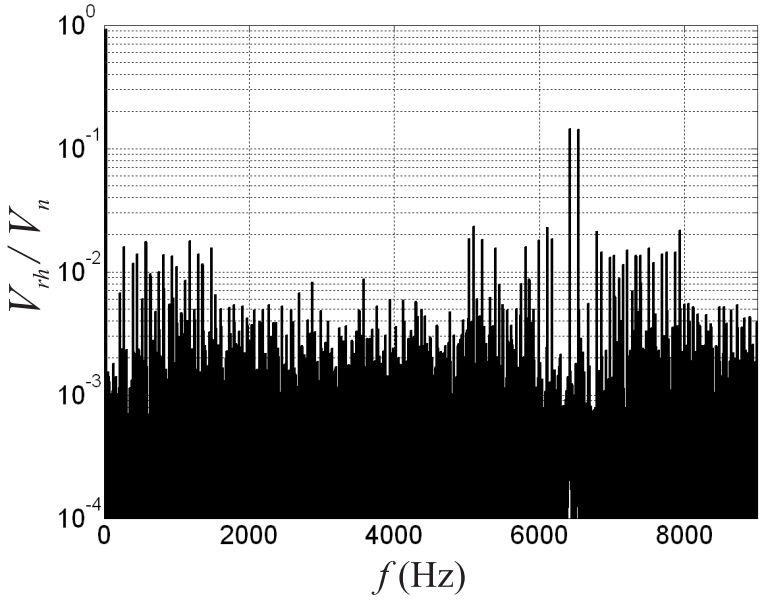

Figure 5.9 - Example 5.II: Normalized line-to-line rotor voltage spectrum.

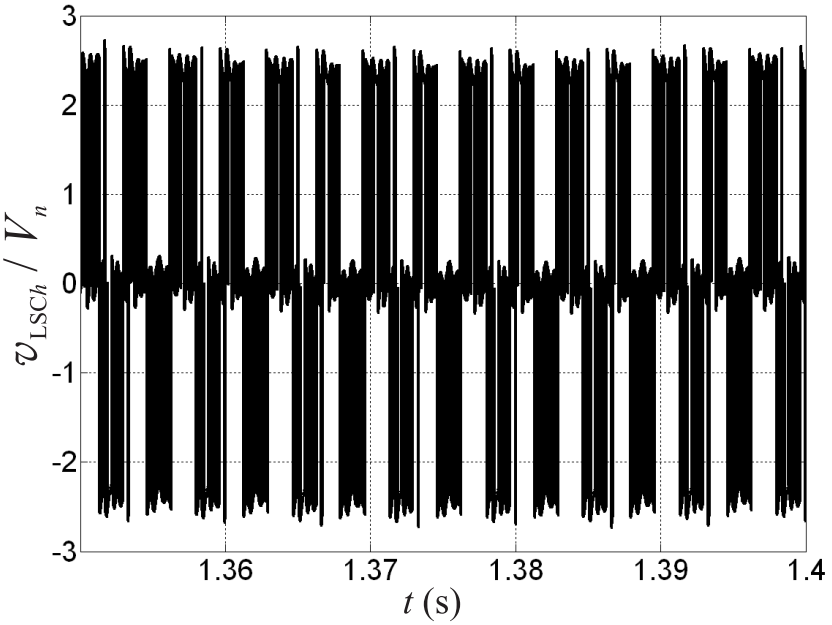

Figure 5.10 - Example 5.II: Normalized line-to-line LSC voltage oscillogram.

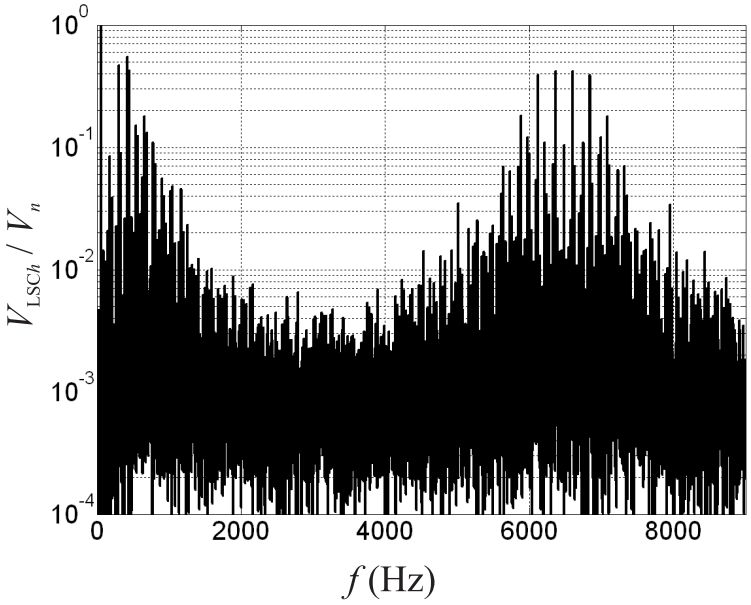

Figure 5.11 - Example 5.II: Normalized line-to-line LSC voltage spectrum.

minor harmonics components are caused by PWM operation of the LSC connected to the same PCC.

The stator voltage oscillogram (Figure 5.14) and spectrum (Figure 5.15) resemble the ones obtained for the PCC. This result can be justified by observing that only the fundamental current component flows through the feeder that connects the DFIG stator to the PCC, therefore the harmonic voltage drop on the feeder impedance is negligible.

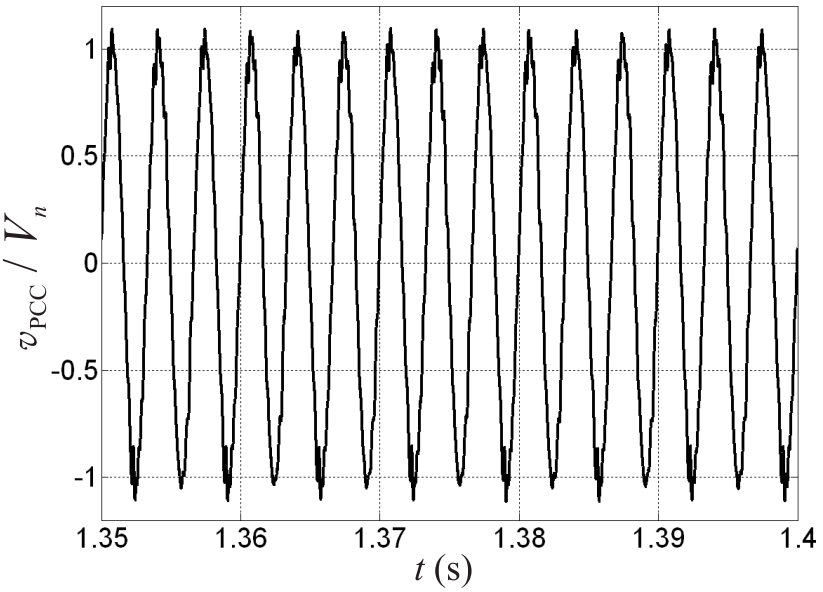

Figure 5.12 - Example 5.II: Normalized line-to-neutral voltage oscillogram at the PCC.

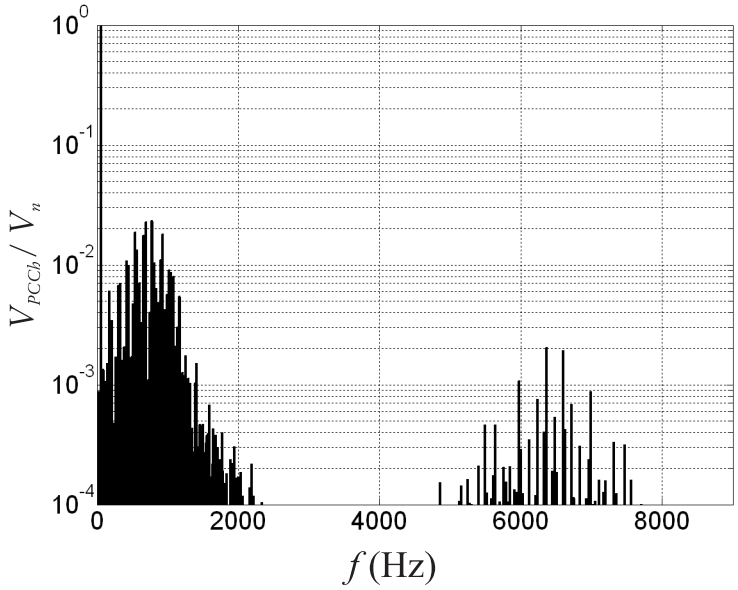

Figure 5.13 - Example 5.II: Normalized line-to-neutral voltage spectrum at the PCC.

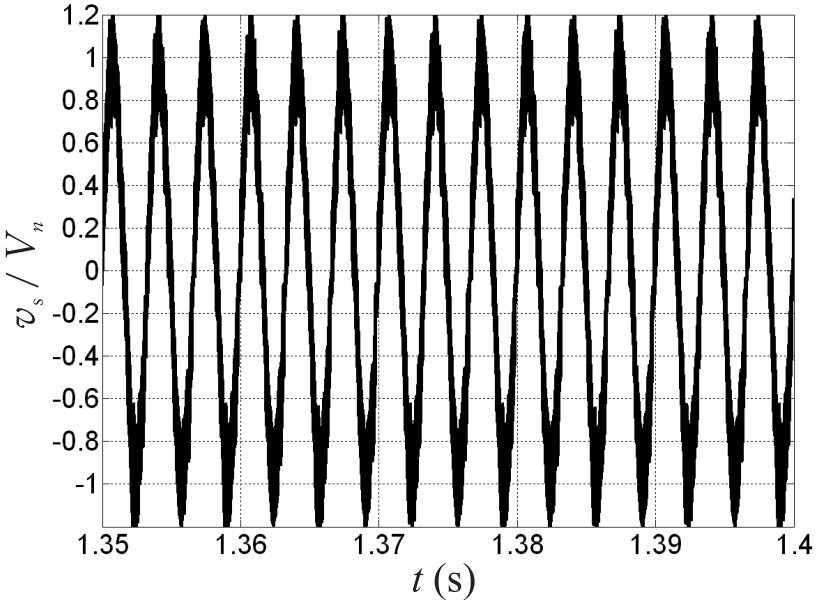

Figure 5.14 - Example 5.II: Normalized line-to-neutral stator voltage oscillogram.

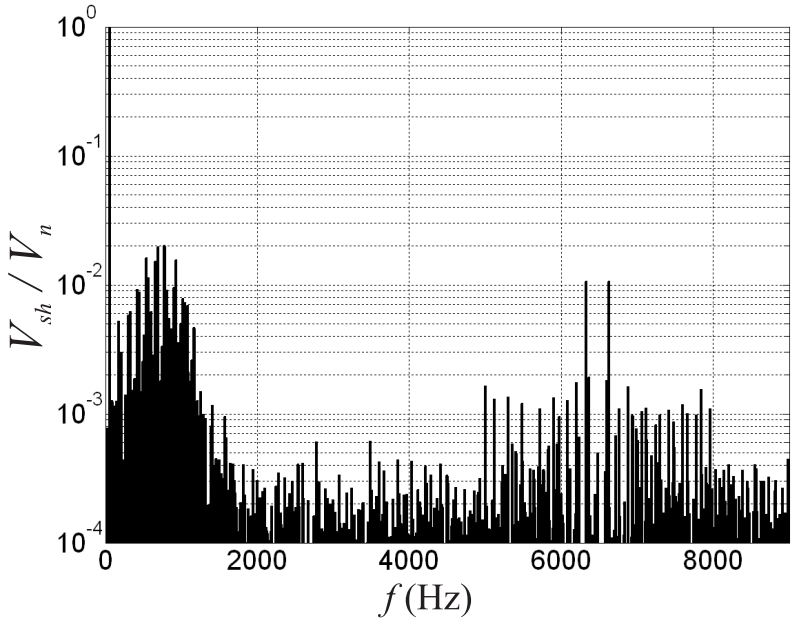

Figure 5.15 - Example 5.II: Stator line-to-neutral voltage spectrum.

5.4 Triplen harmonics compensation

Triplen[25] harmonics include the odd multiples of the 3^{rd} harmonic (ex. 3^{rd}, 9^{th}, 15^{th}, 21^{st} etc.). Since triplen harmonics are additive in the neutral and result in a zero-sequence current [92], their effect is different from the positive- and negative-sequence harmonics [136] . Consequences of triplen harmonics include: large currents circulating in the neutral (that present a fire hazard and result in a degradation of the neutral insulation), transformer overheating, elevated neutral potential and EMI (electromagnetic interference). Single-phase power supplies for equipment such as electronic loads and PCs are the most significant source of triplen harmonics [136]. Due to their detrimental effect on the grid operation, compensation of triplen harmonics is important and will be studied in the following sections.

Induction machine windings are never connected to the ground [76] to avoid the flow of zero-sequence triplen harmonics in the machine's windings. The flow of triplen harmonics would cause harmful power loss and parasitic torques [75] that would reduce the life time of the windings insulation and of the bearings. As a results, no triplen harmonics can be injected by the DFIG and when compensation by means of RSC modulation [110] is performed the cancellation of the triplen harmonics injected by the NLL cannot be obtained.

On the contrary, the connection of the dc-link to the ground as shown in Figure 5.16 allows the injection of the zero-sequence triplen harmonics from the LSC terminals (reference). A triplen harmonic injected by the NLL does not flow in the mains if a current with the same magnitude and frequency and shifted by 180^o is injected by the LSC.

This is the same principle described for the compensation of direct and inverse current components; however, triplen harmonics compensation requires a dedicate analysis and a different control system design [92] because the zero-sequence pattern includes the neutral and zero-sequence circuit is independent from the positive- and negative-sequence equivalent circuits (appendix E).

5.5 LSC subsystem zero-sequence equivalent circuit

Figure 5.17 shows the zero-sequence equivalent circuit for the LSC subsystem and the pattern of the zero-sequence current injected by the NLL. The zero-sequence equivalent resistance R_{L0} and inductance L_{L0} are calculated as follows [92, 137][26]:

$$R_{L0} = R_L + 3R_{LN} \tag{5.7}$$

[25]The term 'triplen' has been introduced by Vladimir Karapetoff in 1928 in a letter to AIEE.
[26]The relations (5.7) and (5.8) are derived in appendix F.

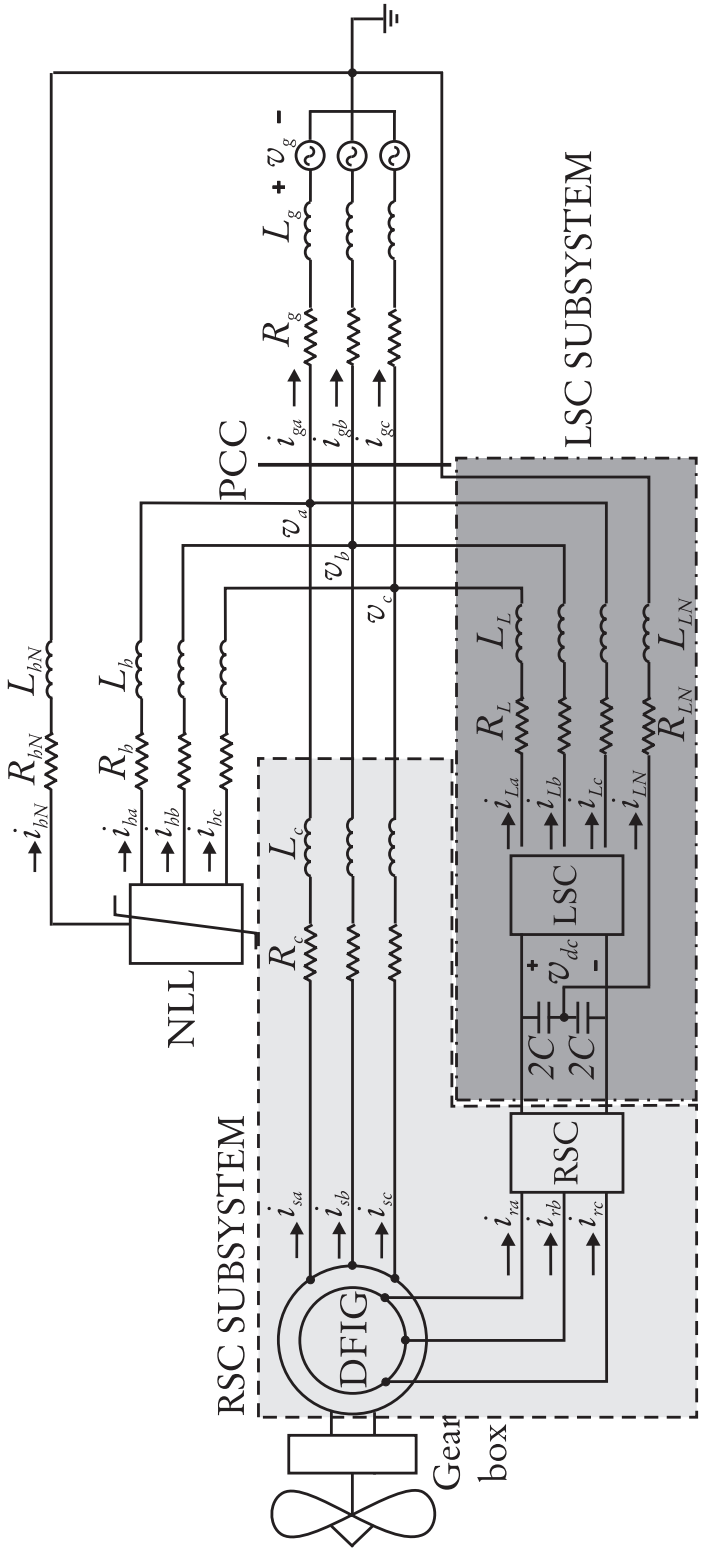

Figure 5.16 - Modification of the system configuration: the dc-link is connected to the neutral. The capacitor C shown in Figure 3.1 has been replaced by the series of two equivalence capacitors $2C$. The step-up transformer is not shown for simplicity.

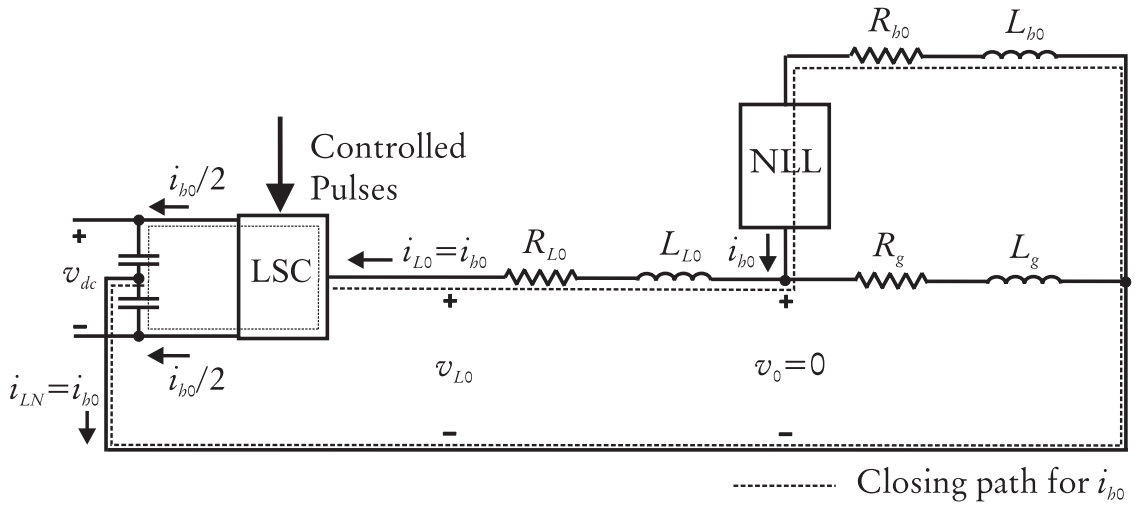

Figure 5.17 - The zero-sequence equivalent circuit for the LSC subsystem.

$$L_{L0} = L_L + 3L_{LN} \tag{5.8}$$

where R_{LN} and L_{LN} are the neutral resistance and inductance; and R_L and L_L are the phase resistance and inductance for the line that connect the LSC to the PCC 5.16.

The zero-sequence current injected by the NLL i_{h0} is calculated by applying the Fortescue transformation [138]:

$$i_{h0} = \frac{1}{3}(i_{ha} + i_{hb} + i_{hc}) \tag{5.9}$$

When compensation by means of LSC modulation is implemented, the following relation applies between the zero-sequence current components injected by the NLL (i_{h0}) and by the LSC (i_{L0}):

$$i_{L0} = -i_{h0} \tag{5.10}$$

The zero-sequence current flows in the dc-link and then through the ground, and returns to the NLL. The equality (5.10) means that no zero-sequence current component flow in the grid resistance R_g and inductance L_g and in the RSC subsystem.

Figure 5.18 shows in detail the zero-sequence current flow in the dc-link: due to the dc-link symmetry the capacitor currents shown in Figure 5.18 are equal to half the zero-sequence current injected by the NLL:

$$i_{c10} = i_{c20} = \frac{i_{h0}}{2} \tag{5.11}$$

Given the relation (5.11), the zero-sequence voltage drops on the capacitors v_{c10} and

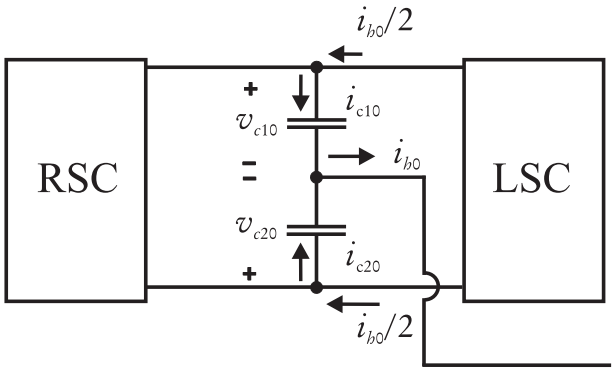

Figure 5.18 - Detailed representation of the zero-sequence current flow in the dc-link.

v_{c20} are instantaneously equal in magnitude and opposite in phase:

$$v_{c10} = -v_{c20} \tag{5.12}$$

Figure 5.19 exemplifies this concept: the voltages v_{c10} and v_{c20} are plotted as a function of time, while compensation by means of LSC modulation is implemented and a triplen harmonic current of the third order (h=3) is injected by the NLL. Figure 5.19 shows that the sum of the voltages amplitude v_{dc10} and v_{dc20} is instantaneously equal to the rated voltage (1200 V), although the capacitors voltages are not perfectly constant and equal to half the rated value. The voltage ripple frequency is equal to 180 Hz; the ripple is caused by the voltage drops on the LSC power switches (the IGBTs parameters are listed in appendix A).

5.5.1 Transfer functions for the grounded dc-link

Positive- and negative-sequence transfer function

The relation (5.12) means that the zero-sequence current flow in the dc-link has no effect on the dc-link voltage v_{dc} magnitude. Moreover, the connection to ground of the common terminal of the capacitors $2C$ does not alter the positive- and negative-sequence current flow in the dc-link, because these components do not flow through the ground resistance R_{LN} and impedance L_{LN}.

The above considerations imply that the connection in series of two capacitors $2C$ is equivalent to the single capacitor C for the positive- and negative-sequence current components and that the dc-link transfer function (4.53) derived in chapter 4 is still valid for the system modified as in Figure 5.16.

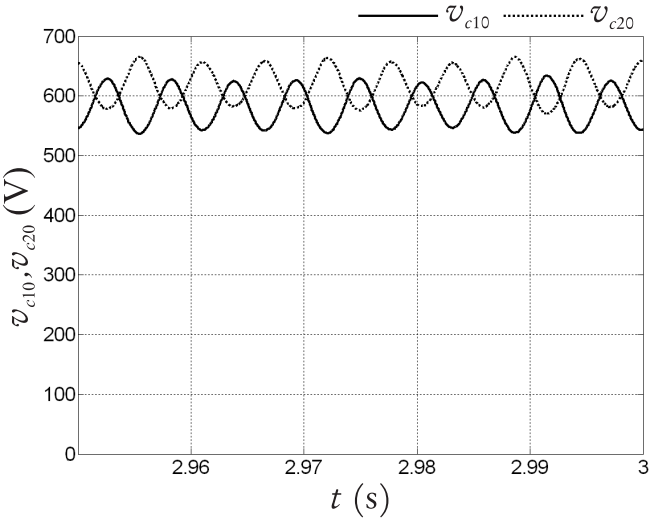

Figure 5.19 - Voltages v_{c10} and v_{c20} as a function of time, when compensation by means of LSC modulation is implemented and a triplen harmonic of frequency 180 Hz is injected by the NLL.

Zero-sequence transfer function

Since the zero-sequence harmonics flow through the neutral, the zero-sequence transfer function is different from the positive- and negative-sequence transfer function and is derived by using the circuit shown in Figure 5.17.

If harmonic compensation by means of LSC modulation is implemented, no zero-sequence current is allowed to flow on the grid and the zero-sequence voltage at the PCC is nil:

$$v_0 = \frac{1}{3}(v_a + v_b + v_c) = 0 \tag{5.13}$$

Given the above result, the KVL for the circuit shown in Figure 5.17 is:

$$v_{L0} = R_{L0} + L_{L0}\ \frac{d}{dt} i_{L0} \tag{5.14}$$

By applying the Laplace transform to (5.14), the zero-sequence transfer function for the LSC subsystem is obtained:

$$\frac{I_{L0}}{V_{L0}} = \frac{1}{R_{L0} + s\ L_{L0}} \tag{5.15}$$

The above transfer function is used in the design of the zero-sequence controller as shown in Figure 5.20. The input for the controller PI_4 is the current error ΔI_{L0}, the output is the auxiliary voltage V_{L0}. The values for the proportional and integral gains k_{p4} and k_{i4} are

determined by using the gain and phase margin test and they are listed in appendix A.

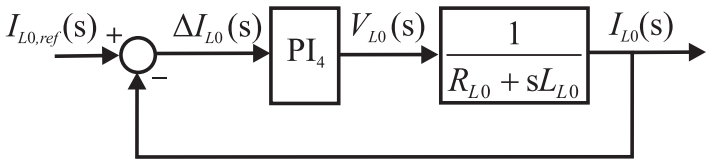

Figure 5.20 - Closed-loop including the integral controller and the zero-sequence transfer function.

5.6 LSC Block diagram including the zero-sequence

The control of the zero-sequence current component is independent from the d and q components. For this reason, the triplen harmonics compensation results in the addition of a third branch to the block diagram presented in Figure 5.2. This design implies that if no triplen harmonics are injected by the NLL, the zero-sequence inputs are nil and the original block diagram of Figure 5.2 is restored.

Figure 5.21 illustrates the complete control diagram for the LSC converter when compensation by means of LSC modulation is implemented. The first and second branches are the same used in Figure 5.2: the same variables and PI controller parameters are used.

The lower branch describes the control for the zero-sequence component. The input is the inverse of the zero-sequence current injected by the NLL (i_{h0}). The controller used for the zero-sequence is the PI controller shown in Figure 5.20. Note than in the zero-sequence controller branch, there is no auxiliary voltage because the zero-sequence transfer function is independent from the d and q transfer function.

5.7 Examples including triplen harmonics

5.7.1 Example 5.III

The NLL injects a triplen harmonic current and the corresponding spectrum is presented in Figure 5.22.b:

$$i_{ha} = i_{hb} = i_{hc} = 0.2 I_n \cos(3\omega_1 t) \quad \text{p.u.} \tag{5.16}$$

The grid current spectrum (Figure 5.22.a) contains a dominant fundamental component at 60 Hz; the third harmonic current magnitude is approximately two order of magnitude

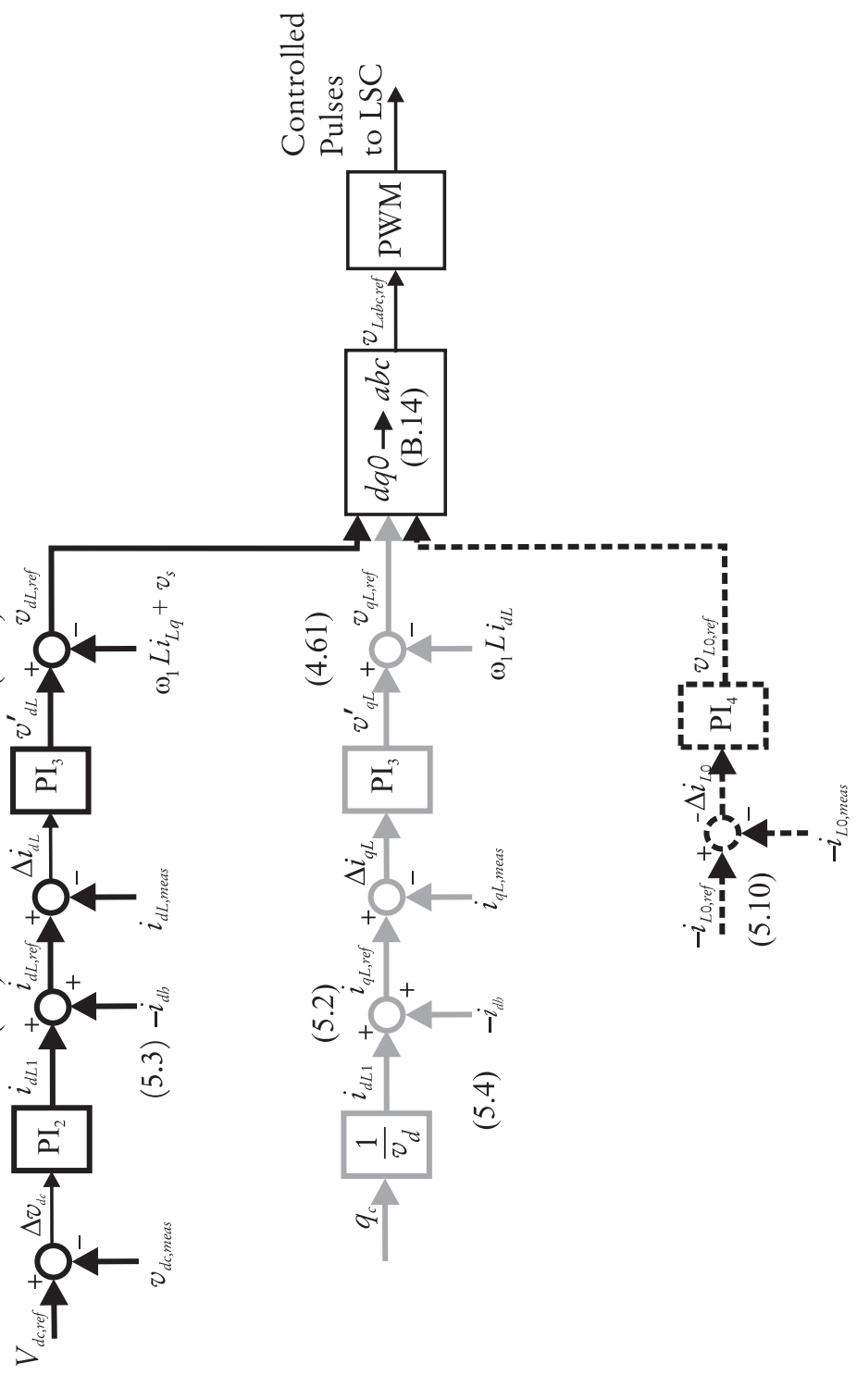

Figure 5.21 - Block diagram for the control of the LSC subsystem including the zero-sequence component, compensation by means of LSC modulation.

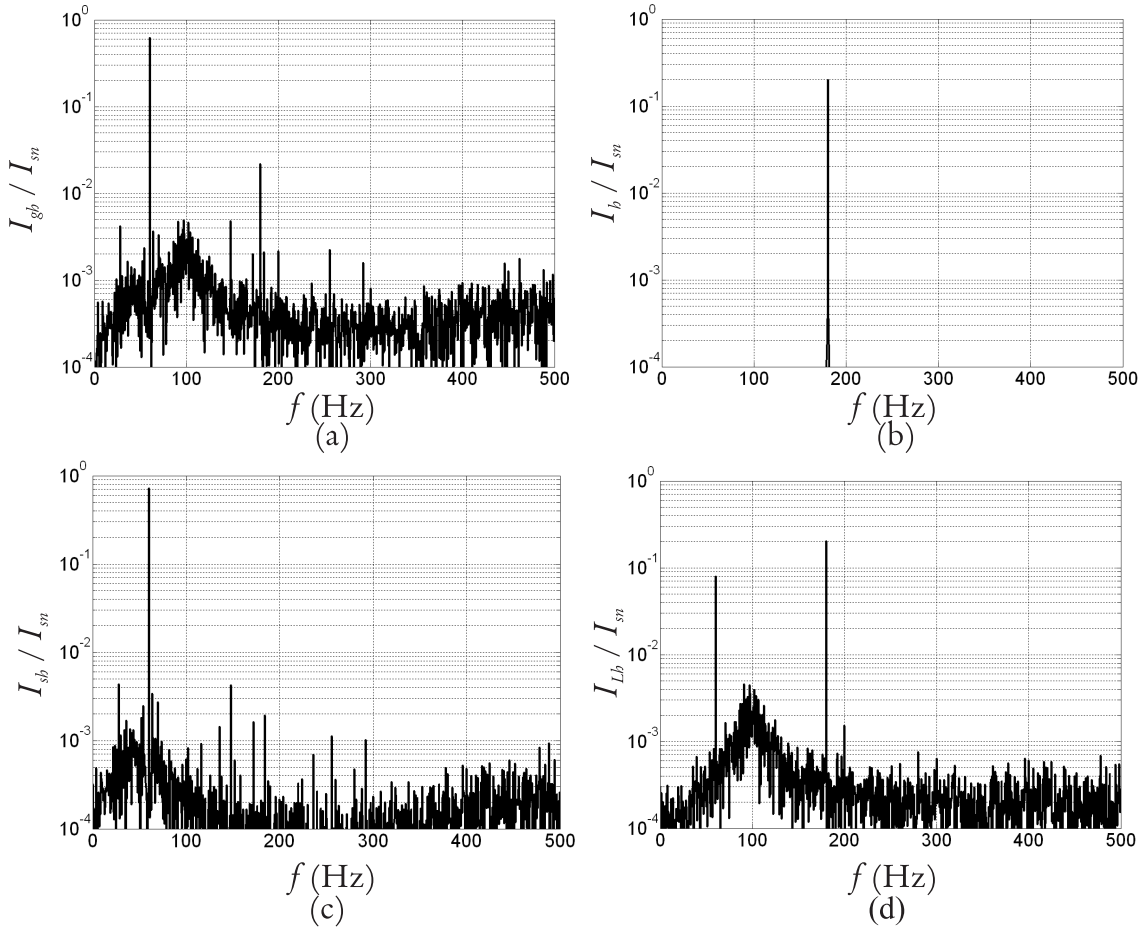

Figure 5.22 - Example 5.III: normalized current amplitude spectra; (a) grid current, (b) NLL current, (c) stator current and (d) LSC current.

smaller than the fundamental components; other components are present due to power converters' operation and to the non idealities included in the solid state devices model.

The stator current spectrum is depicted in Figure 5.22.c: the fundamental harmonic component at 60 Hz is responsible for the fundamental power flow and the high order harmonic components are due to the coupling between the stator windings and the rotor windings.

The LSC is injecting a first and third harmonic (Figure 5.22.d); the first harmonic current corresponds to the active power flow through the rotor and controls the dc-link voltage magnitude. The third harmonic amplitude is equal to the one injected by the NLL. The third harmonic current is not compensated perfectly on the grid because the third harmonic component current injected by the LSC is not exactly out of phase with respect to the third harmonic current injected by the NLL. This behaviour is due to the difficulty to identify the zero-sequence current pattern and to the consequent imperfections of the control system.

The LSC and RSC power loss for Example 5.III are very similar to the one obtained for Example 5.I. This result is explained by observing that in both examples the NLL is injecting a single harmonic component only with amplitude equal to 0.2 p.u. Given the above, derating is not applied in Example 5.III as in Example 5.I.

5.7.2 Example 5.IV

Example 5.IV - Current spectra

The NLL injects the currents listed in Table 5.2 and the corresponding current spectrum is shown in Figure 5.23.b.

Table 5.2 - Example 5.IV: Harmonic currents injected by the NLL.

h	I_h/I_n	Sequence
3	0.20	0
5	0.20	+
7	0.14	−

The grid current spectrum (Figure 5.23.a) contains a dominant fundamental component at 60 Hz; the third, fifth and seventh components amplitudes are significantly smaller than the one illustrated in Figure 5.23.b; other harmonic components are attributed to the connection of the LSC to the PCC and to the nonidealities introduced in the model.

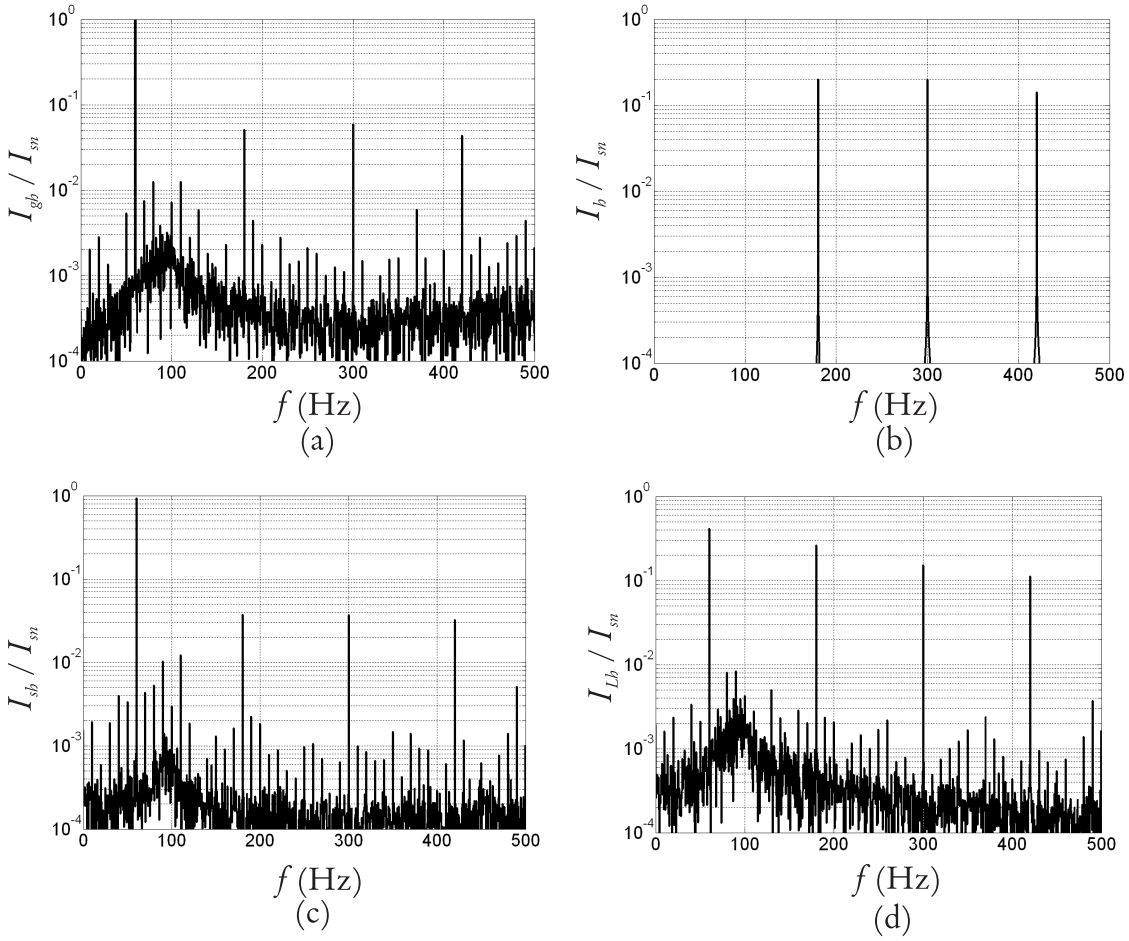

Figure 5.23 - Example 5.IV: Normalized current amplitude spectra; (a) grid current, (b) NLL current, (c) stator current and (d) LSC current.

The stator current spectrum is shown in Figure 5.23.c: the first harmonic current is responsible for the fundamental power flow and the other minor components are due to the coupling with the RSC through the rotor.

The LSC current spectrum dominant component are the first, the third, fifth and seventh harmonics (Figure 5.23.d); the first harmonic current corresponds to the active power flow through the rotor; the amplitude of the third, fifth and seventh harmonic currents are equal to the one represented in Figure 5.23.b. The NLL harmonic current components are not canceled perfectly due to the imperfections in the zero-sequence current compensator, as already pointed out for Example 5.III.

Example 5.IV - Power loss

The RSC and LSC power loss is shown in Figure 5.24. The majority of power loss is due to the flow of harmonic currents: at low rotor speed, when the fundamental current flow is small, the power loss is close to the rated value and it is mainly caused by the harmonic currents. When the rotor speed increases above the rated value, the power loss is unacceptable and DFIG derating is necessary.

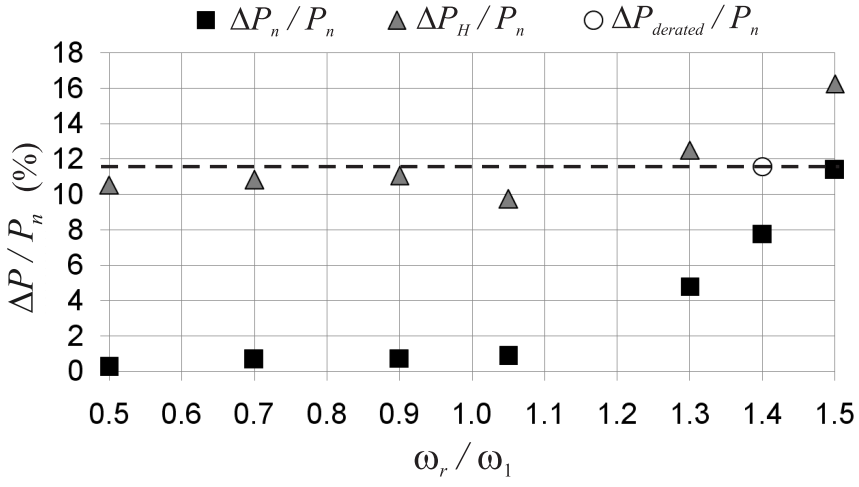

Figure 5.24 - Example 5.IV: Normalized power loss for in the RSC and LSC as function of the normalized rotor speed; base values are the rated stator power and the synchronous speed. Three patterns are shown: the rated power loss ratio $\Delta P_n/P_n$, the power loss ratio when harmonic compensation is implemented $\Delta P_H/P_n$ and the power loss ratio when DFIG derating is applied $\Delta P_{derated}/P_n$.

DFIG derating for Example 5.IV is presented in Figure 5.25 and is applied for super-synchronous speeds. DFIG derating helps to reduce the RSC and LSC power loss at high

rotor speeds. In order to reduce the power loss in the RSC and LSC to the rated value at $\omega_r/\omega_1 = 1.5$, derating equal to 0.5 is needed. As observed in chapter 3, practical derating is limited to 0.7.

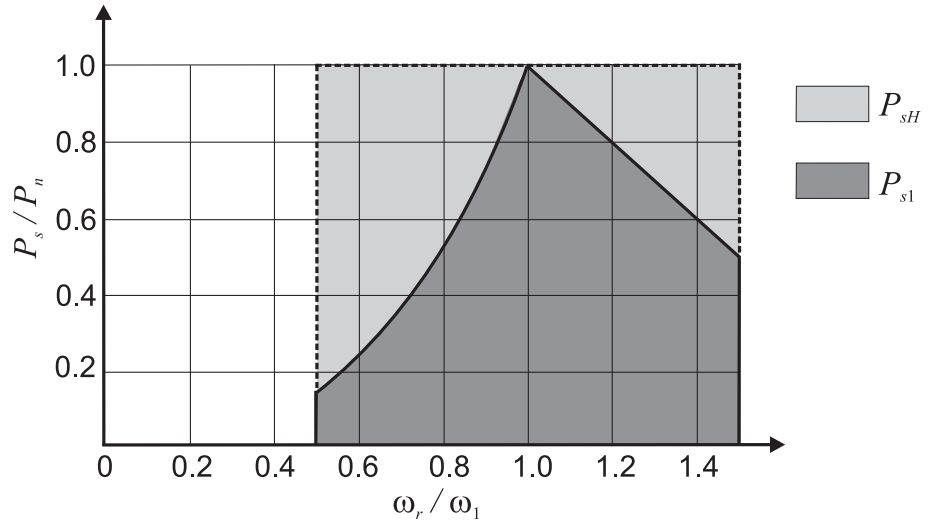

Figure 5.25 - Example 5.IV: Modified power curve as function of the normalized rotor speed ω_r/ω_1; DFIG derating is implemented at supersynchronous speed.

5.7.3 Example 5.V

Example 5.V - Current spectra

The NLL injects the currents listed in Table 5.3 and the corresponding current spectrum is depicted in Figure 5.23.b. The same current injection studied in Example 5.III with an additional third harmonic is assumed.

Table 5.3 - Example 5.V: Harmonic currents injected by the NLL.

h	I_h/I_n	Sequence
0.05	0.10	+
3	0.20	0
5	0.20	+
7	0.14	−
7.5	0.10	+

The grid current spectrum (Figure 5.23.a) contains a dominant fundamental component at 60 Hz; as in the previous Examples, the reduction of the third harmonic current is not as good as the cancellation of the other harmonic components.

The stator current spectrum is depicted in Figure 5.23.c: the first harmonic current is responsible for the fundamental power flow and the other minor components are due to the coupling with the RSC through the rotor.

The LSC current spectrum dominant component are the first components and the harmonic components listed in Table 5.3 (Figure 5.23.d) responsible for the active power flow through the rotor. The other harmonics correspond to the ones injected by the NLL. There are also other components due to the imperfection of the control system, and due to the fact that the LSC PWM reaches saturation as described in appendix H.

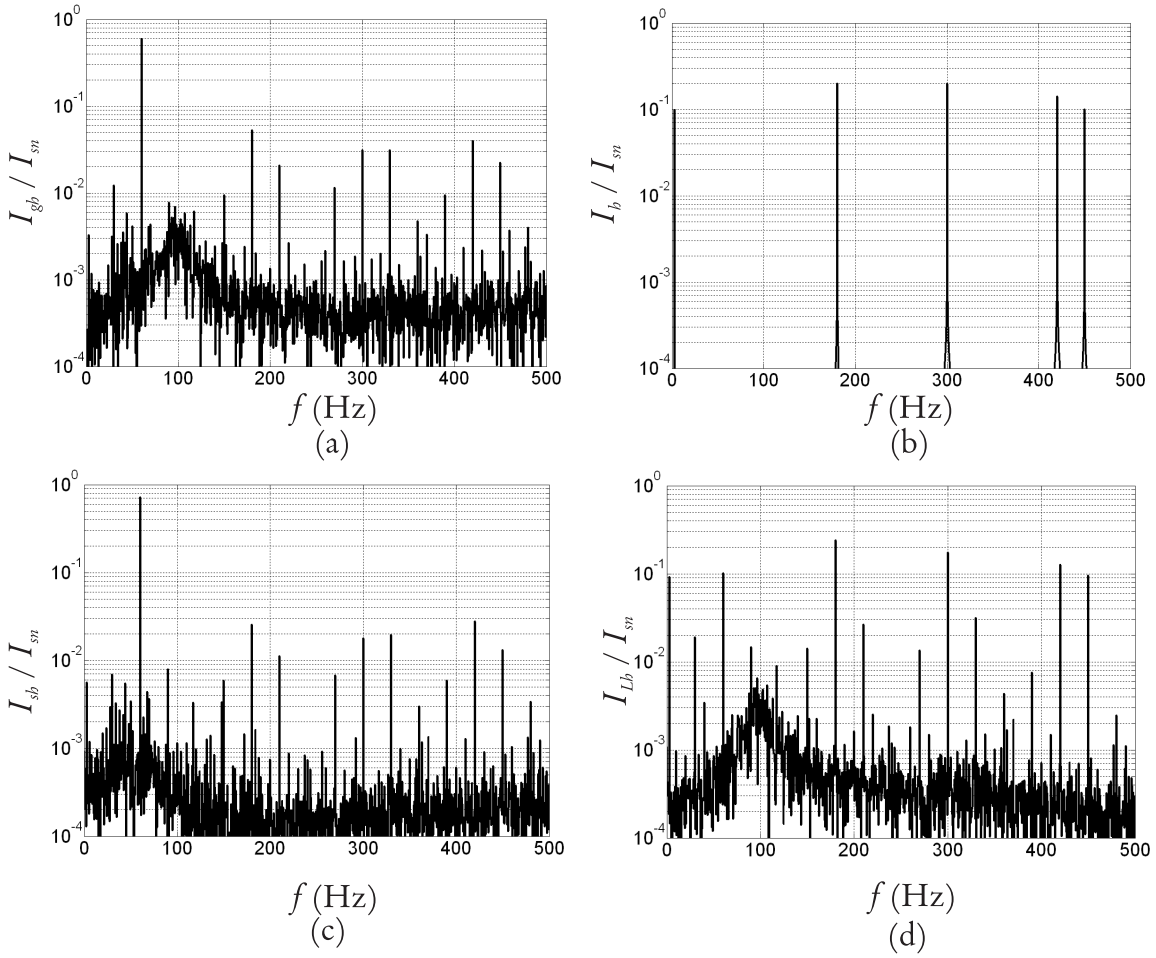

Figure 5.26 - Example 5.V: Normalized current amplitude spectra; (a) grid current, (b) NLL current, (b) stator current and (c) LSC current.

The grid current and grid voltage THD (total harmonic distortion) [25, 26] are significantly reduced when harmonic compensation is applied. Table 5.4 shows that current and voltage THD measured at the PCC (Figure 3.1) before and after the compensation is implemented. In the last column of Table 5.4 the percent reduction is shown.

Table 5.4 - Example 5.V: Voltage and current THD at the PCC.

THD	No Compensation	LSC modulation	% Reduction
Current	0.25	0.075	-333 %
Voltage	0.11	0.055	-50 %

Example 5.V - Power loss

The power loss in the RSC and LSC are presented in Figure 5.27 as function of the normalized rotor speed. The majority of power loss is caused by the harmonic currents flown. For this example, DFIG derating does not result in a successful reduction of the power loss below the rated value.

Figure 5.27 shows that even DFIG derating does not allow to achieve this result, because the majority of the power loss in the RSC and LSC are caused by the harmonic power flow. This examples teaches that if the harmonic current injection from the NLL includes many harmonic components with significant amplitudes, it is not possible to operate the LSC as AF and to guarantee the safe and continuous operation of the solid state devices, due to the high power loss.

DFIG derating for Example 5.IV is presented in Figure 5.28: similarly to the previous example, the required derating is too severe.

Example 5.V - Voltage oscillograms and spectra

The normalized line-to-line rotor voltage oscillogram and spectrum are displayed in Figure 5.29 and 5.30, respectively.

The normalized line-to-line LSC voltage oscillogram and spectrum are presented in Figure 5.31) and Figure 5.30, respectively.

The normalized PCC voltage oscillogram is displayed in Figure 5.33, the corresponding spectrum is shown in Figure 5.34. Similarly to Example 5.II, the PCC voltage is practically sinusoidal, and the spectrum is dominated by the fundamental component.

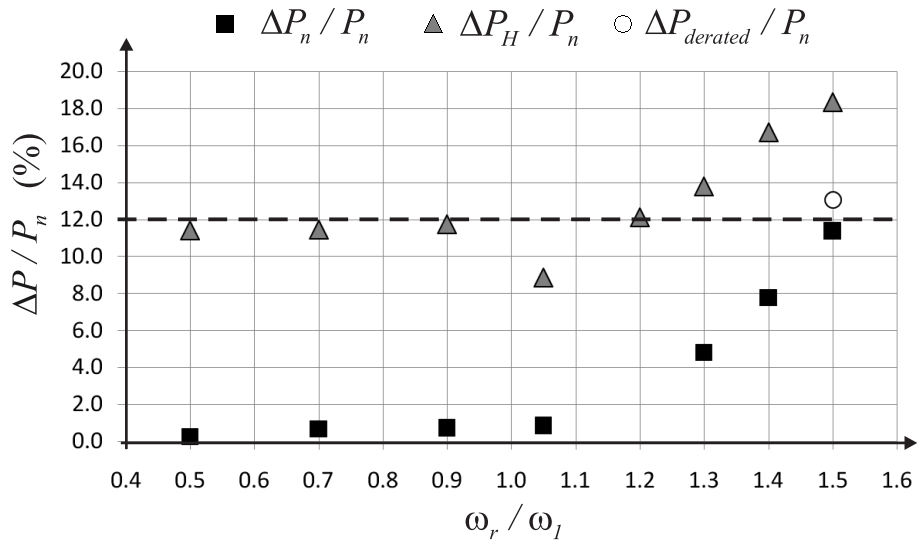

Figure 5.27 - Example 5.V normalized power loss for in the RSC and LSC as function of the normalized rotor speed; base values are the rated stator power and the synchronous speed. The rated power loss ratio $\Delta P_n/P_n$, the power loss ratio when harmonic compensation is implemented $\Delta P_H/P_n$ and the power loss ratio when DFIG derating is applied $\Delta P_{derated}/P_n$ are shown.

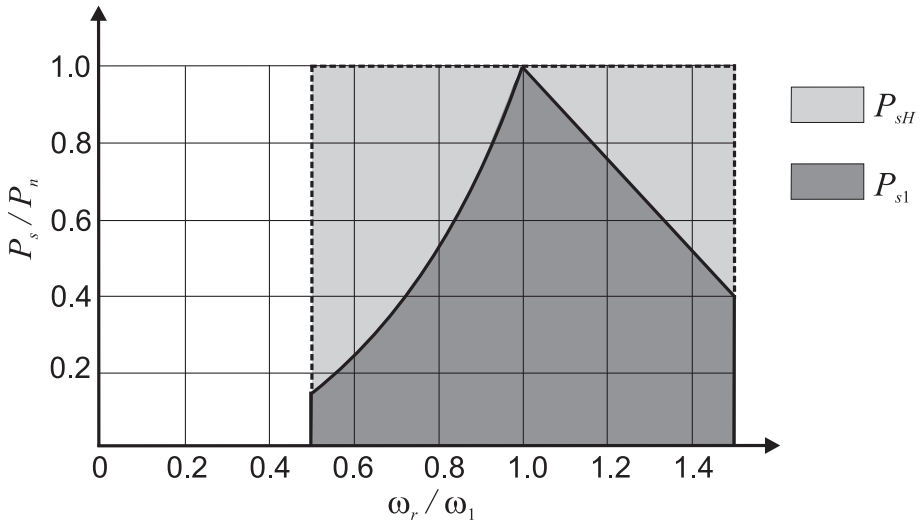

Figure 5.28 - Example 5.V: Modified power curve as function of the normalized rotor speed ω_r/ω_1; DFIG derating is implemented at supersynchronous speed.

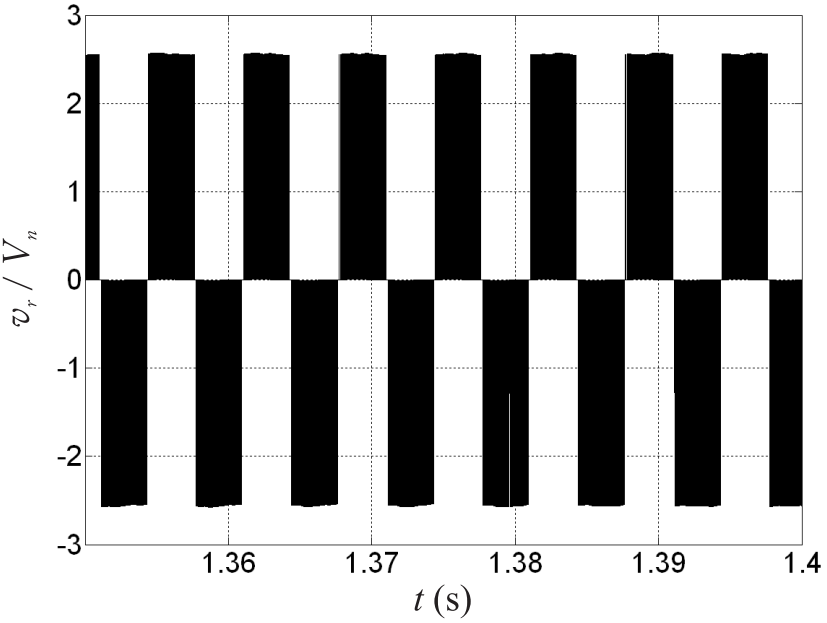

Figure 5.29 - Example 5.V - Normalized line-to-line rotor voltage oscillogram.

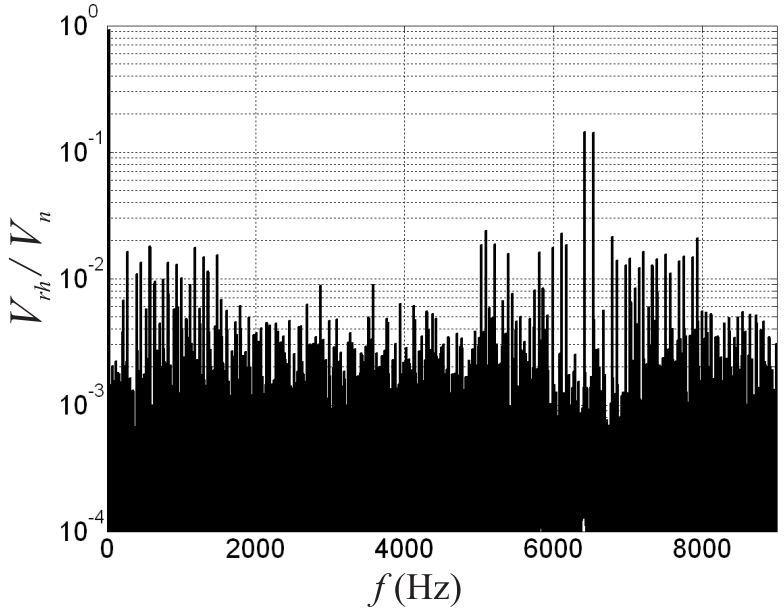

Figure 5.30 - Example 5.V - Normalized line-to-line rotor voltage spectrum.

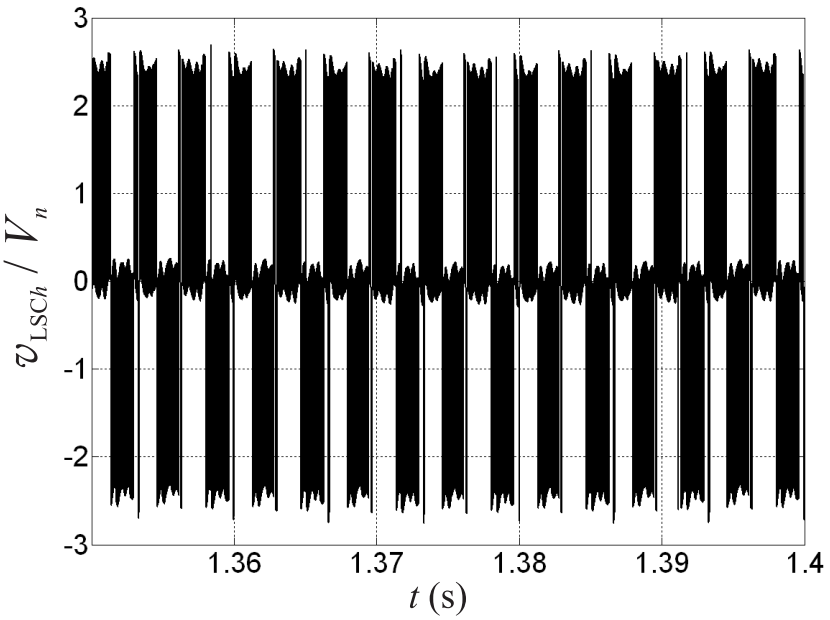

Figure 5.31 - Example 5.V - Normalized line-to-line LSC voltage oscillogram.

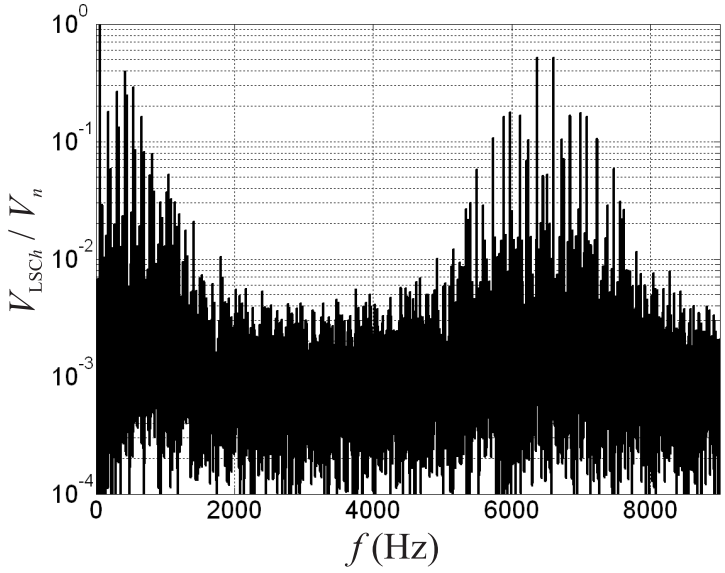

Figure 5.32 - Example 5.V - Normalized line-to-line LSC voltage spectrum.

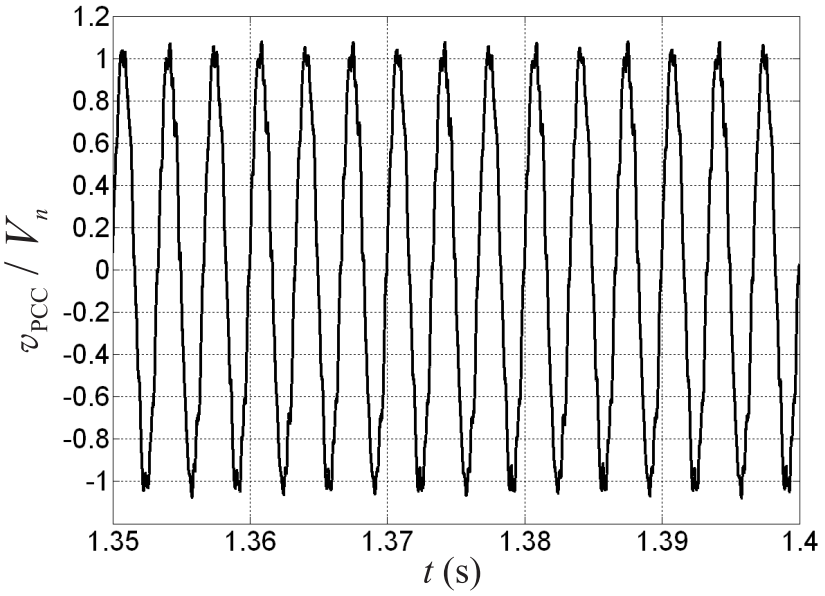

Figure 5.33 - Example 5.V - Normalized line-to-ground voltage oscillogram at the PCC.

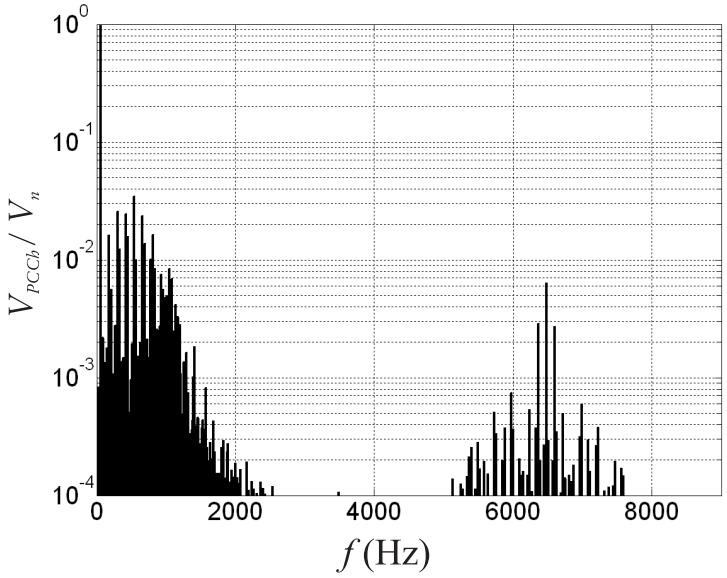

Figure 5.34 - Example 5.V - Normalized line-to-ground voltage spectrum at the PCC.

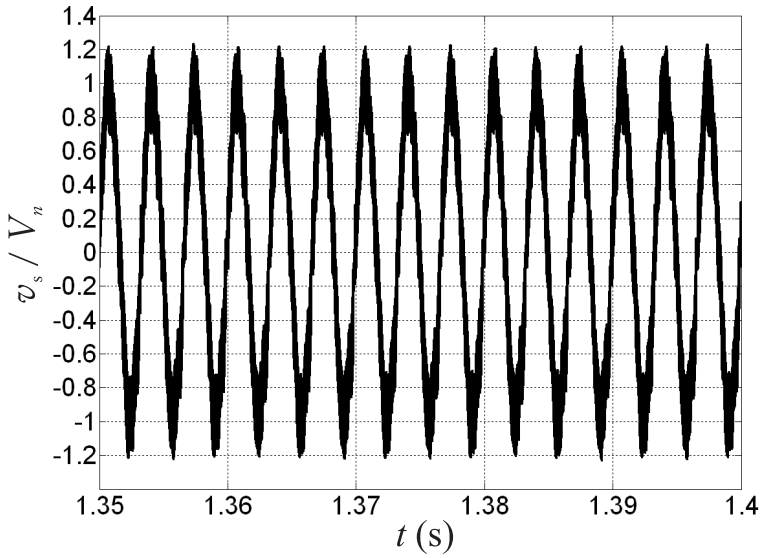

Figure 5.35 - Example 5.V - Normalized line-to-ground stator voltage oscillogram.

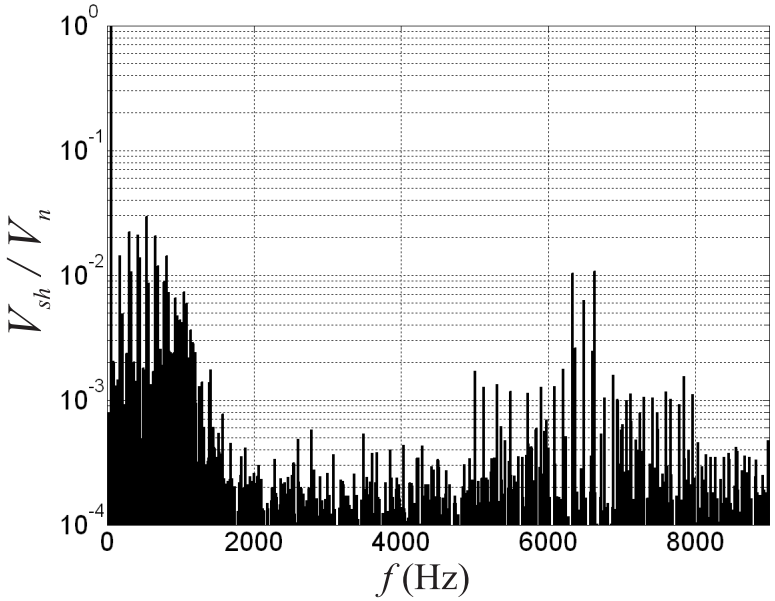

Figure 5.36 - Example 5.V - Normalized line-to-ground stator voltage spectrum.

The stator voltage oscillogram (Figure 5.35) and spectrum (Figure 5.36) are very similar to the ones shown for the PCC voltage. This result is very similar to the one obtained for Example 5.II and has the same explanation: the current flowing from the DFIG stator to the grid is practically sinusoidal, therefore there is no harmonic voltage drop on the line impedance and no voltage distortion at the DFIG terminals.

5.8 Conclusions

The control system to perform 'compensation by means of LSC modulation' has been presented. Simulation results prove that this method is a valid alternative to the compensation by means of RSC modulation described in chapter 4. The major advantage of compensation by means of LSC modulation is the possibility to compensate triplen harmonics if the dc-link is connected to the neutral.

The last two examples show a drawback of the proposed method: since the power converters are rated for a power smaller than the DFIG, compensation by means of LSC modulation may result in excessive power loss in the RSC and LSC and therefore damage of the solid state devices. It has also been shown that DFIG does not allow the reduction of the power loss to the rated value. This result suggests that in practical applications it may not be convenient to compensate all the harmonic currents injected by the NLL by using current injection by the LSC.

Chapter 6

Compensation by Means of Combined Modulation: Steady-State Analysis

6.1 Introduction

The first part of this chapter deals with the comparison of 'compensation by means of RSC modulation' (chapter 4) and 'compensation by means of LSC modulation' (chapter 5).

In the second part, a third concept for harmonic compensation is presented, named 'compensation by means of Combined Modulation (CM)'.

6.2 Comparison between compensation by means of RSC and of LSC modulation

The comparison between the two compensation methods is implemented with the help of a case study characterized by the following assumptions:

- The currents injected by the NLL are listed in Table 4.3: the NLL spectrum includes harmonic components multiple of the fundamental, interharmonics, subharmonics and triplen harmonics and it has been chosen because it exemplifies the harmonic current content injected by practical NLLs. The NLL current spectrum is depicted in Figure 6.1.
- At the DFIG stator terminals, the power factor (PF) is unity.
- The blade pitch angle is nil, β=0: this allows maximum power capture from the wind [10, 94].
- Operation at maximum wind speed, corresponding to maximum normalized rotor speed $\omega_r/\omega_1 = 1.5$ (according to the tracking characteristic reported in Fig. A.1) is considered.

- The obtained results correspond to steady-state conditions: the NLL current spectrum and the wind speed are assumed constant.

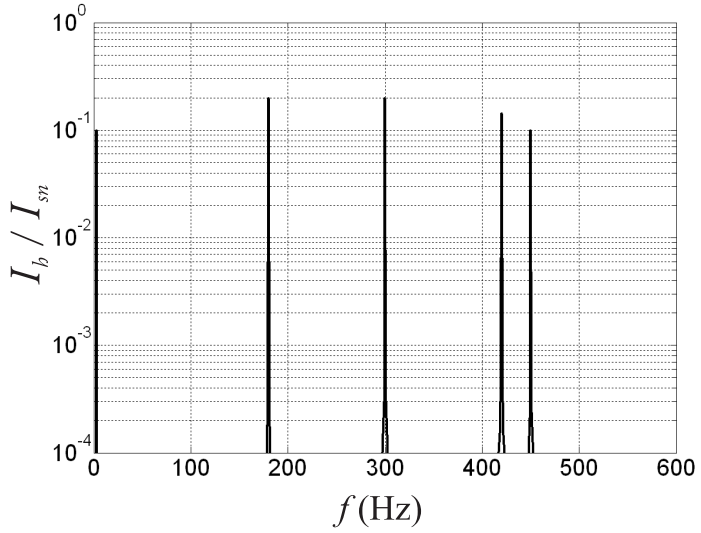

Figure 6.1 - Comparison between compensation by means of RSC modulation and of LSC modulation: normalized NLL current spectrum.

6.2.1 Current spectra and THDs

The normalized current spectra at the PCC, at the stator terminals and at the LSC terminals are shown Figure 6.2.a, 6.2.b and 6.2.c respectively. For both the compensation methodologies, the amplitude of the current harmonics in the grid spectrum is lower than in the NLL spectrum, as obtained by comparing Figure 6.2.a with Figure 6.1. Compensation by means of RSC modulation results in a slightly cleaner spectrum, except for the triplen harmonic that cannot be injected from the stator terminals. Figure 6.2.b shows that the stator contains the harmonic currents corresponding to the ones injected by the NLL when RSC modulation is implemented. Figure 6.2.c shows that the LSC feeder current spectrum contains the harmonic currents corresponding to the ones injected by the NLL when LSC modulation is considered.

The performances of the two compensation methodologies can be better quantified by comparing the current THD at the PCC for three cases: no harmonic compensation, compensation by means of RSC modulation and compensation by means of LSC modulation. The numerical values for the current THD are listed in Table 6.1.

The current spectra illustrated in Figure 6.2 and of the current THD variations shown in

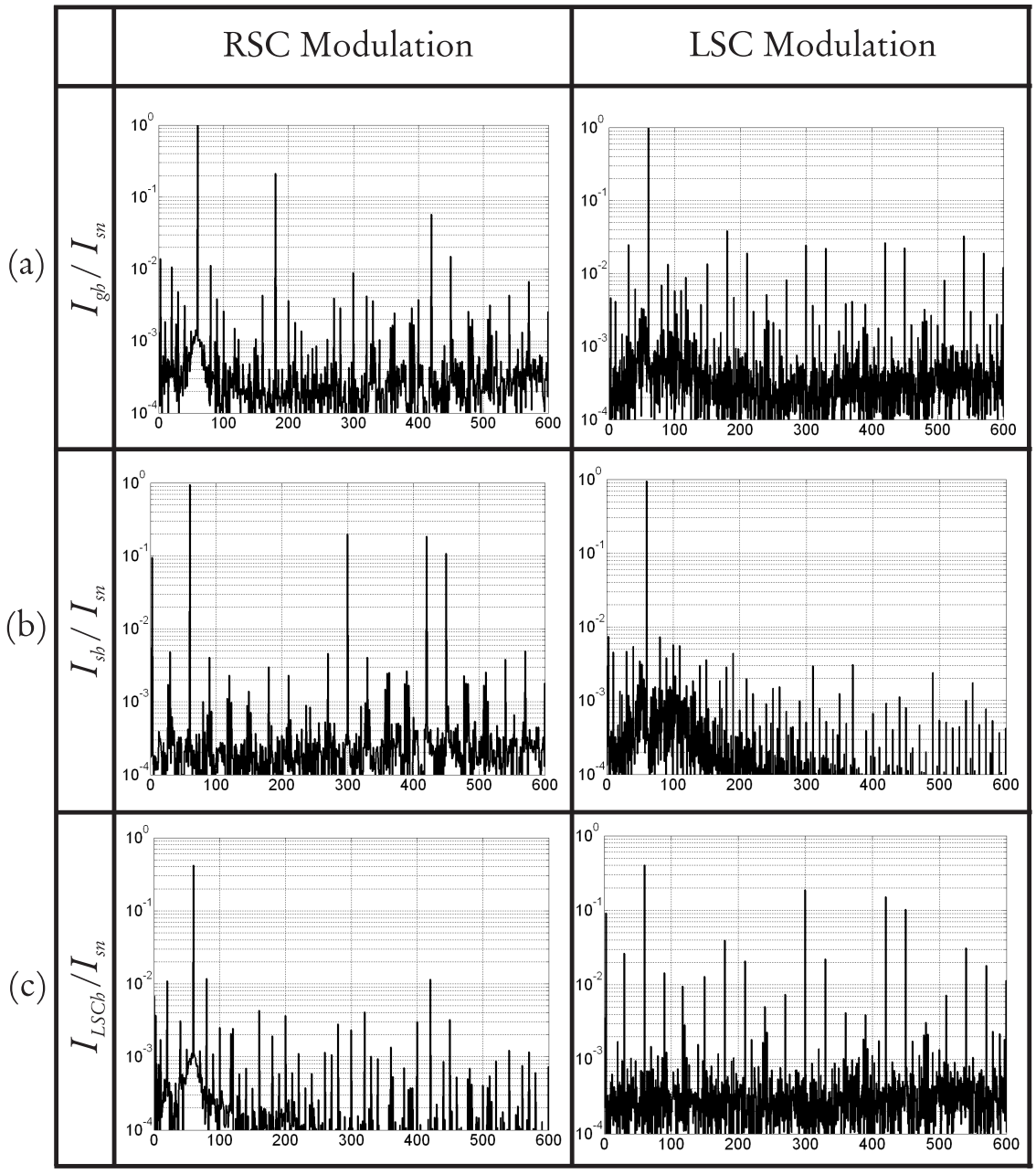

Figure 6.2 - Comparison between compensation by means of RSC modulation and of LSC modulation: normalized current spectra; (a) grid current, (b) stator current and (c) LSC feeder current. For all the figures, x-axis: f (Hz) ; y-axis: harmonic current amplitude, p.u. (base value is the DFIG rated current).

Table 6.1 - Comparison between compensation by means of RSC modulation and of LSC modulation: current THD at the PCC.

THD	No Comp.	RSC mod.	LSC mod.
Current	0.25	0.16	0.075

Table 6.1 teach that compensation by means of RSC modulation results in a lower current distortion than compensation by means of LSC modulation.

6.2.2 Voltage spectra and THD

Table 6.2 - Comparison between compensation by means of RSC modulation and compensation by means of LSC modulation: voltage THD at the PCC.

THD	No Comp.	RSC mod.	LSC mod.
Voltage	0.11	0.047	0.055

The normalized voltage spectrum at the PCC, at the stator terminals, at the rotor terminals and at the LSC terminals are shown in Figure 6.3.a, 6.3.b, 6.3.c and 6.3.d respectively. In terms of voltage at the PCC, the two compensation methodologies are equivalent: the spectra depicted in the first row of Figure 6.3 show a dominant fundamental component and residual high frequency components, due to the power converters' PWM.

The amplitude of the harmonic components is lower for the stator voltages (Figure 6.3.b) than for the rotor voltages (Figure 6.3.c), because the DFIG acts as a filter for the harmonics generated by the RSC.

The spectra depicted in Figure 6.3.c and Figure 6.3.d show clearly how the role of the RSC and of the LSC are interchanged for each compensation methodology: the rotor and LSC spectra for the case of compensation by means of RSC modulation are similar to the LSC and rotor spectra respectively for the case of compensation by means of LSC modulation.

By observing the results in Figures 6.3.b,.c and .d one learnes that compensation by means of LSC modulation results in a general higher harmonic distortion at the stator terminals, rotor terminals and LSC terminals then compensation by means of RSC modulation. This result is confirmed by comparing the voltage THD at the PCC for three cases: no harmonic compensation, compensation by means of RSC modulation and compensation

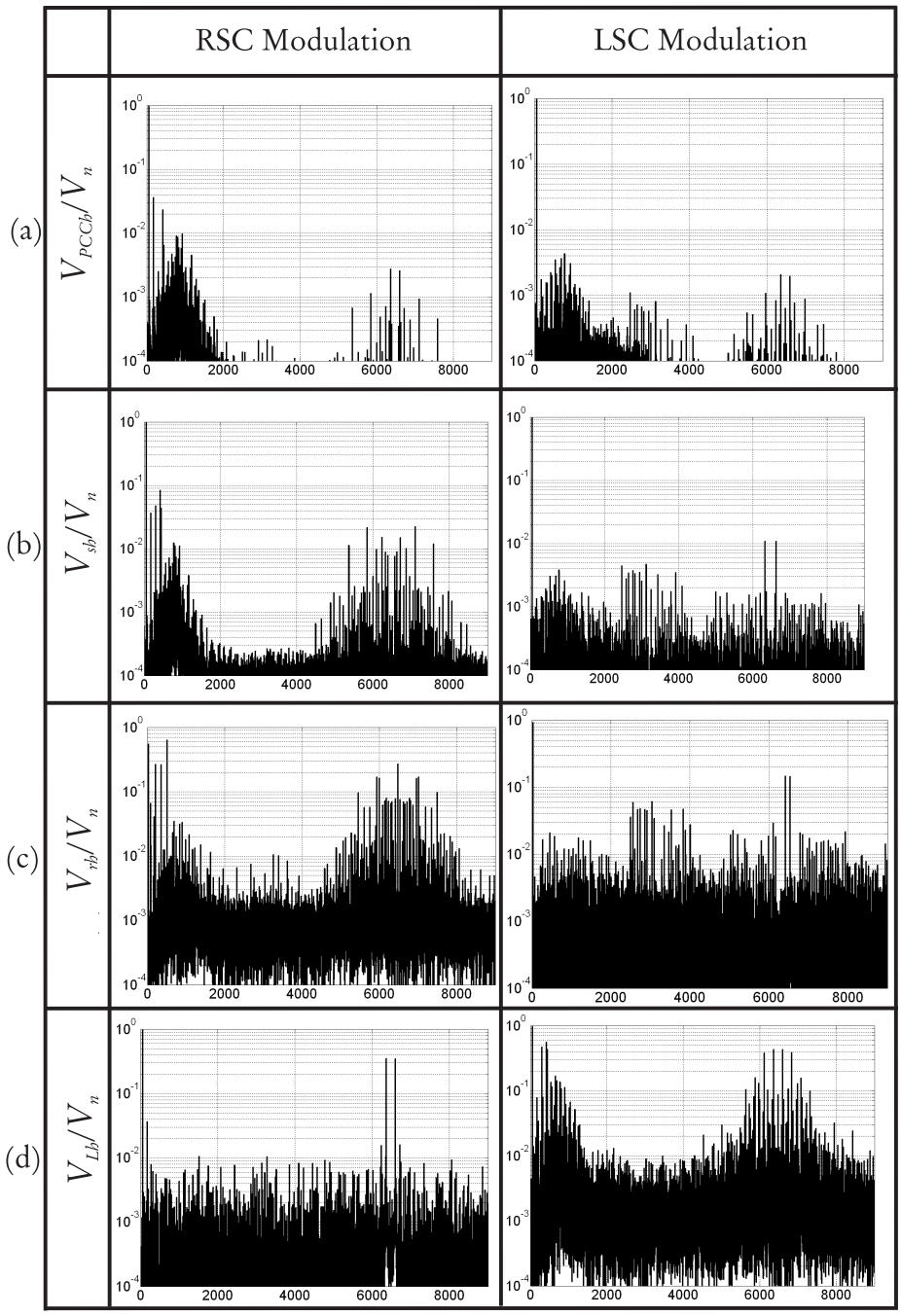

Figure 6.3 - Comparison between compensation by means of RSC modulation and of LSC modulation: Voltage amplitude spectra (a): PCC voltage, (b): stator voltage, (c): rotor voltage and (d): LSC feeder voltage. For all the figures, x-axis: f (Hz); y-axis: harmonic voltage amplitude, p.u. (base value is the DFIG rated voltage).

by means of LSC modulation. The numerical results are listed in Table 6.2. Compensation by means of RSC modulation results in a lower THD for the voltage at the PCC: this conclusion is similar to the one obtained from the comparison of the grid current THD variations (Table 6.1).

6.2.3 Power loss and derating

Figures 6.4 and 6.5 show the windings power loss and the RSC and LSC power loss respectively. In both cases the x-axis variable is the normalized rotor speed. Figure 6.6 presents the fundamental stator current for the case study, assuming unit power factor at the stator terminals. Under this condition, the fundamental stator current is directly proportional to the stator active power.

When compensation by means of RSC modulation is implemented, the windings loss rises significantly above the rated value as shown by the left plot of Figure 6.4. DFIG derating is needed to reduce the winding power loss. On the contrary, from the right plot of Figure 6.4 one concludes that, when compensation by means of LSC modulation is applied, the winding loss is always equal or below the rated value.

When compensation by means of LSC modulation is implemented, the RSC and LSC power loss rises significantly above the rated value as shown by the right plot of Figure 6.5. DFIG derating is needed to reduce the RSC and LSC power loss below the rated value. On the contrary, the left plot of Figure 6.5 shows that when compensation by means of RSC modulation is implemented, the RSC and LSC power loss is always below the rated value.

Figure 6.6 shows that the fundamental current trajectory for the two compensation methodologies is very similar: this result is expected since the same case study and the same system topology are assumed.

6.2.4 Summary of the comparison

The analysis developed in chapter 4, chapter 5 and in the previous sections shows that either compensation by means of RSC modulation or compensation by means of LSC modulation can be used to cancel the harmonic currents injected by a NLL connected in proximity ofthe WECS. The results of the comparison are summarized in Table 6.3.

Compensation by means of RSC modulation is slightly superior from the point of view of current and voltage spectra; compensation of LSC modulation has the indisputable advantage of allowing compensation of triplen harmonics (5.4). The power loss and consequent derating is very similar.

Although the simulation results provided in the previous sections applies to a particular

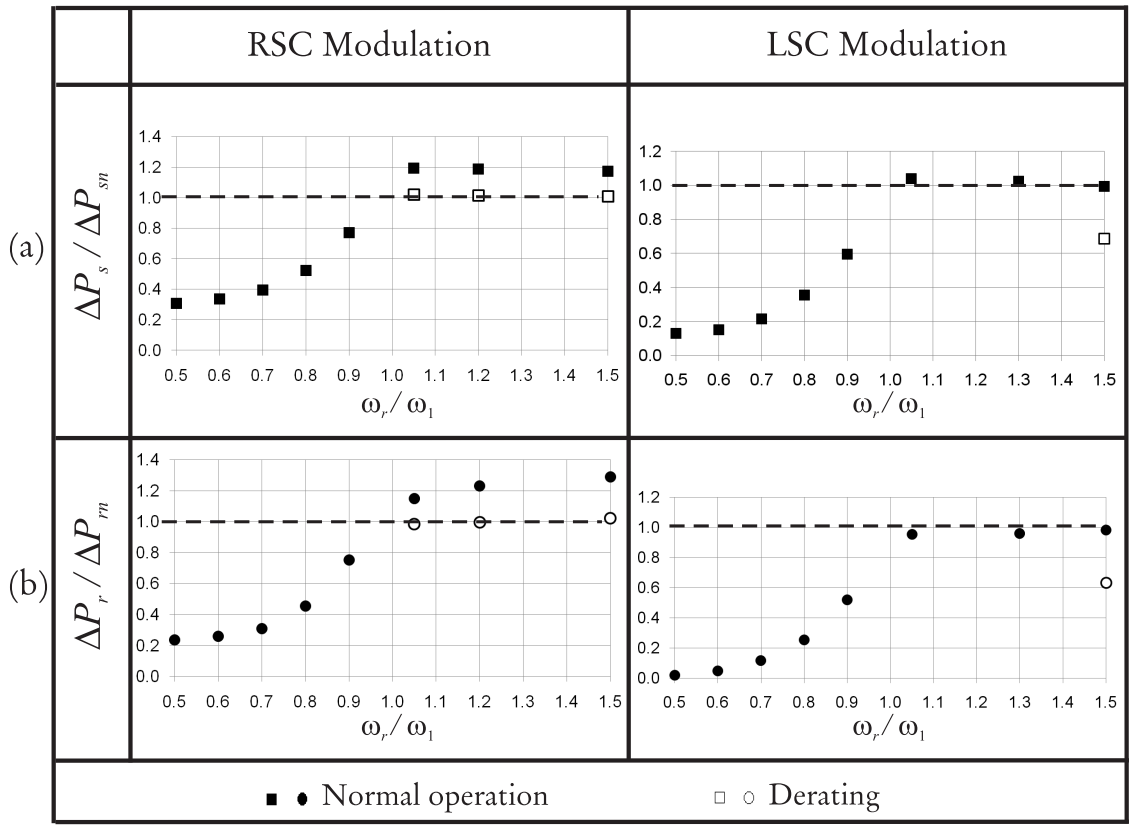

Figure 6.4 - Comparison between compensation by means of RSC modulation and of LSC modulation: normalized winding power loss; (a) Stator winding power loss and (b) rotor windings power loss. DFIG derating is implemented according to the curves shown in Figure 6.6 for each compensation methodology.

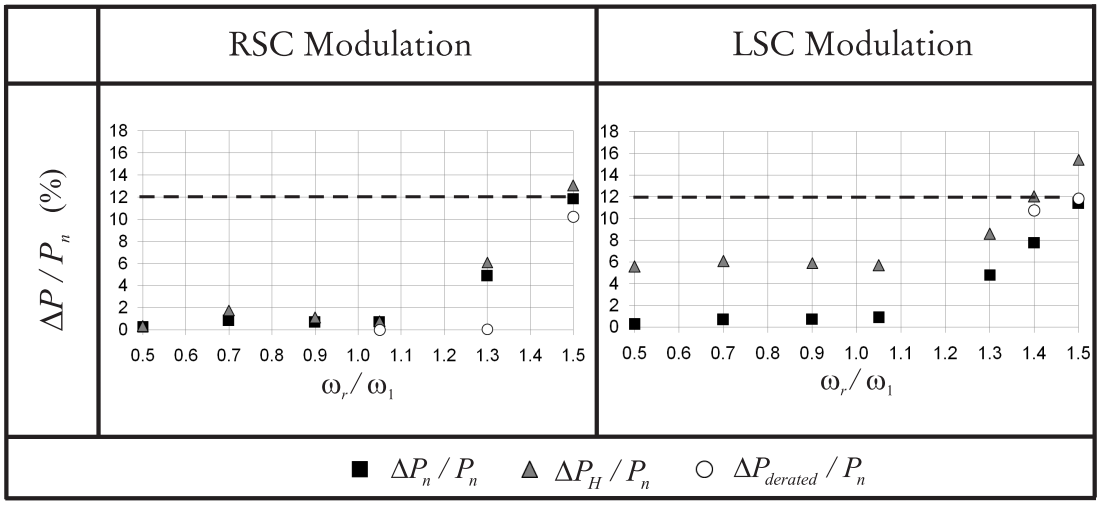

Figure 6.5 - Comparison between compensation by means of RSC modulation and of LSC modulation: RSC and LSC power loss. Three trajectories are presented; $\Delta P_n/P_n$: normalized power loss at rated conditions (sinusoidal operation); $\Delta P_H/P_n$: normalized power loss when harmonic compensation is applied; $\Delta P_{derated}/P_n$: normalized power loss when derating is implemented according to Figure 6.6.

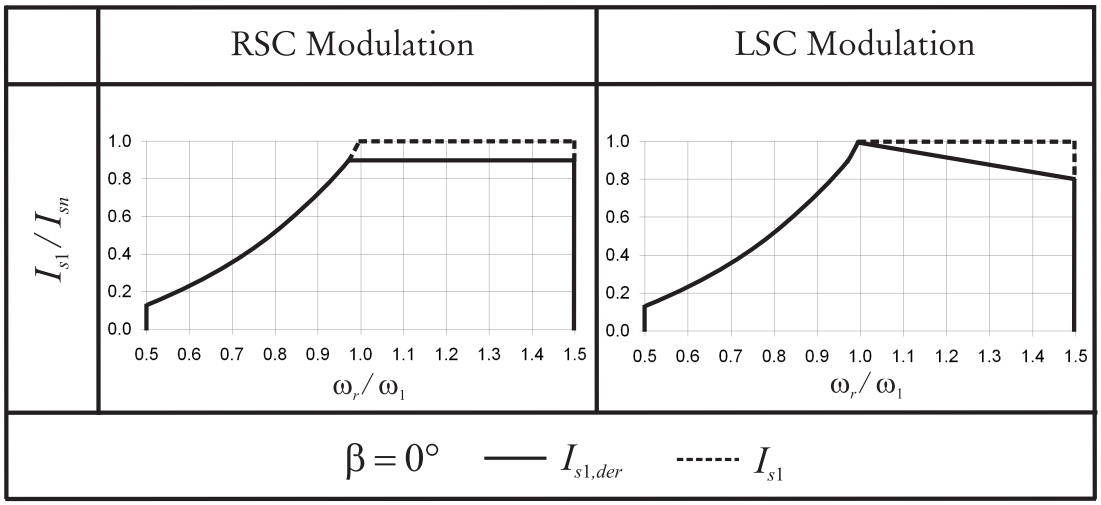

Figure 6.6 - Comparison between compensation by means of RSC modulation and of LSC modulation: DFIG fundamental stator current, under the assumption of unity power factor at the stator terminals.

Table 6.3 - Comparison between compensation by means of RSC modulation and of LSC modulation: Summary of the results.

Item	RSC or LSC?
Current Spectra	RSC
Voltage Spectra	RSC
Derating	Similar
Triplen	LSC

harmonic current injection and to a specific system configuration, they exemplify the control system response for more general situation. Some of the most important factors and parameters that affect the control system response can be summarized as follows:

1. Stator feeder length:

   The length of the feeder that connects the PCC to the stator terminals is an important variable when compensation by means of RSC modulation is implemented. When this method is applied, the harmonic currents flow from the stator to the grid results in harmonic voltage drop on the line impedance, and in distortion of the voltage at the stator terminals (chapter 4). The importance of this parameter when the transient phenomena take place is addressed in chapter 8.

2. RSC and LSC rated power:

   When sinusoidal operation is assumed, the RSC and LSC rated power is proportional to the maximum slip, (3.36). When harmonic compensation is implemented, the LSC and RSC rated power must be increased to withstand the estimated harmonic power flow and the rms current increase.

   This concept is explained by means of an example: the RSC and LSC rated power is 30% of the DFIG rated power ($P_{n,\mathrm{RSC}} = P_{n,\mathrm{LSC}} = 0.3P_n$) and a single harmonic current injection h=5 with amplitude 0.2 p.u. is assumed. Simulation results indicate that at $\omega_r/\omega_1 = 1.5$, the power converter loss is approximately 50 % higher than the rated value for both compensation by means of RSC modulation and compensation by means of LSC modulation. When the power converters rated powre is $0.5P_n$, it results that the power loss increase for both compensation methods is a few percent, as presented in chapters 4 and 5.

This result for a single harmonic injection indicates that the use of a WECS as an AF and power generator simultaneously requires to oversize the power converters.

3. Triplen harmonics:

   Triplen harmonics can be canceled only by means of LSC modulation if the dc-link is connected to the neutral. The RSC modulation cannot be used for this purpose, because the DFIG winding are never connected to the neutral (chapter 5).

6.3 Harmonic compensation by means of Combined Modulation (CM)

6.3.1 Control system and block diagrams

The system under study is the one presented in Figure 5.16: since the system configuration is identical to the one studied in chapter 5, the same transfer functions apply.

Compensation by means of Combined Modulation is implemented according to these principles:

- The triplen harmonics compensation ($h = 3k$) is obtained by LSC modulation
- The compensation of the other harmonics ($h \neq 3k$) is obtained by RSC modulation.

In the equivalent Park domain (section 4.3), the above principles are expressed as follows:

1. The stator positive- and negative-sequence currents are equal in magnitude and 180^o out of phase with respect to the positive- and negative-sequence currents injected by the NLL:

$$i_{sd} = -i_{hd} \tag{6.1}$$

$$i_{sq} = -i_{hq} \tag{6.2}$$

2. The zero-sequence current injected by the LSC equal in magnitude and 180^o out of phase with respect to the zero-sequence NLL current injected by the NLL

$$i_{L0} = -i_{h0} \tag{6.3}$$

The block diagrams implementing the power converters control are derived from the ones presented in chapters 4 and 5: the same block diagram illustrated in Figure 4.9 is used to

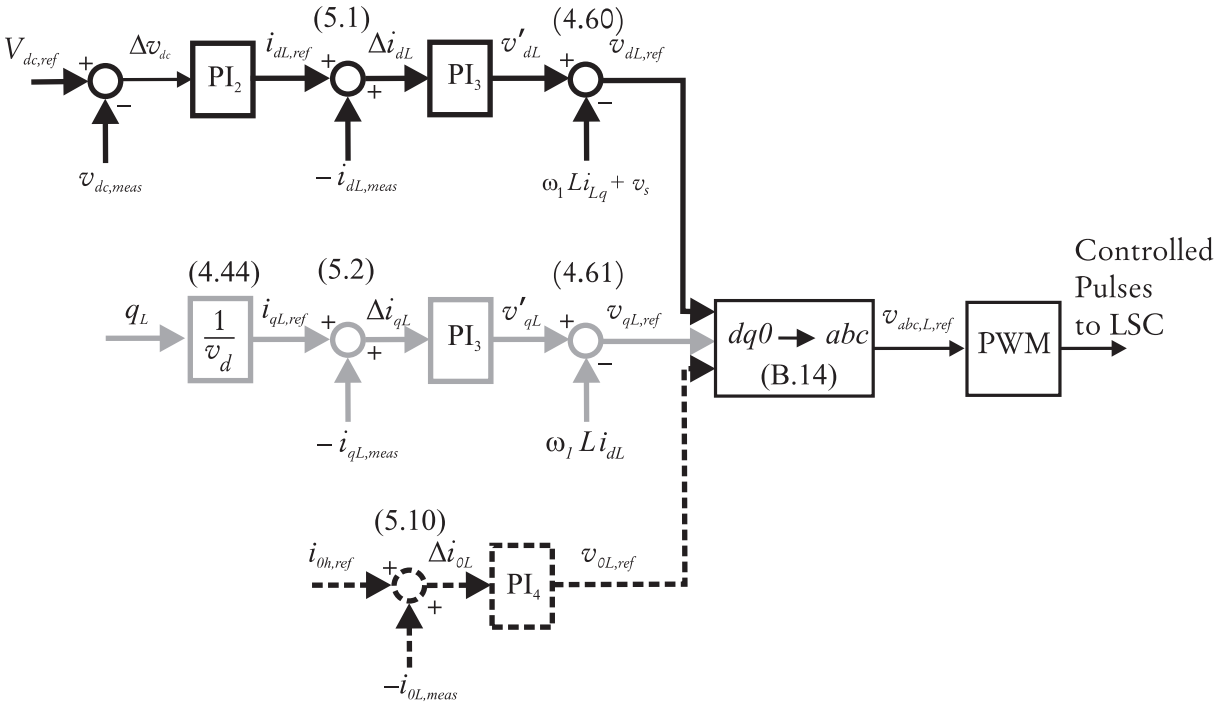

Figure 6.7 - Block diagram for the control of the LSC subsystem, compensation by means of Combined Modulation.

control the RSC. The block diagram shown in Figure 5.21 for the LSC control is simplified as shown in Figure 6.7 when compensation by means of CM is applied. The block diagram presented in Figure 6.7 is obtained by removing the NLL positive- and negative-sequence currents i_{hd} and i_{hq} from the diagram shown in Figure 5.21, since the RSC modulation results in the compensation of those components.

The value of the proportional and integral gains used in the block diagrams of Figure 4.9 and Figure 6.7 are listed in Table A.7.

6.4 Simulation results for compensation by means of CM

6.4.1 Example 6.I

Example 6.I - Current spectra

The amplitude of the harmonic currents injected by the NLL are listed in Table 6.4. This first example is assumed to explain the control system operation and to compare the power loss distributions with the ones obtained for compensation by means of RSC modulation

and of LSC modulation.

Table 6.4 - Example 6.I: Harmonic currents injected by the NLL.

h	I_h/I_n	Sequence
3	0.20	0
5	0.20	+

The normalized current spectra are presented in Figure 6.8. The grid current spectrum is presented in Figure 6.8.a: the main component is at 60 Hz; the third and fifth harmonic components are significantly reduced with respect to the NLL current spectrum (Figure 6.8.b).

The fifth harmonic component is sinked by the stator (Figure 6.8.c), the third harmonic component by the LSC (Figure 6.8.d).

The power loss distribution is not presented in details because the plots resemble the ones presented in chapters 4 and 5. The DFIG loss are equal to the ones shown in Figure 4.16 for Example 6.I; the power converter loss shows a pattern similar to the one presented in Figure 5.4 for Example 6.I. The power loss patterns indicate that no derating is necessary.

6.4.2 Example 6.II

The NLL spectrum is the one chosen to compare compensation by means of RSC and of LSC modulation: the harmonic currents are listed in Table 4.3 and the corresponding spectrum is displayed in Figure 6.9.b.

Example 6.II - Current spectra

The current amplitude spectra are shown in Figure 6.9: the LSC is responsible for the injection of the third order harmonic current (Figure 6.9.d), while the stator is responsible for the injection of all the other harmonics (Figure 6.9.c). The resulting grid current spectrum is relatively clean (Figure 6.9.a), by observing that the NLL current spectrum introduce a severe distortion (Figure 6.9.b).

The improvement of the current waveform can be better quantified by analyzing the grid current oscillograms presented in Figure 6.10. The upper oscillogram shows the current waveform before harmonic compensation is applied; the lower oscillogram shows the current oscillogram when compensation by means of Combined Modulation is implemented. The waveform improvement is relevant, although there are residual distortions.

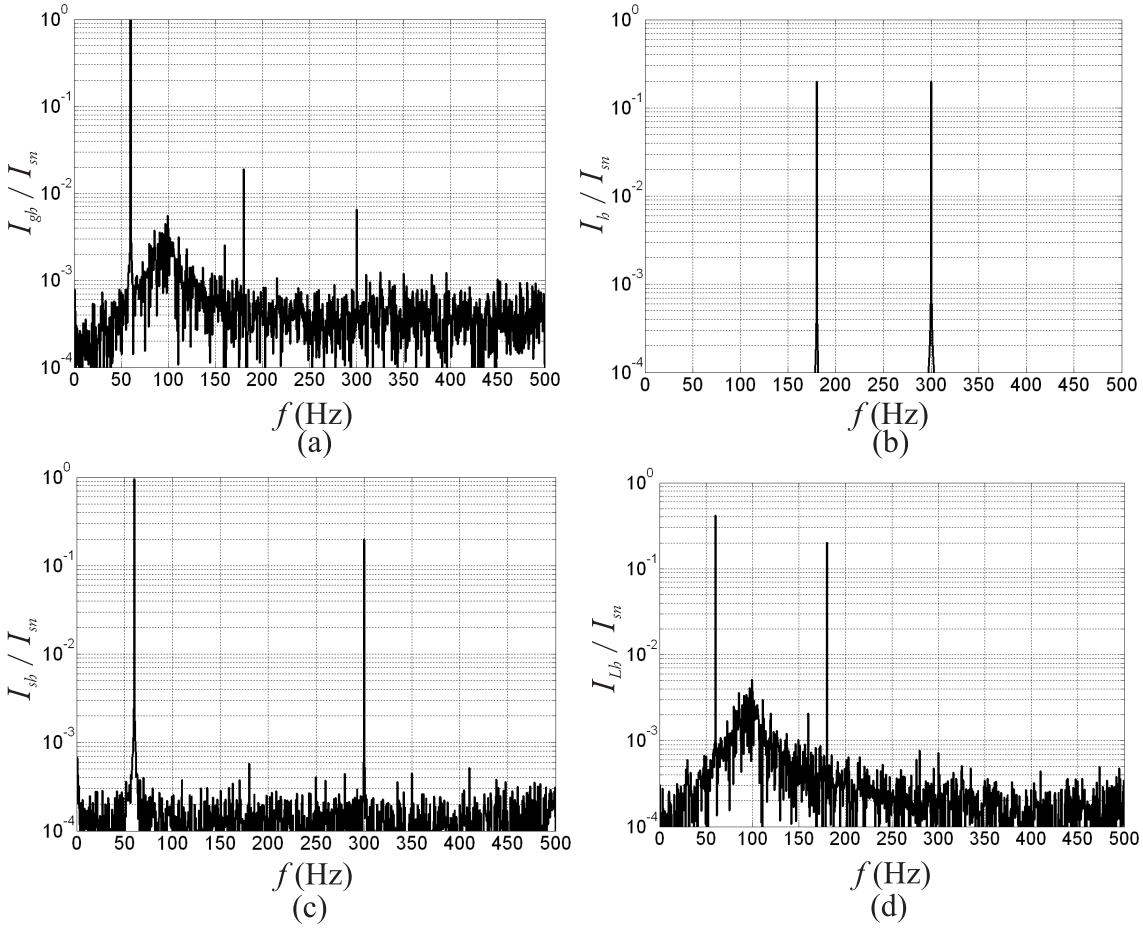

Figure 6.8 - Example 6.I: normalized current amplitude spectra; (a) grid current, (b) NLL current, (c) stator current and (d) LSC current.

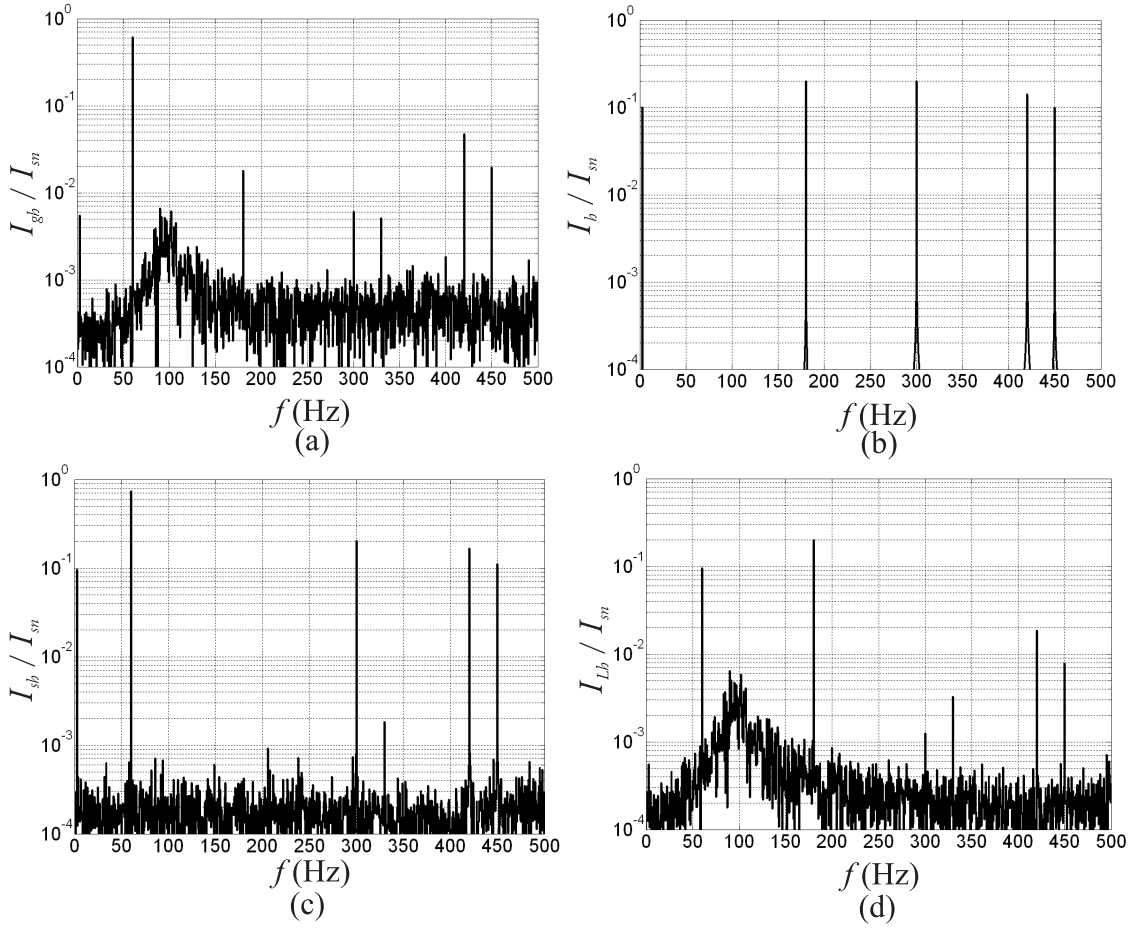

Figure 6.9 - Example 6.II: Normalized current amplitude spectra; (a) grid current, (b) NLL current, (b) stator current and (c) LSC current.

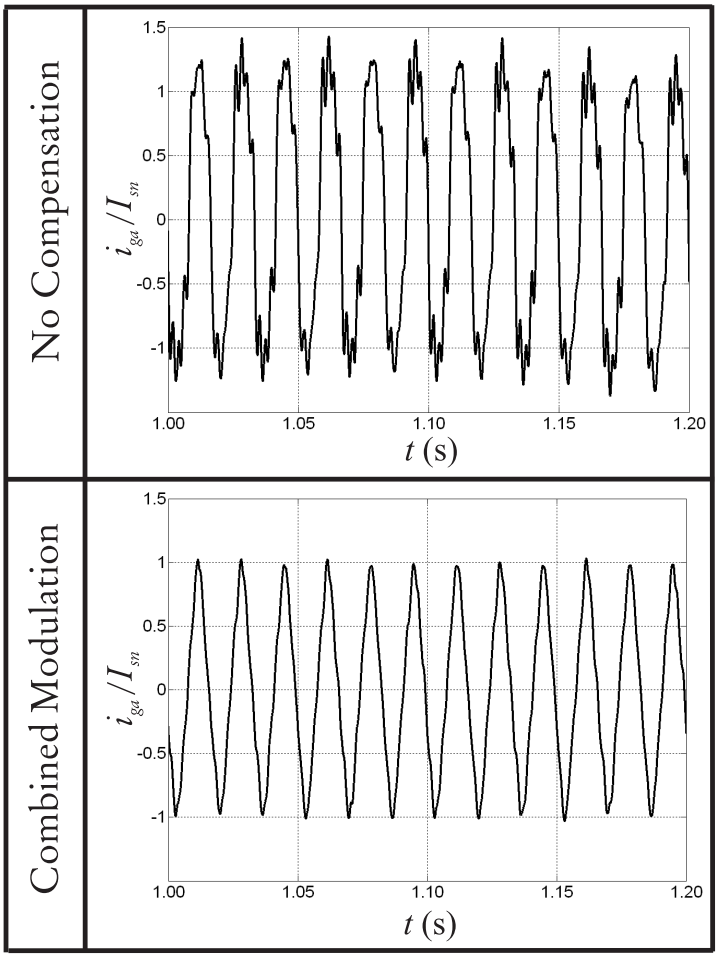

Figure 6.10 - Example 6.II: Normalized grid current oscillogram, base value is DFIG rated current; (a) Current oscillogram before harmonic compensation and (b) after harmonic compensation.

Example 6.II - Voltage spectra

The voltage spectra are shown in Figures 6.11 - 6.12.

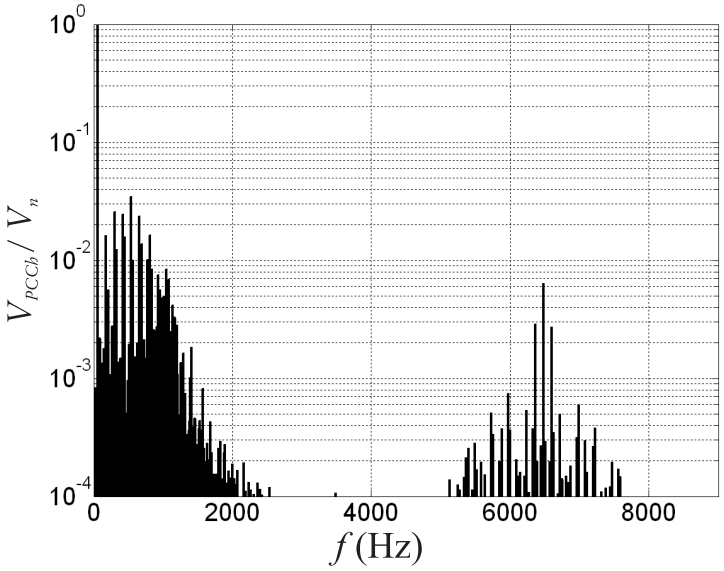

Figure 6.11 - Example 6.II: Normalized line-to-neutral PCC voltage amplitude spectrum.

The normalized stator voltage oscillogram is shown in Figure 6.15. The upper diagram shows the stator voltage oscillogram before harmonic compensation is applied: the waveform is a sinusoid with minor distortions, principally due to the coupling between stator and rotor and the consequent presence of high harmonic components. The lower oscillogram shows that when compensation by means of Combined Modulation is applied, the stator windings are injecting harmonic currents and the consequent voltage drop on the line impedance causes voltage distortion at the stator windings terminals and the resulting peak voltage is approximately 1.15 p.u.

Example 6.II: Current and voltage THDs

The current and voltage THDs are presented in Table 6.5.

Example 6.II: Power loss

Figures 6.16 and 6.17 present the RSC and LSC power loss and the winding power loss, respectively.

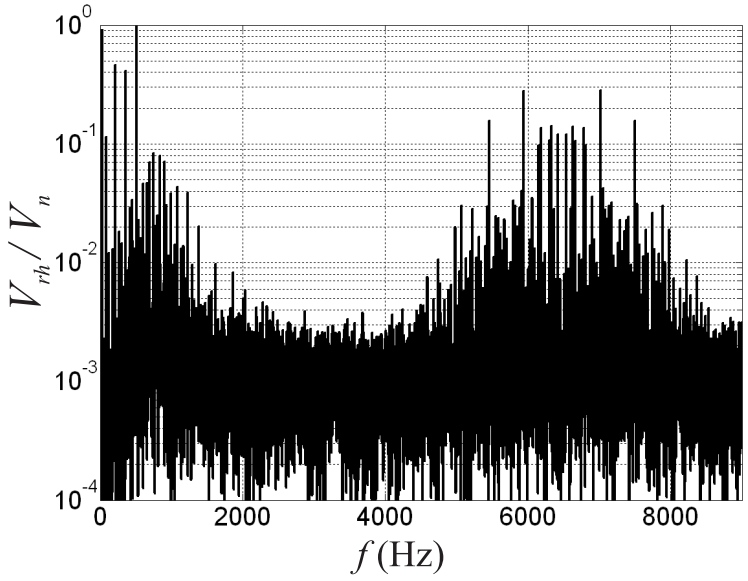

Figure 6.12 - Example 6.II: Normalized line-to-line rotor voltage amplitude spectrum.

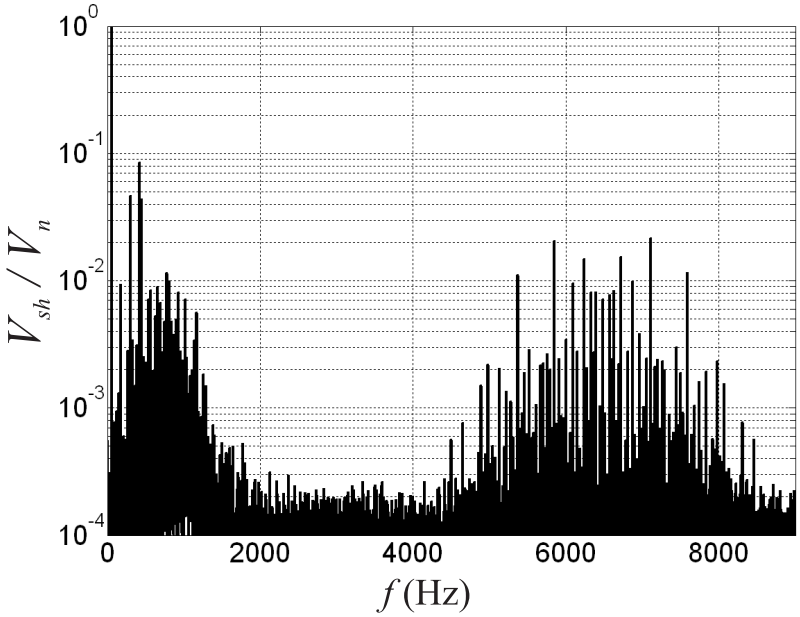

Figure 6.13 - Example 6.II: Normalized line-to-neutral stator voltage amplitude spectrum.

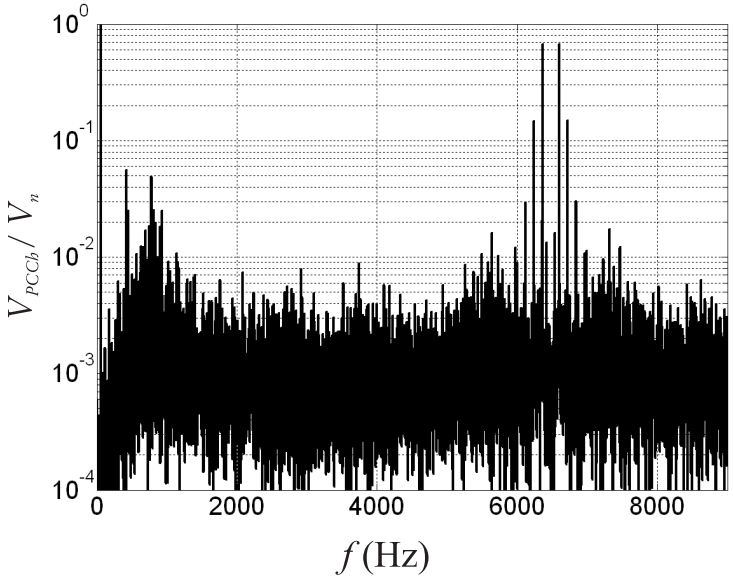

Figure 6.14 - Example 6.II: Normalized line-to-line LSC voltage amplitude spectrum.

Table 6.5 - Example 6.II: Current and voltage THD at the PCC

THD	No Compensation	RSC mod.	LSC mod.	CM
Current	0.25	0.050	0.075	0.070
Voltage	0.11	0.030	0.055	0.040

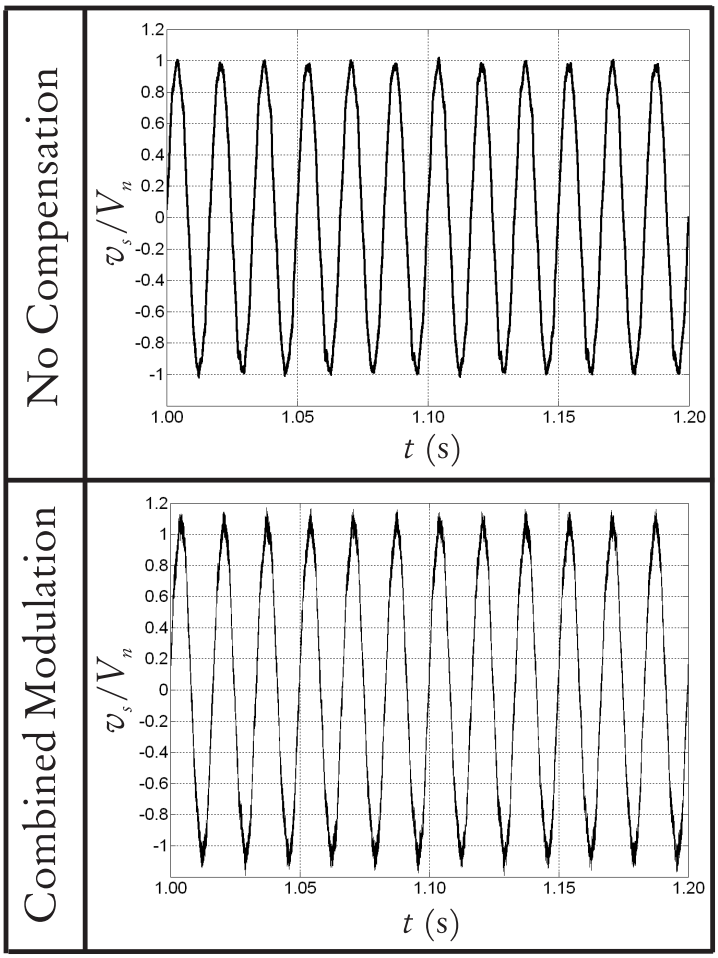

Figure 6.15 - Example 6.II: Normalized stator voltage oscillogram.

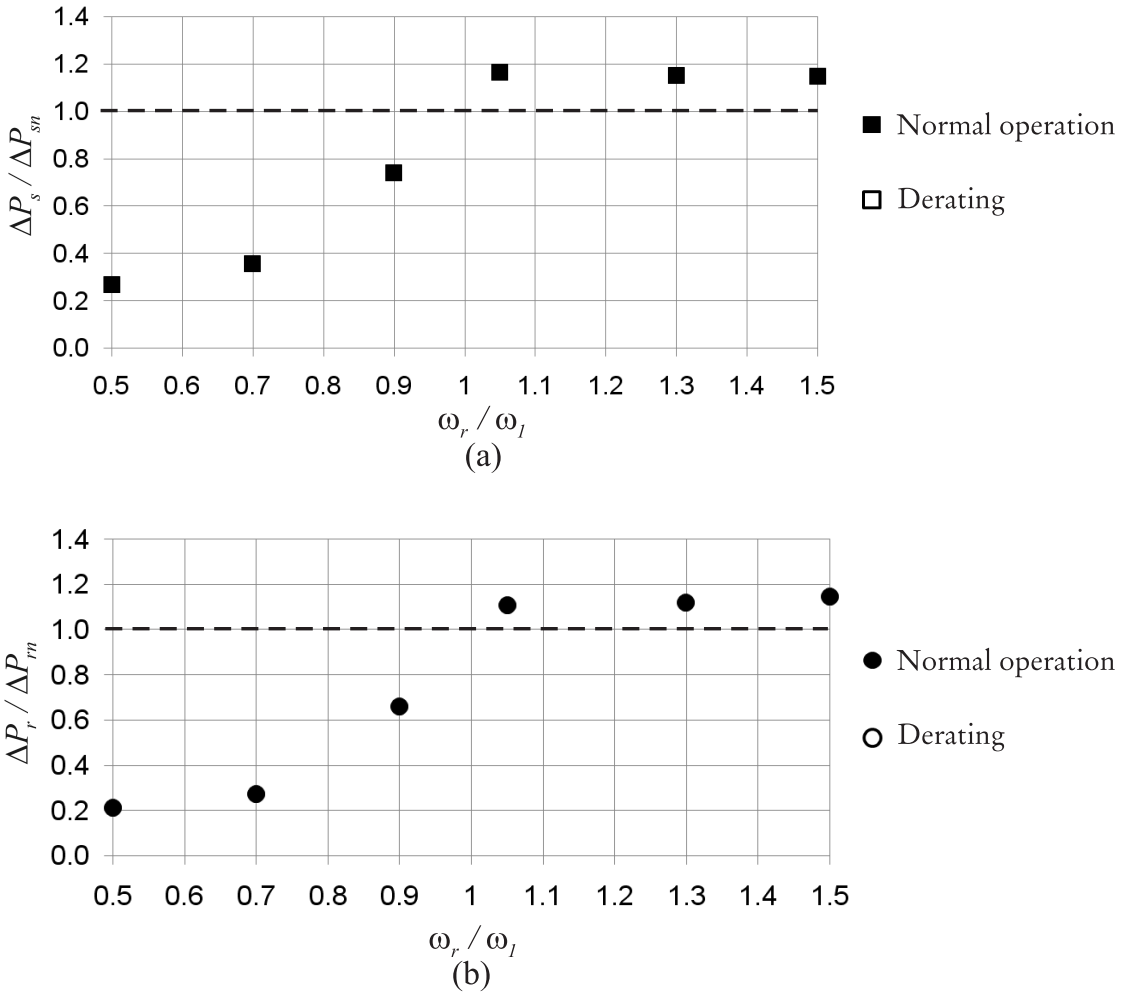

Figure 6.16 - Example 6.II: Normalized winding power loss: (a) Stator and (b) rotor.

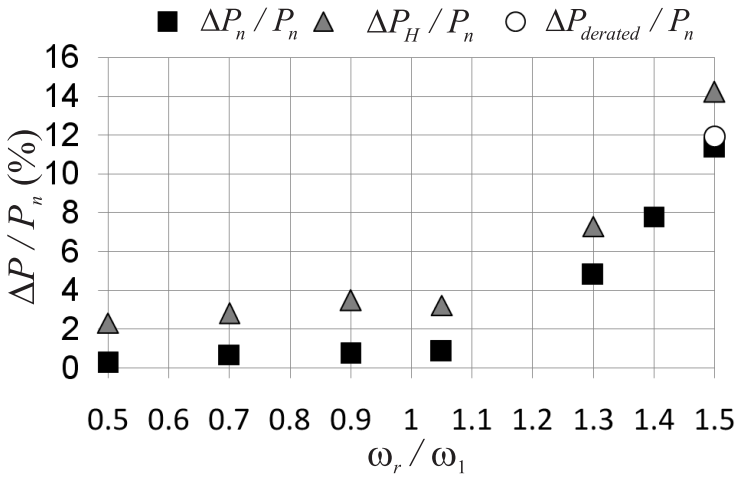

Figure 6.17 - Example 6.II: Normalized RSC and LSC power loss.

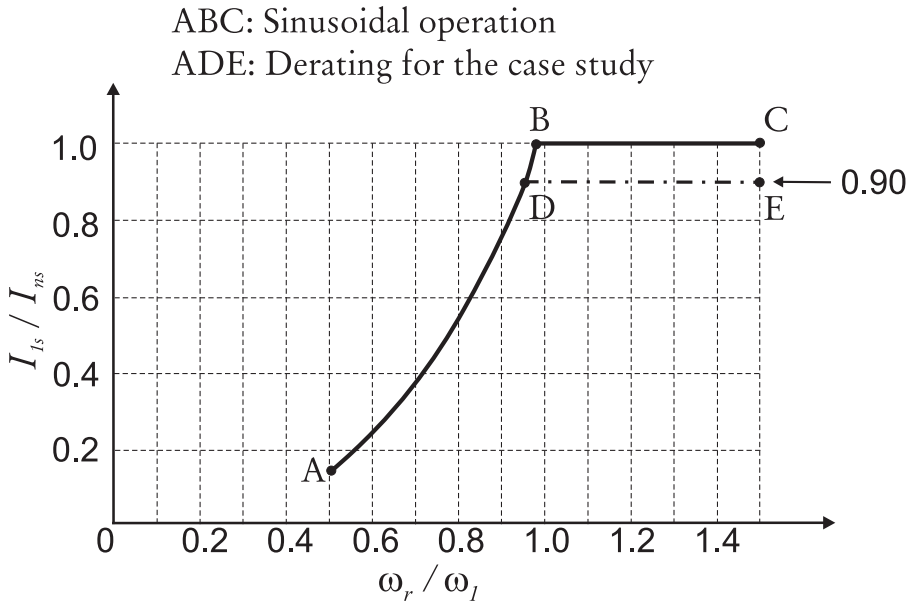

Figure 6.18 - Example 6.II: Normalized fundamental stator current curve as function of normalized rotor speed.

Figure 6.18 presents the normalized fundamental stator curve as function of the normalized rotor speed ω_r/ω_1. Two trajectories are presented: ABC is the stator fundamental curve for sinusoidal operation; ADE is the fundamental stator curve when Combined Modulation and consequent derating are implemented.

By comparing the results presented in Figures 6.16 - 6.18 with the plots illustrated in Figures 6.4-6.6 one concludes that compensation by means of Combined Modulation results in a more uniform split of the power loss among the WECS components and in a less conservative derating.

6.4.3 Example 6.III - Three-phase diode rectifier

The NLL is represented by a three-phase diode rectifier: the NLL configuration is shown in Figure 6.19, where the dc-current load I_d/I_n=0.2.

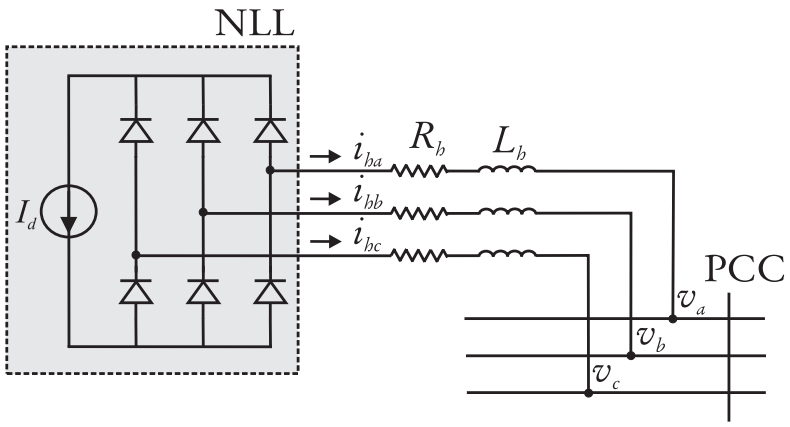

Figure 6.19 - Example 6.III: A three-phase diode rectifier is connected to the PCC.

Example 6.III - Current spectra

The current spectra are presented in Figure 6.20. Figure 6.20.b shows the typical spectrum of a three-phase bridge rectifier: the dominant harmonics are the fifth and seventh components, no triplen harmonic is present. The stator is responsible for injecting the compensating currents (Figure 6.20.c), according to compensation by means of CM. No harmonic current is inected by the LSC (Figure 6.20.d).

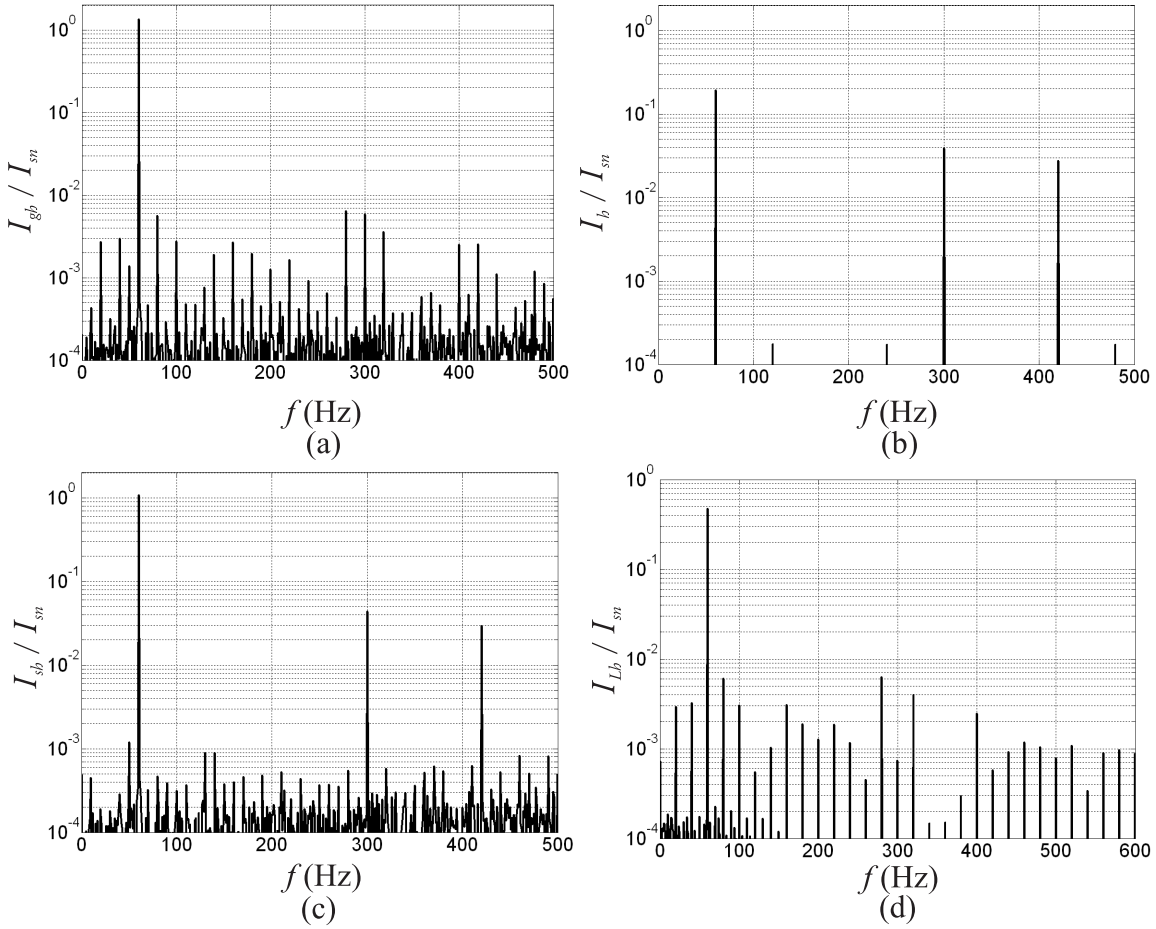

Figure 6.20 - Example 6.III: Normalized current amplitude spectra; (a) grid current, (b) NLL current, (c) stator current and (d) LSC current.

Example 6.III: Current and voltage THDs

The control system operation results in a reduction of the voltage and current THDs, according to the results listed in Table 6.6.

Table 6.6 - Example 6.III: Current and voltage THDs.

THD	No Comp.	CM
Voltage	0.007	0.008
Current	0.068	0.04

Example 6.III: Power loss

The DFIG normalized winding loss are illustrated in Figure 6.21. The DFIG winding loss are above the rated value due to the significant amount of harmonic currents flowing in the DFIG windings: for this particular example, the stator windings are responsible for the injection of a significant amount of harmonic currents, thus explaining the increasing winding loss. On the contrary, the LSC is not injecting any harmonic current (compare Figures 6.26.c and 6.26.d) and the power loss in the RSC and LSC are comparable with the ones presented in Examples 5.1-5.IV. Example 6.III leads to the conclusion that compensation by means of Combined Modulation is an improvement of the other two methodologies but depending on the NLL current spectrum may not result in an uniform partition of the power loss among the WECS components.

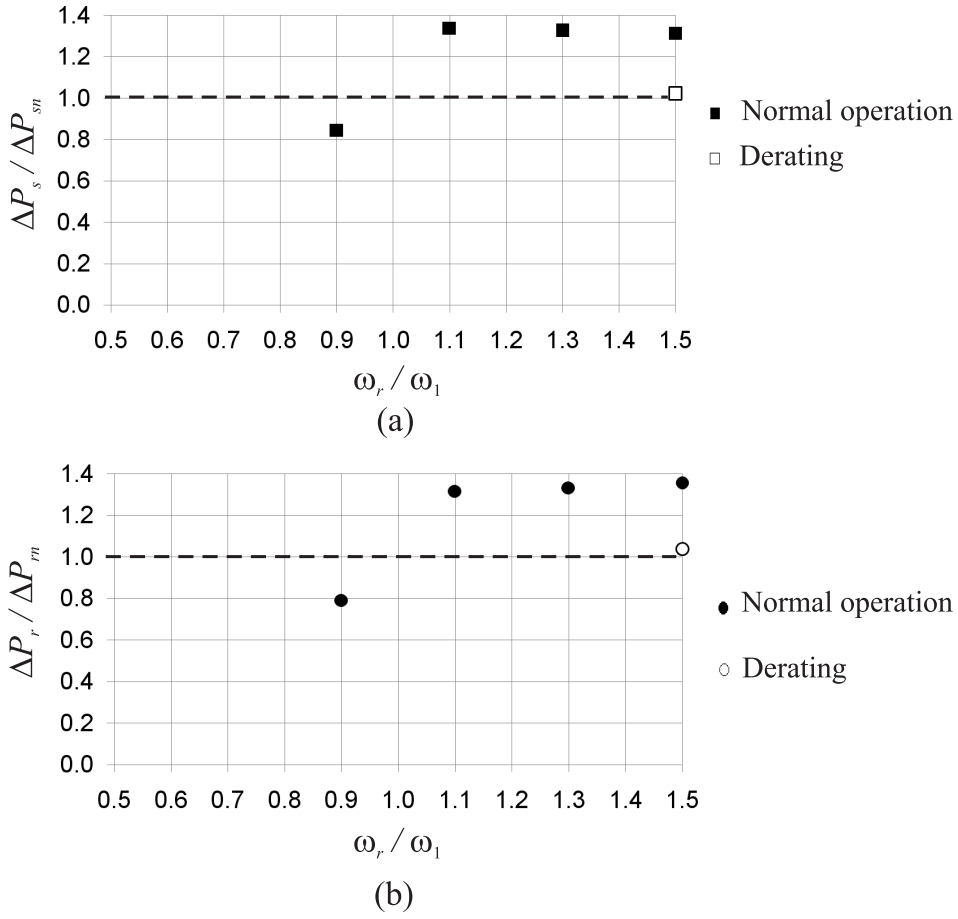

Figure 6.21 - Example 6.III: Normalized winding power loss as function of the normalized rotor speed, compensation by means of CM is applied; (a) stator winding loss and (b) rotor winding loss.

6.4.4 Example 6.IV - Three single-phase diode rectifier

The NLL is represented by single-phase diode rectifier connected between phase a,b,c and neutral respectively. The NLL configuration is shown in Figure 6.19, where I_d/I_n=0.2.

The above configuration has been chosen because it exemplifies the operation of a power system with balanced load, that results in a severe neutral current.

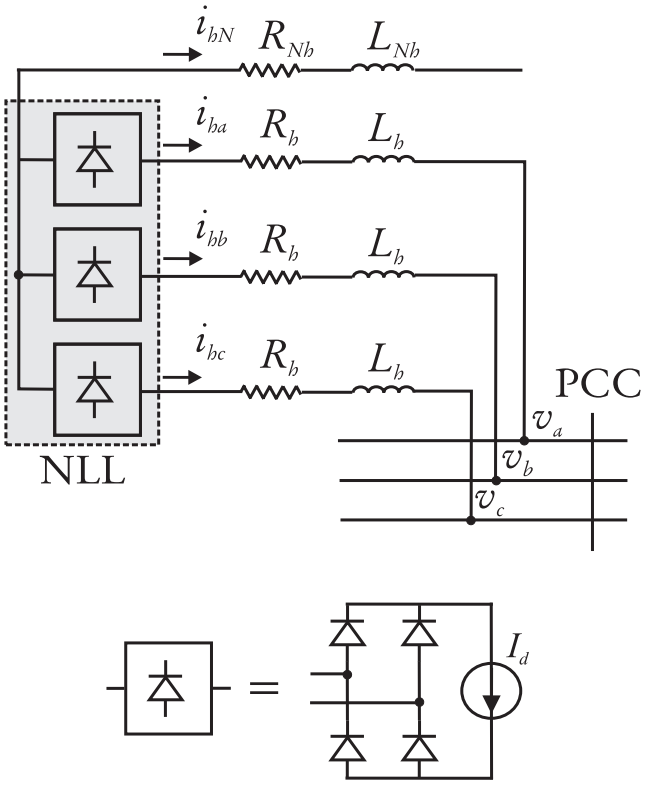

Figure 6.22 - Example 6.IV: Three single-phase diode rectifiers connected between phase and neutral.

Example 6.IV - Current spectra

The current amplitude spectra are displayed in Figure 6.23. Figure 6.23.a shows the current spectrum measured at the single-phase diode rectifiers terminals. The stator current spectrum (Figure 6.23.b) contains the fundamental component as well as the positive- and negative-sequence harmonic currents $h = 3k \pm 1$. The LSC current spectrum (Figure 6.23.c) contains the fundamental component and the triplen component with frequency $f = 3f_1$ Hz. Consequently the grid current spectrum (Figure 6.23.d) is relatively clean being dominated by the fundamental frequency.

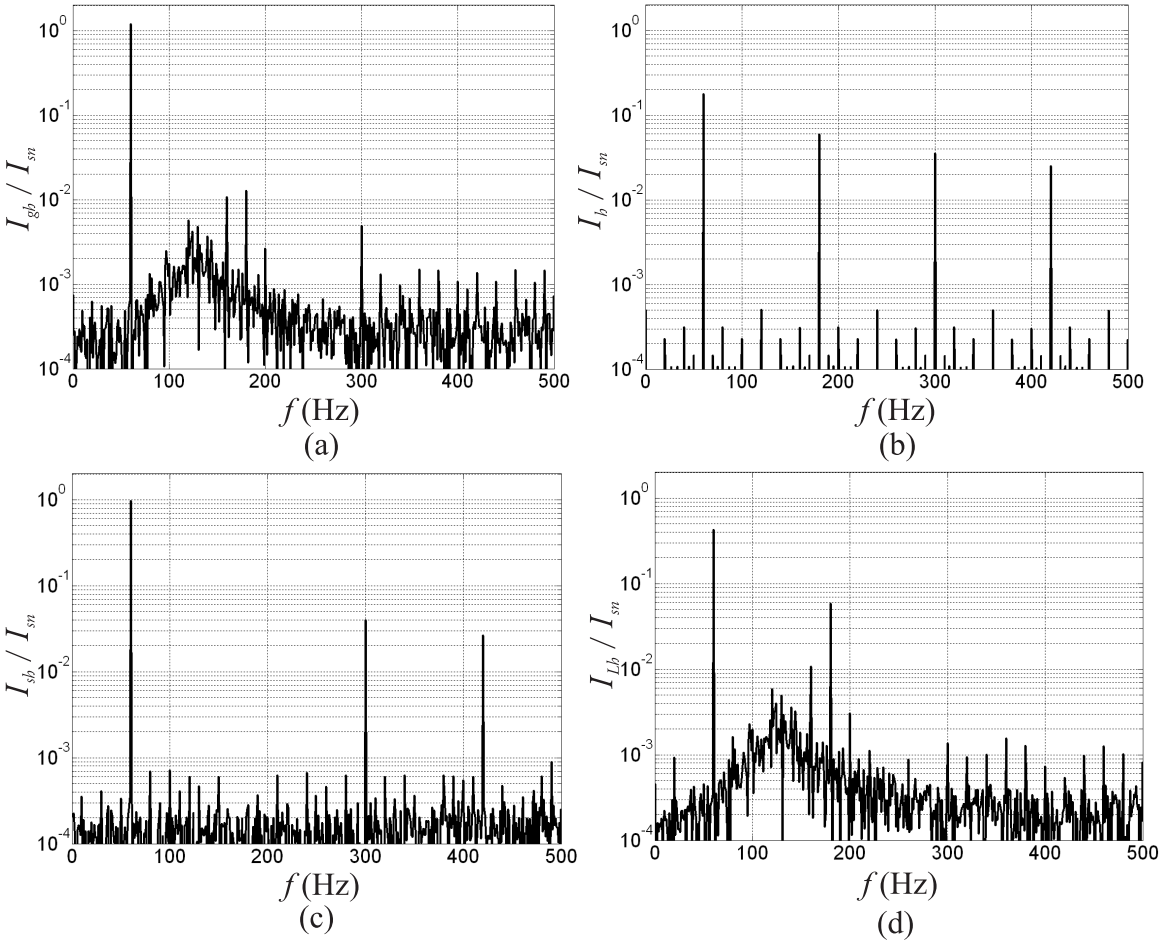

Figure 6.23 - Example 6.IV: normalized current amplitude spectra; (a) grid current, (b) NLL current, (c) stator current and (d) LSC current.

Example 6.IV: Current and voltage THDs

The control system operation results in a reduction of the voltage and current THD, according to the results listed in Table 6.6.

The AF operation results in a significant reduction of the voltage and current THD, as shown in Table 6.7. The current THD is reduced from 0.24 to 0.030, meaning a variation equal to −87.5%. The voltage THD variation consequent to the cancellation of harmonic currents is −45.0%.

Table 6.7 - Current and voltage THD for Example 6.IV, without compensation and with compensation by means of CM.

THD	No Comp.	CM	% Difference
Voltage	0.24	0.030	−87.5 %
Current	0.10	0.055	−45.0 %

Example 6.IV: Power loss and derating

The winding loss are the same obtained for Example III and presented in Figure 6.21, since the same harmonic current injection is supplied by the DFIG windings in both examples.

The RSC and LSC power loss and the fundamental stator current trajectory are shown in Figures 6.24 and 6.25, respectively.

At supersynchronous speed, both the winding loss and the RSC and LSC power loss are above the rated value. The WECS derating trajectory allows reducing the power losses to or below the rated values.

The normalized grid current oscillogram is presented in Figure 6.20.a. Similarly to the previous examples, the harmonics injected by the NLL are filtered by the WECS.

6.5 Conclusions

The comparison between compensation by means of RSC modulation and of LSC modulation allows identifying the advantages and the drawbacks of each compensation methodology. The results obtained from the comparison suggest to define a third compensation methodology, named 'compensation by means of Combined Modulation'. This technique provides similar results in terms of grid current spectrum improvement, and a more uniform

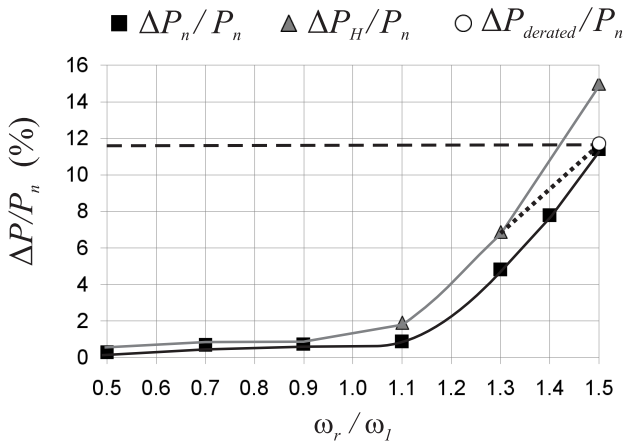

Figure 6.24 - Example 6.IV: normalized RSC and LSC power loss as function of the normalized rotor speed, compensation by means of CM is applied. Three curves are shown: $\Delta P_n/P_n$: normalized power loss at rated conditions (sinusoidal operation); $\Delta P_H/P_n$: normalized power loss when the DFIG is used as AF; $\Delta P_{derated}/P_n$: normalized power loss when derating is implemented according to Figure 6.25.

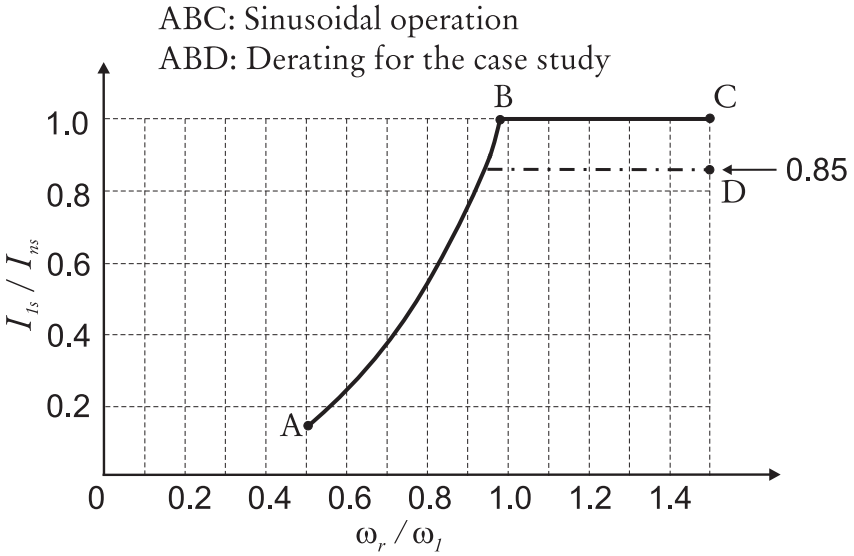

Figure 6.25 - Example 6.IV: normalized fundamental stator current trajectory, base values is the rated stator current. Compensation by means of CM is applied

.

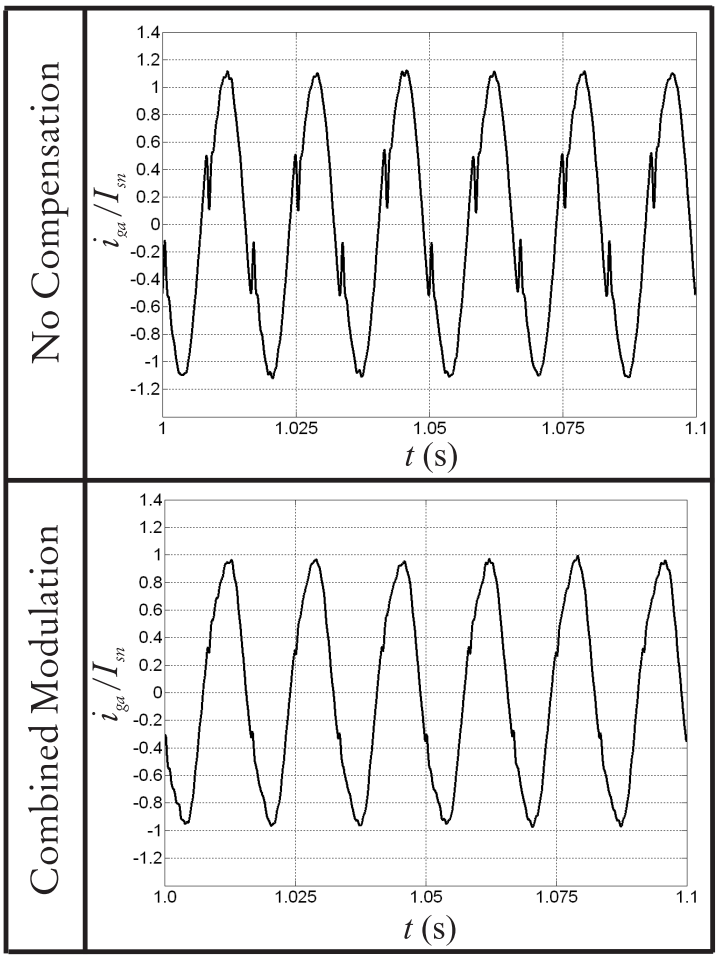

Figure 6.26 - Example 6.IV: Grid current oscillogram: (a) without harmonic compensation and (b) with harmonic compensation.

distribution of the power loss among the WECS components, compared to the other two techniques.

The analysis of simulation results allows concluding that compensation by means of Combined Modulation is the most efficient technique among the ones presented in chapters 4-6 to use a WECS as an AF. However, Example 6.III shows that depending on the load distribution, compensation by means of Combined Modulation may lead to a non uniform distribution of the harmonic current injection from the power converters.

Part III

Harmonic Compensation: Transient Operation

Introduction to Part III

Transient analysis is necessary to validate the control system design because it allows studying the following fundamental aspects of the WECS operation:

- Mechanical stress. In the DFIG, high currents caused by faults or transients may result in high magnetic forces between the windings resulting in the mechanical damage of the windings insulation. Transient analysis allows estimating such forces and therefore gives indications on the winding insulation desing.
- Thermal stress. The solid state devices are the most sensitive components of the WECS to temperature rise. The calculation of the transient peak and rms currents result in the choice of the components able to withstand the most severe conditions.
- Voltage oscillations. Voltage variations at the transmission level caused by WECS operation affects the loads connected to the same PCC and should be limited. The dielectric inside the dc-link capacitor may be damaged by the dc-link voltage increase.
- Low Voltage Ride Through (LVRT) capability (chapter 1) must be verified.

The mechanical transients have a larger time constant than the electrical transients [12, 16, 139, 140]. While the mechanical response can be ignored when voltage variations are assumed (chapter 7), an accurate model of the mechanical system is necessary to study the WECS response to wind variations (chapter 8). The mechanical model of the WECS proposed in this work includes the following components:

- Aerodynamic model, that provides the relationship between the wind speed and the mechanical power extracted by the wind turbine;
- Shaft model, that represents the coupling between the wind turbine and the electric generator;
- Pitch control model, that calculates the pitch angle β based on the wind speed and power set point.

Chapter 7

WECS Transient Response to Voltage Sags

7.1 Introduction

Voltage variations on the transmission line affect the waveform, magnitude and phase shift of the voltage supplied to both the DFIG and the LSC and alter the power flow from the WECS to the grid. The detailed response of a WECS to voltage variations highly depends on the system's topology and on its control system [141]: the WECS analyzed in the present chapter has the characteristics described in appendix A and implements compensation by means of CM (chapter 6).

The goal of the present study is the analysis of the transient response of this specific WECS to voltage sags[27]: in particular, the LVRT ability (chapter 1) of the studied system is assessed and the effects of WECS operation on other loads connected to the same PCC are quantified.

It is assumed that no other additional phenomena take place during the voltage sag and in the instants following the fault clearance: in particular, the NLL current spectrum and the wind characteristic don't change. As a result, the mechanical torque applied to the generator is constant and the shaft speed is constant too: this assumption is justified by observing that the mechanical time constants are significantly larger than any typical fault duration [12, 139, 142].

7.2 DFIG behavior during voltage sags

The DFIG behavior during voltage sags has been extensively studied in the literature [10, 39, 143, 144] and is briefly summarized in the following paragraphs.

[27] According to IEEE Standard 1159 [24], 'The term *sag* is used in the power quality community as a synonym to the IEC term *dip*. The category short duration variations is used to refer to voltage dips and short interruptions. The term *swell* is introduced as an inverse to sag (dip)'. Categories and characteristics of voltage transient phenomena in power systems according to different standards are described in [113].

In steady-state operation, the bulk of power absorbed by the wind turbine is delivered to the grid through the stator; a small fraction of the total power flows through the power converters that connect the rotor to the PCC, as illustrated in Figure 2.16. The power flow balance is maintained during transient too, but the separation of power flow between the stator and the rotor may be different from the one typical of steady-state operation.

During a voltage sag, the power delivered to the grid by the DFIG stator is reduced and the power delivered through the power converters increases thus resulting in a higher dc-link voltage and current flow through the solid state devices. Simultaneously, the stator flux decreases since the voltage amplitude at the stator terminals is reduced during the fault [88, 142]: this means that the energy stored in the magnetizing field is reduced and the release of this causes a transient reactive current flow in the stator windings.

After the fault clearance, the stator voltage rated value is restored: a second transient takes place in the WECS to reestablish the power flow distribution prior to the fault and the magnetic field in the air-gap. The stator current amplitude may exceed the rated current during this second transient due to the combination of two phenomena:

1. the DFIG absorbs reactive current needed to produce the magnetic field;
2. the phase shift between the stator fundamental voltage phasor and to the PCC fundamental voltage phasor may be different from the pre-fault condition.

The second phenomenon can be explained by means of the phasor diagrams represented in Figure 7.1. This figure displays the phasors corresponding to the fundamental voltage at the PCC and at the stator terminal prior and after the fault. Prior to the fault, a certain phase angle φ_1 is measured between the phasors $\overline{V}_{s1}$ and $\overline{V}_1$, corresponding to fundamental voltage induced in the stator windings and voltage at the PCC, respectively. During the voltage sag, the angular speed of the stator may be different from the rated value ω_1. When the fault is cleared, the phase shift φ_2 is expected to be different from φ_1. If $\varphi_2 >> \varphi_1$, the difference between the phasor voltages $\bar{V}_{s2}$ and $\bar{V}_2$ is significant, thus leading to high stator currents.

The above described phenomena prove the vulnerability of the DFIG to the voltage variations and the need to study the transient response for each new installation.

The stator and rotor windings can withstand a current higher than the rated one if the insulation temperature is not excessive [145] and heads of the windings are not damaged by the magnetic forces generated by the short-circuit currents.

The maximum admissible surge currents that can be withstood by the RSC and LSC solid state devices are defined in the components' datasheet and they are generally limited

by the maximum allowable junction temperature. During and after the fault, the current flow increase in the power converters may be significant thus causing a permanent damage of the solid state devices [34]. In case of threatening transient currents, protection devices are necessary to limit the current flow through the solid state devices One of the most popular, although controversial, devices intended to limit the current flow is the crowbar [43, 146]: details on the crowbar operation are given in appendix 7.A.

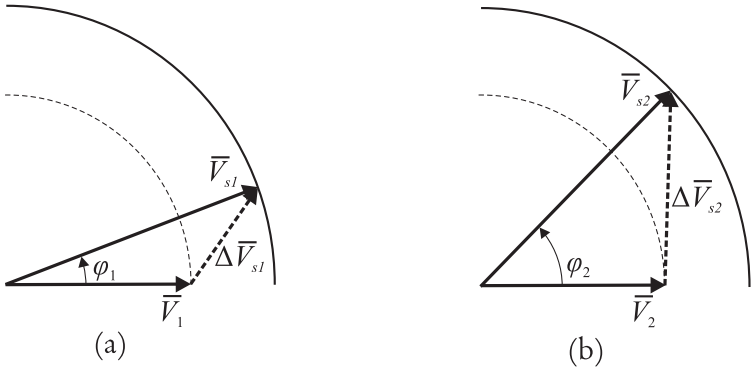

Figure 7.1 - Phasors diagrams representing the voltage at the PCC and the voltage induced in the stator's windings: (a) phasor diagram before the sag takes place and (b) phasor diagram after the fault is cleared. The stator current is proportional to the voltage difference $\Delta\overline{V}_s$. This diagram shows that before and after the fault the fundamental voltage phasor amplitudes are unaltered, but due to different phase shifts ($\varphi_1 \neq \varphi_2$), the amplitude of $\Delta\overline{V}_s$ may increase after the fault clearance, thus causing high stator currents.

7.3 Organization of the study

The study of the WECS dynamical response to voltage variation at the PCC is organized as follows:

- The voltage sags are classified using three parameters that describe the voltage amplitude and phase shift at the PCC.
- The operating conditions of the WECS prior to the voltage sag are established, based on the wind speed and on the NLL characteristics.
- Simulations are carried out: the voltage sags are defined based on the LVRT requirements for wind power plants.

- The oscillograms corresponding to the most significant electrical quantities are displayed for different types of fault.
- Contour plots are presented, thus giving a complete picture of the WECS transient response to voltage variations.
- Based on simulation results and power loss calculations, LVRT ability for the studied installation is carried out and the effect of harmonic compensation on the WECS performance following a voltage disturbance is assessed.

7.4 Voltage sag classification

The voltage sag classification used in the present chapter is based on the study reported in [147]. Three characteristics define the severity of a voltage sag:

1. Sag amplitude
2. Phase shift
3. Sag duration

The above characteristics are defined as follows:

1. **Sag amplitude** α,β

   As illustrated in Figure 7.2, the amplitude of the voltage sag is defined by the scale parameters α and β. Those parameters affect the magnitude of the phasors $\overline{V}_a$, $\overline{V}_b$ and $\overline{V}_c$, corresponding to the phase voltages at the high-voltage of the step up transformer[28]. The values of the scale parameters for different types of faults are listed in Table 7.1. For three-phase symmetrical faults $\alpha = \beta$; for single-phase sags, $0 \leq \alpha \leq 1$ and β=1 because only the magnitude of phase a voltage changes. For phase-to-phase sags the reverse conditions apply: $0 \leq \beta \leq 1$ and α=1 because the magnitude of phases b and c voltage changes with the same ratio. The asymmetrical fault is described by the simultaneous variation of α and β.

2. **Phase angle** ε

   The phase angle is described by the parameter ε, depicted in Figure 7.2. The value of ε during the fault is determined by three-phase transformers installed between the point where the fault takes place and the load. Different primary and secondary

[28]This is the point where the voltage dip is measured according to [73]

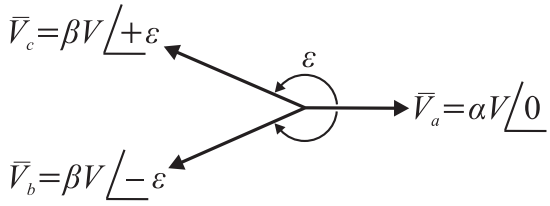

Figure 7.2 - Voltage phasor diagram used to describe seven fault types listed in [147]. α and β are the scale parameters, ε is the phase angle.

connections of the transformer windings and different typed of fault result in positive or negative phase shifts with respect to the rated value $\varepsilon = 120$ deg. In practice, only a few degrees variation around the rated value is observed [147].

3. **Sag duration Δt**

   The fault duration is chosen according to the LVRT requirements (chapter 1) defined by in the WECC white paper [148], illustrated in Figure 7.3. The LVRT requirement is a function of the voltage sag amplitude: the less severe the sag amplitude, the longer the DFIG is required to remain connected. The LVRT requirements apply to any kind of voltage sag (three-phase, phase-to-phase or phase-to-ground).

7.5 WECS operation at the moment of fault

Each simulation is characterized by the voltage parameters α,β and by the angle ε described in the previous section and by two additional quantities that define WECS operation at the moment of fault:

1. **Rotor speed ω_r/ω_1**

   The rotor speed is a function of the wind speed, according to the wind turbine tracking characteristic (Figure A.1). The rotor speed is related to the torque applied to the

Table 7.1 - Fault characteristics for the phasor diagram shown in Figure 7.2.

Type	α	β	ε
Three-phase	0 to 1	α	120 deg
Single-phase	0 to 1	1	120 deg
Phase-to-phase	1	0 to 1	0 to 180 deg

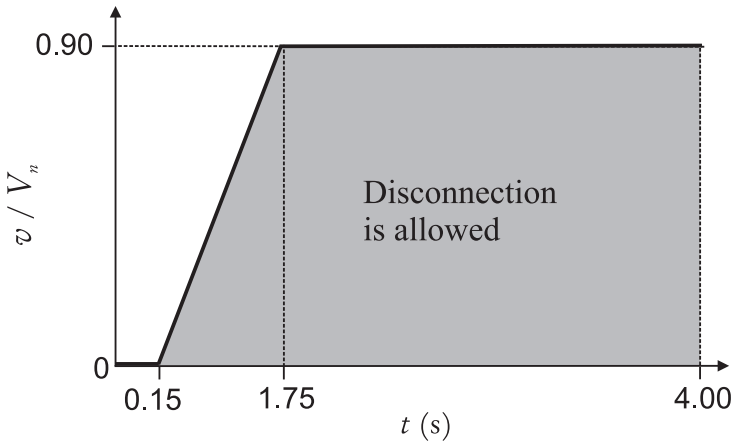

Figure 7.3 - LVRT requirement according to WECC white paper [148]. The normalized voltage amplitude at the high side of the step-up transformer is plotted in function of time, and the region where the WECS is allowed to disconnect is indicated by the gray area. For voltage variations above the black trajectory, the WECS must stay connected to the grid.

DFIG shaft: in general, at lower rotor speed the torque is significantly lower than the rated value. On the contrary, maximum rotor speed corresponds to the rated mechanical torque. The value of the torque impressed at the DFIG shaft when the voltage sag take place determines the power flow through the WECS components and therefore the current amplitudes during the transients that follow the fault.

2. **Derating $\mathscr{D}$**

   As described in chapter 3, the derating trajectory depends on both the NLL current spectrum and the control method. In the following sections, the NLL is given by three single-phase diode rectifiers connected phase-to-neutral (Figure 6.22). Compensation by means of CM is implemented; therefore, the derating trajectory assumed in the following sections is the one illustrated in Figure 6.25.

7.6 Simulation results - Oscillograms

In the following sections, oscillograms obtained from the simulations[29] of phase-to-phase and three-phase voltage sags are displayed. The most representative variables of the system's behavior have been selected:

- Stator current

[29]The simulation software and parameters are the same used in chapters 4 - 6.

- Voltage measured at the PCC
- LSC current
- dc-link voltage

The instant of fault is $t_f = 2$s for all simulations, while the fault duration Δt varies from 140 ms to 1000 ms.

7.6.1 Phase-to-phase voltage sag, Δt=140 ms

The phase-to-phase voltage sag is characterized by the parameters listed in Table 7.2.

Table 7.2 - Phase-to-phase voltage sag characteristics.

Item	Value	Unit
α	1	N.A.
β	0	N.A.
ε	120	deg
Δt	140	ms
ω_r/ω_1	1.5	p.u.
$\mathscr{D}$	0.85	p.u.

Grid voltage at the PCC

The normalized PCC phase-to-ground voltage amplitudes for phases a, b and c are shown in Figures 7.4-7.6. The oscillograms for the three phase voltages at the PCC must be verified because, due to the phase shift between the three phases, the peak voltages may be different from phase to phase.

The voltage sag takes place during the interval $2 \leq t \leq 2.14$ s and involves phases b and c. Phase a voltage slightly increase during the fault: this behavior is due to the decay of the magnetizing stator flux.

After the fault clearance, both phase a and b voltage amplitude is restored without any overshoot. On the contrary, a visible surge (1.4 p.u.) appears on phases c voltage. This peak is due to the phase shift between the voltage at the PCC and the voltage at the stator terminals at the moment of voltage sag clearance, and may affect the operation of other loads connected at the same PCC.

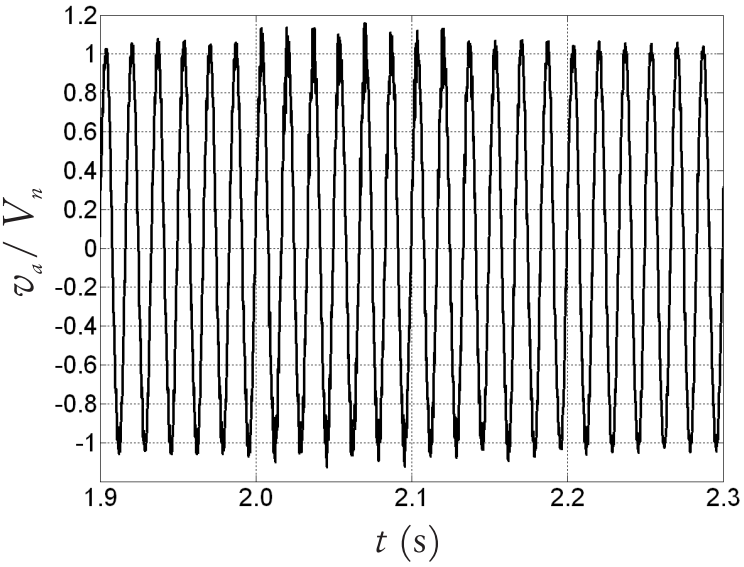

Figure 7.4 - Phase-to-phase fault: normalized phase a PCC voltage oscillogram, base value is DFIG rated voltage, $\Delta t = 140$ ms.

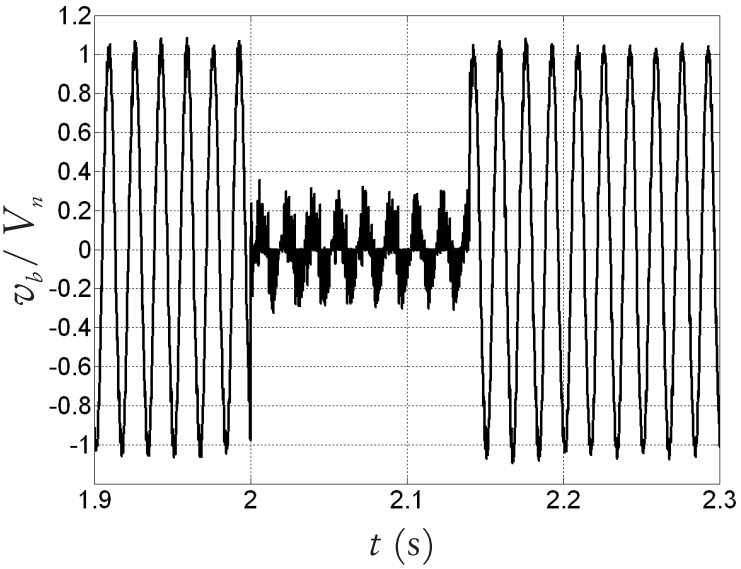

Figure 7.5 - Phase-to-phase fault: normalized phase b PCC voltage oscillogram, base value is DFIG rated voltage, $\Delta t = 140$ ms.

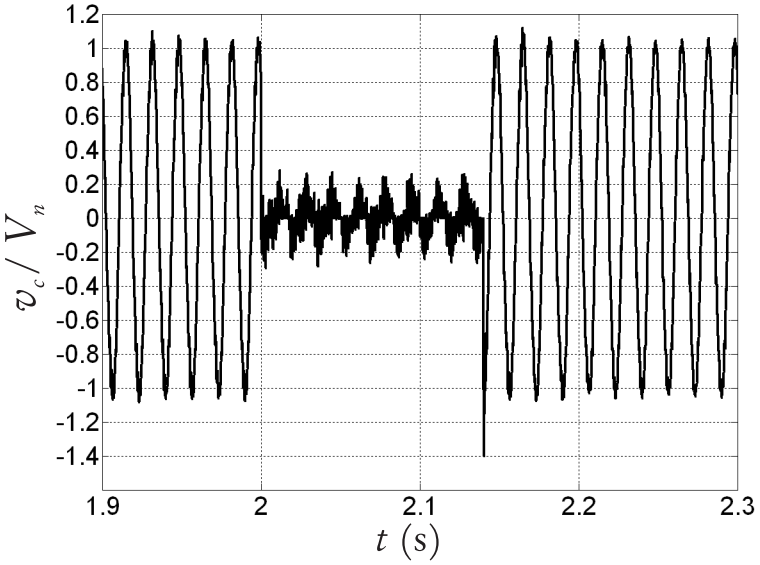

Figure 7.6 - Phase-to-phase fault: normalized phase c PCC voltage oscillogram, base value is DFIG rated voltage, $\Delta t = 140$ ms.

Stator current

The normalized stator current phase oscillograms are shown in Figures 7.7 - 7.9 for phase a,b and c respectively. While the stator phase b current is higher than the rated value during the fault (Figure 7.8), phases a and c currents are lower (Figure 7.7 and 7.9)).

After the fault clearance ($t > 2.14$ s), the sudden magnetization of the machine results in currents amplitude above the rated values for all three phases.

Both during the fault and after the fault clearance, the peak stator currents are only a few p.u. higher than the rated values and the overvoltages die out in a few periods: this behavior does not results in a tripping of the CBs installed for the protection of the stator windings. The verification of the winding temperature rise during the fault proves that the temperature rise in the windings is only a few degrees °Cand do not compromise the physical properties of the winding insulation. The procedure applied to verify the temperature rise is described in appendix 7.B.1.

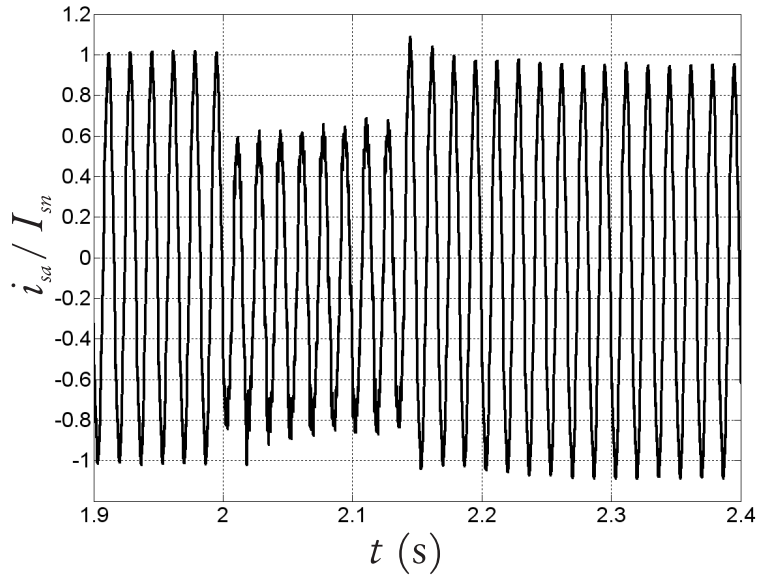

Figure 7.7 - Phase-to-phase fault: normalized phase a stator current oscillogram, base value is DFIG rated stator current, $\Delta t = 140$ ms.

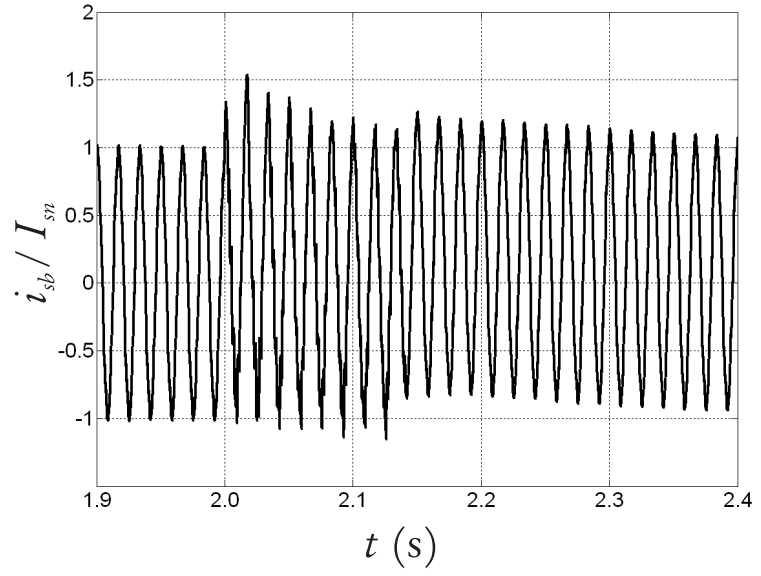

Figure 7.8 - Phase-to-phase fault: normalized phase b stator current oscillogram, base value is DFIG rated stator current, $\Delta t = 140$ ms.

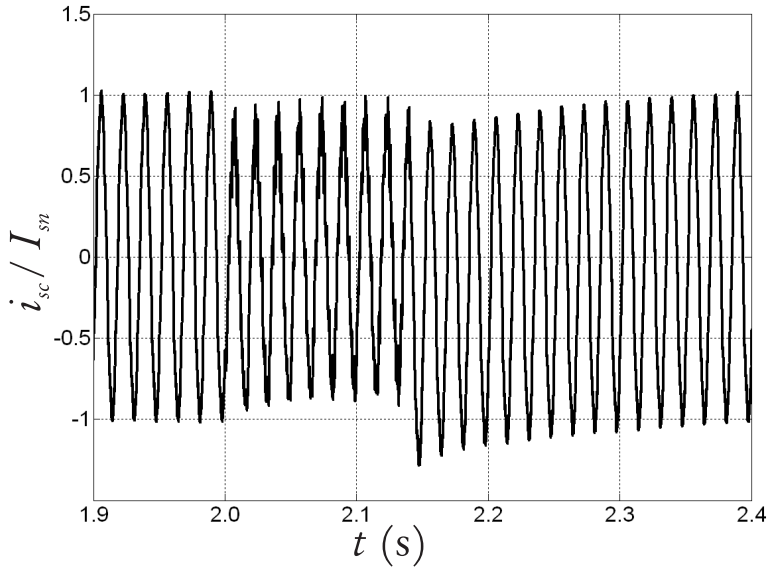

Figure 7.9 - Phase-to-phase fault: normalized phase c stator current oscillogram, base value is DFIG rated stator current, $\Delta t = 140$ ms.

LSC current and dc-link voltage

The normalized LSC current oscillograms are shown in Figures 7.10-7.12 for phase a,b and c respectively; the dc-link normalized voltage oscillogram is displayed in Figure 7.13. The three current plots are very similar, due to the symmetry of the system.

During the fault, the power flow through the rotor and the power converter increases but, due to the intrinsic voltage limitations in the power converter three-phase voltages[30] and to the low value of the voltage at the PCC, the power deliver to the grid through the power converters is limited. This results in increasing LSC currents and dc-link voltage for $2 \leq t \leq 2.14$ s.

After the fault clearance, the power flow through the power converters is reduced and the dc-link controller brings the dc-link voltage amplitude to the rated value. The transients following the fault clearance result in voltage oscillations around the rated value. The oscillations are caused by the fact that the dc-link controller (chapter 4) is not intended to be fast, but to maintain the stability of the dc-link voltage magnitude. The LSC current amplitudes decrease to the value prior to the fault in a few periods. This is because the

[30]Appendix H provides the details of the RSC and LSC control through PWM and it shows that the three-phase voltage at the power converters' terminal is limited by the intrinsic characteristics of the control by means of PWM. More in detail, the amplitude modulation coefficient m_a, that is proportional to the three-phase voltage amplitude, is limited to a fixed value, as illustrated in Figure H.3.

current controller is faster than the dc-link controller (the PI controllers parameters are listed in appendix A).

For the studied fault, the peak current amplitude is 1.5 times the rated LSC current. In order to verify the temperature increase in the power converters, both the peak value and the rms value of the LSC current must be considered. The temperature rise is verified according to the procedure described in appendix 7.B.2. For the assumed fault, the temperature increase in the solid state devices is below 140 °C, for an ambient temperature of 40 °C.

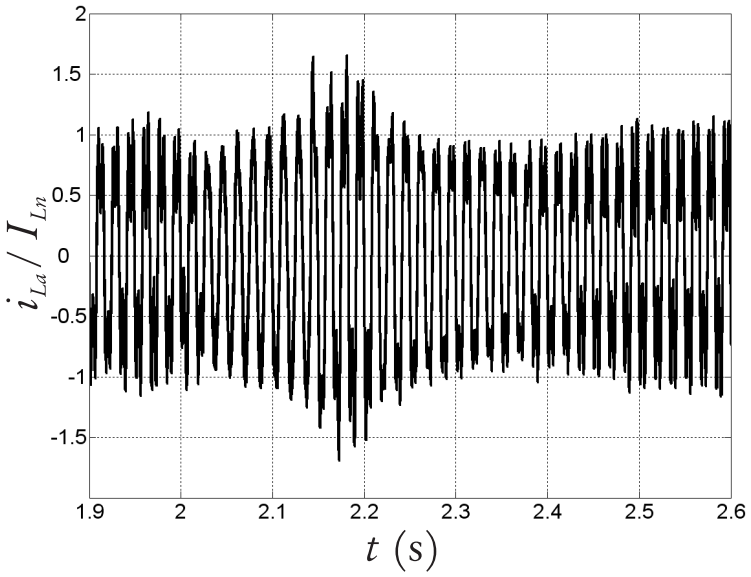

Figure 7.10 - Phase-to-phase fault: normalized phase a LSC current oscillogram, base value is LSC rated current, $\Delta t = 140$ ms.

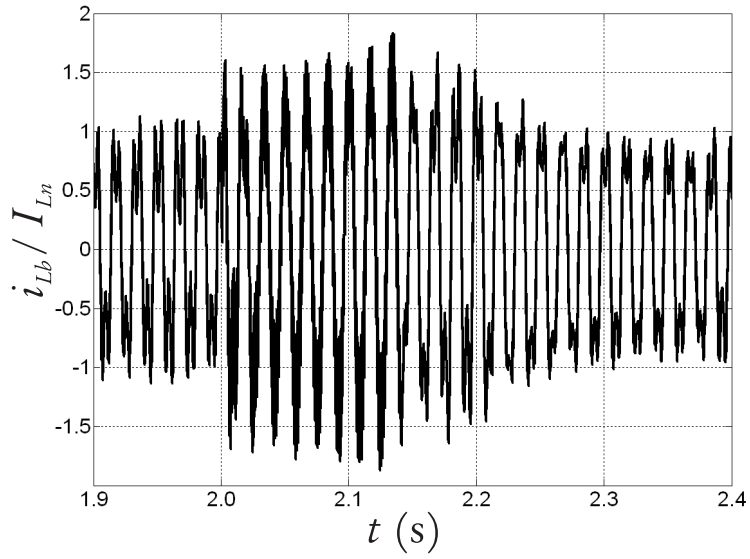

Figure 7.11 - Phase-to-phase fault: normalized phase b LSC current oscillogram, base value is LSC rated current, $\Delta t = 140$ ms.

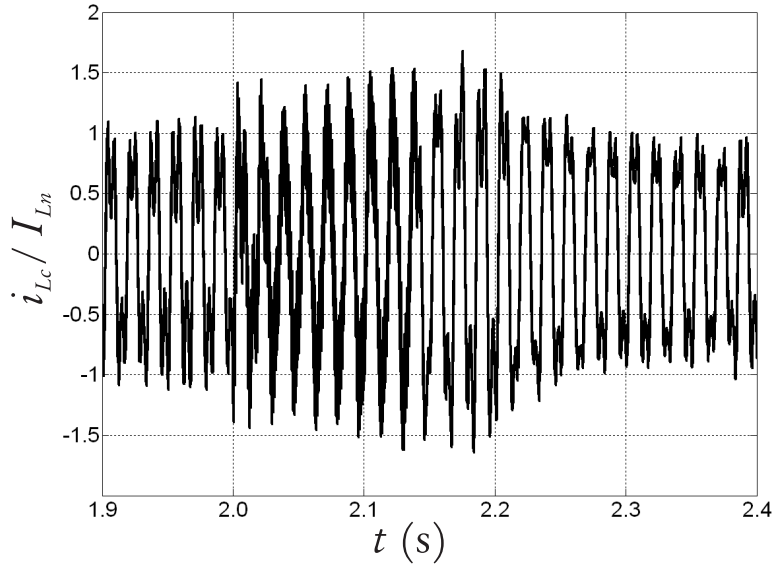

Figure 7.12 - Phase-to-phase fault: normalized phase c LSC current oscillogram, base value is LSC rated current, $\Delta t = 140$ ms.

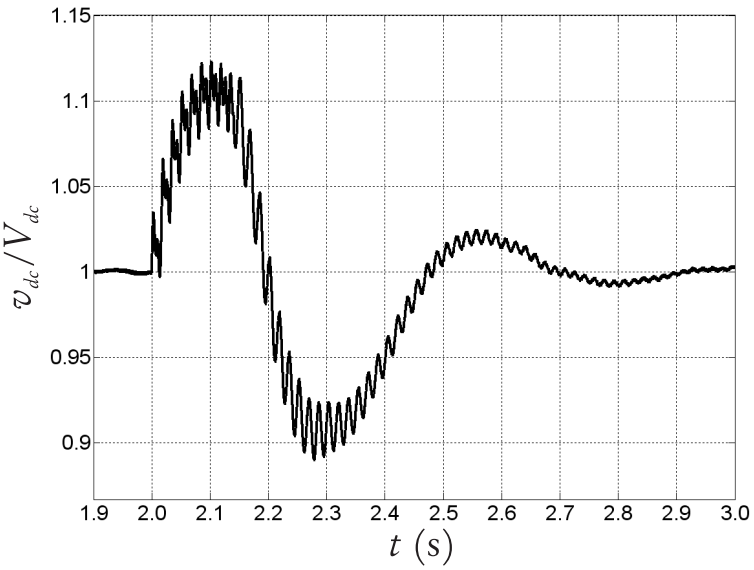

Figure 7.13 - Phase-to-phase fault: normalized dc-link voltage oscillogram, base value is dc-link rated voltage, $\Delta t = 140$ ms.

7.6.2 Symmetrical fault Δt=140 ms

Symmetrical faults are less frequent than single-phase or phase-to-phase faults, but they results in the most severe transients. The characteristics of the symmetrical fault studied in this section are listed in Table 7.3.

Table 7.3 - First symmetrical voltage sag - characteristics.

Item	Value	Unit
α	0	N.A.
β	0	N.A.
ε	120	deg
Δt	140	ms
ω_r/ω_1	1.5	p.u.
$\mathscr{D}$	0.85	p.u.

PCC voltage amplitude for $\Delta t = 140$ ms

The normalized PCC phase-to-ground voltage amplitudes for phases a, b and c are shown in Figures 7.14-7.16. The measured peak voltage is the same as the one obtained from the previous simulation (1.4 p.u.) and it is detected on phase c after the voltage restoration. The same value is obtained because the same reclosing time is assumed.

This result allows one to conclude that in case of small residual voltage amplitude during the fault, the effect of phase shift on the magnitude of voltage peak is more evident than the effect due to the variation of the magnetic field magnitude.

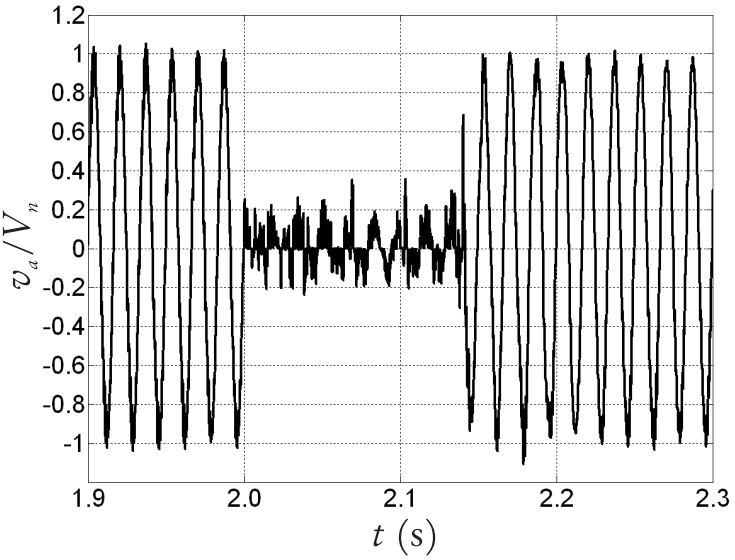

Figure 7.14 - Symmetrical fault: normalized phase a PCC voltage oscillogram, base value is DFIG rated voltage, $\Delta t = 140$ ms.

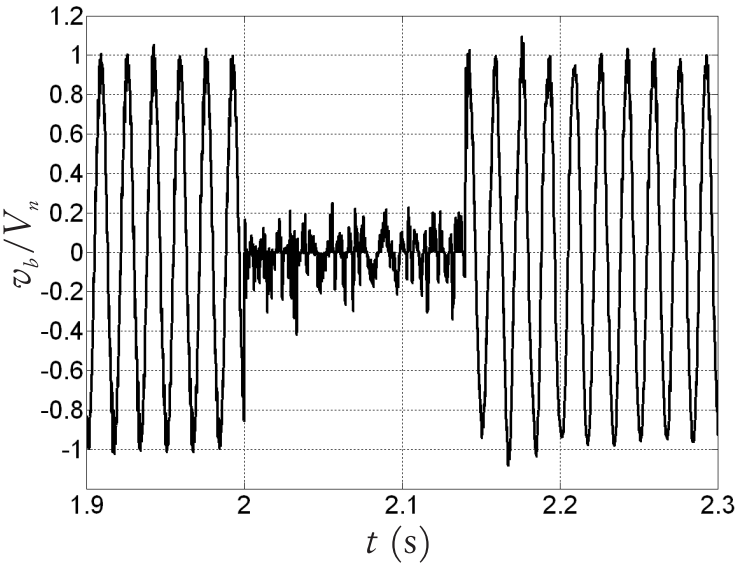

Figure 7.15 - Symmetrical fault: normalized phase b PCC voltage oscillogram, base value is DFIG rated voltage, $\Delta t = 140$ ms.

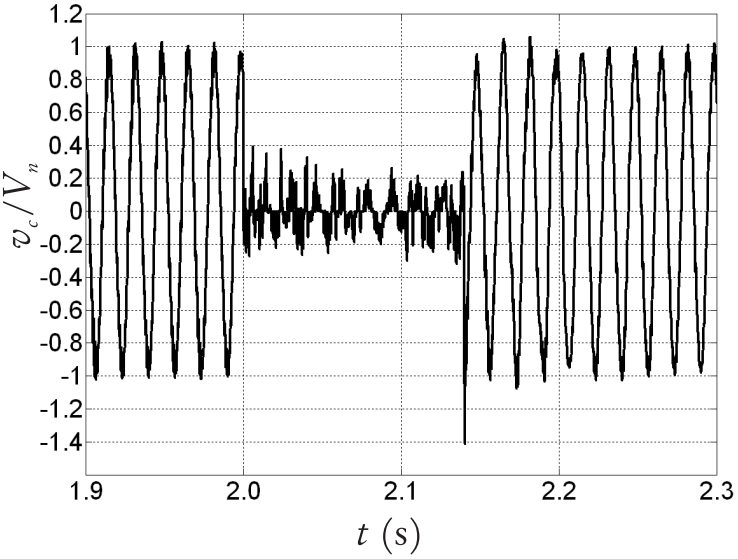

Figure 7.16 - Symmetrical fault: normalized phase c PCC voltage oscillogram, base value is DFIG rated voltage, $\Delta t = 140$ ms.

Stator current for $\Delta t = 140$ ms

The normalized stator current oscillograms for phases a, b and c are shown in Figures 7.17-7.19: a first transient takes place during the voltage sag ($2.00 < t < 2.14$ s) and a more severe transient starts immediately after the fault clearing ($t > 2.14$ s). For all three phases, the first transient results in a current peak amplitude equal to approximately 1.5 p.u., and the second transient results in a peak equal to approximately 2.5 p.u.

Both peak values listed above are below five times the rated stator current and lasts about two cycles: therefore the CBs installed to protect the DFIG do not trip. The thermal analysis (appendix 7.B.1) proves that the temperature rise in the machine's windings is only a few degrees °C, and does not affect the mechanical and dielectric properties of the winding's insulation.

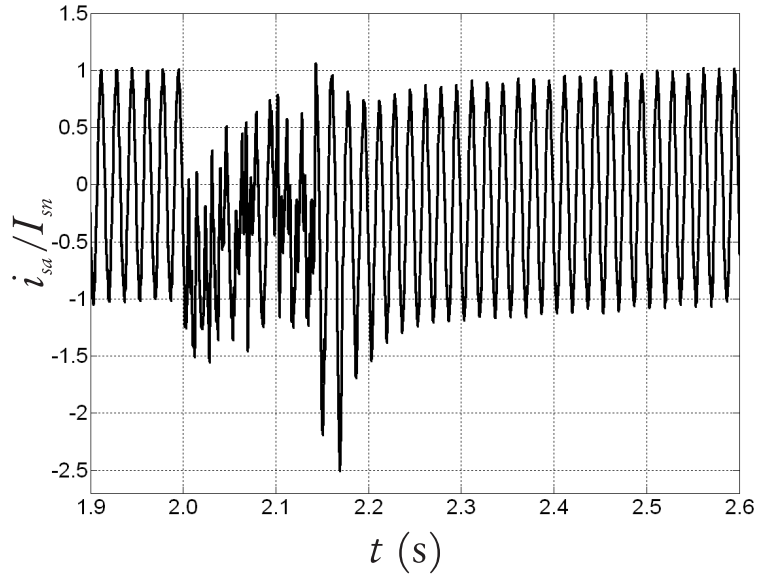

Figure 7.17 - Symmetrical fault: normalized phase a stator current oscillogram, base value is DFIG rated stator current, $\Delta t = 140$ ms.

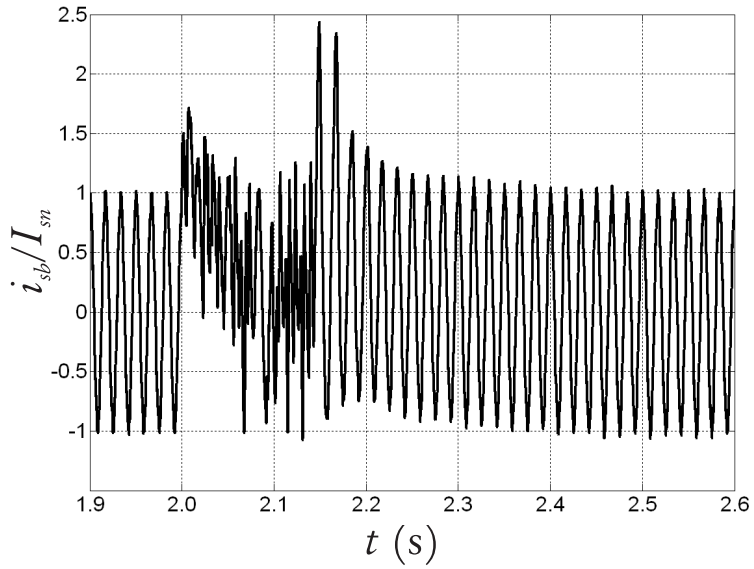

Figure 7.18 - Symmetrical fault: normalized phase b stator current oscillogram, base value is DFIG rated stator current, $\Delta t = 140$ ms.

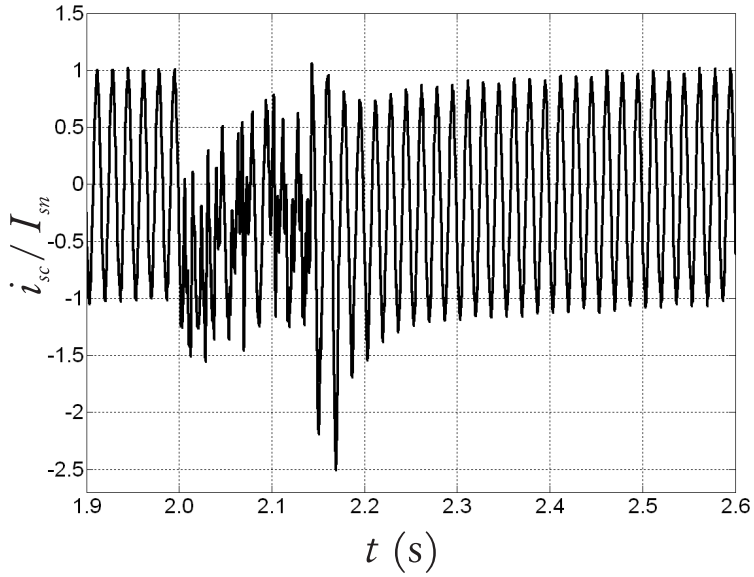

Figure 7.19 - Symmetrical fault: normalized phase c stator current oscillogram, base value is DFIG rated stator current, $\Delta t = 140$ ms.

LSC current and dc-link voltage for $\Delta t = 140$ ms

The normalized LSC current oscillogram are illustrated in Figures 7.20-7.22. The normalized dc-link voltage oscillogram is plotted in Figure 7.23.

In case of a three-phase fault, the peak values of the LSC currents and of the dc-link voltages are higher than for the phase-to-phase fault because the symmetrical fault causes higher power flow through the power converters.

The dc-link voltage oscillogram after the fault clearance is significantly different than the one displayed in the previous sections. Figure 7.23 shows that the dc-link voltage oscillates around 0.9 p.u. for $2.2 \lessapprox t \gtrapprox 2.9$ ms, and then rises to the rated value that is reached at $t=$ 3.4 s. This behavior is explained as follows: the generator absorbs reactive power from the grid for its magnetization after the fault, and this process slows the recovery of the dc-link voltage [142].

The current amplitude pattern results in higher power loss in the solid state devices and consequent temperature rise. The thermal analysis for the solid state devices is presented in appendix 7.B.2: during symmetrical faults the temperature rise in the solid state devices can be significant; however, if the fault duration is limited to a few hundreds milliseconds, the maximum temperature remains below the limit value of 140 °C.

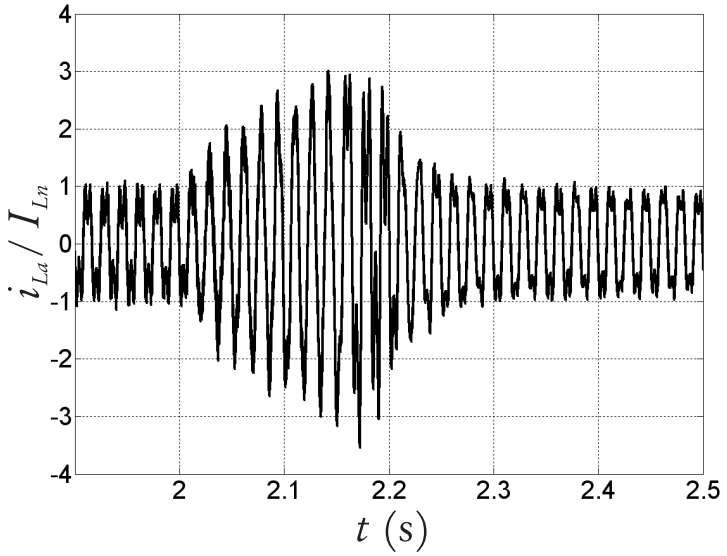

Figure 7.20 - Symmetrical fault: normalized phase a PCC voltage oscillogram, base value is DFIG rated voltage, $\Delta t = 140$ ms.

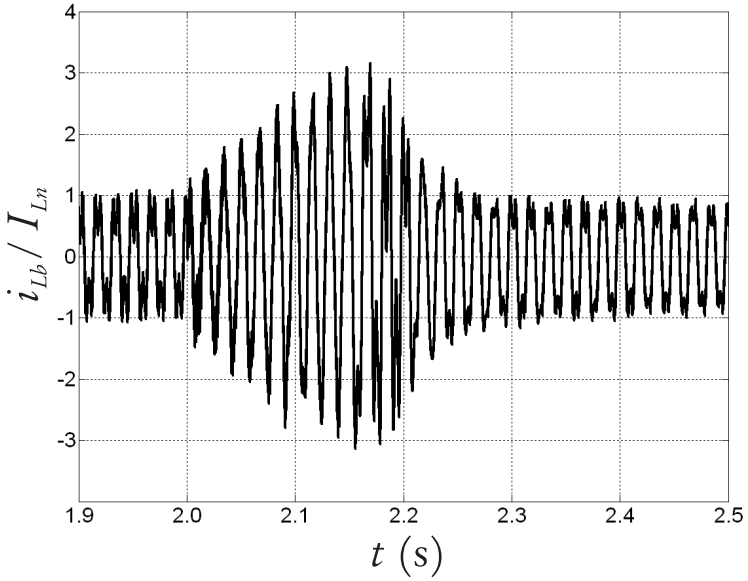

Figure 7.21 - Symmetrical fault: normalized phase b LSC current oscillogram, base value is LSC rated current, $\Delta t = 140$ ms.

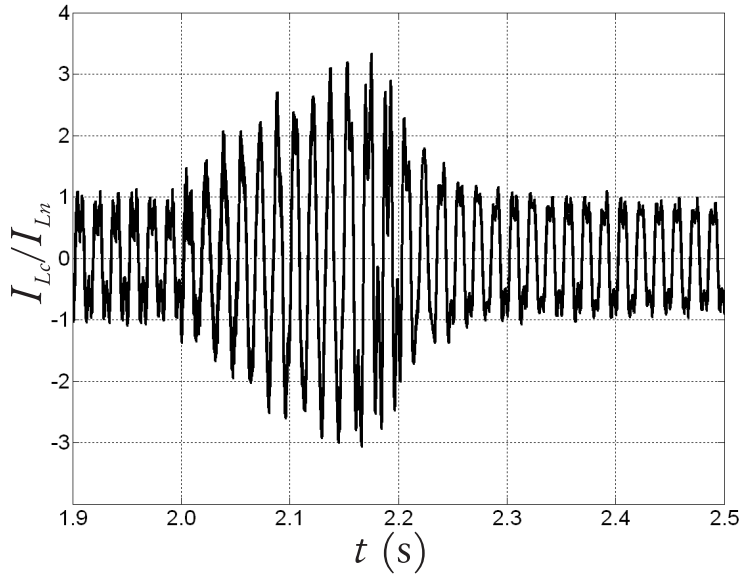

Figure 7.22 - Symmetrical fault: normalized phase c LSC current oscillogram, base value is LSC rated current, $\Delta t = 140$ ms.

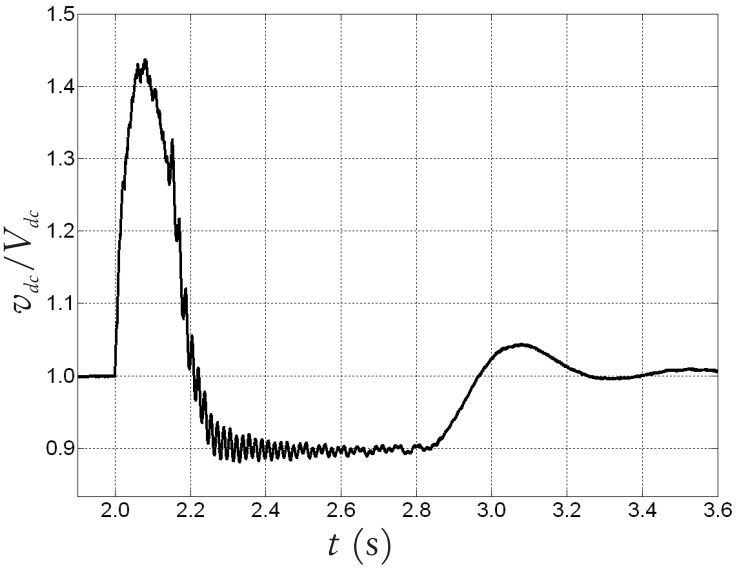

Figure 7.23 - Symmetrical fault: normalized dc-link voltage oscillogram, base value is dc-link rated voltage, $\Delta t = 140$ ms.

7.6.3 Symmetrical fault Δt=140 ms, sinusoidal operation

In the present section, the WECS is not injecting harmonic currents: this case is analyzed to compare the results with the ones presented in the previous section and to see the effects of harmonic compensation on the currents and voltage peak values. The simulation characteristics are listed in Table 7.4: the only difference with respect to Table 7.3 is derating equal to unity.

Table 7.4 - First symmetrical voltage sag, harmonic compensation not implemented - characteristics.

Item	Value	Unit
α	0	N.A.
β	0	N.A.
ε	120	deg
Δt	140	ms
ω_r/ω_1	1.5	p.u.
$\mathscr{D}$	1	p.u.

Phase c voltage oscillogram at the PCC is displayed in Figure 7.24. The peak voltage magnitude is approximately 1.1 p.u. and occurs after the fault clearance. This value is lower than 1.4 p.u., obtained from the simulations when compensation by means of CM is implemented (Figure 7.16). This result can be justified as follows: harmonic currents injection from the stator windings result in harmonic voltage drop on the stator, that leads to higher peak voltage at the PCC than for sinusoidal operation.

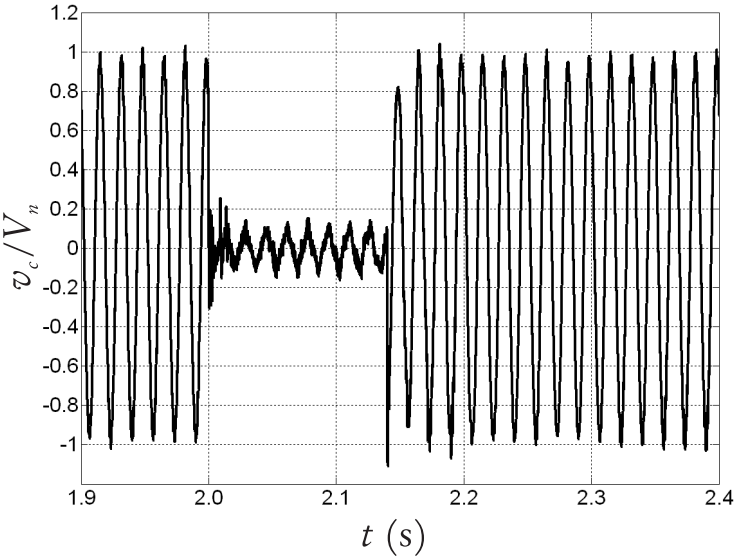

Figure 7.24 - Symmetrical fault: normalized phase a PCC voltage oscillogram, base value is DFIG rated voltage, $\Delta t = 140$ ms, harmonic compensation is not implemented.

The normalized stator current oscillogram for phase a is presented in Figure 7.25. The peak stator current is about 3 p.u., higher than the value detected in Figure 7.17. When harmonic currents are injected from the stator windings and consequent derating of the DFIG is applied, a lower fundamental current amplitude flows in the machine's windings both in steady-state operation and during the transients. As a consequence, DFIG derating results in a less severe transient for the stator currents with respect to the case when the machine is operating at full power.

The normalized LSC current oscillogram for phase a is presented in Figure 7.25. The peak LSC current is about 3 p.u. as in Figure 7.20. This means that the use of the WECS as a harmonic compensator does not modify the current flow in the power converters during the transients following a voltage sag. This conclusion, however, depends on the type of modulation that is implemented: for the current simulations, compensation by means of

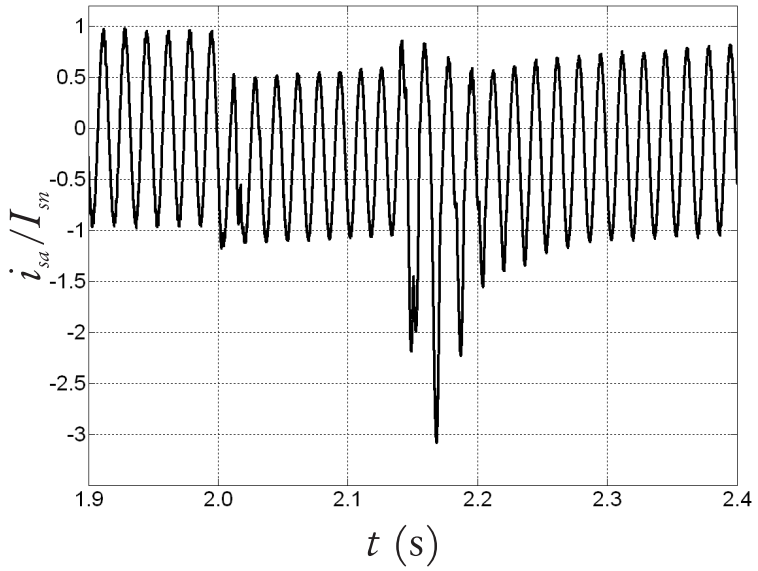

Figure 7.25 - Symmetrical fault: normalized phase a stator current oscillogram, base value is DFIG rated stator current, $\Delta t = 140$ ms, harmonic compensation is not implemented.

CM has been assumed, thus resulting in the injection of the third harmonics only from the power converters (chapter 6). If compensation by means of LSC modulation (chapter 5) is applied, a higher number of harmonic currents is injected by the power converters and it is expected that the harmonic current flow will have a more significant on the LSC current oscillograms.

The normalized dc-link voltage oscillogram is presented in Figure 7.27. The peak voltage is above 1.5. p.u., higher than the value detected in Figure 7.20. The power flowing in the power converters is higher for sinusoidal operation, since derating is equal to unity and the rated power is flowing in the DFIG at the moment of fault.

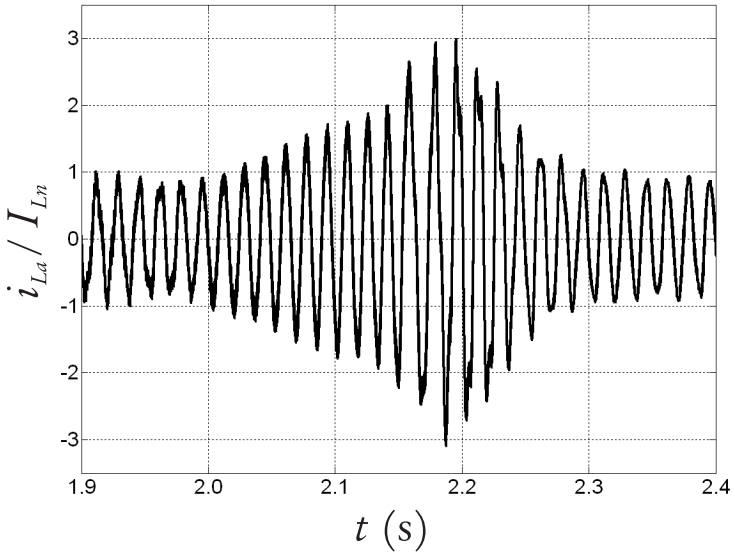

Figure 7.26 - Symmetrical fault: normalized phase a LSC current oscillogram, base value is LSC rated current, $\Delta t = 140$ ms, harmonic compensation is not implemented.

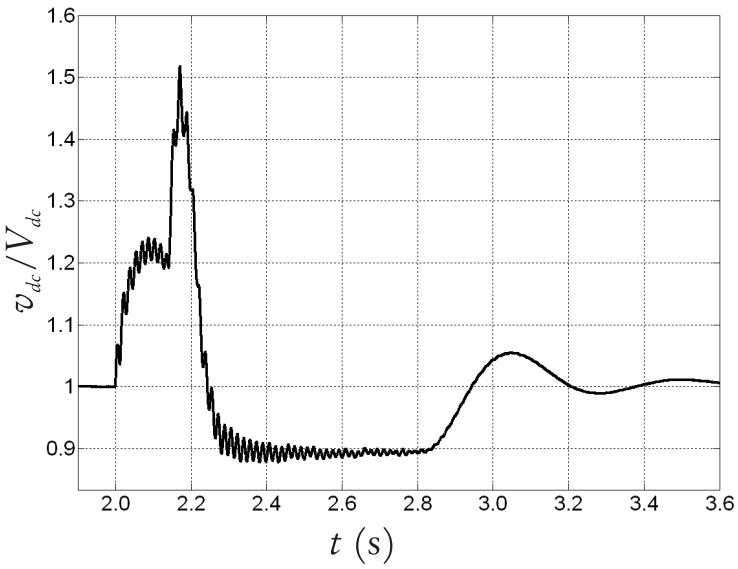

Figure 7.27 - Symmetrical fault: normalized dc-link voltage oscillogram, base value is dc-link rated voltage, $\Delta t = 140$ ms, harmonic compensation is not implemented.

7.6.4 Symmetrical fault Δt=200 ms

The characteristics of the second symmetrical fault are listed in Table 7.5: the only difference with respect to the case described in Table 7.3 is the fault duration increased to 200 ms. Harmonic compensation by means of CM is applied, thus resulting in derating the system to 0.85 p.u.

Table 7.5 - Second symmetrical voltage sag - characteristics.

Item	Value	Unit
α	0	N.A.
β	0	N.A.
ε	120	deg
Δt	200	ms
ω_r/ω_1	1.5	p.u.
$\mathscr{D}$	0.85	p.u.

The only electrical quantity that is significantly affected by Δt increase is the LSC current. The LSC current oscillogram for the second symmetrical fault is shown in Figure 7.28: the measured peak current amplitude is higher and last longer than in the previous case. However, according to the thermal analysis conducted in appendix 7.B.2 the maximum temperature is still below the limit of 140 °C.

7.6.5 Symmetrical fault Δt=1000 ms

The characteristics of the third symmetrical fault are listed in Table 7.6: the fault duration is further increased to 1000 ms.

Figure 7.29 shows that for $\Delta t > 800$ ms the LVRT ability is lost: the dc-link voltage does not recover and goes to zero. This result arises from the fact that the DFIG is completely demagnetized and the WECS is disconnected from the grid. This situation is unlikely to happen in the practice, but is presented to show the system response in extreme situations.

The LSC current oscillogram is displayed in Figure 7.30: the current amplitude assumes high values during the transient following the fault, and eventually drops to zero due to the WECS disconnection from the grid. Thermal analysis shows that the current transient results in unacceptable junction temperature, and protections must be installed to disconnect the power converters when such conditions are met.

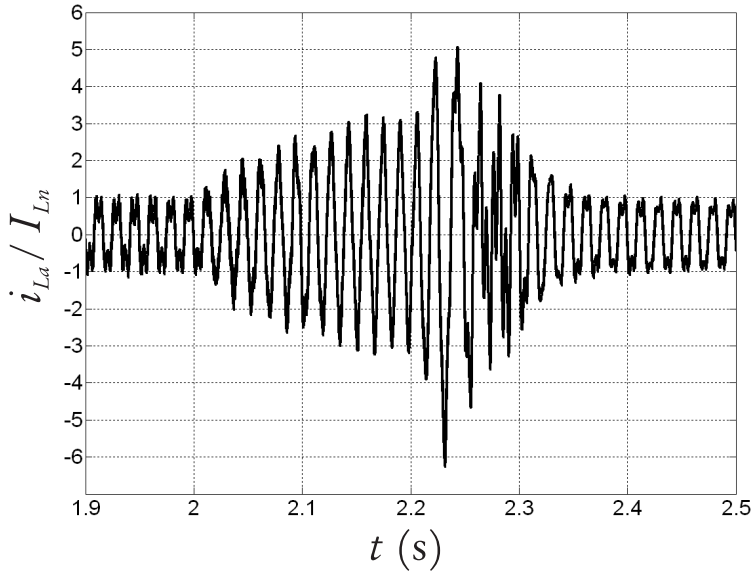

Figure 7.28 - Symmetrical fault: normalized LSC current oscillogram, base value is LSC rated current, $\Delta t = 200$ ms.

Table 7.6 - Third Symmetrical voltage var - characteristics.

Item	Value	Unit
α	0	N.A.
β	0	N.A.
ε	120	deg
Δt	1000	ms
ω_r/ω_1	1.5	p.u.
$\mathscr{D}$	0.85	p.u.

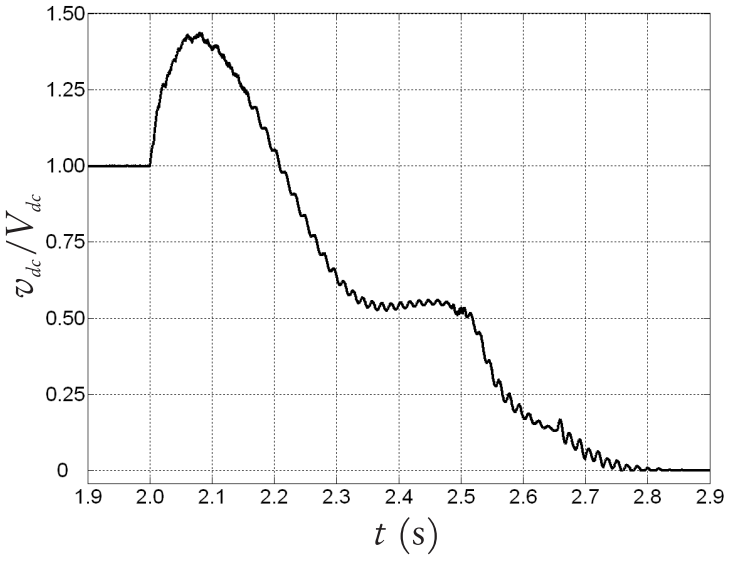

Figure 7.29 - Symmetrical fault: normalized dc-link voltage oscillogram, base value is dc-link rated voltage, $\Delta t = 1000$ ms.

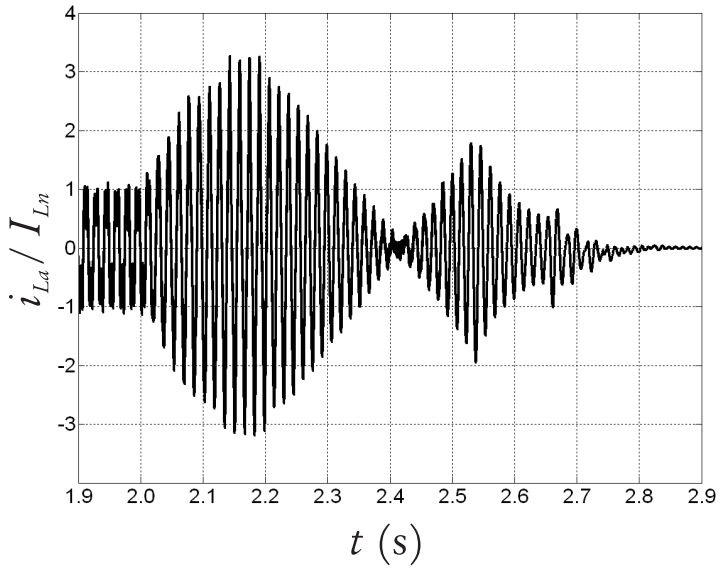

Figure 7.30 - Symmetrical fault: normalized LSC current oscillogram, base value is LSC rated current, $\Delta t = 1000$ ms.

The stator current oscillogram is shown in Figure 7.31. The stator current drops to zero at 2.9 s, due to the disconnection of the DFIG from the grid.

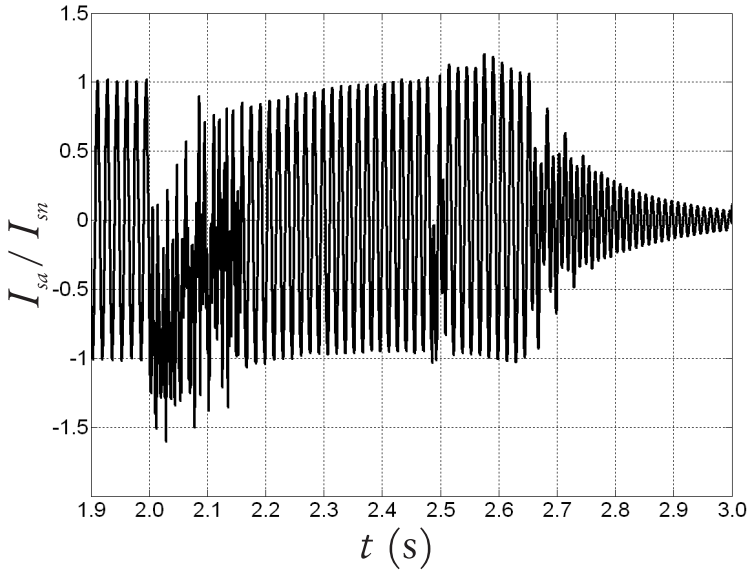

Figure 7.31 - Symmetrical fault: normalized stator current oscillogram, base value is DFIG rated stator current, $\Delta t = 1000$ ms.

7.7 Conclusions based on the oscillograms

The oscillograms presented in the previous sections allow one to conclude that LVRT capability is verified for faults that fall outside the gray area of the diagram shown in Figure 7.3. When the fault conditions fall within the gray area, the LVRT ability is not guaranteed any more.

The comparison between the case when harmonic compensation is implemented by the WECS and the case when harmonic compensation is not implemented shows that harmonic compensation has a positive effect on LVRT capability: derating allows the reduction of fundamental power flow within the WECS and therefore results in less severe transients following a voltage sag.

A more accurate analysis, carried out in the next sections, provide a clearer distinction between the fault conditions when the LVRT ability is verified and the ones when the safe operation and the integrity of the WECS components cannot be guaranteed.

7.8 Simulation results - Countour plots

In the following sections, the system response to voltage sags is investigated in detail and the results are presented as contour plots.

Countour plots allow to represent a three-dimensional surface z on a xy plane: the points that correspond to the same height are connected by means of countour lines. The area between two contour lines is colored according to the magnitude assumed by the surface z.

The following electrical quantities are represented as contour plots for each type of fault that is investigated:

1. peak voltage at the PCC

   The peak voltage at the PCC may have negative effect on other loads connected in proximity of the WECS: this is due to the fact that the loads are intended to operate at rated voltage and the presence of voltage dips or spikes may results in their malfunctioning or damage.

2. peak stator current

   From the oscillograms illustrated in the previous sections, results that the critical time of the transient occurs after the fault clearance, when the current reaches its peak value. The steady state value is restored within three or four cycles. The peak current has two consequences:

(a) Excessive magnetic forces that can mechanically damage or distort the conductors at the heads of the windings

(b) Increased conductor temperature.

The DFIG designer has the responsibility to address the mechanical integrity of the machine when stressed by the magnetic forces. Conservative computations of the temperature rise are based on the peak stator current appendix 7.B.1.

3. peak LSC current

   The thermal analysis carried out in appendix 7.B.2 allows determining the hot spot temperature of the solid state devices installed within the LSC and the RSC. The conclusion from it analysis is that for rms currents equal or below to 2 p.u., the junction limit temperature of 140^o is not reached, while for currents values above 2 p.u. such temperature is reached in a few milliseconds.

   In the level curves presented in the following sections, the peak value of the LSC current is displayed and it is used to estimate the temperature rise in the solid state devices. This choice is conservative, because the peak value of any waveform is always higher than the rms, and results in a simplification of the study, because, being the amount of harmonic components in the LSC current dependent on the compensation methodology, the rms current value is variable, while the peak value is independent on the harmonic current injection, as proved in Section 7.6.3.

4. peak dc-link voltage

   The dc-link peak voltage controls the maximum electric field intensity within the dielectric material of the capacitor. Too high peak voltage may lead to an insulation breakdown and arc within the capacitor.

For any simulation, the values of the parameters that describe WECS operation at the moment of fault (section 7.5) are as follows:

- $\mathscr{D}$=0.85
- $\omega_r/\omega_1 = 1.5$

7.8.1 Single-phase voltage sag

The contour plots for single-phase voltage sag are shown in Figures 7.32 - 7.35. The independent variables are the sag duration Δt and the scale parameter α. The other two parameters shown in Figure 7.2 are constant: $\beta = 1$ and $\varepsilon = 2\pi/3$.

Figure 7.32 displays the normalized transient peak voltage $\hat{V}_{PCC}/\hat{V}_n$ in function of sag duration $0 \leq \Delta t \leq 3.2$ and scale parameter $0 \leq \alpha \leq 1$. A grey shade scale is used to present the results, where white color indicates the rated value and dark color the highest values assumed by the normalized peak voltage. The contour plot shows that the highest value of the peak voltage are reached for α close to zero. This result can be explained as follows: for α close to zero, the power transiting through stator phase a is almost nil, while the power transferred through phases b and c is equal to the rated value, thus resulting in the most severe transients at the beginning of the fault and after fault clearance. The oscillograms displayed in the previous sections showed that the peak voltage is reached after fault clearance; for the single-phase fault, the maximum peak voltage is about 16 % above the rated value. As a final observation, the countour plot for maximum peak voltage shows that this value is practically independent of time.

The contour plot displayed in Figure 7.33 shows the normalized stator current peak amplitude $\hat{I}_s/\hat{I}_{sn}$ in function of sag duration $0 \leq \Delta t \leq 3.2$ and scale parameter $0 \leq \alpha \leq 1$; the grey scale used to represent the current peak value varies between 0 and 2.2. The highest value for the stator peak current are reached for values of α close to zero, for the same reasons explained for the previous contour plot. For the contour plot describing stator current peak, the highest values are concentrated around the region $\Delta t \approx 140$ ms. According to the requirements illustrated in Figure 1.6, any WECS is required to stay connected for fault duration below 140 ms, therefore LVRT ability of the system for fault durations close to this value must be investigated.

The thermal analysis carried out in appendix 7.B.2 proves that the peak value of 2.2 p.u. does not affect significantly the temperature rise in the stator windings. Moreover, the CB will not trip because the peak value of the stator current is below 5 p.u., that is the threshold typically set for CBs' relays [127].

Figures 7.34 show the countour plot for the peak values assumed the LSC current $\hat{I}_{LSC}/\hat{I}_{LSCn}$. The characteristics of this plot are very similar to the ones presented for countour plot displayed in Figure 7.32: highest peak values for the LSC current are obtained for values of α close to zero and the curve levels are independent from time duration. The peak value assumed by the LSC current is about 2.1 p.u.: thermal analysis carried out in appendix 7.B.2. prove that for rms currents equal to twice the rated current, the hot spot temperature always below the critical threshold of 140^oC (Figure 7.53). Since the contour plot displays the peak value and not the rms value of the LSC current, it results the solid devices temperature will not rise above the threshold under any condition in case of single-phase faults.

The last results provided for single-phase fault are shown in Figure 7.35 where normal-

ized peak voltage at the dc-link $\hat{V}_{dc}/V_{dc,n}$ is presented. The contour lines are independent of the fault duration, and the normalized peak voltage value is about 20% above the rated value. This value is not compromising the operation and the safety of the dc-link capacitor.

From the analysis of the graphs presented in Figures 7.32 - 7.35, it results that LVRT ability is verified for single-phase sags, even for conditions more severe than the one expressed by the typical LVRT requirements (Figure 1.6).

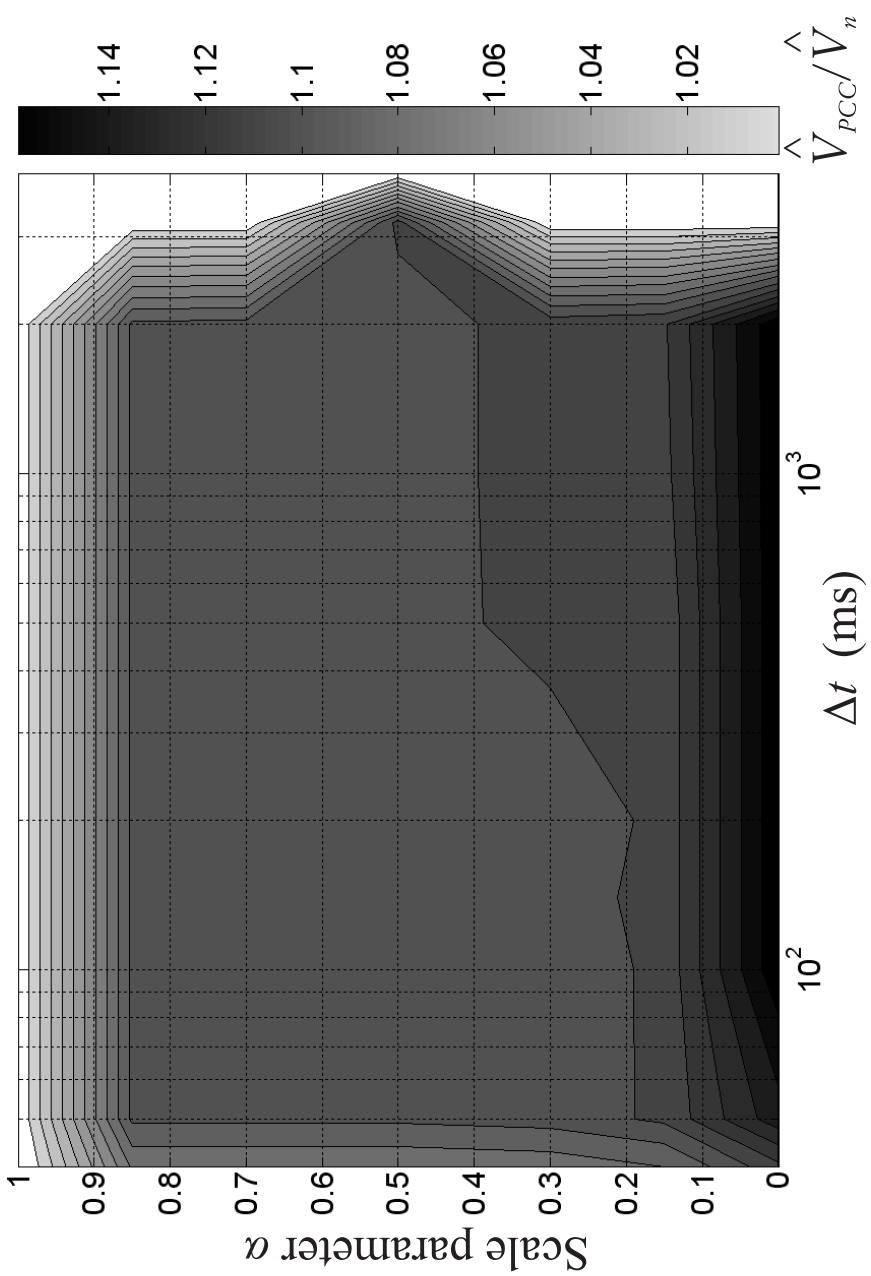

Figure 7.32 - Single-phase sag: normalized PCC peak voltage contour plot. x-axis: Δt (ms); y-axis: scale parameter α.

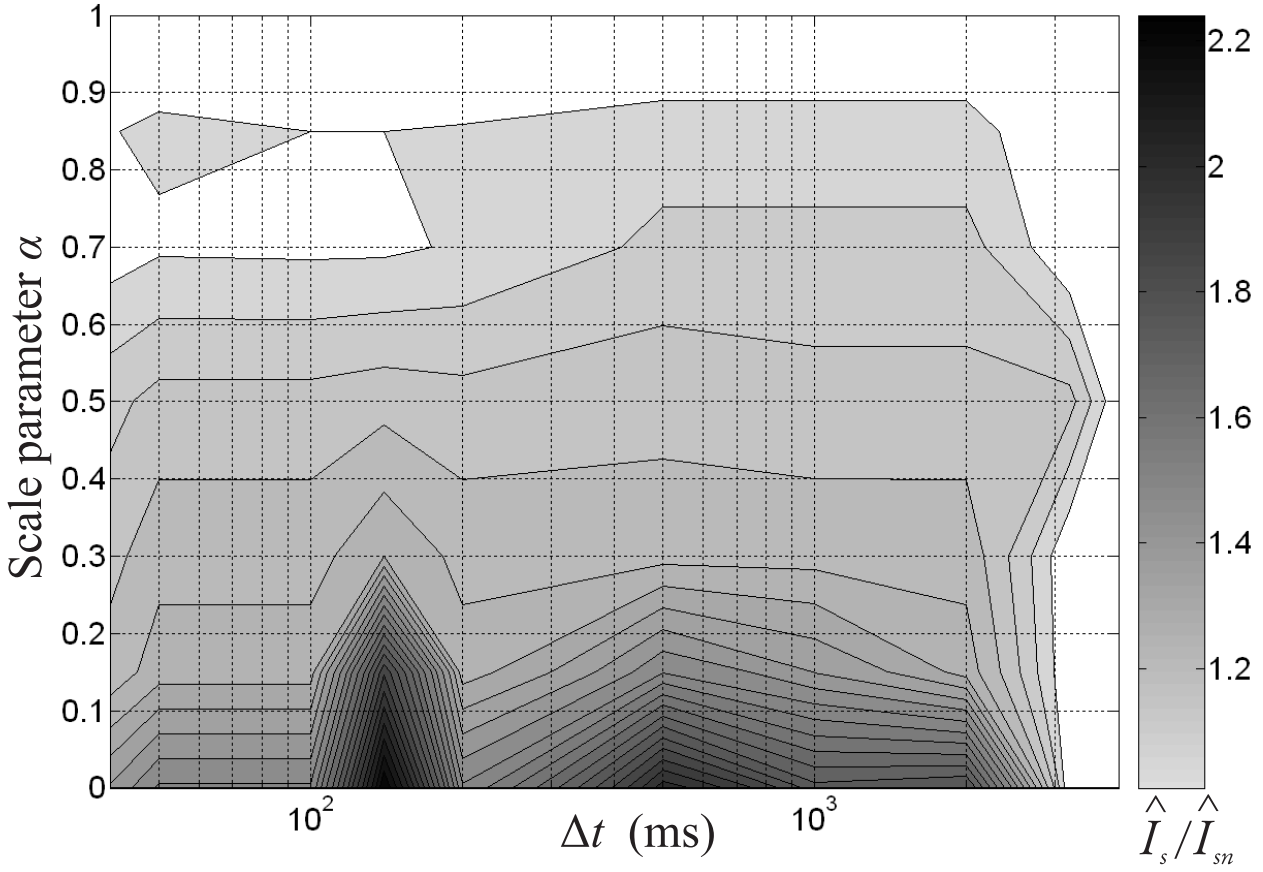

Figure 7.33 - Single-phase sag: normalized stator peak current contour plot. x-axis: Δt (ms); y-axis: scale parameter α.

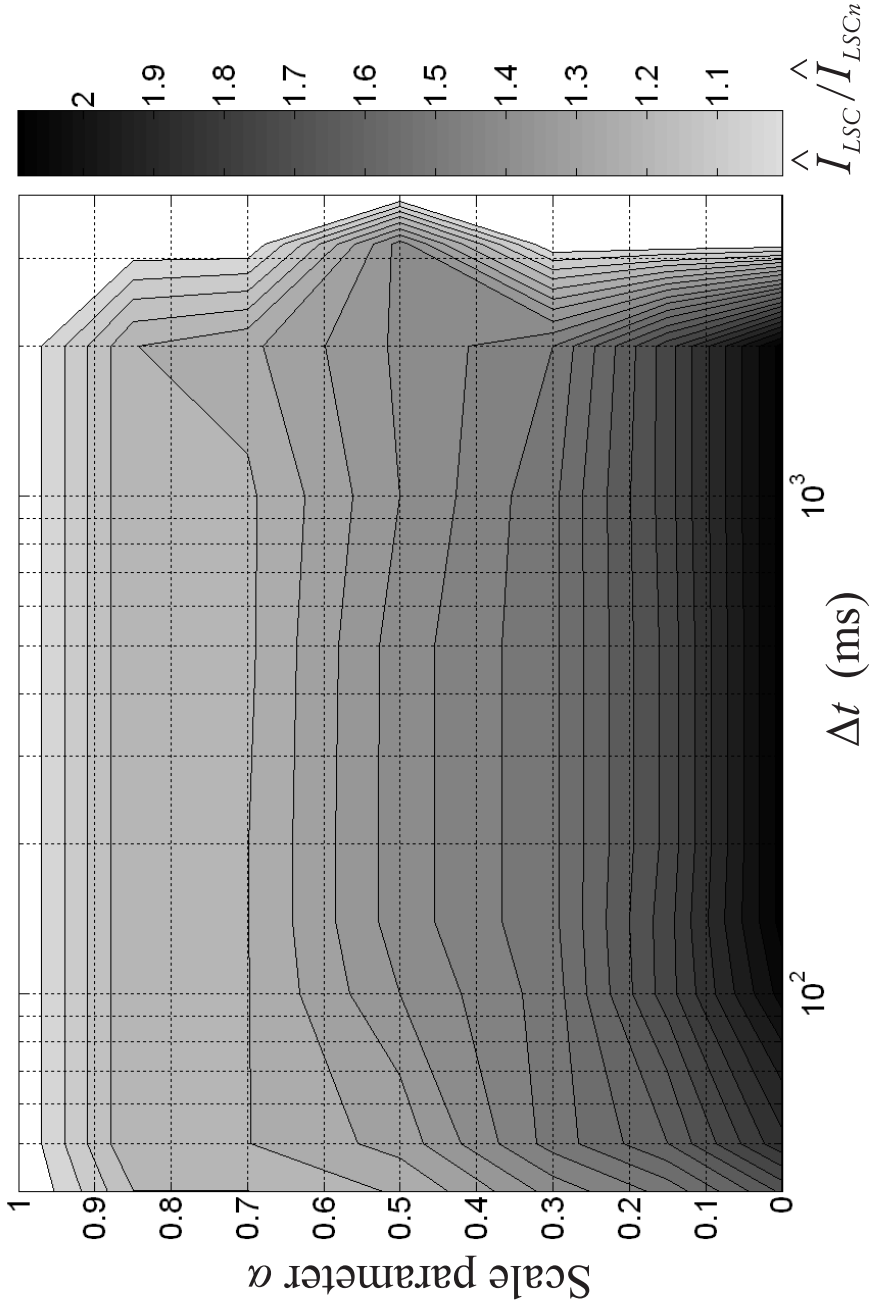

Figure 7.34 - Single-phase sag: normalized LSC peak current contour plot. x-axis: Δt (ms); y-axis: scale parameter α.

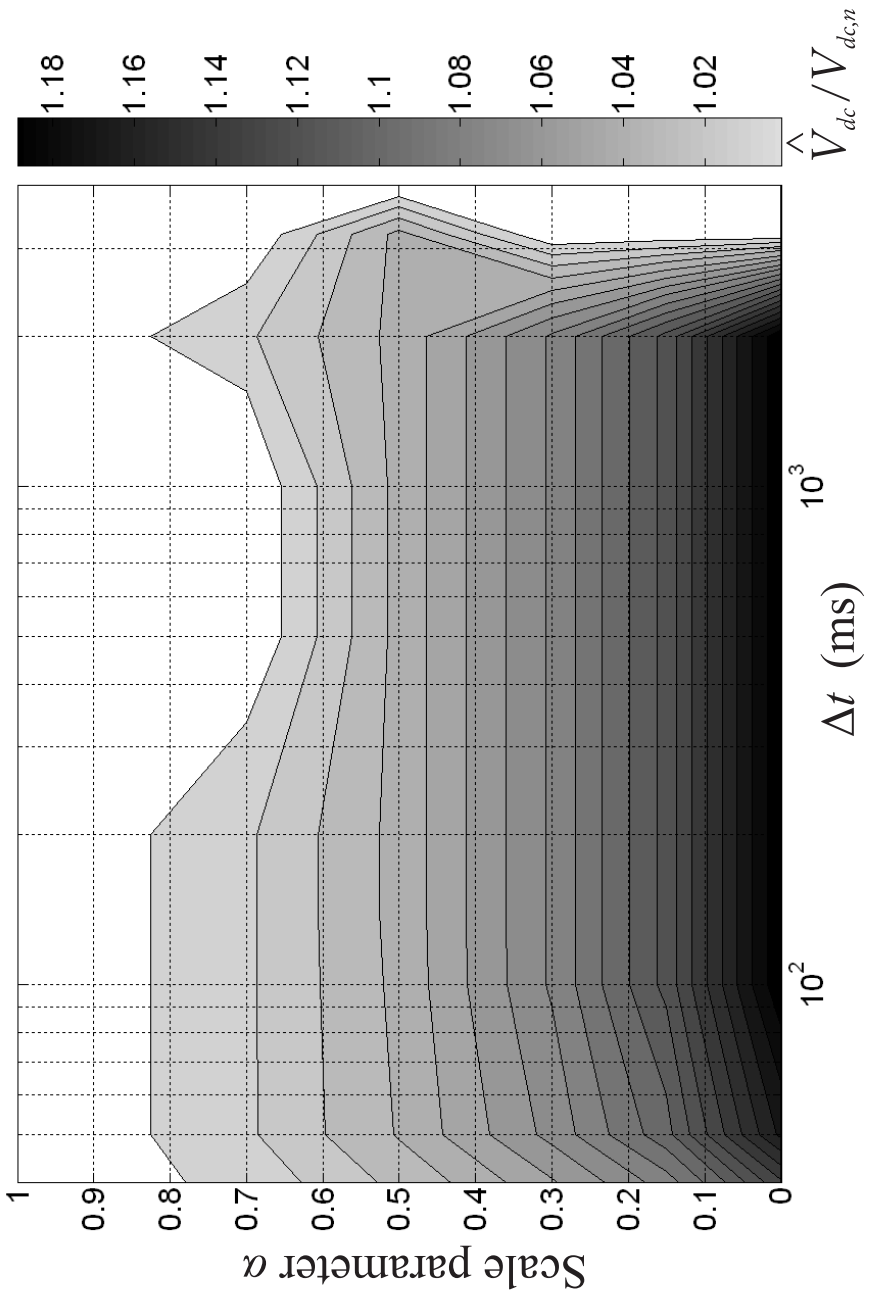

Figure 7.35 - Single-phase sag: normalized dc-link peak voltage contour plot. x-axis: Δ_t (ms); y-axis: scale parameter α.

7.8.2 Phase-to-phase voltage sag

The contour plots for phase-to-phase voltage sag are shown in Figures 7.36 - 7.39. The independent variables are the sag duration Δt and the scale parameter β. The other two parameters shown in Figure 7.2 are constant: $\alpha = 1$ and $\varepsilon = 2\pi/3$.

Figure 7.36 summarizes the normalized transient peak voltage $\hat{V}_{PCC}/\hat{V}_n$ in function of sag duration $0 \leq \Delta t \leq 3.2$ and scale parameter $0 \leq \beta \leq 1$. The behavior is very similar to the one observed in the case of single-phase fault (Figure 7.32). The highest peak voltages are reached for β close to zero, and they are independent of time. The peak amplitudes are more severe for the case of phase-to-phase voltage sag than for the case of single-phase fault, being respectively 1.6 p.u. and 1.16 p.u.

The contour plot displayed in Figure 7.37 shows the normalized stator current peak amplitude $\hat{I}_s/\hat{I}_{sn}$ in function of sag duration $0 \leq \Delta t \leq 3.2$ and scale parameter $0 \leq \beta \leq 1$. The grey scale used to represent the current peak value varies between 0 and 1.55 and the results obtained from thermal analysis on stator windings (appendix 7.B.2.) prove that peak value reached by the stator current does not compromise the integrity of the stator winding insulation. Similarly to the contour plot displayed for single-phase fault, the highest value for the stator peak current are reached for values of the scale parameter close to zero and they are independent of time. It is worth to observe that the peak stator current is generally higher in the case of phase-to-phase fault than in the case of single phase fault; however the contour plot for peak stator current in presence of single-phase fault presents higher peaks in the region around 140 ms. This result shows that reclosing time is a critical parameter for the study of the transients following fault clearance.

Figures 7.38 illustrates the peak values assumed by the LSC current $\hat{I}_{LSC}/\hat{I}_{LSCn}$. The behavior of this plot is very similar to the corresponding one presented for single-phase voltage sag. Higher peak values for the LSC current are obtained for values of β close to zero, the curve levels are independent of time duration and the peak value is close to twice the rated current. As already discussed for the single-phase fault, the thermal analysis carried out in appendix 7.B.2. proves that for this peak value the threshold temperature in the power converters is not reached.

The last results provided for single-phase fault are summarized in Figure 7.39 where normalized peak voltage at the dc-link $\hat{V}_{dc}/V_{dc,n}$ is presented. The results are again very similar to the ones obtained for single phase fault; however, the peak voltage is only 10% above the rated value, thus resulting in an even lower less severe fault condition for the phase-to-phase voltage sag.

The above discussion on the results provided in Figures 7.36 - 7.39 proves that LVRT

ability is verified for the phase-to-phase voltage sag for a wide spectrum of sag amplitude and duration, that goes beyond the typical LVRT requirements.

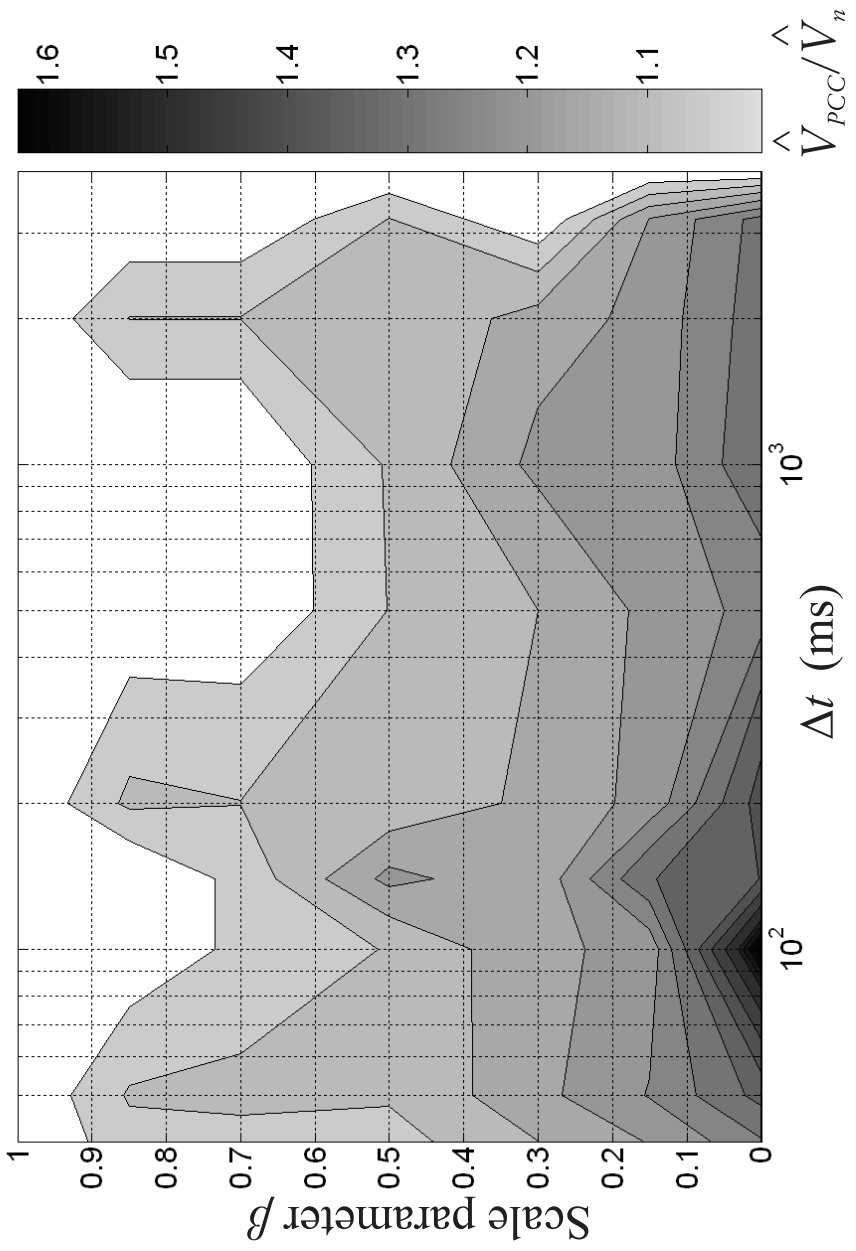

Figure 7.36 - Phase-to-phase sag: normalized PCC peak voltage contour plot. x-axis: Δt (ms); y-axis: scale parameter β.

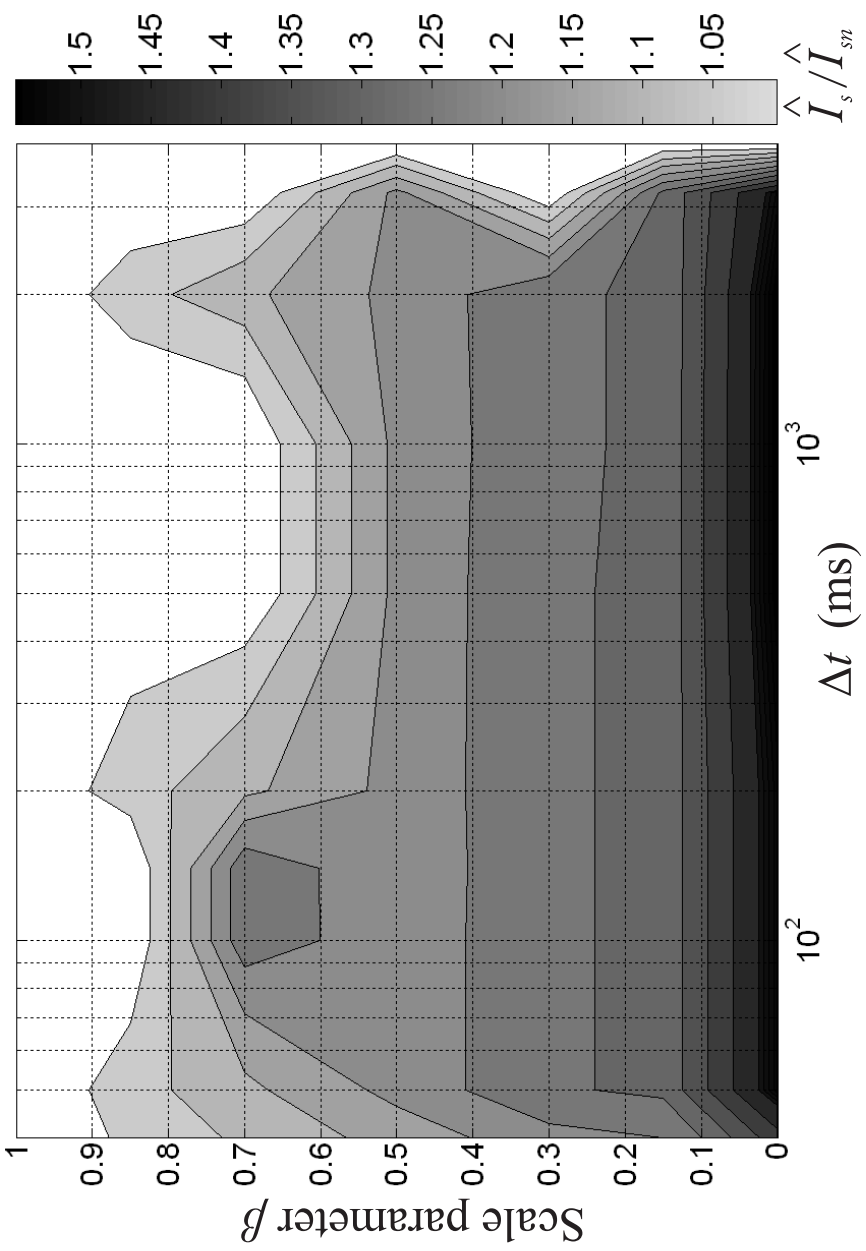

Figure 7.37 - Phase-to-phase sag: normalized stator peak current contour plot. x-axis: Δt (ms); y-axis: scale parameter β.

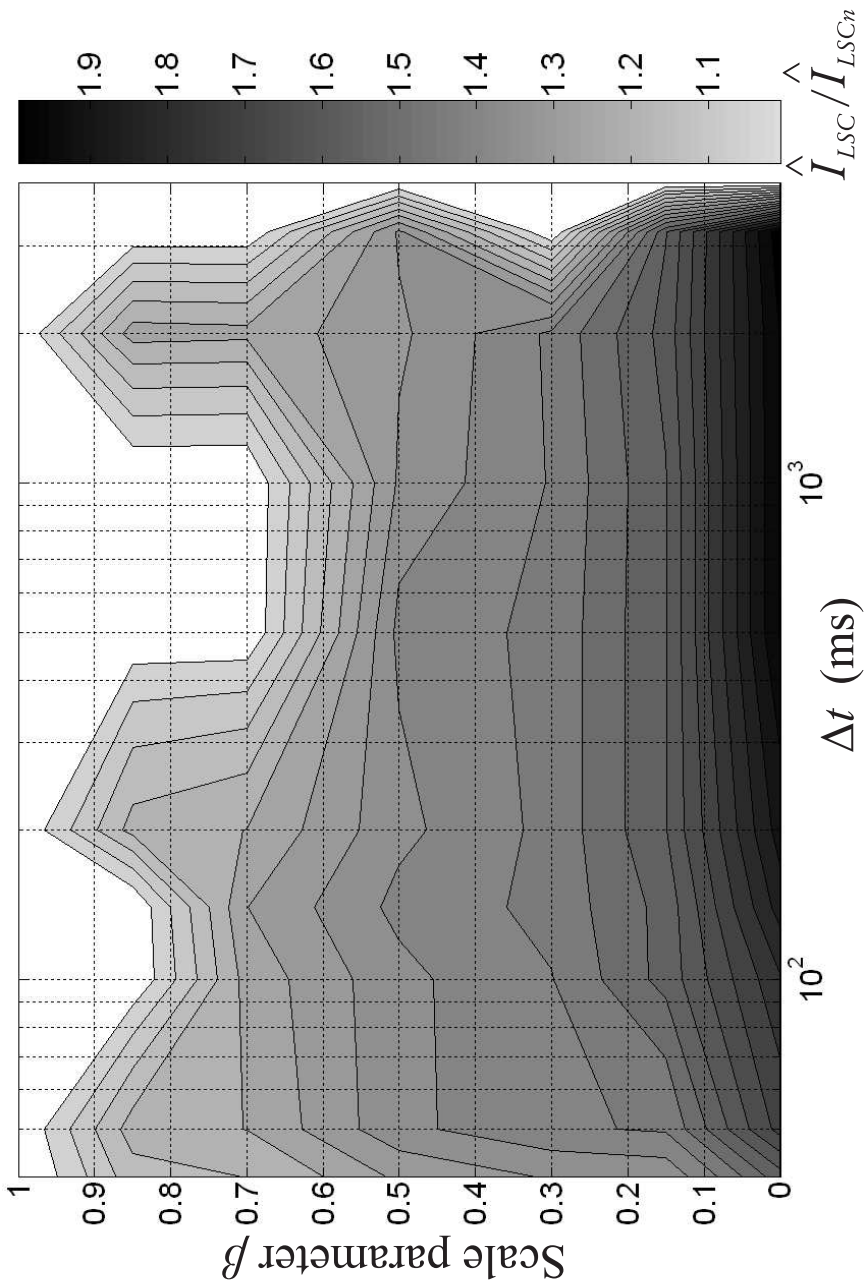

Figure 7.38 - Phase-to-phase sag: normalized LSC peak current contour plot. x-axis: Δt (ms); y-axis: scale parameter β.

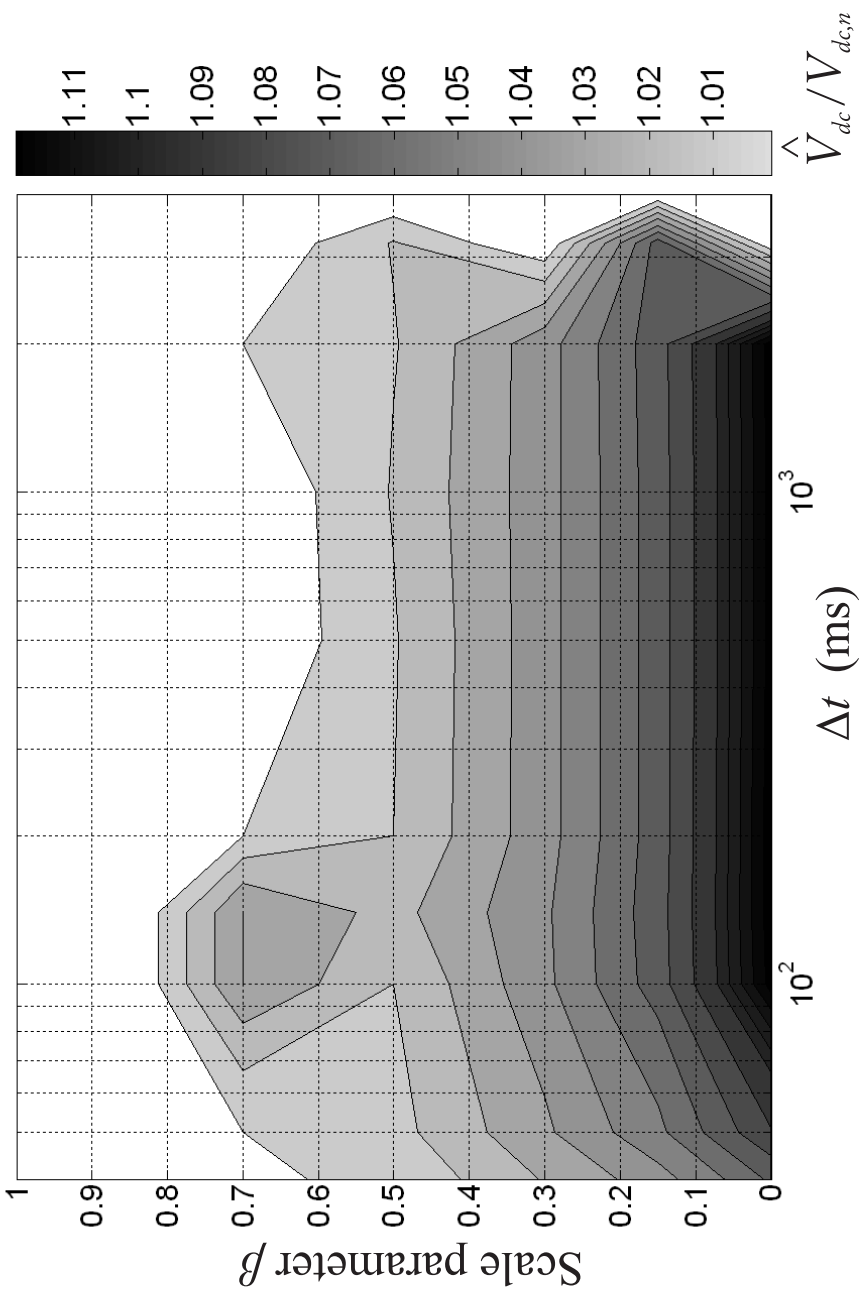

Figure 7.39 - Phase-to-phase sag: normalized dc-link peak voltage contour plot. x-axis: Δt (ms); y-axis: scale parameter β.

7.8.3 Thee-phase symmetrical voltage sag

The contour plots for the three-phase voltage sag are shown in Figures 7.40 - 7.44. The independent variables are the sag duration Δt and the scale parameters $\alpha = \beta$. The phase shift is constant: $\varepsilon = 2\pi/3$.

In the countour plots displayed in Figures 7.40 - 7.44, a dotted line and a rectangle delimited by the letters ABCD are shown. The dotted line represents the LVRT requirements described in section 7.4. The rectangle shows the area where LVRT ability of the system cannot be guaranteed. The dotted line and the rectangle are not shown in the contour plots obtained for single-phase and phase-to-phase voltage sags because for those faults LVRT ability is verified under any working condition.

Figure 7.40 describes the normalized transient peak voltage $\hat{V}_{PCC}/\hat{V}_n$ in function of sag duration $0 \leq \Delta t \leq 3.2$ and scale parameter $0 \leq \alpha = \beta \leq 1$. The highest peak voltages are approximately 1.5 p.u. and they are reached for $\alpha = \beta$ close to zero. The value assumed by the peak voltage is dependent on fault duration and the most critical area is between 100 ms and 140 ms.

The contour plot displayed in Figure 7.41 shows the normalized stator current peak amplitude $\hat{I}_s/\hat{I}_{sn}$ in function of sag duration $0 \leq \Delta t \leq 3.2$ and scale parameter $0 \leq \beta \leq 1$. The highest value for the stator peak current is 3.55 p.u. and is reached for values of $\alpha = \beta$ close to zero. However, for $\Delta t \approx 140$ ms, high stator currents are reached even for values of the scale parameters close to 0.5. p.u. Although the peak stator current amplitude for three-phase voltage sag is significantly higher than for single-phase and phase-to-phase voltage sags, it results that this value does not result in a significant temperature rise, according to the thermal analysis carried out in appendix 7.B.2. The CB will not trip because the peak value of the stator current is always below 5 p.u.

The countour plot depicted in Figures 7.42 show the normalized peak LSC current $\hat{I}_{LSC}/\hat{I}_{LSCn}$. The highest peak current values are obtained for $\alpha = \beta$ close to zero. The detail of this plot for $40 \leq \Delta t \leq 1000$ (ms) and $0 \leq \alpha = \beta \leq 0.1$ is depicted in Figure 7.43. In case of three-phase symmetrical voltage sag, the LSC current amplitude reaches peak values close to 10 times the rated current. Such high values are not allowed because they will lead to the destruction of the power converters' solid state devices; this situation is also aggravated by observing that such peaks are obtained in correspondence of long fault durations. According to the thermal analysis carried out in appendix 7.B.2., the threshold temperature in the switches is reached after a few milliseconds for rms currents equal to 4 p.u. For higher rms currents the temperature rise above the threshold is almost instantaneous. As a conclusion, for LSC peak currents above 3 p.u. and with durations

higher than 150 ms the LVRT capability of the system under study cannot be guaranteed: the rectangle ABCD encloses such area.

After this description, the reason why the rectangle ABCD is depicted in all the diagrams reported in Figures 7.40 - 7.44 is clear: for symmetrical fault with $\alpha = \beta \leq 0.1 p.u.$ and $\Delta t \geq 150$ ms the system LVRT ability is not verified. The values assumed by the peak voltage at the PCC, the peak stator current and the dc-link voltage are not critical within this area, but the fact that LSC peak currents are too high limits the performances of the complete system.

Since the area delimited by the rectangle ABCD lies below the dotted line, the studied system controlled by means of CM can be operated within the requirements defined by the majority of the utilities [55, 67, 68].

The results obtained for normalized peak voltage at the dc-link $\hat{V}_{dc}/V_{dc,n}$ are presented in Figure 7.44. The contour lines are independent of the fault duration, and the peak value is about 60% above the rated value. This voltage amplitude may be critical for the operation of the dc-link, but since it is within the rectangle ABCD, the system is not allowed to operated in this region.

The contour plots obtained for symmetrical faults confirm that the three-phase voltage sag represent the most severe fault condition for a WECS. The amplitudes for all the electrical quantities peak values are significantly higher than for single-phase and phase-to-phase faults. The most severe transients are obtained for $\alpha = \beta$ close to zero: this result is justified by considering that under this condition the power delivered to the grid through the stator is almost nil. The quantity that is limiting the performances of the entire system is the LSC current.

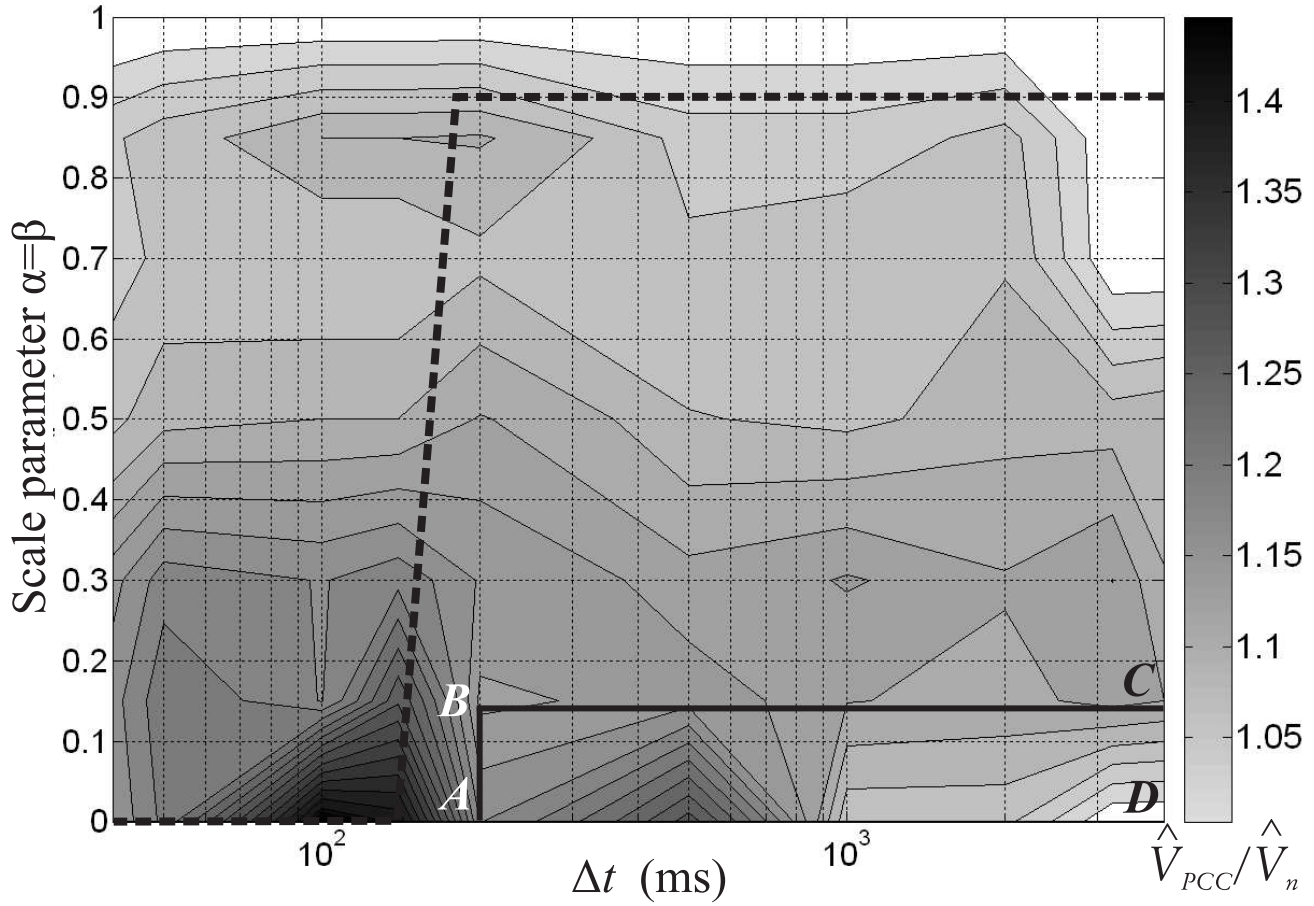

Figure 7.40 - Three-phase symmetrical sag: normalized PCC peak voltage contour plot. x**-axis:** Δt **(ms);** y**-axis: scale parameter** $\alpha = \beta$**.**

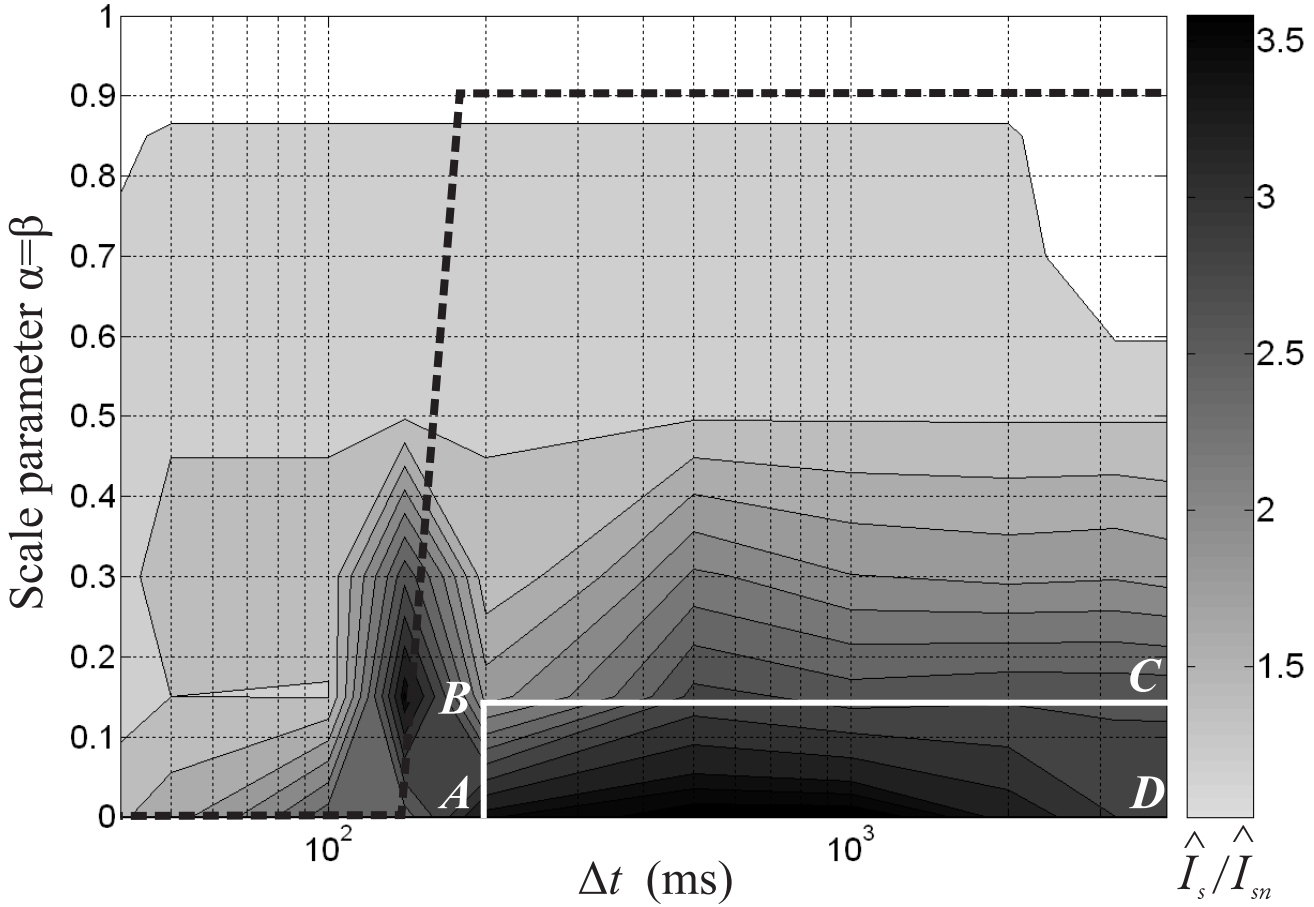

Figure 7.41 - Three-phase symmetrical sag: normalized stator peak current contour plot. x-axis: Δt (ms); y-axis: scale parameter $\alpha = \beta$.

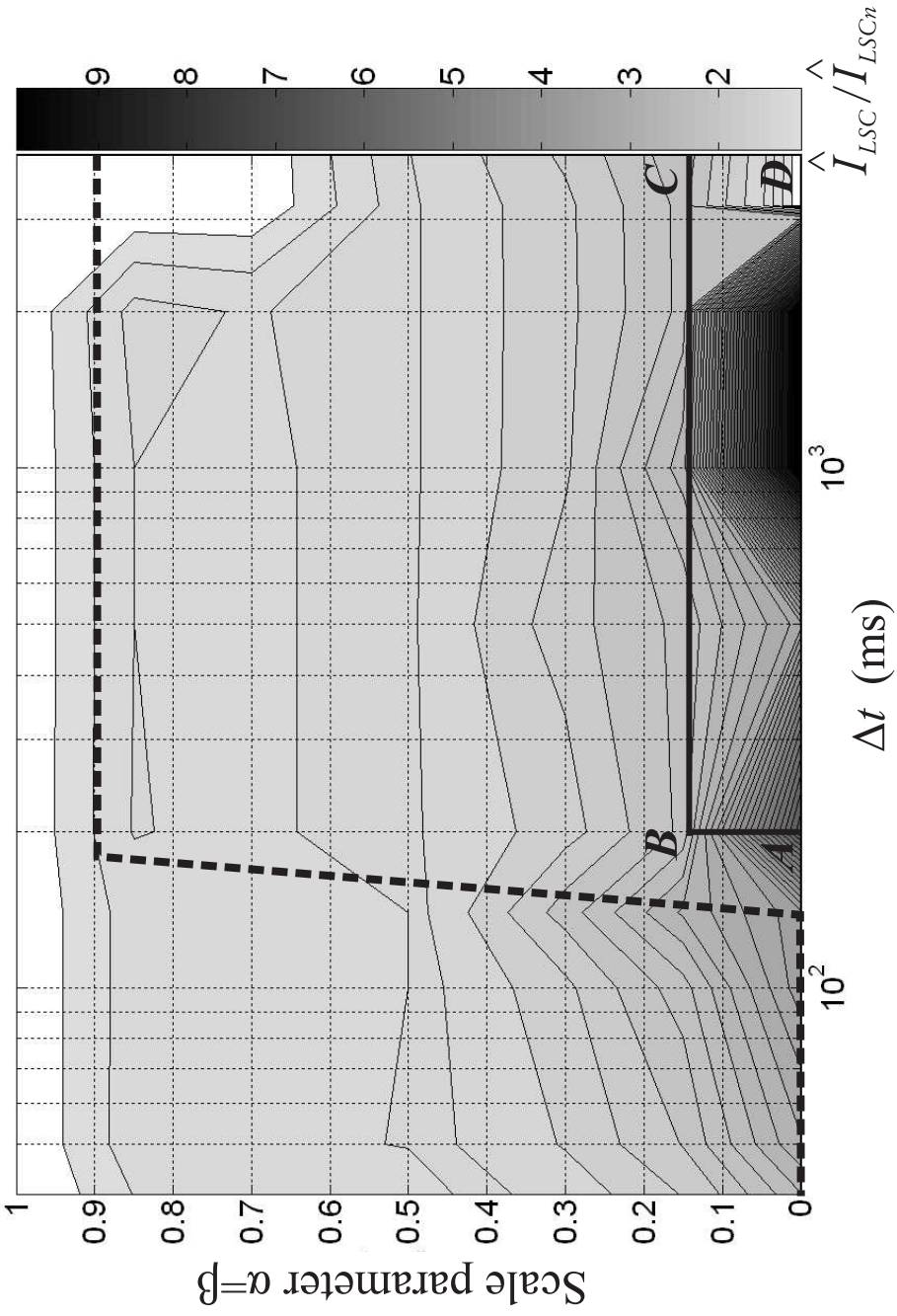

Figure 7.42 - Three-phase symmetrical sag: normalized LSC peak current contour plot. x-axis: Δt (ms); y-axis: scale parameter $\alpha = \beta$.

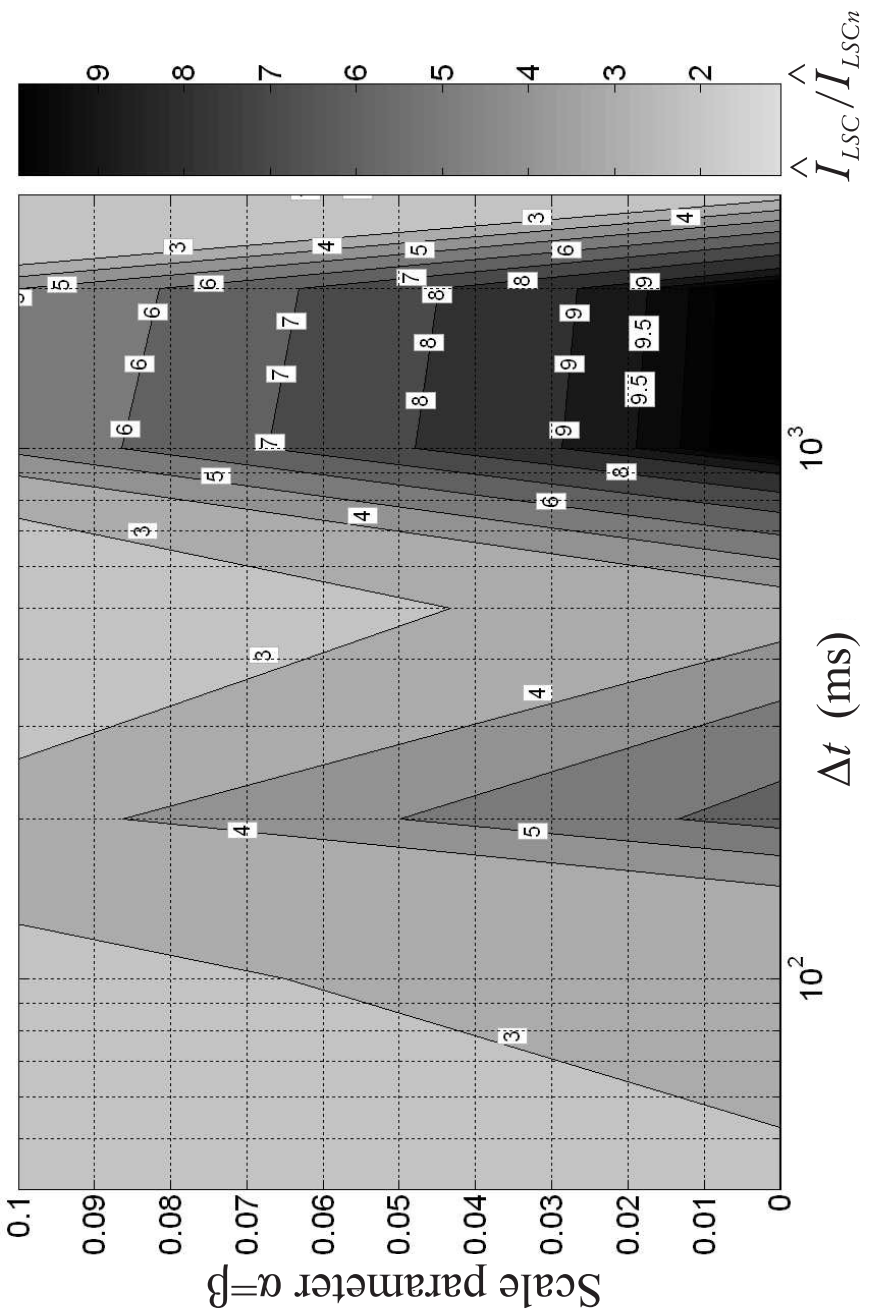

Figure 7.43 - Three-phase symmetrical sag: detail of the normalized LSC peak current contour plot for $40 \leq \Delta t \leq 1000$ (ms) and $0 \leq \alpha = \beta \leq 0.1$.

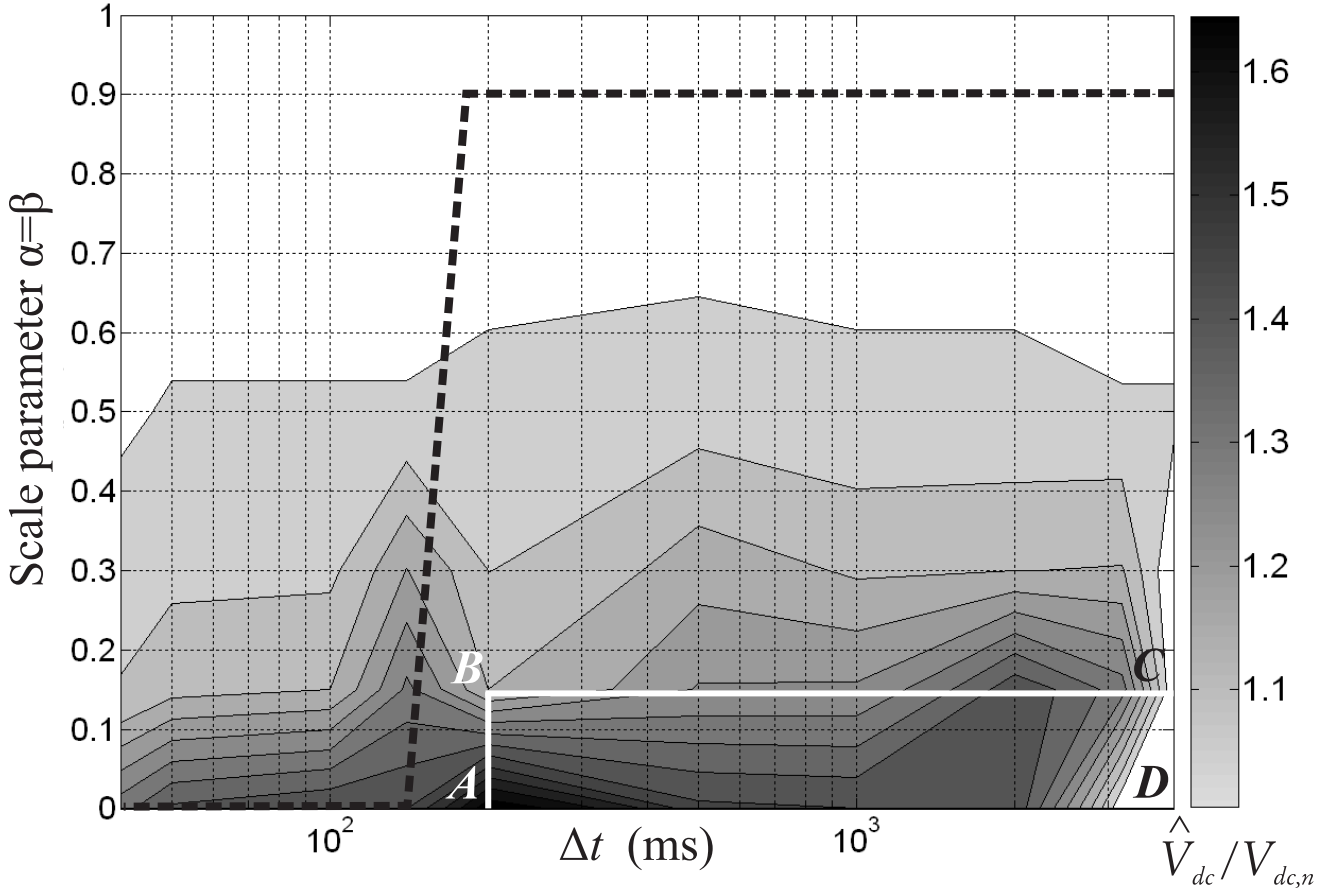

Figure 7.44 - Thee-phase symmetrical sag: normalized dc-link peak voltage contour plot. x-axis: Δt (ms); y-axis: scale parameter $\alpha = \beta$.

7.8.4 Phase-to-phase voltage sag with phase shift

The contour plots for the phase-to-phase sag with phase shift are shown in Figures 7.45 - 7.48. The independent variables are the sag duration Δt and the phase shift ε. The values assumed by the scale parameters are: $\alpha = 1$ and $\beta = 0.85$. The scale parameters are typical of a mild fault conditions, and they are chosen to identify the effect of the phase shift on the amplitudes of the electrical quantities.

Figure 7.45 displays the normalized transient peak voltage $\hat{V}_{PCC}/\hat{V}_n$ in function of sag duration $0 \leq \Delta t \leq 3.2$ and phase shift $100 \leq \varepsilon \leq 140$. This contour plot shows that when the phase shift changes with respect to the rated value, the peak voltage at the PCC rises significantly up to 1.3 p.u. for phase shift equal to 140 deg. Although a phase shift variation of 20 deg is rarely obtained in the practice, this plot shows that even for mild voltage sag characteristics, the effect of phase shift on the PCC voltage variation can be significant.

The contour plot displayed in Figure 7.46 shows the normalized stator current peak amplitude $\hat{I}_s/\hat{I}_{sn}$. The behavior of the contour lines is similar to the one described for the plot related to voltage at the PCC since any deviation (positive or negative) from the rated condition results in an increase of peak stator current, independent of the voltage sag duration. The peak stator current, however, is only about 1.45 p.u. thus not compromising the windings' insulator integrity.

The countour plot depicted in Figure 7.47 shows the peak values assumed by the normalized LSC current $\hat{I}_{LSC}/\hat{I}_{LSCn}$. The behavior is similar to the one described for the peak voltage at the PCC and for the peak stator current, and the peak LSC current of 1.7 p.u. is reached. The peak current is below 2 p.u. and does not affect the safe operation of the power converters' solid state devices.

Figure 7.48 displays the contour lines for the normalized peak voltage at the dc-link $\hat{V}_{dc}/V_{dc,n}$. The peak value of 1.1. p.u. is obtained, and does not result in an threaten for the dc-link capacitor.

If a more severe fault conditions were chosen, the peak values obtained from the contour plots would have been obtained; however, the contour plots are representative of the contribution of phase shift.

The conclusion learned from the diagrams presented in this section is that any phase shift variations increase the peak values assumed by the electrical quantities; if a severe fault condition is combined with a significant fault variations, the results obtained in sections 7.8.1-7.8.3 may be reviewed. In detail, LVRT ability may not be guaranteed any more under any condition of single-phase and phase-to-phase faults, and the rectangle ABCD may be extended.

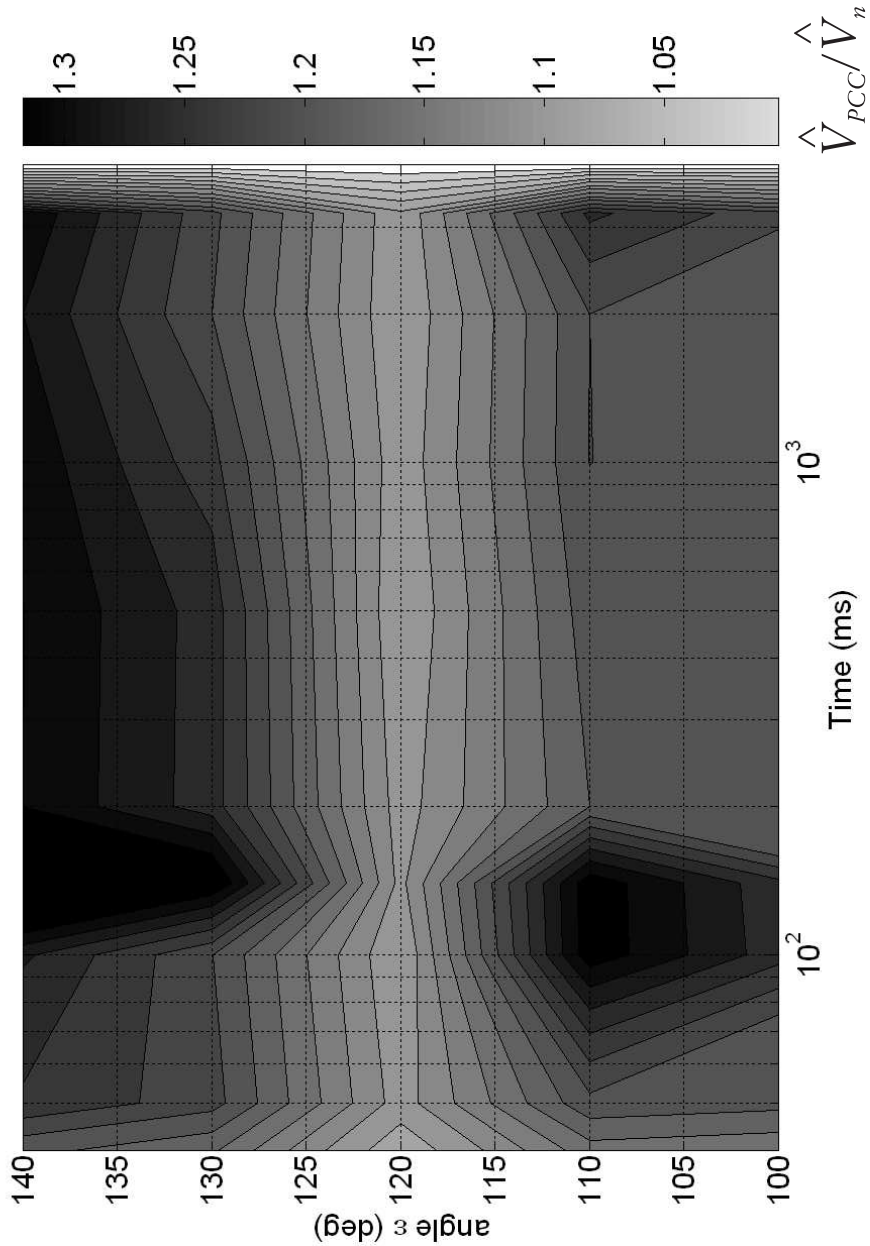

Figure 7.45 - Phase-to-phase voltage sag with phase shift: normalized PCC peak voltage contour plot. x-axis: Δt (ms); y-axis: phase angle ε (deg).

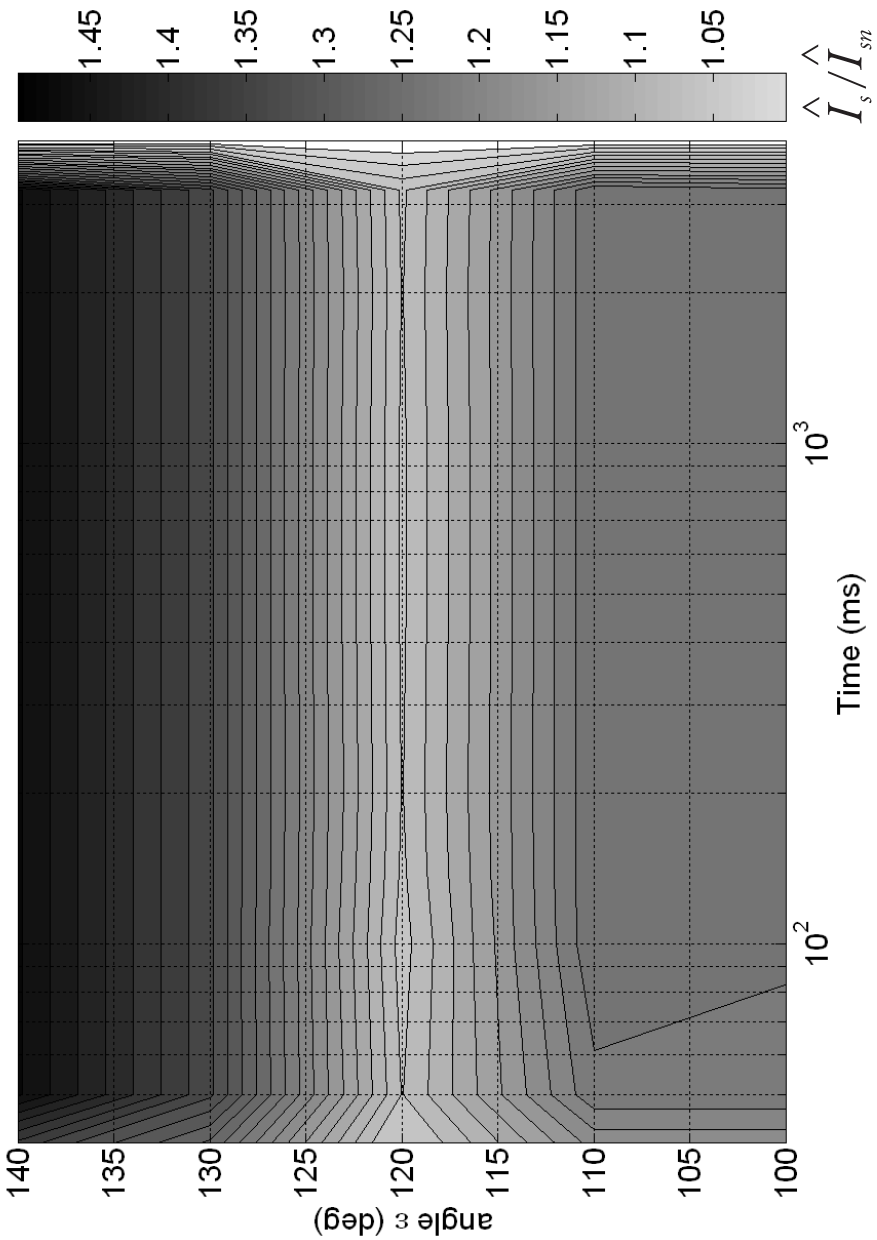

Figure 7.46 - Phase-to-phase voltage sag with phase shift: normalized stator peak current contour plot. x-axis: Δt (ms); y-axis: phase angle ε (deg).

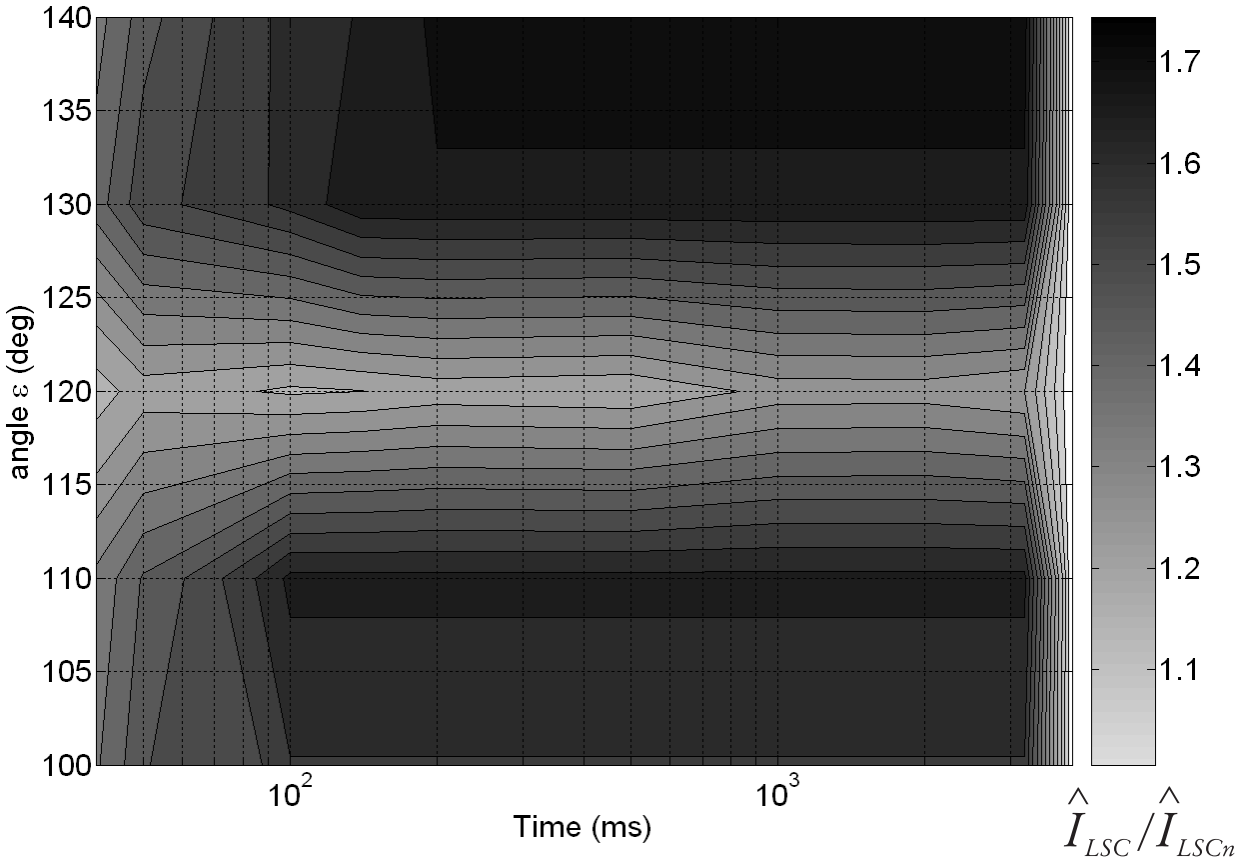

Figure 7.47 - Phase-to-phase voltage sag with phase shift: normalized LSC peak current contour plot. x-axis: Δt (ms); y-axis: phase angle ε (deg).

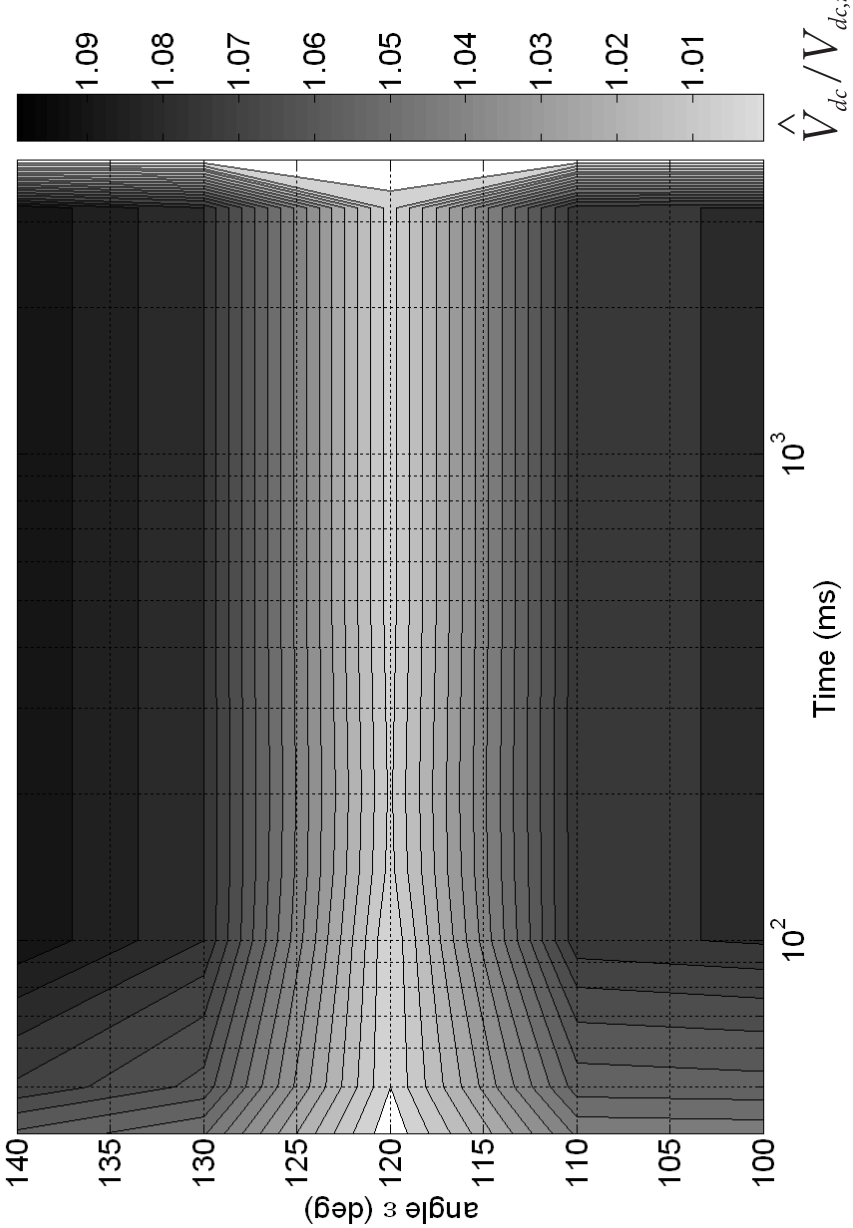

Figure 7.48 - Two-phase voltage sag with phase shift: normalized dc-link peak voltage contour plot. x-axis: Δt (ms); y-axis: phase angle ε (deg).

7.9 LVRT assessment and conclusions

The oscillograms and contour plots displayed in the previous sections show the values assumed by the principal electric quantities during four types of voltage sags, characterized by different amplitudes and durations. The studied conditions cover a broad spectrum of voltage variations that may take place in typical power grids.

The conclusion from the study carried out in the present chapter is that LVRT ability of the WECS under study is guaranteed for the majority of the faults; contour plots allowed to identify the region where LVRT cannot be verified, that corresponds to symmetrical faults with almost zero residual voltage and relatively long duration. Since this region is below the trajectory illustrated in Figure 1.6, the LVRT requirements are guaranteed.

The effects of harmonic current injection on the dynamic response of the system has been evaluated in section 7.6.3 by comparing the oscillograms obtained for the same fault condition with and without harmonic compensation implemented by the WECS. From these oscillograms, it results that the harmonic currents flow does not affect the peak values assumed by the electrical quantities, except that for the voltage at the PCC. On the contrary, derating of the machine results in a reduction of the peak currents trough the stator and the power converters and in a lower dc-link voltage peak, since derating results in a lower fundamental power flowing through the WECS components.

Appendix 7.A: Use of the crowbar to limit LSC current during the voltage sags

The crowbar is a three-phase rectifier installed on the rotor side circuit to protect the DFIG during faults [22, 142, 145, 146, 149, 150]. The purpose of the crowbar is to provide a path to dissipate the excess of energy injected by the rotor and therefore to reduce the amplitude of the current flowing through the power converters. The crowbar current i_{cr} is zero under normal operation. If either the rotor current or the dc-link voltage levels exceed their limits, the crowbar is activated [151]. When the crowbar is triggered, the rotor side converter is disconnected from the rotor and the controllability of the DFIG is lost during the voltage dip: this is the main drawback of the crowbar protection.

During the time the crowbar is active, the DFIG behaves as a squirrel cage induction generator with a variable rotor resistance until the moment when the crowbar is cut off and the rotor side converter resumes normal operation. During the transient that follows the crowbar deactivation, the DFIG absorbs reactive power from the grid need for reestablish the amplitude of the magnetic field [142].

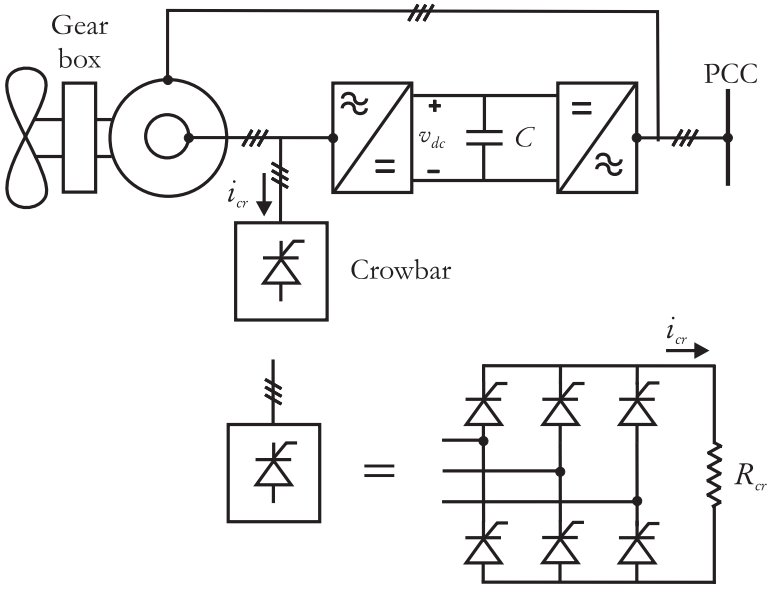

Figure 7.49 - The crowbar model used in the simulation.

The installation of the crowbar in wind power plant is controversial: some authors consider the crowbar more a threat than a benefit due to the disconnection of the power converters and to the loss of their control during crowbar operation [144]. Other authors claim that the crowbar is necessary to guarantee zero-voltage ride through [39, 152]. In [9] it is remarked that the details of crowbar operation are vendor dependent and therefore difficult to generalize across all turbines of the same topology.

This appendix is dedicated to study the effects of crowbar installation in the system under study. The crowbar is modeled by the three-phase rectifier depicted in Figure 7.49 and connected in parallel to the RSC [146]. The dc-load is a resistor. The value of the resistor R_{cr} is an important design parameter. Small values of the rotor resistance implies high rotor current, high values of the rotor resistance result in too high rotor voltage [142, 145]. In the present work, R_{cr}= 2 p.u.

The effect of the crowbar on the LSC current amplitude for two symmetrical fault with different fault durations is studied. Symmetrical faults are assumed because they create the most stressful conditions in the WECS. Figure 7.50 shows the LSC current for the symmetrical fault described in Table 7.3, with $\Delta t = 140$ ms. By comparing this oscillogram with the one presented in Figure 7.20, it results that the peak current amplitude is lowered from 3 p.u. to 1.8 p.u. when the crowbar is installed.

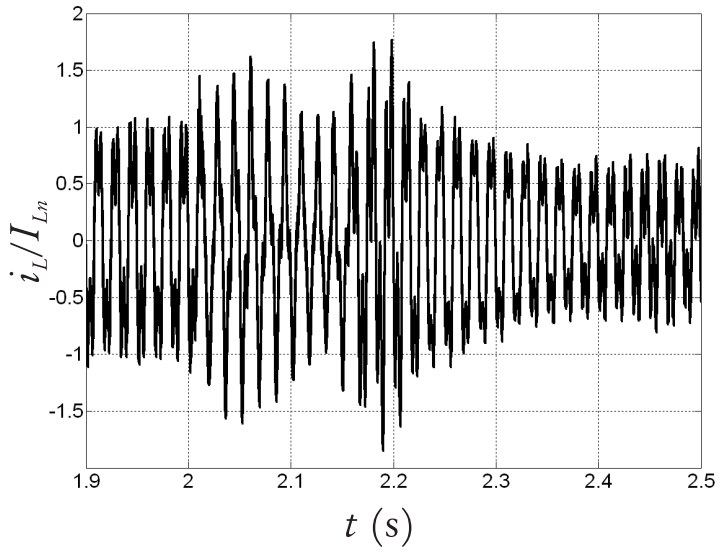

Figure 7.50 - Symmetrical fault with crowbar installed: normalized LSC current oscillogram, base value is LSC rated current, $\Delta t = 140$ ms.

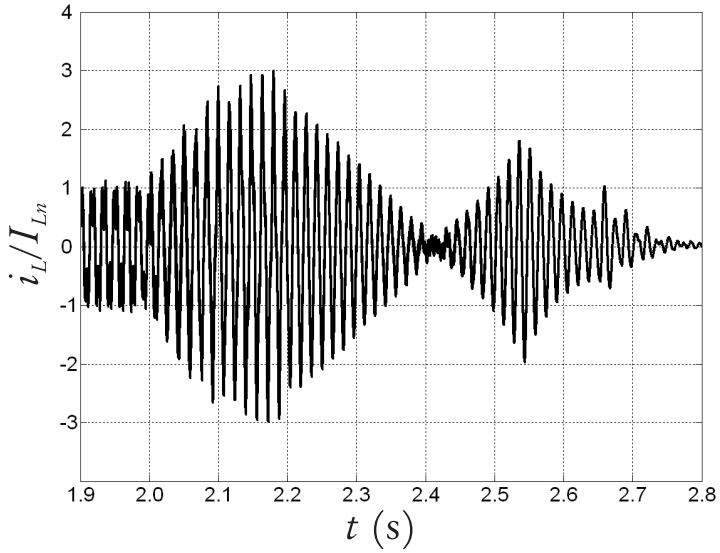

Figure 7.51 - Symmetrical fault with crowbar installed: normalized LSC current oscillogram, base value is LSC rated current, $\Delta t = 1000$ ms.

Appendix 7.B: Thermal effects during voltage sag

7.B.1 Winding temperature rise

The stator currents increase that follows the voltage sag results in higher power dissipation in the stator windings. The fault duration is short compared to the thermal time constant of the stator windings: for this reason, the heating process is adiabatic.

The following equation governs the adiabatic process:

$$R\ I_s^2 \Delta t = C_{th} \Delta T \tag{7.1}$$

where I_s is the rms stator current, R is the copper resistance (assumed constant), C_{th} is the winding thermal capacitance and ΔT is the temperature rise (K). The value of both R and the C_{th} depends on the winding dimensions (displayed in Figure 3.20) and of the conductor physical properties and (7.1) can be rewritten as follows:

$$\left(\rho \frac{l}{A}\right) I_s^2 \Delta t = \left(A l \gamma c_s\right) \Delta T \tag{7.2}$$

where:

l is the length of the conductor (m)

A is the cross-section area of the conductor (m)

ρ is the conductivity (Ω/m)

γ is the density (Kg/m^3)

c_s is the specific thermal capacitance (J/ Kg °C)

The temperature rise is obtained from 7.2 as:

$$\Delta T = \frac{\rho (I_s/A)^2 \Delta t}{\gamma c_s} = \frac{\rho \gamma^2 \Delta t}{\gamma c_s} \tag{7.3}$$

where the current density is $\gamma = I_{rms}/A$.

If the material used for the windings is copper and the windings designed in appendix 3.A are used, the following substitutions are made in (7.3): $\rho = 16.78\text{n}\Omega$/m, c_s=385 J/Kg °C, γ=8900 kg/m^3, A=384 mm^2

yielding to the simplified formula for the calculation of the adiabatic temperature rise:

$$\Delta T = 0.08192(I_s/I_n)^2 \Delta t \tag{7.4}$$

The last result shows that the copper properties combined with the geometrical characteristics of the winding yield an insignificant temperature rise for the transients conditions. The analysis provided in the previous sections shows that the peak current in the stator windings is generally a few p.u. and the duration of the transients is lower than three periods.

This conclusion is reinforced by the results provided in Table 7.7. In this table it is shown that the temperature rise is below one degree even for significantly high stator currents and long transients. Note that in this table the peak value of the stator current is used: this approximation is conservative, and is made since the results provided by the contour plots display the peak current. It is worth to notice that although the peak values are assumed, the temperature rise is very small.

Table 7.7 - Stator windings temperature rise ΔT as function of $I_{s,rms}/I_{sn}$ and Δt, according to (7.3). It is assumed that the conductive material used for the stator windings is copper.

I_s/I_{sn} (A)	Δt (s)	ΔT (°C)
3	0.05	0.0371
4	0.05	0.0659
5	0.05	0.103

7.B.2 Solid state devices temperature rise

The thermal equivalent circuit for a solid state device subjected to power flow $p(t)$ is represented in Figure 7.52.

The solid state equivalent thermal resistance and capacitance are obtained from the datasheet [134]; the power loss is the sum of conduction loss and switching loss [34]:

$$p(t) = p_{cond} + p_{sw} = RI_{rms}^2 + f_{tri}E_{sw} \tag{7.5}$$

where E_{sw} is the switching energy loss during the switching time and f_{tri} is the modulating signal frequency (see appendix H for definitions related to PWM).

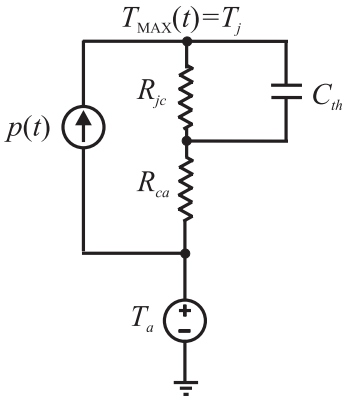

Figure 7.52 - Equivalent thermal circuit for a solid state device characterized by thermal resistance R_{th} and thermal capacitance C_{th}. The ambient temperature is T_a, the power loss injected in the switch is $p(t)$.

The following data are used for the switch thermal analysis [134]:

R=0.143 mΩ

R_{th}=0.055 °C/w

C_{th}=1.5 J/ °C

E=190 mJ/pulse

I_{LSCn}=840 A

f_{tri}=6480 Hz

T_a=40 °C.

For the present analysis, it is assumed that during the fault the switching loss p_{sw} does not change. The rms current through the switch is obtained by using the LSC current oscillograms presented in sections 7.6 and 7.8.

The maximum temperature oscillograms are illustrated in Figures 7.53-7.55 for different current amplitudes and durations. These oscillograms show that for increasing values of the rms current through the solid state devices, the maximum temperature limits is reached for shorter values of Δt.

In detail, when the current rms into the solid state devices is twice the rated current, the steady state temperature is below 140 deg for any fault duration (Figure 7.53). For $I_{rms} = 3 \cdot I_{LSCn}$, the temperature of 140 °Cis reached after 155 ms (Figure 7.54). For $I_{rms} = 4 \cdot I_{LSCn}$, the temperature of 140 °Cis reached after 47 ms (Figure 7.55).

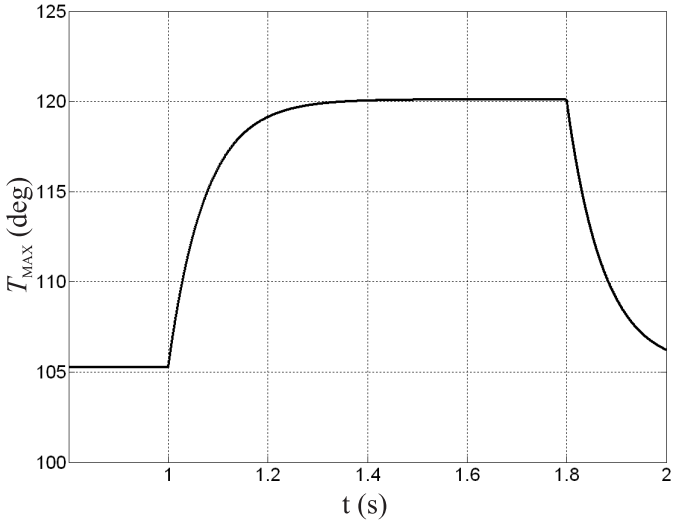

Figure 7.53 - Symmetrical fault: maximum temperature oscillograms, $I_{rms} = 2 \cdot I_{LSCn}$, Δt = 800 ms.

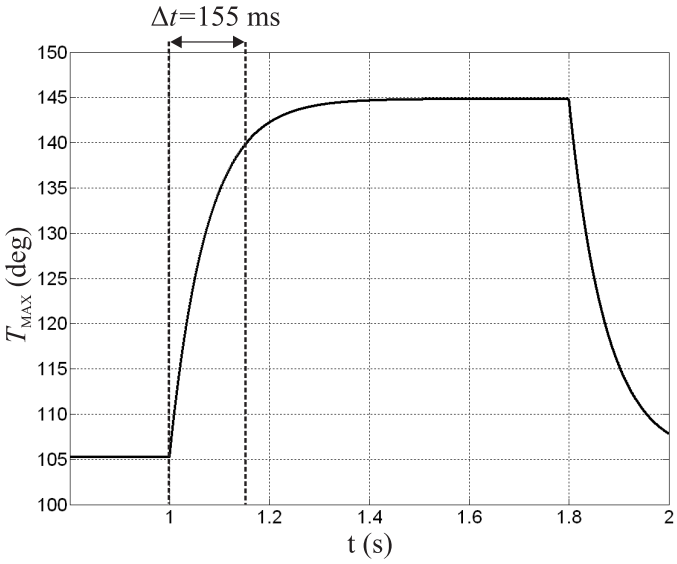

Figure 7.54 - Symmetrical fault: maximum temperature oscillograms, $I_{rms} = 3 \cdot I_{LSCn}$, Δt = 800 ms.

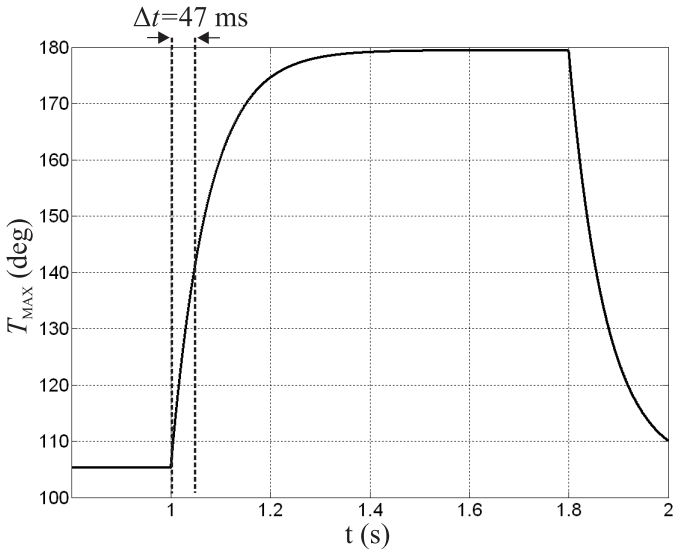

Figure 7.55 - Symmetrical fault: maximum temperature oscillograms, $I_{rms} = 4 \cdot I_{LSCn}$, Δt = 800 ms.

Chapter 8

WECS Transient Response to Wind Speed Variation

8.1 Introduction

Wind speed variation is a second transient phenomenon that affects the operation of wind generators[31].

The present chapter is intended to study in detail the effects of wind speed variations on the quality of the energy delivered by the WECS at the PCC and to assess if the transient phenomena affect the ability to perform harmonic compensation. The following assumptions are made:

- The chosen WECS has the characteristics described in appendix A and is controlled to perform compensation by means of CM (chapter 6).
- The system response to wind speed variations is principally determined by the mechanical transient: both the shaft control and the blades pitch control are characterized by high time constants (in the order of seconds), while the response of the power electronics is assumed to be instantaneous [153].
- Three identical single-phase diode rectifiers (Figure 6.22) are the NLL.

8.2 Mechanical system model

For WECSs based on DFIG technology (Type C configuration, chapter 1), the mechanical section consists of the wind turbine, the low speed shaft, the gearbox and the high speed shaft that support the wind generator rotor windings [32]. The gearbox is needed to rise the

[31] The characteristics of wind speed distribution and the wind power fluctuations are described in appendix C.

[32] The mechanical system is different for WECSs based on Type D configuration - Direct drive.

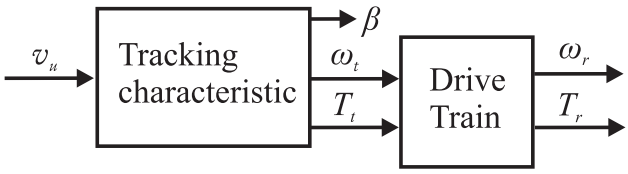

Figure 8.1 - Overview of the mechanical control: the input of the control system is the upstream wind speed v_u, the output are the pitch angle β, the generator speed ω_r and the generator torque T_r.

low turbine velocity to an appropriate value for the operation of the electric generator; the turbine velocity and the generator velocity are related by the gearbox ratio N_{gb} as follows:

$$\omega_r = N_{gb}\omega_t \tag{8.1}$$

Typical values of gearbox ratio for variable speed wind turbines based on DFIG are in the order of 100:1 [36].

The concept of the mechanical system control is depicted in Figure 8.1, where two blocks are shown:

1. *Tracking characteristic*: The input variable is the upstream wind speed v_u; the output variables are the turbine torque T_t, turbine speed ω_t and pitch angle β.

2. *Drive train*: The input variables are the turbine speed and torque are the input for the drive model. The output variables are the generator speed ω_r and the generator torque T_r.

Each block is described in details in the following sections.

8.2.1 Tracking characteristic and pitch control

The use of the tracking characteristic for variable speed operation is described in appendix C: the tracking characteristic defines a relation between the upstream wind speed v_u, the turbine angular speed ω_r, the power extracted from the wind P_t and the pitch angle β (Figure C.5). Increasing the pitch angle β results in a limitation of the power absorbed by the turbine (section C.4.1) for wind speeds above the rated value [12]; for wind speed below the rated value the angle β is kept equal to zero[33]. The tracking characteristic used in the present work is displayed in Figure A.1.

[33]As mentioned in chapter 3, pitch angle control may be used to implement DFIG derating because it results in a lower fundamental power flow

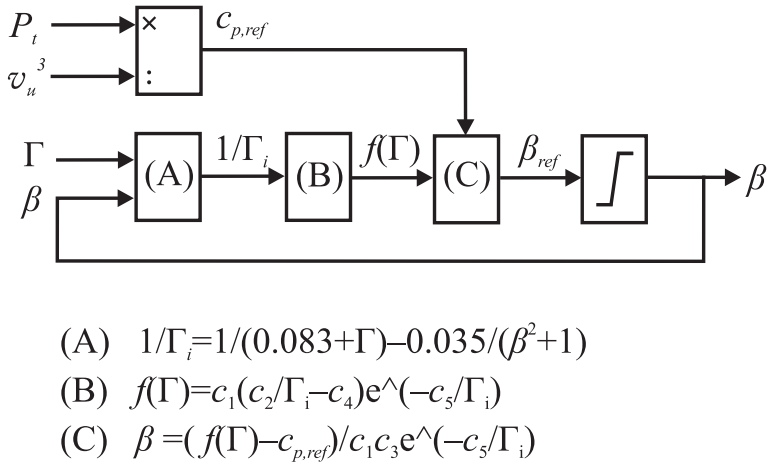

Figure 8.2 - Block diagram for the control of the pitch angle β: the input are the wind speed v_u and the turbine extracted power P_t.

The control system for the determination of the angle β is illustrated in Figure 8.2: the turbine reference power $P_{t,ref}$ is derived from the tracking characteristic depending on the measured wind speed. The ratio between the mechanical power $P_{t,ref}$ and the cube of the wind speed v_u results in the reference power coefficient $c_{p,ref}$ (C.4). The reference pitch angle β_{ref} that corresponds to$c_{p,ref}$ is obtained by inverting (C.4):

$$\beta_{ref} = \frac{c_1(\frac{c_2}{\Gamma_i} - c_4)e^{-c_5/\Gamma_i} - c_{p,ref}}{c_1 c_3 e^{-c_5/\Gamma_i}} \tag{8.2}$$

According to [12, 127], the rate of change that limits the pitch angle variation falls within the interval:

$$5^o/\text{s} < \dot{\beta} < 20^o/\text{s} \tag{8.3}$$

In this work, the selected speed is 10^o/sec. This feature is modeled by including a rate limiter in the block diagram shown in Figure 8.2. The output of the rate limiter is the actual value of the angle β. Table 8.1 displays the values of the mechanical quantities (P_t,ω_t and β) as a function of the wind speed are listed in t

8.2.2 Drive train model

The drive train is described by means of a two-mass model [154, 155, 156] as illustrated in Figure 8.3. In this model, the mass of the drive train is ignored; the two degree of freedom

Table 8.1 - Relation between wind speed, turbine angular speed, power extracted from the wind and blade pitch angle from the tracking characteristic displayed in Figure A.1; v_u=6 m/s is the cut-in speed; v_u=12 m/s is the cut-off speed.

v_u (m/s)	ω_r/ω_1 (p.u.)	P_t/P_n (p.u.)	β (deg)
6	0.50	0.125	0
7	0.58	0.198	0
8	0.67	0.296	0
9	0.75	0.422	0
10	0.83	0.579	0
11	0.92	0.770	0
12	1.00	1.000	0
13	1.08	1.000	3.1
14	1.17	1.000	7.1
15	1.25	1.000	10.3
16	1.33	1.000	12.2
17	1.42	1.000	13.65
18	1.50	1.000	14.7

of the system are the angular position of the turbine θ_t and the angular position of the electrical generator θ_r, measured with respect to an arbitrary reference; in this case the vertical axis has been chosen.

The equations that govern the system are:

$$T_t - T_k = (J_t\ddot{\theta}_t + D_t\dot{\theta}_t) \tag{8.4}$$

$$T_k - T_r = (J_r\ddot{\theta}_r + D_r\dot{\theta}_r) \tag{8.5}$$

$$T_k = k(\theta_t - \theta_r) \tag{8.6}$$

where

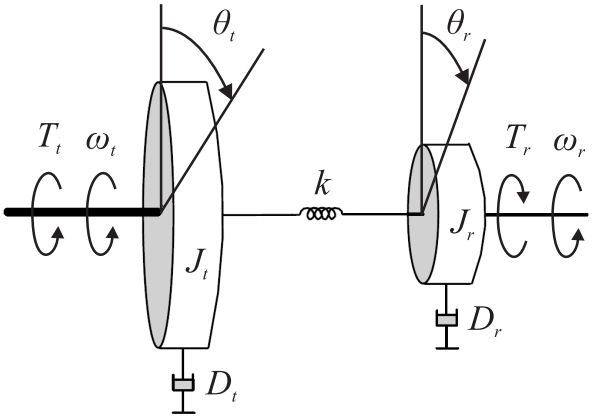

Figure 8.3 - Two mass model used to describe the drive train: the rotating mass on the left corresponds to the wind turbine, the rotating mass on the right corresponds to the electrical generator and the central spring represents the gearbox and the shaft connecting the two rotating masses.

- T_t and T_r (Nm) are the turbine and generator torques;
- J_t and J_r (kg m^2) are the turbine and generator inertias;
- D_t and D_r (kg m^2/s) are the turbine and generator damping coefficients;
- ϑ_t and ϑ_r (rad/s) are the turbine and generator angular positions;
- k (Nm/rad) is the spring constant.

In the differential system (8.4)-(8.6), the variables T_t and ω_t are known; the parameters J_r, J_t and k are also known. The damping coefficients D_t and D_r are ignored: this approximation allows simplifying the system solution without introducing significant deviations from the actual results.

The torque across the spring is determined:

$T_k = T_t - J_t\ddot{\theta}_t$

The generator angle (and consequently the mechanical speed) is carried out:

$\theta_r = \theta_t - T_k/k$

The generator torque is obtained:

$T_r = T_k - J_r\ddot{\theta}$

8.2.3 Solution of the mechanical system

The response of the mechanical system including the wind turbine and the shaft (Figure 8.1) is obtained by solving the following steps:

1. The reference mechanical power P_t and turbine speed ω_t are calculated from the upwind speed v_u by using the data listed in Table 8.1. In case of wind speed magnitude above the rated value, the pitch angle controller is activated and $\beta \neq 0$

   The turbine torque is obtained as follows:

   $$T_t = \frac{P_t}{\omega_t} \tag{8.7}$$

2. The values of T_t and ω_t are the input for the mechanical system (8.4-8.6). The output variables are the generator torque and speed T_r and ω_r.

3. The two mechanical variables T_r and ω_r are the input for the electrical generator.

8.3 Simulation results

The electrical and mechanical responses to different wind speed variations are studied in the following sections. The case studies are chosen to exemplify the wind transients encountered in typical sites: for this reason, different wind speeds with different rates of change are simulated.

The first simulation assumes ideal mechanical response. In the following simulations, the electromechanical actual response is assumed.

The characteristics of the system, including the mechanical parameters, are listed in appendix A. In this set of simulations, the line length is ℓ=1 km.

8.3.1 Slow wind speed variation below the rated value, ideal mechanical response

The wind speed varies between 6 m/s and 8 m/s for $2 \leq t \leq 6$ s, as shown in Figure 8.4; since during the whole simulation time the wind speed is below the rated value, the pitch angle β is equal to zero and the pitch angle control is not activated.

The mechanical system is assumed to be ideal, by ignoring the turbine and generator inertias and damping coefficients, and assuming a rigid shaft (In Figure 8.1, this means $J_t = J_g = 0$, $D_t = D_g = 0$ and k=0). The choice of an ideal mechanical response allows studying exclusively the effects of the wind speed variation on the system's response. The

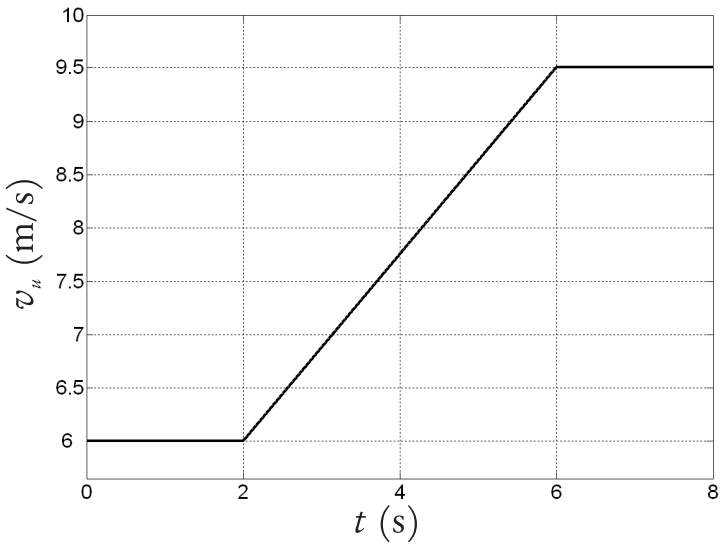

Figure 8.4 - Slow wind speed variation below the rated value, ideal mechanical response: wind speed variation versus time.

effects caused by the mechanical delays and oscillations will be quantified in the following case studies. The shaft speed variation for the ideal mechanical system is presented in Figure 8.5: the shaft speed increases following the same trend of the wind speed.

The dc-link voltage oscillogram is displayed in Figure 8.6. As already observed in the dynamic study carried out in chapter 7, the dc-link voltage control is designed to be stable, not to be fast. Since wind speed variation causes variation in the power flow through the converters, the dc-link voltage oscillogram is not kept exactly constant. In particular, for 2 $\leq t \leq$ 6 s, the dc-link voltage is slightly below the rated value. For $t \geq$ 6 s, when steady state operation is reached, the dc-link oscillogram is noisy.

The voltage measured at the PCC is shown in Figure 8.7 and the corresponding THD is shown in Figure 8.8. The voltage is roughly constant and minimally distorted in spite of the varying power injected into the grid; this observation is numerically quantified by the constant value assumed by the voltage THD[34]. The average voltage THD is about 2 %, but presents some oscillations. These oscillations may be due to numerical truncations, or to low order harmonics circulating in the systems. The oscillations that the dc-link voltage amplitude present (Figure 8.13) may justify the origin of these harmonics.

The constant voltage is a result that is not affected significantly by the line parameters (R_g and L_g): different simulations has been carried out where the line parameters have been increased up to 10 times the values listed in appendix A, with no significant variations

[34]The THD window width is 10 periods of the fundamental harmonic.

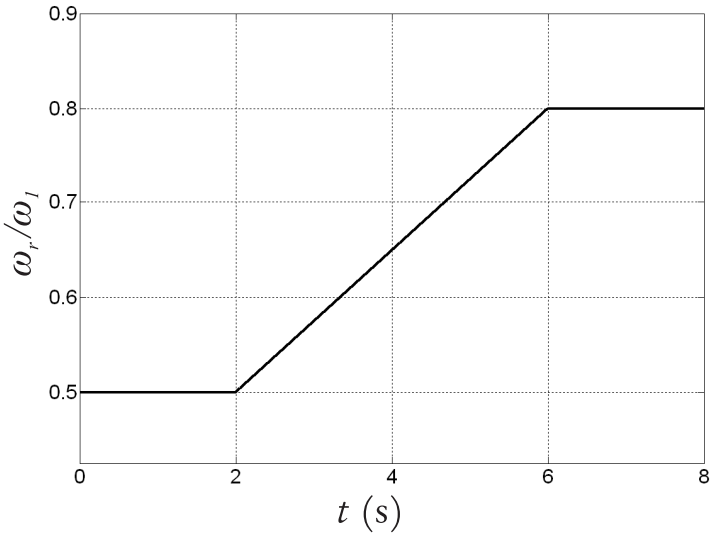

Figure 8.5 - Slow wind speed variation below the rated value, ideal mechanical response: normalized generator speed ω_r/ω_1 versus time.

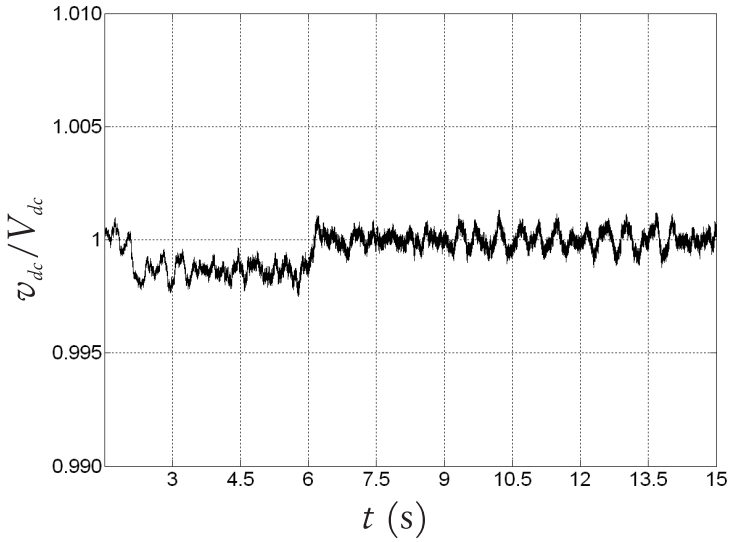

Figure 8.6 - Slow wind speed variation below the rated value, ideal mechanical response: dc-link voltage versus time.

in the voltage oscillogram at the PCC.

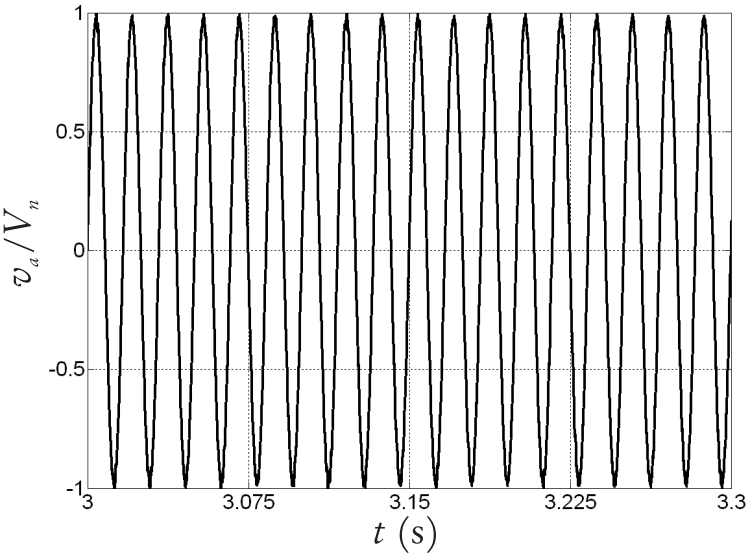

Figure 8.7 - Slow wind speed variation below the rated value, ideal mechanical response: voltage at the PCC for $3 \leq t \leq 3.3$ s.

The normalized current oscillogram measured at the PCC is plotted in Figure 8.9: for $2 \leq t \leq 6$ s, the fundamental component of the grid current increases due to the increase power captured from the wind. A detail of this oscillogram is presented in Figure 8.10: since the grid current waveform has low distortion, the corresponding current THD is below 10 %, as illustrated in Figure 8.11. The current THD decreases in time due to the increase of the fundamental current component delivered to the grid[35].

The power at the PCC is displayed in Figure 8.12. The power delivered to the grid increases repeating the same trend of the current measured at the PCC (Figure 8.9), since the voltage magnitude does not change significantly in time (Figure 8.7).

[35] An alternative quantification of the distortion at the PCC is given by the non fundamental effective apparent power S_{eN} defined by the IEEE Standard 1459 - 2000 [157]. For the system assumed in the present analysis, the fact that the low THD and the symmetry of the system and of the loads result in a value for S_{eN} very close to the current THD. This observation agrees with the IEEE Standard, where, for the above described conditions, it is assumed $S_{eN} \approx \text{THD}_i$.

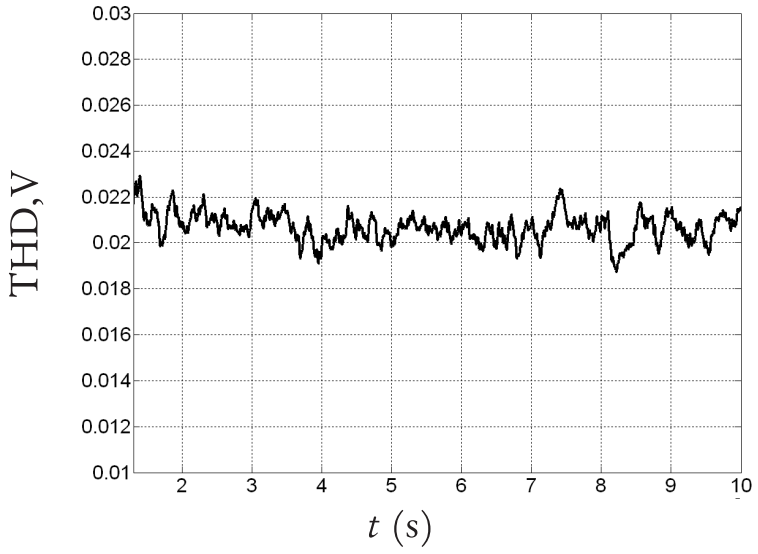

Figure 8.8 - Slow wind speed variation below the rated value, ideal mechanical response: voltage THD measured at the PCC versus time.

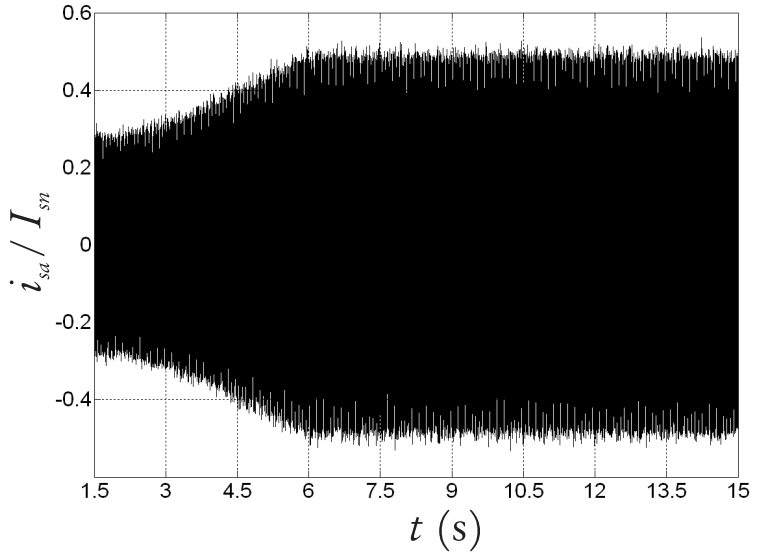

Figure 8.9 - Slow wind speed variation below the rated value, ideal mechanical response: grid current versus time.

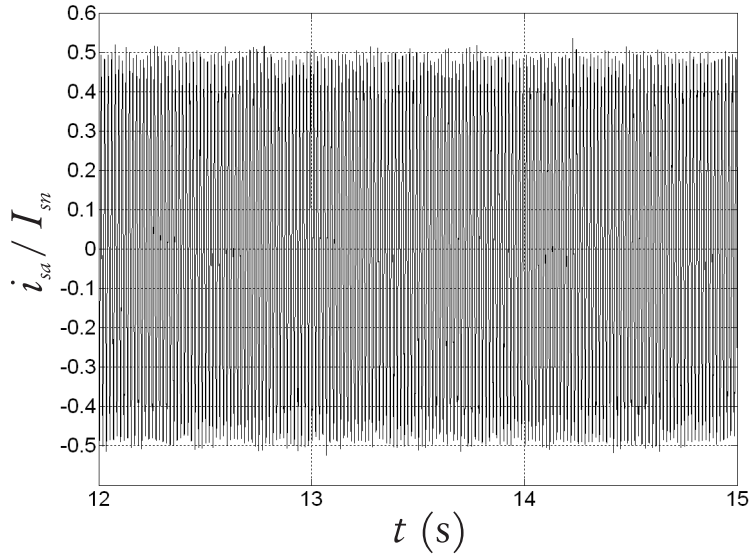

Figure 8.10 - Slow wind speed variation below the rated value, ideal mechanical response: grid current for $12 \leq t \leq 15$ s.

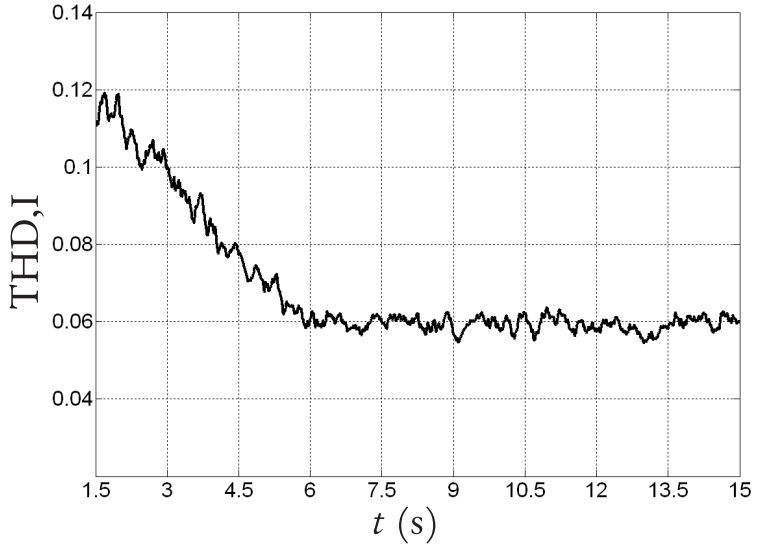

Figure 8.11 - Slow wind speed variation below the rated value, ideal mechanical response: grid current THD versus time.

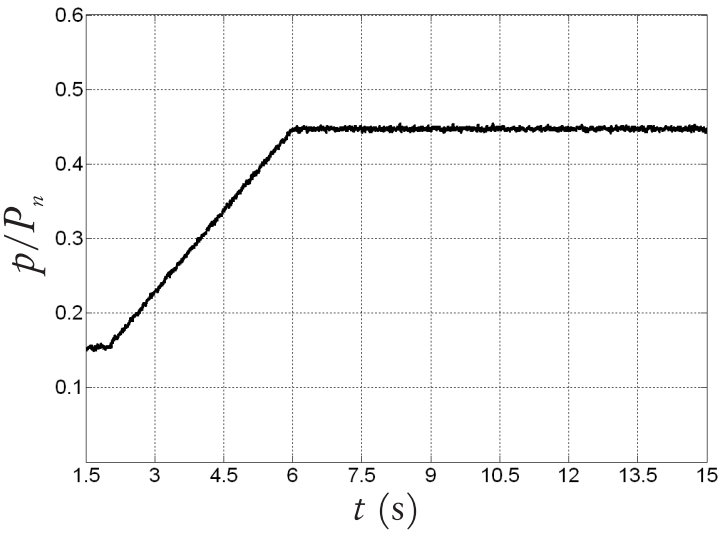

Figure 8.12 - Slow wind speed variation below the rated value, ideal mechanical response: grid power versus time.

8.3.2 Slow wind variation below the rated value, real mechanical response

For the second simulation, the same wind speed variation shown in Figure 8.4 is assumed, but the inertias of the mechanical system and the elastic coupling between turbine and generator are taken into account.

Due to non idealities of the mechanical system, the generator response is delayed and slower than the wind variation: while the wind speed variation takes place for $2 < t < 6$ s (Figure 8.4), the transient of the mechanical system is slightly delayed and lasts around 100 seconds, as illustrated in Figure 8.13. To visualize better the different dynamics, in Figure 8.14 the wind speed variation and the rotor speed transient are shown on the same time scale.

The dc-link voltage oscillogram is displayed in Figure 8.15. For $2 < t < 6$ s, the dc-link voltage variation is more evident than in the case of ideal mechanical response (Figure 8.6); nevertheless, the voltage drop with respect to the rated value is still very small. A more significant difference is related to the long term transient: the dc-link voltage variation follows the rotor speed oscillations, although with a reduced amplitude. The dc-link voltage magnitude oscillations are caused by the variation of power flow through the RSC and the LSC.

The stator current oscillogram is presented in Figure 8.16. The fundamental component

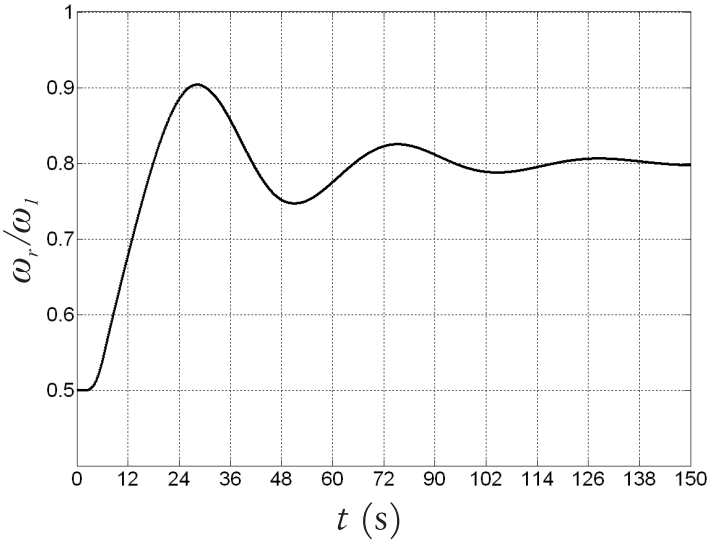

Figure 8.13 - Slow wind variation below the rated value, real mechanical response: normalized generator speed ω_r/ω_1 versus time.

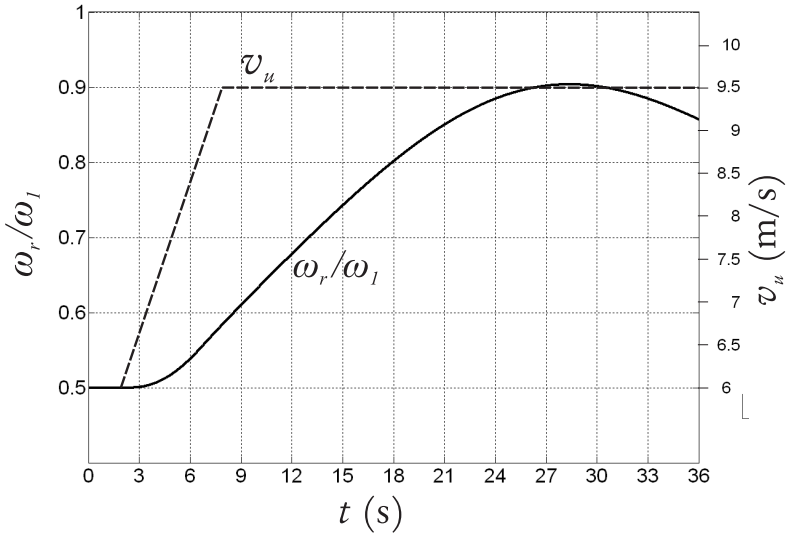

Figure 8.14 - Slow wind variation below the rated value, real mechanical response: wind speed and normalized generator speed for $0 \leq t \leq 36$ s.

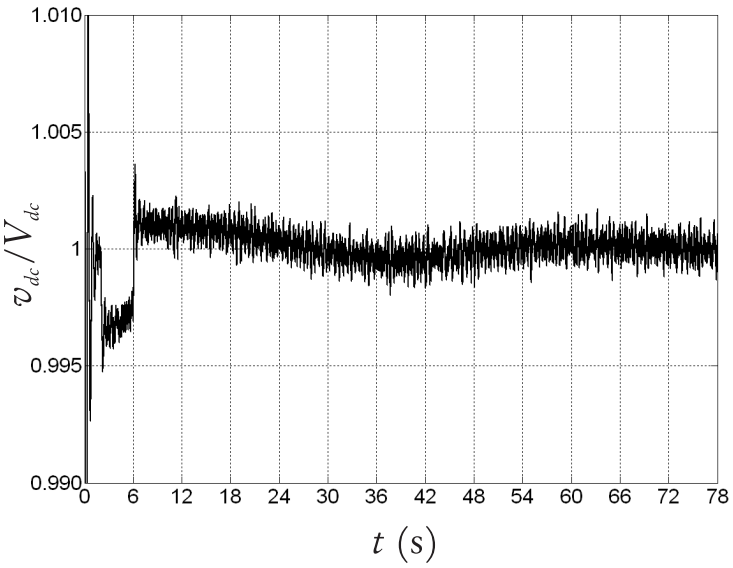

Figure 8.15 - Slow wind variation below the rated value, real mechanical response: dc-link voltage versus time.

of the stator current is derived from the mechanical power extracted from the wind. Since the response of the power converters is practically instantaneous [153], the stator current rises to the rated value simultaneously to the increase of the wind speed. The spikes in the stator current oscillogram are due to the harmonic current injection.

Figure 8.17 shows the oscillogram of the rotor current for the whole simulation time. Since the rotor is magnetically coupled to the stator, a similar transient takes place in the stator current oscillogram (Figure 8.16) and in the rotor current oscillogram (Figure 8.17), for $2 \leq t \leq 6$ s. The oscillations in the shaft speed (Figure 8.13) result in a variation in rotor current frequency. Figures 8.18 and 8.19 help visualizing the variation in rotor current frequency by dysplaing the details of rotor current oscillograms for two different time intervals. The rotor current frequency corresponding to the two time intervals is calculated in Table 8.2. In the same table, the value of the slip is calculated too; since the steady state value of the normalized rotor speed is 0.8 for the given wind speed, it is expected to obtain a steady state slip equal to 20 %.

The remaining results show the performance at the PCC. The voltage oscillogram presented in Figure 8.7 shows the voltage at the PCC for $6 \leq t \leq 6.3$ s. The voltage is roughly constant in spite of the variation of power injected into the grid and in spite of the variations of rotor speed. As a consequence, the voltage THD is low and approximately constant. These results are very similar to the ones presented in the case of ideal mechanical response.

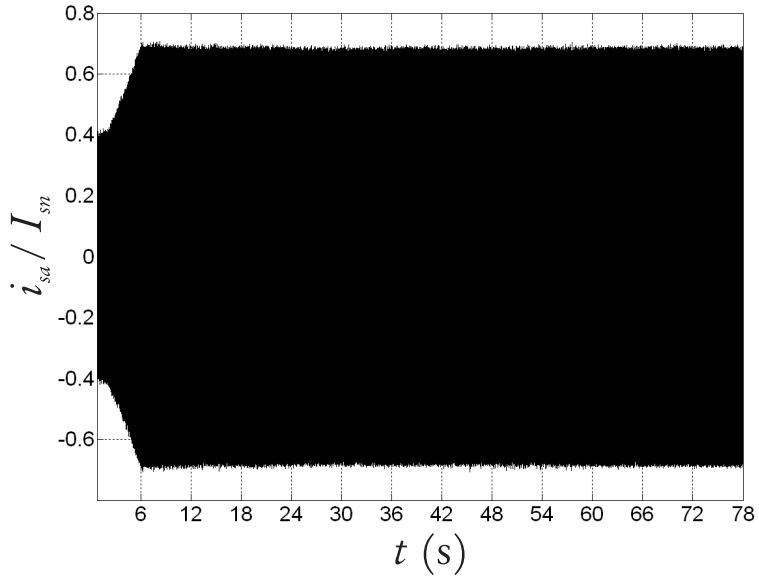

Figure 8.16 - Slow wind variation below the rated value, real mechanical response: stator current versus time.

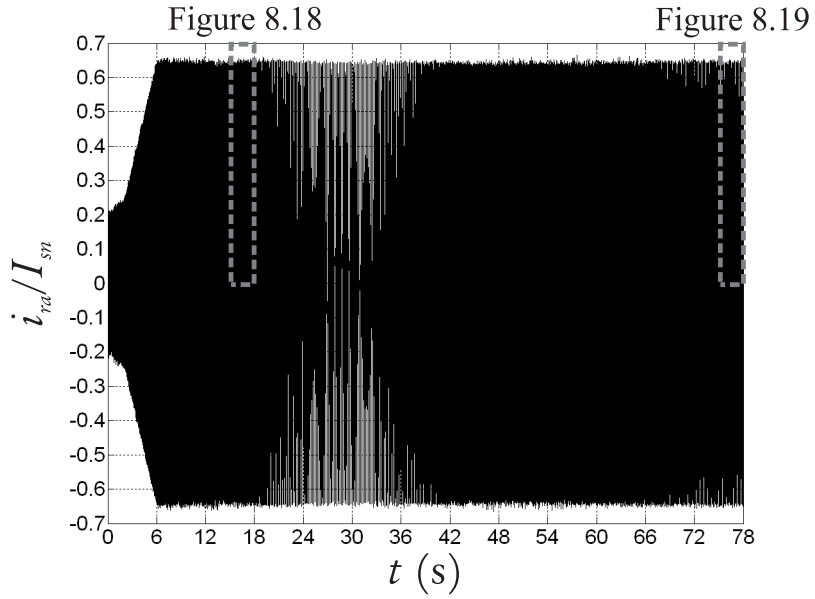

Figure 8.17 - Slow wind variation below the rated value, real mechanical response: normalized rotor current versus time.

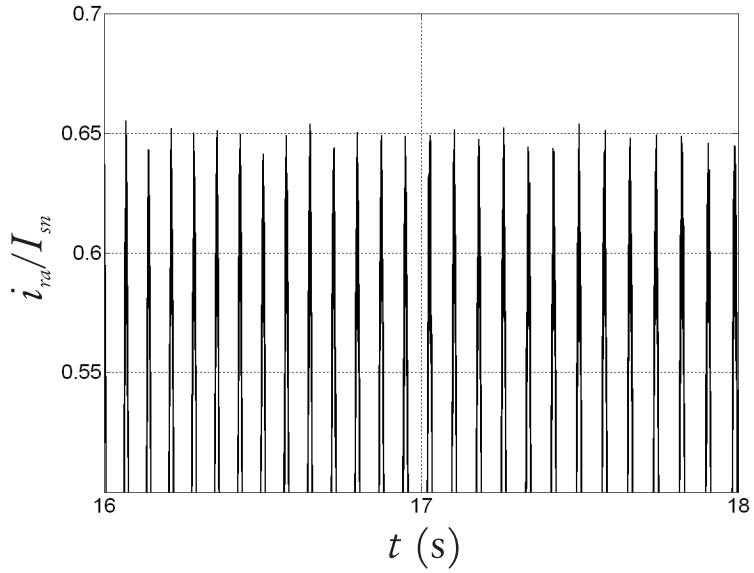

Figure 8.18 - Slow wind variation below the rated value, real mechanical response: normalized rotor current for 16 $\leq t \leq$ 18 s.

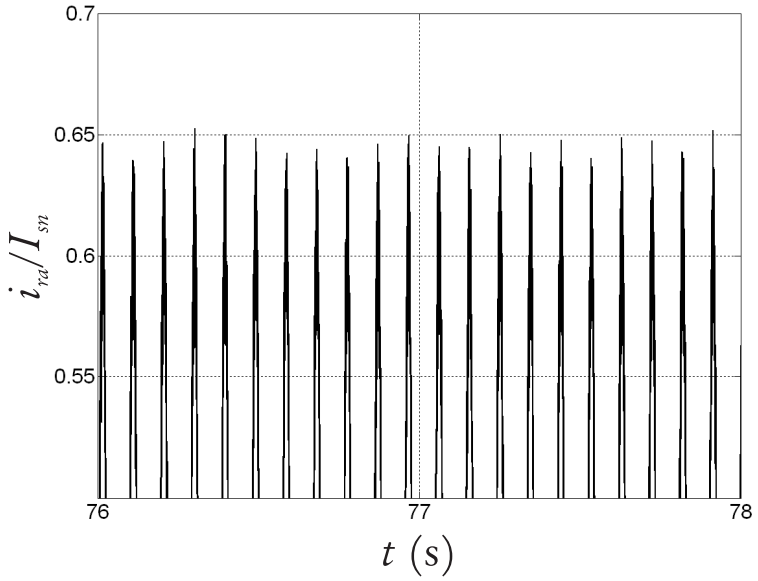

Figure 8.19 - Slow wind variation below the rated value, real mechanical response: normalized rotor current for 76 $\leq t \leq$ 78 s.

Table 8.2 - Rotor current frequency calculated for two different time intervals: the rotor current is obtained as the ratio of the number of periods and the time interval.

	t_1 (s)	t_2 (s)	Δ_t (s)	N	$f_r = \mathrm{N}/\Delta t$ (Hz)	slip
Figure 8.18	16	18	2	≈ 21	≈ 10.5	≈ 21.67
Figure 8.19	76	78	2	≈ 26	≈ 13	≈ 17.5

In particular, this is due to the fact that the line connecting the WECS to the PCC is stiff. In section 8.4 the effects of line lenght will be investigated.

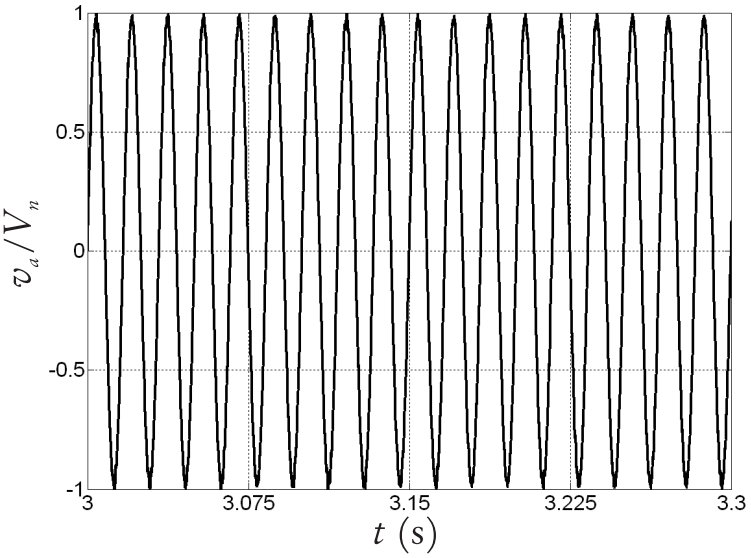

Figure 8.20 - Slow wind speed variation below the rated value, real mechanical response: voltage at the PCC for 3$\leq t \leq$ 3.3 s.

The grid current oscillogram is illustrated in Figure 8.22; a detail of this plot for $12 \leq t \leq 15$ s is displayed in Figure 8.23.

The oscillogram depicted in Figure 8.22 shows that the current delivered to the grid increases due to the higher power captured from the wind, similarly to the results presented in the previous simulations. However, for the present case, there are low frequency oscillations due to the variations of the shaft speed (Figure 8.13). The low frequency oscillations do no affect significantly the current distortion; this observation is quantified numerically by studying the current THD oscillogram represented in Figure 8.24. The THD decreases fast for $t \leq 6$ s in correspondence of the wind speed increase, due to the increasing amplitude

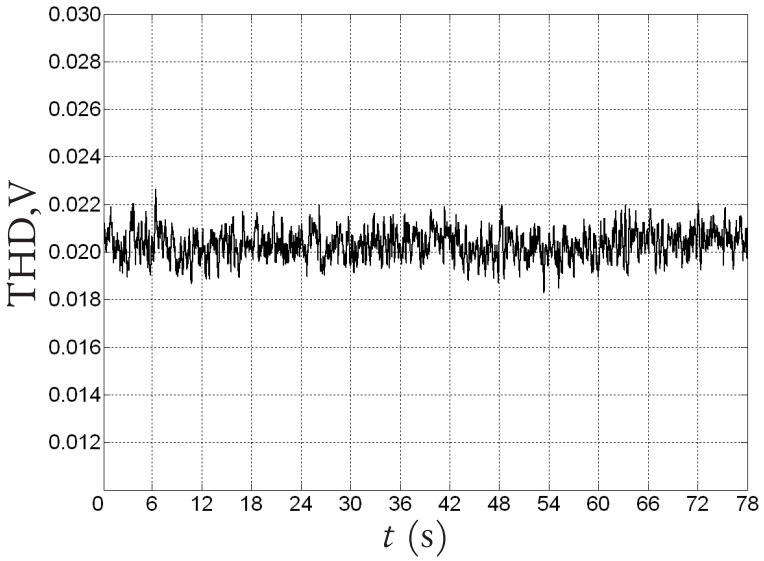

Figure 8.21 - Slow wind variation below the rated value, real mechanical response: voltage THD measured at the PCC, versus time.

of the fundamental component of the grid current. For $t \geq 6$ s, the current THD stabilizes around the value 0.06.

By comparing the two details of the grid current oscillogram Figure 8.10 and Figure 8.23, one concludes that the mechanical transient contributes to slow the grid current response.

The total power delivered at the PCC is depicted in Figure 8.25. The power delivered to the grid increases due to the increasing stator current. The initial slope is slower than in Figure 8.12. The oscillation around the average value are caused by the variation of the shaft speed.

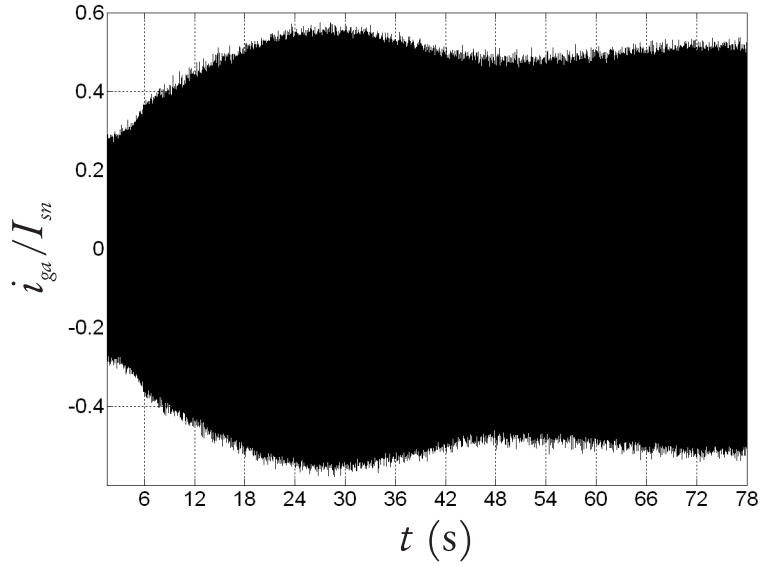

Figure 8.22 - Slow wind variation below the rated value, real mechanical response: grid current versus time.

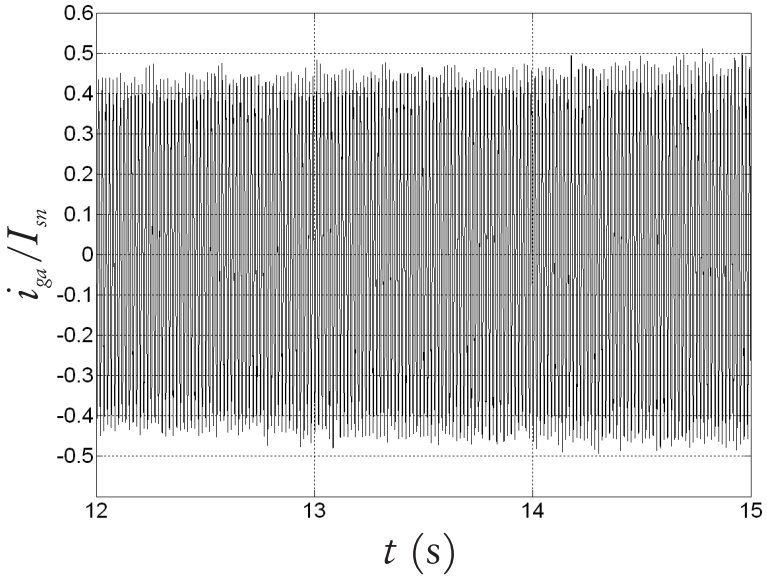

Figure 8.23 - Slow wind variation below the rated value, real mechanical response: grid current for $12 \leq t \leq 15$ s.

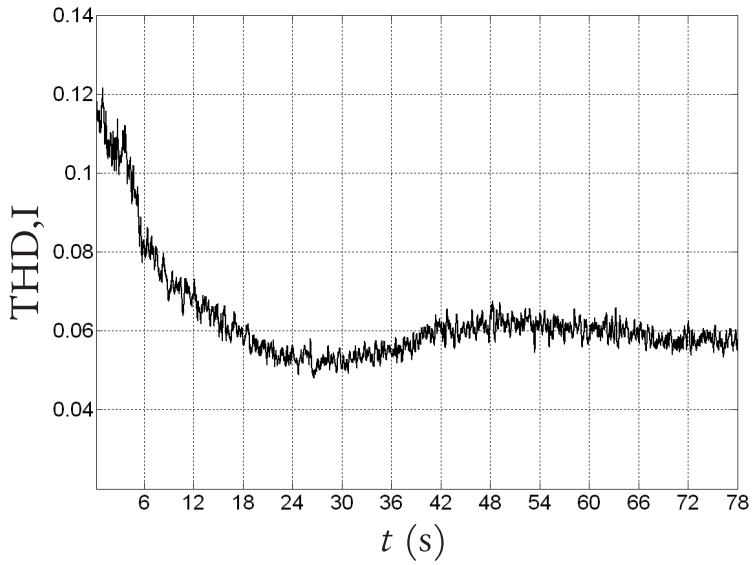

Figure 8.24 - Slow wind variation below the rated value, real mechanical response: grid current THD versus time.

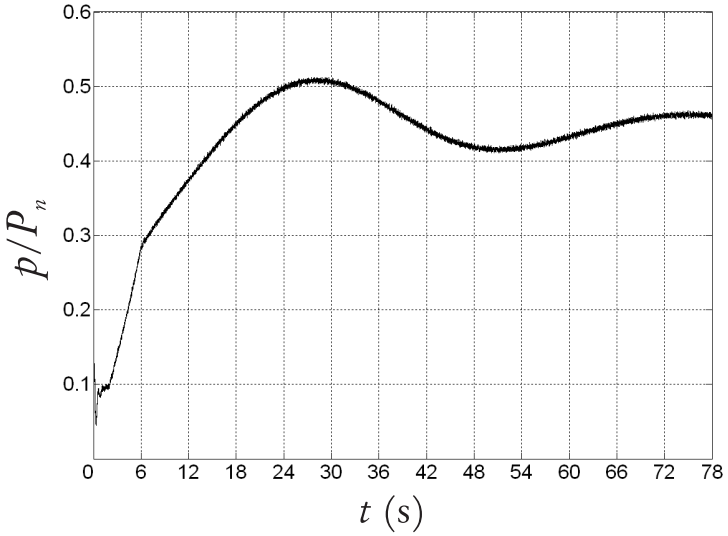

Figure 8.25 - Slow wind variation below the rated value, real mechanical response: grid power versus time.

8.3.3 Slow wind variation above the rated value, real mechanical response

The wind speed variation for the present case is presented in Figure 8.4: for $2 \leq t \leq 6$ s, the wind speed ramps from 12 to 14 m/s.

Since the initial wind speed is equal to the design value and then further increases, a corresponding increase of the angle β is expected. The pitch angle variation is displayed in Figure 8.27: the assumed wind variation is relatively slow and therefore the rate limiter doesn't affect the trajectory of β. One observes that although the wind speed variation is linear, the variation of β follows a non linear trajectory, due to the many variables that are involved in the pitch angle control (section 8.2.1). The initial value of β is higher than zero because derating is applied: an angle equal to 1.7 deg for a wind speed of 12 m/s allows reducing the power absorption from the wind to 0.8 of the rated value, according to (C.5).

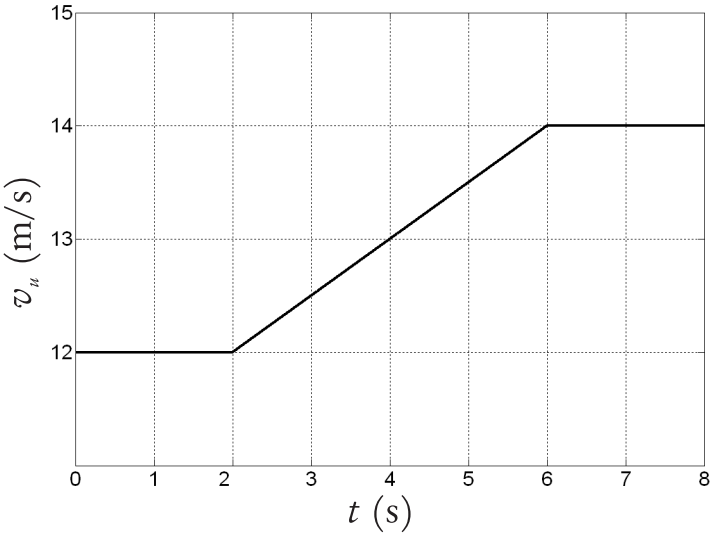

Figure 8.26 - Slow wind variation above the rated value, real mechanical response: wind speed variation versus time.

The shaft speed variation is presented in Figure 8.5. The shaft speed increases due to the increase of the wind speed, and the oscillations are due to the elastic coupling between the turbine and the generator. This result is similar to the one displayed in the previous example (Figure 8.13); however the oscillations amplitude is larger, due to the higher wind speed values assumed in the present simulation and to the consequent higher power absorbed from the wind.

The stator current oscillogram is presented in Figure 8.29. This oscillogram shows that

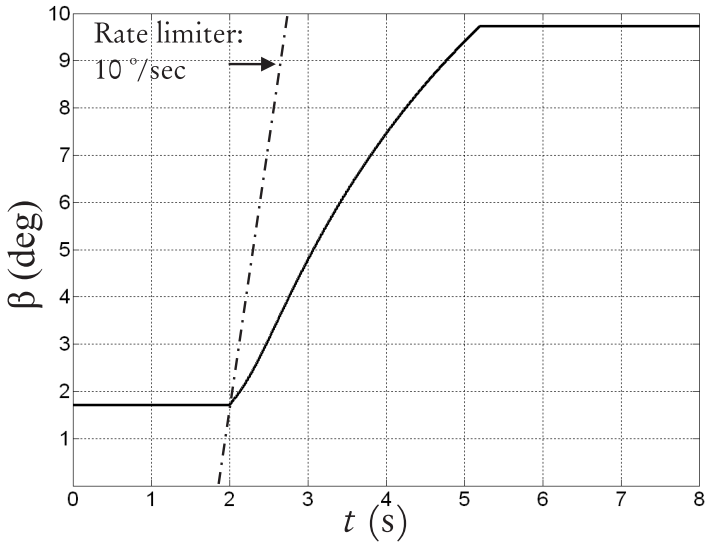

Figure 8.27 - Slow wind variation above the rated value, real mechanical response: pitch angle variation versus time.

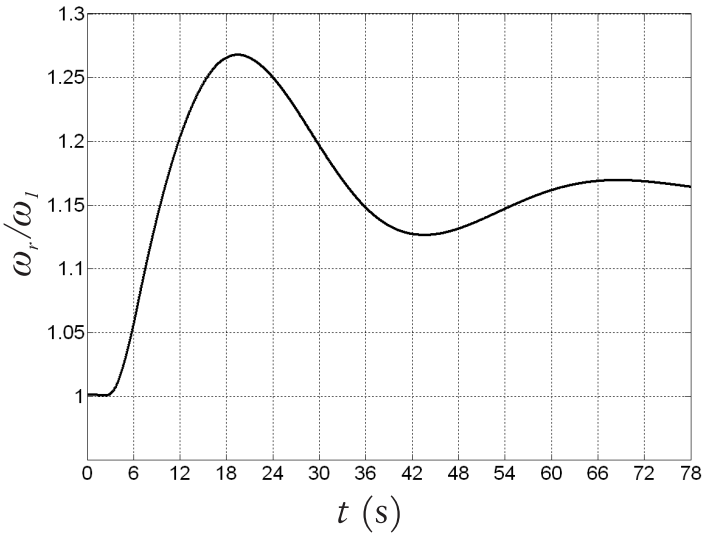

Figure 8.28 - Slow wind variation above the rated value, real mechanical response: normalized generator speed ω_r/ω_1 versus time.

the stator current is constant and equal to the rated value through the entire simulation. This result is expected since for the assumed wind speeds the power absorbed by the turbine is equal to the rated power and determines the amplitude of the fundamental stator current component.

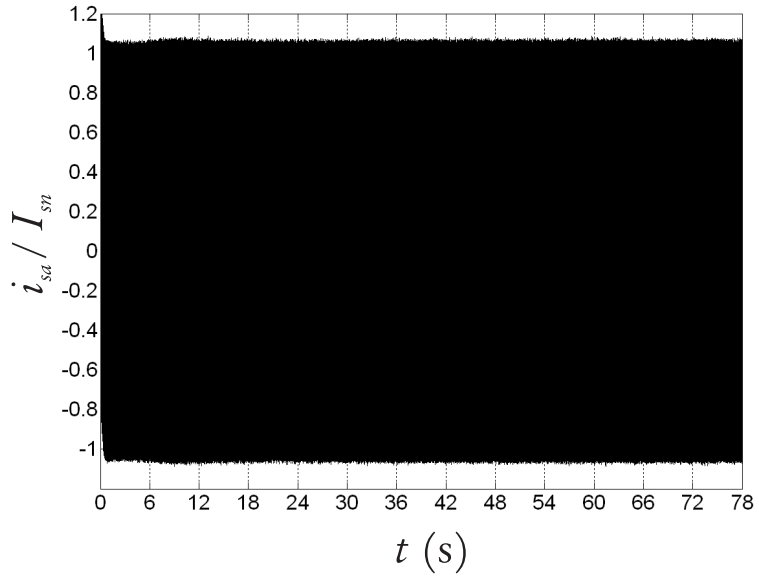

Figure 8.29 - Slow wind variation above the rated value, real mechanical response: stator current versus time.

The voltage at the PCC is displayed in Figure 8.30: the oscillogram shows a constant amplitude and negligible distortion, similarly to the previous simulations. As a consequence, the voltage THD is constant and small, as illustrated in Figure 8.31.

The grid current oscillogram is presented in Figure 8.32: the effect of the mechanical system's oscillations is similar to the one studied in the previous sections. In spite of the low frequency oscillations, the current distortion is minimal: the current THD oscillogram represented in Figure 8.33 is constant and very low, due to the high fundamental current injection.

The total power delivered at the PCC is depicted in Figure 8.34. Similarly to the previous simulation, the mechanical system's oscillations are reflected in the power transferred to the main grid.

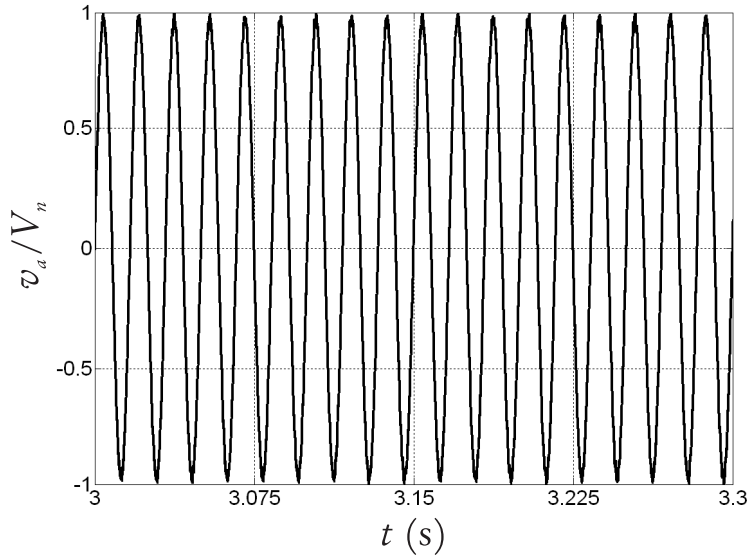

Figure 8.30 - Slow wind variation above the rated value, real mechanical response: voltage at the PCC versus time.

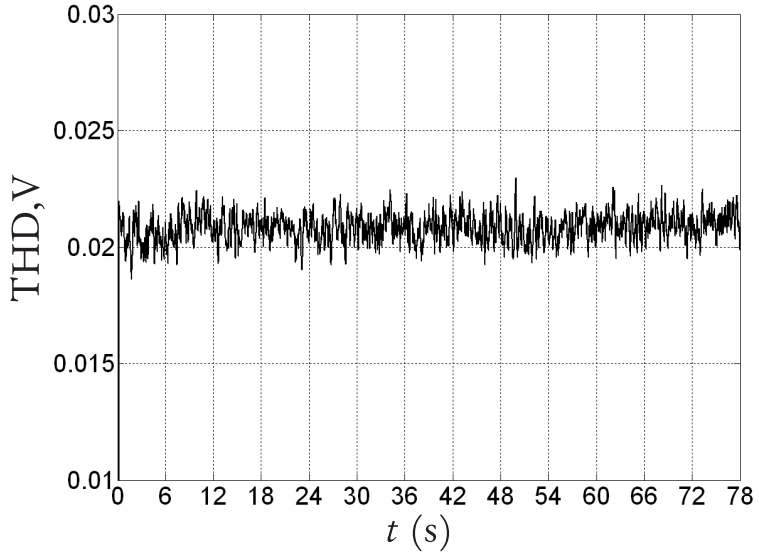

Figure 8.31 - Slow wind variation above the rated value, real mechanical response: voltage THD measured at the PCC versus time.

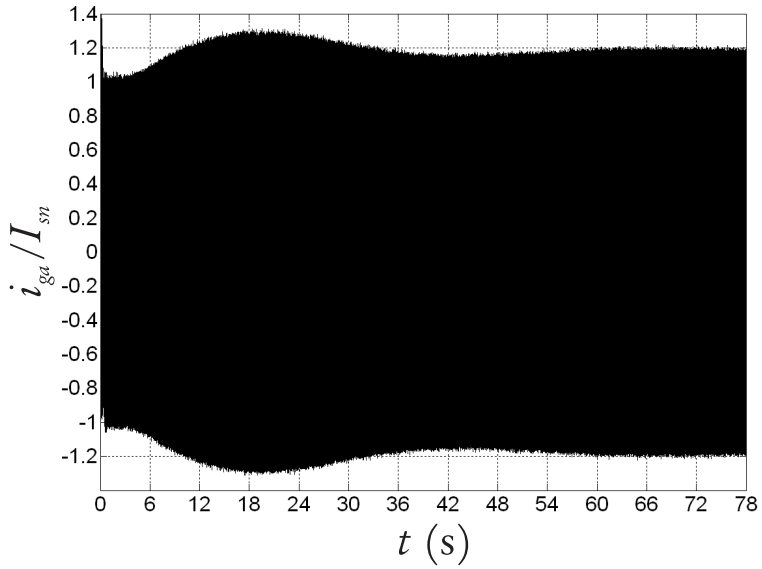

Figure 8.32 - Slow wind variation above the rated value, real mechanical response: normalized grid current versus time.

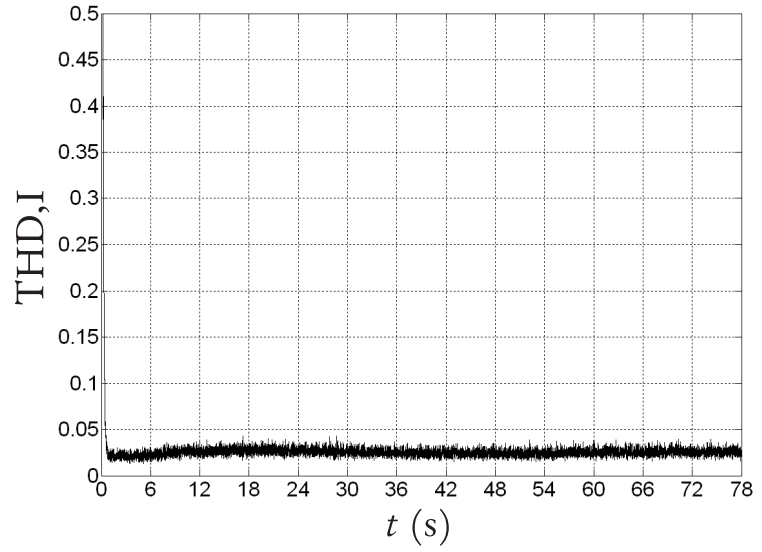

Figure 8.33 - Slow wind variation above the rated value, real mechanical response: normalized grid current THD versus time.

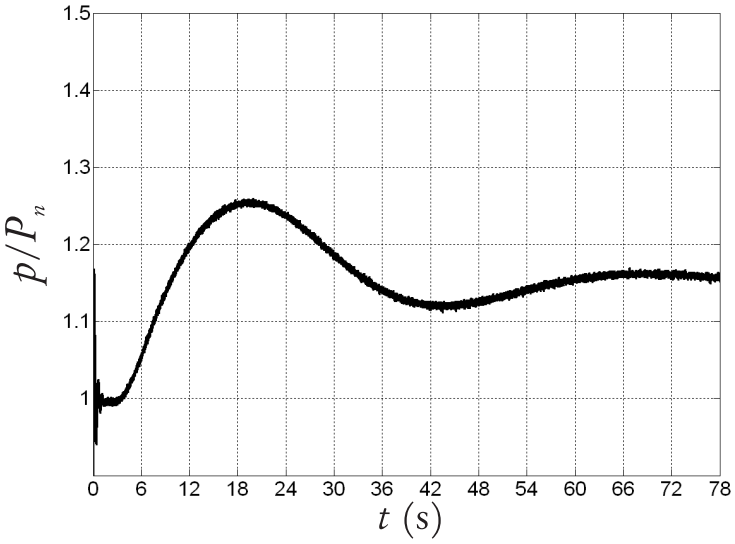

Figure 8.34 - Slow wind variation above the rated value, real mechanical response: normalized grid power versus time.

8.3.4 Fast wind variation above the rated value, real mechanical response

The wind speed variation is presented in Figure 8.4: for $2 \leq t \leq 3$ s, the wind speed ramps from 12 to 16 m/s. As a result, the wind speed variation is characterized by an higher slope with respect to the previous cases.

Being the wind speed equal or above the rated values for all the simulation time, the pitch angle β is expected to be different from zero, according to Table 8.1. For the present case study, since the wind speed variation is very rapid, the consequent dynamics of the pitch angle is fast: therefore the inertia of the blades, represented by the rate limiter in Figure 8.2, acts to slow the increase of β. As a result, the pitch angle β varies following a ramp (Figure 8.36) and the steady state value is reached with a delay with respect to the wind speed[36].

Due to the delay of β variation with respect to the wind variation, it results that the mechanical power absorbed by the turbine is greater than the rated power for $2 \leq t \leq 4.2$ s.

The shaft speed response is shown in Figure 8.5 and it presents a delay with respect to the wind speeds and transient oscillations as in the previous cases.

[36]If a more complete model of the β regulator were used, oscillations superposed to the linear variation would have been detected. However, for the purpose of the present work, the assumed simplified model is an acceptable approximation.

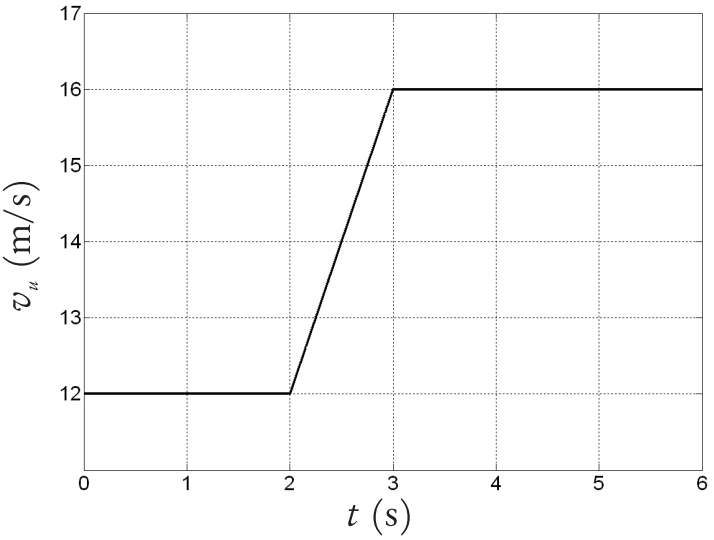

Figure 8.35 - Fast wind variation above the rated value, real mechanical response: wind speed variation versus time.

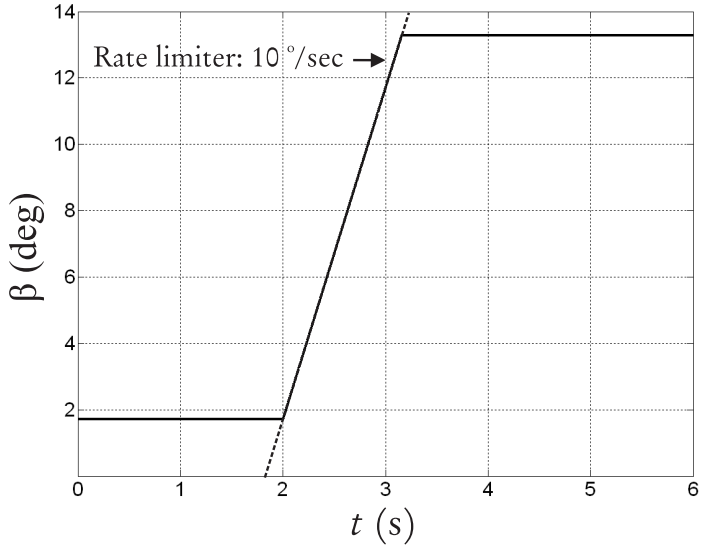

Figure 8.36 - Fast wind variation above the rated value, real mechanical response: pitch angle variation versus time.

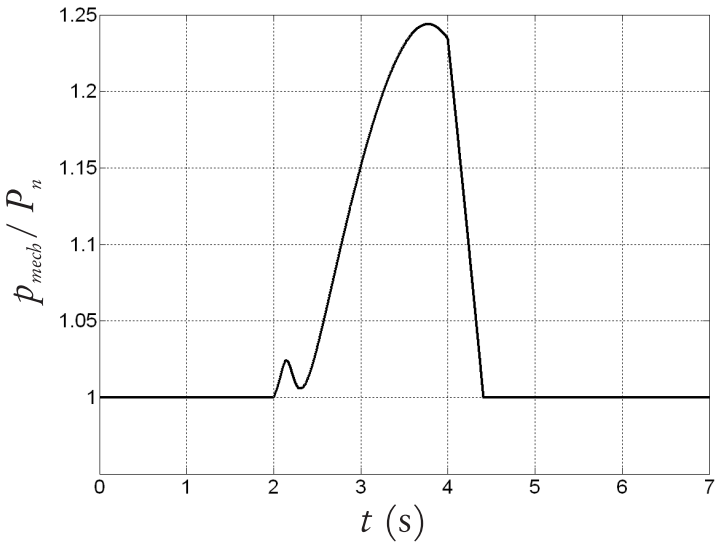

Figure 8.37 - Fast wind variation above the rated value, real mechanical response: normalized power absorbed from the wind versus time.

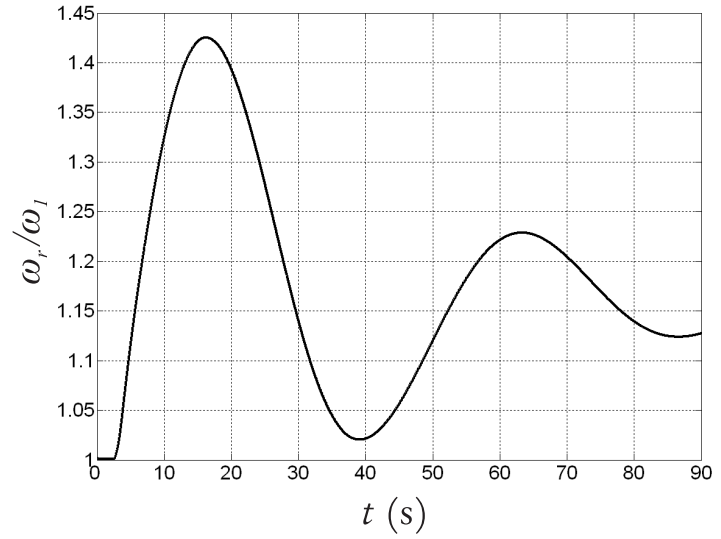

Figure 8.38 - Fast wind variation above the rated value, real mechanical response: normalized generator speed ω_r/ω_1 versus time.

The power delivered to the grid is plotted in Figure 8.39. Two types of disturbances can be identified, as a result of the mechanical system response. The first disturbance is a glitch caused the delay of the pitch angle response (for $2 \leq t \leq 4.2$). The second disturbance is caused by oscillations of the current amplitude due to shaft speed variations.

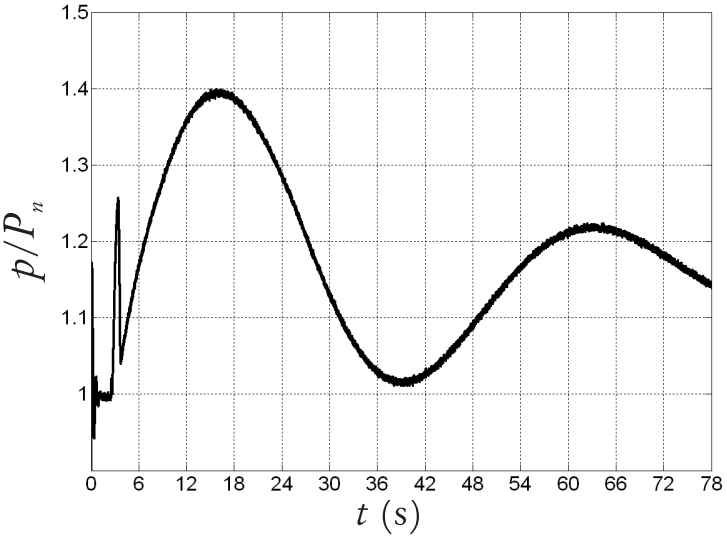

Figure 8.39 - Slow wind variation with mechanical transient: grid power.

The current delivered to the grid has a similar trend as the power (Figure 8.40). The current THD is approximately constant since the amplitude of the fundamental grid current is significantly high, as shown in Figure 8.41.

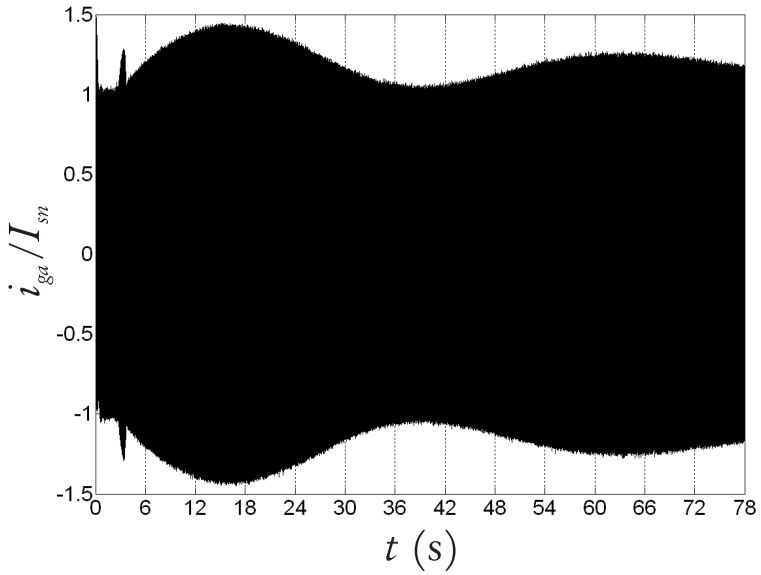

Figure 8.40 - Fast wind variation with mechanical transient: normalized grid current versus time.

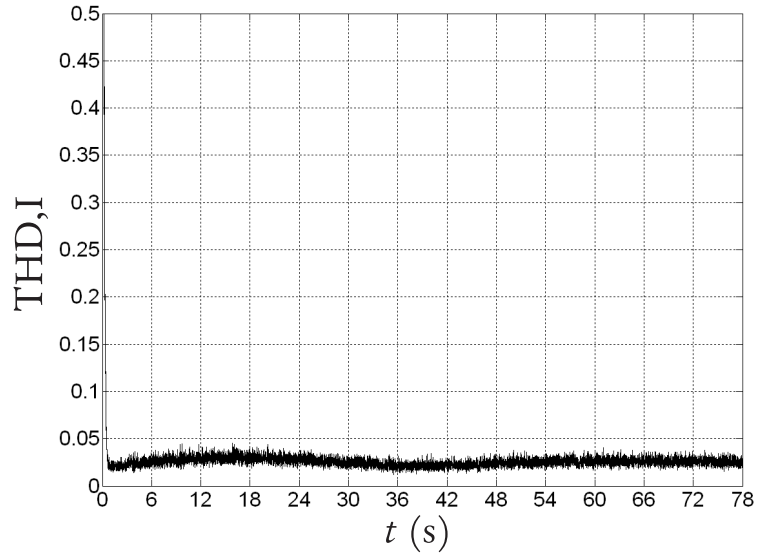

Figure 8.41 - Fast wind variation with mechanical transient: normalized grid current THD versus time.

8.4 Effects of the line length

The simulation results illustrated in the previous sections show that, while the amplitude of the current injected by the WECS into the grid may be significantly affected by the wind speed variation, the voltage is practically constant. This result depends on the particular configuration assumed: the transmission line is short, meaning that the voltage drop across $\bar{Z}_g$ is negligible: therefore, the voltage at the PCC is practically coincident with the voltage impressed by the equivalent voltage source v_g (Figure 3.1).

This configuration has been chosen to simplify the analysis, but is not realistic. As discussed in chapter 1, in-land and off-shore large wind plants are generally built in remote location, where the wind blows faster, there is more space for the installation of the turbines and there are less complaints from the residents regarding landscape alteration and acoustic noise. The choice to build wind power plants far from the residential areas implies a long transmission line to transfer the wind power to the users [7].

The scope of this section is to identify the effects of the line length on the voltage and current oscillograms. The same speed variations described in Sections 8.3.2-8.3.4 are assumed, while the line impedance $\overline{Z}_g$ has been increased by a factor of ten to model a longer transmission line.

The case of slow speed variation below the rated value is studied first and the results are displayed in Figure 8.42. The active power and current waveforms (Figures 8.42.a and .b, respectively) overlap with the ones presented in Figures 8.22 and 8.25, since they depend on the wind speed and the power extracted from the turbine only and not on the line length. The normalized line-to-ground voltage measured at the PCC presents a minimal deviation from the rated value (Figure 8.42.c): this result can be attributed to the fact that the assumed wind speed variation results in a small increase of the current delivered to the grid and the changes in the voltage drop across $\overline{Z}_g$ are not detectable.

The results for the case of slow speed variation above the rated value are displayed in Figure 8.43. Similarly to the previous case, the active power and current waveforms (Figures 8.43.a and .b, respectively) overlap with the one obtained for short transmission line. The normalized line-to-ground voltage measured at the PCC presents a swall in correspondance of the current increase during the interval $6 \leq t \leq 36$ s (Figure 8.43.c). During this time interval, the current injected into the grid increase by 20 % of the rated value, and the variation of the voltage drop across Z_g has a visible effect on the voltage at the PCC.

The system response to a fast wind speed variation above the rated value is the last case study, and the results are presented in Figure 8.44. The active power and current waveforms displayed in Figures 8.44.a and .b, correspond to one obtained for the case of short line.

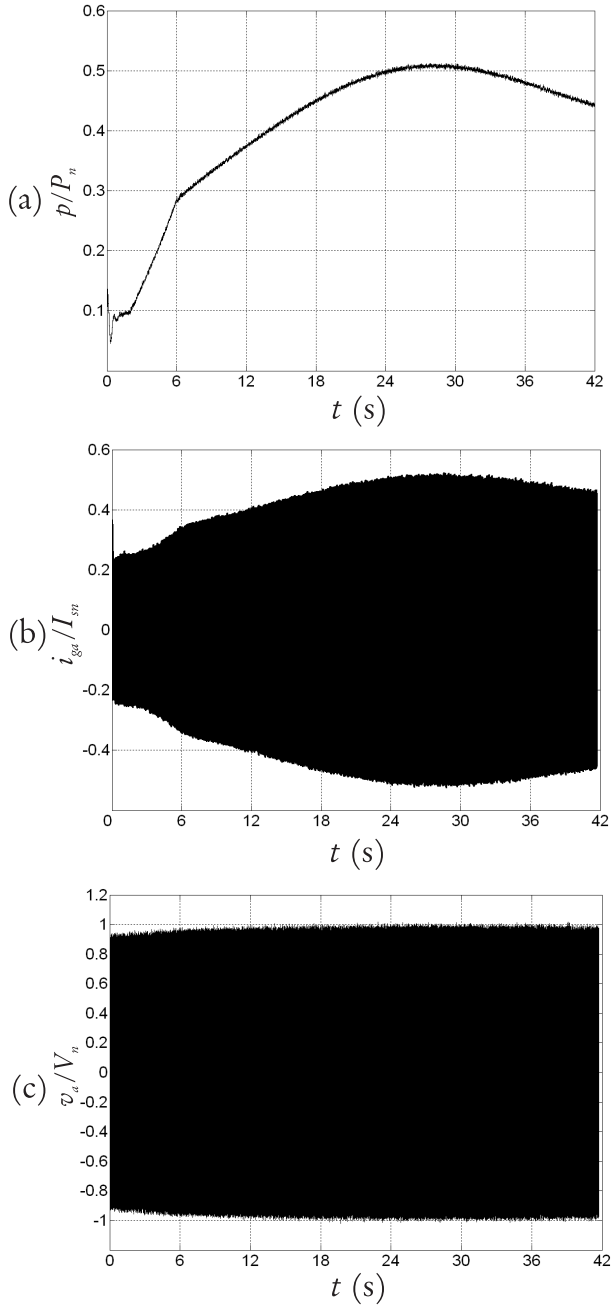

Figure 8.42 - Normalized oscillograms for wind speed variation below the rated value, ℓ=10 km: (a) Instantaneous active power, (b) Line current and (c) Voltage at the PCC.

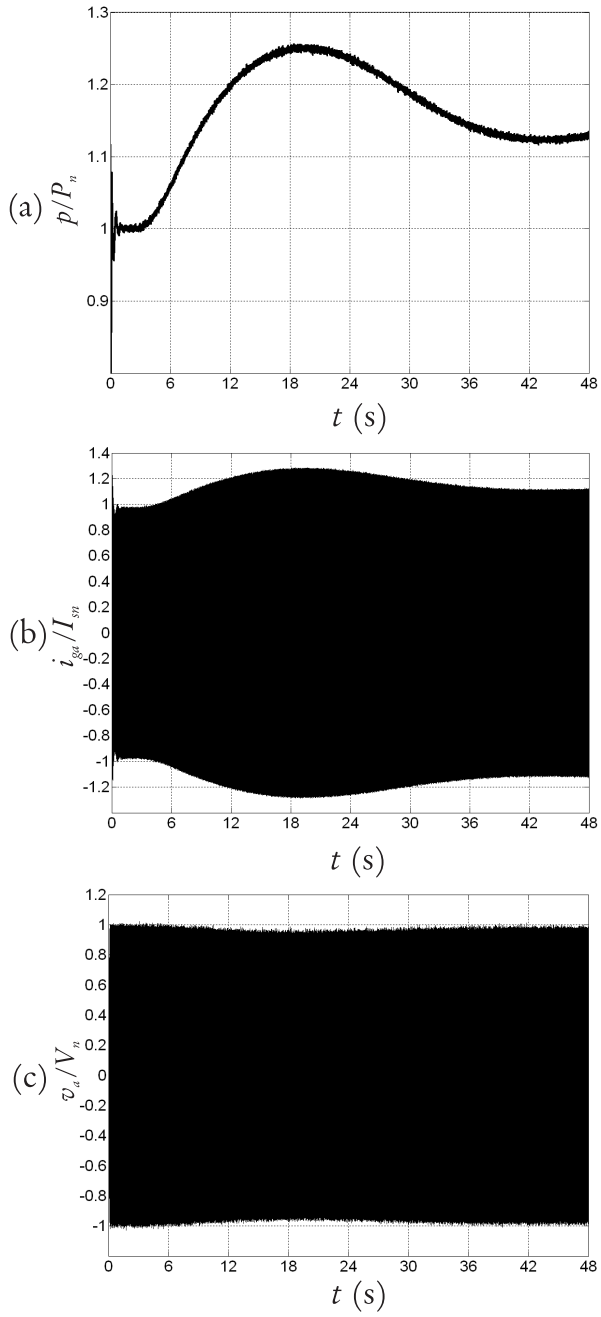

Figure 8.43 - Normalized oscillograms for slow wind speed variation above the rated value, ℓ=10 km: (a) Instantaneous ctive power, (b) Line current and (c) Voltage at the PCC.

The normalized line-to-ground voltage measured at the PCC present a dip equal to 20 % of the rated voltage. This result is due to the significant variation in the grid current injected by the WECS.

The last results indicate that if the transmission line is long and the wind speed varies suddenly and significantly, the oscillations of the voltage amplitude at the PCC are not acceptable. They may lead to malfunctioning and damage of other loads connected to the same PCC and to grid instability.

A further observation results from observing the voltage waveforms in Figure 8.42-8.44. The voltage at the PCC is equal to the rated value when the rated current is injected by the WECS. For current magnitude lower than the rated value, the voltage at the PCC is less than the rated value; conversely, for current magnitude above the rated value, the voltage rises above 1 p.u. This last observations suggest implementation of voltage regulation by control of the reactive power injection.

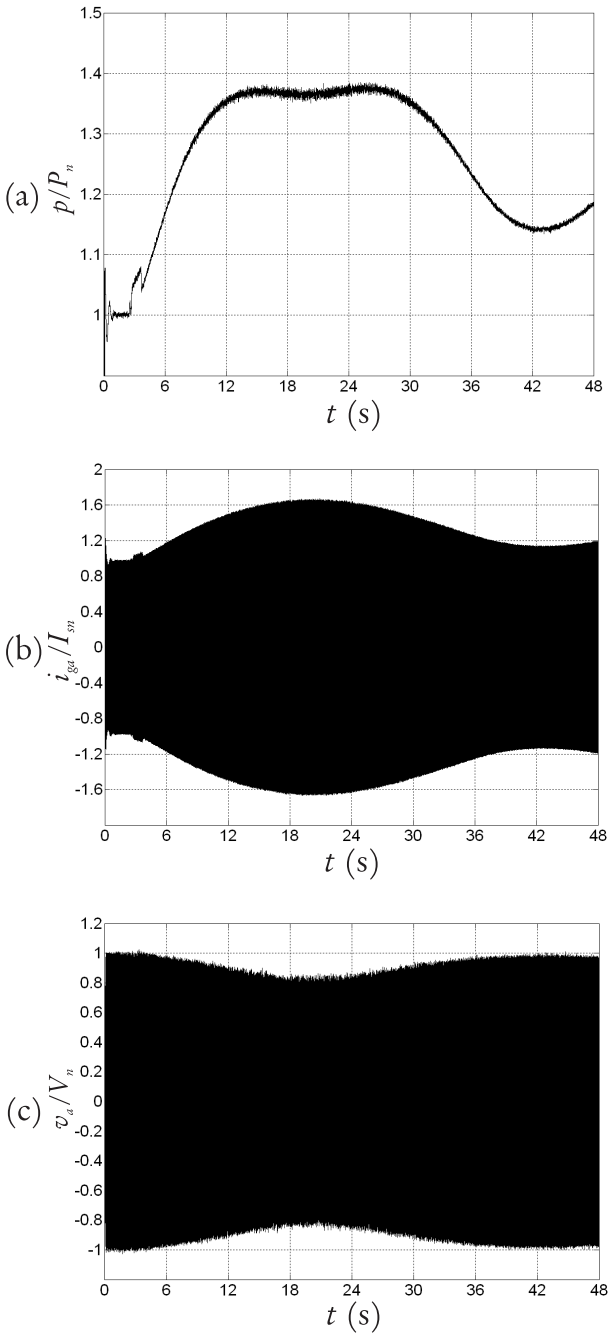

Figure 8.44 - Normalized oscillograms for fast wind speed variation above the rated value, ℓ=10 km: (a) Instantaneous active power, (b) Line current and (c) Voltage at the PCC.

8.4.1 Reactive power control

WECSs based on DFIG technology have the ability to control active and reactive power independently (chapter 1: this property can be used to perform voltage regulation. Implementing voltage regulation by proper modulation of the RSC and LSC results in several advantages, including rapidity of regulation and use of the already installed system components. However, the physical limitations of the DFIG must be taken into account in the design of the reactive power control. The DFIG physical limitations to inject reactive power consist in: stator current amplitude limitation, rotor current amplitude limitation and stability limits [64, 65, 118, 158].

The above listed limitations are exemplified for a a 2.75 MW unit in Figure 8.45, where the stator reactive power is plotted as function of the stator active power. Reactive power injection is upper limited by the stability limit, lower power injection is limited by the stator current limit, and it results that the DFIG ability to limit reactive power is not symmetric [64].

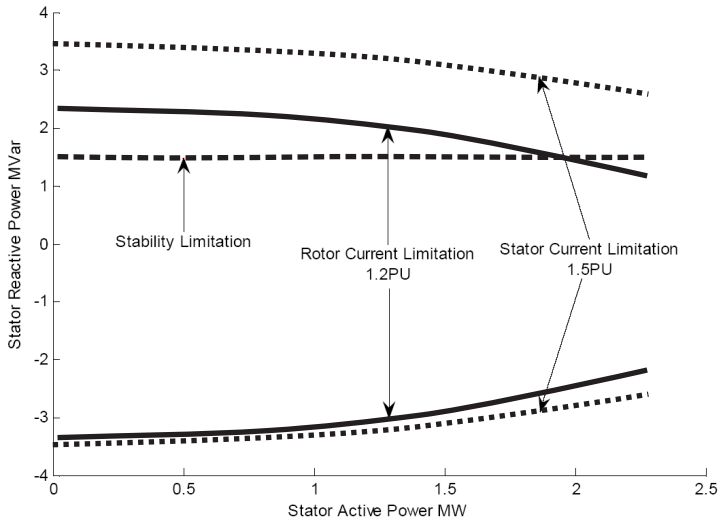

Figure 8.45 - PQ curve for a 2.75 MW DFIG [158]: the stator reactive power is plotted as function of the stator active power. Three different limitations for the reactive power output are shown: stator current limitation, rotor current limitation and stability limitation.

The block diagram that implements reactive power control and voltage regulation for the system under study is defined in the equivalent dq reference frame and is presented in Figure 8.46. In the stator-voltage equivalent frame, the instantaneous reactive power

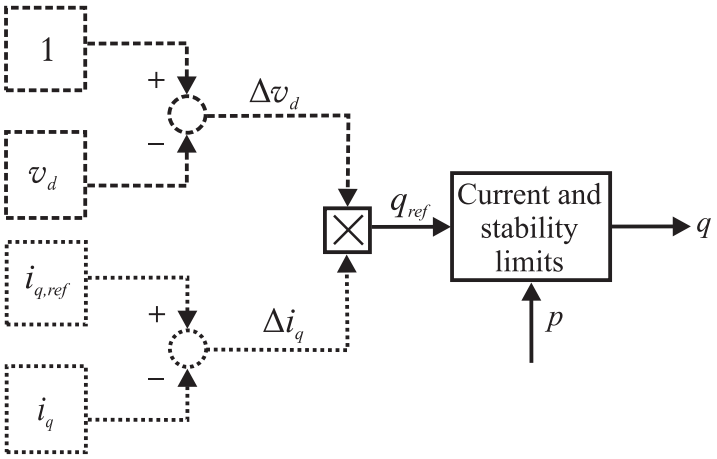

Figure 8.46 - Block diagram used for reactive power regulation: the reference signal for q is obtained from the values assumed by v_d and i_q

.

(appendix E) at the PCC is expressed as follows:

$$q = v_d i_q \tag{8.8}$$

and the values of v_d[37] and i_q are used to generate the reference values for q.

If the voltage at the PCC differs from the reference value, the error term $\Delta v_d = 1 - v_d$ is generated, as shown in the dashed section of the block diagram displayed in Figure 8.46.

The reference value of the q-axis current depends on the PF at the WECS terminal: in the present work, $i_{q,ref}$=0, since it is assumed that the WECS is operated as power generator only (chapter 4). However, due to wind speed variations and consequent transient, the actual value of i_q differs from the refence value, and a second error term Δi_q is obtained.

The product of Δv_d and Δi_q gives the reference instantaneous reactive power q_{ref}. Note that in steady state operation, this term is nil. The reference instantaneous reactive power q_{ref} is the first input for the block that implements the limitations illustrated in Figure 8.45. The active instantaneous power injected by the DFIG is the second input.

The result of the block diagram presented in Figure 8.46 is the signal q, which is the input for the block diagram presented in Figure 4.9.

[37]The normalized q-axis voltage is nil both in steady-state and in transient operation because the DFIG operation does not result in any changes of the system frequency; therefore of the space vector $\bar{v}$is always aligned with the d-axis of the equivalent reference frams. The DFIG used for wind generation differs from the synchronous machine because variations in the power delivered to the grid do no translate in frequency variation. This is due to the fact that the rotor absorbs the power variation and the rotor current frequency is decoupled from the grid frequency by means of the power converters [84].

The improvement of the voltage oscillograms following the implementation of reactive power regulation are displayed in Figures 8.47 and Figure 8.48.

Figure 8.47.a presents the result for the case of slow wind speed variation under the rated wind speed value (Figure 8.4). The instantaneous active power and the current waveforms are not affected by the reactive power regulation (Figure 8.47.a and .b). The reactive power variation is minimal in this case, as presented in Figure 8.47.c. This minimal variation is enough to make the voltage at the PCC constant, as displayed in Figure 8.47.d.

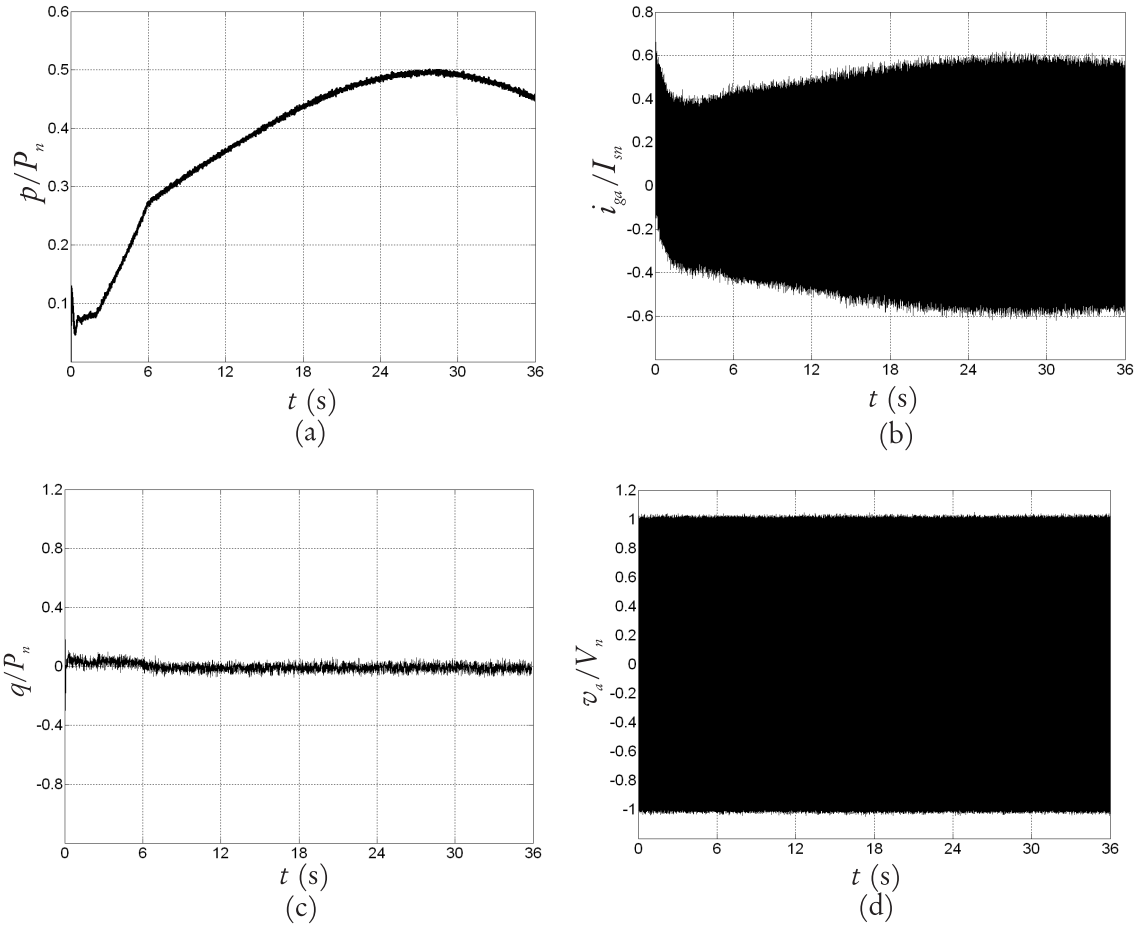

Figure 8.47 - Normalized oscillograms for slow wind speed variation below the rated value, ℓ=10 km; (a) Instantaneous active power, (b) Line current, (c) Reactive power and (d) Line-to-line voltage.

Figure 8.48 deals with the case of fast wind speed variation above the rated value. As in the previous case, the instantaneous active power and the current waveforms are not affected by the reactive power regulation (Figure 8.48.a and .b). Figure 8.48.c shows that

the reactive power variation is significant in this case since the results presented in the previous section showed a severe voltage dip, caused by the current amplitude oscillation. As a result of the implemented control, the voltage at the PCC is maintained practically constant, as displayed in Figure 8.48.d. A voltage spike is detected in correspondance of the current glitch at time $t = 4$ s. This result shows that if the blade control is not fast enough, sudden active power variations cannot be mitigated even when reactive power control is applied.

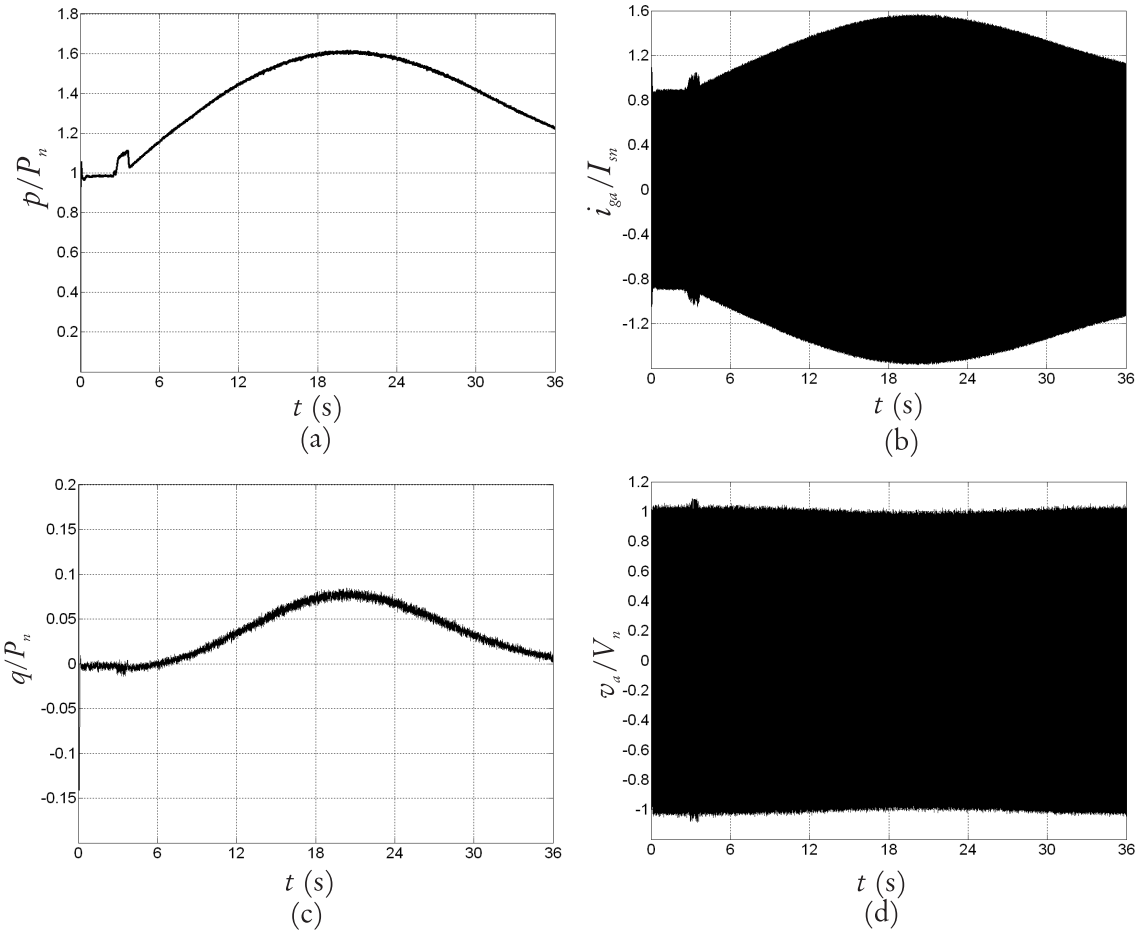

Figure 8.48 - Normalized oscillograms for fast wind speed variation above the rated value, ℓ=10 km; (a) Instantaneous active power, (b) Line current, (c) Reactive power and (d) Line-to-line voltage.

Additional observations on reactive power control

- Voltage regulation has been implemented by regulating the reactive power injected by the DFIG. A similar concept may be applied to the regulation of the reactive power injected by the LSC [65], since the LSC is connected to the same PCC. The injection of reactive power from the LSC converter presents limitations too, dictated by the rated LSC apparent power and the rms current flowing in the solid state devices.

- For any methods applied to regulate reactive power injection, if the WECS is operating at full active power, the reactive power injection (either from the DFIG or from the LSC) in steady state operation must be nil. Given that reactive power injection from the WECS cannot be guaranteed continuously, this method has been proposed only for regulating the voltage during transient operations. The installation of additional devices dedicated to reactive power compensation may be necessary for power factor and voltage regulation, depending on the specific installation (chapter 1).

- The majority of the grid codes worldwide requires the PF of the wind power plants to be mainained above 0.95. In United States, the FERC regulations [72, 73] indicate that the ability for the wind generator to operate within a specific PF range must be demonstrated only if the Impact Study conducted by the Transmission Operator and therefore no general rule is defined. If specific values of the PF are required by the grid operation, at low wind speed, when the active power injected from the WECS into the grid is only a fraction of the rated power, the reactive power injected or extracted must be consequently limited, thus adding further contraints to the ones illustrated in Figure 8.45.

8.5 Conclusions

In this chapter the response system response to wind speed variation has been investigated. This study requires to model the mechanical part of the WECS, composed by the wind turbine and the shaft.

Simulation results show that the ability to compensate harmonics is not altered by the wind speed variation and the following transients: the control signals defining the harmonic currents injected by the WECS depend on the NLL current spectum only and are not affected by the fundamental current flow.

Other conclusions resulting from the conducted analysis are:

- The shaft response is delayed with respect to the wind speed variation, due to the

turbine and DFIG inertia. The mechanical system response is oscillatory, being the system underdamped. However, since the frequency of the mechanical system response is low, the oscillations caused by the mechanical transients do no affect the current and voltage THD, that are measured every few electrical cycles (8 to 10).

- The lenght of the line that connects the WECS to the system affect the severity of the voltage oscillations following the wind speed variation.
- The effect of wind gusts on the grid current and voltage are significant only when high wind speed variations are assumed, since the blade pitch dynamics contributes to delay the mechanical system response and the power oscillations are large. At low wind speed, the pitch angle is permanently equal to zero, and since the power absorbed by the turbine is a small ratio of the rated power, wind gusts do not have a significant effect on the grid waveforms.
- The control of reactive power injected by the WECS helps to maintain a constant grid voltage. The maximum reactive power injection depends on the operating point of the turbine.

Chapter 9

Research Results and Future Works

9.1 Research results

The achievements of this thesis are the following:

1. Three alternatives control systems are proved to be effective in compensating the harmonic currents injected by a NLL supplied by the same feeder as the WECS. It has been verified that any harmonic current (positive-, negative-, zero-sequence, interharmonics, subharmonics) can be reduced by implementing the designed proposed systems. The advantages and drawbacks of each control system are identified.

2. The effects of the proposed operation on the WECS steady-state performances have been investigated: this study is necessary to avoid the damage of the WECS components. The use of the WECS as a power generator and harmonic compensator results in additional power loss and voltage distortion: both these effects have been analytically studied and quantified in terms of the harmonic currents injected by the NLL and in terms of the WECS equivalent parameters.

3. Derating is necessary to maintain the power loss within the WECS components below to a critical level because it results in a lowering of the fundamental power extracted by the turbine. Transient analysis allows verifying that derating has beneficial effects by limiting the amplitude of the currents flowing in the WECSs in response to a voltage dip at the PCC. Practical derating can be obtained by pitching the turbine blades, being this mechanism available in the majority of the modern wind turbines.

4. The study of the system response to voltage dips and wind speed variation proves that the system capability to compensate harmonics is not affected during transient operation: according to the proposed design, the harmonic current injection is a function of the currents measured at the NLL terminals and of the system transfer function, that are independent from the fundamental power flow.

5. Wind transient analysis shows that the main effect of wind speed variation on the grid operation is the grid voltage oscillation in case of long transmission line. The voltage fluctuation can be limited by implementing reactive power control.

6. An engineering economic analysis proves that the economical feasibility of the proposed approach is a function of the cost of the AF and of electric energy.

9.2 Future works

The following topics have been identified for further research on the subject of AF operation of a WECS:

- The definition of a function to optimize the amount of harmonic currents injected by each power converter. Simulation results show that compensation by means of combined modulation is the most effective way to implement current cancellation; however, depending on the NLL current spectrum, harmonic compensation may results in excessive power loss in some of the WECS components and need for severe derating, while other components are used below their capability.

- The definition of the control system starting from the currents measured on the grid, instead than from the currents measured at the NLL terminals. The control systems designed in the present research are suitable for the case of a dominant NLL connected in proximity of the WECS. In the majority of the applications, the situation is different: the harmonic currents measured at the PCC are not generated by a single load, but by a number of loads connected at the same PCC or at different points of the transmission/distribution system.

- A finer control system to regulate reactive power injection. At the moment, it is assumed that reactive power is injected only in presence of voltage distortion caused by fluctuations of the wind speed. In steady state operation, zero reactive power injection is assumed, according to the operation of the majority of moder wind turbines. The improved control system will allow regulating the PF at the WECS terminals as function of the Transmission Operator requirements and of the active power injection. At the same time, limitations in terms of rated VA and of power loss increase must be included into the control system.

- The implementation of harmonic compensation and reactive power injection at no-wind: this application is possible due to the connection of the power converters to the grid.

- The study of a similar mechanism by means of other WECS configurations (for example direct-drive) and solar plants.
- The study of the steady-state performance of alternative control system designs and the comparison with the ones used in the present work, based on PI controllers and PWM of the power converters.

Bibliography

[1] J. C. Smith and B. Parson, "What does 20% look like?," *Power and Energy Magazine, IEEE*, vol. 5, no. 6, pp. 22–33, Nov. - Dec. 2007.

[2] Z. Chen and F. Blaabjerg, "Wind energy: The world's fastest growing energy source," *IEEE Power Electronics Society Newsletter*, vol. 18, no. 3, pp. 15–19, 2006.

[3] J. Andrews and N. Jelley, *Energy Science - principles, technologies and impacts*, Oxford University Press, 116-117 High St, Oxford, U.K., 2007.

[4] World Wind Energy Association, "World wind energy report 2008," Tech. Rep.

[5] J. Arai, K. Iba, T. Funabashi, Y. Nakanishi, K. Koyanagi, and R. Yokoyama, "Power electronics and its applications to renewable energy in Japan," *Circuits and Systems Magazine, IEEE*, vol. 8, no. 3, pp. 52–66, Third Quarter 2008.

[6] US Wind Energy Projects AWEA, "www.awea.org/projects/," .

[7] R. Piwko, R. DeMello, R. Gramlich, W. Lasher, D. Osborn, C. Dombek, and K. Porter, "What comes first?," *Power and Energy Magazine, IEEE*, vol. 5, no. 6, pp. 68–77, Nov. - Dec. 2007.

[8] U. S. Department of Energy, "20% Wind Energy by 2030," Tech. Rep., May 2008.

[9] R. Zavadil, N. Miller, A. Ellis, E. Muljadi, E. Camm, and B. Kirby, "Queuing up," *Power and Energy Magazine, IEEE*, vol. 5, no. 6, pp. 47 – 58, Nov.-Dec. 2007.

[10] T. Ackermann, *Wind Power in Power Systems*, John Wiley and Sons, Hoboken, NJ 07030-5774, US, 2005.

[11] A. S. Laxson P.W. Carlin and E. B. Muljadi, "The history and state of the art of variable-speed wind turbine technology," *Wind Energy*, vol. 6, pp. 129–59, 2003.

[12] S. Heier, *Grid Integration of Wind Energy Conversion Systems*, J. Wiley & Sons, 111 River Street, Hoboken, NJ 07030-5774, US, 1998.

[13] R. Thresher, M. Robinson, and P. Veers, "To capture the wind," *Power and Energy Magazine, IEEE*, vol. 5, no. 6, pp. 34–46, Nov.-Dec. 2007.

[14] E. Muljadi, C. P. Butterfield, J. Chacon, and H. Romanowitz, "Power quality aspects in a wind power plant," in *Power Engineering Society General Meeting, 2006*, Montreal, Canada, 18-22 June 2006.

[15] Wachtel S., J. Marques, E. Quitman, and M. Schellschmidt, "Wind energy converters with FACTS capabilities and the benefits for the integration of wind power plants into power systems," in *Proc. European Wind Energy Conference and Exhibition (EWEC)*, Milan, 4, May 7-10 2007, pp. 1761–65.

[16] F. Blaabjerg and Z. Chen, *Power Electronics for Modern Wind Turbines*, Synthesis Lectures on Power Electronics. Morgan & Claypool, U.S., 2006.

[17] B. Parson, M. Milligan, B. Zavadil, D. Brooks, B. Kirby, K. Dragoon, and J. Caldwell, "Grid impacts of wind power: A summary of recent studies in the United States," *Wind Energy*, vol. 7, no. 1, pp. 87–108, Apr./Jun. 2004.

[18] R. A. Walling, R. Saint, R. C. Dugan, J. Burke, and L. A. Kojovic, "Summary of distributed resources impact on power delivery systems," *IEEE Trans. on Power Del.*, vol. 23, no. 3, pp. 1636 – 44, July 2008.

[19] J. C. Smith, M. R. Milligan, E. A. DeMeo, and B. Parsons, "Utility wind integration and operating impact state of the art," *IEEE Trans. Pow. System*, vol. 22, no. 3, pp. 900–908, Aug. 2007.

[20] C. Kalich J. King M. R. Milligan C. Murlay B. Oakleaf E. A. DeMeo, G. A. Jordan and M. J. Schuerger, "Accomodating wind's natural behavior," *Power and Energy Magazine, IEEE*, vol. 5, no. 6, pp. 59–67, Nov.-Dec. 2007.

[21] P. Fairley, "Steady As She Blows," *IEEE Spectrum*, vol. 40, no. 8, pp. 35–39, Aug. 2003.

[22] A. D. Hansen, G. Michalke, P. Sorensen, and T. Lund, "Co-ordinated voltage control of DFIG wind turbines in uninterrupted operation during grid faults," *Wind Energy*, vol. 10, no. 1, pp. 51–68, 2007.

[23] M. Prodanovic, K. De Brabandere, J. Van den Keybus, T. Green, and J. Driesen, "Harmonic and reactive power compensation as ancillary services in inverter-based

distributed generation," *IET Gener. Transm. Distr.*, vol. 1, no. 3, pp. 432–38, March. 2007.

[24] IEEE Power Engineering Society Standard 1159, *Recommended Practice for Monitoring Electric Power Quality*, 1995.

[25] IEEE Power Engineering Society Standard 519, *Recommended Practices and Requirements for Harmonic Control in Electrical Power Systems*, 1992.

[26] IEEE Power Engineering Society Standar 519, *Correction to IEEE Recommended Practices and Requirements for Harmonic Control in Electrical Power Systems*, 1992.

[27] L. H. Hansen, P. H. Madsen, F. Blaabjerg, H. C. Christersen, U. Lindhard, and K. Eskildsen, "Generators and power electronics technology for wind turbines," in *Proc. Industrial Electronics Society, IEEE 2002 27th Annual Conference IECON*, Denver, US, Nov. 29 - Dec. 1 2001, pp. 2000–2005.

[28] M. T. Abolhassani, H. A. Toliyat, and P. Enjeti, "Stator flux oriented control of an integrated alternator/active filter for wind power applications," in *Proc. Electric Machines and Drives Conference IEMDC 2003, IEEE Intern.*, Madison, NJ, US, 1-4 June 2003, pp. 461 – 467.

[29] M. T. Abolhassani, P. Niazi, H. A. Toliyat, and P. Enjeti, "Integrated Doubly Fed Electric Alternator/Active Filter (IDEA), a Viable Power Quality Solution, for Wind Energy Conversion Systems," *IEEE Trans. En. Conv.*, vol. 23, no. 2, pp. 642–650, June 2008.

[30] M. T. Abolhassani, H. A. Toliyat, and P. Enjeti, "An electromechanical active harmonic filter," in *Proc. Electric Machines and Drives Conference IEMDC 2001, IEEE Intern.*, Cambridge, MA, US, 17-20 June 2001, pp. 349 – 355.

[31] B. Toufik, M. Machmoum, and F. Poitiers, "Doubly Fed Induction Generator with active filtering function for wind energy conversion system," in *Proc. Power Electronics and Applications (EPE), 2005 European Conference on*, Dresden, Germany, 11-14 Sept 2005, pp. 1–9.

[32] E. Tremblay, A. Chandra, and P. Lagace, "Grid-side converter control of DFIG wind turbines to enhance power quality of distribution network," in *Proc. Power Engineering Society General Meeting*, Montreal, Canada, 18-22 June 2006, pp. 1542–47.

[33] F. Blaabjerg, Z. Chen, R. Teodorescu, and F. Iov, "Power Electronics in Wind Turbines Systems," in *Proc. CES/IEEE-PELS Int. Power Electronics and Motion Control Conference (IPEMC)*, Shangai, China, August 13-16 2006, pp. 1–11.

[34] N. Mohan, T. M. Undeland, and W. P. Robbins, *Power Electronics: converters, applications and design, 3rd edition*, J. Wiley & Sons, 111 River Street, Hoboken, NJ 07030-5774, US, 2003.

[35] J.A. Baroudi, V. Dinavahi, and A.M. Knight, "A review of power converter topologies for wind generators," in *Proc. Electric Machines and Drives, IEEE Intern. Conf. on*, San Antonio, TX, US, 15-18 May 2005, pp. 458–465.

[36] D. Aguglia, P. P. Viarouge, R. Wamkeue, and J. Cros, "Selection of gearbox ratio and power converters ratings for wind turbines equipped with Doubly-Fed Induction Generators," in *Proc. Electric Machines & Drives Conference, 2007. IEMDC '07. IEEE International*, Antalya, Turkey, 3-5 May 2007, pp. 447 – 52.

[37] Wind Turbine Generators: A Comparison of Machine Technologies M. Bradt, "mywebspace.wisc.edu/bradt/web/wind/windturbinegenerators%28bradt%29.pdf," .

[38] Vestas Wind Power Solutions, "www.vestas.com/en/wind-power-solutions," .

[39] I. Erlich, H. Wrede, and C. Feltes, "Dynamic behavior of DFIG-based wind turbines during grid faults," in *Proc. Power Conversion Conference 2007. PCC '07*, Nagoya, Japan, 2-5 Apr. 2007, pp. 1195–1200.

[40] J. Lopez, P. Sanchis, X. Roboan, and L. Marroyo, "Dynamic Behavior of the Doubly Fed Induction Generator During Three-Phase Voltage Dips," *IEEE Trans. Energy Convers.*, vol. 22, no. 3, pp. 709–717, Sept. 2007.

[41] A. Petersson and S. Lundberg, "Energy efficiency comparison of electrical systems for wind turbines," in *Proc. IEEE NordicWorkshop Power Industrial Electron. (NORpie/2002)*, Stockholm, Sweden, 2002.

[42] M. Kayikci and J. V. Milanovic, "Reactive power control strategies for DFIG-based plants," *IEEE Trans. Energy Convers.*, vol. 22, no. 2, pp. 389–396, June 2007.

[43] J. Niiranen, "Voltage dip ride through of a double-fed generator equipped with an active crowbar," in *Proc. NordicWind Power Conference*, Gothenburg, Sweden, Mar 2004.

[44] M. Behnke and A. Ellis, "Reactive Power Planning for Wind Power Plant Interconnections," in *Proc. Power and Energy Society General Meeting - Conversion and Delivery of Electrical Energy in the 21st Century, 2008 IEEE*, Pittsburgh, PA, US, 20-24 July 2008, pp. 1–4.

[45] Y. Higuchi, N. Yamamura, M. Ishida, and T. Hori, "An improvement of performance for small-scaled wind power generating system with permanent magnet type synchronous generator," in *Proc. 26th Annual Conference of the IEEE Industrial Electronics Society (IECON2000)*, Nagoya, Aichi, Japan, 22-28 Oct. 2000, pp. 1037–1043.

[46] I. Schiemenz and M. Stiebler, "Control of a permanent magnet synchronous generator used in a variable speed wind energy system," in *Proc. IEEE International Electric Machines and Drives Conference (IEMDC 2001)*, MIT, Boston, MA, US, 23 Mar. 2001, pp. 872–877.

[47] A. C. Williamson E. Spooner and G. Catto, "Modular design of permanent-magnet generators for wind turbines," *IEE Proc.-B, Electric Power Applicat.*, vol. 143, no. 5, pp. 388–395, Sept. 1996.

[48] D. Grenier and J. P. Loue, "Use of an extension of the Park's transformation to determine control laws applied to a non-sinusoidal permanent magnet synchronous motor," in *Proc. ENE*, Brighton, 13-16 Sept. 1993, pp. 32–37.

[49] K. Tan and S. Islam, "Optimum Control Strategies in Energy Conversion of PMSG Wind Turbine System without Mechanical Sensors," *IEEE Trans. En. Conv.*, vol. 19, no. 2, pp. 392–399, June 2004.

[50] H. Polinder, F. F. A. van der Pijl, G. de Vilder, and P. J. Tavner, "Comparison of direct-drive and geared generator concepts for wind turbines," *IEEE Trans. on En. Conv.*, vol. 21, no. 3, pp. 725–33, Sept. 2006.

[51] Cape Wind Website, "www.capewind.org/," .

[52] C. Meyer, M. Hoing, A. Peterson, and R.W. De Doncker, "Control and design of dc grids for offshore wind farms," *IEEE Trans. Ind. Appl.*, vol. 43, no. 6, pp. 1475 – 82, Nov.-Dec. 2007.

[53] R. Li J. C. Clare G. M. Asher S. V. Bozhko, R. Blasco-Gimenez, "Control of Offshore DFIG-Based Wind Farm Grid With Line-Commutated HVDC Connection," *IEEE Trans. En. Conv*, vol. 22, no. 1, pp. 71–78, Mar. 2007.

[54] B. Andresen and K. Johansen, "Grid code and wind farm control requirements - what to control, why, where and how," in *Proc. 7th International Workshop on Large Scale Integration of Wind Power and on Transmission Networks for Offshore Wind Farms*, Madrid, Spain, 26 - 27 May 2008, pp. 1–6.

[55] J. L. Dallachy and I. Tait, "Guidance note for the connection of wind farms," *2.2.2, SP TRansmission and Distribution, Scottish Hydro-Electric*, vol. 2.2.2, 2002.

[56] S. K. Salman and B. Badrzadeh, "New approach for modelling doubly-fed induction generator (DFIG) for grid-connection studies," in *Proc. European Wind Energy Conference (EWEC)*, London, U.K., 22-25 Nov 2004, pp. 1–13.

[57] J. O. G. Tande, "Exploitation of wind-energy resources in proximity to weak electric grids," *Applied Energy*, vol. 65, no. 1, pp. 395–401, 2000.

[58] A. I. Estanqueiro, J. O. Tande, and J. A. Peas Lopes, "Assessment of power quality characteristics of wind farms," in *Power Engineering Society General Meeting, 2007. IEEE*, Tampa, FL, US, 24-28 June 2007, pp. 1–4.

[59] L. Rossetto, P. Tenti, and A. Zuccato, "Electromagnetic compatibility issues in industrial equipment," *IEEE Ind. Appl. Mag.*, vol. 5, no. 6, pp. 34–46, Nov.-Dec. 1999.

[60] AA. Larsson, "Flicker emission of wind turbines during continuous operation," *IEEE Trans. Energy Convers.*, vol. 17, no. 1, pp. 114–118, March 2002.

[61] T. Sun, Z. Chen, and F. Blaabjerg, "Flicker study on variable speed wind turbines with doubly fed induction generators," *IEEE Trans. on Energy Conv.*, vol. 20, no. 4, pp. 896–905, Dec. 2005.

[62] M. P. Papadopoulos, S. A. Papathanassiou, S. T. Tentzerakis, and N. G. Boulaxis, "Investigation of the flicker emission by grid connected wind turbines," in *Proc. 8th Int. Conf. Harmonics Quality of Power*, Athens, Greece, 14-16 Oct. 1998, pp. 1152–1157.

[63] IEEE Power Engineering Society Standard P1547, *Standard for Distributed Resources Interconnected with Electric Power Systems*, 2002.

[64] T. Lund, P. Sorensen, and J. Eek, "Reactive power capability of a wind turbine with doubly fed induction generator," *Wind Energy*, vol. 30, no. 10, pp. 379–394, Apr. 2007.

[65] A. Tapia, G. Tapia, and J. X. Ostolaza, "Reactive power control of wind farms for voltage control applications," *Elsevier - Renewable Energies*, vol. 29, no. 1, pp. 377–392, 2004.

[66] J. W. Smith, T. Key, and R. C. Dugano, "Power quality considerations for wind generation," Tech. Rep., EPRI PEAC Corporation, Knoxville, TN.

[67] Guidance Notes for Power Park Developers, "www.nationalgrid.com," .

[68] E.ON Netz, *Erg ånzende Netzanschlussregeln fur Windengieanlagen, www.eon.com*, 2001.

[69] B. Ernst, B. Oakleaf, M. L. Ahlstrom, M. Lange, C. Moehrlen, B. Lange, U. Focken, and K. Rohrig, "Predicting the Wind," *Power and Energy Magazine, IEEE*, vol. 5, no. 6, pp. 78–89, Nov.-Dec. 2007.

[70] IEC Standard 61400-21, *Measurement and assessment of power quality characteristics of grid connected wind turbines*, 2001.

[71] J. S. Rohatgi and V. Nelson, *Wind Characteristics: An Analysis for the Generation of Wind Power*, Alternative Energy Institute, Cayon, TX, 79015, US, 1994.

[72] FERC Order No. 661 - Final Rule, *Interconnection for Wind Energy*, 2005.

[73] FERC Order No. 661A - Order on Rehearing and Clarification, *Interconnection for Wind Energy*, 2005.

[74] J. K. Lemming, "Cost Reduction Potentials in Wind," Tech. Rep., Ris National Laboratory, Technical University of Denmark DTU, Presentation at the IEA Technology Learning and Deployment Workshop June 11-12, 2007.

[75] B. K. Bose, *Power Electronics and AC drives*, Prentice-Hall, Upper Saddle River, NJ, 07458, US, 2001.

[76] A. E. Fitzgerald, C. Kingsley, and S. D. Umans, *Electric machinery, 5th Edition*, McGraw-Hill, 6th Avenue, New York City, NY, 10001-6309, US, 1990.

[77] A. S. Langsdorf, *Theory of Alternating Current Machinery*, McGraw-Hill, 6th Avenue, New York City, NY, 10001-6309, US, 1937.

[78] P. C. Krause, O. Wasynczuk, and S. D. Sudhoff, *Analysis of Electric Machinery and Drive Systems*, Wiley-IEEE Press, 111 River Street, Hoboken 07030-5774, NJ, US, 2002.

[79] O. Darrigol, *Electrodynamics from Ampere to Einstein*, Oxford University Press, 116-117 High St, Oxford, Oxfordshire, OX1 4BZ, U.K., 2000.

[80] G. Ferraris, "Rotazioni elettrodinamiche prodotte per mezzo di correnti alternate (electrodynamic rotations produced by alternating currents)," *The Electrician*, vol. 36, no. 1, pp. 246–263, 1888.

[81] Electro Magnetic Motor, *N. Tesla*, Patent 381968, March 1st 1888.

[82] N. Mohan, *Advanced Electric Drives. Analysis, Control and Modeling using Simulink*, Mnpere, P.O. Box 14503, Minneapolis, MN, 55414, US, 2001.

[83] P. G. Cummings, "Estimating effect of system harmonics on losses and temperature rise of squirrel-cage motors," *IEEE Trans. Ind. Appl.*, vol. IA-22, no. 6, pp. 1121–1126, Nov. 1986.

[84] I. Boldea, *Variable Speed Generators*, CRC Press, 2000 NW Corporate Blvd Boca Raton, FL 33431, US, 2006.

[85] L. Jiao, B. Ooi, G. Joos, and F. Zhoub, "Doubly-fed induction generator (DFIG) as a hybrid of asynchronous and synchronous machine," *Electric Power Systems Research*, vol. 76, no. 1, pp. 33–37, 2005.

[86] I. Cadirci and M. Ermis, "Double-output induction generator operating at sub-synchronous and super-synchronous speeds: Steady-state optimization and wind-energy recovery," *IEE Proc.-B, Electric Power Applicat.*, vol. 139, no. 5, pp. 429–442, 1992.

[87] M. S. Erlicki, "Inverter rotor drive of an induction motor," in *Proc. IEEE Winter Power Meeting*, New York City, NY, US, 31 Jan. - 5 Feb. 1965, pp. 1–12.

[88] W. Leonhard, *Control of Electrical Drives*, Electric driving. Springer-Verlag, Berlin, Germany, 2001.

[89] R. Pena, J.C. Clare, and G.M. Asher, "Doubly Fed Induction Generator Using Back-to-Back PWM Converters and its Application to Variable-Speed Wind-Energy Generation," *IEE Proc.-B, Electric Power Applicat.*, vol. 143, no. 3, pp. 231–241, May 1996.

[90] I. Boldea and S. A. Nasar, *The induction machine handbook*, CRC Press, 2000 NW Corporate Blvd Boca Raton, FL 33431, US, 2002.

[91] Chapman, *Electrical Machines*, Cambridge, US, 1978.

[92] W. D. Stevenson, *Elements of Power System Analysis*, McGraw-Hill, 6th Avenue, New York City, NY, 10001-6309, US, 1992.

[93] V. Akhmatov, *Induction generators for wind power*, Multi-Science Publishing Company, 111 River Street, Hoboken 07030-5774, NJ, US, 2005.

[94] M. R. Patel, *Wind and Solar Power Systems*, CRC Press, 2000 NW Corporate Blvd Boca Raton, FL 33431, US, 1999.

[95] S. Li and S. Sinha, "A simulation analysis of double-fed induction generator for wind energy conversion using pspice," in *Proc. Power Engineering Society General Meeting, 2006. IEEE*, Montreal, CA, 18-22 June 2006, pp. 1–8.

[96] R. Datta and V.T. Ranganathan, "Variable-speed wind power generation using doubly fed wound rotor induction machine a comparison with alternative scheme," *IEEE Trans. Energy Convers.*, vol. 17, no. 3, pp. 414–421, Sept. 2002.

[97] N. K. Trehan, "Ancillary services-reactive and voltage control," in *Proc. IEEE Winter Power Meeting*, Columbus, OH, US, 28 Jan. - 2 Feb. 2001, pp. 1341–46.

[98] FERC Order No. 888, *Promoting Wholesale Competition Through Open Access Non-discriminatory Transmission Services by Public Utilities; Recovery of Stranded Costs by Public Utilities and Transmitting Utilities*, 1996.

[99] H. Akagi, "New trends in active filters for power conditioning," *IEEE Trans. Ind. Appl.*, vol. 32, no. 6, pp. 1312 – 1322, Nov.-Dec. 1996.

[100] R. C. Dugan, M. F. McGranaghan, and H. W. Beaty, *Electrical Power Systems Quality*, Electrical Engineering. McGraw-Hill, 6th Avenue, New York City, NY, 10001-6309, US, 1996.

[101] F. L. Hoadley, "Curb the disturbance," *Industry Applications Magazine, IEEE*, vol. 14, no. 5, pp. 25–33, Sept. - Oct. 2008.

[102] D. A. Paice, *Power Electronic Converter Harmonics*, IEEE Press, 111 River Street, Hoboken 07030-5774, NJ, US, 1996.

[103] M. S. Erlicki and A. E. Emanuel, "New Aspects of Power Factor Improvement Part I - Theoretical Basics," *IEEE Trans. Ind. and Gen. Appl*, vol. IGA4, no. 4, pp. 441–446, July/Aug. 1968.

[104] A. E. Emanuel, "New Aspects of Power Factor Improvement Part II - Practical Circuits," *IEEE Trans. Ind. and Gen. Appl*, vol. IGA4, no. 4, pp. 447–455, July/Aug. 1968.

[105] L. Asiminoaei, F. Blaabjerg, and S. Hansen, "Detection is key - harmonic detection methods for active power filter applications," *IEEE Ind. App. Magazine*, vol. 13, no. 4, pp. 22–33, July-Aug. 2007.

[106] H. Akagi, Y. Kanazawa, and A. Nabae, "Instantaneous reactive power compensators comprising switching devices without energy storage components," *Trans. Ind. Appl.*, vol. IA-20, no. 3, pp. 625–630, May 1984.

[107] H. Akagi, A. Nabae, and S. Atoh, "Control strategy of active power filters using multiple voltage-source PWM converters," *IEEE Trans. Ind. Appl.*, vol. IA-22, no. 3, pp. 460–465, May 1986.

[108] G. Superti Furga and G. Todeschini, "Discussion on instantaneous p-q strategies for control of active filters," *IEEE Trans. on Power Electronics*, vol. 23, no. 4, pp. 1945 – 55, July 2008.

[109] I. Takahashi and M. Nishitoba, "Universal power distortion compensator using secondary excitation of a rotating machine," *Electrical Engineering in Japan*, vol. 107, no. 2, pp. 73–80, 1987.

[110] G. Todeschini and A. E. Emanuel, "Wind energy conversion system as an active filter: Design and comparison of three control systems," *Submitted for publication to IET Renewable Power Generation*, Sept. 2009.

[111] G. Todeschini and A. E. Emanuel, "The DFIG as Harmonic Compensator by Means of RSC Modulation: Control System and Derating for Steady State Performance," in *Proc. Applied Power Electronics Conference and Exposition (APEC) 2010, Twenty-Fifth Annual IEEE*, Palm Beach, CA, February 21-25 2010.

[112] R. Richter, *Elektrische Maschinen (Electrical Machines)*, Verlag Birkhauser, Germany, 1951.

[113] E. F. Fuchs and M. A. S. Masoum, *Power Quality in Power Systems and Electrical Machines*, Academic Press, 6th Avenue, New York City, NY, 10001-6309, US, 2008.

[114] Transformers Committee of the IEEE Power Engineering Society C57-110, *IEEE Recommended Practice for Establishing Transformer Capability When Supplying Nonsinusoidal Load Currents*, 1998.

[115] P. K. Sen and H.A. Landa, "Derating of induction motors due to waveform distortion," *IEEE Trans. Ind. Appl.*, vol. 26, no. 6, pp. 1102 – 1107, Nov.-Dec. 1990.

[116] A. E. Emanuel, "Estimating the effects of harmonic voltage fluctuations on the temperature rise of squirrel cage motors," *IEEE Trans. Ener. Conv.*, vol. 6, no. 1, pp. 162–169, March 1991.

[117] A. Testa, M.F. Akram, R. Burch, G. Carpinelli, G. Chang, V. Dinavahi, C. Hatziadoniu, W.M. Grady, E. Gunther, M. Halpin, P. Lehn, Y. Liu, R. Langella, M. Lowenstein, A. Medina, T. Ortmeyer, S. Ranade, P. Ribeiro, N. Watson, J. Wikston, and W. Xu, "Interharmonics: Theory and modeling," *IEEE Trans. Pow. Del.*, vol. 22, no. 4, pp. 2335 – 48, Oct. 2007.

[118] A. Petersson, *Analysis, Modeling and Control of Doubly-Fed Induction Generators for Wind Turbines*, Ph.D. thesis, Chalmers University of Technology, Goteborg, Sweden, 2005.

[119] F. Abrahamsen, *Energy optimal control of induction motor drives*, Ph.D. thesis, Aalborg University, Aalborg, Denmark, 2000.

[120] M.Gopal, *Modern Control System Theory - Second Edition Revised*, New Age International Publishers, 1994.

[121] A. K. Jain, R. Tirumala, N. Mohan, T. Gjengedal, and R. M. Halet, "Harmonics and flicker control in wind farms," in *Wind Power and the Impacts on Power Systems Workshop*, Oslo, Norway, 17-18 June 2002, pp. 1–5.

[122] R. Datta and V. T. Ranganathan, "Decoupled control of active and reactive power for a grid-connected doublyfed wound rotor induction machine without position sensors," in *Proc. of the 1999 IEEE Industry Applications Conference*, Phoenix, AZ, US, Oct. 1999, p. 262328.

[123] L. Morel, H. Godfroid, A. Mirzaian, and J. Kauffmann, "Double-fed induction machine: converter optimisation and field oriented control without position sensor," *IEE Proc. Electr. Power Appl.*, vol. 145, no. 4, pp. 36068, July 1998.

[124] C. L. Phillips and R. D. Harbor, *Feedback Control Systems (Fourth Edition)*, Prentice Hall, Upper Saddle River, NJ 07548, US, 2000.

[125] R. E. Best, *Phase-Locked Loops. Theory, Design and Applications*, Mc Graw Hill, 6th Avenue, New York City, NY, 10001-6309, US, 1984.

[126] Philips Semiconductors, *An overview of the phase-locked loop (PLL)*, 1988.

[127] Simulink User Guide, "www.mathworks.com," 2008.

[128] H. Akagi, E. H. Watanabe, and M. Aredes, *Instantaneous power theory and applications to power conditioning*, IEEE Press, 111 River Street, Hoboken 07030-5774, NJ, US, 2007.

[129] M. Yin, G. Li, M. Zhou, G. Liu, and C. Zhao, "Study on the control of DFIG and its responses to grid disturbances," in *Proc. Power Engineering Society General Meeting*, Montreal, Canada, 18-22 June 2006.

[130] P. T. Krein, *Elements of power electronics*, The Oxford series in electrical and computer engineering. Oxford University Press, 116-117 High St, Oxford, Oxfordshire, OX1 4BZ, U.K., 1998.

[131] Chee-Mun Ong, *Dynamic Simulation of Electric Machinery Using Matlab/Simulink*, Prentice Hall, Upper Saddle River, NJ 07548, US, 1998.

[132] Simulink Product Page, "www.mathworks.com/products/simulink/," 2008.

[133] J. G. Proakis and D. K. Manolakis, *Digital Signal Processing: Principles, Algorithms, and Applications (Fourth Edition)*, Prentice Hall, Upper Saddle River, NJ 07548, US, 2006.

[134] Powerex CM900DU-24NF, "www.pwrx.com," Accessed March 2009.

[135] M. Kruger-Gotzmann, C. Schiller, and G. Zwarg, "Wind power installation with separate primary and secondary cooling circuits," .

[136] T. M. Gruzs, "A survey of neutral currents in Three-Phase computer power systems," *IEEE Trans. Ind. Appl.*, vol. 26, no. 4, pp. 719–725, 1990.

[137] P. M. Anderson, *Analysis of Faulted Power Systems*, The Iowa State University Press, Ames, Iowa, 50010 US, 1973.

[138] C. L. Fortescue, "Method of symmetrical coordinates applied to the solution of polyphase networks," *Trans. AIEEE*, vol. 37, no. 1, pp. 1027–1140, 1918.

[139] P. K. Kovacs, *Transient Phenomena in Electrical Machines*, Elsevier, 52 Vanderbilt Avenue, New York City, NY, 1983.

[140] F. Iov, A. D. Hansen, C. Jauch, P. Soresen, and F. Blaabjerg, "Advanced Tools for Modeling, Design and Optimization of Wind Turbine Systems," in *Nordic Wind Power Conference*, Chalmers University of Technology, 1-2 March 2004 2004, pp. 1–12.

[141] I. Slama-Belkhodja J. Arbi and S. Arnaltes Gomez, "Control of a dfig-based wind system in presence of large grid faults: analysis of voltage ride through capability," in *Proc. 9th International Conference Electric Power Quality and Utilisation*, Barcelona, Spain, 9-11 October 2007, pp. 1–6.

[142] A. D. Hansen and G. Michalke, "Fault ride-threou capability of DFIG wind turbines," *Science Direct - Renewable Energy*, vol. 32, no. 1, pp. 1594–1610, 2006.

[143] J. Morren and S. W. H. de Haan, "Ridethrough of wind turbines with doubly-fed induction generator during a voltage dip," *IEEE Trans. Energy Convers.*, vol. 20, no. 3, pp. 435–441, June 2005.

[144] D. Xiang, L. Ran, P. J. Tavner, and S. Yang, "Control of a doubly fed induction generator in a wind turbine during grid fault ride-through," *IEEE Trans. on Energy Conv.*, vol. 21, no. 3, pp. 652–662, Sept. 2006.

[145] J. Morren and S. W. H. de Haan, "Short-circuit current of wind turbines with doubly fed induction generator," *IEEE Trans. Energy Convers.*, vol. 22, no. 1, pp. 174 – 180, March 2007.

[146] S. Seman, N. Niiranen, S. Kanerva, and A. Arkkio, "Analysis of a 1.7 MVA Doubly Fed Wind-Power Induction Generator during Power Systems Disturbances," in *Proc. Nordic Workshop on Power and Industrial Electronics*, Trondheim, Norway, 14-16 June 2004, pp. 1–6.

[147] M. H. J. Bollen, *Understanding Power Quality Problems - Voltage Sags and Interruptions*, IEEE Press, 445 Hoes Lane, P.O. Box 1331, Piscataway, NJ 08855-1331, 2000.

[148] Wester Energy Coordinating Council, *The Technical Basis for the New WECC Voltage Ride-Though (VRT) Standard*, June 13, 2007.

[149] A. Geniusz and S. Engelhardt, "Riding through grid faults with modified multiscalar control of Doubly Fed Asynchronous Generators for wind power systems," in *Proc. Intern. Conf. for Power Electronics - Intelligent Motion - Power Quality PCIM Europe*, Nrnberg, Germany, May/June 2006, pp. 1195–1200.

[150] N. Jenkins F. M. Hughes, O. Anaya-Lara and G. Strbac, "A Power System Stabilizer for DFIG-based Wind Generation," *IEEE Trans. Pow. Systems*, vol. 21, no. 2, pp. 763– 772, May 2006.

[151] S. Seman, N. Niiranen, and J.-P. Virtanen, R.; Matsinen, "Low Voltage Ride-Through Analysis of 2 MW DFIG Wind Turbine - Grid Code Compliance Validations," in *Proc. Power and Energy Society General Meeting - Conversion and Delivery of Electrical Energy in the 21st Century, 2008 IEEE*, Pittsburgh, PA, US, 20-24 July 2008, pp. 1–6.

[152] Peng L., B. Francois, and Y. Li, "Improved Crowbar Control Strategy of DFIG Based Wind Turbines for Grid Fault Ride-Through," in *Proc. Applied Power Electronics Conference and Exposition, 2009. APEC 2009. Twenty-Fourth Annual IEEE*, Washington, DC, 15-19 Feb. 2009, pp. 1932–38.

[153] Private Communication, *R. Piwko*, 2009.

[154] C. Carrillo, A. E. Feijo, J. Cidrs, and J. Gonzlez, "Power fluctuations in an isolated wind plant," *IEEE Trans. En. Conv*, vol. 19, no. 1, pp. 217–21, March 2004.

[155] A.G. Abo-Khalil and Lee Dong-Choon, "Dynamic modeling and control of wind turbines for grid-connected wind generation system," in *Proc. Power Electronics Specialists Conference, 2006. PESC '06. 37th IEEE*, Jeju, South Korea, 18-22 June 2006, pp. 1 – 6.

[156] J. P. Den Hartog, *Mechanical Vibrations*, Dover Publications, Mineola, NY, US, 1985.

[157] IEEE Power Engineering Society Standar 1459, *Trial-Use Standard Definitions for the Measurement of Electric Power Quantities Under Sinusoidal, Nonsinusoidal, Balanced, or Unbalanced Conditions*, 2000.

[158] Y. Zhou, P. Bauer, and J. A. Ferreira, "Reactive power limitation of doubly fed induction generator and its application on coordinated hybrid wind farm contol," in *Proc. EWEC 2008*, 31 March - 3 April 2008, pp. 1–8.

[159] R. H. Park, "Two-Reaction Theory of Synchronous Machines - Generalized Method of Analysis, Part I," *AIEE Transactions*, vol. 48, no. 1, pp. 716–727, July 1929.

[160] H. C. Stanley, "An Analysis of the Induction Motor," *AIEE Transactions*, vol. 57, no. 1, pp. 751–755, 1938.

[161] G. Kron, *Equivalent Circuits of Electric Machinery*, J. Wiley and Sons, New York City, NY, US, 1951.

[162] D. S. Brereton, D. G. Lewis, and C. G. Young, "Representation of induction motor loads during power stability studies," August 1957.

[163] E. Clarke, *Circuit Analysis of A-C Power Systems*, General Electric series. J. Wiley & Sons, 111 River Street, Hoboken, NJ 07030-5774, US, 1947.

[164] C.J. Retter, *Matrix and Space-Phasor Theory of Electrical Machines*, Akadèmiai Kiadó, Budapest, Hungary, 1987.

[165] G. H. Golub and C. F. Van Loan, *Matrix Computations*, Mathematical Sciences. John Hopkis University Press, 6th Avenue, New York City, NY, 10001-6309, US, 1996.

[166] D. Y. Ohm, "Dynamic model of induction motors for vector control," in *www.drivetechinc.com/articles/IM98VC1.pdf*, 1998, pp. 1–8.

[167] P. Vas, *Vector Control of AC machines*, Oxford Science Publications, 116-117 High St, Oxford, Oxfordshire, OX1 4BZ, U.K., 1990.

[168] E. Muljadi and C. P. Butterfield, "Pitch-controlled variable-speed wind turbine generation," in *1999 IEEE Industry Applications Society Annual Meeting*, Phoenix, AZ, 3-7 October 1999, pp. 1–8.

[169] T. Burton, D. Sharpe, N. David, and E. Bossanyi, *Wind Energy Handbook*, John Wiley & Sons Inc., Hoboken, NJ 07030-5774, US, 2001.

[170] A. Tapia, G. Tapia, J. X. Ostolaza, and J. R. Saenz, "Modeling and Control of a Wind Turbine Driven Doubly Fed Induction Generator," *IEEE Trans. En. Conv.*, vol. 18, no. 2, pp. 194–204, June 2003.

[171] A. Betz, *Wind-Energie und ihre Ausnutzung durch Windmhlen*, Bandenhoeck & Ruprect, Gottingen, Germany, 1926.

[172] W.E. Leithead, S. de la Salle, and D. Reardon, "Role and objectives of control for wind turbines," *IEE Proc. Generation, Transmission and Distribution*, vol. 138, no. 2, pp. 135–48, March 1991.

[173] Johson, "Adaptive torque control of variable speed wind turbines," Tech. Rep. NREL/TP-500-36265, National Renewable Energy Laboratory, 1617 Cole Boulevard, Golden, CO 80401-3393, Aug. 2004.

[174] F. D. Bianchi, H. De Battista, and R. G. Mantz, *Wind Turbines Control Systems*, Advances in Industrial Control. Springer - Verlag, London, U.K., 2007.

[175] 1.5 MW Wind Turbine Technical Specifications GE Energy, "www.gepower.com/prodserv/products/windturbines/en/15mw/specs.htm," 2008.

[176] D. S. Zinger and E. Muljadi, "Annualized wind energy improvement using variable speed," *IEEE Trans. on Ind. Appl.*, vol. 6, no. 33, pp. 1444 – 47, Nov.-Dec. 1997.

[177] Danish Wind Industry Association, "www.windpower.org/en/tour/," 2008.

[178] L. Fingersh and P. Carlin, "Results from the NREL Variable-Speed Test Bed," in *Proceedings of the 17th ASME Wind Energy Symposium*, Reno, NV, US, 12-15 Jan. 1998, pp. 233–37.

[179] G. Niglio and G. Scorsoni, "Short term forecasting of wind power in Italy - the GSE experience," in *7th International Workshop on Large Scale Integration of Wind Power and on Transmission Networks for Offshore Wind Farms*, Madrid, Spain, 26-27 May 2008, pp. 1–4.

[180] P. V. O'Neil, *Advanced Engineering Mathematics*, Thomson, 1120 Birchmount Road, Toronto, Ontario, M1K 5G4, Canada, 2007.

[181] M. T. Thompson, *Intuitive Analog Circuit Design*, Electrical Engineering - Circuit Design. Newnes - Elsevier, 30 Corporate Drive, Suite 400, Burlington, MA 01803, US, 1994.

[182] Matlab Control System Toolbox, "www.mathworks.com/products/control," 2008.

[183] G. C. Paap, "Symmetrical Components in the Time Domain and Their Application to Power Network Calculations," *IEEE Trans. on Power Systems*, vol. 15, no. 2, pp. 522 – 28, May 2000.

[184] P. W. Bridgman, *The Logic of Modern Physics*, Macmillan, New York, 1927.

[185] L. S. Czarnecki, "On some misinterpretations of the instantaneous reactive power $p - q$ theory," *IEEE Trans. Pow. Electr.*, vol. 19, no. 3, pp. 828–36, May 2004.

[186] A. E. Emanuel, "Poynting vector and physical meaning of non active powers," *IEEE Trans. Instr. Meas.*, vol. 54, no. 4, pp. 1457–62, Aug. 2005.

[187] S. Togasawa, T. Murase, H. Hakano, and A. Nabae, "Reactive power compensation based on a novel cross-vector theory," *IEEJ Trans. Ind. Appl*, vol. 114, no. 3, pp. 340–41, March 1994.

[188] H. Akagi, S. Ogasawara, and H. Kim, "The theory of instantaneous power in Three-Phase four-wire systems: A comprehensive approach," in *Proc. Industry Applications Conference, 1999. Thirty-Fourth IAS Annual Meeting. Conference Record of the 1999 IEEE*, Phoenix, AZ, 3-7 Oct. 1999, pp. 431 – 439.

[189] A. M. Trzynadlowski, "An overview of modern PWM techniques for three-phase, voltage-controlled, voltage-source inverters," in *Proc. IEEE International Symposium on Industrial electronics, (ISIE 96)*, Warsaw, Poland, 17-20 June 1996, pp. 25–39.

Appendix A

System data

Table A.1 - DFIG parameters.

P_n	=	1.50	MW
$\cos\varphi_n$	=	0.90	
V_n	=	575	V
$\mathbb{P}$	=	3	
R_s	=	0.00706	p.u.
L_{ls}	=	0.171	p.u.
R_r	=	0.005	p.u.
L_{lr}	=	0.156	p.u.
L_m	=	2.9	p.u.
H	=	5.04	s
$\mathbb{F}$	=	0.01	p.u.

Table A.2 - Supply line and transformer parameters.

R_g	=	0.1153	Ω / km
L_g	=	1.05	mH / km
ℓ	=	10	km
V_1	=	575	V
V_2	=	13	kV
X_T	=	0.1	p.u.

Table A.3 - RC load / filter parameters.

R_f	=	18.37	Ω
ωC_f	=	0.367	Ω
Q	=	50	

Table A.4 - Power converters and dc-link parameteres.

Switches		IGBT	
R_{on}	=	8	m Ω
P_n	=	7.25	MW
f_{tri}	=	6480	Hz
C	=	0.6	F
$V_{dc,nom}$	=	1200	V
R_L	=	0.003	Ω
L_L	=	0.3	H

Table A.5 - PI controllers parameteres for compensation by means of RSC modulation.

	k_i	k_p
RSC current controller	k_{i1} =4	k_{p1} =8
LSC current controller	k_{i2} =0.1	k_{p2} =5
dc-link voltage controller	k_{i3} =0.001	k_{p3} =0.025
zero sequence controller	absent	absent

Table A.6 - PI controllers parameteres for compensation by means of LSC modulation.

	k_i	k_p
RSC current controller	k_{i1} =0.1	k_{p1} =5
LSC current controller	k_{i2} =4	k_{p2} =8
dc-link voltage controller	k_{i3} =0.001	k_{p3} =0.025
zero sequence controller	k_{i4} =0.002	k_{p4} =400

Table A.7 - PI controllers parameteres for compensation by means of combined modulation.

	k_i	k_p
RSC current controller	k_{i1} =4	k_{p1} =8
LSC current controller	k_{i2} =4	k_{p2} =8
dc-link voltage controller	k_{i3} =0.001	k_{p3} =0.025
zero sequence controller	k_{i4} =0.002	k_{p4} =400

Table A.8 - System rated power loss (in % with respect to the rated power of the DFIG).

Name	**Symbol**	**Value**
Stator windings	ΔP_{sn}	2.6 %
Rotor windings	ΔP_{rn}	1.8 %
Power converters	ΔP =	12%

Table A.9 - Definition of base quantitites [92].

Name	**Symbol**	**Expression**	**Unit**
Base voltage	V_B		V
Base power	S_B	$S_B = \sqrt{3}\ V_B\ I_B$	VA
Base current	I_B	V_B^2/S_B	A
Base Impedance	Z_B	$V_B^2/S_B = V_B/(\sqrt{3}\ I_B)$	Ω

Table A.10 - Base quantities chosen for the system shown in Figure 3.1.

$V_B = 575$ V
$S_B = 1.667$ MVA
$I_B = 1675$ A
$Z_B = 0.982\ \Omega$

Table A.11 - Parameters of the two mass model.

Name	**Symbol**	**Value**
Generator inertia	J_r	5.04 s
Turbine inertia	J_t	4.45 s
Spring constant	k	0.001 N/m

Tracking characteristic

The tracking characteristic of the wind turbine is shown in Figure A.1.

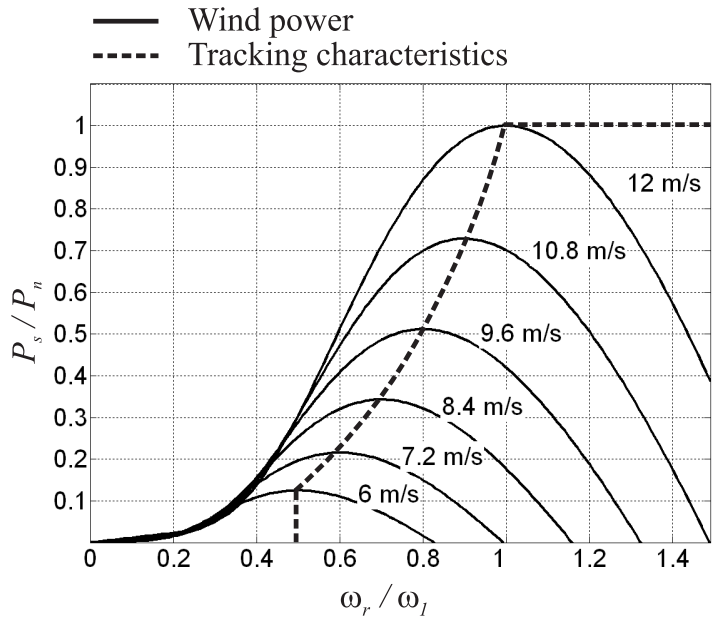

Figure A.1 - Tracking characteristic of the wind turbine used in this work: the power captured from the wind is expressed as function of time, for different wind speeds.

Appendix B

Reference Frame Theory and Vector Control

B.1 Introduction

The study of the dynamic behavior of the induction machine needs the use of particular methodologies, due to the complexity of the problem: mutual coupling between stator and rotor, position-dependence of mutual inductances are a couple of the challenges [90]. A common procedure to study the induction and synchronous machine dynamics is the transformation of the machine variables in an equivalent reference frame.

The first formulation of the reference frame theory was developed by R. H. Park [159] in 1929: he formulated a change of variables which replaces the voltages, currents and flux linkages associated with the stator windings into variables associated with fictitious windings fixed with the rotor (rotor reference frame). H. C. Stanley [160], G. Kron [161] and D. S. Bereton [162] developed other changes of variables. In 1965 Krause et al. noted that all those transformations are different expressions of a more general transformation that eliminates time-varying inductances by referring the stator and rotor to a reference frame that may rotate at any angular velocity or remain stationary [78]. This general reference frame is called 'arbitrary reference frame'.

In the following sections, the reference frame theory principles are summarized and the vector control is introduced.

B.2 Clarke and Park transformations

Clarke transformation [163] and the more general Park transformation [164] help to simplify the dynamic analysis of the three-phase machine because

1. the time-varying machine parameters are replaced by constant values,

2. two parameters are used instead of three.

B.2.1 Clarke transformation

The concept of Clarke transformation[38] [75, 139, 163] is shown in Figure B.1: three phase axes a, b, c are replaced by two perpendicular axes α and β. In order to obtain a perfect correspondence between the actual and the transformed system, an arbitrary single phase (homopolar or zero-sequence) component is added. It will be shown that in the electrical machine, the homopolar component resulting from the transformation is nil and, as a result, only two variables will be used after the transformation is applied.

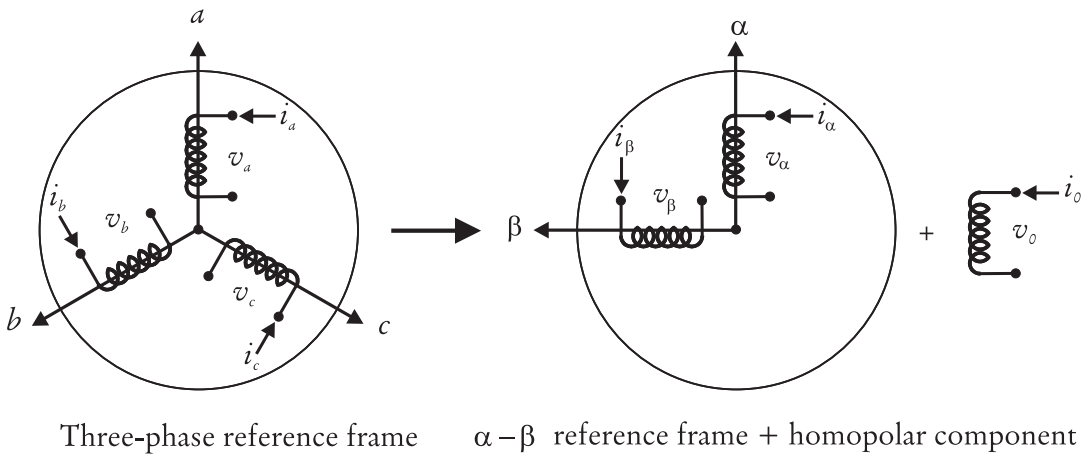

Figure B.1 - The Clarke transformation concept: the three phase axes a, b, c are replaced by two perpendicular axes d,q and a homopolar component.

Referring to the notation shown in Figure B.1, the α-axis is aligned with the a axis of the three-phase windings, and hence the projection of the three-phase system on the $\alpha\beta$ frame is obtained as:

$$\begin{bmatrix} y_\alpha \\ y_\beta \\ y_0 \end{bmatrix} = k \begin{bmatrix} \cos(0) & \cos(2\pi/3) & \cos(4\pi/3) \\ \sin(0) & \sin(2\pi/3) & \sin(4\pi/3) \\ w & w & w \end{bmatrix} \begin{bmatrix} y_a \\ y_b \\ y_c \end{bmatrix} \tag{B.1}$$

where the coefficients k and w are introduced for generalization.

The transformation matrix $[T(0)]$ is:

$$[T(0)] = k \begin{bmatrix} \cos(0) & \cos(2\pi/3) & \cos(4\pi/3) \\ \sin(0) & \sin(2\pi/3) & \sin(4\pi/3) \\ w & w & w \end{bmatrix} \tag{B.2}$$

[38] In the literature (for example in [48])this transformation is named also 'Concordia Transformation'.

The system contains two unknowns, k and w. The values of these coefficients can be chosen arbitrarily, or additional constrains can be considered to make matrix (B.2) to satisfy specific properties.

First of all, the matrix (B.2) has to be invertible, in order to apply the reverse transformation from the equivalent system to the three-phase system. The matrix (B.2) is invertible if its determinant is different from zero:

$$\det[\mathrm{T}(0)] = \sqrt{3}\ k\ w\ \frac{3}{2} \neq 0$$

The previous condition is verified if $k \neq 0$ and $w \neq 0$. Moreover, the orthogonality condition [163, 165] is added to (B.2). The orthogonality condition is expressed as:

$$[T(0)]\ [T(0)]^T = [I] \tag{B.3}$$

where the $[I]$ is the identity matrix:

$$[I] = \begin{bmatrix} 1 & 0 & 0 \\ 0 & 1 & 0 \\ 0 & 0 & 1 \end{bmatrix}$$

and the superscript ^{T} indicate the transpose.

The orthogonality condition (B.3) is chosen for two reasons:

1. The calculations are simplified because if $[T_0]$ is orthogonal, the inverse is equal to the transpose [165]: $[T(0)]^T = [T(0)]^{-1}$,

2. If the transformation matrix is orthogonal, the same power is absorbed/delivered by the original and the transformed system. This can be proved in a few steps. If $p = v_a\ i_a + v_b\ i_b + v_c\ i_c$ is the power absorbed by the three-phase system, then applying (B.1) the following is obtained:

$$\begin{aligned} p &= [v_{a,b,c}]^T\ [i_{a,b,c}] = [[T(0)]^{-1}[v_{\alpha,\beta,0}]]^T\ [T(0)]^{-1}[i_{\alpha,\beta,0}] \\ &= [v_{\alpha,\beta,0}]^T[[T(0)]^{-1}]^T\ [T(0)]^{-1}[i_{\alpha,\beta,0}] \\ &= [v_{\alpha,\beta,0}]^T[[[T(0)]\ [T(0)]^T]^{-1}[i_{\alpha,\beta,0}] \\ &= [v_{\alpha,\beta,0}]^T[i_{\alpha,\beta,0}] \end{aligned}$$

   The last equation is true only if orthogonality condition (B.3) applies.

Substituting (B.2) in (B.3) gives:

$$[T(0)]\,[T(0)]^T = k^2 \begin{bmatrix} 3/2 & 0 & 0 \\ 0 & 3/2 & 0 \\ 0 & 0 & 3\,w^2 \end{bmatrix} = \begin{bmatrix} 1 & 0 & 0 \\ 0 & 1 & 0 \\ 0 & 0 & 1 \end{bmatrix} \tag{B.4}$$

hence:

$$k = \sqrt{\frac{2}{3}}$$

$$w = \sqrt{\frac{1}{2}}$$

and the matrix $[T(0)]$ is:

$$[T(0)] = \sqrt{\frac{2}{3}} \begin{bmatrix} \cos(0) & \cos(2\pi/3) & \cos(4\pi/3) \\ \sin(0) & \sin(2\pi/3) & \sin(4\pi/3) \\ \sqrt{1/2} & \sqrt{1/2} & \sqrt{1/2} \end{bmatrix} = \sqrt{\frac{2}{3}} \begin{bmatrix} 1 & -1/2 & -1/2 \\ 0 & \sqrt{3}/2 & -\sqrt{3}/2 \\ \sqrt{1/2} & \sqrt{1/2} & \sqrt{1/2} \end{bmatrix} \tag{B.5}$$

If the matrix (B.5) is substituted in (B.1), the α, β and 0 components are:

$$\begin{cases} y_\alpha &= \sqrt{\frac{2}{3}}\Big[y_a - \frac{1}{2}y_b - \frac{1}{2}y_c\Big] \\ y_\beta &= \sqrt{\frac{2}{3}}\Big[\frac{\sqrt{3}}{2}y_b - \frac{\sqrt{3}}{2}y_c\Big] \\ y_0 &= \sqrt{\frac{2}{3}}\Big[\frac{1}{\sqrt{2}}y_a + \frac{1}{\sqrt{2}}y_b + \frac{1}{\sqrt{2}}y_c\Big] \end{cases} \tag{B.6}$$

B.2.2 Park transformation

The Park transformation [75, 164] is a generalization of the Clarke transformation, because in the Park domain the dq axes rotates at arbitrary speed ω_a, as shown in Figure B.2. The zero-sequence axis is fixed as in the Clarke transformation.

By referring to the notation of Figure B.2, the angle between α and d varies in time:

$$\vartheta_a = \omega_a t$$

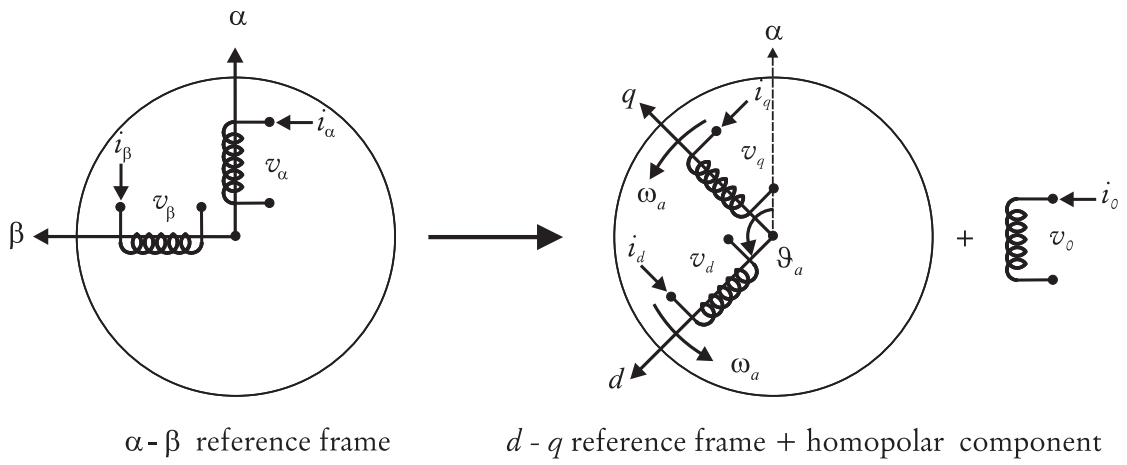

Figure B.2 - The concept of Park transformation: the two perpendicular axes d and q rotate with speed ω_a. The zero-sequence axis is fixed.

and the dq axes are obtained from the $\alpha\beta$ axes by applying the following transformation:

$$\begin{bmatrix} y_d \\ y_q \\ y_0 \end{bmatrix} = \begin{bmatrix} \cos(\vartheta_a) & \sin(\vartheta_a) & 0 \\ -\sin(\vartheta_a) & \cos(\vartheta_a) & 0 \\ 0 & 0 & 1 \end{bmatrix} \begin{bmatrix} y_\alpha \\ y_\beta \\ y_0 \end{bmatrix} \tag{B.7}$$

where the rotation matrix is:

$$[\Pi(\vartheta_a)] = \begin{bmatrix} \cos(\vartheta_a) & \sin(\vartheta_a) & 0 \\ -\sin(\vartheta_a) & \cos(\vartheta_a) & 0 \\ 0 & 0 & 1 \end{bmatrix} \tag{B.8}$$

The complete transformation from the a, b, c reference frame to the dq reference frame

is obtained as a combination of (B.5) and (B.7):

$$\begin{aligned}
\begin{bmatrix} y_d \\ y_q \\ y_0 \end{bmatrix} &= [\Pi(\vartheta_a)]\,[T(0)] \begin{bmatrix} y_a \\ y_b \\ y_c \end{bmatrix} \\
&= \begin{bmatrix} \cos(\vartheta_a) & \sin(\vartheta_a) & 0 \\ -\sin(\vartheta_a) & \cos(\vartheta_a) & 0 \\ 0 & 0 & 1 \end{bmatrix} \sqrt{\frac{2}{3}} \begin{bmatrix} 1 & -1/2 & -1/2 \\ 0 & \sqrt{3}/2 & -\sqrt{3}/2 \\ \sqrt{1/2} & +\sqrt{1/2} & \sqrt{1/2} \end{bmatrix} \begin{bmatrix} y_a \\ y_b \\ y_c \end{bmatrix} \\
&= \sqrt{\frac{2}{3}} \begin{bmatrix} \cos(\vartheta_a) & \cos(\vartheta_a - 2\pi/3) & \cos(\vartheta_a - 4\pi/3) \\ \sin(\vartheta_a) & \sin(\vartheta_a - 2\pi/3) & \sin(\vartheta_a - 4\pi/3) \\ \sqrt{1/2} & \sqrt{1/2} & \sqrt{1/2} \end{bmatrix} \begin{bmatrix} y_a \\ y_b \\ y_c \end{bmatrix} \\
&= [T(\vartheta_a)] \begin{bmatrix} y_a \\ y_b \\ y_c \end{bmatrix}
\end{aligned} \tag{B.9}$$

where the matrix $[T(\vartheta_a)]$ for the Park transformation is:

$$\begin{aligned}
[T(\vartheta_a)] &= \sqrt{\frac{2}{3}} \begin{bmatrix} \cos(\vartheta_a) & \cos(\vartheta_a - 2\pi/3) & \cos(\vartheta_a - 4\pi/3) \\ \sin(\vartheta_a) & \sin(\vartheta_a - 2\pi/3) & \sin(\vartheta_a - 4\pi/3) \\ \sqrt{1/2} & \sqrt{1/2} & \sqrt{1/2} \end{bmatrix} \\
&= \begin{bmatrix} \cos(\omega_a t) & \cos(\omega_a t - 2\pi/3) & \cos(\omega_a t - 4\pi/3) \\ \sin(\omega_a t) & \sin(\omega_a t - 2\pi/3) & \sin(\omega_a t - 4\pi/3) \\ \sqrt{1/2} & \sqrt{1/2} & \sqrt{1/2} \end{bmatrix}
\end{aligned} \tag{B.10}$$

The second formulation of (B.10) is shows that the transformation angle is a function of time, because the axes are rotating.

B.2.3 The space vector

The dq components can be combined in a unique space vector [166]; as a result, the three-phase system correspond to a space vector that embeds the information of the d and q equivalent circuits and to a scalar zero-sequence component.

If the Clarke transformation (B.5) is applied, the space vector and the zero-sequence

component have the following formulation:

$$\begin{cases} \bar{y}_{\alpha\beta} = \sqrt{\dfrac{2}{3}} \left\{ y_a + \bar{\alpha} y_b + \bar{\alpha}^2 y_c \right\} \\ y_0(t) = \dfrac{1}{\sqrt{3}} \left\{ y_a + y_b + y_c \right\} \end{cases} \tag{B.11}$$

where $\bar{\alpha} = \exp(j2\pi/3)$ is the Fortescue operator. According to (B.11), in a balanced three-phase system the zero-sequence component is nil [75].

If the Park transformation (B.10) is implemented, the space vector formulation is:

$$\bar{y}_{dq} = \bar{y}_{\alpha\beta}\ exp(-j\vartheta_a) \tag{B.12}$$

The zero-sequence component formulation does not change in the Park domain with respect to the Clarke domain, since the third line of the matrices (B.5) and (B.10) is the same.

B.2.4 Inverse transformations

From (B.1) and applying the orthogonality condition (B.3) the phase quantities are obtained from the α, β and 0 quantities as follows:

$$\begin{aligned} \begin{bmatrix} y_a \\ y_b \\ y_c \end{bmatrix} &= [T(0)]^{-1} \begin{bmatrix} y_\alpha \\ y_\beta \\ y_0 \end{bmatrix} = [T(0)]^T \begin{bmatrix} y_\alpha \\ y_\beta \\ y_0 \end{bmatrix} \\ &= \sqrt{\frac{2}{3}} \begin{bmatrix} \cos(0) & \sin(0) & \sqrt{1/2} \\ \cos(2\pi/3) & \sin(2\pi/3) & \sqrt{1/2} \\ \cos(4\pi/3) & \sin(4\pi/3) & \sqrt{1/2} \end{bmatrix} \begin{bmatrix} y_\alpha \\ y_\beta \\ y_0 \end{bmatrix} \end{aligned} \tag{B.13}$$

and from (B.9), the phase quantities a, b, c are derived from the d,q,0 quantities:

$$\begin{aligned} \begin{bmatrix} y_a \\ y_b \\ y_c \end{bmatrix} &= [T(\vartheta_a)]^T \begin{bmatrix} y_\alpha \\ y_\beta \\ y_0 \end{bmatrix} \\ &= \sqrt{\frac{2}{3}} \begin{bmatrix} \cos(\vartheta_a) & \sin(\vartheta_a) & \sqrt{1/2} \\ \cos(\vartheta_a - 2\pi/3) & \sin(\vartheta_a - 2\pi/3) & \sqrt{1/2} \\ \cos(\vartheta_a - 4\pi/3) & \sin(\vartheta_a - 4\pi/3) & \sqrt{1/2} \end{bmatrix} \begin{bmatrix} y_d \\ y_q \\ y_0 \end{bmatrix} \end{aligned} \tag{B.14}$$

B.3 The induction machine dynamic model

B.3.1 Stator windings representation in the equivalent frame

The three-phase stator windings of an induction machine are now considered. The windings and their components are shown in Figure B.3: the resistance of the windings is R_s, the auto-inductance is L_s, the mutual inductance is M_s.

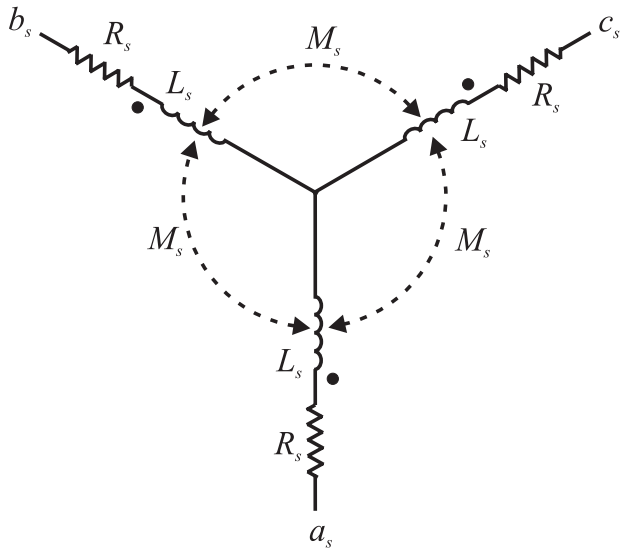

Figure B.3 - Induction machine stator windings.

The Kirchhoff Voltage Law and the constitutive relation for the stator windings in matrix representation are:

$$[v_s] = [R_s][i_s] + \frac{d}{dt}[\lambda_s] \tag{B.15}$$

$$[\lambda_s] = [L_s][i_s] \tag{B.16}$$

where:

$$[v_s] = \begin{bmatrix} v_{as} \\ v_{bs} \\ v_{cs} \end{bmatrix} \quad ; \quad [\lambda_s] = \begin{bmatrix} \lambda_{as} \\ \lambda_{bs} \\ \lambda_{cs} \end{bmatrix} \quad ; \quad [i_s] = \begin{bmatrix} i_{as} \\ i_{bs} \\ i_{cs} \end{bmatrix}$$

$$[R_s] = \begin{bmatrix} R_s & 0 & 0 \\ 0 & R_s & 0 \\ 0 & 0 & R_s \end{bmatrix} \quad \text{and} \quad [L_s] = \begin{bmatrix} L_s & M_s & M_s \\ M_s & L_s & M_s \\ M_s & M_s & L_s \end{bmatrix}$$

If the Clarke transformation (B.3) is applied to (B.15) and (B.16), the following is obtained:

$$[v_{\alpha\beta 0s}] = [T(0)][v_s] = [T(0)][R_s][i_s] + \frac{d}{dt}[T(0)][\lambda_s] \tag{B.17}$$

and

$$[\lambda_{\alpha\beta 0s}] = [T(0)][\lambda_s] = [T(0)][L_s][i] \tag{B.18}$$

where

$$[v_{\alpha\beta 0s}] = \begin{bmatrix} \lambda_{\alpha s} \\ \lambda_{\beta s} \\ \lambda_{0s} \end{bmatrix} \quad \text{and} \quad [\lambda_{\alpha\beta 0s}] = \begin{bmatrix} \lambda_{\alpha s} \\ \lambda_{\beta s} \\ \lambda_{0s} \end{bmatrix}$$

By applying the orthogonality property (B.3) to (B.18), it results:

$$[\lambda_{\alpha\beta 0s}] = [T(0)][L_s][i] = ([T(0)][L_s][T(0)]^{-1})([T(0)][i]) = [L_s]'[i_{\alpha\beta 0s}] \tag{B.19}$$

where:

$$[L_s]' = [T(0)][L_s][T(0)]^{-1} = \begin{bmatrix} L_s - M_s & 0 & 0 \\ 0 & L_s - M_s & 0 \\ 0 & 0 & L_s + 2\ M_s \end{bmatrix}$$

$$[i_{\alpha\beta 0s}] = \begin{bmatrix} i_{\alpha s} \\ i_{\beta s} \\ i_{0s} \end{bmatrix}$$

Substitution of (B.19) in (B.17) it results:

$$[v_{\alpha\beta 0s}] = ([T(0)][R_s][T(0)]^{-1})([T(0)][i]) + \frac{d}{dt}[T(0)][\lambda_s] = [R_s][i_{\alpha\beta 0s}] + \frac{d}{dt}[L_s]'[i_{\alpha,\beta,0,s}] \tag{B.20}$$

From (B.19) and (B.20), the following observations are carried out:

- the diagonal matrix $[R_s]$ is not altered by the transformation: $[T(0)][R_s][T(0)]^{-1} = [R_s]$.
- The transformed inductance matrix $[L_s]'$ is diagonal: there is no mutual inductance between the $\alpha\beta$ axes. This result derives from the fact that the $\alpha\beta$ axes are orthogonal, as shown in Figure B.3.
- The Clarke transformation requires a simultaneous transformation of the machine parameters and of the electric quantities in order to obtain an equivalent machine

with the same air-gap flux.

- As already pointed out, when the Park transformation is applied to symmetric three-phase systems, the resulting homopolar component is nil, because the sum of the phase quantities is zero. For this reason, in the following developments only the two-dimensional vectors $[y_{\alpha\beta s}]$ and $[y_{dqs}]$ will be used.
- The transformed matrix is symmetric: $[L_s]' = [L_s]'^T$. This condition must be verified because the symmetry of the original matrix $[L_s]$ cannot be altered by the transformation.

If the axis are rotating, the matrix $[\Pi(\vartheta)]$ is applied to (B.20)[39]:

$$\begin{aligned}
[v_{dqs}] &= [\Pi(\vartheta)][v_{\alpha\beta 0s}] \\
&= [\Pi(\vartheta)]([R_s][i_{\alpha\beta s}] + \frac{d}{dt}[L_s]'[i_{\alpha\beta s}]) \\
&= [\Pi(\vartheta)][R_s][i_{\alpha\beta s}] + [T(\vartheta)]\frac{d}{dt}[L_s]'[i_{\alpha\beta s}]) \\
&= [\Pi(\vartheta)][R_s][\Pi(\vartheta)]^T[T(\vartheta)][i_{\alpha\beta s}] + [\Pi(\vartheta)]\frac{d}{dt}[L_s]'[\Pi(\vartheta)]^T[\Pi(\vartheta)][i_{\alpha\beta s}]) \\
&= [R_s][i_{dqs}] + [T(\vartheta)][L_s]'[T(\vartheta)]^T[i_{dqs}] + [\Pi(\vartheta)][L_s]'\frac{d}{dt}[\Pi(\vartheta)]^T[i_{dqs}]) \qquad \text{(B.21)} \\
&= [R_s][i_{dqs}] + [\psi_{dqs}] + [\Pi(\vartheta)][L_s]'\frac{d}{d\vartheta}\frac{d\vartheta}{dt}[\Pi(\vartheta)]^T[i_{dqs}]) \\
&= [R_s][i_{dqs}] + [\psi_{dqs}] + \omega_a[\Pi(\vartheta)][L_s]'\frac{d}{d\vartheta}[\Pi(\vartheta)]^T[i_{dqs}]) \\
&= [R_s][i_{dqs}] + [\psi_{dqs}] + \omega_a[\Pi(\vartheta)]\frac{d}{d\vartheta}[\Pi(\vartheta)]^T[L_s]'[i_{dqs}]) \\
&= [R_s][i_{dqs}] + [\psi_{dqs}] + \omega_a[B][\psi_{dqs}])
\end{aligned}$$

where:

$$[B] = [\Pi(\vartheta)]\frac{d}{d\vartheta}[\Pi(\vartheta)]^T = \begin{bmatrix} 0 & -1 & 0 \\ 1 & 0 & 0 \\ 0 & 0 & 0 \end{bmatrix}$$

[39] Observing that the information given by (B.19) is embedded in (B.20), in the following only (B.20) will be considered.

The stator windings representation in the dq variables is:

$$\begin{cases} v_{ds} = R_s\ i_{ds} + \dfrac{d}{dt}\ \lambda_{ds} - \omega_a\ \lambda_{qs} \\ v_{qs} = R_s\ i_{qs} + \dfrac{d}{dt}\ \lambda_{qs} + \omega_a\ \lambda_{ds} \end{cases} \tag{B.22}$$

B.3.2 Stator and rotor windings representation in the equivalent frame

The stator and rotor windings are shown in Figure B.4; the winding parameters are:

R_s = stator winding resistance

R_r = rotor winding resistance

L_s = stator winding auto inductance

L_r = rotor winding auto inductance

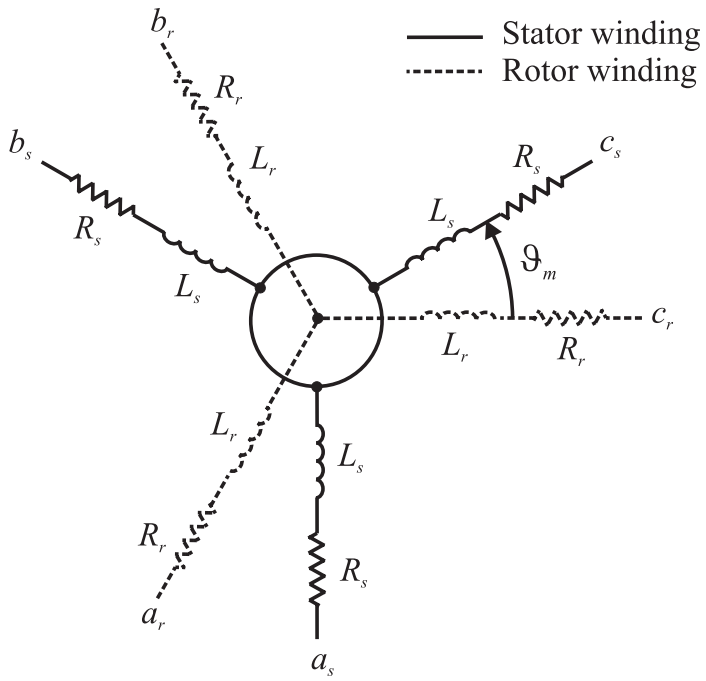

Figure B.4 - Stator and rotor windings of a three-phase machine.

For the sake of simplicity, the mutual inductances are not shown in Figure B.4; however, the following mutual inductances will be included in the mathematical analysis:

- M_s = mutual inductance between stator windings;
- M_r = mutual inductance between rotor windings;
- $M_{ij}(\vartheta_m)$ = mutual inductances between stator winding i and rotor windings j, where $i, j \in \{a, b, c\}$. The mutual inductances $M_{ij}(\vartheta_m)$ are function of the angle ϑ_m between the rotor axis a_r and the stator axis a_s (Figure B.4) [82].

Kirchhoff's laws and the constitutive equations are similar to (B.15) and (B.16), but in this case six-dimensional vectors are considered:

$$\begin{bmatrix} v_s \\ v_r \end{bmatrix} = \begin{bmatrix} [R_s] & 0 \\ 0 & [R_r] \end{bmatrix} \begin{bmatrix} i_s \\ i_r \end{bmatrix} + \frac{d}{dt} \begin{bmatrix} \lambda_s \\ \lambda_r \end{bmatrix} \tag{B.23}$$

$$\begin{bmatrix} \lambda_s \\ \lambda_r \end{bmatrix} = \begin{bmatrix} [L_s] & [M(\vartheta_m)] \\ M(\vartheta_m) & L_r \end{bmatrix} \begin{bmatrix} i_s \\ i_r \end{bmatrix} \tag{B.24}$$

where:

$$\begin{bmatrix} v_s \\ v_r \end{bmatrix} = \begin{bmatrix} v_{as} \\ v_{bs} \\ v_{cs} \\ v_{ar} \\ v_{br} \\ v_{cr} \end{bmatrix} \quad ; \quad \begin{bmatrix} i_s \\ i_r \end{bmatrix} = \begin{bmatrix} i_{as} \\ i_{bs} \\ i_{cs} \\ i_{ar} \\ i_{br} \\ i_{cr} \end{bmatrix}$$

$$[R_s] = \begin{bmatrix} R_s & 0 & 0 \\ 0 & R_s & 0 \\ 0 & 0 & R_s \end{bmatrix} \quad ; \quad [R_r] = \begin{bmatrix} R_r & 0 & 0 \\ 0 & R_r & 0 \\ 0 & 0 & R_r \end{bmatrix}$$

$$[L_s] = \begin{bmatrix} L_s & M_s & M_s \\ M_s & L_s & M_s \\ M_s & M_s & L_s \end{bmatrix} \quad ; \quad [L_r] = \begin{bmatrix} L_r & M_r & M_r \\ M_r & L_r & M_r \\ M_r & M_r & L_r \end{bmatrix}$$

and

$$[M(\vartheta_m)] = \begin{bmatrix} M_{aa}(\vartheta_m) & M_{ab}(\vartheta_m) & M_{ac}(\vartheta_m) \\ M_{ba}(\vartheta_m) & M_{bb}(\vartheta_m) & M_{bc}(\vartheta_m) \\ M_{ca}(\vartheta_m) & M_{cb}(\vartheta_m) & M_{cc}(\vartheta_m) \end{bmatrix}$$

Due to the symmetry in the geometry of the machine, $[M(\vartheta_m)]$ is symmetric, however it is full and dependent on the rotor position ϑ_m. The dq representation of the systems is convenient because if the stator and rotor windings are referred to the same frame (Figure B.5), the mutual inductance matrix is diagonalized and the time dependence is eliminated.

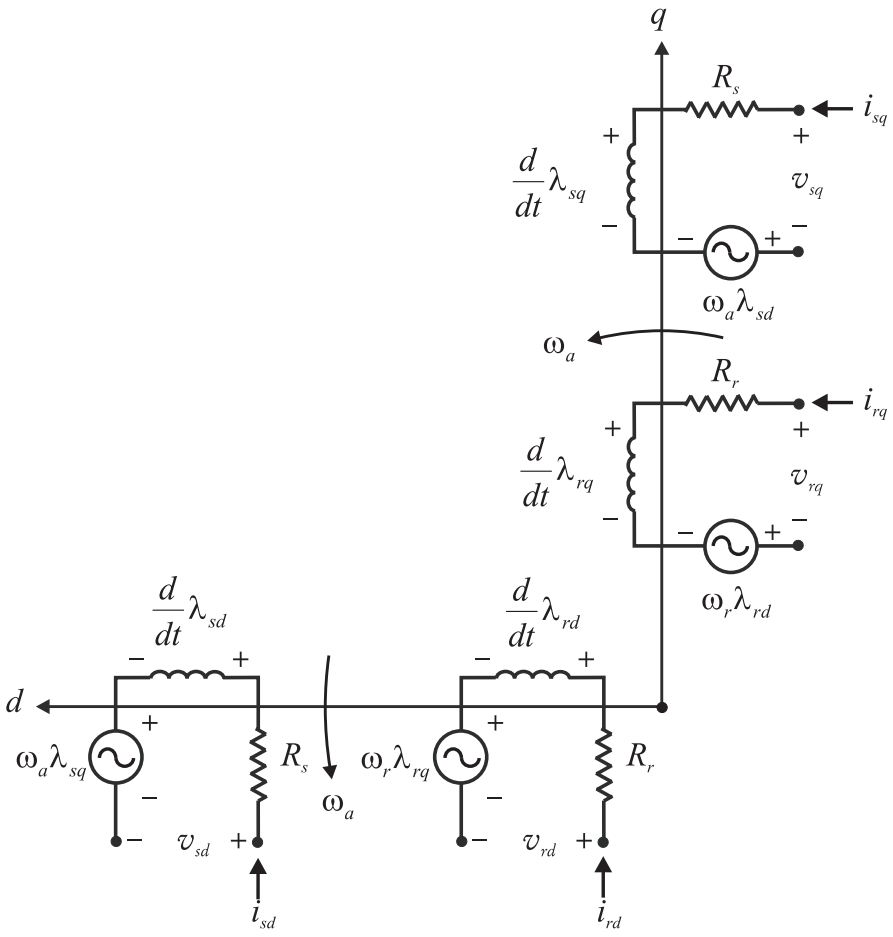

Figure B.5 - Representation of the stator and rotor windings in a dq reference frame rotating at speed ω_a

.

Two transformations characterized by different angles are applied to the stator and rotor windings respectively. The angles between the windings are shown in Figure B.6.

The dq axes are rotating at speed $\omega_a = \vartheta_a t$ while the stator windings are fixed in space. The angle between the d axis and the a_s axis is defined as ϑ_a (Figure B.6).

The rotor windings rotate with speed $\omega_m = \frac{d}{dt}\vartheta_m$ respect to the stator, the angle between the d axis and the a_r axis is defined as ϑ_r (Figure B.6).

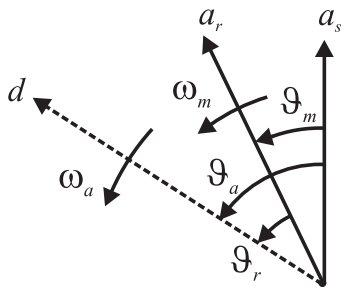

Figure B.6 - Angles between stator winding a_s, rotor winding a_r and d axis in stator reference frame.

If the stator and rotor windings are referred to the same dq reference frame, the angles for the transformations are ϑ_a for the stator windings and ϑ_r for the rotor windings.

The transformation of the systems (B.23) and (B.24) is expressed by the following block diagonal matrix [165]:

$$[T] = \begin{bmatrix} T(\vartheta_a) & 0 \\ 0 & T(\vartheta_r) \end{bmatrix} \tag{B.25}$$

where, referring to the notation of Figure B.6:

- ϑ_a is the angle of the d axis respect to the stator;
- ϑ_r is the angle of the d axis respect to the rotor.

Moreover, according to Figure B.6, the following relation apply:

$$\vartheta_a = \vartheta_m + \vartheta_r \tag{B.26}$$

The matrix (B.25) applied to (B.23) and (B.24) results in the following systems [75, 90]:

$$\begin{cases} v_{ds} = R_s i_{ds} + \dfrac{d}{dt}\lambda_{ds} - \omega_a \lambda_{qs} \\ v_{qs} = R_s i_{qs} + \dfrac{d}{dt}\lambda_{qs} + \omega_a \lambda_{ds} \\ v_{dr} = R_r i_{dr} + \dfrac{d}{dt}\lambda_{dr} - \omega_r \lambda_{qr} \\ v_{qr} = R_r i_{qr} + \dfrac{d}{dt}\lambda_{qr} + \omega_r \lambda_{dr} \end{cases} \tag{B.27}$$

where:

$$\omega_r = \frac{d}{dt}\vartheta_r = \omega_a - \omega_m \tag{B.28}$$

is the velocity of the d axis with respect to the rotor winding a_r (Figure B.6)

and

$$\begin{cases} \lambda_{ds} = L_s i_{ds} + M i_{dr} \\ \lambda_{qs} = L_s i_{qs} + M i_{qr} \\ \lambda_{dr} = L_r i_{dr} + M i_{ds} \\ \lambda_{qr} = L_r i_{qr} + M i_{qs} \end{cases} \tag{B.29}$$

where M is the magnetizing inductance [75].

The equivalent circuits of the induction machine on the d and q axes that correspond to (B.27) and (B.29) are represented in Figure B.7 applying the following relations:

- $L_{ls} = L_s - M$
- $L_{lr} = L_r - M$

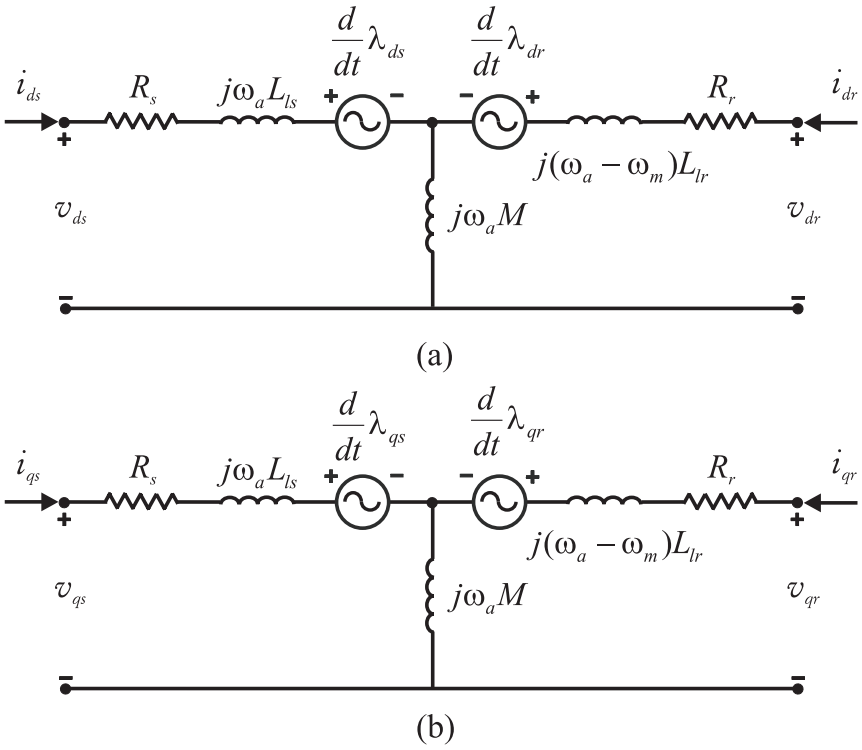

Figure B.7 - Dynamic equivalent circuits of a DFIG referred to an dq reference frame rotating with speed ω_a.

The above relations (B.27) and (B.29) can be expressed in terms of space vectors (B.12) as follows:

$$\begin{cases} \bar{v}_s = R_s \bar{i}_s + \dfrac{d}{dt}\bar{\psi}_s + j\omega_a \bar{\psi}_s \\ \bar{v}_r = R_r \bar{i}_r + \dfrac{d}{dt}\bar{\psi}_r + j(\omega_a - \omega_m)\bar{\psi}_r \end{cases} \tag{B.30}$$

and

$$\begin{cases} \bar{\lambda}_s = L_s \bar{i}_s + M \bar{i}_r \\ \bar{\lambda}_r = M \bar{i}_s + L_r \bar{i}_r \end{cases} \tag{B.31}$$

The circuit representation in terms of space vectors on an arbitrary reference frame (Figure B.8) is obtained from (B.30) and is named Park domain representation:

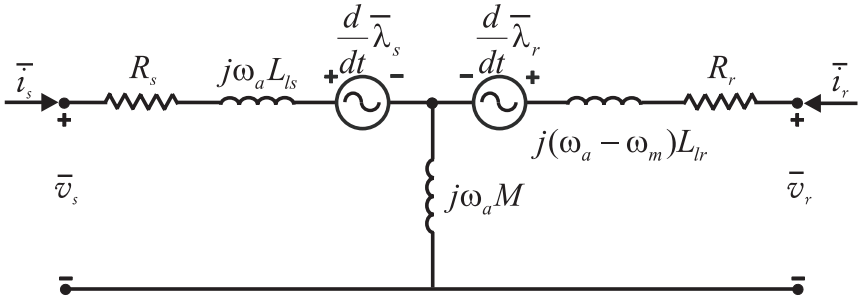

Figure B.8 - Dynamic equivalent circuit of a DFIG referred to an dq reference frame rotating with speed ω_a in terms of space vectors (Park domain representation).

B.3.3 Reference frame selection

In the previous sections, a reference frame rotating with arbitrary speed ω_a has been considered in applying the Park transformation (B.10).

In the practical applications [75, 82, 88, 167], the choice for the rotating speed is limited to two options:

1. $\omega_a = 0$
2. $\omega_a = \omega_1$

The first option coincides with the fixed reference frame (or Clarke transformation); the second option corresponds to the synchronously rotating reference frame.

The d-axis of the fixed reference frame is generally aligned with the stator winding a_s [75]; the rotating reference frame may be aligned with the stator flux, rotor flux, air gap flux, stator voltage... according to the control objectives [75, 82].

In a synchronously rotating frame, the positive sequence quantities appear as dc components; this is the reason why the synchronously rotating frame is widely implemented in motors' simulations.

Let us consider a generic three-phase positive sequence system:

$$\begin{cases} y_a = \hat{Y}\cos(\omega_1 t) \\ y_b = \hat{Y}\cos(\omega_1 t - 2\pi/3) \\ y_c = \hat{Y}\cos(\omega_1 t - 4\pi/3) \end{cases} \tag{B.32}$$

where $\hat{Y}$ is the peak value of the waveform.

By applying (B.6) the α and β components are obtained (while the zero-sequence component is nil):

$$\begin{aligned} y_\alpha &= \sqrt{\frac{2}{3}}(y_a - \frac{1}{2}y_b - \frac{1}{2}y_c) = \sqrt{\frac{2}{3}}\frac{3}{2}y_a = \sqrt{\frac{3}{2}}\hat{Y}\cos(\omega_1 t) \\ y_\beta &= \sqrt{\frac{2}{3}}(\frac{\sqrt{3}}{2}v_b - \frac{\sqrt{3}}{2}v_c) \\ &= \frac{1}{\sqrt{2}}(v_b - v_c) \\ &= \frac{1}{\sqrt{2}}\hat{Y}[\cos(\omega_1 t - 2\pi/3) - \cos(\omega_1 t - 4\pi/3)] = \\ &= \frac{1}{\sqrt{2}}\hat{Y}[\cos(\omega_1 t)\cos(2\pi/3) + \sin(\omega_1 t)\sin(2\pi/3) \\ &\quad -\cos(\omega_1 t)\cos(4\pi/3) - \sin(\omega_1 t)\sin(4\pi/3)] \\ &= \frac{1}{\sqrt{2}}\hat{Y}\frac{\sqrt{3}}{2}2\sin(\omega_1 t) = \sqrt{\frac{3}{2}}\hat{Y}\sin(\omega_1 t) \end{aligned} \tag{B.33}$$

and it results that they vary sinusoidally.

Further application of (B.10) with $\omega_a = \omega_1$ to (B.33) the dq components on the synchronously rotating frame are derived:

$$\begin{aligned} y_d &= y_\alpha\cos(\omega_1 t) + y_\beta\sin(\omega_1 t) \\ &= \sqrt{\frac{3}{2}}\hat{Y}[\cos(\omega_1 t)^2 + \sin(\omega_1 t)^2] = \sqrt{\frac{3}{2}}\hat{Y} \\ y_q &= -y_\alpha\sin(\omega_1 t) + y_\beta\cos(\omega_1 t) \\ &= \sqrt{\frac{3}{2}}\hat{Y}[-\cos(\omega_1 t)\sin(\omega_1 t) + \sin(\omega_1 t)\cos(\omega_1 t)] = 0 \end{aligned} \tag{B.34}$$

The last expressions that shows that in a synchronously rotating reference frame the dq components are constant (dc value).

The convenience of the synchronously rotating reference frame representing the system (B.32) can be summarized in two points:

1. two equivalent quantities are used instead of three
2. the equivalent quantities are constant in time.

B.3.4 Torque expression in the synchronous reference frame

In the previous paragraph the instantaneous power expression have been applied to the generic three phase load. In the following, the induction machine shown in Figure B.4 will be considered. The instantaneous power absorbed by the machine is the sum of the rotor and stator power [166]:

$$p = p_s + p_r = v_{sa}\ i_{sa} + v_{sb}\ i_{sb} + v_{sc}\ i_{sc} + v_{ra}\ i_{ra} + v_{rb}\ i_{rb} + v_{rc}\ i_{rc} \tag{B.35}$$

According to (E.7), the instantaneous power (E.1) can be expressed in the equivalent reference frame as follows:

$$p = v_{ds}\ i_{ds} + v_{qs}\ i_{qs} + v_{dr}\ i_{dr} + v_{qr}\ i_{qr} \tag{B.36}$$

By substituting (B.27) in (B.36):

$$\begin{aligned} p &= (R_s\ i_{ds} + \frac{d}{dt}\ \lambda_{ds}\ - \omega_a\ \lambda_{qs}\ )i_{ds} \\ &\quad +(R_s\ i_{qs} + \frac{d}{dt}\ \lambda_{qs}\ + \omega_a\ \lambda_{ds}\ )i_{qs} \\ &\quad +(R_r\ i_{dr} + \frac{d}{dt}\ \lambda_{dr}\ - \omega_r\ \lambda_{qr}\ )i_{dr} \\ &\quad +(R_r\ i_{qr} + \frac{d}{dt}\ \lambda_{qr}\ + \omega_r\ \lambda_{dr}\ )i_{qr} \\ &= R_s\ i_{ds}^2 + \frac{d}{dt}\ \lambda_{ds}\ i_{ds} - \omega_a\ \lambda_{qs}\ i_{ds} \\ &\quad +R_s\ i_{qs}^2 + \frac{d}{dt}\ \lambda_{qs}\ i_{qs} + \omega_a\ \lambda_{ds}\ i_{qs} \\ &\quad +R_r\ i_{dr}^2 + \frac{d}{dt}\ \lambda_{dr}\ i_{dr} - \omega_r\ \lambda_{qr}\ i_{dr} \\ &\quad +R_r\ i_{qr}^2 + \frac{d}{dt}\ \lambda_{qr}\ i_{qr} + \omega_r\ \lambda_{dr}\ i_{qr} \end{aligned} \tag{B.37}$$

The following three terms can be identified in (B.37):

1. Joule loss:

$$P_j = R_s i_{ds}^2 + R_s i_{qs}^2 + R_r i_{dr}^2 + R_r i_{qr}^2 \tag{B.38}$$

2. Rate of change of the stored magnetic energy:

$$\frac{d}{dt}W_\mu = \frac{d}{dt}\lambda_{ds} i_{ds} + \frac{d}{dt}\lambda_{qs} i_{qs} + \frac{d}{dt}\lambda_{dr} i_{dr} + \frac{d}{dt}\lambda_{qr} i_{qr} \tag{B.39}$$

3. Mechanic power:

$$\begin{aligned} p_m &= -\omega_a \lambda_{qs} i_{ds} + \omega_a \lambda_{ds} i_{qs} - \omega_r \lambda_{qr} i_{dr} + \omega_r \lambda_{dr} i_{qr} \\ &= -(\omega_m + \omega_r)(L_s i_{qs} + L_m i_{qr}) i_{ds} + (\omega_m + \omega_r)(L_s i_{ds} + L_m i_{dr}) i_{qs} \\ &\quad -\omega_r (L_r i_{qr} + L_m i_{qs}) i_{dr} + \omega_r (L_r i_{dr} + L_m i_{ds}) i_{qr} \\ &= \omega_m M (i_{dr} i_{qs} - i_{qr} i_{ds}) \end{aligned} \tag{B.40}$$

and the torque expression is obtained from the (B.40):

$$\begin{aligned} T_e &= \frac{p_m}{\omega_m} = M(i_{dr}i_{qs} - i_{qr}i_{ds}) \\ &= M\Big[\frac{1}{M}i_{qs}(\lambda_{ds} - L_s) - \frac{1}{M}i_{ds}(\lambda_{qs} - L_s)\Big] \\ &= i_{ds}\ \lambda_{qs} - i_{qs}\lambda_{ds} \end{aligned} \tag{B.41}$$

B.4 Vector control

In chapter 2 it was shown that the DFIG stator current affects both the torque and the air-gap flux simultaneously (the same conclusions apply to the squirrel cage machine [75, 78]).

On the contrary, in a dc motor with independent excitation, the air gap flux is controlled by the excitation current, the torque is controlled by the armature current [75].

The induction machine can be controlled as the dc machine if the vector control method is used.

Let us consider a reference frame synchronous with the stator voltage (Figure 4.7)

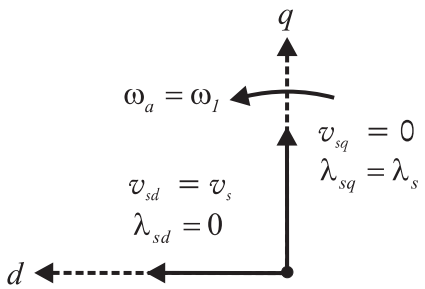

Figure B.9 - Stator voltage reference frame.

As visualized in Figure B.9, the following conditions are met in the stator reference frame:

$$\begin{aligned} &\omega_a = \omega_1 \\ &v_{ds} = v_s \\ &v_{qs} = 0 \\ &\lambda_{ds} = 0 \\ &\lambda_{qs} = \lambda_s \end{aligned} \tag{B.42}$$

By substituting (B.42) in the torque expression (B.41), the following is obtained:

$$T_{edq} = i_{ds}\lambda_s \tag{B.43}$$

If the reference frame is synchronous with the stator voltage, according to the system (B.42) and to Figure 4.7, then:

- the air gap flux λ_s is proportional to the current i_{qs}.
- the torque T_e is proportional to the current i_{ds}.

The decoupling of torque and flux control is obtained for different reference frames, as shown in [75, 77, 82, 167].

Appendix C

Principles of Wind Turbine Aerodynamics

C.1 Introduction

The understanding of the principles that regulate the turbine operation is fundamental to properly design the control of the electric generator and the origins of the disturbances that may affect the quality of the energy delivered to the grid.

Scope of this appendix is to provide these fundamental principles; the reader that may be interested in more in depth analysis will find further details in the literature dedicated to this subject, such as [3, 12, 94, 168, 169].

C.2 Turbine operation and power coefficient

The kinetic energy w_a of an air mass m moving with speed v is:

$$w_a = \frac{1}{2}mv^2 \tag{C.1}$$

while the power p_a is defined as the derivative of the kinetic energy and can be expressed as [3, 94, 168, 170]:

$$p_a = \frac{1}{2}\dot{m}v^2 = \frac{1}{2}(\rho A_t v)v^2 = \frac{1}{2}\gamma_a A_t v^3 \tag{C.2}$$

where

p_a (w) is the moving air power,

A_t (m^2) is the area swept by the rotor blades (rotor swept area);

γ_a (kg/m^3) is the air density .

The power expression (C.2) shows that the power in the upstream wind varies linearly with the density of the air sweeping the blades, and with the cube of the wind speed. Thus a 10% increase in wind speed means a 33% increase in avaliable power [8].

Only a ratio of the the upstream wind power can be extracted by the blades: some power is left in the downstream wind which moves with reduced speed (Figure C.1).

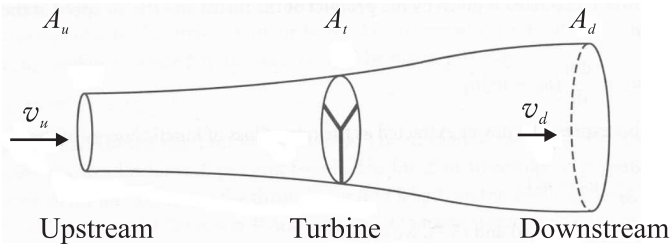

Figure C.1 - Wind speed variation caused by the turbine operation: the upstream wind speed v_u is reduced in the downstream wind v_d [3].

.

As a consequence, the actual power extracted by the rotor blades is the difference between the upstream and the downstream wind powers:

$$p_m = \frac{1}{2}\gamma_a A_t (v_u^3 - v_d^3) \tag{C.3}$$

where:

p_m (w) is the mechanical power extracted by the rotor;

v_u (m/s) is the upstream wind velocity;

v_d (m/s) is the downstream wind velocity.

In 1919 Albert Betz [171] proved that no wind turbine can convert more than 16/27 (59.3%) of the upstream kinetic energy of the wind into mechanical energy. This limit has nothing to do with inefficiencies in the generator, but it is intrinsic in the process of power extraction from the wind. According to Betz's analysis, the power (C.3) can be written as a function of the upstream wind velocity:

$$p_m = \frac{1}{2}\gamma_a A_t c_p v_u^3 \tag{C.4}$$

where c_p is named 'power coefficient' that quantifies the efficiency of the power extraction from the wind [94, 169, 171].

The analytical expression of c_p is complex, because it depends on the blades geometry [10, 93] and on the turbine speed. A widely used simplified expression that uses a polynomial

representation is as follows [12, 93, 127, 169]:

$$c_p(\Gamma, \beta) = c_1\Big(\frac{c_2}{\Gamma'} - c_3\beta - c_4\Big)e^{-c_5/\Gamma'} + c_6 t \tag{C.5}$$

where

- Γ is the tip speed ratio, defined as the relative speed of the blade tip with respect to the wind speed:
$$\Gamma = \frac{R\ \omega_t}{v_u} \tag{C.6}$$
(R is radius of the blade and ω_t is the rotational speed of the turbine);
- β named 'pitch angle' of the turbine blades (more details are provided in section C.4.1);
- Γ' is defined as:
$$\frac{1}{\Gamma'} = \frac{1}{\Gamma + 0.083} - \frac{0.035}{\beta^2 + 1}$$
- $c_1 = 0.5176$, $c_2 = 116$, $c_3 = 0.4$, $c_4 = 5$, $c_5 = 21$ and $c_6 = 0.0068$.

Table C.1 shows the relation between v_u, Γ and c_p. In Figure C.2, c_p is plotted in function of Γ; the pitch angle β is a parameter. From the curves presented in Figure C.2, one learns that c_p is a single-maximum function.

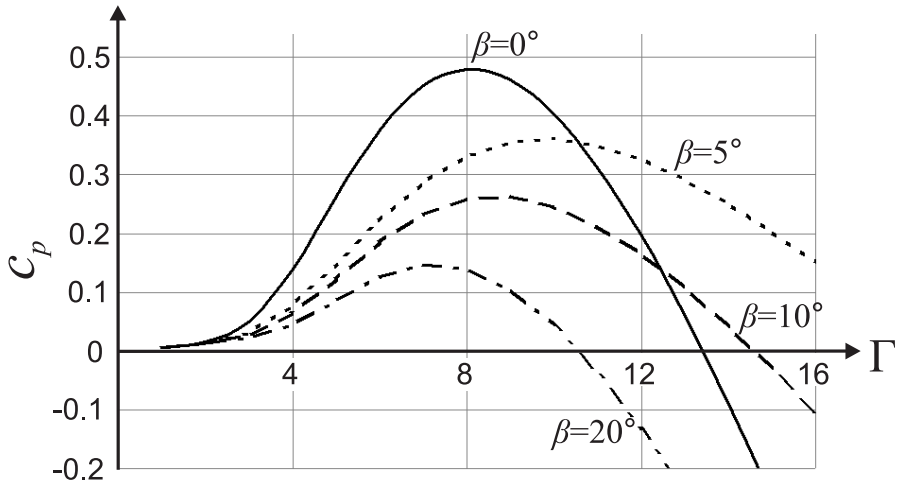

Figure C.2 - Typical relations between C_p and Γ for modern three-blades wind turbine, the pitch angle β is a parameter. The curves are obtained by applying (C.6).

Table C.1 - Relation between wind speed v_u, tip speed ration Γ, power coefficient c_p, and blade pitch angle β.

v_u	0		3.1		7.1		10.3		12.2		13.65		14.7	
Γ	$1/\Gamma'$	c_p	$1/\Gamma'$	c_p	$1/\Gamma'$	c_p	$1/\Gamma'$	c_p	$1/\Gamma'$	c_p	$1/\Gamma'$	c_p	$1/\Gamma'$	c_p
1	0.965	0.007	0.800	0.007	1.369	0.007	0.548	0.007	0.506	0.007	0.478	0.008	0.460	0.008
1.5	0.632	0.010	0.571	0.010	0.813	0.010	0.430	0.013	0.404	0.014	0.386	0.016	0.374	0.017
2	0.465	0.015	0.444	0.016	0.578	0.014	0.354	0.023	0.336	0.027	0.323	0.029	0.315	0.031
2.5	0.365	0.026	0.363	0.026	0.448	0.019	0.301	0.041	0.288	0.046	0.278	0.050	0.272	0.052
3	0.298	0.050	0.307	0.045	0.366	0.029	0.261	0.066	0.251	0.071	0.244	0.075	0.239	0.078
3.5	0.251	0.088	0.266	0.072	0.309	0.046	0.231	0.095	0.223	0.100	0.218	0.103	0.214	0.105
4	0.215	0.140	0.234	0.106	0.268	0.070	0.207	0.127	0.201	0.129	0.196	0.130	0.193	0.130
4.5	0.187	0.200	0.209	0.145	0.236	0.101	0.188	0.158	0.183	0.157	0.179	0.155	0.176	0.153
5	0.165	0.263	0.189	0.187	0.211	0.136	0.172	0.186	0.167	0.181	0.164	0.175	0.162	0.170
5.5	0.147	0.323	0.173	0.227	0.191	0.171	0.158	0.210	0.154	0.200	0.152	0.190	0.150	0.182
6	0.132	0.376	0.159	0.265	0.174	0.205	0.147	0.229	0.143	0.213	0.141	0.199	0.139	0.187
6.5	0.119	0.419	0.147	0.299	0.160	0.236	0.137	0.242	0.134	0.220	0.132	0.201	0.130	0.186
7	0.108	0.451	0.137	0.329	0.148	0.262	0.128	0.249	0.125	0.221	0.124	0.197	0.122	0.179
7.5	0.098	0.472	0.128	0.354	0.138	0.284	0.120	0.251	0.118	0.216	0.116	0.188	0.115	0.166
8.1	0.088	**0.480**	0.119	0.377	0.128	0.302	0.112	0.246	0.110	0.204	0.109	0.169	0.108	0.142
8.5	0.081	0.474	0.112	0.391	0.120	0.312	0.106	0.236	0.104	0.187	0.103	0.148	0.102	0.118
9.0	0.075	0.458	0.106	0.400	0.113	0.316	0.101	0.222	0.099	0.167	0.098	0.123	0.097	0.089
9.5	0.069	0.431	0.100	0.405	0.107	0.316	0.096	0.204	0.095	0.142	0.094	0.093	0.093	0.057
10	0.064	0.396	0.096	0.406	0.102	0.311	0.092	0.182	0.090	0.115	0.089	0.061	0.089	0.021
10.5	0.059	0.352	0.091	0.403	0.097	0.302	0.088	0.157	0.086	0.084	0.086	0.026	0.085	-0.018
11	0.055	0.302	0.087	0.396	0.092	0.289	0.084	0.129	0.083	0.050	0.082	-0.012	0.081	-0.059

The maximum achievable value of c_p is below 0.5 for high-speed, two-blade turbines, and between 0.2 and 0.4 for slow speed turbines with more blades [94, 169]. This concept is visualized in Figure C.3 where c_p is plotted as function of Γ, and the number of blades is a parameter ($\beta = 0$ is assumed).

When $n = 1$, the curve is flat: c_p changes very little over a wide tip speed ratio range but the maximum C_p is low because the drag losses are high. If the number of blades is high, the curve is narrow with a sharp peak making the turbine very sensitive to tip speed ratio changes. If the number of blades further increases, the maximum c_p is relatively low due to stall losses.

The best compromise is achieved with $n = 3$, but two blades is an acceptable alternative because although the maximum c_p is a little lower the spread of the peak is wider and that might result in a larger energy capture.

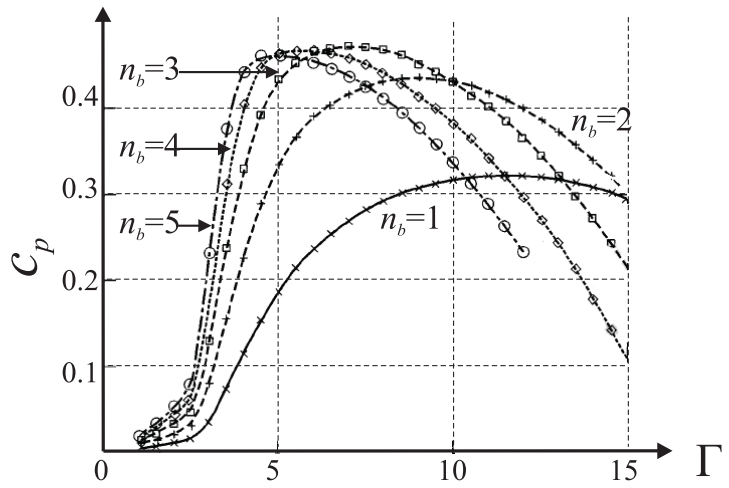

Figure C.3 - c_p curves as function of Γ; the number of blades is a parameter ($\beta = 0$) [169].

C.3 Fixed and variable-speed operation

In the earlier 1990s wind turbines operated at constant speed, meaning that the wind turbine angular speed is constant regardless the wind speed. The fixed-speed design is simple, reliable and cheap. Its disadvantages are low efficiency and limited power quality control. While the second aspect will be analyzed in chapter 1, the limited efficiency is explained by analyzing Figure C.4.a. The wind power potential plotted as a function of the rotor speed; the wind speed is a parameter. Since the power is proportional to the cube of

the wind speeds, the curves that describe the wind power potential are cubic functions: for higher wind speed, higher power potential is obtained at different rotor speeds.

The thick vertical line represents the power captured by a turbine operating at fixed-speed (ω_r/ω_1=1) showing that the power extracted matched the peak wind power potential only for v_u=10 m/s.

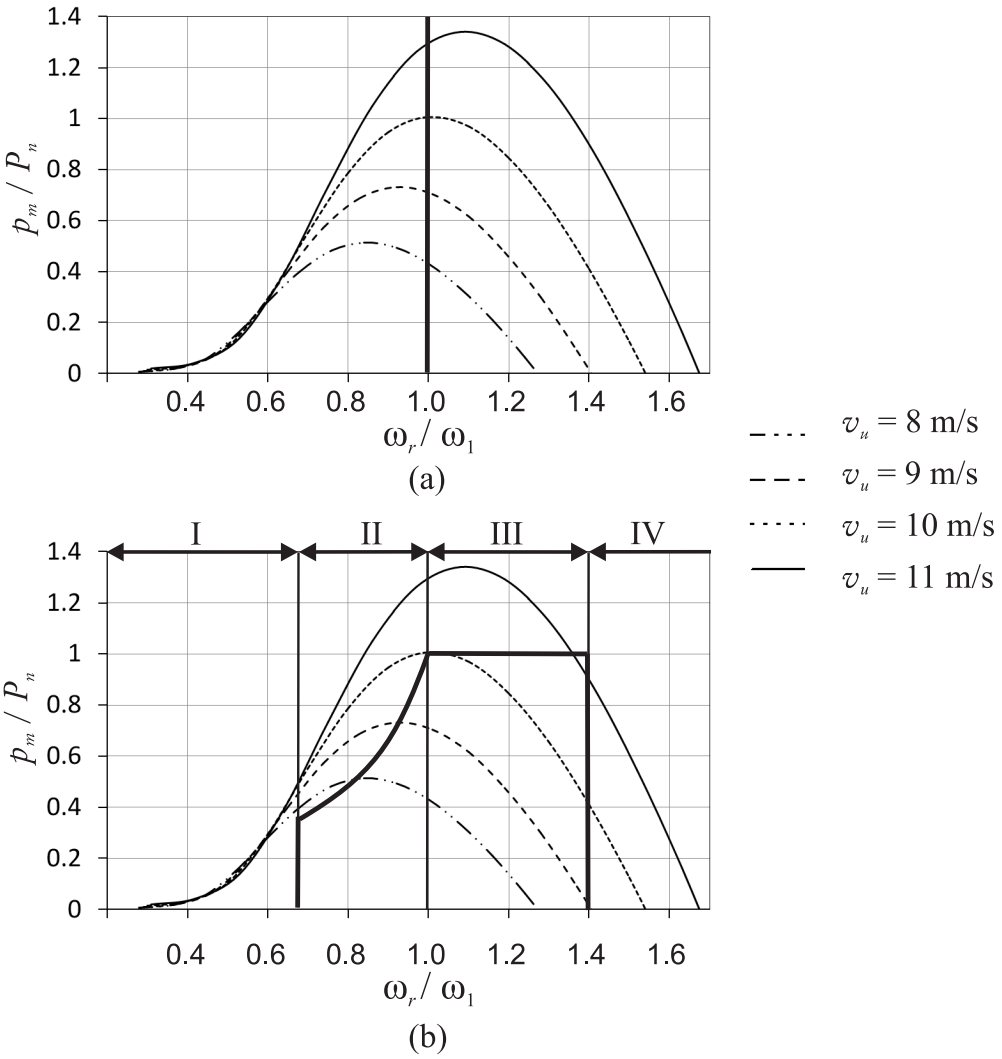

Figure C.4 - Power extracted from a wind turbine as a function of the shaft speed: (a) fixed speed operation and (b) variable speed operation.

Given the disadvantages of variable speed operation, the last generations of wind turbines operate with variable speed to achieve maximum aerodynamic efficiency over a wide range of wind speeds [172]. The rotational speed of the turbine is varied according to the

wind speed to maximize the tip speed ratio (C.6) and to increase the power capture. Above a certain rotational speed, the power output of the turbine is limited due to mechanical, thermal and safety reasons. Figure C.4.b presents the power curve of a variable speed wind turbine and four different control regions can be identified [13, 94, 173, 174]:

- Region I: Below the cut-in speed, it is not efficient to turn on the turbine, and $p_m = 0$;
- Region II (Maximum c_p region): Between the cut-in speed and the rated speed, the rotor speed varies with the wind speed in order to operate at constant Γ corresponding to the maximum c_p for the turbine.
- Region III (Maximum power region): Between the rated speed and the cut-out speed, the machine is operated at constant power: this result is obtained in the majority of the installations by pitching the blades (section C.4.1). In this region, c_p is below the optimum value.
- Region IV: Above the cut-out speed, the rotor is shut off to prevent structural overloads and damage.

The threshold wind speeds values for typical modern turbines operated in variable-speed are [13, 172, 175]: rated speed: 12 m/s; cut-in speed: 5 m/s ; cut-out speed: 22 m/s.

The advantages of variable-speed wind turbines with respect to fixed-speed turbines are: increased energy capture, improved power quality and reduced mechanical stress. Although the actual power capture increase largely depends on the wind pattern and control design [13, 93, 94, 169, 176], the advantages in terms of power quality have been making variable-speed turbine the dominant technology in wind power [10]. The disadvantages are a more complex electrical design (chapter 1) and higher costs.

C.4 Power capture control

There are several methods to control wind turbines power output, some of them are common to both fixed- and variable-speed operated wind turbines [10, 13, 93, 169, 172, 173, 176, 177, 178].

C.4.1 Pitch control

In order to implement this control operation, the rotor blades have to be able to turn around their longitudinal axis (to pitch) as shown in Figure C.5. This Figure presents a top view of the turbine blade: the angle β is measured with respect to the rotor plane: $\beta = 0$ means

maximum power capture. When the wind speed is higher than the rated value, the blade pitch mechanism which pitches (turns) the rotor blades slightly out of the wind. When the rotor speed reach the design limit, the pitch angle is 90^o: at this point, the turbine is shut off. Conversely, the blades are turned back into the wind whenever the wind drops.

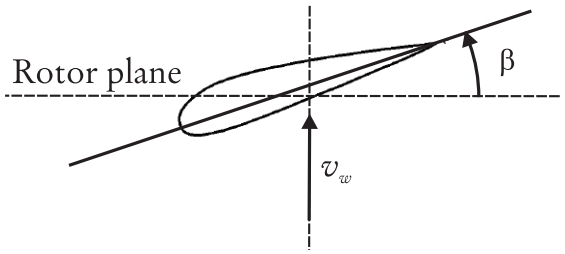

Figure C.5 - Top-view of a turbine blade, assuming wind speed v_u perpendicular to the rotor plane. The pitch angle β is the angle between the rotor plane and the turbine longitudinal axis [12, 169].

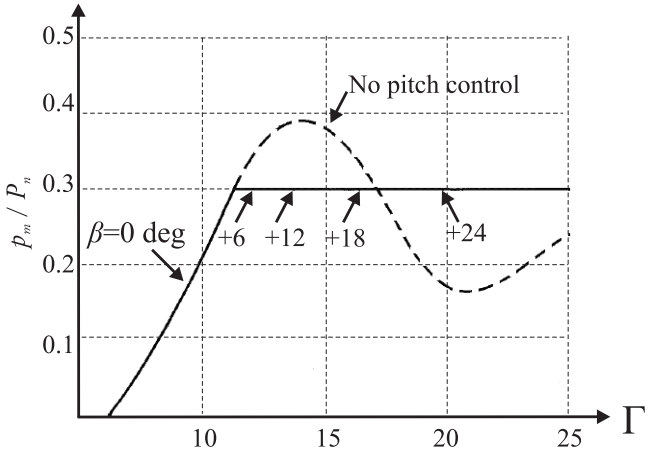

Figure C.6 - Normalized mechanical power absorbed by the turbine as a function of Γ: increasing of the pitch angle β allows limiting the power absorption at high wind speeds [169].

The pitch mechanism is usually operated using hydraulics or electric stepper motors. The velocity of the control system is within the range $\dot{\beta}$=5:20 deg/sec [12].

Figure C.6 shows the power captured from the turbine as function of the tip speed. When the rated power is reached, the pitch angle increases in order to maintain the rated power. Pitch adjustment is utilized to reduce power for wind speed higher than the rated value, rarely or never used for low wind speeds.

C.4.2 Passive stall control

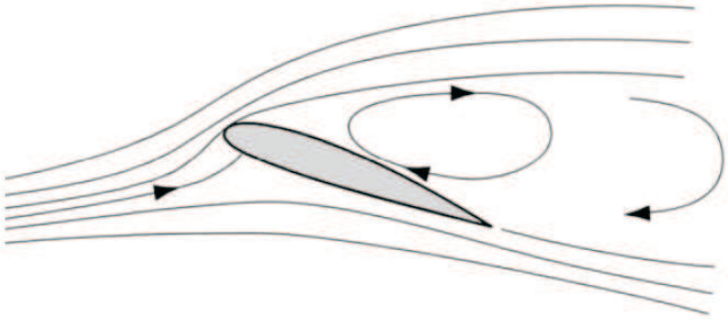

Figure C.7 - Passive stall control principle: above a certain wind speed, the turbulences created by the wind cause a drop in the power capture [169].

Stall controlled wind turbines have the rotor blades bolted onto the hub at a fixed angle. A rotor blade for a stall controlled wind turbine is twisted slightly along its longitudinal axis, in order to ensure that the rotor blade stalls gradually rather than abruptly when the wind speed reaches its critical value. When the wind speed becomes too high, it creates turbulence on the side of the rotor blade which is not facing the wind as shown in Figure C.7 and the driving torque is reduced.

As the blade pitch is fixed, the turbine rotor is quite simple as there is no blade pitch system required (no additional hydraulics, electrics, or pitch bearings) making the turbine cheap and simple.

On the other hand, stall control represents a complex aerodynamic design problem, that include the study of the structure dynamics. Some drawbacks of the passive stall control include:

- reduced efficiency towards rated speeds
- higher loads, particularly on blades and tower
- larger wake deficits resulting in greater array losses for the farm
- increased wake turbulence
- noise is caused by higher angle of attack during operation
- severe vibrations are to transition period around rated speed where blades are coming in and out of stall during each rotation
- sensitive to dirty blades (rated power can be significantly reduced)

C.4.3 Active stall control

An increasing number of larger wind turbines (1 MW and up) are being developed with an active stall power control mechanism. Technically the active stall machines resemble pitch controlled machines, since they have pitchable blades [177].

In order to get a reasonably large torque (turning force) at low wind speeds, the machines will usually be programmed to pitch their blades much like a pitch controlled machine at low wind speeds.

When the machine reaches its rated power, however, the blades are pitched in the opposite direction from what a pitch controlled machine does. In other words, it will increase the angle of attack of the rotor blades in order to make the blades go into a deeper stall, thus wasting the excess energy in the wind [12].

One of the advantages of active stall is that one can control the power output more accurately than with passive stall, so as to avoid overshooting the rated power of the machine at the beginning of a gust of wind. Another advantage is that the machine can be run almost exactly at rated power at all high wind speeds. A normal passive stall controlled wind turbine will usually have a drop in the electrical power output for higher wind speeds, as the rotor blades go into deeper stall.

As with pitch control it is largely an economic question whether it is worthwhile to pay for the added complexity of the machine, when the blade pitch mechanism is added.

C.4.4 Yaw control

A possibility to control the power absorption is to yaw the rotor as presented in Figure C.8. In this Figure, γ is the angle created by the wind speed and the rotor axis: increasing values of γ result in a reduction of the power capture. This technique is in practice used only for small wind turbines (1 kW or less), because it produces cyclically varying stress in the rotor, which may ultimately damage the entire structure [12, 169].

C.5 Wind and energy distributions

C.5.1 Weibull distribution

Wind speed distribution is a fundamental parameter in the determination of the feasibility of a wind power plant and in the design of its component.

Experimental measurements of the wind speeds in different locations show that the Weibull probability distribution can be used to describe the wind patterns with good approximation [94, 179] in most sites all over the world [69].

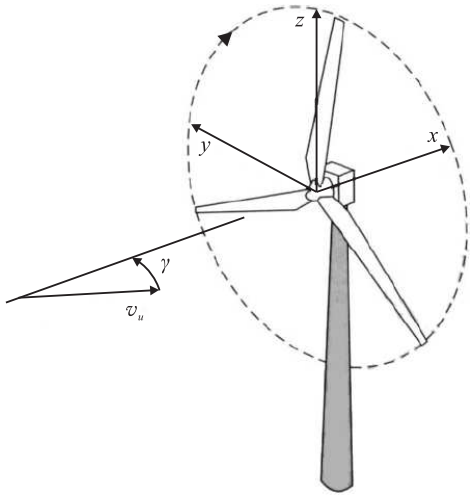

Figure C.8 - Yaw control concept: in order to reduce the power absorption, the angle γ between the rotor plane and the upwind is increased [169].

The Weibull probability distribution function w has the following expression:

$$w = \frac{k}{c^k}\, v_u^{k-1}\, e^{-(v_u/c)^k} \tag{C.7}$$

where

c is the scale parameter;

k is the shape parameter.

The Weibull distribution (C.7) with $k = 1$ simplifies in the exponential distribution, with $k = 2$ results in the Rayleigh distribution. For $k > 3$, it approaches the normal distribution (Gaussian distribution).

Typical values of the parameters c and k for that describe wind distributions are [94]:

- $5 < c < 10$
- $1.5 < k < 2.5$

Given the above values, one concludes that at most sites the Rayleigh distribution ($k = 2$) is a simple and accurate enough representation of the wind speed with just one parameter, the scale parameter c. Figure C.9 shows the Rayleigh distribution as a function of wind speed, for different values of the scale parameter c. For greater values of c, the curves shift right to the higher wind speeds, meaning that more number of days have high winds.

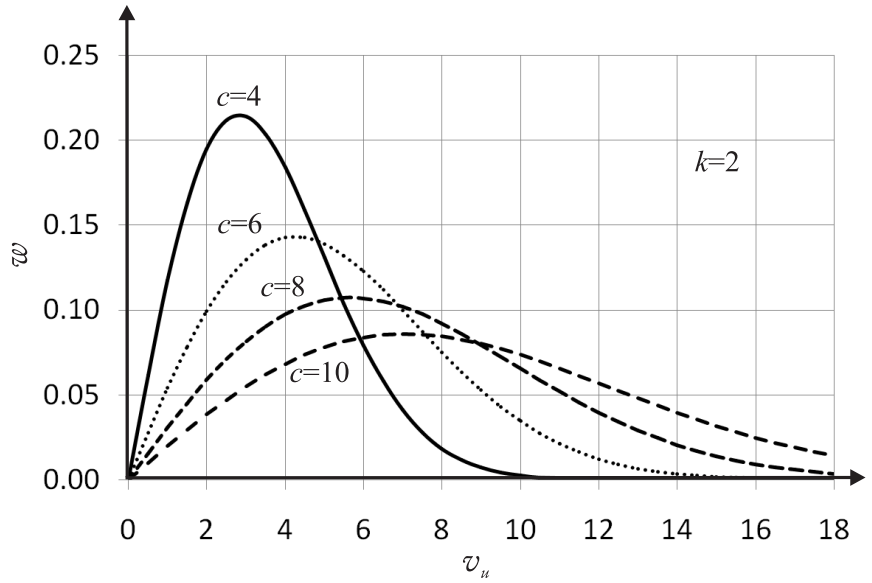

Figure C.9 - Weibull distribution as function of the wind speed, c is a parameter, $k = 2$.

C.5.2 Effect of height

The wind speed is a function of height above the ground. To correctly determine the wind energy potential in a site, the wind resource map drawn for 100-m elevation should be considered, since this is the operating hub energy for many modern wind turbines [13].

The wind shear at ground surface causes the the wind speed increase with height: for this reason, the height of the wind turbine has been increasing continuously in the last years. The wind power increase at a certain height h_2 with respect to a reference point at height h_1 is quantified by means of the following expression:

$$v_{u2} = v_{u1}\left(\frac{h_1}{h_2}\right)^{\alpha} \tag{C.8}$$

where

- v_{u1} = upstream wind speed measured at the reference height h_1,
- v_{u2} = upstream wind speed estimated at the height h_2,
- α = ground surface friction coefficient.

The wind speed increase as a function of height is shown in Figure C.10, the friction coefficient α is a parameter. For urban areas, $0.4 \leq \alpha \leq 3$, for farmland $0.002 \leq \alpha \leq 0.3$,

for open sea, 0.001≤ α ≤0.0001 [3, 94]. This last data allows understanding that the wind speed on the ocean is more constant than on the land and is not a function of the height.

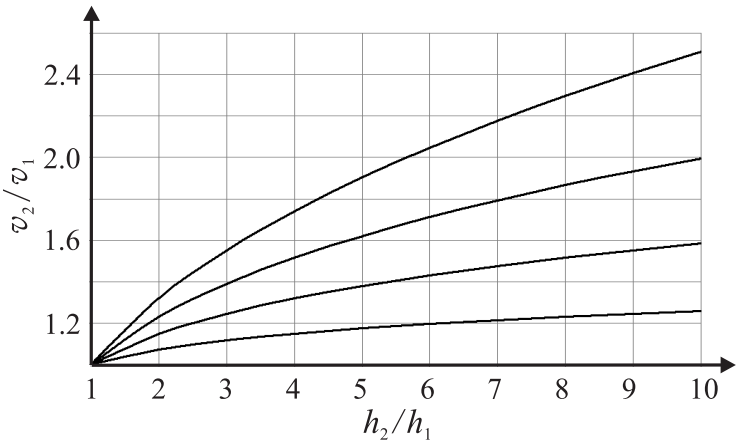

Figure C.10 - Upstream wind speed as a function of height. The upstream wind speed v_{u2} estimated at height h_2 is normalized with respect to the wind speed v_{u1} measured at the reference height h_1. The friction coefficient α is a parameter.

The wind speed does not increase with height indefinitely: the data collected at Merida airport in Mexico show that typically the wind speed increases with height up to about 450 m and then decreases [94]. The wind speed at 450 m can be four to five times greater than the ground speed.

C.5.3 Energy distribution

Since the mechanical power extracted from the wind is proportional to the cube of the wind speed (C.2), a small increase of wind speed results in a noticeable increase of power production. This positive effect is counterbalanced by observing in Figure C.9 that high wind speed take place with lower probability.

The energy distribution function allows to quantify the amount of energy captured from the wind in a year period:

$$e = \frac{\int_{v_u}^{v_u+\Delta v_u} p_a w dv}{\Delta v_u} \tag{C.9}$$

where

p_a is the power in the moving air (C.2),

w is the Weibull distribution,

v_u is the wind speed.

Figure C.11 presents the Weibull distribution w with $k = 2$ and $c = 6$ and the corresponding energy distribution function e as a function of wind speed v_u. The peak of the energy function is different from the peak of the wind distribution [94].

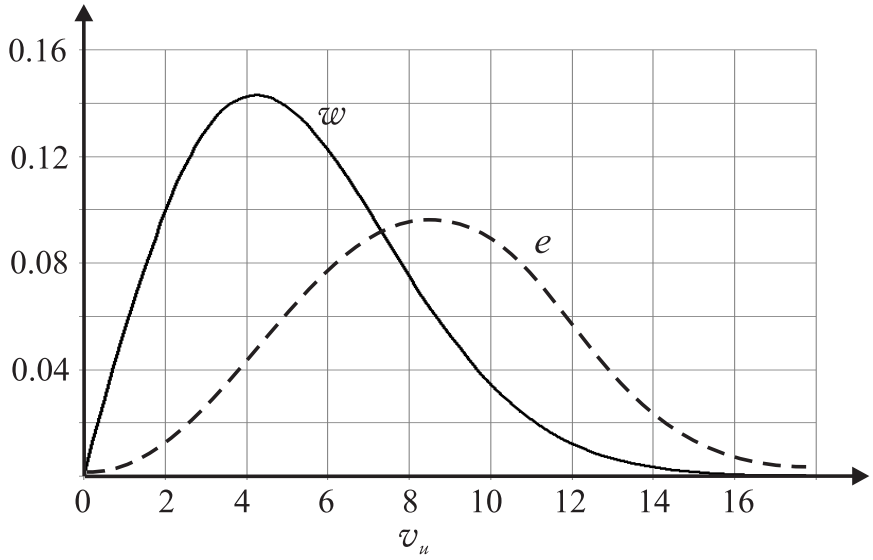

Figure C.11 - Weibull distribution w and corresponding energy distribution e.

C.5.4 Wind power fluctuations

The variability of wind speed is one of the most challenging characteristics in the design of the power plants, because it affects both the quality of wind energy and the operation of wind turbines. Managing the variability of wind generation is the key aspect associated to the optimal integration of that renewable energy into electricity grids.

Two main types of wind fluctuations can be identified:

1. *Probabilistic* variability of wind generation can be expressed using various time scales: seasonal variations, diurnal cycles, microvariations due to local turbulences. The amplitude of the variation is not of the same order for these three different timescales. [71]. Only an accurate weather forecast allows predicting the variability of wind energy production caused by probabilistic wind fluctuations; given the above listed mechanisms for probabilistic variability, forecasting of wind power generation is generally performed at different time scales:

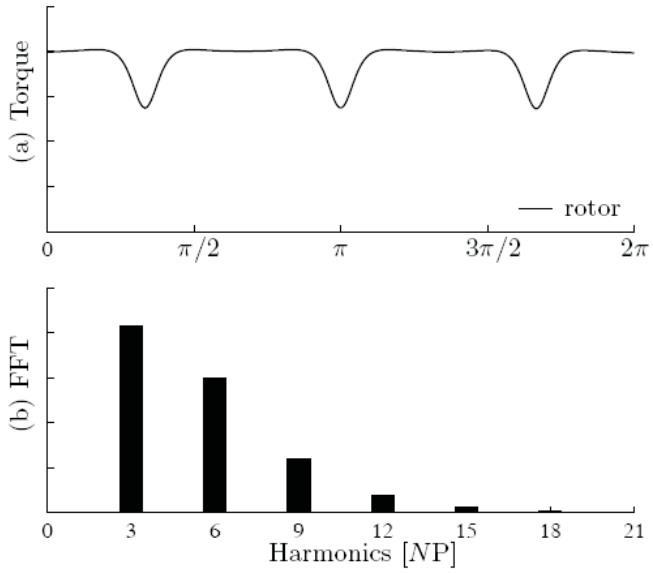

Figure C.12 - Tower shadow effect for three-bladed wind turbine: (a) Normalized rotor torque fluctuations and (b) Fast Fourier Transform [12].

(a) Very short-term forecasts (from milliseconds up to a few minutes): used for the turbine active control [179].

(b) Short-term forecast (48−72 hours): needed for the power system management. These predictions are used to decide on the use of conventional power plants (Unit commitment) and for the optimization of the scheduling of these plants (Economic dispatch).

(c) Long term-forecast (up to 5−7 days ahead): necessary for planning the maintenance of wind farms, or conventional power plants or transmission lines. Planning of maintenance operations is critical for offshore wind farms, due to their high maintenance costs.

2. *Deterministic* wind fluctuations depend on the geometry of wind turbines. 'Wind shear' (or 'wind gradient') has already been described in section C.5.2 and affects the operation of wind turbine since the wind speed at the top and at the bottom of the rotor swept area may vary significantly when the blades length increases. This process causes unequal loads on the rotor and therefore may result in fatigue.

   'Tower shadow' refers to the reduced torque when the blade faces the tower, as presented in Figure C.12.a. Since in the majority of the modern wind turbines the num-

ber of blades is equal to three, tower shadow gives rise to triplen multiples harmonic components of the torque, as illustrated in Figure C.12.b [12, 174].

Appendix D

Principles of Control Systems

D.1 Notation and feedback control design

The control system design is defined according to a standard procedure, that includes the following steps:

1. The definition of the system mathematical model. The mathematical model is a set of differential equations that describes the dynamic relations between the system input variables and the output variables. When linear and time-invariant systems are studied, it is assumed that the system coefficients are constant in time. In the practice, very few systems satisfy this requirement;
2. The linearization of the system equations performed and the application of the Laplace transformation [180]: this step allows determining the system transfer function $H(s)$.
3. The formulation of the control law and of its parameters: the control manipulates the output of the system to force the state variables to follow a determined pattern.

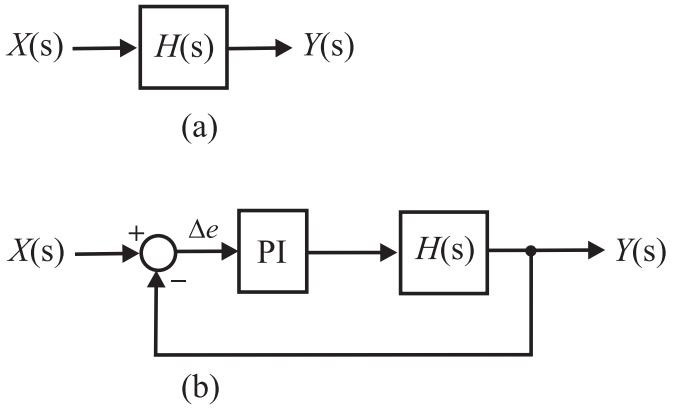

Figure D.1 - Block diagrams for elementary control systems: (a) open-loop and (b) closed-loop with compensator.

Figure D.1.a presents the block diagram corresponding to a first-order system in the Laplace domain:

$X(\mathrm{s})$ is the Laplace transform of the input signal.

$Y(\mathrm{s})$ is the Laplace transform of the output signal.

$H(\mathrm{s})$ is the system transfer function:

$$H(\mathrm{s}) = \frac{Y(\mathrm{s})}{X(\mathrm{s})} \tag{D.1}$$

A typical control system diagram for the first-order systems is presented in Figure D.1.b: this block diagram includes a controller and a feedback loop: the output signal is used to derive an error term that is the input for the controller.

Closed-loop topologies have the following advantages over open-loop [75, 124]:

- disturbance rejection,
- guaranteed performance even with model uncertainties,
- reduced sensitivity to parameter variations,
- improved reference tracking performance.

The disadvantages are:

- stability problem (the feedback loop introduces additional poles that may lead to unsteadiness),
- more complex design,
- loss of system gain.

Among the controllers most used in the practice, are the Proportional Integral controllers, that are briefly described in the following section.

D.2 PI controllers

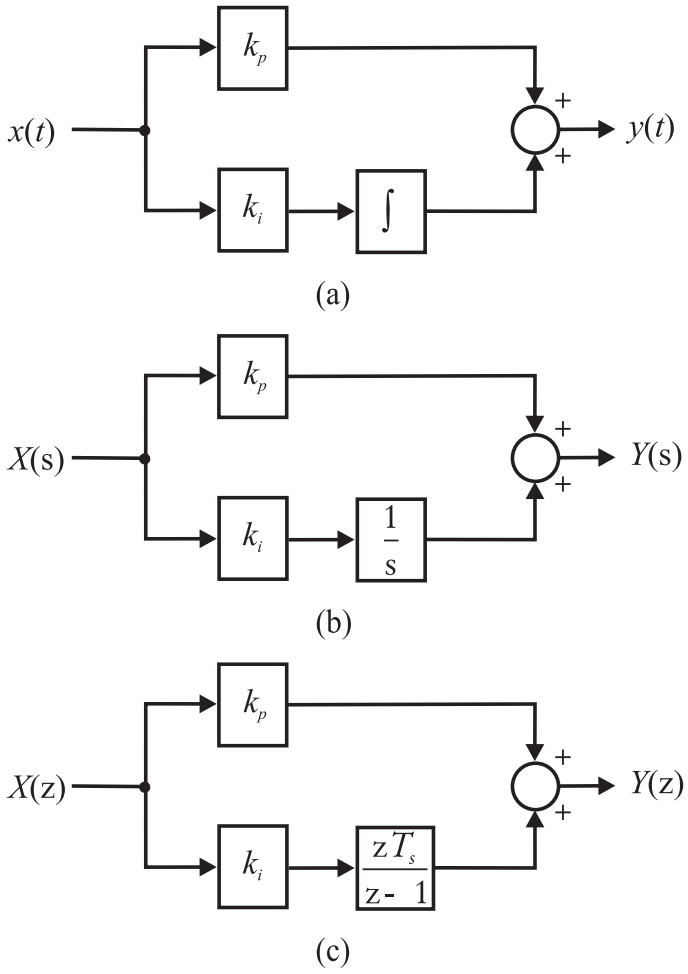

Figure D.2 - Representation of the PI controller operation in different domains: (a) continuous-time domain, (b) Laplace domain and (c) discrete-time domain.

The proportional integral (PI) controllers are widely used in control systems for power converters [89, 124, 130]. By referring to the notation of Figure D.2.a, the PI controller expression in continuous time domain is:

$$y(t) = k_p\ x(t) + k_i \int_0^T x(t)\ dt \tag{D.2}$$

The use of the two terms of PI controller is justified as follows[40] [124, 130]:

[40]The use of the derivative term would lead to a PID controller, but the derivative control is discarded in control of power converters because the commutation spikes and the switch functions have derivatives with

- the proportional term $k_p\ x(t)$ increases the speed of the response; it is proportional to the input $x(t)$ that corresponds to the error (difference between the reference value and the measured value).
- the integral term $k_i\ \int_0^T\ dt$ reduces the steady-state error. The integrator alone does not work because in case of large disturbances the *integrator windup* phenomenon may arise: the integrator continues to cumulate error and drive the output too high (windup phenomenon). The use of a proportional stage reduces the windup.

In this work, the PI controllers were designed by applying the following steps:

1. The transfer functions (Laplace domain) of the system are identified. For the system shown in Figure 3.1 the transfer functions are determined in chapter 4.
2. For each transfer function, the closed loop system shown in Figure D.1.b is designed. The PI controller formulation in the Laplace domain is as follows (Figure D.2.b):

$$Y(s) = k_p\ X(s) + \frac{k_i}{s} X(s) \tag{D.3}$$

3. The choice of the proportional gain and integral gain is based on the phase margin and gain margin test [181]. According to this methodology, a system is considered stable if the loop transmission phase margin is higher than 45^o and the closed loop gain margin is higher than 3 dB. In the proposed design, the parameters k_p and k_i are chosen to obtain a phase margin of 60^o to obtain a safe design; the constrain on the gain margin is always verified with this choice.
4. The closed loop transfer function, the step response and the phase and gain margin are plotted by using the functions provided in Matlab Control System Toolbox [182].
5. The controller are discretized by mapping the Laplace domain in the Z-domain [124, 133]. This step is necessary because the fixed-step discrete-time solver is used; the expression of the PI controller in the Z-domain (Figure D.2.c.) is:

$$Y(z) = k_p\ X(z) + \frac{k_i\ T_s\ z}{z-1}\ X(z) \tag{D.4}$$

high values [124, 130].

Appendix E

Theory of Instantaneous Powers

E.1 Introduction

In Appendix B the concept of Park transformation has been illustrated and its applications to the modeling and control of the induction machine have been described.

In the following sections, the theory of instantaneous powers will be described: mathematically, the instantaneous powers are obtained by applying a procedure that resembles the Park transformation. However, the theory of instantaneous power has been developed in the 80's only for the analysis of power flow in three-phase systems, without any reference to the rotating machines [183].

E.2 Definition of instantaneous powers for three-wires three-phase systems

In [106] the first definition of instantaneous powers in dq reference frame is presented, referring to the case of three-phase three-wire systems. The instantaneous apparent power $\overline{s}$ is

$$\overline{s} = \overline{v}_{dq}\ \bar{i}_{dq}^{\,*} = (v_d i_d + v_q i_q) + j(v_d i_q - v_q i_d) \tag{E.1}$$

where

$$\begin{bmatrix} v_d \\ v_q \end{bmatrix} = \sqrt{\frac{2}{3}} \begin{bmatrix} 1 & -1/2 & -1/2 \\ 0 & +\sqrt{3}/2 & -\sqrt{3}/2 \end{bmatrix} \begin{bmatrix} v_a \\ v_b \\ v_c \end{bmatrix} \tag{E.2}$$

$$\begin{bmatrix} i_d \\ i_q \end{bmatrix} = \sqrt{\frac{2}{3}} \begin{bmatrix} 1 & -1/2 & -1/2 \\ 0 & +\sqrt{3}/2 & -\sqrt{3}/2 \end{bmatrix} \begin{bmatrix} i_a \\ i_b \\ i_c \end{bmatrix} \tag{E.3}$$

and the voltage and current space vectors are defined as follows:

$$\begin{aligned} \overline{v}_{dq} &= v_d + j v_q \\ \bar{i}_{dq} &= i_d + j i_q \end{aligned} \tag{E.4}$$

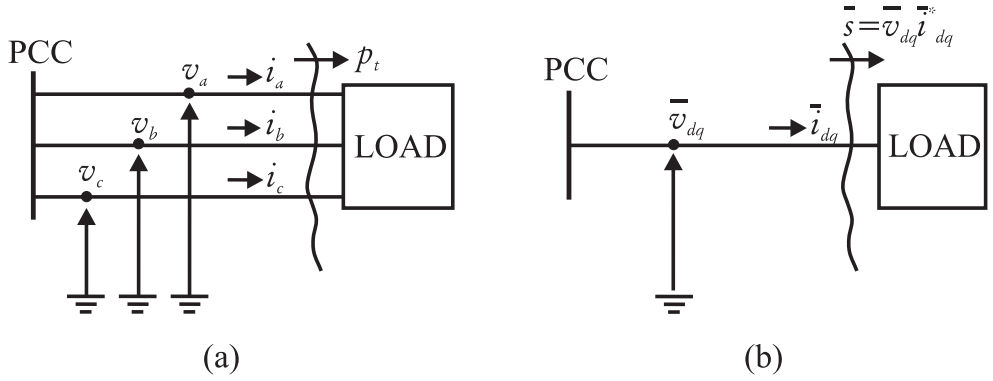

Figure E.1 - (a) Three phase load and (b) equivalent space vectors representation.

The instantaneous active power p and instantaneous imaginary power q[41] are defined respectively as:

$$p = v_d i_d + v_q i_q \tag{E.5}$$

$$q = v_d i_q - v_q i_d \tag{E.6}$$

In Figure E.1.a a three-phase isolated load is shown and in Figure E.1.b its corresponding representation in terms of space vectors is illustrated.

The correspondence between the power definitions in the three-phase systems and in the Park domain have been a source of discussion for many years [106, 185, 186]. The main reason for such a conflict is attributed in the lack of straightforward power definitions for the three-phase systems. However, the analysis of this problem goes beyond the scope of this work.

For the present analysis the instantaneous active power, as defined in (E.5), corresponds to the conventional three-phase power p_t expression:

$$\begin{aligned} p_t &= v_a i_a + v_b i_b + v_c i_c = [v_a\ v_b\ v_c]^T\ [i_a\ i_b\ i_c] \\ &= [v_d\ v_q]^T [T(\vartheta)][T(\vartheta)]^T [i_d\ i_q] = [v_d v_q]^T\ [i_d\ i_q] = v_d i_d + v_q i_q = p \end{aligned} \tag{E.7}$$

The previous result applies because the transformation from three-phase domain to dq domain is orthogonal [165].

[41] According to the nomenclature introduced in [106], the power quantity defined in (E.6) is named *imaginary power*. This quantity belongs to the set of the *non-active powers* [116, 157]. Although the imaginary power shares some properties with the non-active powers, it maintains its own identity because it is defined by a unique formulation. In [184] the correspondence between meanings and operation is described in detail.

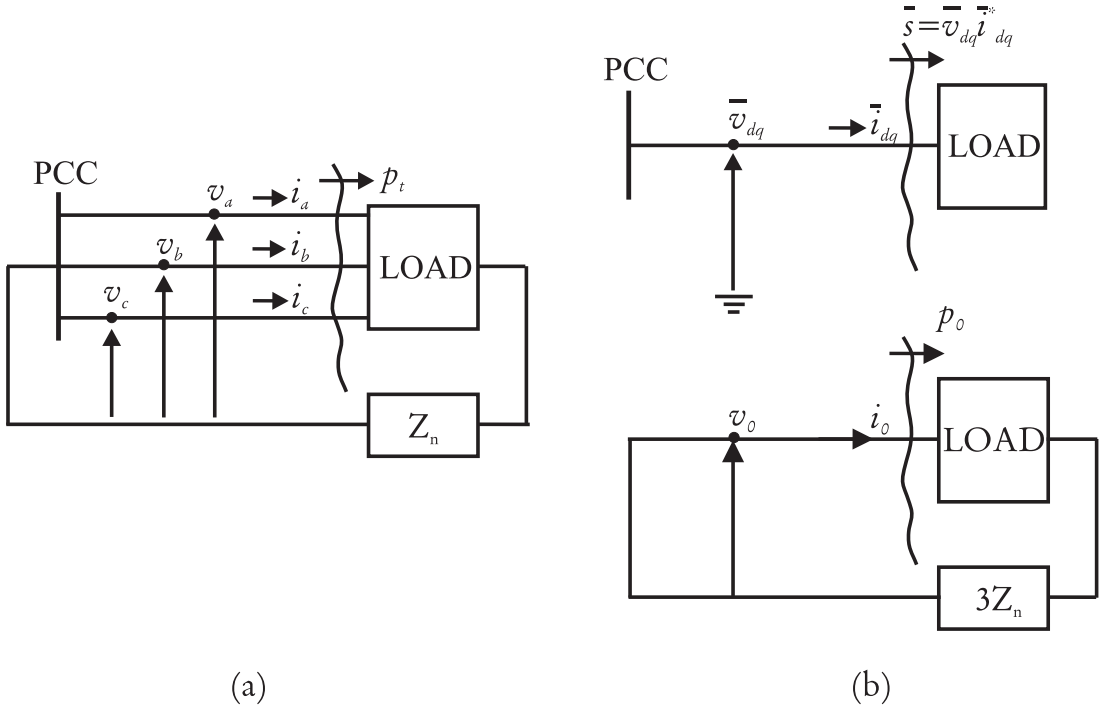

Figure E.2 - (a) Three-phase four wires load and (b) equivalent representation in terms of space vectors and zero-sequence component.

E.3 Definition of instantaneous powers for four-wires three-phase systems

When four-wires three-phase systems are considered, the flow of currents in the neutral wires results in zero-sequence voltage and current, defined as follows:

$$v_0 = \frac{1}{3}(v_a + v_b + v_c) \tag{E.8}$$

$$i_0 = \frac{1}{3}(i_a + i_b + i_c) \tag{E.9}$$

The instantaneous power (E.5) definition is modified as follows by the introduction of the zero-sequence components[42]:

$$p = v_d i_d + v_q i_q + v_0 i_0 \tag{E.10}$$

[42]In the present exposition, the approach defined in [106] is used. Following publications such as [187] propose a different definition of instantaneous powers when four-wires systems are considered. However, in [188] it is proved that the original definitions [106] give the same results, although they were defined for three-wires systems

E.4 Instantaneous powers as function of the PF at the load terminals

The instantaneous active and imaginary powers (E.5) and (E.6) depend on the PF at the load terminals. This consideration applies to any three-phase load, including three-phase machines. The three-phase voltages and currents at the machine's terminals are expressed as follows:

$$\begin{cases} v_a = \hat{V}\cos(\omega_1 t) \\ v_b = \hat{V}\cos(\omega_1 t - 2\pi/3) \\ v_c = \hat{V}\cos(\omega_1 t - 4\pi/3) \end{cases} \tag{E.11}$$

$$\begin{cases} i_a = \hat{I}\cos(\omega_1 t) \\ i_b = \hat{I}\cos(\omega_1 t - 2\pi/3) \\ i_c = \hat{I}\cos(\omega_1 t - 4\pi/3) \end{cases} \tag{E.12}$$

According to (B.33) and (B.34), the voltage and currents space vectors corresponding to (E.11) and (E.12) are respectively:

$$\begin{cases} v_{dq} = \sqrt{\frac{3}{2}}\hat{V} \\ i_{dq} = \sqrt{\frac{3}{2}}\hat{I} \end{cases} \tag{E.13}$$

Given the waveforms (E.11) and (E.12) the instantaneous powers (E.5) and (E.6) are as follows:

$$\begin{cases} p = \sqrt{\frac{3}{2}}\hat{V}\sqrt{\frac{3}{2}}\hat{I} = \frac{3}{2}\hat{V}\hat{I} \\ q = 0 \end{cases} \tag{E.14}$$

From the above derivations it is learned that if the power factor is unity, the instantaneous reactive power q is zero and the value of the instantaneous active power p is a constant. If the rms value is used instead of the peak value the instantaneous active power p corresponds to the power measured at the load terminals with the wattmeter:

$$p = \frac{3}{2}\hat{V}\hat{I} = 3VI\cos\varphi = 3VI \tag{E.15}$$

where V and I are the rms values for the voltage and currents. If the voltages (E.11) are

considered and the three-phase currents are as follows:

$$\begin{cases} i_a = \hat{I}\cos(\omega_1 t - \gamma) \\ i_b = \hat{I}\cos(\omega_1 t - 2\pi/3 - \gamma) \\ i_c = \hat{I}\cos(\omega_1 t - 4\pi/3 - \gamma) \end{cases} \tag{E.16}$$

where γ is the displacement between the voltage and the current in the time domain, the PF is not unity. The same angle γ is used for the three phase because it is assumed that the system is symmetric.

The α and β current components that correspond to (E.16) are:

$$\begin{cases} i_\alpha = \sqrt{\frac{3}{2}}\hat{I}\cos(\omega_1 t - \gamma) \\ i_\beta = \sqrt{\frac{3}{2}}\hat{I}\sin(\omega_1 t - \gamma) \end{cases} \tag{E.17}$$

and the d and q current components result as follows:

$$\begin{cases} v_d = \sqrt{\frac{3}{2}}\hat{I}\cos(\gamma) \\ i_d = \sqrt{\frac{3}{2}}\hat{I}\sin(\gamma) \end{cases} \tag{E.18}$$

Under the conditions (E.11) and (E.16), the following space vectors are obtained:

$$\begin{cases} \overline{v}_{dq} = \sqrt{\frac{3}{2}}\hat{V} \\ \bar{i}_{dq} = \sqrt{\frac{3}{2}}\hat{I}\cos(\gamma) + j\ \sqrt{\frac{3}{2}}\hat{I}\sin(\gamma) \end{cases} \tag{E.19}$$

Substituting the space vectors expressions (E.19) in the instantaneous powers definition (E.5) and (E.6), the following is obtained:

$$\begin{cases} p = \sqrt{\frac{3}{2}}\hat{V}\ \sqrt{\frac{3}{2}}\hat{I}\cos(\gamma) = \frac{3}{2}\hat{V}\hat{I}\cos(\gamma) \\ q = \sqrt{\frac{3}{2}}\hat{V}\ \sqrt{\frac{3}{2}}\hat{I}\sin(\gamma) = \frac{3}{2}\hat{V}\hat{I}\sin(\gamma) \end{cases} \tag{E.20}$$

It is learned from (E.20) that if the PF $\neq 1$, the instantaneous imaginary power is not

zero. When $\gamma = 0$ (PF = 1), (E.14) is obtained as a particular case. When $\gamma = \pm\pi/2$:

$$\begin{cases} p = \sqrt{\frac{3}{2}}\hat{V}\ \sqrt{\frac{3}{2}}\hat{I}\cos(\pm\pi/2) = 0 \\ q = \sqrt{\frac{3}{2}}\hat{V}\ \sqrt{\frac{3}{2}}\hat{I}\sin(\pm\pi/2) = \frac{3}{2}\hat{V}\hat{I} \end{cases} \tag{E.21}$$

The condition $\gamma = \pm\pi/2$ corresponds to the case of purely inductive or capacitive load (zero power factor): the results (E.20) confirm that in this case there is no absorption of active power.

As a conclusions, the systems (E.14) and (E.20) describes the case of minimum and maximum imaginary power absorption, that corresponds to the unitary power factor ($\gamma = 0$) and zero power factor ($\gamma = \pm\pi/2$) respectively. For other values of the power factor, the instantaneous imaginary power will assume intermediate values.

Appendix F

Fortescue Transformation

The Fortescue transformation [138] is a similarity transformation used for the study of unbalanced polyphase systems. This method has been intensively used for the analysis of faults in the three-phase systems. In the following sections, the Fortescue transformation will be presented for the case of three-phase systems.

F.1 Fortescue transformation and equivalent impedances

According to Fortescue theorem, three unbalanced phasors $\overline{Y}_a, \overline{Y}_b, \overline{Y}_c$ can be resolved into three balanced systems of phasors $\overline{Y}_+, \overline{Y}_-, \overline{Y}_0$:

$$\begin{bmatrix} \overline{Y}_+ \\ \overline{Y}_- \\ \overline{Y}_0 \end{bmatrix} = \mathrm{A} \begin{bmatrix} \overline{Y}_a \\ \overline{Y}_b \\ \overline{Y}_c \end{bmatrix} = \begin{bmatrix} \overline{Y}_+ \\ \overline{Y}_- \\ \overline{Y}_0 \end{bmatrix} = \begin{bmatrix} a^2 & a & 1 \\ a & a^2 & 1 \\ 1 & 1 & 1 \end{bmatrix} \begin{bmatrix} \overline{Y}_a \\ \overline{Y}_b \\ \overline{Y}_c \end{bmatrix} \tag{F.1}$$

where

$\overline{Y}_+$ is the positive-sequence component;

$\overline{Y}_-$ is the negative-sequence component;

$\overline{Y}_0$ is the zero-sequence component;

$a = e^{j2\pi/3}$ is the Fortescue operator;

A is the Fortescue matrix:

$$\mathrm{A} = \begin{bmatrix} a^2 & a & 1 \\ a & a^2 & 1 \\ 1 & 1 & 1 \end{bmatrix} \tag{F.2}$$

.

The zero-sequence component is the same obtained from the Clarke's transformation (B.6), except for a scale factor. In [92] it is shown that if the matrix A is premultiplied by the coefficient 2/3, then the zero sequence component obtained by applying the Clarke

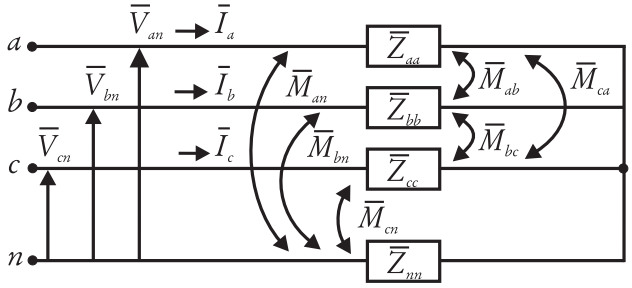

Figure F.1 - The four-wire three-phase system used to describe the sequence transformation: the phases impedances and mutual inductances are shown

transformation is the same obtained by applying the Fortescue transformation. However, in principle the meaning of the zero-sequence component is the same for both transformations, because this component exists only if the sum of the three-phase components is zero.

The four-wire three-phase system shown in Figure F.1 is considered. The mutual inductances between the phases and between the phases and the ground are equal. The phase-to-neutral voltage are expressed as follows

$$\begin{bmatrix} \overline{V}_{an} \\ \overline{V}_{bn} \\ \overline{V}_{cn} \end{bmatrix} = \begin{bmatrix} \overline{Z}_{aa} + \overline{Z}_{nn} & \overline{Z}_{nn} + \overline{M}_{ab} + \overline{M}_{bn} & \overline{Z}_{nn} + \overline{M}_{ca} + \overline{M}_{cn} \\ \overline{Z}_{nn} + \overline{M}_{ab} + \overline{M}_{an} & \overline{Z}_{bb} + \overline{Z}_{nn} & \overline{Z}_{nn} + \overline{M}_{bc} + \overline{M}_{cn} \\ \overline{Z}_{nn} + \overline{M}_{ca} + \overline{M}_{an} & \overline{Z}_{nn} + \overline{M}_{bc} + \overline{M}_{bn} & \overline{Z}_{cc} + \overline{Z}_{nn} \end{bmatrix} \begin{bmatrix} \overline{I}_a \\ \overline{I}_b \\ \overline{I}_c \end{bmatrix} \tag{F.3}$$

and the impedance matrix Z is defined as follows:

$$Z = \begin{bmatrix} \overline{Z}_{aa} + \overline{Z}_{nn} & \overline{Z}_{nn} + \overline{M}_{ab} + \overline{M}_{bn} & \overline{Z}_{nn} + \overline{M}_{ca} + \overline{M}_{cn} \\ \overline{Z}_{nn} + \overline{M}_{ab} + \overline{M}_{an} & \overline{Z}_{bb} + \overline{Z}_{nn} & \overline{Z}_{nn} + \overline{M}_{bc} + \overline{M}_{cn} \\ \overline{Z}_{nn} + \overline{M}_{ca} + \overline{M}_{an} & \overline{Z}_{nn} + \overline{M}_{bc} + \overline{M}_{bn} & \overline{Z}_{cc} + \overline{Z}_{nn} \end{bmatrix} \tag{F.4}$$

If the system is symmetric, the following substitution apply:

$$\begin{array}{rcrcrcl} \overline{Z}_{aa} & = & \overline{Z}_{bb} & = & \overline{Z}_{cc} & = & \overline{Z} \\ \overline{M}_{ab} & = & \overline{M}_{bc} & = & \overline{M}_{ca} & = & \overline{M}_m \\ \overline{M}_{an} & = & \overline{M}_{bn} & = & \overline{M}_{cn} & = & \overline{M}_{mn} \end{array} \tag{F.5}$$

and the impedance matrix Z_{symm} is:

$$Z_{symm} = \begin{bmatrix} \overline{Z} + \overline{Z}_{nn} & \overline{Z}_{nn} + \overline{M}_m + \overline{M}_{mn} & \overline{Z}_{nn} + \overline{M}_m + \overline{M}_{mn} \\ \overline{M}_m + \overline{M}_{mn} & \overline{Z}_{nn} + \overline{Z} + \overline{Z}_{nn} & \overline{Z}_{nn} + \overline{M}_m + \overline{M}_{mn} \\ \overline{M}_m + \overline{M}_{mn} & \overline{M}_m + \overline{M}_{mn} & \overline{Z}_{nn} + \overline{Z} + \overline{Z}_{nn} \end{bmatrix} \tag{F.6}$$

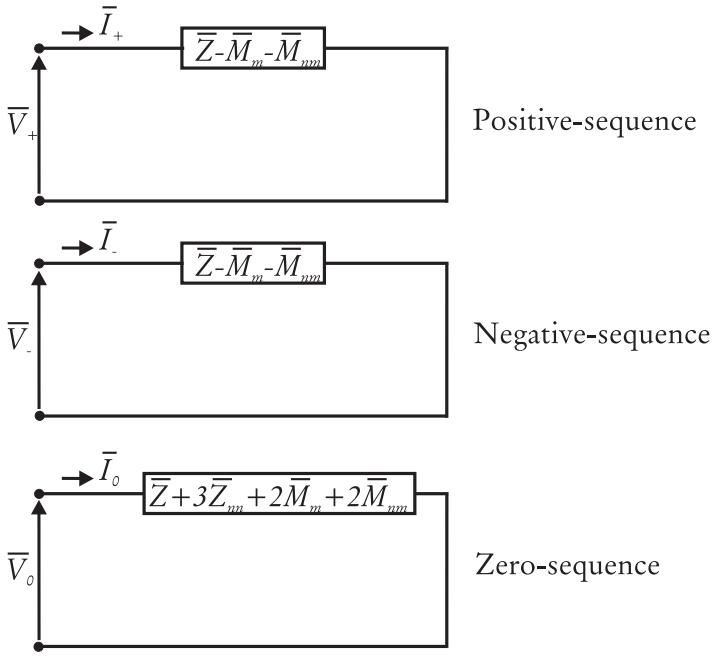

Figure F.2 - The positive-, negative- and zero-sequence equivalent circuits for the system depicted in Figure F.1, with the substitutions listed in (F.5).

The equivalent voltages are obtained by applying the transformation (F.1) to the system (F.3); the equivalent impedances are obtained as [92, 137]:

$$\begin{aligned} Z_{eq} &= \mathrm{A}\ Z_{symm}\ \mathrm{A}^{-1} = \begin{bmatrix} Z_+ \\ Z_- \\ Z_0 \end{bmatrix} \\ &= \begin{bmatrix} \overline{Z} - \overline{M}_m - \overline{M}_{mn} & 0 & 0 \\ 0 & \overline{Z} - \overline{M}_m - \overline{M}_{mn} & 0 \\ 0 & 0 & \overline{Z} + 3\ \overline{Z}_n + 2\overline{M}_m + 2\overline{M}_{mn} \end{bmatrix} \end{aligned} \tag{F.7}$$

The matrix Z_{eq} is diagonal because the original system matrix is symmetric. Therefore, the resulting positive-, negative- and zero-sequence equivalent circuits are decoupled, as illustrated in Figure F.2.

Appendix G

Engineering Economic Evaluation

G.1 Introduction

Scope of the present appendix is to determine the economical feasibility of the proposed use of the WECS as a power generator and Active Filter simultaneously.

From an economical point of view, the reduction of power delivered to the grid caused by derating results in a decrease of the annual income from the wind energy sale. At the same time, the proposed method allows to save on the cost of the AF installation.

A brief economical analysis will help to estimate under which conditions the proposed method is more economical than the installation of an AF.

G.2 Derating and power loss

For a typical wind speed distribution (section C.5.1) the energy curve at sinusoidal conditions is the continuous trajectory depicted in Figure G.1 [10, 94]. When harmonic compensation and consequent derating are applied, the energy probability curve is lowered for wind speeds above the design value, as shown by the dashed curve in Figure G.1. The area between the two energy curves is the annual energy loss (ΔW).

The cost of annual energy lost due to derating is:

$$CW = u_W \Delta W \quad (\$/\text{y}) \tag{G.1}$$

where u_W ($\$/kWh$) is the cost of electric energy.

The annual cost of the AF is:

$$CF = u_{AF} P_{AF} \frac{i \cdot (1+i)^N}{(1+i)^N - 1} u_{AF} \quad (\$/\text{y}) \tag{G.2}$$

where P_{AF} is the active filter rated power, u_{AF} is the cost of the AF ($\$/\text{k}VA$), N is the number of years (budget life), i is the annual interest.

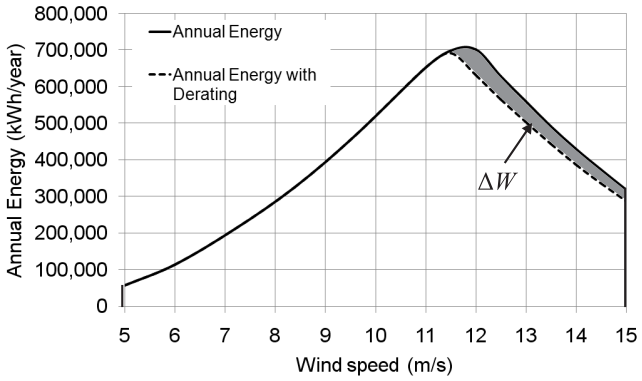

Figure G.1 - Energy distribution for the variable-speed wind turbine described in appendix A. The continuous line is the energy capture distribution at sinusoidal operation, the dotted line is the curve when derating is applied.

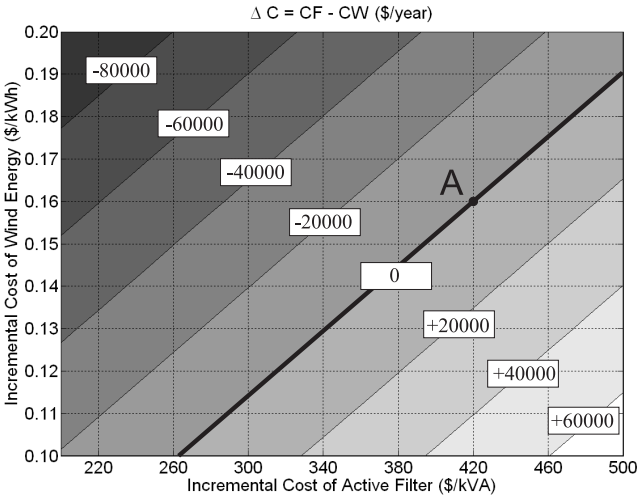

Figure G.2 - The difference between the savings and the loss for each year, when harmonic compensation by means of RSC modulation is assumed; $\mathscr{D}_s = 0.8$, $i = 0.05$ and the wind speed probability function is described with a Weibull distribution with shape parameter $k = 2$ and scale parameter $c = 8$.

The difference between the annual cost of the AF and the cost of annual energy loss is

$$\Delta C = CF - CW \quad (\$/\text{year}) \tag{G.3}$$

If $\Delta C > 0$, the use of the WECS as AF is more economical than investing in a dedicated AF. In Figure G.2, the level curve plot of ΔC is shown as a function of u_W and u_{AF}, assuming i=0.05 and N=20. The preliminary results show that if the condition

$$u_{AF} \geq \frac{8000}{3}\, u_w - 860 \quad (\$/\text{kVA}) \tag{G.4}$$

is met, then $\Delta C > 0$ and the use of the WECS as AF may be considered. A numerical example helps to quantify condition (G.3). The point A in Figure G.2 has $u_{AF,\text{A}} = 420$ \$/kVA and $u_{w,\text{A}} = 0.16$ \$/kWh. If, for the same incremental cost of electric energy ($u_{w,\text{A}} = 0.13$ \$/kWh), u_{AF} is higher than 420 \$/kVA, then the use of WECS is more economical than the installation of an AF; the reverse applies if u_{AF} is lower than 420 \$/kVA.

Although simplified, the analysis presented above allows to identify the mail parameters that affect the economic benefit of the proposed application: the wind characteristic, the cost of AF and of electric energy. The study conducted above results in a first estimate on the economic implications of using a WECS as AF and of consequent derating.

Appendix H

Pulse Width Modulation (PWM)

Pulse Width Modulation (PWM) is a technique used to control the output voltage of a three-phase inverter. The schematic of the three-phase inverter is shown in Figure H.1.

The switches of the inverter (S_1 to S_6) are controlled so that the output voltage follows a sinusoidal waveform.

Figure H.2 shows how the pulses the govern the states of the switches are generated.

The three-phase reference voltages (control signal) are compared with a triangular waveform (modulating signal) at higher frequency (Figure H.2.a).

The ratio between the amplitude of $v_{con,a}$, $v_{con,b}$ and $v_{con,c}$ and v_{tri} is named amplitude modulation:

$$m_a = \frac{\hat{v}_{con}}{\hat{v}_{tri}} \tag{H.1}$$

where

$\hat{V}_{con}$ is the peak value of the control signal

$\hat{V}_{tri}$ is the peak value of the modulating signal

The ratio between the frequency of $v_{con,a}$,$v_{con,b}$ and $v_{con,c}$ and v_{tri} is named frequency

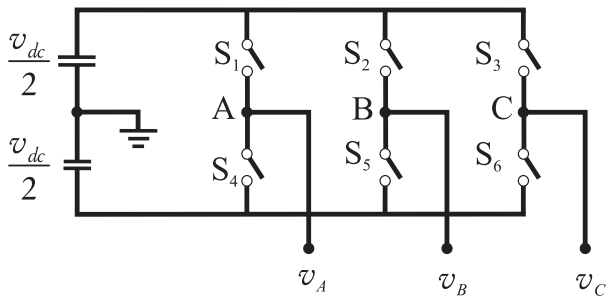

Figure H.1 - Schematic representation of a three-phase inverter: the dc-side is made of two identical capacitors with central tap connected to the ground.

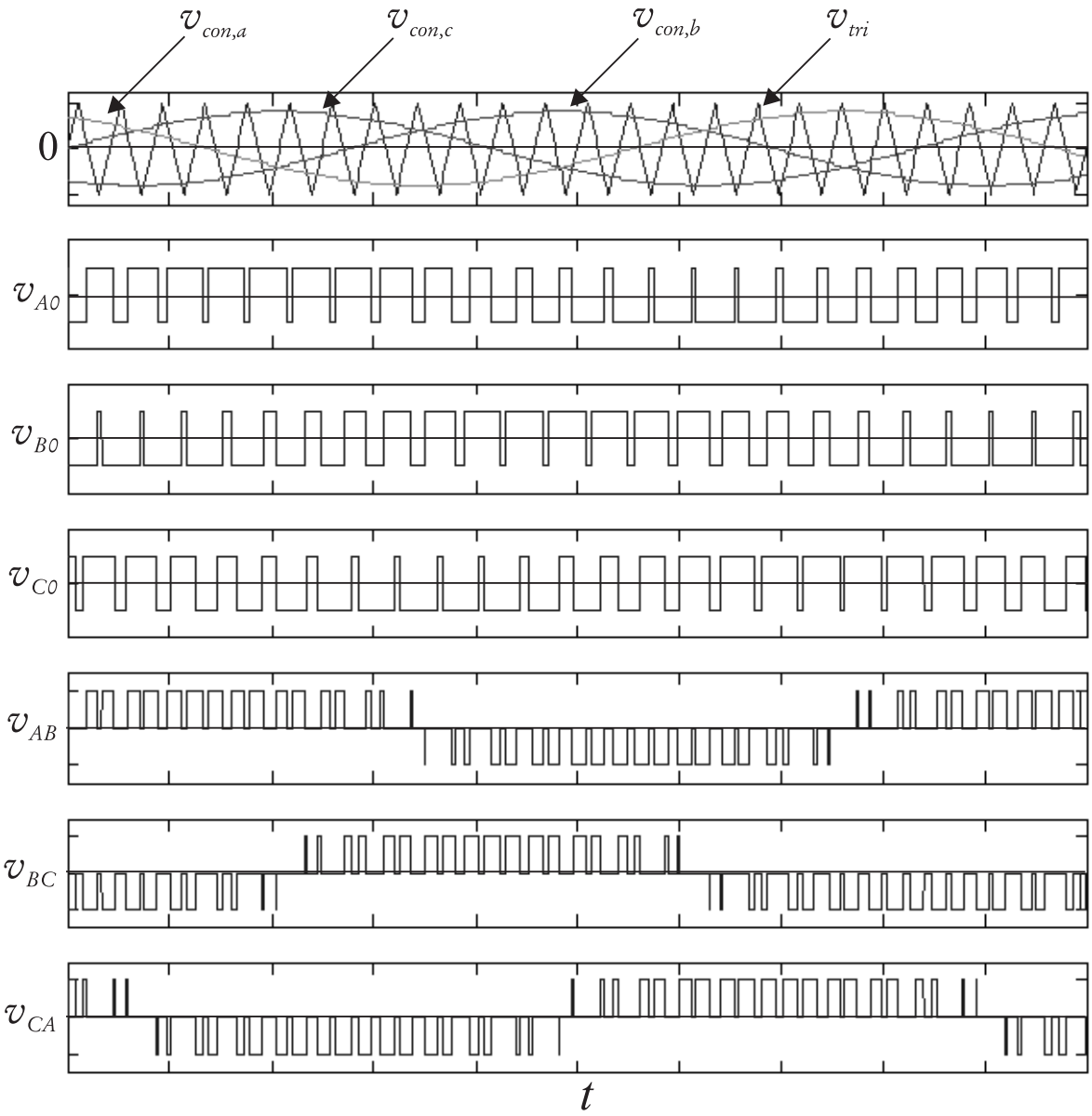

Figure H.2 - Waveforms for the generation of switching signals for PWM modulation [34].

modulation:

$$m_f = \frac{f_{tri}}{f_{con}} \tag{H.2}$$

where

f_{con} is the control signal frequency

f_{tri} is the modulating signal frequency

Figure H.2.b,c,d show the output phase voltages, according to the law:

$$\begin{cases} v_{i0} = v_{dc}/2 & \text{if} \quad v_{con,i} > v_{tri} \\ v_{i0} = 0 & \text{if} \quad v_{con,i} < v_{tri} \\ \text{where} & i = a, b, c \end{cases} \tag{H.3}$$

Figure H.2.e,f,g show the output line to line voltages, obtained as:

$$\begin{cases} v_{ab} = v_{a0} - v_{b0} \\ v_{bc} = v_{b0} - v_{c0} \\ v_{ca} = v_{c0} - v_{a0} \end{cases} \tag{H.4}$$

The following comments apply to the modulation index [34]:

- Figure H.3 shows that if $m_a < 1$, there is a linear relation between the amplitude of the output voltage and the amplitude of the control voltages. This is the reason why in the normal applications $m_a < 1$. In the linear region, the rms line to line output voltage is proportional to the amplitude modulation index m_a and to the dc side voltage v_{dc}:

$$V_{LL,rms} = \frac{m_a}{2\sqrt{2}} v_{dc}, \tag{H.5}$$

- Figure H.4 shows that the spectrum of the output voltage contains harmonics that are multiple of m_f. This is the reason why, in the normal applications, m_f is an integer number with value greater than 20 [189].

.

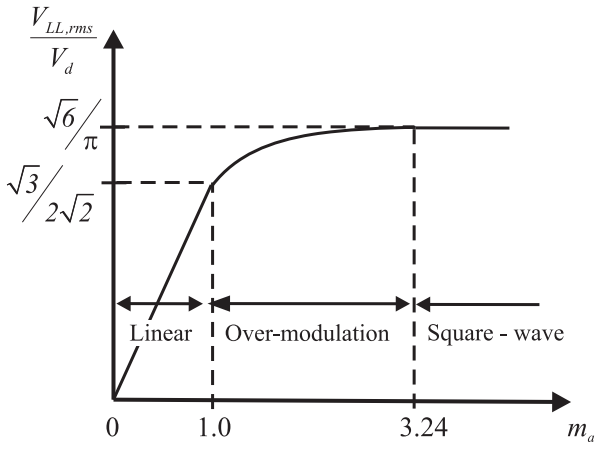

Figure H.3 - Relation between the amplitude of the output voltage and the amplitude modulation index m_a.

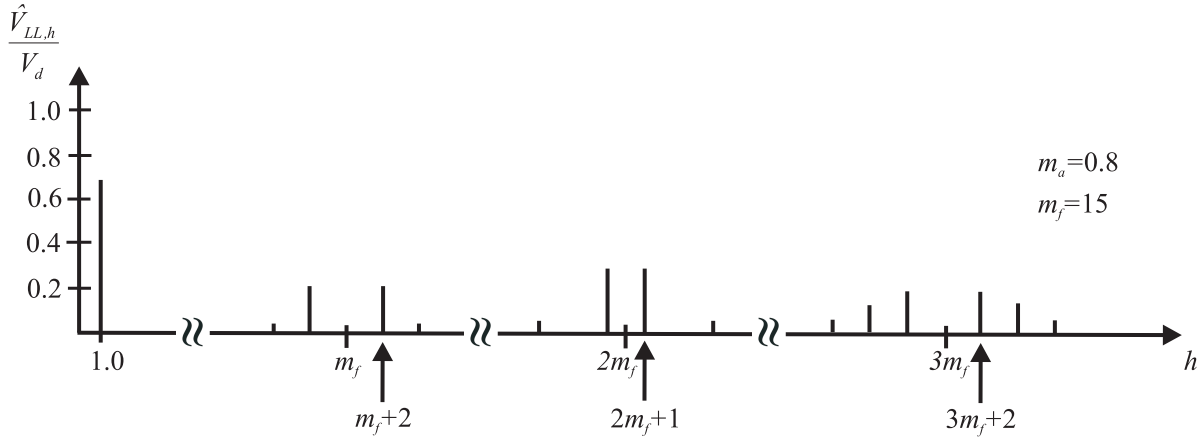

Figure H.4 - Frequency spectrum of the three-phase voltage: the output frequencies are multiples of the switching frequency.